2021 RETROSPECTIVE: STRUCTURAL MATERIALS

EDITED BY: John L. Provis
PUBLISHED IN: Frontiers in Materials

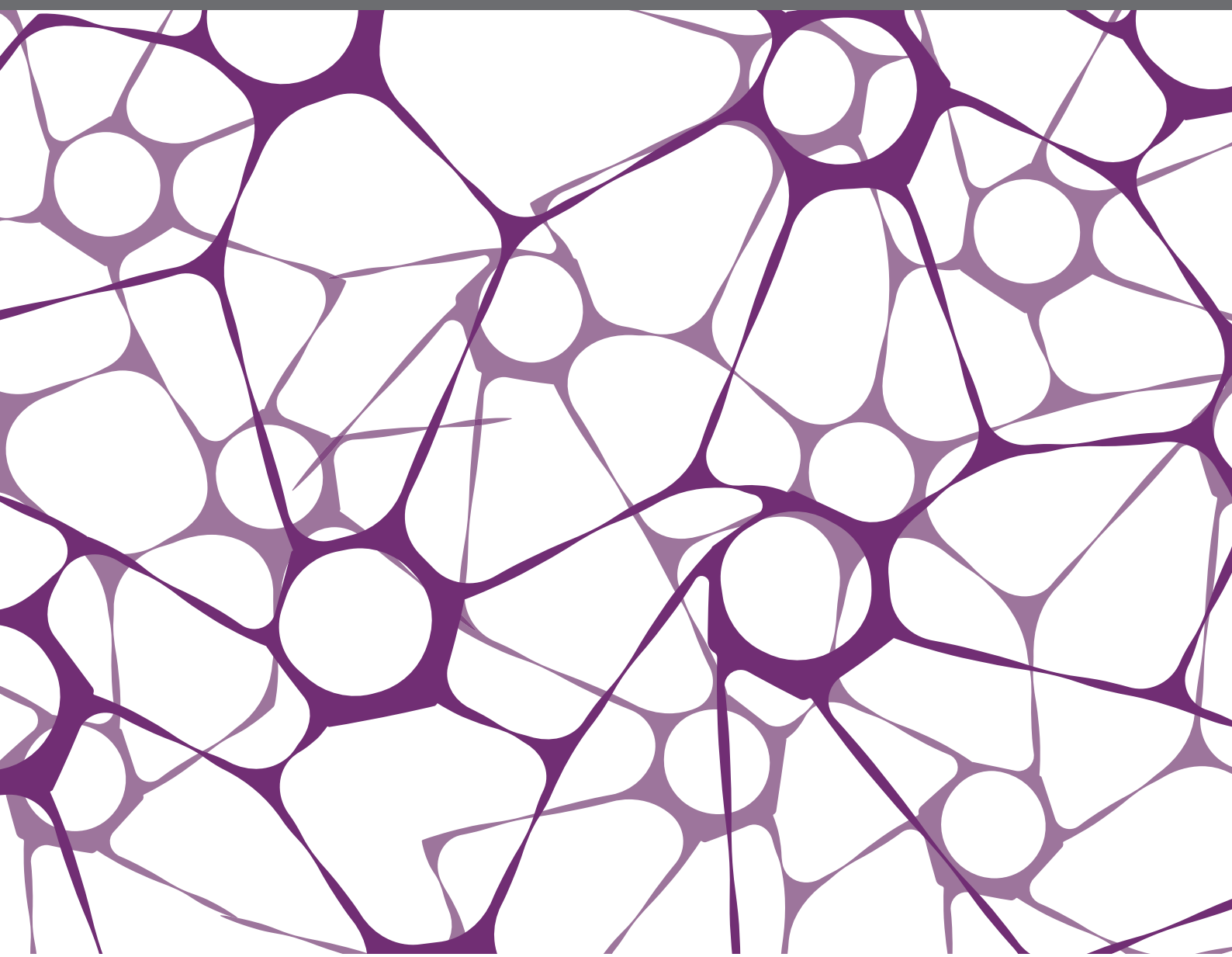

frontiers Research Topics

frontiers

ISSN 1664-8714
ISBN 978-2-83250-049-1
DOI 10.3389/978-2-83250-049-1

About Frontiers

Frontiers is more than just an open-access publisher of scholarly articles: it is a pioneering approach to the world of academia, radically improving the way scholarly research is managed. The grand vision of Frontiers is a world where all people have an equal opportunity to seek, share and generate knowledge. Frontiers provides immediate and permanent online open access to all its publications, but this alone is not enough to realize our grand goals.

Frontiers Journal Series

The Frontiers Journal Series is a multi-tier and interdisciplinary set of open-access, online journals, promising a paradigm shift from the current review, selection and dissemination processes in academic publishing. All Frontiers journals are driven by researchers for researchers; therefore, they constitute a service to the scholarly community. At the same time, the Frontiers Journal Series operates on a revolutionary invention, the tiered publishing system, initially addressing specific communities of scholars, and gradually climbing up to broader public understanding, thus serving the interests of the lay society, too.

Dedication to Quality

Each Frontiers article is a landmark of the highest quality, thanks to genuinely collaborative interactions between authors and review editors, who include some of the world's best academicians. Research must be certified by peers before entering a stream of knowledge that may eventually reach the public - and shape society; therefore, Frontiers only applies the most rigorous and unbiased reviews.
Frontiers revolutionizes research publishing by freely delivering the most outstanding research, evaluated with no bias from both the academic and social point of view. By applying the most advanced information technologies, Frontiers is catapulting scholarly publishing into a new generation.

What are Frontiers Research Topics?

Frontiers Research Topics are very popular trademarks of the Frontiers Journals Series: they are collections of at least ten articles, all centered on a particular subject. With their unique mix of varied contributions from Original Research to Review Articles, Frontiers Research Topics unify the most influential researchers, the latest key findings and historical advances in a hot research area! Find out more on how to host your own Frontiers Research Topic or contribute to one as an author by contacting the Frontiers Editorial Office: frontiersin.org/about/contact

2021 RETROSPECTIVE: STRUCTURAL MATERIALS

Topic Editor:
John L. Provis, The University of Sheffield, United Kingdom

Citation: Provis, J. L., ed. (2022). 2021 Retrospective: Structural Materials. Lausanne: Frontiers Media SA. doi: 10.3389/978-2-83250-049-1

Table of Contents

frontiers in Materials

ORIGINAL RESEARCH
published: 02 February 2021
doi: 10.3389/fmats.2020.622479

Stability Evaluation and Mechanism of Asphalts Modified With Various Rubber Powder Contents

Hengxiao Xue[1]*, *Yuanbo Cao*[1], *Qi Liu*[2], *Hongfei Zhang*[1] and *Mingliang Zhang*[1]

[1]College of Highways, Chang'an University, Xi'an, China, [2]School of Transportation, Southeast University, Nanjing, China

Ground tires are one of the main sources of urban solid waste. Rubber powder-modified asphalt provides an effective method to solve the problem, and it presents good high- and low-temperature performance in sustainable pavement construction. However, the storage properties of rubber powder-modified asphalts prepared from the traditional low-temperature shear mixing method are unstable, which restricts their application. In this study, four test methods (the softening-point test; the dynamic shear rheological test; the Laboratory Asphalt Stability Test; and fluorescence image analysis) and six evaluation indexes (the softening-point difference S_{diff}, the segregation percentage S_p, the segregation index I_{se}, the segregation rate R_s, the degradation rate R_d, and the stability index I_{st}) were employed to analyze the storage abilities of asphalts modified by various activated rubber powder contents. The results show that the storage properties have a positive correlation with rubber powder content in the modified asphalt, and a rubber powder content of 60% is proven to be the optimum mixing amount. The rubber powders can distribute uniformly in the asphalt matrix when mixed below the optimum mixing amount; otherwise a rubber powder agglomeration is formed. The quantitative morphology analysis results are in good agreement with the laboratory test conclusions. The activated rubber powder shows better compatibility compared with ordinary rubber powders and presents a promising method to treat waste ground tires.

Keywords: rubber powder-modified asphalts, stability evaluation, mechanism, sustainable pavement, fluorescence imaging method

OPEN ACCESS

Edited by:
Antonio Caggiano, Darmstadt University of Technology, Germany

Reviewed by:
Juan Xie, Changsha University of Science and Technology, China
Józef Haponiuk, Gdansk University of Technology, Poland
Xiaoming Huang, Southeast University, China

***Correspondence:**
Hengxiao Xue
xhx1570@126.com

Specialty section:
This article was submitted to Structural Materials, a section of the journal Frontiers in Materials.

Received: *29 October 2020*
Accepted: *22 December 2020*
Published: *02 February 2021*

Citation:
Xue H, Cao Y, Liu Q, Zhang H and Zhang M (2021) Stability Evaluation and Mechanism of Asphalts Modified With Various Rubber Powder Contents. Front. Mater. 7:622479. doi: 10.3389/fmats.2020.622479

INTRODUCTION

Waste tires are significant contributors to urban solid waste (Siddika et al., 2019; Luo et al., 2020). In pavement construction, rubber powder-modified asphalt presents good performance in both high- and low-temperature working conditions (Ding et al., 2019), and it provides a sustainable solution to the solid waste problem (Ma et al., 2017; Zhang et al., 2020). However, due to the compatibility problem between rubber powder and asphalt (Li et al., 2019), the storage ability of modified asphalt has drawn much attention in sustainable pavement construction (Guo et al., 2020; Ma et al., 2020). The main factors affecting the storage properties of modified asphalts include the properties of asphalts and rubber powders and the compatibility between them (Yu et al., 2018). Therefore, an effective method to improve the storage stability of rubber powder-modified asphalt is to activate the surface of rubber powder (Liao and Li, 2004; Yu et al., 2018; Li et al., 2019). The light component in asphalt may also affect the distribution properties of rubber powder (Sienkiewicz et al., 2017).

Recently, much attention has been paid to the storage stability of rubber powder-modified asphalt (Bahia and Zhai, 2000). The segregation test provides an evaluation method to assess the storage ability of modified asphalt. The test is easily performed and has low cost (Zhong-Yang et al., 2018). The National Highway Cooperation Research Program (NCHRP) of the United States has developed a new Laboratory Asphalt Stability Test (LAST) to evaluate the stability of modified asphalt based on the segregation test (Bahia and Zhai, 2000). Li Ping developed a Modified Asphalt Stability Test (MAST) on the basis of the LAST (Li, 2005). Yin Jiming evaluated the storage stability of modified asphalt with LH-1 stabilizer utilizing the MAST method and test-tube method (Yin, 2008).

Chemical and physical modifications are the two main methods to improve the stability of rubber powder-modified asphalt (Artamendi et al., 2006; Zhang et al., 2017). The physical method is to diminish the rubber powder particles at high temperature and high-speed shearing condition (Maccarrone, 1991); the compatibility between rubber powder and asphalt can be improved by increasing the specific surface area (Shi, 2011). The chemical method is by activating the surface of rubber powder or adding stabilizer. The activated rubber powder has better surface activity in the asphalt matrix, which makes it easier to disperse during shear mixing (Mu et al., 2020).

Research shows that rubber powder-modified asphalt prepared by the activation of modified rubber powder has lower viscosity and better stability in the same condition compared with ordinary rubber powder (Lu et al., 2014; Ma et al., 2017; Hallmark-Haack et al., 2019). Recently, the terminal blend (TB) method has been widely accepted as a means of modifying asphalts with rubber powder. The high-speed loading treatment was applied on base asphalt after mixing with high-content rubber powder at high temperature (Tan et al., 2020). The TB method ensures that the rubber powders have good distribution properties after fully swelling. The depolymerization level of rubber powder is increased significantly; hence, the storage stability of modified asphalt can be improved (Presti, 2013).

To summarize the previous research achievements, the segregation test method, the LAST method, and the dynamic mechanical method were employed to assess the storage stability of modified asphalts in this study. To further research the storage stability mechanism, fluorescence microscope (FM) technology was used to scan the micro-properties of modified asphalt. The correlation between the laboratory test results and mechanism of storage properties of rubber powder-modified asphalt can be established, which could provide a reference for improving the service ability of sustainable pavements.

TESTS AND METHODS

Materials

The 40-mesh activated rubber powder was pre-swelled with 20% waste oil. The microwave treatment on rubber powder was selected as 2 min because toxic gases were produced after 2 min, and the rubber powders started to burn (Yin et al., 2021). The rubber powders were obtained from the waste meridian tire plant of Tianjin City, and the detailed properties of the rubber powder can be seen in **Table 1**. Filtered motor oil was employed as the waste oil in this study, with a density of 0.89 g/cm^3. To prepare the modified asphalt, the shearing temperature is selected as 230–240°C, the shearing rate is 3,000 r/min, and the shearing time is 5 h. The asphalts used were SK-90# from South Korea, and the properties of the asphalt can be seen in **Table 2**.

Evaluation Methods

Segregation Test

The segregation test (T0661-2011) is the most widely used method to evaluate the storage stability of polymer-modified asphalt. According to the specification of "Standard Test Methods of Bitumen and Bituminous Mixtures for Highway Engineering" (JTG E20-2011, 2011), the testing procedure can be summarized briefly as below:

(1) The asphalt sample is heated at the recommended temperature, and then 50 ± 0.5 g of asphalt is poured into the separation tube.
(2) The segregation tube is conditioned vertically in the oven for 48 ± 1 h at 163 ± 5°C.
(3) After heating and segregation, the separation tube is removed together with the test tube rack and placed into a freezer vertically for cooling for at least 4 h to make the asphalt sample solidify.
(4) The separation tube is cooled in a temperature-controlled box for 4 h until the solidification of asphalt.

TABLE 1 | Properties of waste rubber powder tires.

	Properties	American standard	Chinese standard	Actual value
Physical index	Relative density (g/cm^3)	1.1–1.2	1.1–1.3	1.26
	Moisture content (%)	≤0.75	<1	0.83
	Metal content (%)	<0.1	<0.03	0.02
	Fiber content (%)	--	<1	0.8
Chemical index	Acetone extract (%)	≤25	≤22	10.55
	Ash content (%)	≤8	≤8	2.43
	Carbon black content (%)	20–40	≥28	34.78
	Rubber hydrocarbon content (%)	40–55	≥42	52.24
	Natural rubber content (%)	16–24	≥30	30.56

TABLE 2 | Properties of SK-90# asphalt.

Properties		Specification value	SK-90#
The penetration (25°C, 100 g, 5 s)/0.1 mm		80–100	89.9
Softening point/°C		⩽42	45.5
Ductility (5 cm/min, 10°C)/cm		⩽100	>100
RTFOT (163°C, 85 min)	Loss of quality/%	⩾±0.8	0.07
	Penetration ratio/%	⩽54	70
	Ductility at 10°C/cm	⩽6	9.0

(5) The segregation tube is cut into upper, middle, and lower sections, in preparation for the test.

The segregation test sample can be seen in **Figure 1**, and asphalts modified by various rubber powder content (20%, 25%, 30%, 40%, 50%, 60%, and 70%) were used.

Dynamic Mechanical Method

The dynamic shear rheological (DSR) test is widely accepted in studying the rheological properties of asphalts and has the advantages of easy operation and high testing precision. The evaluation indexes of DSR are complex shear modulus G^* and phase angle δ. Recently, the DSR method was introduced to analyze the storage ability of rubber powder-modified asphalt by comparing the rheological property differences of modified asphalts between upper and lower sections of the segregation tube (Bahia et al., 1998). In this study, the rheological property differences in the upper and lower sections of various asphalts were assessed utilizing the DSR method, and the storage abilities of tested asphalts were analyzed.

Laboratory Asphalt Stability Test (LAST)

The LAST is a part of the National Highway Cooperation Research Program (NCHRP) 9–10 project, and it was developed to study the storage stability of asphalt binders modified by elastomers, plastomers, and solid additives (Polacco et al., 2015). This method involves the use of a small storage cabinet composed of an internal heater, an external heater, an agitator, and a temperature control device, which was designed to simulate the actual storage conditions.

Fluorescence Imaging Method

A fluorescence microscope (FM) was used to scan the target with 420 nm wavelength monochromatic light or 365 nm wavelength ultraviolet and observe distribution properties of targets according to the fluorescence shape.

According to the mechanism of modified asphalt, the rubber powders distribute in the asphalt matrix after shear mixing. The fluorescence reaction occurs on the rubber powder when lighted by various lasers. Asphalts are black and opaque and have no fluorescence reaction. The fluorescence reaction difference between rubber powder and asphalt can be used to present the distribution properties. **Figure 2** shows the FM device and the distribution of rubber powders in modified asphalt.

Evaluation Index

Softening-Point Difference

The softening-point difference between the upper and lower section separation pipe is the most commonly used method in assessing the storage stability of polymer-modified asphalt. Generally, it is considered that the storage stability of modified asphalt can meet the requirement of application if the softening-point difference is less than 2.5°C.

The softening-point measurement was conducted based on the T0606-2011 in "Standard Test Methods of Bitumen and Bituminous Mixtures for Highway Engineering" (JTG E20-2011, 2011), and the softening-point difference can be calculated according to the following equation:

$$S_{\text{diff}} = \left|S_t - S_b\right|, \tag{1}$$

FIGURE 1 | Segregation test.

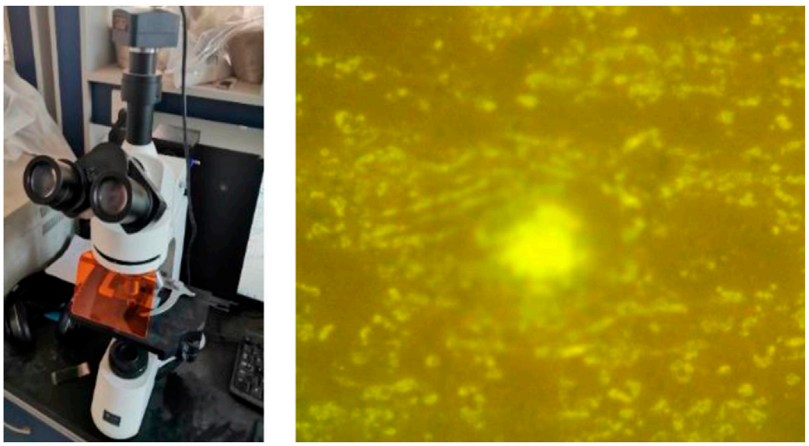

FIGURE 2 | Fluorescence microscope and fluorescence micro-images.

where S_t- is the softening-point value of the upper part of the separation tube, ˚C, and S_b- is the softening-point value of the lower part of the separation tube, ˚C.

Segregation Percentage

The segregation percentage is used to evaluate the storage stability of polymer-modified asphalt. This is a recently developed evaluation method based on the ASTM D 5892-00 (Bahia and Zhai, 2000; ASTM D5892-00, 2001). The complex shear modulus G^* of the upper and lower sections of the segregation test is measured at high temperature utilizing the DSR method (25 mm parallel plate, 54˚C testing temperature, and 10 rad/s frequency), and then the segregation percentage can be calculated according to **Eq. 2**. A smaller segregation percentage means better storage stability.

$$S_p = \frac{\max\left(G_t^*, G_b^*\right) - G_{avg}^*}{G_{avg}^*} \times 100, \tag{2}$$

where G_t^* and G_b^* are the complex shear modulus values of the upper and lower sections of the separation tube and G^*_{avg} is the average value of the complex shear modulus of the upper and lower sections.

Segregation Index

The segregation index (I_{se}) is calculated based on the logarithm of complex shear modulus ratio, which can be used to evaluate the storage stability of polymer-modified asphalt (Li et al., 2019), and I_{se} can be calculated according to **Eq. 3**. It can be concluded that a smaller absolute value of I_{se} means better storage stability of modified asphalt. The complex shear modulus in this research was acquired with the testing parameters of an 8 mm parallel plate, 25˚C testing temperature, and 10 rad/s frequency.

$$I_{se} = \log\left(\frac{G_b^*}{G_t^*}\right). \tag{3}$$

Segregation Rate and Degradation Rate

The complex shear modulus G^* and phase angle δ can be used to calculate the segregation rate and degradation rate at high and medium temperatures. The storage stability of the asphalt binder was evaluated using **Eqs. 4** and **5** to calculate the segregation rates of samples at different times over 48 h, and the same data were also used to calculate degradation ratios according to **Eqs. 6** and **7**. It is considered that segregation or degradation occurs if the index value is out of the range of 0.8–1.2.

$$R_{sHT} = \frac{\left(G^*/\sin\delta\right)_t}{\left(G^*/\sin\delta\right)_b}, \tag{4}$$

$$R_{sIT} = \frac{\left(G^*/\sin\delta\right)_t}{\left(G^*/\sin\delta\right)_b}, \tag{5}$$

$$R_{dHT} = \frac{\left(G^* \cdot \sin\delta\right)_t + \left(G^* \cdot \sin\delta\right)_b}{2\left(G^* \cdot \sin\delta\right)_{in}}, \tag{6}$$

$$R_{dIT} = \frac{\left(G^*/\sin\delta\right)_t + \left(G^*/\sin\delta\right)_b}{2\left(G^*/\sin\delta\right)_{in}}, \tag{7}$$

where $G^*/\sin\delta$ is the rutting factor and $G^*\cdot\sin\delta$ is the fatigue factor. *HT* and *IT* represent the high and medium temperature, respectively; *t* and *b* represent the upper and lower sections of the separation tube, respectively; and *in* represents the initial value.

Stability Index

The fluorescence area of rubber powders in the asphalt matrix was analyzed using Image Pro Plus software. The stability index (I_{st}) can be calculated according to **Eq. 8**. I_{st} can evaluate the storage ability of modified asphalts based on the morphology method.

$$I_{st} = \frac{S_t}{S_b}, \tag{8}$$

where S_t is the fluorescence area of rubber powder in upper section and S_b is the fluorescence area of rubber powder in lower section.

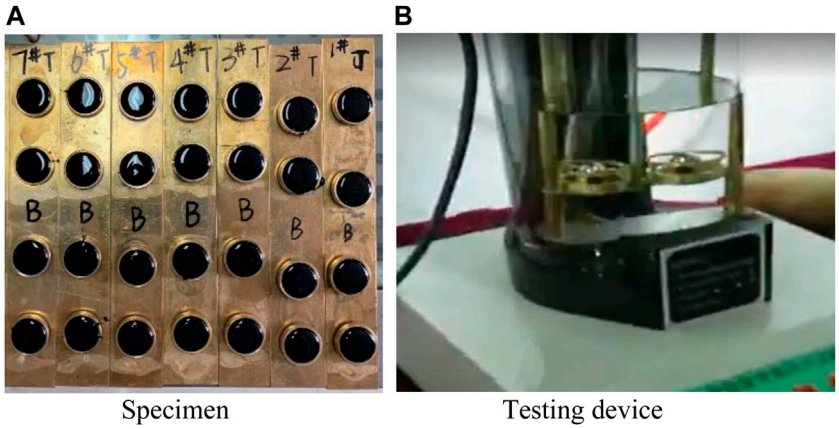

FIGURE 3 | Softening-point test. **(A)** Specimen. **(B)** Testing device.

RESULTS AND ANALYSIS

Softening-Point Difference

To study the softening-point difference between the upper and lower sections of the segregation tube, asphalts with various activated rubber powder contents of 20%, 25%, 30%, 40%, 50%, 60%, and 70% were employed. To further understand the effect of storage time, the softening-point difference asphalts (50%, 60%, and 70%) from the upper and lower sections of the segregation pipe were measured after pouring for 1, 2, 3, 4, and 5 h, and four replicates were tested for each parameter.

Figure 3 shows the poured softening-point specimen and the softening-point measurement, using a softening-point meter, and **Figure 4** presents the developing rules of softening-point difference with various rubber powder contents.

As can be seen in **Figure 4**, with the increase in the activated rubber powder content, the softening-point difference gradually decreases. The softening-point difference reaches its maximum at 20% and its minimum at 70%. It can be concluded that the storage stability of 20% rubber powder-modified asphalt is the worst, and that of 70% is the best.

To research the softening-point difference between the upper and lower sections of the separation pipe, the 50%, 60%, and 70% activated rubber powder content modified asphalts were tested at various shear times (1, 2, 3, 4, and 5 h), and the test results can be seen in **Figure 5**.

In **Figure 5**, the softening-point difference of asphalts modified with different rubber powder contents decreases as shear time increases. The overall softening-point difference curves of 50% rubber powder content asphalt are higher than those of 60%, but they present a similar trend. For the asphalt of 70% rubber powder content, the curve drops rapidly in the first 2 h under the effect of high-speed shear loading and then stays stable in the last 3 h.

Segregation Percentage

The developing rules of segregation percentage value of modified asphalt at the rubber powder content range from 20% to 70%, as shown in **Figure 6**.

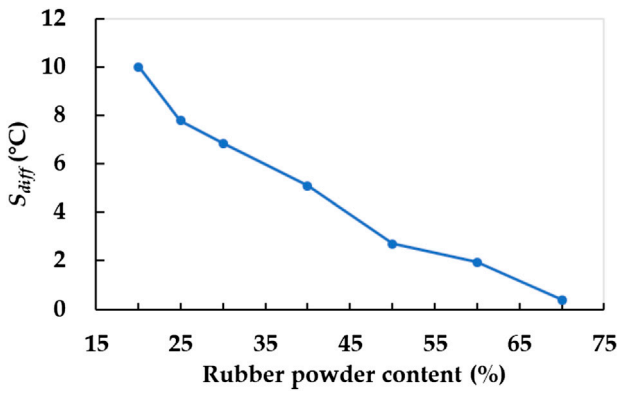

FIGURE 4 | Variation of softening-point difference with content.

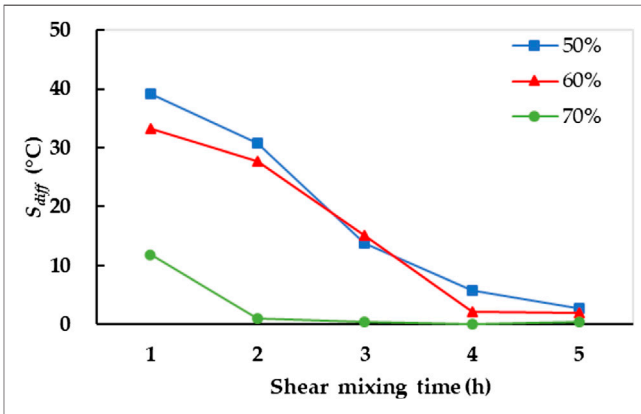

FIGURE 5 | Variation of softening-point difference of asphalt modified by high-content activated rubber powder with shear time.

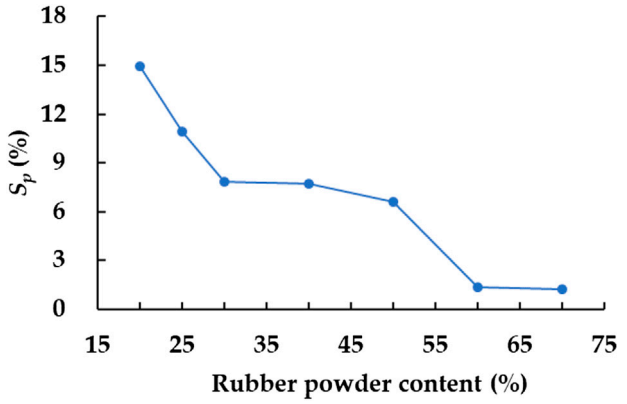

FIGURE 6 | The change of segregation percentage with dosage.

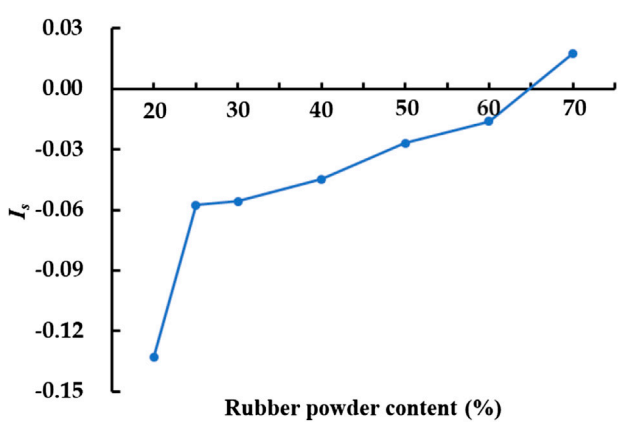

FIGURE 7 | The change of segregation rate at various rubber powder contents.

It can be seen in **Figure 6** that the segregation percentage gradually decreases with the increase in rubber powder content. The segregation percentage value reached its maximum value of 14.92% at the rubber powder content of 20% and reached its minimum value of 1.24% at the rubber powder content value of 70%. Two inflection points can also be seen at the rubber powder contents of 30% and 60% in the curve.

Segregation Index

The developing rules of segregation rate at various rubber powder contents can be seen in **Figure 7**.

It can be seen from **Figure 7** that the segregation index (I_{se}) increases gradually along with the increase in activated rubber powder content. The segregation index of 20% rubber powder-modified asphalt has the biggest absolute value among all. The absolute values of 60% and 70% are the two lowest, and the zero point can be found between 60% and 70% rubber powder content.

Segregation Rate and Degradation Rate

The high-temperature and medium-temperature segregation rates of different modified asphalts with rubber powder content varying from 20% to 70% can be seen in **Figures 8A** and **B**.

Figure 8A illustrates that, with the increase in the rubber powder content, the segregation rate increases from 0.32 to 0.99. According to the specification of the LAST, the standard segregation rate is required to vary from 0.8 to 1.2. It can be seen that asphalts modified by 60% and 70% rubber powder contents are applicable in actual working condition.

In **Figure 8B**, the segregation rates at medium temperature of tested asphalts are all between 0.8 and 1.2, and it can be concluded that the segregation rate index is not sensitive to the variation of rubber powder content in modified asphalt. Combining **Figures 8A** and **8B**, the rubber powder content between 60% and 70% presents the best storage ability in both conditions.

The high-temperature and medium-temperature degradation rates of different modified asphalts with rubber powder content varying from 20% to 70% can be seen in **Figures 9A** and **9B**.

In **Figure 9**, the degradation rates of all the tested modified asphalts in high and medium temperatures are between 0.8 and 1.2, and there is no clear tendency along with the increases of rubber powder content. It can be concluded that the degradation rate index cannot differentiate the difference among asphalts with various rubber powder contents significantly.

Stability Index

A fluorescence microscope (FM) was employed to research the microscopic rubber powder distribution properties of modified asphalts under high-temperature and high-speed shear mixing, and the observation results of 50%, 60%, and 70% activated rubber powder content asphalts can be seen in **Figure 10**.

It can be seen in **Figure 10** that the rubber powder distribution density of various asphalts is relatively large.

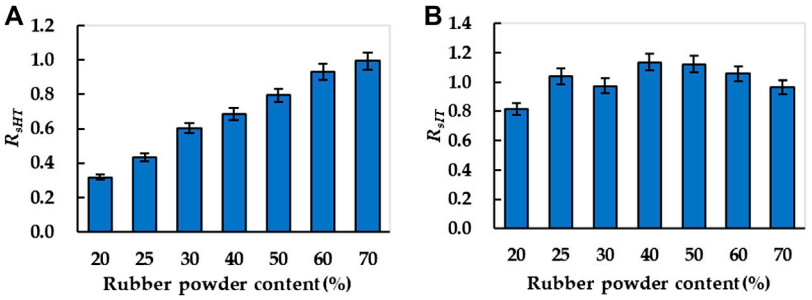

FIGURE 8 | The variation of segregation rate with the amount of the rubber powder. **(A)** High temperature. **(B)** Medium temperature.

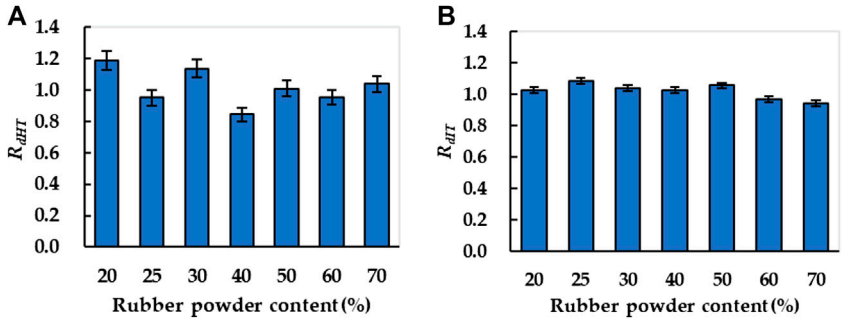

FIGURE 9 | The variation of degradation rate with the amount of rubber powder. **(A)** High temperature. **(B)** Medium temperature.

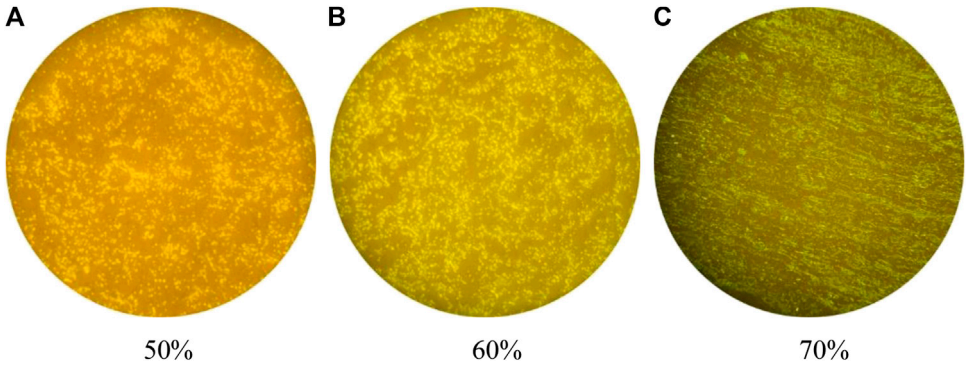

FIGURE 10 | Fluorescence images of asphalt modified by high-content activated rubber powder. **(A)** 50%, **(B)** 60%, and **(C)** 70%.

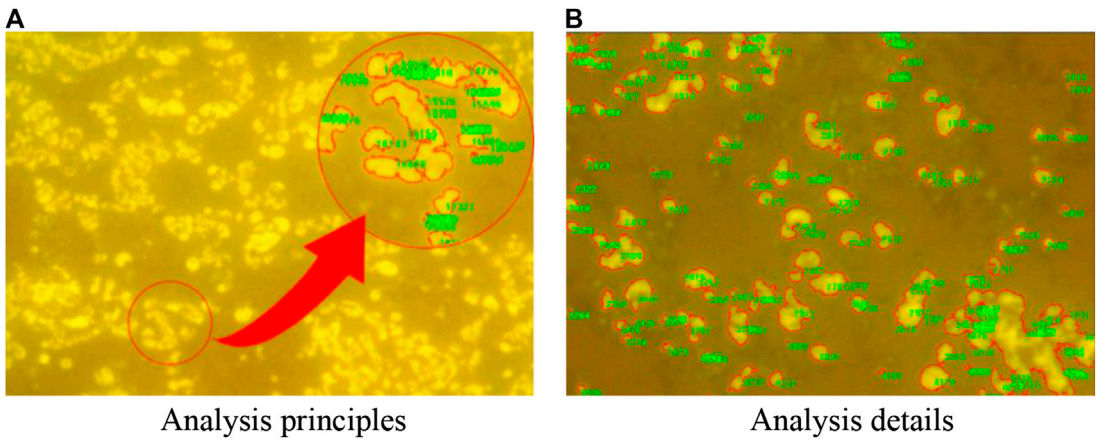

FIGURE 11 | Fluorescence image using IPP software. **(A)** Analysis principles. **(B)** Analysis details.

Among them, the 50% and 60% rubber powder content asphalts have similar morphology, but the rubber powder distribution density of 60% asphalt is higher than that of 50% asphalt. For 70% asphalt, the rubber powder distribution structure in the matrix changes, and small crosslinking phases can be found. It can be concluded that there is not enough light component in asphalt, and the rubber powder cannot be dispersed sufficiently.

To further understand the micro-distribution properties of modified asphalt quantitatively, Image Pro Plus software was utilized to analyze the fluorescent images, as shown in **Figure 11**.

Based on the fluorescence microscopy method and IPP software, the upper and lower section in the separation pipe of 50%, 60%, and 70% rubber powder content asphalts were measured, and the stability indexes were calculated to indicate the storage abilities of

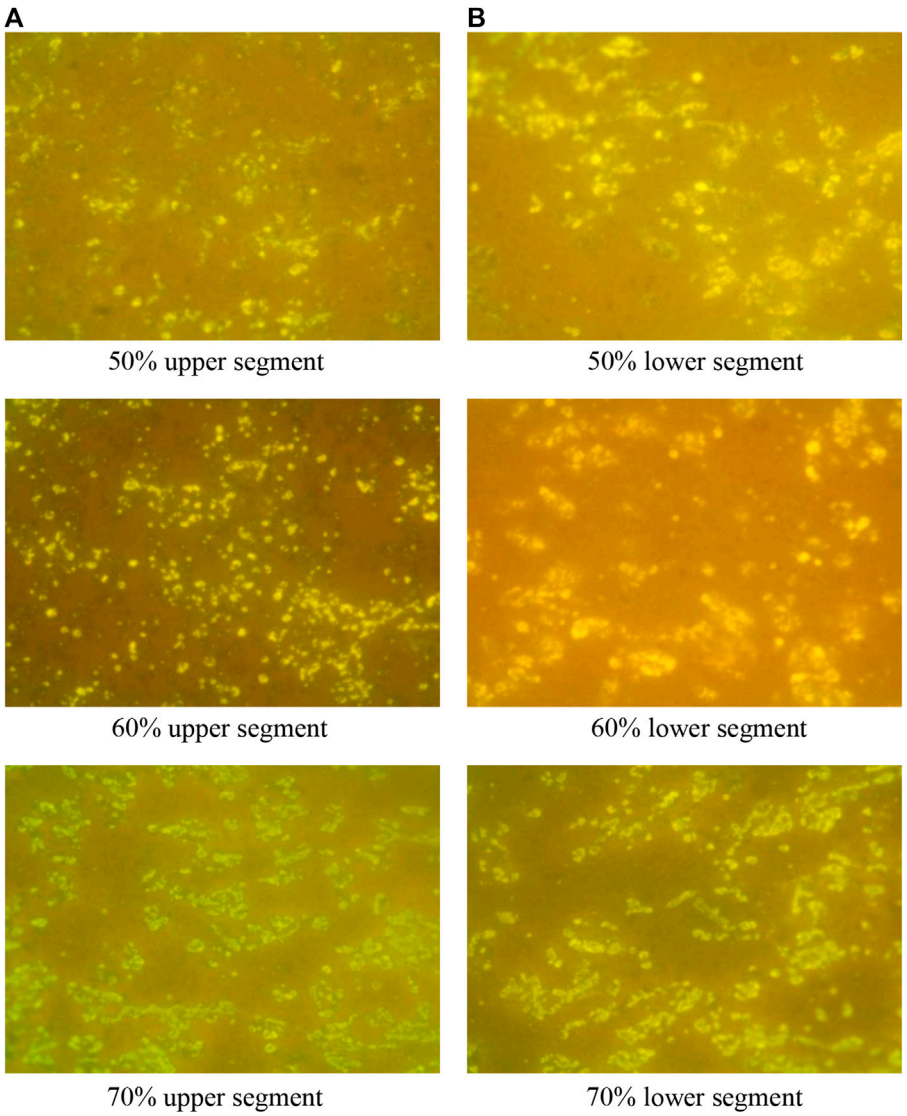

FIGURE 12 | Fluorescence images of various modified asphalts. **(A)** 50% upper segment, 60% upper segment, and 70% upper segment. **(B)** 50% lower segment, 60% lower segment, and 70% lower segment.

TABLE 3 | Stability index of various modified asphalts (I_{st}).

Rubber powder content (%)	Total area *S*		Maximum area *M*		Stability index I_{st}
	Upper section	Lower section	Upper section	Lower section	
50	472,568	500,346	47,116	53,205	0.944
60	533,086	560,972	50,826	55,486	0.950
70	583,957	619,645	52,909	60,914	0.942

various asphalts. The fluorescence images and stability indexes of the three tested asphalts can be seen in **Figure 12** and **Table 3**.

It can be seen from **Figure 12** that the rubber powders agglomerate when their content is as large as 70%, especially in the lower segment. In **Table 3**, the stability index (I_{st}) of the 70% asphalt is the lowest among all, which shows that the rubber powder content of 70% exceeds the optimum proportion of modified asphalt. The rubber powder content of 60% has the highest I_{st} value, and it has the best rubber powder distribution structure. Therefore, it can be concluded that asphalt modified by the 60% rubber powder content presents the best storage ability.

DISCUSSION

Ground tire rubber can be utilized to modify asphalts in sustainable pavement construction and provide an effective method to diminish the effects of urban solid waste. However, the storage problems of asphalts modified by ordinary rubber powder restrict its further application, and the storage ability decreases as the rubber powder content increases for the ordinary modified asphalts.

According to this research, the storage abilities of asphalts modified by activated rubber powder have a positive correlation with rubber powder content, which presents a different tendency than the asphalts modified by ordinary rubber powder. The reasons can be explained by two main factors as follows. Firstly, the low-content activated rubber powder can disperse uniformly in the asphalt matrix but settles easily at the bottom of segregation tube in heated storage conditions. This is due to the low viscosity of asphalt caused by the existence of waste oil. Secondly, the activated rubber powder is prepared based on the combination of microwave treatment and waste oil pre-swelling, which improves its compatibility and distribution properties in the asphalt matrix.

In **Figure 5**, the softening-point differences of 50% and 60% rubber powder content modified asphalts decrease over shear mixing time. It can be concluded that the activated rubber powders depolymerized during shear mixing and formed a stable distribution structure. The 60% rubber powder content asphalt presents better distribution properties compared to that of 50%. For the 70% rubber powder content asphalt, the curve tends to flatten after shear mixing for 2 h, which means that the swelling process is finished in the first 2 h, and there is not enough light component in the asphalt matrix. The rubber powder distributed in asphalt exceeds the optimum dosage.

Based on the segregation percentage test results in **Figure 6**, the best two rubber powder contents are 60% and 70% compared with the five other groups. There is also an inflection point at 60% content, after which the storage ability of modified asphalt has no significant improvement.

As shown in **Figure 7**, the segregation index was employed to indicate segregation level of modified asphalt. Based on **Eq. 3**, asphalt modified by 60% rubber powder content has the lowest absolute value among all, indicating that 60% rubber content has the optimal distribution structure. In addition, the absolute value of various modified asphalts presents an overall decreasing trend with the increase in rubber powder content, which agrees well with the conclusions of the softening-point difference tests.

Based on the segregation rate and degradation rate shown in **Figures 8** and **9**, only the segregation rate at high temperature presents a clear tendency for various rubber powder contents, and 60% and 70% rubber powder contents can meet the requirement of the LAST specification. The difference among modified asphalts cannot be differentiated significantly, and the evaluation results have no clear correlation with the other tests. It can be seen that the evaluation indexes are not applicable in this study.

According to the fluorescence microscope (FM) scanning results in **Figure 10**, the rubber powders in 50% and 60% modified asphalts distribute uniformly, but for 70% modified asphalt, rubber powder agglomeration is formed, and the boundaries of rubber powder are not clear. In addition, the stability indexes (I_{st}) of various modified asphalts were calculated using Image Pro Plus software, and the 60% rubber powder content has the highest I_{st} value among all, which indicates that asphalt modified by 60% rubber powder content has the best storage ability. The FM scanning results are in close accordance with the other test conclusions.

Therefore, the activated rubber powder-modified asphalt provides an effective method to solve the waste ground tire problem, but the storage ability of modified asphalt needs to be researched. In this study, 60% activated rubber powder content is proven to have the best storage properties.

CONCLUSION

(1) The storage properties of modified asphalts have a positive correlation with activated rubber powder content. The 60% rubber powder content is proven to be the optimum mixing amount, and more rubber powder cannot improve the storage ability of asphalt significantly. The modified asphalts are in good homogenization condition after shear mixing for 5 h.
(2) The evaluation results of softening-point difference, segregation percentage, and segregation index are all in good agreement with each other, but the segregation rate and degradation rate cannot differentiate the storage ability differences among various modified asphalts significantly.
(3) The rubber powders can distribute uniformly in the asphalt matrix when their contents are below 60%. For the content of 70%, rubber powder agglomeration is formed, and the boundaries of rubber powder are not clear. Based on the quantitative morphology analysis, asphalts modified by 60% rubber powder content have the largest stability index, which indicates their superior storage ability. The FM analysis results are in accordance with the conclusions of the laboratory test.
(4) The activated rubber powders have better compatibility with asphalts and present better storage properties in asphalt compared to the ordinary rubber powder asphalts. This provides a promising method to solve the waste ground tire problems.

DATA AVAILABILITY STATEMENT

The original contributions presented in the study are included in the article/Supplementary Material, further inquiries can be directed to the corresponding author.

AUTHOR CONTRIBUTIONS

The authors contributed to the present study as follows: HX and YC: conceptualization; HX and QL: methodology; YC, HZ, and MZ: validation; HX: formal analysis, writing—original draft

preparation, and funding acquisition; YC: investigation and writing—review and editing; QL: resources, software, and visualization; HZ and MZ: data curation; HZ: supervision; MZ: project administration. All authors have read and agreed to the published version of the manuscript.

FUNDING

This research was funded by the National Natural Science Foundation of China (51908055) and Fundamental Research Funds for the Central Universities (CN) (300102219103).

REFERENCES

Artamendi, I., Khalid, H. A., and Page, G. C. (2006). Diffusion kinetics of bitumen into waste tyre rubber. *Am. Assoc. Phys. Teach. J.* 20 (3), 22–33.

ASTM D5892-00 (2001). *Standard specification for type IV polymer-modified asphalt cement for use in pavement construction*. West Conshohocken, PA: ASTM International.

Bahia, H. U., and Zhai, H. (2000). Storage stability of modified binders using the newly developed LAST procedure. *J. Road Mat. Pavement Des.* l (1–2), 53–73. doi:10.1080/14680629.2000.9689884

Bahia, H. U., Zhai, H., and Rangel, A. (1998). Evaluation of stability, nature of modifier, and short-term aging of modified binders using new tests: LAST, PAT, and modified RTFO. *Transport. Res. Rec.* 1638, 64–71. doi:10.3141/1638-08

Ding, X., Chen, L., Ma, T., Ma, H., Gu, L., Chen, T., et al. (2019). Laboratory investigation of the recycled asphalt concrete with stable crumb rubber asphalt binder. *Construct. Build. Mater.* 203, 552–557. doi:10.1016/j.conbuildmat.2019.01.114

Guo, F., Zhang, J., Pei, J., Ma, W., Hu, Z., and Guanand, Y. (2020). Evaluation of the compatibility between rubber and asphalt based on molecular dynamics simulation. *Front. Struct. Civ. Eng.* 14 (2), 435–445. doi:10.1007/s11709-019-0603-x

Hallmark-Haack, B. L., Hernandez, N. B., Williams, R. C., and Cochran, E. W. (2019). Ground tire rubber modification for improved asphalt storage stability. *Energy Fuels* 33 (4), 2659–2664. doi:10.1021/acs.energyfuels.8b03558

JTG E20-2011. (2011). *Standard test methods of bitumen and bituminous mixtures for highway engineering*, Beijing, China: Ministry of Transport.

Li, H., Dong, B., Zhao, D., Guo, P., and Zhang, J. (2019). Physical, rheological and stability properties of desulfurized rubber asphalt and crumb rubber asphalt. *Arabian J. Sci. Eng.* 44 (5), 5043–5056. doi:10.1007/s13369-018-3684-2

Li, P. (2005). Study on aging performance and storage stability of SBS modified asphalt. Master's thesis, China: Chang'an University.

Liao, M., and Li, X. (2004). Stability and influencing factors of rubber powder modified asphalt. *J. Petroleum Chem. Eng. Univ.* 17 (4), 38–41.

Lu, Q., Huang, W., and Cai, C. (2014). Properties and application prospect of terminal blending rubber asphalt. *J. Chongqing Jiaotong Univ.* 33 (04), 51–55. doi:10.3969/j.issn.1674-0696.2014.04.11

Luo, P., Sun, Y., Wang, S., Wang, S., Lyu, J., Zhou, M., et al. (2020). Historical assessment and future sustainability challenges of Egyptian water resources management. *J. Clean. Prod.* 263, 121154. doi:10.1016/j.jclepro.2020.121154

Ma, J., Sun, G., Sun, D., Zhang, Y., Falchetto, A. C., Lu, T., et al. (2020). Rubber asphalt modified with waste cooking oil residue: optimized preparation, rheological property, storage stability and aging characteristic. *Construct. Build. Mater.* 258, 120372. doi:10.1016/j.conbuildmat.2020.120372

Ma, T., Wang, H., He, L., Zhao, Y., Huang, X., Chen, J., et al. (2017). Property characterization of asphalt binders and mixtures modified by different crumb rubbers. *J. Mater. Civ. Eng.* 29 (7), 04017036. doi:10.1061/(ASCE)MT.1943-5533.0001890

Maccarrone, S. (1991). Properties of polymer modified binders and relationships to mix and pavement performance. *Asph. Pav. Technol.* 60 (2), 2–10.

Mu, D., Luo, P., Lyu, J., Zhou, M., Huo, A., Duan, W., et al. (2020). Impact of temporal rainfall patterns on flash floods in Hue City, Vietnam. *J. Flood Risk Manag.* 2020, e12668. doi:10.1111/jfr3.12668

Polacco, G., Filippi, S., Merusi, F., and Stastna, G. (2015). A review of the fundamentals of polymer-modified asphalts: asphalt/polymer interactions and principles of compatibility. *Adv. Colloid Interface Sci.* 224, 72–112. doi:10.1016/j.cis.2015.07.010

Presti, D. L. (2013). Recycled tyre rubber modified bitumens for road asphalt mixtures: a literature review. *Construct. Build. Mater.* 49 (6), 863–881. doi:10.1016/j.conbuildmat.2013.09.007

Shi, J. (2011). *Study on activating modification of ground tyre rubber powder*. Qingdao, China: Qingdao University of Science and Technology.

Siddika, A., Al Mamun, M. A., Alyousef, R., Mugahed Amran, Y. H., Aslani, F., and Alabduljabbar, H. (2019). Properties and utilizations of waste tire rubber in concrete: a review. *Construct. Build. Mater.* 224, 711–731. doi:10.1016/j.conbuildmat.2019.07.108

Sienkiewicz, M., Borzędowska-Labuda, K., Wojtkiewicz, A., and Janik, H. (2017). Development of methods improving storage stability of bitumen modified with ground tire rubber: a review. *Fuel Process. Technol.* 159, 272–279. doi:10.1016/j.fuproc.2017.01.049

Tan, X., Zhang, J., Guo, D., Sun, G., Zhou, Y., and Zhang, W. (2020). Preparation and repeated repairability evaluation of sunflower oil-type microencapsulated filling materials. *J. Nanosci. Nanotechnol.* 20 (3), 1554–1566. doi:10.1166/jnn.2020.17338

Yin, J. (2008). *Reasearch on compatibility performance and anti-aged performance of activated scrap rubber powder modified asphalt*. Yangzhou, China: Yangzhou University.

Yin, L., Yang, X., Shen, A., Wu, H., Lyu, Z., and Li, B. (2021). Mechanical properties and reaction mechanism of microwave-activated crumb rubber-modified asphalt before and after thermal aging. *Construct. Build. Mater.* 267, 120773. doi:10.1016/j.conbuildmat.2020.120773

Yu, J., Ren, Z., Yu, H., Wang, D., Svetlana, S., Korolev, E., et al. (2018). Modification of asphalt rubber with nanoclay towards enhanced storage stability. *Materials* 11 (11), 2093. doi:10.3390/ma11112093

Zhang, C., Yang, F., Li, Q., and Yu, Y. (2017). Research progress in storage stability of rubber powder modified asphalt. *Synthetic Rubber Industry* 40 (05), 409–412.

Zhang, Y., Luo, P., Zhao, S., Kang, S., Wang, P., Zhou, M., et al. (2020). Control and remediation methods for eutrophic lakes in the past 30 years. *Water Sci. Technol.* 81 (6), 1099–1113. doi:10.2166/wst.2020.218

Zhong-Yang, G., Zhi-Yang, X. U., and Ju-Nan, S. (2018). Influence of different development time on rheological property of rubber powder modified asphalt. *Northern Commun.* 12, 51–54.

Conflict of Interest: The authors declare that the research was conducted in the absence of any commercial or financial relationships that could be construed as a potential conflict of interest.

The reviewer XH declared a shared affiliation with one of the authors, QL, to the handling editor at time of review.

frontiers in Materials

ORIGINAL RESEARCH
published: 16 February 2021
doi: 10.3389/fmats.2020.580938

Effects of Brazing Technology on Hermeticity of Alumina Ceramic-Metal Joint Used in Nuclear Power Plants

Nengmei Deng[1], *Jun Zhao*[2]*, *Lilin Yang*[2] *and Zhiqin Zheng*[3,4,5,6]*

[1]City College, Southwest University of Science and Technology, Mianyang, China, [2]Sichuan College of Architecture and Technology, Deyang, China, [3]Nuclear Wastes and Environmental Safety Laboratory, Southwest University of Science and Technology, Mianyang, China, [4]Sichuan Civil-military Integration Institute, Southwest University of Science and Technology, Mianyang, China, [5]School of Life Science and Engineering, Southwest University of Science and Technology, Mianyang, China, [6]School of Environmental and Resources, Southwest University of Science and Technology, Mianyang, China

Taking the brazing mechanism of alumina ceramics and kovar alloys as the main research object, based on the molybdenum–manganese metallization method, the influence of the direct and indirect brazing processes on the morphology of the final connected layer is explored. Combined with SEM, EDS, the microscopic morphology, and hermeticity affecting the final ceramic–metal composite component is discussed. Finally, through the indirect brazing process, various ceramic–metal composite joints with good airtightness satisfying the requirements were prepared.

Keywords: layers, kovar, alumina ceramics, brazing, molybdenum-manganese layers

OPEN ACCESS

Edited by:
Antonio Caggiano, Darmstadt University of Technology, Germany

Reviewed by:
Songbai Xue, Nanjing University of Aeronautics and Astronautics, China
Junlei Qi, Harbin Institute of Technology, China

***Correspondence:**
Jun Zhao
17683146919@163.com
Zhiqin Zheng
ddblyy@yeah.net Jun Zhao

Specialty section:
This article was submitted to Structural Materials, a section of the journal Frontiers in Materials

Received: *02 August 2020*
Accepted: *07 October 2020*
Published: *16 February 2021*

Citation:
Deng N, Zhao J, Yang L and Zheng Z (2021) Effects of Brazing Technology on Hermeticity of Alumina Ceramic-Metal Joint Used in Nuclear Power Plants. Front. Mater. 7:580938. doi: 10.3389/fmats.2020.580938

INTRODUCTION

With the depletion of conventional energy, nuclear energy has become an important energy source, and nuclear power has also become an important part of the power industry. Climate change is becoming more pessimistic, and nuclear power is a clean energy. Improving the nuclear power industry is an important approach for world energy development. It meets the growing energy needs of industrial and agricultural production and ensures social stability and harmony (Nehrenheim, 2018; Ul'yanin et al., 2018; ZohuriB, 2019).

However, in the process of nuclear power development, many key technologies, including sealing and connecting technology between ceramics and metals, still need to be developed. Nowadays, electrical penetration is mainly made of polymer as a sealing material, but the polymer has poor high-temperature and radiation resistance, low air tightness, and a short working life. Since the late 1930s, the process of joining ceramics with metals or other materials has steadily advanced. Similar to the connection process between other materials, the connection process between ceramics and other materials is initially more of an art than a science, and the development of proprietary properties in this field has exacerbated this situation. After World War II, Pulfrich (Telefunken) and Vatter (Siemens and Halske, A.G.) achieved the metallization of ceramic to produce a surface that can be wetted by the brazing alloy in subsequent joining operations. Also, a large number of patents on metallization and joining processes were issued to Pulfrich, Vatter, or the company that employed them. Some of these patents are most prominently listed in reference (Clarke et al., 1965).

Subsequently, the sealing and connection technology between ceramics and metals has become more and more important. Due to the use of ceramics as a structural material has broadened its scope of application for the future. For example, when the first space station was established in outer space, the ceramic and metal connectors played a key role in the construction and operation of the first

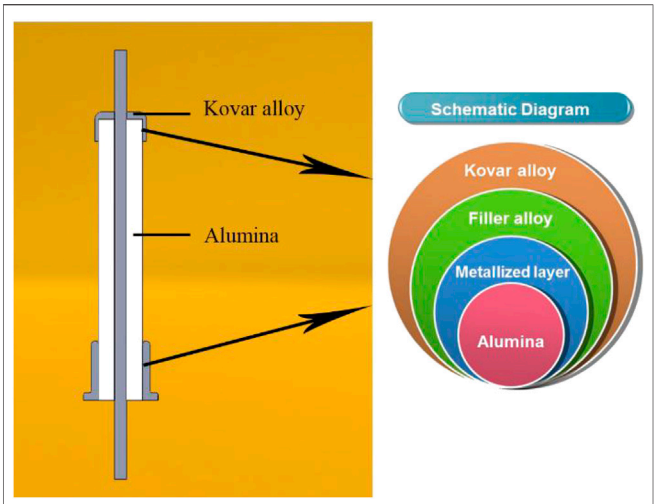

FIGURE 1 | The structure diagram of seal tightness test assembly.

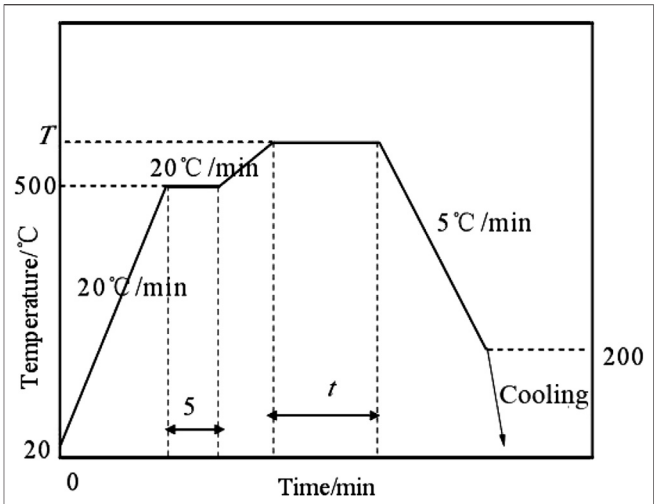

FIGURE 2 | The technology curve of brazing experiments with Ag-Cu-Ti solder.

space station. Nuclear and solar energy equipment have been used to provide energy. Ceramic and metal connectors have been used in these devices to convert nuclear and solar energy into electricity. Likewise, a ceramic coating can be used to provide the required firing frequency to control and maintain the proper temperature level inside the space station structure. The performance of spacecraft today is often dependent on the strength provided by ceramic–metal joints, corrosion resistance, and the ability to protect from high temperatures. The main methods to realize permanent sealing between metal parts and ceramic components are hot pressing connection (Berndt et al., 1985), gradient powder connection (Pattee et al., 1968; Giraldez and Horner, 1994), air pressure connection, active metal brazing (Erdemir et al., 2011; Walker et al., 2011), electron beam welding (Solfest and Strangman, 1989), glass solder (Sandhage et al., 1996), ceramic brazing (Nascimento et al., 2003), *in situ* ceramic sintering (Yoshimura and Suchanek, 1997), and *in situ* glass crystallization (Jain, 2004).

In this work, the connection between alumina ceramic and Kovar alloy is achieved by active brazing. The main research contents are as follows: Vacuum brazing of alumina ceramics and Kovar alloys was carried out using commercial Ag-Cu-Ti brazing filler metal. The effect of interface structure and process parameters on interface morphology was further analyzed, and the sealing mechanism of interface formation was clarified. The airtightness of the alumina ceramic and the Kovar alloy sealing joint is tested, the influencing factors are analyzed, and the optimum process conditions are preferred. By comparing the presence or absence of a molybdenum–manganese metallization layer, the alumina ceramic and Kovar alloy were sealed to explore the effect of the molybdenum–manganese metallization layer on the sealing effect, explore effective sealing, reduce the defective rate, and save production costs (Tomlinson, 1986; Aita, 1992; Mulpuri and Sarin, 1996; Choy, 2003; Li et al., 2008; Fernie et al., 2009).

EXPERIMENTS

Experimental Process

A. Alumina ceramics do not have a molybdenum–manganese metallization layer during the direct brazing process. The brazing material is a silver–copper–titanium solder paste:

First, separately clean 95% alumina ceramic and Kovar.

Second, for parts assembly, first clean the ceramic tube and Kovar in an ultrasonic cleaning machine for 30 min and then soak in the cleaning solution at 70–80°C for 10 min. Then the ceramic tube and Kovar were washed with distilled water 3–5 times and then washed with absolute ethanol. Finally, the cleaned ceramic and Kovar alloy were dried in an oven at 120°C; then, the silver copper wire was cleaned with an alcohol swab, wound in a circle with clean tweezers, and then fixed on the weld. Kovar was placed on ceramic tiles coated with silver–copper solder and was ready for sintering after being fixed and placed in a graphite jig.

Third, in the ceramic–metal brazing process, the metallized alumina ceramic tube prepared in step 2 is assembled with nickel-plated Kovar alloy and silver–copper solder and then placed in a dedicated graphite mold. Then the assembled sample is brazed and sealed at a temperature of 10^{-3}–10^{-4} Pa and 750–900°C for 2–5 min.

Fourth, in the performance test, the insulation and airtightness of the resulting seals were examined separately.

B. For the indirect brazing process route, the selected metallized alumina ceramic and Kovar alloy are brazed and sealed. The selected brazing material is silver–copper brazing wire. The rest of the specific steps are similar to the A process (Véchembre and Fox, 2001; Ionkin et al., 2011).

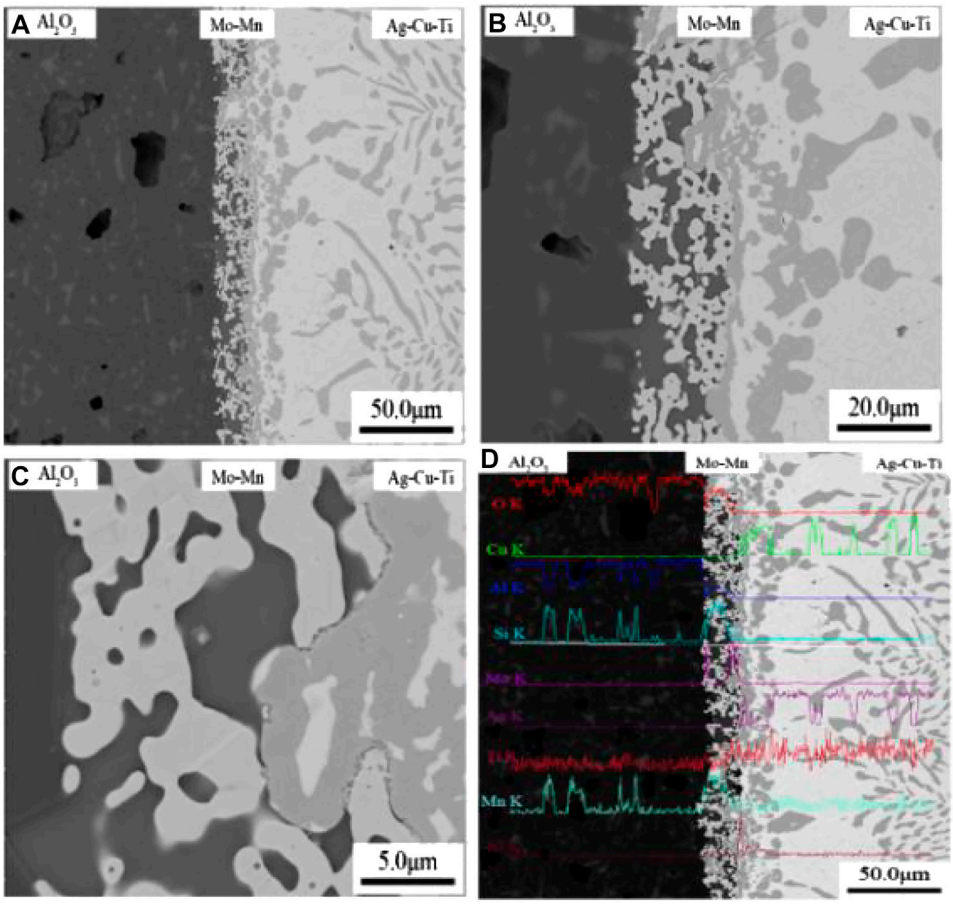

FIGURE 3 | (**A**–**D**) The interface morphologies of alumina ceramic/solder (780°C/2 min).

Brazing Procedure

The brazing experiment is carried out in a vacuum brazing furnace. The device is mainly composed of vacuum, heating, digital display, recording, and control systems. It can provide an ultimate vacuum of 7×10^{-4} Pa and a maximum heating of 1,600°C. These performance parameters are sufficient to meet the experimental requirements of this topic.

Before the experiment, the surface oxide film of Kovar was removed with 400#, 800#, and 1000# sandpaper and cleaned with deionized water and acetone, respectively. The alumina ceramic surface was cleaned with ethanol and acetone, respectively. Assemble the process airtight specimens as shown in **Figure 1**. The diameter and wall thickness of the alumina tube was 2 and 0.1 mm, and the size of the Kovar alloy was 3 mm.

The brazing process curve used is shown in **Figure 2**, where *t* is the holding time. Considering the ceramic part and the Kovar alloy member easily generate large residual stress in the joint during sealing, the ceramic framework is also very sensitive to stress concentration, so a smaller cooling rate is used to reduce the residual stress in the joint.

RESULTS

Effects of Indirect Brazing on Interface Morphology of Joints

Interface Morphology Analysis of Alumina Ceramics/Molybdenum–Manganese Metallization Layer/Solder Layer

Selecting commercial silver–copper–titanium wire and alumina ceramics with a molybdenum–manganese layer (nickel-plated) as experimental materials, the aluminum oxide ceramic/molybdenum–manganese metallization layer was prepared by a sealing process with a sealing temperature of 780°C and a holding time of 2 min (Huh et al., 2011).

Figure 3 is an SEM image of the interface morphology of the alumina ceramic/molybdenum manganese layer (nickel plated)/binder. From **Figure 3A**, it can be seen that there is a significant molybdenum–manganese metallization layer between the solder and the alumina ceramic. **Figure 3B** indicates that the thickness of the molybdenum–manganese layer is about 20 microns. From **Figure 3C**, we can see that the wettability between the molybdenum–manganese metallization layer and the solder is

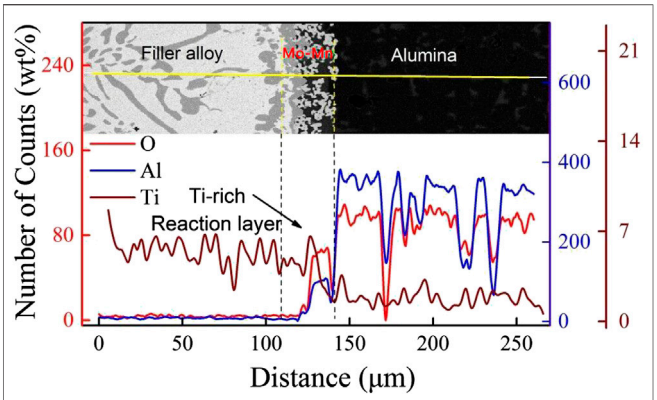

FIGURE 4 | The element distribution of O-Al-Ti on the interface microstructure (780°C/2 min).

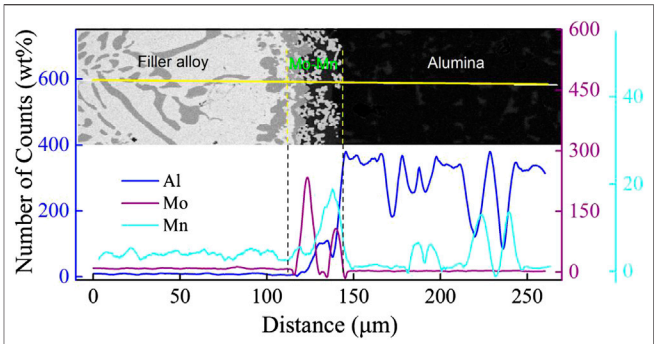

FIGURE 5 | The element distribution of Al-Mo-Mn on interface microstructure (780°C/2 min).

better. The dark and irregular long bands in the solder layer are silver–copper eutectic structures. **Figure 3D** shows the distribution of elements enriched at the interface layer. In order to further clarify the product composition at the interface, the distribution of some elements was selected (Khanna, 2011).

Figure 4 presents that, in the position where the active titanium element is enriched in the molybdenum–manganese metallization layer, other elements begin to enrich at corresponding positions, and it can be seen that the titanium element is very active and has a wide distribution range.

From **Figure 5**, it can be seen that the molybdenum–manganese metallurgy layer has started to migrate into the interior of the alumina ceramics, and a complex reaction has occurred with other glass-phase materials in the alumina. Based on the above analysis, it is further proven that the $MnO{\cdot}Al_2O_3$ spinel produced by the reaction of manganese oxide and aluminum oxide in the molybdenum–manganese layer contributes to sealing, and other manganese oxides also react with silica and other oxides in alumina ceramics. $MnO{\cdot}SiO_2$ and other materials are also helpful for sealing (Chien et al., 2008).

Analysis of Interface Morphology of Alumina Ceramics/Solder Layer/Kovar Alloy Layer

Figure 6 shows the SEM photos and elemental distribution profiles of the interface morphology of alumina ceramic/brazing/cobalt alloys. As shown in **Figure 6C**, it can be clearly observed that the solder and kovar layers have obvious reaction intermediates. The irregular dark banded product in the solder layer is a silver–copper eutectic structure. To further investigate the reactions occurring at the interface, a representative element is selected to analyze the complex reactions at the interface. As shown in **Figure 7**, there is no significant migration of aluminum, and the active element, titanium, is relatively evenly distributed throughout the interfacial structure with a wide distribution depth. At the same time as shown in **Figure 8**, a complex chemical reaction occurs between the elements in the solder layer and the elements in the Kovar alloy. Based on the analysis of their relative contents in the energy spectrum, it can be speculated that they are in the interface between the two. The $TiFe_2$, $TiNi_3$ intermetallic layer was formed (Vinod, 2013).

The Effect of the Direct Brazing Process on Interface Microstructure

The commercial silver–titanium–titanium solder paste and nonmetallized alumina ceramics were selected as the experimental materials. The interface morphology of alumina ceramic/solder layer/Kovar alloy layer was prepared at a sealing temperature of 900°C and a holding time of 2 min.

Figure 9 shows the alumina ceramic/braze/Kovar alloy interface topography. As can be seen from the figure, there are significant microcracks in the solder layer, the wettability at the ceramic interface is poor, the wetting effect with the kovar alloy layer is also not good, and no obvious reaction interface layer is observed. At the same time, the solder layer itself fails to form a dense connection layer, which directly leads to a lower sealing performance of the sealing joint and a greater leakage rate.

Figure 10 shows the results of the energy spectrum analysis of the element at the interface of the joint after direct brazing process conditions. From the figure, it can be seen that there is no change in the oxygen and aluminum elements at the location where the active element titanium is enriched, indicating that the two elements do not react with the active element. In addition, the active elements are mainly concentrated on the solder layer and cannot fully migrate inside the Kovar alloy layer and the alumina ceramics. This shows that, under the direct soldering process conditions, the solder paste of this type fails to fully match the ceramic and Kovar alloy interface. Wet and chemical reactions occur at the interface. At the same time, combined with the results of the elemental distribution shown in **Figure 11**, in the enriched position of the titanium element, the three main constituent elements in the Kovar alloy layer undergo a complex chemical reaction of iron, cobalt, nickel, and titanium elements and are enriched in the titanium element. Synchronous enrichment occurs in the location. It is further proved that the wettability of the solder layer and Kovar alloy is significantly better than that of the alumina ceramic layer. According to the distribution of

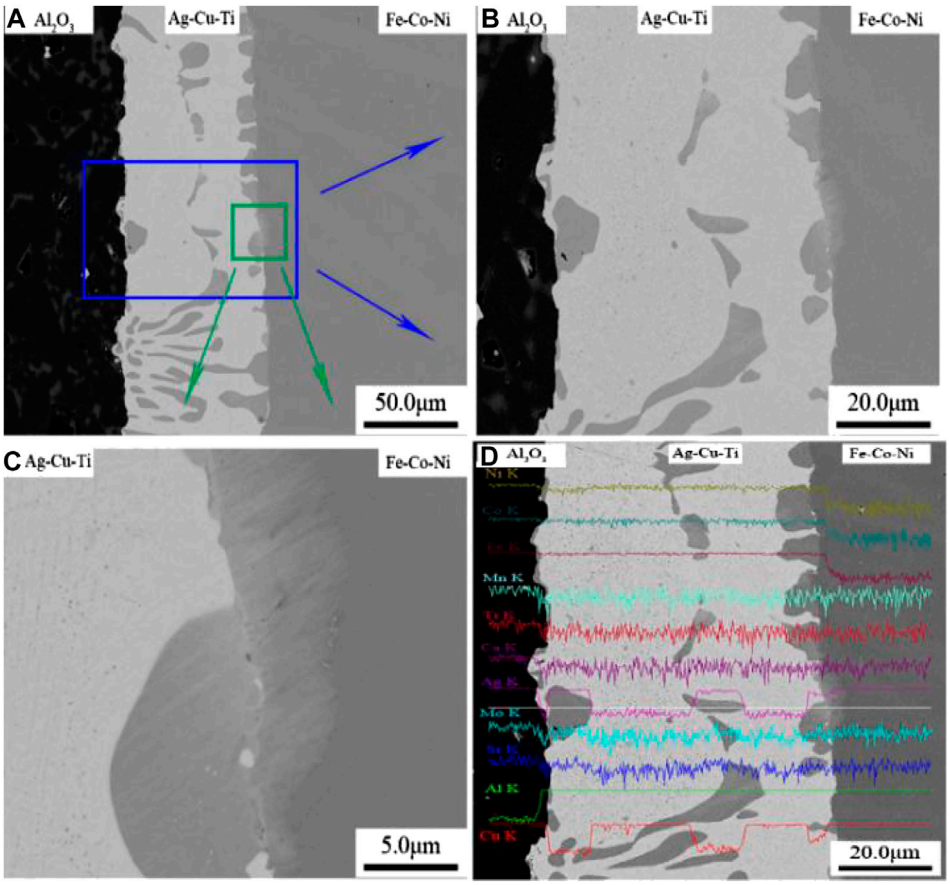

FIGURE 6 | (**A**–**D**) The interface morphologies of alumina ceramic/solder/Kovar alloy (780°C/2 min).

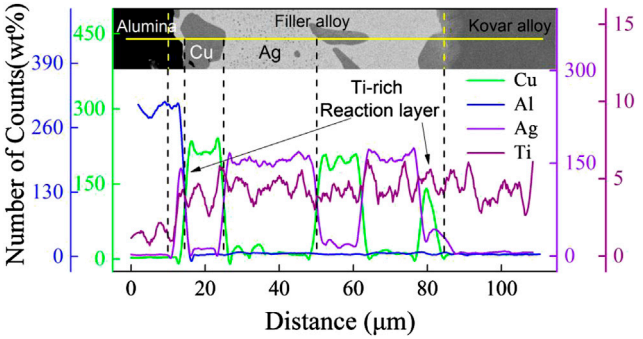

FIGURE 7 | The element distribution of Cu-Al-Ag-Tion interface microstructure (780°C/2 min).

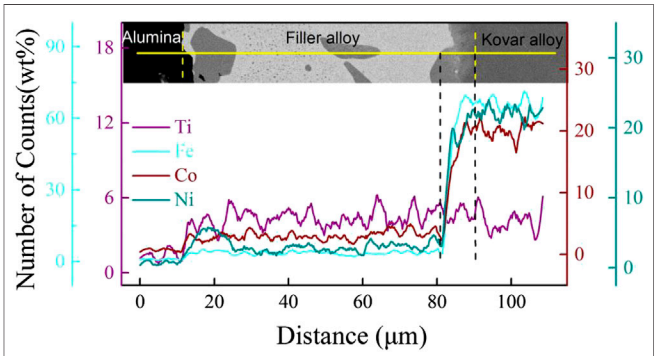

FIGURE 8 | The element distribution of Ti-Fe-Co-Nion interface microstructure (780°C/2 min).

elemental content, $TiFe_2$, and $TiNi_3$ intermetallic compound layers exist at the reaction interface.

Table 1 shows the hermeticity and insulation of the ceramic metal seal joints under the two brazing conditions.

Based on the above analysis and experimental data, the ceramic metal sealed joints prepared by the indirect brazing process show excellent performance indicators.

CONCLUSION

During direct and indirect braze welding, the joints were tested for hermeticity, insulation, and other properties. A well-formed seal was prepared. First, the presence of the molybdenum–manganese metallization layer improves the hermeticity of the sealing structure, which is beneficial to

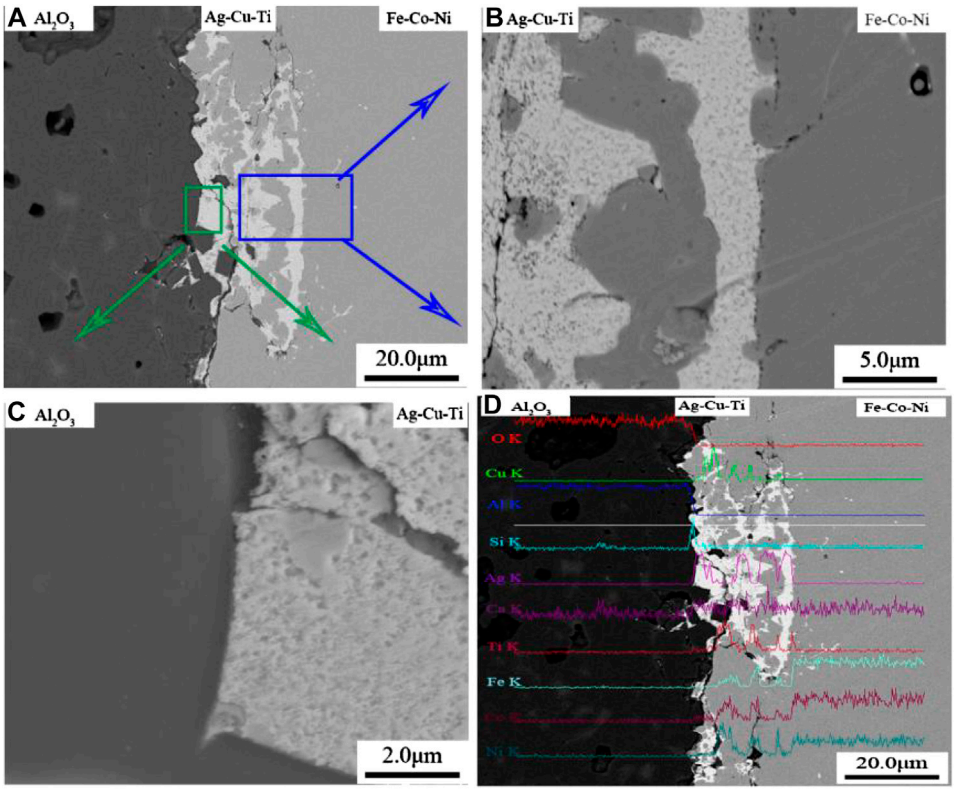

FIGURE 9 | The interface morphologies of alumina ceramic/solder/Kovar alloy (900°C/2 min).

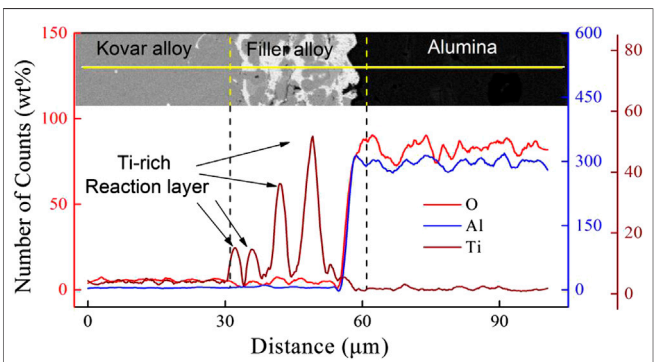

FIGURE 10 | The element distribution of O-Al-Ti (900°C/2 min).

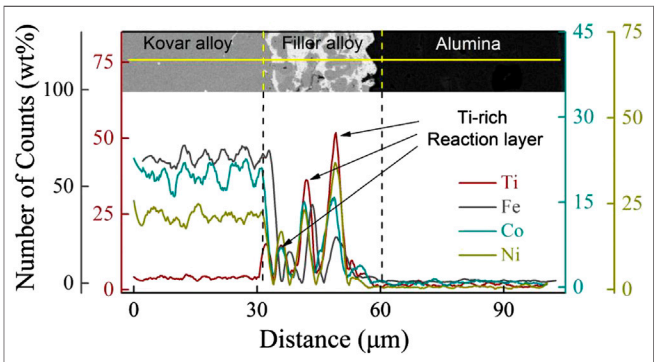

FIGURE 11 | The element distribution of Ti-Fe-Co-Ni (900°C/2 min).

the wetting of the solder layer and the ceramic and, thus, achieves effective sealing with the Kovar alloy layer. Then, the active element titanium in the sealing process and the Kovar alloy in the iron and nickel elements react to generate the $TiFe_2$, $TiNi_3$ intermetallic compound layer, which is conducive to achieving the formation of the seal. Last, the leakage rate of ceramic metal sealed joints prepared under indirect brazing process conditions is $<8.0 \times 10^{-9}$ Pa m^3/s, insulation resistance $>2.6 \times 10^{10}$ Ω. The research promotes the sealing connection technology between ceramic and metal, which can be applied in the construction of nuclear power plants.

TABLE 1 | The hermetic and insulating results of the joint.

Brazing process	Insulation resistance/Ω	Leakage rate/Pa·m^3/s
Indirect brazing	3.6×10^{11}	1.2×10^{-12}
Direct brazing	2.5×10^{11}	6.0×10^{-7}

DATA AVAILABILITY STATEMENT

The original contributions presented in the study are included in the article/Supplementary Material, further inquiries can be directed to the corresponding author/s.

AUTHOR CONTRIBUTIONS

Conceptualization, methodology, formal analysis, data curation and writing, J.Z.; Measurement, ZZ.

FUNDING

Funded by Longshan academic talent research supporting program of SWUST (NO. 18lzxt03; NO. 18zx309); Southwest University of Science and Technology Natural Science Foundation (NO. 18zx7125; Fundamental Science on Nuclear Wastes and Environmental Safety Laboratory (NO. 18kfhk02); Shock and Vibration of Engineering Materials and Structures Key Laboratory of Sichuan Province (NO. 18kfgk06).

REFERENCES

Aita, C. R. (1992). Phase maps for sputter deposited refractory metal oxide ceramic coatings: review of niobium oxide, yttrium oxide, and zirconium oxide growth. *Mater. Sci. Technol.* 8 (8), 666–672. doi:10.1179/mst.1992.8.8.666

Berndt, D., Neidig, A., Wahl, G., and Wittmer, M. (1985). *Method of direct bonding copper foils to oxide-ceramic substrates*. U.S. Patent 4,505,418[P].

Chien, C.-H., Chen, T., Lin, W.-B., Hsieh, C.-C., Wu, Y.-D., and Yeh, C.-H. (2008). Experimental and statistical study in adhesion features of bonded interfaces of IC packages. *Microelectron. Reliab.* 48 (1), 140–148. doi:10.1016/j.microrel.2007.03.002

Choy, K. (2003). Chemical vapour deposition of coatings. *Prog. Mater. Sci.* 48 (2), 57–170. doi:10.1016/s0079-6425(01)00009-3

Clarke, J. F., Ritz, J. W., and Girard, E. H. (1965). *State-of-the-art review of ceramic-to-metal joining*. Attleboro, MA, Metals And Controls, Inc., 9–10.

Erdemir, A., Eryilmaz, O. L., Urgen, M., and Kazmanli, K. (2011). *Method to produce catalytically active nanocomposite coatings*. U.S. Patent Application 13/250,760[P].

Fernie, J. A., Drew, R. A. L., and Knowles, K. M. (2009). Joining of engineering ceramics. *Int. Mater. Rev.* 54 (5), 283–331. doi:10.1179/174328009x461078

Giraldez, E. M., and Horner, M. H. (1994). *Compact multilayer ceramic-to-metal seal structure*. U.S. Patent 5,279,909[P].

Huh, J.-Y., Hong, K.-K., Cho, S.-B., Park, S.-K., Lee, B.-C., and Okamoto, K. (2011). Effect of oxygen partial pressure on Ag crystallite formation at screen-printed Pb-free Ag contacts of Si solar cells. *Mater. Chem. Phys.* 131 (1), 113–119. doi:10.1016/j.matchemphys.2011.07.075

Ionkin, A. S., Fish, B. M., Li, Z. R., Lewittes, M., Soper, P. D., Pepin, J. G., et al. (2011). Screen-printable silver pastes with metallic nano-zinc and nano-zinc alloys for crystalline silicon photovoltaic cells. *ACS Appl. Mater. Interfaces.* 3 (2), 606–611. doi:10.1021/am1011996

Jain, H. (2004). Transparent ferroelectric glass-ceramics. *Ferroelectrics* 306 (1), 111–127. doi:10.1080/00150190490458446

Khanna, V. K. (2011). Adhesion–delamination phenomena at the surfaces and interfaces in microelectronics and MEMS structures and packaged devices. *J. Phys. Appl. Phys.* 44 (3), 034004. doi:10.1088/0022-3727/44/3/034004

Li, X., Dong, Z., Westwood, A., Brown, A., Zhang, S., Brydson, R., et al. (2008). Preparation of a titanium carbide coating on carbon fibre using a molten salt method. *Carbon* 46 (2), 305–309. doi:10.1016/j.carbon.2007.11.020

Mulpuri, R. P., and Sarin, V. K. (1996). Synthesis of mullite coatings by chemical vapor deposition. *J. Mater. Res.* 11 (6), 1315–1324. doi:10.1557/jmr.1996.0166

Nascimento, R. M. d., Martinelli, A. E., and Buschinelli, A. J. A. (2003). Review Article: recent advances in metal-ceramic brazing. *Cerâmica* 49 (312), 178–198. doi:10.1590/s0366-69132003000400002

Nehrenheim, E. (2018). "Energy and natural resources," in *Encyclopedia of the Anthropocene*. Amsterdam, Netherlands: Elsevier, 441–442. doi:10.1016/b978-0-12-809665-9.05353-2

Pattee, H. E., Evans, R. M., and Monroe, R. E. (1968). *Joining ceramics and graphite to other materials*. Columbus, OH: Battelle Memorial Institute.

Sandhage, K. H., Schmutzler, H. J., Wheeler, R., and Fraser, H. L. (1996). Mullite joining by the oxidation of malleable, alkaline-earth-metal-bearing bonding agents. *J. Am. Ceram. Soc.* 79 (7), 1839–1850. doi:10.1111/j.1151-2916.1996.tb08004.x

Solfest, P. A., and Strangman, T. E. (1989). *Ceramic thermal barrier coating with alumina interlayer*. U.S. Patent 4,880,614[P].

Tomlinson, W. J. (1986). Low temperature metallization of debased alumina. *Surf. Coating. Technol.* 27 (1), 23–28. doi:10.1016/0257-8972(86)90041-1

Ul'yanin, Y. A., Kharitonov, V. V., and Yurshina, D. Y. (2018). Forecasting the dynamics of the depletion of conventional energy resources. *Stud. Russ. Econ. Dev.* 29 (2), 153–160. doi:10.1134/S1075700718020156

Véchembre, J. B., and Fox, G. R. (2001). Sintering of screen-printed platinum thick films for electrode applications. *J. Mater. Res.* 16 (4), 922–931. doi:10.1557/jmr.2001.0131

Vinod, P. N. (2013). The fire-through processed screen-printed Ag thick film metal contacts formed on an electrochemically etched porous silicon antireflection coating of silicon solar cells. *RSC Adv.* 3 (11), 3618–3622. doi:10.1039/c2ra20354e

Walker, C., Romero, J., and Stokes, R. (2011). Active-brazed ceramic-tungsten carbide assemblies for seal applications. *Microsc. Microanal.* 17 (S2), 1844–1845. doi:10.1017/s1431927611010099

Yoshimura, M., and Suchanek, W. (1997). *In situ* fabrication of morphology-controlled advanced ceramic materials by soft solution pocessing. *Solid State Ionics* 98 (3), 197–208. doi:10.1016/s0167-2738(97)00103-3

Zohuri, B. (2019). "Nuclear energy research and development roadmap," in *Small modular reactors as renewable energy sources*. Berlin, Germany: Springer, 95–116.

Conflict of Interest: The authors declare that the research was conducted in the absence of any commercial or financial relationships that could be construed as a potential conflict of interest.

frontiers in Materials

ORIGINAL RESEARCH
published: 10 March 2021
doi: 10.3389/fmats.2021.633345

Comparison of Multilayer Transparent Wood and Single Layer Transparent Wood With the Same Thickness

Yan Wu[1,2]*, *Yajing Wang*[1,2] *and Feng Yang*[3]*

[1]College of Furnishings and Industrial Design, Nanjing Forestry University, Nanjing, China, [2]Co-Innovation Center of Efficient Processing and Utilization of Forest Resources, Nanjing, China, [3]Fashion Accessory Art and Engineering College, Beijing Institute of Fashion Technology, Beijing, China

In this paper, poplar was used as raw material, sodium chlorite was used to delignify it in acidic environment, and then epoxy resin was vacuum impregnated in the delignified wood template to prepare transparent wood. Moreover, in order to imitate the lamination method of plywood, the multilayer transparent wood was prepared by means of staggered vertical lamination. The purpose of this paper is to study the physical and chemical properties of multilayer transparent wood, and to explore the application potential of multilayer transparent wood as a new material by comparing with single layer transparent wood with the same thickness. The weight of wood components in the transparent wood prepared in this experiment accounts for about 30–45% of the weight of composite materials. Scanning electron microscopy (SEM) measurements, Fourier transform attenuated total reflection infrared spectroscopy (ATR-FTIR) characterization, weight gain measurements, UV transmittance measurements, color difference measurements, water contact angle measurements and mechanical properties measurements were used to study. The results showed that as the thickness of the transparent wood increased, the cracks between the resin and the wood cell wall increased, and the interface showed an uneven state. In the case of the same thickness, the multilayer transparent wood was made by laminating transparent wood sheets, with fewer internal cracks and smooth interfaces. Its light transmittance is better than single layer transparent wood. Moreover, compared with single layer transparent wood with the same thickness, the lightness of multilayer transparent wood decreased, and tended to yellow and red. Due to the removal of lignin, the tensile strength of transparent wood decreased during the preparation process. However, it can be seen from the mechanical strength test that the tensile strength of multilayer transparent wood is much higher than that of single layer transparent wood. To a certain extent, multilayer transparent wood can improve the mechanical strength of transparent wood. To conclude, multilayer transparent wood is a kind of natural transparent material with large thickness, good light transmission and excellent mechanical properties, and it has a good development prospect.

Keywords: transparent wood, multilayer transparent wood, epoxy resin, acid delignification, thickness

OPEN ACCESS

Edited by:
Antonio Caggiano, Darmstadt University of Technology, Germany

Reviewed by:
Lars A. Berglund, Royal Institute of Technology, Sweden
Shifeng Zhang, Beijing Forestry University, China

***Correspondence:**
Yan Wu
wuyan@njfu.edu.cn
Feng Yang
yangfeng@bift.edu.cn

Specialty section:
This article was submitted to Structural Materials, a section of the journal Frontiers in Materials

Received: *27 November 2020*
Accepted: *28 January 2021*
Published: *10 March 2021*

Citation:
Wu Y, Wang Y and Yang F (2021) Comparison of Multilayer Transparent Wood and Single Layer Transparent Wood With the Same Thickness. Front. Mater. 8:633345. doi: 10.3389/fmats.2021.633345

INTRODUCTION

As a natural green material, wood has good physical and chemical properties, including high strength, low thermal conductivity, non-toxic, and biodegradable (Cabane et al., 2014; Vay et al., 2015). Therefore, wood is widely used in various fields, such as construction, furniture, and decoration (Iwamoto et al., 2005). In recent years, as people pay more attention to the global environment, more and more people have realized the importance of green and sustainable development (Xia et al., 2020), and wood, as the most abundant organic polymer resource on the earth, has also received more and more attention (Cabane et al., 2016; Wang et al., 2017). In addition, wood can be modified to improve some of its own defects, such as enhancing the hydrophilicity of wood surface, so as to better connect with adhesive (Wang et al., 2020). Moreover, the internal components of wood can also be extracted and applied, such as lignin applied to antioxidant components (Dong et al., 2020). In the past research, researchers also have developed modified wood with specific properties such as anti-corrosion wood, wood sponge, transparent wood, etc.

Transparent wood (TW) is a kind of wood with a certain light transmittance, which improves the opacity of the wood itself, and can be used as a new functional material to replace other light-transmitting materials, such as glass. Compared with glass, transparent wood has more excellent physical and chemical properties. The advantages of its wide range of raw materials, environmental protection in the manufacturing process, and excellent thermal stability can effectively solve the safety and environmental problems caused by the fragility of glass. Before the concept of transparent wood was proposed, transparent paper had been widely used in various fields. Transparent paper is prepared by extracting nano cellulose from wood and then modifying it. The method is to fill the holes in the paper with a substance with a refractive index similar to that of cellulose fibers and fillers to make the paper an optically uniform medium, in order to improve the transparency of paper (Gao et al., 2013; Jia et al., 2017). Similar to this method, in 1992, Fink (1992) first proposed the concept of transparent wood. It changed according to three different ways of light passing through a transparent object, namely, reflection, refraction and absorption on the outer surface and the inner surface. Therefore, the method of preparing transparent wood was proposed to first use a bleaching solution to chemically remove the lignin, and then fill the material with a refractive index similar to that of cellulose to eliminate the light scattering at the boundary between wood cells and obtain transparent wood. In 2016, Li et al. (2016) successfully prepared a transparent wood by impregnating the prepolymerized methyl methacrylate (PMMA) into the nanoporous cellulose template. This transparent wood has a light transmittance of 85% and a haze of about 70%. Moreover, by compressing the wood template, Li et al. changed the volume proportion of cellulose in transparent wood, thus adjusting the optical properties of transparent wood. This paper combines the function and structure of transparent wood, which lays a good foundation for further optimization of transparent wood technology. Zhu et al. (2016) selected the radial cutting direction (R-wood) and longitudinal cutting direction (L-wood) of balsa wood as experimental materials to prepare transparent wood considering the structural characteristics of wood anisotropy. Comparing R-wood and L-wood of the same thickness, it was found that the transparency and haze of R-wood are higher than that of L-wood, while the mechanical strength of R-wood is lower than that of L-wood. It is proved that wood has different characteristics in different directions. Considering the practical use of transparent wood as a kind of structural timber, L-wood was used in this paper.

In addition to the research on the structure of transparent wood, the preparation method of transparent wood is also one of the topics that researchers focus on. According to the transparency principle of wood, the preparation of transparent wood can be divided into two parts, that is, decolorization and impregnating resin. The decolorization treatment is mainly to remove the light-absorbing substances in the wood, that is, lignin, and to provide channels for subsequent resin impregnation. At present, the commonly used decolorization treatment methods can be divided into two categories: removing lignin and modifying lignin. The main chemicals used to remove lignin are sodium hypochlorite, sodium chlorite and sodium sulfite. Sodium hypochlorite destroys the aromatic ring structure of lignin through oxidation and chlorination, so as to achieve the effect of removing lignin. For example, Jia et al. (2017) bleached balsa wood with 5% sodium hypochlorite solution to achieve the purpose of delignification. Sodium chlorite decomposes chlorine, chlorine dioxide and water by generating unstable chlorous acid in an acidic environment. These substances can degrade and dissolve lignin. This is currently one of the most widely used decolorization processes. Li et al. (2016), Tang et al. (2018), Gan et al. (2017), Vasileva et al. (2017) all used sodium chlorite solution to successfully prepare delignified wood templates under acidic conditions. Sodium sulfite is in an alkaline environment, through the reaction of SO^{3-} and lignin, the lignin is sulfonated and then dissolved in water, thereby achieving the function of delignification. This method Li et al. (2016) and Yu et al. (2017) are used in the preparation of transparent wood. Considering that the above methods can effectively remove lignin to achieve the effect of wood decolorization, but it will cause certain pollution to the environment. In 2017, Li et al. (2017) proposed a new environment-friendly method, which retained 80% of the lignin. By modifying the lignin, the chromogenic groups were removed, so as to achieve the purpose of decolorization. The impregnation resin part is mainly for the choice of resin. At present, the commonly used resins are polymethyl methacrylate (PMMA), epoxy resin and polyvinylpyrrolidone (PVP). Considering the process and cost comprehensively, this experiment uses sodium chlorite as a decolorizing agent to decolorize the wood, and then selects epoxy resin as the impregnating resin to fill the pores of the wood to prepare transparent wood.

As a structural material, transparent wood can be actually used in energy-saving buildings. In 2019, Li et al. (2019) used 2–5 cm thick translucent wood composite materials as the wall structure, and

demonstrated the huge potential of translucent wood as a new type of energy-saving building material by means of models. In 2020, Mi et al. (2020) prepared a beautiful and transparent wood with high light transmittance, high haze, and excellent UV resistance. It can be used as materials such as house walls and ceilings to effectively provide light to the room. However, the development of transparent wood is still restricted by thickness and material. At present, the thickness of transparent wood can only reach a few centimeters, and the raw materials used are mostly porous wood with lighter density, such as balsa wood, beech wood, etc., which are restricted by mechanical strength in the actual application process. Therefore, increasing the thickness of transparent wood is a topic that researchers are more concerned about. However, it is difficult to immerse the chemicals in the thick wood, so the expected experimental results cannot be achieved. Foster et al. (2019) thought that the current research on transparent wood mainly focuses on single layer transparent wood, and the excellent mechanical properties of multilayer transparent wood are also worthy of attention. They prepared 1-layer and 2-layer transparent wood, and proved that the multilayer board has better mechanical properties through the comparison of mechanical properties. Chen et al. (2019) also pointed out that most of the previous studies focused on the total transmittance of transparent wood at a specific thickness and the angular distribution of light passing through transparent wood at different thickness. They proposed that the light scattering, haze and transmittance can be adjusted by surface modification or lamination of the delignified wood template, which laid a foundation for the preparation of multilayer transparent wood. In addition, Qin et al. (2018) studied the preparation and properties of multilayer transparent wood from different tree species. He used balsa wood, paulownia wood, and white basswood as raw materials to laminate transparent veneers in the same direction and cross-laminated. This method prepared transparent multilayer wood, compared the light transmittance and mechanical properties of the two lamination methods. It was concluded that the cross-laminated method could improve the anisotropy of wood and eliminate the difference between the parallel and cross grain tensile, which had great advantages.

This experiment imitates the production process of plywood, that is, odd layer laminated veneer, and each layer of fiber is perpendicular to each other (Liu et al., 2010) to prepare multilayer transparent wood. Poplar wood was used as raw material to prepare delignified wood template by using sodium chlorite, and then transparent wood was prepared by placing it in epoxy resin impregnation solution. The physical and chemical properties of multilayer transparent wood and single layer transparent wood with the same thickness were compared in order to prepare transparent wood with thicker thickness and better mechanical properties, so as to broaden the application range of transparent wood.

EXPERIMENTAL PART

Materials

Poplar log(OW) is provided by Shantou Yihua life science and Technology Co., Ltd. The specifications used are shown in **Table 1**. The air-dry density of poplar is 0.113 g/cm^3, the absolute dry density is 0.087 g/cm^3, and the moisture content is 10.543%. Among them, as shown in **Figure 1**, the fiber direction 0° refers to the fiber arrangement direction, and 90° refers to the direction perpendicular to the fiber.

Sodium chlorite, concentration 80%, provided by Shanghai Macklin Co., Ltd. Glacial acetic acid, analytical grade, provided by Nanjing Chemical Reagent Co., Ltd. Anhydrous ethanol, analytically pure, provided by Nanjing Chemical Reagent Co., Ltd. E51 type epoxy resin is a low-molecular liquid bisphenol A type epoxy resin, provided by Kunshan Jiulimei Electronic Materials Co., Ltd., its epoxy value (equivalent/100 g) = 0.48–0.54, viscosity (mpas/25°C) is 11000–14000, volatile matter (%) ≤ 2, color number ≤ 2. B210 type epoxy resin curing agent is a new type of amine greenhouse curing agent modified by polyetheramine. It is provided by Kunshan Jiulimei Electronic Materials Co., Ltd. Its viscosity (mpas/25°C) is 200–300, The relative density at 20°C is 1.03–1.08 g/cm^3, and the amine value (KOHmg/g) is 300–400.

Electric heating constant temperature blast drying oven, model: DHG-9643BS-III, provided by Shanghai Xinmiao Medical Equipment Manufacturing Co., Ltd. Electronic balance, model: UTP-313, provided by Shanghai Huachao Electric Co., Ltd. ScienceTOOL laboratory oil-free vacuum pump, Model: R410, provided by American Saints International Group. Plastic vacuum dryer, Model: PC-3, provided by Shanghai Sanmu Industrial Co., Ltd. Digital display three-purpose constant temperature water tank, model: HH-600, provided by Jintan Provided by City Guowang Experimental Instrument Factory. Heat-collecting constant temperature heating magnetic stirrer, model: DF-101Z, provided by Nanjing Wozhong Instrument Equipment Co., Ltd.

Experimental Methods

In this experiment, sodium chlorite was used to prepare delignified wood template under acidic conditions. Then, the material with a refractive index similar to that of cellulose was filled into the wood pores to obtain transparent wood. In addition, a single layer transparent wood sheet was laminated and composited into a multilayer transparent wood by a staggered vertical lamination method.

Pre-Processing

The poplar was dried in an electric heating constant temperature blast drying oven, at 102°C for 12 h.

Preparation of the Wood Templates

A sodium chlorite aqueous solution with a concentration of 3.5 wt% was prepared, a glass rod was used to stir evenly, then an appropriate amount of glacial acetic acid was dropped into the solution, the pH value of the solution was adjusted to 4.6, and the delignified solution was obtained after stirring evenly again. The absolutely dry poplar was put into the delignification solution. Then, a digital display and a three-purpose thermostat water tank was used to keep the solution temperature at 85°C. The poplar was taken out after 4–8 h of reaction. The extracted poplar wood was washed with distilled water for three times, and the delignification solution on the surface was removed, and then dehydrated in absolute ethanol for 24 h to obtain the delignified wood templates.

TABLE 1 | Raw material specifications of poplar.

Thickness (h)/mm	Length (L)/mm	Width (b)/mm	Fiber direction	Air-dry quality (M_1)/g	Absolute dry quality (M_0)/g
0.5	40	20	0°/90°	0.067	0.062
1.5	40	20	0°	0.116	0.105
2.5	40	20	0°	0.151	0.137

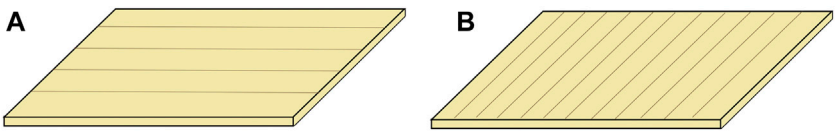

FIGURE 1 | Schematic diagram of wood fiber direction **(A)**. Fiber direction is 0° **(B)**. Fiber direction is 90°).

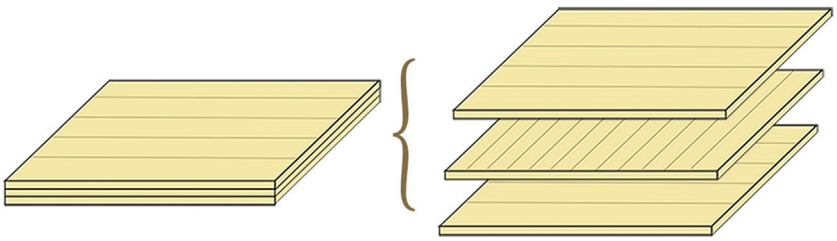

FIGURE 2 | Schematic diagram of 3-layer transparent wood lamination.

Preparation of the Transparent Wood

The delignified wood template was put into a plastic vacuum dryer. Then, an oil-free vacuum was used to pump it into vacuum, and dry it in vacuum for 10–20 min. The epoxy resin impregnation solution was prepared according to the weight ratio of epoxy resin to curing agent of 2:1, which was stirred evenly with a magnetic stirrer for standby. After vacuum drying, the appropriate amount of epoxy resin impregnation solution was poured into the delignified wood template, and it was immersed in vacuum environment for 25–30 min. Finally, the impregnated samples were taken out and placed in two pieces of silica gel to cure at room temperature in a vacuum environment for 12 h to obtain the transparent wood.

Preparation of the Multilayer Transparent Wood

The samples which were vacuum impregnated with epoxy resin impregnation solution for 25–30 min were taken out, and then they were laminated. As shown in **Figure 2**, **3**, 3-layers of transparent wood (0°/ 90°/ 0°) and 5-layers of transparent wood (0°/ 90°/ 0°/ 90°/ 0°). Then put them in two pieces of silica gel, clamp them with a clamp, give them a certain pressure, cure at room temperature in a vacuum environment for 12 h to obtain multilayer transparent wood.

Characterization

In order to facilitate the description of the characterization of the samples, this study numbered the sample types that would appear in the test. Specifically, A refers to poplar logs with a thickness of 0.5 mm and a fiber direction of 0°. DW-A refers to a delignified wood template with a thickness of 0.5 mm and a fiber direction of 0°. TW-A refers to transparent wood with a thickness of 0.5 mm and a fiber direction of 0°. B refers to poplar logs with a thickness of 0.5 mm and a fiber direction of 90°. DW-B refers to a delignified wood template with a thickness of 0.5 mm and a fiber direction of 90°. TW-B refers to transparent wood with a thickness of 0.5 mm and a fiber direction of 90°. C refers to a 1.5 mm thick poplar log with a fiber direction of 0°. DW-C refers to a delignified wood template with a thickness of 1.5 mm and a fiber direction of 0°. TW-C refers to transparent wood with a thickness of 1.5 mm and a fiber direction of 0°. D refers to poplar logs 2.5 mm thick and with a fiber direction of 0°. DW-D refers to a delignified wood template with a thickness of 2.5 mm and a fiber direction of 0°. TW-D refers to 2.5 mm thick transparent wood with a fiber direction of 0°. OW-3 refers to three layers of poplar logs. DW-3 refers to the 3-layer delignified wood template. TW-3 refers to three layers of transparent wood. OW5 refers to five layers of poplar logs. DW-5 refers to 5-layer delignified wood template. TW-5 refers to five layers of transparent wood.

Scanning Electron Microscope Measurements

The sample was cut along the transverse direction, and the surface of the cut sample was polished by ultra-thin slicer, and then adhered to the observation disk for vacuum gold plating. Then, the gold-plated samples were put into a scanning electron

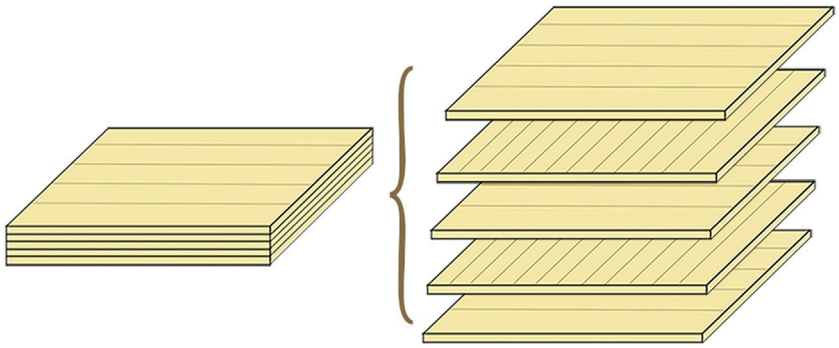

FIGURE 3 | Schematic diagram of 5-layer transparent wood lamination.

microscope (model: Quanta 200, provided by Fei Co., Ltd.) to observe the changes of pores and interfaces before and after treatment.

Fourier Transform Attenuated Total Reflection Infrared Spectroscopy Characterization

A Fourier Transform Infrared Spectrometer (Model VERTEX 80V, provided by Bruker Spectrometer Company, United States) was used to test and analyze the chemical groups in the sample. By observing the chemical group vibration of the sample under light irradiation with a wavenumber of 400–4,000 cm^{-1}, the changes in the chemical group of the sample before and after processing were analyzed.

Weight Gain Rate Measurements

The samples before and after impregnation were placed on an electronic balance (model: UTP-313, provided by Shanghai Huachao Electric Co., Ltd.) for measurement, and the weight gain rate was calculated according to **Eq. 1**. The weight gain rate of different thickness samples was compared, and the difference of weight gain rate between multilayer transparent wood samples and transparent wood with the same thickness was compared.

$$W = \frac{M_a - M_b}{M_b} \times 100\% \quad (1)$$

In formula, **W** represents weight gain rate, $\mathbf{M_a}$ represents mass after impregnation, $\mathbf{M_b}$ represents mass before impregnation.

UV Transmittance Measurements

TW samples with different thickness and multilayer transparent wood were tested by ultraviolet visible light photometer (model: Lambda 950, provided by PerkinElmer company, United States), and the transmittance of transparent wood samples was obtained in the visible light range, that is, the wavelength of 350–800 nm. The difference of light transmittance between multilayer transparent wood and transparent wood with the same thickness was compared. At the same time, in order to improve the accuracy of the data, samples under the same experimental conditions were selected for more than two repeated tests.

Color Difference Measurements

Color analysis of each sample was performed by PANTON color detector (model: RM200, provided by Ashley Co., Ltd.). Record the *L*a*b* value of each sample, and analyze the color difference of samples before and after treatment. In order to reduce the test error, this test selects three points on the same sample to record respectively, and then calculates the average value to get the relatively accurate *L*a*b* value. In order to ensure the same background color during the test, the samples were placed on A4 paper for testing.

Water Contact Angle Measurements

The contact angle tester [model: drop shape analyzer (DSA) 100 s, provided by Kruss Scientific Instruments Shanghai Co., Ltd.] was used to measure the surface properties of the samples before and after treatment. The contact angle of water droplets on the surface of the samples was observed, and the hydrophobicity of the samples before and after treatment was compared.

Mechanical Performance Measurements

The longitudinal tensile test was carried out on the original sample, delignified sample and transparent sample by the precise electronic mechanics experimental machine (model: AG-IC, provided by Shimadzu production Institute, Japan). The tensile rate was set at 5 mm/min and the maximum load force was 10,000 N. Recorded the maximum tensile load, compared the change of tensile strength before and after treatment, and compared the tensile strength of multilayer transparent samples and transparent samples with the same thickness.

RESULTS AND DISCUSSION

Scanning Electron Microscope Analysis

The changes of porosity of wood before and after treatment were observed by SEM. As shown in **Figure 4**, the cross-sectional pores of sample A and B have changed after delignification and transparency treatment. Both sample A and B are poplar

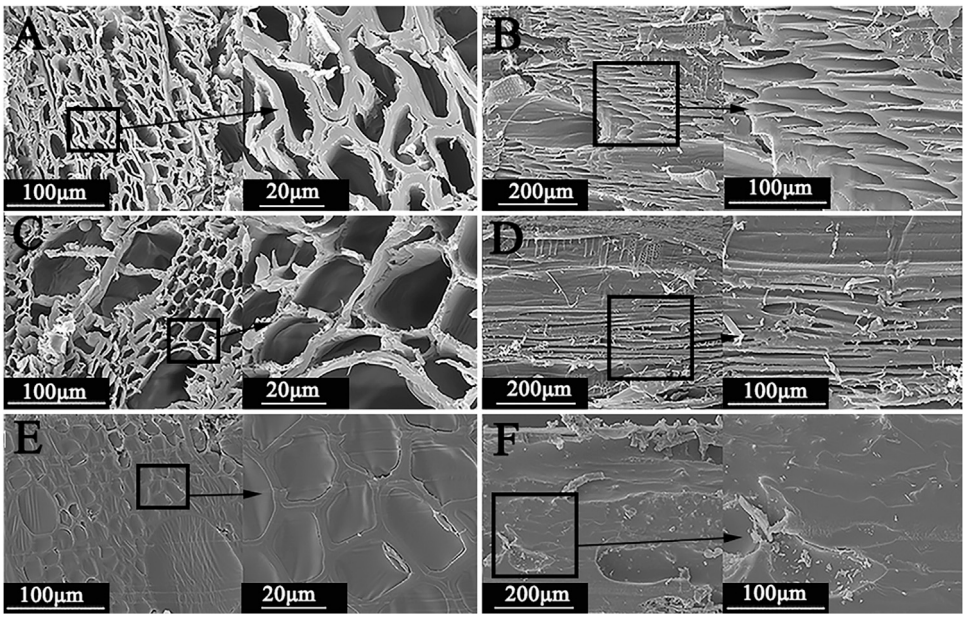

FIGURE 4 | SEM image of poplar with thickness of 0.5 mm before and after treatment (**A**.A; **B**.B; **C**. DW-A; **D**. DW-B; **E**.TW-A; **F**.TW-B).

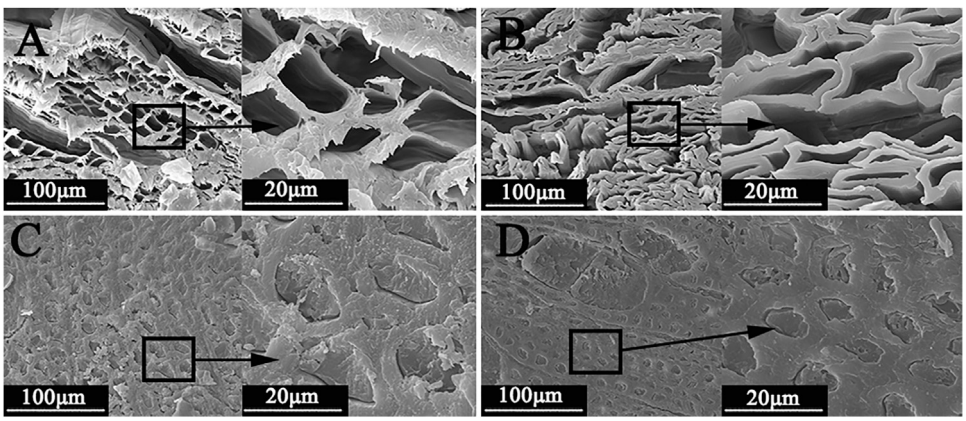

FIGURE 5 | SEM image of poplar with thickness of 1.5 mm and 2.5 mm after delignification and transparency treatment (**A**. DW-C; **B**. DW-D; **C**.TW-C; **D**. TW-C).

wood with a thickness of 0.5 mm, but the fiber direction is different. **Figures 4A,B** show the internal pore structure of sample A and B before treatment. The parenchyma cells and tube pores of poplar can be seen from sample A, and the sectional morphology of parenchyma cells and tube pores can be seen in sample B. It can be seen from **Figure 4C** that after delignification, the cell wall of poplar sample becomes thinner, but the microstructure of the sample is not obviously damaged, and the original cell structure is still maintained. It can be seen from **Figures 4E,F** that the transparent sample contained epoxy resin material, and the interface between the epoxy resin and the wood itself cell wall is good after immersion treatment for the sample with the thickness of 0.5 mm, which is basically no crack (Fang et al., 2017).

It can be seen from **Figure 5** that the changes of thicker samples after delignification treatment and transparency treatment are roughly the same. However, by looking at **Figure 5B**, it can be found that the cell wall of the sample with a thickness of 2.5 mm undergoes swelling and shrinkage after delignification treatment. This is because compared with thin wood, thick wood needed to be soaked in a delignification agent for a longer period of time to remove lignin, and more deionized water was required for operation when washing the residual delignification agent in the wood. This caused thick wood to absorb more water, and the cell wall swelled more obviously. It can be seen from **Figures 5C,D** that there are obvious gaps at the junction between the resin and the cell wall, and there are obvious transverse cracks at the interface. Therefore, compared with the

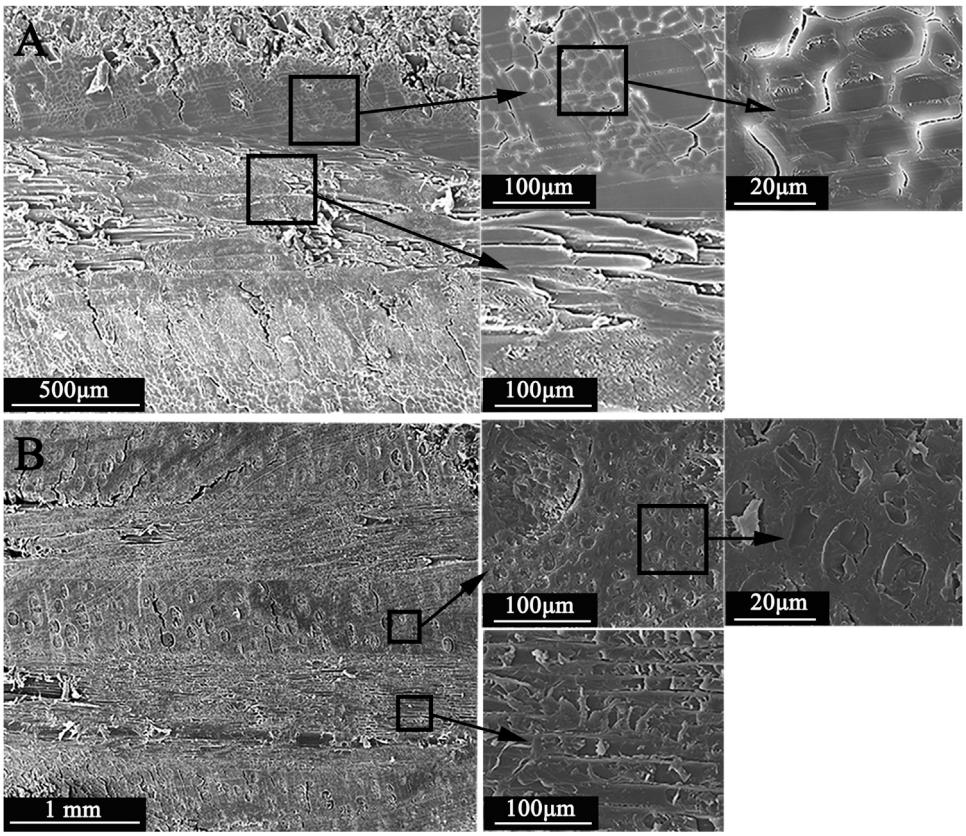

FIGURE 6 | SEM image of multilayer transparent wood (**A**.TW-3; **B**.TW-5).

thin transparent wood, the bonding degree of epoxy resin and wood cells in thick transparent wood is reduced.

It can be seen from **Figure 6** that the multilayer transparent wood was formed by staggered vertical lamination of thin wood, and obvious delamination interface can be seen at the splicing point. Compared with the transparent wood with the same thickness, the multilayer transparent wood has fewer internal cracks, and the epoxy resin has a better combination with the cell wall.

Fourier Transform Attenuated Total Reflection Infrared Spectroscopy Analysis

Since sample A and sample B are different only in fiber direction, sample A was selected for representative test. It can be seen from **Figure 7** that the absorption peaks of the original sample include the stretching vibration of O-H group at 3331 cm^{-1}, the stretching vibration of C-H group at 2921 cm^{-1}, the stretching vibration of C = O group at 1594 cm^{-1}, the stretching vibration of aromatic ring skeleton group of lignin at 1,509 cm^{-1} and the stretching vibration of C = O group at 1,425 cm^{-1}. The test results are consistent with the research results in the literature (Rana et al., 2010; Notburga et al., 2008). After delignification, the absorption peak at 1,509 cm^{-1} disappears in the infrared spectrum of delignified samples. This peak is the stretching vibration peak of aromatic skeleton group of lignin, which prove that lignin was largely removed after delignification. The absorption peaks of E51 epoxy resin include the symmetric stretching vibration of the C-H group on CH_3 at a wavelength of 2,965 cm^{-1}, the antisymmetric stretching vibration of the C-H group on CH_3 at 2,865, 1,606, and 1,508 cm^{-1}. Besides, it include the asymmetric vibration band of the benzene ring skeleton at 1,455 cm^{-1}, the scissor swing vibration of CH_3 at 734 cm^{-1}, the stretching vibration of aliphatic ether C-O-C at 1,241 cm^{-1}, the out of plane deformation of para substituted benzene ring of = CH at 830 cm^{-1}. It is consistent with the results of Zhao (2016). It can be seen from the figure that the infrared spectrum of the transparent sample obtained by vacuum impregnation of epoxy resin E51 has not only the characteristic absorption peak of delignified wood, but also the characteristic peak of epoxy resin E51.

Therefore, from the molecular point of view, the transparent sample contained the molecular groups in the delignified wood template and epoxy resin, and the epoxy resin was successfully polymerized with the delignified wood template.

Analysis of Weight Gain Rate

In the process of preparation, transparent wood needed to be impregnated with resin in vacuum, so that the refractive index of internal material was similar. According to **Eq. 1** in *Weight Gain Rate Measurements*, the weight gain rate of each sample

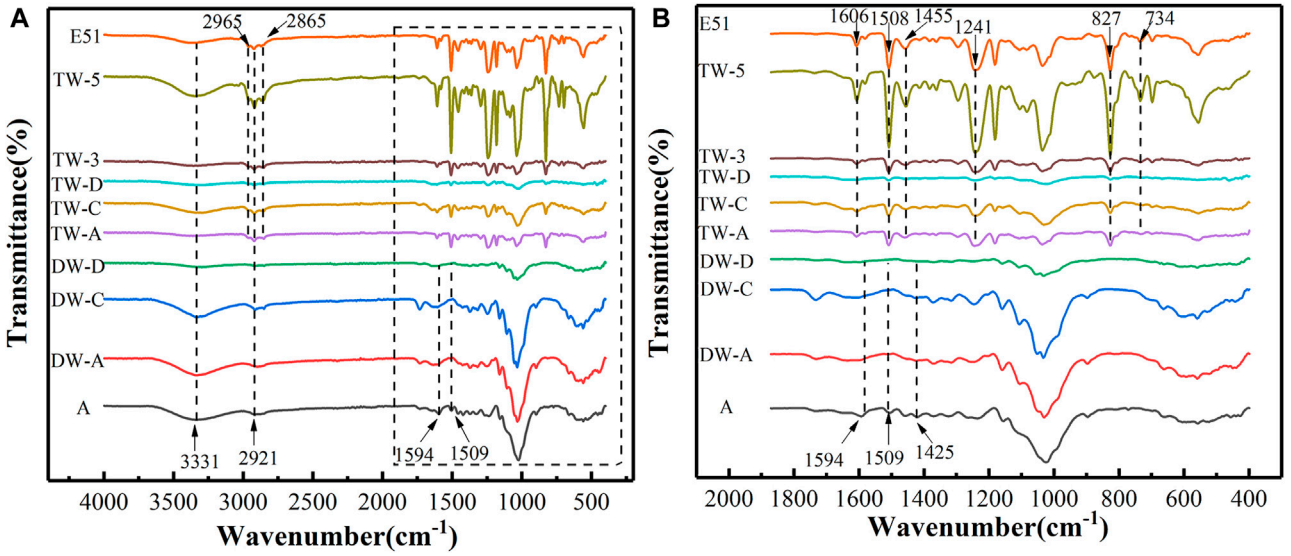

FIGURE 7 | ATR-FTIR of the samples before and after treatment (**B** is the enlarged picture in the dotted box of **A**).

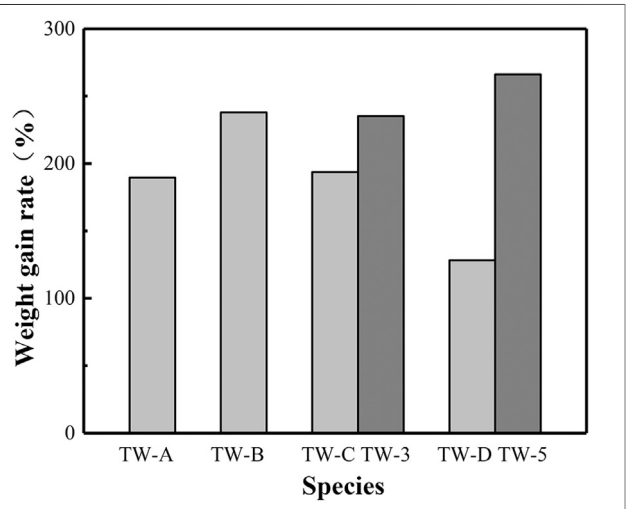

FIGURE 8 | The histogram of weight gain rate of each sample.

impregnated with epoxy resin can be obtained, which reflects the different degree of epoxy resin impregnation in each sample. It can be seen from **Figure 8** that the weight gain rate of single layer transparent poplar wood with thickness of 0.5 and 1.5 mm is about 200%, but the transparent wood with thickness of 2.5 mm is restricted by the thickness direction, and the epoxy resin is difficult to be successfully impregnated into the interior of poplar, and the weight gain rate is greatly reduced, and the weight gain rate is only about 100%. Under the same initial thickness, the weight gain rate of multilayer transparent wood is greater than that of the single layer transparent wood with the same thickness. The weight gain rate of TW-3 is about 40% higher than that of TW-C, and that of TW-5 is about 140% higher than that of TW-D. The results show that the change of weight gain rate is obvious with the increased thickness.

At the same time, due to epoxy resin impregnation in poplar wood, the thickness of transparent sample wood also changed, as shown in **Table 2**, which is the thickness record table of OW and TW. Similar to the results of weight gain rate, the thickness change of multilayer transparent wood is more obvious than that of single layer transparent wood with the same thickness, and the change degree is more obvious with the increase of thickness.

UV Transmittance Analysis

It can be seen from **Figure 9** that OW are opaque under visible light. The light transmittance of TW-A is about 4%, that of TW-B is about 2%, and that of E51 epoxy resin is about 80%. The light transmittance increased with the increase of wavelength. When the visible light is 350–540 nm, the transmittance of TW-C is higher than that of TW-3; when the visible light is 540–800 nm, the transmittance of TW-C is lower than that of TW-3, and the longer the wavelength is, the greater the difference is. The transmittance curve of TW-D coincides with the OW curve, showing an opaque state, while TW-5 have a certain transmittance, and the longer the visible light wavelength is, the higher the transparency is.

It can be seen that the transmittance of transparent veneer with fiber direction of 0° is higher than that of transparent veneer with 90° fiber direction. For thicker samples, multilayer transparent wood can present a certain transmittance, while single layer transparent wood with the same thickness is restricted by the thickness direction, so it is difficult to deal with it, showing a basically opaque state. As shown in **Figure 10**, the macroscopic observation diagram is the same as the test result.

Color Difference Analysis

The *L*a*b* color model consists of a lightness channel and two color channels. L represents the lightness, and the values are all

TABLE 2 | Thickness record of each sample before and after treatment.

Type	Thickness of OW (mm)	Thickness of TW (mm)
0.5 mm thick poplar wood with 0° fiber direction	0.50 (0.035)	0.68 (0.035)
0.5 mm thick poplar wood with 90° fiber direction	0.50 (0.035)	0.74 (0.025)
1.5 mm thick poplar wood	1.50 (0.026)	1.60 (0.090)
3-Layer poplar wood	1.50	—
*The relative thicknesses of different layers are all 0.5 mm	1.95 (0.068)	—
2.5 mm thick poplar wood	2.50	2.57 (0.040)
5-Layer poplar wood	2.50 (0.017)	—
*The relative thicknesses of different layers are all 0.5 mm	3.41 (0.225)	—

The values in brackets are the values of standard deviation.

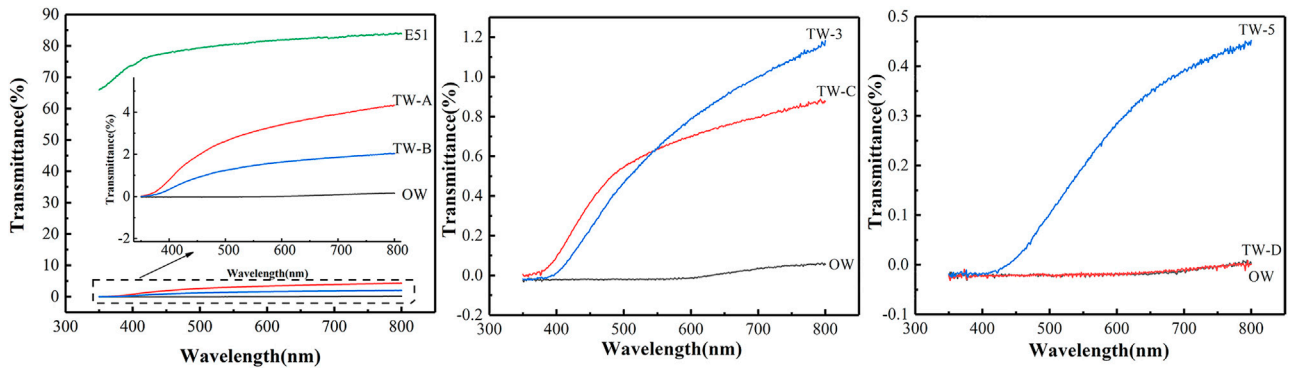

FIGURE 9 | Transmittance before and after treatment.

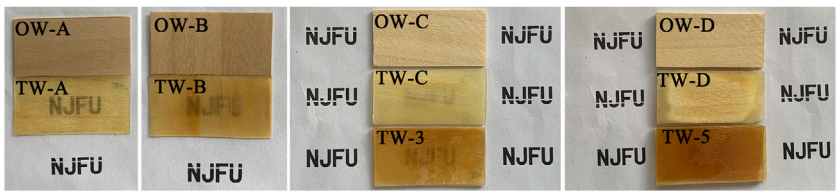

FIGURE 10 | Macroscopic observation diagram of transparent wood.

positive. The larger the value is, the higher the lightness is. a represents the range from green to red, and the value can be divided into positive and negative value. The larger the positive value is, the higher the red saturation of the object is, and the larger the negative value is, the higher the green saturation of the object is. b represents the range from blue to yellow, with positive and negative values. The larger the positive value is, the higher the yellow saturation of the object is, and the larger the negative value is, the higher the blue saturation of the object is (Jia et al., 2017). It can be seen from **Figure 11** that the L value of the single layer transparent sample increases after the transparent treatment, while the value of a and b have no obvious change, indicating that the brightness of the wood increases after the transparency treatment. Comparing multilayer transparent wood with single layer transparent wood with the same thickness, it can be found that the L value of TW-3 and TW-5 is lower than TW-C and TW-D. a value of TW-3 and TW-5 is greater than TW-C. b value of TW-D, TW-3 and TW-5 is greater than that of TW-C and TW-D. This shows that with the same thickness, the brightness of the multilayer transparent wood is lower than that of the single layer transparent wood, and the color tends to be red and yellow. This is consistent with the macro picture shown in **Figure 10**. The multilayer transparent wood presents a transparent texture similar to amber.

Water Contact Angle Analysis

The test time was set to 100°s, and the contact angle between the deionized water droplet and the sample surface was recorded every 5°s to draw a broken line graph. It can be seen from **Figure 12** that poplar wood is a hydrophilic material, and deionized water droplets can be absorbed by poplar wood. When the transparent sample is about 20°s, its contact angle

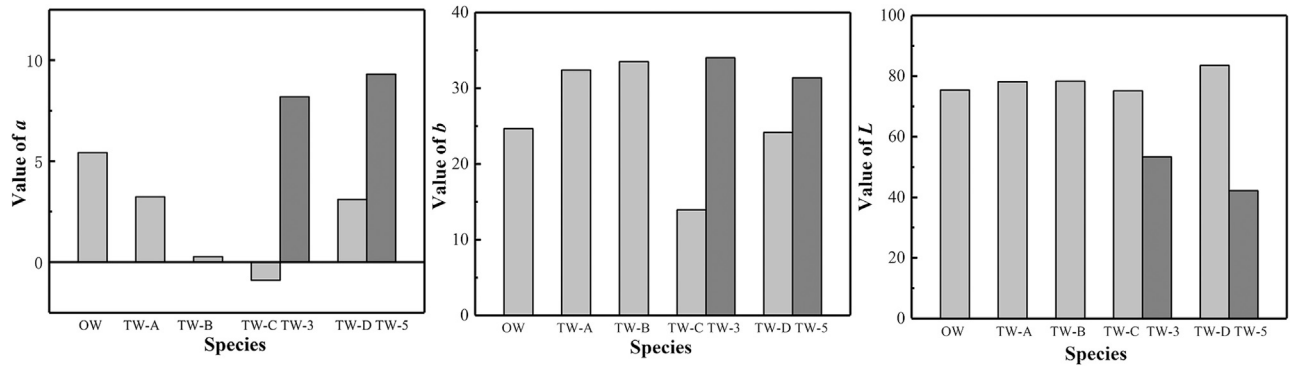

FIGURE 11 | *L*a*b* values of logs and transparent samples.

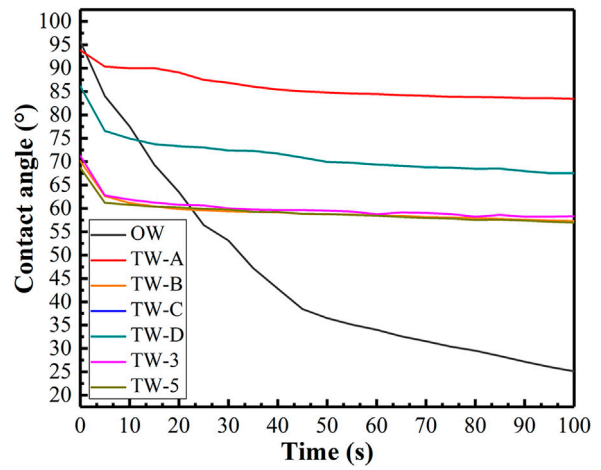

FIGURE 12 | The contact angle of logs and transparent samples over time.

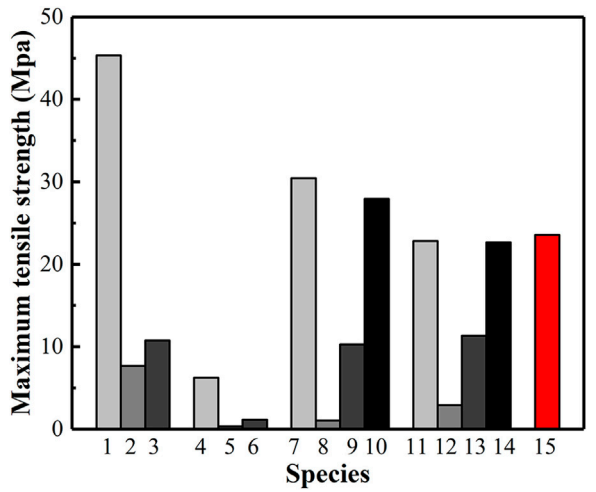

FIGURE 13 | Maximum tensile strength before and after treatment (1. A; 2. DW-A; 3. TW-A; 4. B; 5. DW-B; 6. TW-B; 7. C; 8. DW-C; 9. TW-C; 10. TW-3; 11. D; 12. DW-D; 13. TW-D; 14. TW-5; 15. E51).

begins to stabilize, showing a relatively stable state. This shows that transparent wood has improved the water absorption characteristics of wood to a certain extent, and can effectively reduce the wet expansion and shrinkage of wood due to moisture.

Mechanical Property Analysis

According to p = F/S, the maximum tensile strength of the sample can be calculated (Wu et al., 2020). In this text, S is the product of the h value and the b value in **Table 1**. From **Supplementary Material S1**, the weight loss of delignified wood and the weight proportion of wood components in transparent sample can be calculated. After delignification, the weight of wood will be reduced by 10–15%. It can be seen from **Figure 13** that after delignification, the maximum tensile strength of the sample is significantly reduced. However, after transparency treatment, the maximum tensile strength of the sample is improved, but it still does not reach the strength of the original sample. The weight of wood components in the single layer transparent wood prepared in this experiment accounts for 30–45% of the weight of composite materials, and the weight of wood components in the multilayer transparent wood accounts for about 30% of the weight of composite materials. In addition, it could be found that the maximum tensile strength of single layer transparent wood was about 10°Mpa, while the maximum tensile strength of multilayer transparent wood could reach about 25°Mpa. Obviously, the maximum tensile strength of multilayer transparent wood is greatly improved compared with the transparent wood with the same thickness, which indicates that the tensile strength of multilayer transparent wood is better than that of single layer transparent wood with the same thickness.

CONCLUSION

Single layer transparent wood and multilayer transparent wood can be successfully prepared by the technology adopted in this study. The weight of wood components in the transparent wood prepared in this experiment accounts for about 30–45% of the

weight of composite materials. It can be seen from the SEM images that the greater the thickness of wood is, the more cracks on the interface between epoxy resin and wood cell wall are, showing unsmooth morphological characteristics. There are obvious delamination interfaces in the multilayer transparent wood, compared with the single layer transparent wood with the same thickness. The bonding cracks between epoxy resin and cell wall are less, and the morphology is relatively smooth.

The transparent wood has a certain light transmittance. With the increase of the thickness, the cracks between the cells and the resin inside the transparent wood become more obvious, which leads to the decrease of the transparency. While, compared with the single layer transparent wood with the same thickness, the resin in the multilayer transparent wood combines well with the cell wall, with smaller cracks and relatively flat interface. And through the UV transmittance test, we could find that the transmittance of multilayer transparent wood is greater than that of single layer wood with the same thickness. At the same time, compared with the original wood, the multilayer transparent wood has a certain color difference. Perhaps, this is related to the oxidation of hemicellulose, and the residue of sodium chlorite and lignin. Compared with the single layer transparent wood with the same thickness, the brightness of the multilayer transparent wood decreases, and tends to be yellow and red, showing a transparent texture similar to amber.

In the preparation process, due to the large amount of lignin released, the wood structure was damaged to a certain extent, and the tensile strength of the wood decreased. Compared with untreated wood, the tensile strength of transparent wood was weakened. Multilayer transparent wood can improve this weakness, and its tensile strength is greater than that of single layer transparent wood with the same thickness. In addition, transparent wood can improve the water absorption property of wood to a certain extent, and can effectively reduce the moisture swelling and drying shrinkage of wood due to moisture.

In conclusion, the transmittance and mechanical properties of multilayer transparent wood are better than that of single layer transparent wood. Compared with the single layer transparent wood with the same thickness, the resin in the multilayer transparent wood is better combined with the cell wall, so the light transmittance of the multilayer transparent wood is higher than that of the single-layer transparent wood of the same thickness, and as the thickness increases, this advantage becomes more obvious. Besides, the maximum tensile strength of multilayer transparent wood is more than two times that of single layer transparent wood with the same thickness. Combined with the current process conditions, transparent wood is restricted by the thickness direction. Therefore, multilayer transparent wood can be prepared by lamination, so as to obtain materials with large thickness, high transmittance and excellent mechanical properties. Multilayer transparent wood has a good development prospect in the future.

DATA AVAILABILITY STATEMENT

The original contributions presented in the study are included in the article/**Supplementary Material**, further inquiries can be directed to the corresponding authors.

AUTHOR CONTRIBUTIONS

YWu contributed to conception and design of the study. YWa organized the database, performed the statistical analysis,and wrote the first draft of the manuscript. FY provided the funding support. All authors contributed to manuscript revision, read, and approved the submitted version.

FUNDING

This work was financially supported by the National Natural Science Foundation of China (32071687 and 32001382), the Special Scientific Research Fund of Construction of High-Level Teachers Project of Beijing Institute of Fashion Technology (BIFTQG201805), and the Project of Science and Technology Plan of Beijing Municipal Education Commission (KM202010012001).

ACKNOWLEDGMENTS

I am very grateful to college of Furnishings and Industrial Design of Nanjing Forestry University for their careful training, the teachers and students of 7A331 Laboratory for their help to me, and the help of network resources provided by Nanjing Forestry University to me.

SUPPLEMENTARY MATERIAL

The Supplementary Material for this article can be found online at: https://www.frontiersin.org/articles/10.3389/fmats.2021.633345/full#supplementary-material.

REFERENCES

Cabane, E., Keplinger, T., Künniger, T., Merk, V., and Burgert, I. (2016). Functional lignocellulosic materials prepared by ATRP from a wood scaffold. *Sci. Rep.* 6, 31287. doi:10.1038/srep31287

Cabane, E., Keplinger, T., Merk, V., and Hass, P. (2014). Renewable and functional wood materials by grafting polymerization within cell walls. *ChemSusChem* 7, 1020–1025. doi:10.1002/cssc.201301107

Chen, H., Baitenov, A., Li, Y., Vasileva, E., Popov, S., Sychugov, I., et al. (2019). Thickness dependence of optical transmittance of transparent wood: Chemical modification effects. *ACS Appl. Mater. Interfaces* 11, 35451–35457. doi:10.1021/acsami.9b11816

Dong, H., Zheng, L., Yu, P., Jiang, Q., Wu, Y., Huang, C., et al.(2020). Characterization and application of lignin-carbohydrate complexes from lignocellulosic materials as antioxidants for scavenging *in vitro* and *in vivo* reactive oxygen species. *ACS Sustainable Chem. Eng.* 8, 256–266. doi:10.1021/acssuschemeng.9b05290

Fang, L., Xiong, X., Wang, X., Chen, H., and Mo, X. (2017). Effects of surface modification methods on mechanical and interfacial properties of high-density polyethylene-bonded wood veneer composites. *J. Wood Sci.* 63, 65–73. doi:10.1007/s10086-016-1589-9

Fink, S. (1992). Transparent wood - A new approach in the functional study of wood structure. *Holzforschung* 46, 403–408. doi:10.1515/hfsg.1992.46.5.403

Foster, K., Hess, K., Miyake, G., and Srubar, W.V. (2019). Optical properties and mechanical modeling of acetylated transparent qood composite laminates. *Materials* 12, 2256. doi:10.3390/ma12142256

Gan, W., Xiao, S., Gao, L., Gao, R., Li, J., and Zhan, X. (2017). Luminescent and transparent wood composites fabricated by poly(methyl methacrylate) and γ-Fe2O3@YVO4:Eu3+ nanoparticle impregnation. *ACS Sustainable Chem. Eng.* 5, 3855–3862. doi:10.1021/acssuschemeng.6b02985

Gao, K., Shao, Z., Wu, X., Wang, X., Li, J., Zhang, Y., et al. (2013). Cellulose nanofibers/reduced graphene oxide flexible transparent conductive paper. *Carbohydrate Polymers* 97, 243. doi:10.1016/j.carbpol.2013.03.067

Iwamoto, S., Nakagaito, A. N., Yano, H., and Nogi, M. (2005). Optically transparent composites reinforced with plant fiber-based nanofibers. *Appl. Phys. A.* 81, 1109–1112. doi:10.1007/s00339-005-3316-z

Jia, C., Li, T., Chen, C., Dai, J., Kierzewski, I. M., Song, J., et al. (2017). Scalable, anisotropic transparent paper directly from wood for light management in solar cells. *Nano Energy* 36, 366–373. doi:10.1016/j.nanoen.2017.04.059

Li, H., Guo, X., He, Y., and Zheng, R. (2019). House model with 2-5 cm thick translucent wood walls and its indoor light performance. *Eur. J. Wood Prod.* 77, 843–851. doi:10.1007/s00107-019-01431-w

Li, T., Zhu, M., Yang, Z., Song, J., Dai, J., Yao, Y., et al. (2016c). Wood composite as an energy efficient building material: guided sunlight transmittance and effective thermal insulation. *Adv. Energy Mater.* 6, 1601122. doi:10.1002/aenm.201601122

Li, Y., Fu, Q., Rojas, R., Yan, M., Lawoko, M., and Berglund, L. (2017). Lignin-retaining transparent wood. *ChemSusChem* 10, 3445–3451. doi:10.1002/cssc.201701089

Li, Y., Fu, Q., Yu, S., Yan, M., and Berglund, L. (2016a). Optically transparent wood from a nanoporous cellulosic template: Combining functional and structural performance. *Biomacromolecules* 17, 1358–1364. doi:10.1021/acs.biomac.6b00145

Li, Y., Yu, S., Veinot, J. G. C., Linnros, J., Berglund, L., and Sychugov, I. (2016b). Luminescent transparent wood. *Adv. Opt. Mater.* 5, 1600834. doi:10.1002/adom.201600834

Liu, X., Song, X., and Wu, Y. (2010). Study on hot-pressing technology of the chinese fir plywood. *Fujian Academy of Forestry* 37, 77–80. doi:10.3969/j.issn.1002-7351.2010.03.016

Mi, R., Chen, C., Keplinger, T., Pei, Y., He, S., Liu, D., et al. (2020). Scalable aesthetic transparent wood for energy efficient buildings. *Nat. Commun.* 11. doi:10.1038/s41467-020-17513-w

Notburga, G., Luna, G., Martin, S., Ingo, B., Catherine, C., Tilmann, R., et al. (2008). Situ FT-IR microscopic study on enzymatic treatment of poplar wood cross-sections. *Biomacromolecules* 9, 2194–2201. doi:10.1021/bm800300b

Qin, J., Bai, T., Shao, Y., Shao, X., Li, S., and Hu, Y. (2018). Preparation and characterization of multilayer transparent wood from different tree species. *J. Beijing For. Univ.* 40, 114–120.

Rana, R., Langenfeld-Heyser, R., Finkeldey, R., and Polle, A. (2010). FTIR spectroscopy, chemical and histochemical characterisation of wood and lignin of five tropical timber wood species of the family of Dipterocarpaceae. *Wood Sci. Technol.* 44, 225–242. doi:10.1007/s00226-009-0281-2

Tang, Q., Fang, L., Wang, Y., Zou, M., and Guo, W. (2018). Anisotropic flexible transparent films from remaining wood microstructures for screen protection and AgNW conductive substrate. *Nanoscale* 10, 4344–4353. doi:10.1039/c7nr08367j

Vasileva, E., Li, Y., Sychugov, I., Mensi, M., Berglund, L., and Popov, S. (2017). Lasing from organic dye molecules embedded in transparent wood. *Adv. Opt. Mater.* 5, 1700057. doi:10.1002/adom.201700057

Vay, O., De Borst, K., Hansmann, C., Ller, AT., and Muller, U. (2015). Thermal conductivity of wood at angles to the principal anatomical directions. *Wood Sci. Technol.* 49, 577–589. doi:10.1007/s00226-015-0716-x

Wang, Y., Sun, G., Dai, J., Chen, G., Morgenstern, J., Wang, Y., et al. (2017). A high-performance, low-tortuosity wood-carbon monolith reactor. *Adv. Mater.* 29, 1604257. doi:10.1002/adma.201604257

Wang, Z., Kang, H., Liu, H., Zhang, S., Xia, C., Wang, Z., et al. (2020). Dual-Network Nanocross-linking Strategy to Improve Bulk Mechanical and Water-Resistant Adhesion Properties of Biobased Wood Adhesives. *ACS Sustainable Chem. Eng.* 8, 16430–16440. doi:10.10.1021/acssuschemeng.0c04913

Wu, Y., Zhou, J., Huang, Q., Yang, F., Wang, Y., and Wang, J. (2020). Study on the properties of partially transparent wood under different delignification processes. *Polymers* 12, 661. doi:10.3390/polym12030661

Xia, C., Lam, S., and Sonne, C. (2020). Ban unsustainable mink production. *Science* 370, 1. doi:10.1126/science.abf0461

Yu, Z., Yao, Y., Yao, J., Zhang, L., Chen, Z., Gao, Y., et al. (2017). Transparent wood containing CsxWO3 nanoparticles for heat-shielding window applications. *J. Mater. Chem. A* 5, 6019–6024. doi:10.1039/C7TA00261K

Zhao, J. (2016). Study on the main performance characterization technology of bisphenol a epoxy resin system. Dissertation. Qingdao (China): Qingdao University of Science and Technology.

Zhu, M., Song, J., Li, T., Gong, A., Wang, Y., and Dai, J. (2016). Highly anisotropic, highly transparent wood composites. *Adv. Mater.* 28, 5181–5187. doi:10.1002/adma.201600427

Conflict of Interest: The authors declare that the research was conducted in the absence of any commercial or financial relationships that could be construed as a potential conflict of interest.

frontiers in Materials

ORIGINAL RESEARCH
published: 18 March 2021
doi: 10.3389/fmats.2021.651581

Experimental Study of the Dynamic Compressive and Tensile Strengths of Fly Ash and Slag Based Alkali-Activated Concrete Reinforced With Basalt Fibers

Chong Lian[1,2], *Yubo Wang*[2], *Shan Liu*[2]* *and Yifei Hao*[2]*

[1] Shock and Vibration of Engineering Materials and Structures Key Laboratory of Sichuan Province, Mianyang, China,
[2] School of Civil Engineering, Tianjin University, Tianjin, China

OPEN ACCESS

Edited by:
Faiz Uddin Ahmed Shaikh,
Curtin University, Australia

Reviewed by:
Genwei Wang,
Taiyuan University of Technology, China
Vilma Ducman,
Slovenian National Building and Civil Engineering Institute, Slovenia

***Correspondence:**
Shan Liu
shan_liu@tju.edu.cn
Yifei Hao
hao.yifei@tju.edu.cn

Specialty section:
This article was submitted to Structural Materials, a section of the journal Frontiers in Materials

Received: 10 January 2021
Accepted: 23 February 2021
Published: 18 March 2021

Citation:
Lian C, Wang Y, Liu S and Hao Y (2021) Experimental Study of the Dynamic Compressive and Tensile Strengths of Fly Ash and Slag Based Alkali-Activated Concrete Reinforced With Basalt Fibers. Front. Mater. 8:651581. doi: 10.3389/fmats.2021.651581

The use of industrial by-products, e.g., fly ash, slag, as complete replacement of Portland cement to make alkali-activated concrete (AAC) has become a hot topic due to the contribution to sustainability in construction industry. AAC has comparable compressive strength compared to the ordinary Portland cement concrete (OPC) and has many advantages, such as excellent durability and corrosion resistance. However, similar to OPC, AAC material still has certain shortcomings such as brittleness, low tensile strength, and poor impact resistance, which can be improved by incorporating fibers in the matrix. This paper considers the basalt fiber-reinforced alkali-activated concrete (BFRAAC), and explores the dynamic compressive and tensile strengths through a series of impact tests. The test results show that the dynamic strength of BFRAAC exhibits significant strain rate effect, that is, the material strength increases with the strain rate. Compared to the compressive strength of the material, the strain rate sensitivity of its tensile strength is more marked. Based on the test results, empirical formulas describing the relation between dynamic strength and strain rate of BFRAAC are proposed.

Keywords: alkali-activated concrete, basalt fiber, dynamic compression, dynamic tension, high strain rate

INTRODUCTION

In recent years, alkali-activated concrete (AAC) made of industrial by-products has drawn wide attention (Shaikh and Supit, 2014). AAC is the class of cement free concrete, where the binding phase is derived from the reaction of an alkali metal source with solid calcium silicate or/and aluminosilicate-rich precursors. At present, fly-ash, by-product during coal combustion, and slag, by-product from steel industry, are the main raw materials for the synthesis of AAC with alkaline solutions. The make of AAC can turn a large amount of by-products to resources, which is also beneficial to the environment. Moreover, using AAC to replace ordinary Portland cement concrete (OPC) can also achieve the goal of reducing greenhouse gas emissions for sustainable development in construction industry (Benhalal et al., 2012).

Compared to OPC, previous studies have demonstrated the more excellent durability of AAC (Fernandez-Jimenez et al., 2007). Geiseler et al. pointed out that the use of slag in AAC can greatly improve the ability of concrete to resist chloride (Geiseler et al., 1995). Luga et al. studied the residual strength of fly ash and slag based alkali-activated mortar (AAM) after 45 dry-wet cycles and found that the compressive strength of AAM was increased by 23.9% while that of ordinary Portland cement mortar was decreased from 55 to 18 MPa (Luga, 2015). The excellent resistance to acid and alkali corrosion of AAC was proven by García-Lodeiro et al. (2007). Ana et al. carried out tests and observed good fire resistance of AAC (Ana et al., 2006). By incorporating hydrotalcite into AAC mix, Liu et al. have successfully improved the anti-carbonization performance of AAC and laid the foundation for its structural application (Liu et al., 2021). Besides the durability performance, the quasi-static mechanical properties of AAC have also been widely studied. The quasi-static mechanical properties of AAC have been obtained through uniaxial compression, uniaxial tension, split tension, and bending tests (Deb et al., 2014). The performance of AAC in terms of mechanical properties and durability in comparison with OPC have been well-demonstrated (Ganesan et al., 2014; Haider et al., 2014; Noushini et al., 2016). Based on the study of the mechanical properties of AAC, Tran et al. analyzed the stress characteristics of AAC in structural members, and provided guidance for the structural design with the use of this new type of material (Tran et al., 2019).

As one of the key indicators of structural resistance to highly dynamic loads such as blast and impact, the dynamic strength of AAC has also received widespread attention. Previous study has shown that the dynamic compressive strength of AAC is sensitive to strain rate, and the strain rate sensitivity is dependent on the mix proportion, alkali solution content, curing conditions, etc. (Khan et al., 2018a). Khandelwal et al. studied the dynamic compressive characteristics of high temperature cured alkali-activated mortar under four different strain rates. The results showed that the ultimate compressive strength of AAM increased with the increase of strain rate (Khandelwal et al., 2013). Xin et al. studied the dynamic mechanical properties of AAM with different mix proportions and alkali solutions (Xin et al., 2014). Khan et al. studied the dynamic compressive and splitting tensile strengths of AAM (Khan et al., 2018a). Luo et al. studied the dynamic splitting tensile properties of high-fluidity AAC (Luo and Xu, 2013). Feng et al. studied the dynamic tensile properties of alkali-activated mortar at strain rates ranging from 10^{-7} to 25 s^{-1} (Feng et al., 2014). Menna et al. also conducted a dynamic tensile test of AAC under high-rate loading (Menna et al., 2015).

Similar to OPC, AAC also possesses shortcomings such as being brittle and having low tensile strength and poor resistance to cracking. The addition of short discrete fibers can effectively improve the tensile strength and ductility of AAC to a certain extent. At present, the use of steel fibers or synthetic fibers is the most popular way to reinforce concrete (Ohno and Li, 2014; Khan et al., 2018b). In recent years, basalt fiber has received a lot of attention due to its high tensile strength, low cost, and good corrosion resistance (Sim and Park, 2005). The reinforcing effectiveness of basalt fibers on AAM under quasi-static load has been verified (Punurai et al., 2018). The positive effect of basalt fiber reinforcement on the dynamic compressive strength of AAC was studied (Li and Xu, 2009), where the strain rate achieved in the tests were limited to 100 s^{-1}. However, the contribution of basalt fiber to the dynamic tensile strength of AAC has not yet been studied.

To further understand the reinforcing effects of basalt fibers on the compressive and tensile strengths, this study carried out a series of impact tests on basalt fiber reinforced alkali-activated concrete (BFRAAC). Split Hopkinson pressure bar test system was used to study the dynamic compressive strengths of BFRAAC. INSTRON high strain rate test system was used to carry out splitting tensile tests, while the modified Hopkinson pressure bar test system was adopted to perform spall tests on BFRAAC specimens to achieve different ranges of tensile strain rate. Based on the test results, the dynamic compressive and tensile strengths of BFRAAC material are formulated with respect to strain rate, which provides important reference that needs to be considered in design and analysis of AAC structures subjected to dynamic loadings.

MATERIALS AND PREPARATION OF BFRAAC SPECIMENS

The basalt fiber used in the test is a fiber bundle (12 × 0.9 × 17 μm) by bonding a number of individual fibers with resin as shown in **Figure 1**. The tensile strength of the fiber is 1300 MPa, and the elastic modulus is 53.6 GPa. The BFRAAC specimens were initially considered with different dosages (0.5, 1.0, and 1.5%) of fibers in the mixture. It was found that during the cast of specimens, adding fibers up to 1% can assure the workability of fresh BFRAAC while adding 1.5% fibers resulted in significant fiber balling and more defects in the mixture. Therefore, 1% addition of the basalt fibers was eventually selected to prepare the specimens based on the anti-carbonation AAC mix proposed in Liu et al. (2021). The maximum size of coarse aggregates is limited to 10 mm. The mix proportions of BFRAAC are given in **Table 1**. The basalt fibers were added into the freshly mixed AAC and were mixed for another 2 min to achieve even distribution. The mixture was then poured into cylindrical PVC molds, vibrated and compacted by the shaking table. After that, the end of the PVC tubes were covered by plastic and left in the laboratory environment for 1 day. The specimens were then demolded and placed in the curing room with 25°C and 95% relative humidity for 28 days. Before the tests, the cylindrical specimens were cut into the sizes requested in different test schemes and were ground to assure flat and parallel ends. In this study, the Ø100 × 200 mm and Ø70 ×3 5 mm specimens were prepared for determining the quasi-static compressive and splitting tensile strengths, respectively, of BFRAAC material. In impact tests, the Ø70 × 35 mm specimens were prepared for testing the material strengths under dynamic compression and dynamic splitting tension while the Ø50 × 300 mm specimens were prepared for conducting spall tests to achieve higher tensile strain rates. The quasi-static compressive and splitting tensile strengths of BFRAAC are 39.3 and 3.62 MPa, respectively. The

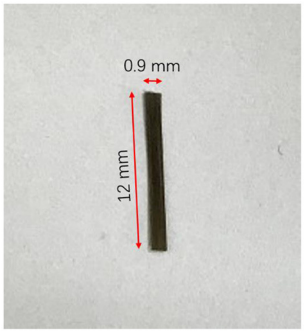

FIGURE 1 | Basalt fiber.

TABLE 1 | Mix proportion of BFRAAC (kg for 1 m^3 of BFRAAC).

Fly ash	Slag	Na_2SiO_3	NaOH	Water	Sand	Stone	Hydrotalcite	Basalt fiber
208	208	160.53	19.73	152.33	708.33	1062.5	25	26.2

Young's modulus of BFRAAC is 24 GPa. These values are used as reference to quantify the dynamic strengths of BFRAAC material at high strain rates.

DYNAMIC COMPRESSIVE TESTS

Test Setup and Method

The dynamic compressive tests on BFRAAC material were carried out by split Hopkinson pressure bar (SHPB) system. As shown in **Figure 2**, the SHPB system includes the impact bar, incident bar, transmission bar, absorption bar, and other components. The bars are made of stainless steel and have the same diameter of 75 mm. The Ø70 × 35 mm cylindrical specimen was placed in between the incident and the transmission bars with the application of grease at specimen-bar interfaces to eliminate the friction. A copper disc as a wave shaper was attached onto the impact end of the incident bar receiving the compressive stress wave from the impact bar. Strain gauges were glued onto the surface at the mid length of the incident and transmission bars to record the incident, reflected and transmitted stress waves. A data acquisition device with frequency of 20 MHz was used to record the strain signals in voltage. An oscilloscope was adopted to monitor the waveforms in the incident and transmission bars. The strain rate in the specimens in SHPB tests can be varied by adopting different levels of pressure in the chamber.

The principle of SHPB test is based on the theory of one-dimensional stress wave propagation in elastic circular bars. This technique is one of the primary methods to study the properties of materials at high strain rates (Balendran et al., 2002). The reliability of the SHPB test results is based on the following two assumptions, namely (1) the one-dimensional stress wave propagation and (2) the stress and strain are uniformly distributed along the length of the specimen (Davies, 1948). According to the one-dimensional stress wave theory, the stress $\sigma(t)$, strain rate $\dot{\varepsilon}(t)$ and strain $\varepsilon(t)$ of the specimen can be calculated by the following three formulas (Khan et al., 2018a).

$$\sigma(t) = E\left(\frac{A}{A_s}\right)\varepsilon_t(t) \tag{1}$$

$$\dot{\varepsilon}(t) = -\frac{2C_0}{L}\varepsilon_r(t) \tag{2}$$

$$\varepsilon(t) = -\frac{2C_0}{L}\int_0^t \varepsilon_r(t)d\tau \tag{3}$$

where $\varepsilon_t(t)$ and $\varepsilon_r(t)$ are the strain histories recorded in the transmission and incident bars, respectively, E and A are the Young's modulus and cross-sectional area of the bars respectively, A_s and L are the cross-sectional area and length of the tested specimen, respectively, and C_0 is the wave velocity in the bars.

The calculated stress and strain rate from recorded strain signals from a typical SHPB compressive test are presented in **Figure 3**. As shown, the value of the strain rate corresponding to the same time instant when the stress reaches its peak is determined as the strain rate of the specimen.

Failure Mode of BFRAAC

The failure mode of BFRAAC is shown in **Figure 4**. It can be seen that the addition of basalt fibers improves the brittleness of AAC material. This can be understood that when cracks were initiated and propagated in the specimen, the basalt fibers along the path of cracks were subjected to pullout load and provide additional energy consumption. Therefore, the cracked parts can be bridged by the added basalt fibers so that the structural integrity of the specimen was kept to some extent.

Strain Rate Effect on BFRAAC Compressive Properties

The stress-strain curves of BFRAAC specimens obtained from SHPB compression tests at different strain rates are shown in **Figure 5**. It can be seen from the figure that with the increase of strain rate, the compressive strength of BFRAAC generally increases, demonstrating the significant strain rate effect.

The dynamic increase factor (DIF, ratio of dynamic to quasi-static strength) is adopted to quantify the strain rate effect on BFRAAC compressive strengths. The relation between DIF of BFRAAC and strain rate from SHPB compression tests is given in **Figure 6**. The lines in the figure represent the fitted relations of the scattered data as defined by Equations 4and 5. It can be seen from the figure that the value of DIF increases with the increase of strain rate. It should be noted that due to the limitation of testing apparatus, the strain rates achieved by SHPB compressive tests cannot be lower than 100/s, which results in the gap between quasi-static and high strain rate conditions. Therefore, a linear relation is assumed in this range, following the common practices in existing studies. The maximum dynamic compressive strength of BFRAAC can be almost twice the static compressive strength.

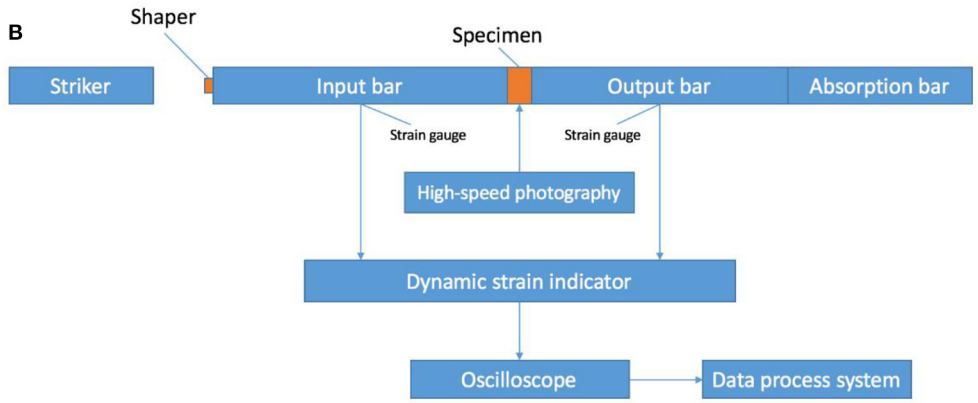

FIGURE 2 | SHPB test system **(A)** photograph **(B)** schematic illustration.

This can be understood that at relatively higher strain rate, more cracks are generated to consume the input energy in the specimen. Moreover, unlike the quasi-static tests in which the cracks mainly propagate via weak parts, i.e., interfacial transition zone between mortar matrix and aggregates, in the specimen, at high strain rate, the cracks have to propagate through coarse aggregates with higher toughness and strength than the mortar matrix, resulting in higher compressive strength of the BFRAAC specimen.

$$CDIF_\sigma = 0.03129\left(\log\dot{\varepsilon}\right) + 1.09388 \text{ for } 10^{-3}/s \leq \dot{\varepsilon} \leq 105.19/s \quad (4)$$

$$CDIF_\sigma = 1.33333\left(\log\dot{\varepsilon}\right) - 1.65711 \text{ for } 105.19/s \leq \dot{\varepsilon} \leq 385.45/s \quad (5)$$

DYNAMIC TENSILE TESTS

Dynamic Splitting Tensile Tests

The dynamic splitting tensile tests on BFRAAC specimens were carried out by using INSTRON high strain rate testing system with force capacity of 100 kN. The test setup is shown in **Figure 7A**. The Ø70 × 35 mm specimens were diametrically placed on the loading platen so that the vertical compressive force can induce splitting tensile stress in the specimen. To avoid stress concentration and compressive failure between specimen and loading platens, wood strips were placed on the upper and lower sides of the cylindrical specimen. The thickness and width of the wood strips are 2.5 and 20 mm, respectively. It should be noted that the influence of the thickness of wood strip on quasi-static or dynamic splitting tensile test results has not been studied. It is

a very interesting topic that should be addressed in future studies. The applied vertical load was recorded by the built-in sensor. The failure mode and distribution of fibers in the matrix are shown in **Figure 7B**. According to the theory of elasticity, the maximum horizontal tensile stress is located at the center of the cylinder. Accordingly, the splitting tensile strength σ_t and strain rate $\dot{\varepsilon}$ of the specimen can be calculated by Equations 6 and 7 (Hao et al., 2016). The strain rate obtained from impact splitting tensile tests on BFRAAC ranges from 0.15 to 2 s^{-1}.

$$\sigma_t = \frac{2P}{\pi DB}\left[1-(b/D)^2\right]^{3/2} \quad (6)$$

$$\dot{\varepsilon} = \frac{\sigma_t}{E_s \times (t_1 - t_0)} \quad (7)$$

where P is the peak vertical load, D and B are the diameter and thickness of the cylindrical specimen, respectively, b is the width of the wood strip for the split tensile test, E_s is the Young's modulus of specimen, and t_0 and t_1 are time instants corresponding to the initiation and peak of the stress.

Spall Tests

The strain rate obtained from dynamic splitting tensile tests is limited to 2 s^{-1}. To achieve higher strain rates, spall tests on Ø50 × 300 mm BFRAAC specimens were further conducted using modified SHPB test system, with removal of transmission bar, as shown in **Figure 8**. The rod specimen was pasted at the end of the incident bar. A copper disc was adopted as wave shaper. Apart from strain gauges at the mid length on the incident bar, additional strain gauges were attached on the surface along the length of the specimen with 50 mm intervals to record the waveform and histories. In spall test, when the impact bar hits the incident bar, a compressive stress wave is generated and propagated in the incident bar. Upon reaching the bar/specimen interface, a portion of the

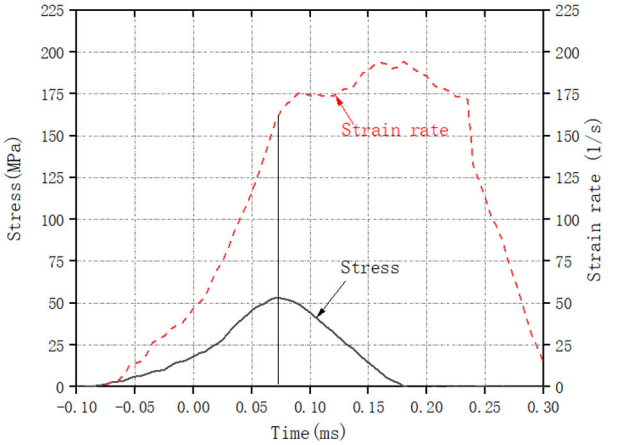

FIGURE 3 | Typical stress and strain rate histories from SHPB test.

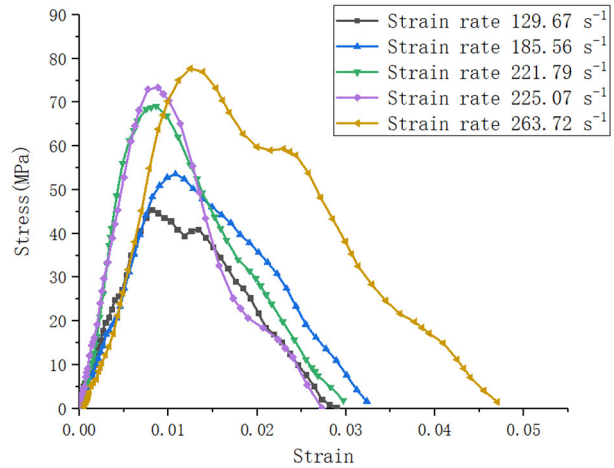

FIGURE 5 | Typical compressive stress-strain relations of BFRAAC at different strain rates.

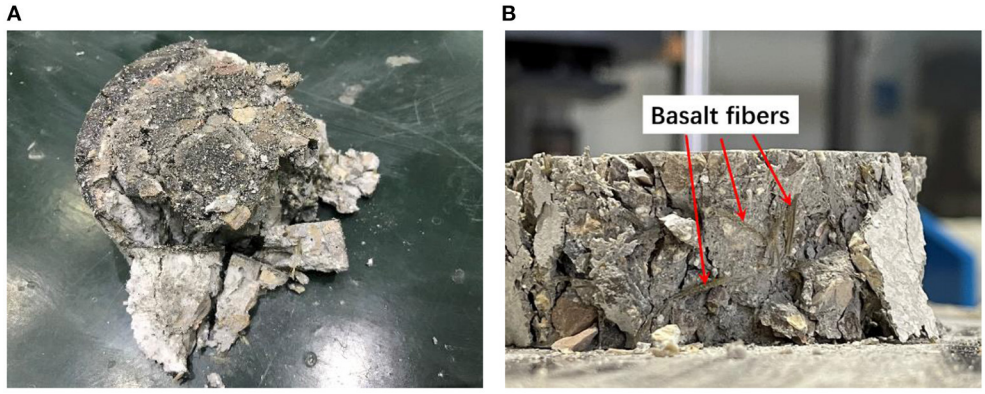

FIGURE 4 | Illustration of the failure mode of BFRAAC under dynamic compression at strain rate of 129.67 s^{-1}. **(A)** Damage and integrity of specimen after impact. **(B)** Fiber distribution in the matrix.

compressive stress wave is transmitted into the specimen and reflected as a tensile wave at the free end of the specimen. Because the tensile strength of BFRAAC is far less than its compressive strength, the tensile stress wave may cause the specimen to be fractured, namely spalled as shown in **Figure 9**. It should be noted that in spall tests, the incident stress wave should be well-controlled to avoid compressive damage to the specimen before the compressive stress wave is reflected as tensile wave.

In spall tests, the theory of one-dimensional stress wave propagation is used to calculate the dynamic tensile strength of BFRAAC material. The wave speed in the tested specimen can be calculated according to the different initiation time instants recorded by the series of strain gauges on the specimen and the intervals among the strain gauges. The reflected tensile stress wave is calculated according to the incident compressive stress waveform, the superposition of compressive and tensile stress waves, and the distance between the free end and the first fracture of the specimen. The dynamic tensile strength of the specimen is determined by the superimposed waveform at the first fracture location. Accordingly, the strain rate of the BFRAAC specimen in spall test is calculated by Equation 8. The strain rate obtained from spall tests on BFRAAC ranges from 10 to 94.5 s^{-1}.

$$\dot{\varepsilon} = \frac{\sigma_d}{E_s \times t} \tag{8}$$

where σ_d is the tensile strength in spall test and t is the time for reflected tensile stress wave to propagate from free end of the specimen and the fracture location.

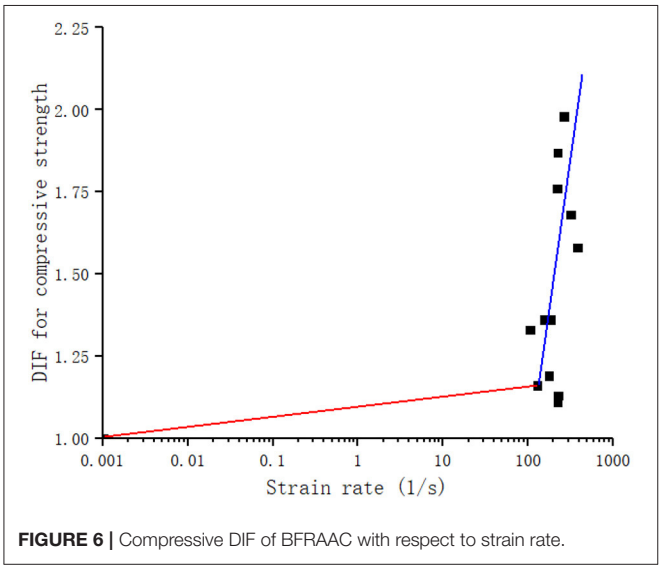

FIGURE 6 | Compressive DIF of BFRAAC with respect to strain rate.

Strain Rate Effect on BFRAAC Tensile Strengths

Based on the results from impact splitting tensile tests and spall tests, the strain rate effects on the tensile strength of BFRAAC material are illustrated in **Figure 10**. As can be seen, similar to compressive DIFs, the tensile DIF of BFRAAC increases with strain rate. Also due to the limitation of testing apparatus, the strain rates achieved in dynamic splitting tensile tests cannot be lower than 0.1/s. Thus, a linear relation is assumed between quasi-static and high strain rate conditions. Empirical formulas are proposed by fitting the scattered data to describe the relation between tensile strength and strain rate as given in Equations 9 and 10.

$$TDIF_\sigma = 0.11973\left(\log\dot{\varepsilon}\right) + 1.59865 \quad \text{for } 10^{-5}/s \le \dot{\varepsilon} \le 0.15/s \tag{9}$$

$$TDIF_\sigma = 2.76717\left(\log\dot{\varepsilon}\right)^2 + 0.78838\left(\log\dot{\varepsilon}\right) + 0.27119 \quad \text{for } 0.15/s \le \dot{\varepsilon} \le 94.5/s \tag{10}$$

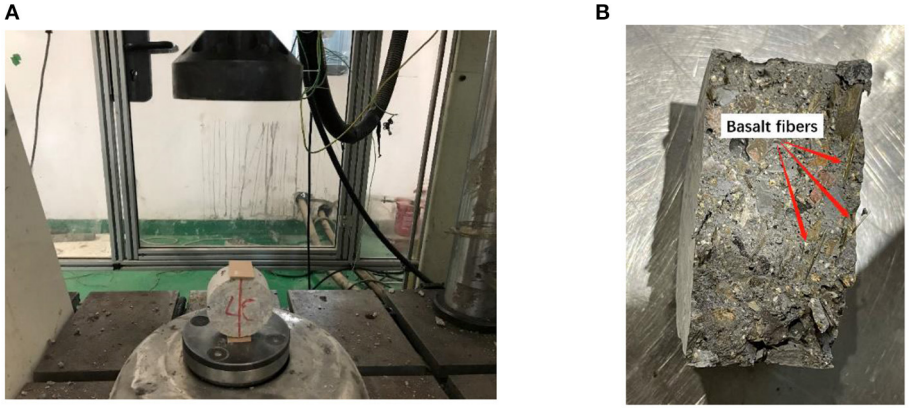

FIGURE 7 | Illustration of dynamic splitting tensile test setup and failure mode of BFRAAC. **(A)** Test setup. **(B)** Failure mode.

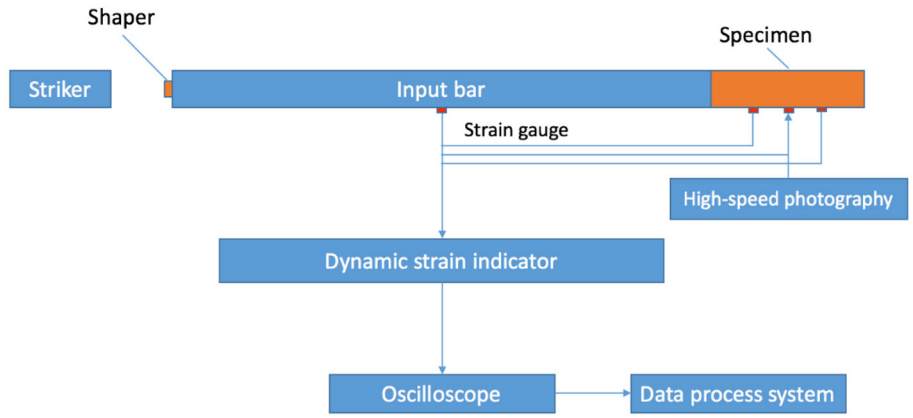

FIGURE 8 | Plan view of the setup of spall test.

FIGURE 9 | Illustration of the failure mode of BFRAAC in spall test at strain rate of 56.8 s^{-1}.

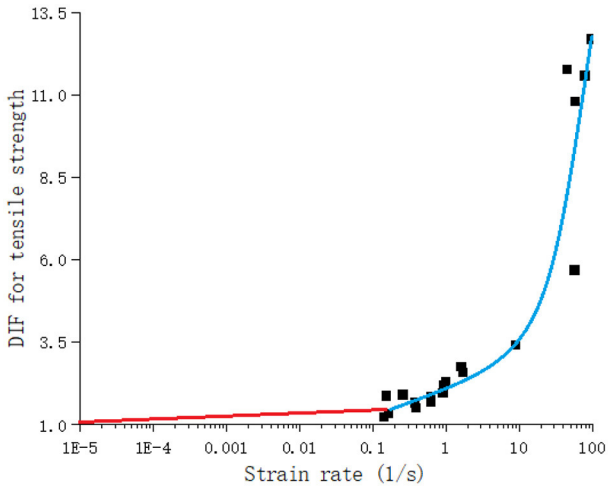

FIGURE 10 | Tensile DIF of BFRAAC with respect to strain rate.

DISCUSSIONS ON THE INERTIA EFFECT IN DYNAMIC TESTS

It is known that inertia in dynamic tests of quasi-brittle materials might influence the testing results, and its influence is dependent on the specimen size and strain rate. For the tests presented in the present study, inertia effect due to lateral confinement is of major concern, which is related to the mechanical properties of the material under triaxial stress state. With regard to the lateral inertia effect on concrete strengths in dynamic compressive tests, it is found that the contribution of lateral inertia of Ø100 mm diameter specimens to the test results is up to 15% for strain rate below 300/s (Hao et al., 2010). In the present study, the tested specimens have smaller diameter (70 vs. 100 mm in Hao et al., 2010), thus less significant influence from lateral inertia confinement. With regard to dynamic splitting tensile tests, it has been reported that the inertia effect only becomes significant when the strain rate is higher than 6/s (Hao and Hao, 2016). In this study, the maximum strain rate achieved in splitting tensile tests is only 2/s. Moreover, spall tests mainly rely on stress wave propagation in long specimen, which is fractured by reflected tensile stress wave rather than the deformation of the specimen itself. Therefore, it is reasonable to deduce that the inertia effect on the dynamic compressive strength of BFRAAC is <15% while in dynamic tensile tests the inertia effect can be ignored. Nonetheless, further study is needed to quantify the mechanical properties of BFRAAC under triaxial loading to identify the sensitivity of material strength to confining pressure, based on which the evaluation of the influence of lateral inertia confinement in dynamic compressive tests can be conducted.

CONCLUSIONS

The dynamic compressive and tensile strengths of basalt fiber reinforced alkali-activated concrete (BFRAAC) material are experimentally investigated in the present study. Tests adopting split Hopkinson pressure bar (SHPB) system, INSTRON high strain rate system and modified SHPB system were carried out to determine the compressive and tensile strengths at high strain rates. It is found that the strengths of BFRAAC material are significantly enhanced with the increase of strain rate. Through the series of tests, the strain rate effects on compressive and tensile strengths of BFRAAC material are analyzed. Empirical relations of the dynamic increase factor and strain rate are proposed based on test data to formulate the strain rate effect. The proposed relations can be used in design and analysis of BFRAAC structures subjected to blast and impact loadings.

DATA AVAILABILITY STATEMENT

The original contributions presented in the study are included in the article/supplementary material, further inquiries can be directed to the corresponding authors.

AUTHOR CONTRIBUTIONS

CL: methodology, validation, formal analysis, investigation, data curation, and writing-original draft. YW: methodology and validation. SL: methodology, investigation, writing-review, and editing. YH: conceptualization, methodology, writing-review, editing, supervision, project administration, and funding acquisition. All authors contributed to the article and approved the submitted version.

FUNDING

The authors would like to acknowledge financial supports from Shock and Vibration of Engineering Materials and Structures Key Laboratory of Sichuan Province, National Natural Science Foundation of China (grant number: 51778415), Natural Science Foundation of Tianjin (grant number: 17JCYBJC42600), Natural Science Foundation of Hebei Province (E2020402079), and National Key Research and Development Program of China (grant number: 2019YFC1907202) for carrying out this study.

REFERENCES

Ana, M., Fernandez-Jimenez, A. P., and Cecilio, L. H. (2006). Engineering properties of alkaliactivated fly ash concrete. *ACI Mater. J.* 103, 106–112. doi: 10.14359/15261

Balendran, R. V., Zhou, F. P., Nadeem, A., and Leung, A. Y. T. (2002). Influence of steel fibres on trength and ductility of normal and lightweight high strength concrete. *Build. Environ.* 37, 1361–1367. doi: 10.1016/S0360-1323(01)00109-3

Benhalal, E., Zahedi, G., Shamsaei, E., and Bahodori, A. (2012). Global strategies and potentials to curb CO_2 emissions in cement industry. *J. Clean. Prod.* 51, 142–161. doi: 10.1016/j.jclepro.2012.10.049

Davies, R. M. (1948). A critical study of the Hopkinson pressure bar. *Philos. Trans. R. Soc. London Ser. A Math. Phys. Sci.* 240, 375–457. doi: 10.1098/rsta.1948.0001

Deb, P. S., Nath, P., and Sarker, P. K. (2014). The effects of ground granulated blast-furnace slag blending with fly ash and activator content on the workability and strength properties of geopolymer concrete cured at ambient temperature. *Mater. Design* 62, 32–39. doi: 10.1016/j.matdes.2014.05.001

Feng, K. N., Ruan, D., Pan, Z., Collins, F., Bai, Y., Wang, C. M., et al. (2014). Effect of strain rate on splitting tensile strength of geopolymer concrete. *Mag. Concr. Res.* 66, 825–835. doi: 10.1680/macr.13.00322

Fernandez-Jimenez, A., García-Lodeiro, I., and Palomo, A. (2007). Durability of alkaliactivated fly ash cementitious materials. *J. Mater. Sci.* 42, 3055–3065. doi: 10.1007/s10853-006-0584-8

Ganesan, N., Abraham, R., Deepa Raj, S., and Sasi, D. (2014). Stress–strain behaviour of confined Geopolymer concrete. *Constr. Buil. Materi.* 73, 326–331. doi: 10.1016/j.conbuildmat.2014.09.092

García-Lodeiro, I., Palomo, A., and Fernández-Jiménez, A. (2007). Alkali–aggregate reaction in activated fly ash systems. *Cem. Concr. Res.* 37, 175–183. doi: 10.1016/j.cemconres.2006.11.002

Geiseler, J., Kollo, H., and Lang, E. (1995). Influence of blast-furnace cements on durability of concrete structures. *ACI Mater. J.* 92, 252–257. doi: 10.14359/9773

Haider, G. M., Sanjayan, J. G., and Ranjith, P. G. (2014). Complete triaxial stress–strain curves for geopolymer. *Constr. Build. Mater.* 69, 196–202. doi: 10.1016/j.conbuildmat.2014.07.058

Hao, Y., and Hao, H. (2016). Finite element modelling of mesoscale concrete material in dynamic splitting test. *Adv. Struct. Eng.* 19, 1027–1039. doi: 10.1177/1369433216630828

Hao, Y., Hao, H., and Chen, G. (2016). Experimental investigation of the behavior of spiral steel fibre reinforced concrete beams subjected to drop-weight impact loads. *Mater. Struct.* 49, 353–370. doi: 10.1617/s11527-014-0502-5

Hao, Y., Hao, H., and Li, Z. X. (2010). Numerical analysis of lateral inertial confinement effects on impact tests of concrete compressive material properties. *Int. J. Prot. Struct.* 1, 145–167. doi: 10.1260/2041-4196.1.1.145

Khan, M. Z. N., Hao, Y., Hao, H., and Shaikh, F. U. A. (2018b). Mechanical properties of ambient cured high strength hybrid steel and synthetic fibers reinforced geopolymer composites. *Cem. Concr. Compos.* 85, 133–152. doi: 10.1016/j.cemconcomp.2017.10.011

Khan, M. Z. N., Hao, Y., Hao, H., and Shaikh, F. U. A. (2018a). Experimental evaluation of quasi-static and dynamic compressive properties of ambient-cured high-strength plain and fiber reinforced geopolymer composites. *Constr. Build. Mater.* 166, 482–499. doi: 10.1016/j.conbuildmat.2018.01.166

Khandelwal, M., Ranjith, P. G., Pan, Z., and Sanjayan, J. G. (2013). Effect of strain rate on strength properties of low-calcium fly-ash-based geopolymer mortar under dry condition. *Arab. J. Geosci.* 6, 2383–2389. doi: 10.1007/s12517-011-0507-0

Li, W., and Xu, J. (2009). Mechanical properties of basalt fiber reinforced geopolymeric concrete under impact loading. *Mater. Sci. Eng.* 505, 178–186. doi: 10.1016/j.msea.2008.11.063

Liu, S., Hao, Y., and Ma, G. (2021). Approaches to enhance the carbonation resistance of fly ash and slag based alkali-activated mortar-experimental evaluations. *J. Clea. Prod.* 280:124321. doi: 10.1016/j.jclepro.2020.124321

Luga, E. (2015). *Properties of fly ash and blast furnace slag geopolymer mortars* (Ph.D. thesis). Institute of Science, Erciyes University, Kayseri, Turkey.

Luo, X., and Xu, J. (2013). Dynamic splitting-tensile testing of highly fluidised geopolymer concrete. *Mag. Concr. Res.* 65, 837–843. doi: 10.1680/macr.12.00172

Menna, C., Asprone, D., Forni, D., Roviello, G., Ricciotti, L., Ferone, C., et al. (2015). Tensile behaviour of geopolymer-based materials under medium and high strain rates. *EPJ Web Conf. EDP Sci.* 01034, 1–4. doi: 10.1051/epjconf/20159401034

Noushini, A., Aslani, F., Castel, A., Gilbert, R. I., Uy, B., and Foster, S. (2016). Compressive stress-strain model for low-calcium fly ash-based geopolymer and heat-cured Portland cement concrete. *Cem. Concr. Compos.* 73, 136–146. doi: 10.1016/j.cemconcomp.2016.07.004

Ohno, M., and Li, V. C. (2014). A feasibility study of strain hardening fiber reinforced fly ash-based geopolymer composites. *Constr. Build. Mater.* 57, 163–168. doi: 10.1016/j.conbuildmat.2014.02.005

Punurai, W., Kroehong, W., Saptamongkol, A., and Chindaprasirt, P. (2018). Mechanical properties, microstructure, and drying shrinkage of hybrid fly ash-basalt fiber geopolymer paste. *Constr. Build. Mater.* 186, 62–70. doi: 10.1016/j.conbuildmat.2018.07.115

Shaikh, F. U. A., and Supit, S. W. M. (2014). Mechanical and durability properties of high volume fly ash (HVFA) concrete containing calcium carbonate ($CaCO_3$) nanoparticles. *Constr. Build. Mater.* 70, 309–321. doi: 10.1016/j.conbuildmat.2014.07.099

Sim, J., and Park, C. (2005). Characteristics of basalt fiber as a strengthening material for concrete structures. *Compos. Part B Eng.* 36, 504–512. doi: 10.1016/j.compositesb.2005.02.002

Tran, T. T., Pham, T. M., and Hao, H. (2019). Rectangular stress-block parameters for fly-ash and slag based geopolymer concrete. *Structures* 19, 143–155. doi: 10.1016/j.istruc.2019.01.006

Xin, L., Jin-yu, X., Weimin, L., and Erlei, B. (2014). Effect of alkali-activator types on the dynamic compressive deformation behavior of geopolymer concrete. *Mater. Lett.* 124, 310–312. doi: 10.1016/j.matlet.2014.03.102

Conflict of Interest: The authors declare that the research was conducted in the absence of any commercial or financial relationships that could be construed as a potential conflict of interest.

frontiers in Materials

ORIGINAL RESEARCH
published: 22 March 2021
doi: 10.3389/fmats.2021.636379

Deformation Texture Evolution in Flat Profile AlMgSi Extrusions: Experiments, FEM, and Crystal Plasticity Modeling

Tomas Manik[1], *Knut Marthinsen*[1]*, *Kai Zhang*[2], *Arash Imani Aria*[1] *and Bjørn Holmedal*[1]

[1]*Department of Materials Science and Engineering, NTNU, Norwegian University of Science and Technology, Trondheim, Norway,* [2]*SINTEF Industry, Trondheim, Norway*

In the present work, the deformation textures during flat profile extrusion from round billets of an AA6063 and an AA6082 aluminium alloy have been numerically modeled by coupling FEM flow simulations and crystal plasticity simulations and compared to experimentally measured textures obtained by electron back-scatter diffraction (EBSD). The AA6063 alloy was extruded at a relatively low temperature (350°C), while the AA6082 alloy, containing dispersoids that prevent recrystallization, was extruded at a higher temperature (500°C). Both alloys were water quenched at the exit of the die, to maintain the deformation texture after extrusion. In the center of the profiles, both alloys exhibit a conventional β-fiber texture and the Cube component, which was significantly stronger at the highest extrusion temperature. The classical full-constraint (FC)-Taylor and the Alamel grain cluster model were employed for the texture predictions. Both models were implemented using the regularized single crystal yield surface. This approach enables activation of any number and type of slip systems, as well as accounting for strain rate sensitivity, which are important at 350°C and 500°C. The strength of the nonoctahedral slips and the strain-rate sensitivity were varied by a global optimization algorithm. At 350°C, a good fit could be obtained both with the FC Taylor and the Alamel model, although the Alamel model clearly performs the best. However, even with rate sensitivity and nonoctahedral slip systems invoked, none of the models are capable of predicting the strong Cube component observed experimentally at 500°C.

Keywords: aluminum, extrusion, texture, crystal plasticity, modeling

OPEN ACCESS

Edited by:
Zhenggang Wu,
Hunan University, China

Reviewed by:
Liang Chen,
Shandong University, China
Cunsheng Zhang,
Shandong University, China

***Correspondence:**
Knut Marthinsen
knut.marthinsen@ntnu.no

Specialty section:
This article was submitted to Structural Materials, a section of the journal Frontiers in Materials

Received: *01 December 2020*
Accepted: *08 January 2021*
Published: *22 March 2021*

Citation:
Manik T, Marthinsen K, Zhang K, Aria AI and Holmedal B (2021) Deformation Texture Evolution in Flat Profile AlMgSi Extrusions: Experiments, FEM, and Crystal Plasticity Modeling. Front. Mater. 8:636379. doi: 10.3389/fmats.2021.636379

INTRODUCTION

Extrusion is an extensively used thermal–mechanical process to produce aluminium profiles for a range of applications. The properties of the profiles, for example, mechanical, fatigue, fracture, corrosion, as well as surface appearance, are strongly dependent on the underlying microstructure and texture, and the desired characteristics of these different properties may vary with applications (Ralston et al., 2010; Dumoulin et al., 2012; Donati et al., 2013). Moreover, in many cases, it is challenging to provide extruded profiles with a consistent and homogenous grain structure and texture both along the length and through the cross section of the profiles. It is, thus, of great importance to understand and be able to predict (model) how different microstructures and textures are generated and how they evolve during and after extrusion, as basis for controlling the final

appearance and properties of extruded profiles (Ralston et al., 2010; Dumoulin et al., 2012; Donati et al., 2013).

The deformation texture after extrusion can be numerically predicted by coupling FEM flow simulations and crystal plasticity models. Aukrust et al. (1997) predicted the deformation texture for flat profile extrusions using the FC- and Relaxed-Constraints (RC)-Taylor model, while Perocheau and Driver (2000) made use of the RC-Taylor hypothesis and a viscoplastic constitutive law for their texture simulations. The deformation texture predictions and their through thickness variations were compared to corresponding experiments and showed reasonable qualitative agreement. At the same time, it was shown that the predictions were improved by considering the nonoctahedral slip systems for high-temperature deformations. More recently, the present authors have modeled the overall deformation texture for extruded round profiles, using the FC-Taylor model and Alamel-type models and deformation histories along different particle paths provided by FEM flow simulations, to predict the through thickness texture variations (Zhang et al., 2018b). Compared to experiments, the Alamel model gave the best predictions.

In the present work, the deformation texture evolutions of extruded flat profiles of AA6xxx aluminium alloys have been numerically investigated and discussed in view of corresponding extrusion experiments. The extrusion trials were carried out in a mini-press laboratory extrusion set-up with immediate water quenching of the profiles at the exit of the die, which made it possible to 'freeze' the deformation texture prior to possible spontaneous recrystallization of the profiles at the die exit. The experimentally textures were characterized by the electron back-scatter diffraction technique (EBSD) in scanning electron microscopy (SEM).

In order to model the deformation texture evolution during extrusion, FEM simulations are carried to provide the strain, strain rate, and temperature along the center particle path. The simulations serve as input to an appropriate deformation texture (crystal plasticity) model. Since this is hot deformation, a special focus is put on the effect of nonoctahedral slip and strain-rate sensitivity on the deformation texture evolution. A careful analysis of the deformation history obtained from the FEM simulations provides information on how the deformation conditions change during extrusion, from the container, through the die, and into the extruded profile, and serves as basis to interpret the as-extruded deformation textures. The novelty of the present work is partly related to the use of the Alamel grain cluster model, in addition to the FC-Taylor model, to model the deformation texture evolution during flat profile extrusion. Furthermore, the fact that both models were implemented using the regularized single crystal yield surface approach, enables any number and type of slip systems (i.e., including nonoctahedral slip), as well as accounting for strain rate sensitivity. These aspects strongly influence the predicted texture during hot deformation, like extrusion, and have in the present work been fitted to experiments with the implementation of an optimization procedure.

MATERIALS AND METHODS

Experimental

The alloys considered in this work, were direct chill cast, then homogenized, extruded, and finally water quenched. An AA6063 alloy (chemical composition in wt% Si 0.4; Mg 0.5; Fe 0.096; Mn 0.017; Ti 0.01; Ga 0.012; Al remaining) and an AA6082 alloy (chemical composition in wt% Si 1.0; Mg 0.7; Fe 0.17; Mn 0.5; Zn 0.01; Al remaining) were investigated. The latter alloy contains dispersoids to suppress recrystallization.

For the AA6063 alloy, billets of 22 mm length and with a 20 mm diameter were machined from the homogenized material and then extruded into rectangular flat profiles of 1.3 mm thickness and 3 mm width in a laboratory scale direct extrusion set-up. This corresponds to an extrusion ratio of 80, which is within the typical extrusion ratio range in the extrusion industry. Prior to extrusion, the container, billet, die, and ram were heated together to the desired testing temperature, which for the results presented in this study were 350°C. The extrusions were performed at a ram speed of 4.5 mm/s and with a ram stroke of 9 mm. At the exit of the die, the extruded profiles were immediately pushed into cold water, which enabled the extruded material to be below 300°C within 2 s after the end of deformation. The low extrusion temperature of 350°C was chosen to prevent possible fast static recrystallization during quenching and thus to preserve the deformed microstructure and texture after extrusion. The ram speed was chosen to provide a profile exit speed comparable to industrial practice of similar alloys. The initial microstructure showed an equiaxed grain structure with an average grain size of diameter of 90 μm. While the material contained primary particles (constituents) with an average diameter of 1.4 μm and volume fraction of about 0.4%, this alloy did not contain second-phase particles (dispersoids) to suppress recrystallization.

For comparison with another alloy, which does not easily recrystallize after deformation, even at higher extrusion temperatures, experiments were also carried out with an AA6082 alloy. In this case, round billets of 100 mm in diameter were extruded into flat bars of 10 mm thickness and 78.5 mm in width, which corresponds to an extrusion ratio of 10. The as-cast textures of both alloys were random. AA6063 and AA6082 are chosen for the present study as they are commonly used extrusion alloys.

The textures of the as-extruded profiles were obtained by EBSD in a field emission scanning electron microscope (FESEM) equipped with the TSL orientation imaging microscopy (OIM) software points. Orientation distribution functions (ODF) were employed to illustrate the textures. The experimental deformation texture of the AA6063 alloy has been presented in an earlier work, and for further experimental details, it is referred to this work (Zhang et al., 2018a).

FEM Simulations

During extrusion, each material point in the billet will go through different and complicated deformation histories, in terms of strain rate, temperature, pressure, and strain, which will vary

TABLE 1 | Material constants of the Sellars–Tegart constitutive equation for AA6063.

α (**MPa**$^{-1}$)	ln(***A***) (**s**$^{-1}$)	***n***	***Q*** (**J mol**$^{-1}$)
0.04	22.5	5.385	141,500

with time and position. In order to predict the extrusion microstructure and texture, an accurate description of the deformation history in terms of these quantities is thus required. The initial step of the modeling exercise is to perform flow simulations by FEM, to provide the deformation history along relevant particle paths as output for the subsequent modeling (Aukrust et al., 1997; Zhang et al., 2015).

In the present work, a commercial FEM code HyperXtrude, assuming steady-state flow, was employed to provide the deformation history along desired path lines. Due to the symmetry of the extrusion profile and the set-up, only a quarter of the geometry was simulated. Hexahedral brick elements were used with a very fine mesh resolution in the bearing channel region, to capture the variations in the deformation field in this region with adequate accuracy. Rigid boundaries were considered for the container and the die towards the aluminium. The temperature of 350°C was specified for the container and the die. A heat transfer coefficient of 10,000 W/(m^2K) was used and full sticking assumed between the aluminium and the container and between the aluminium and the die surface. In the bearing channel, on the other hand, where the experimental set-up used parallel bearings, a full-slip condition was assumed in the simulations, since it can be expected that the bearings are relieved due to die deflection during extrusion.

The Sellars–Tegart constitutive equation was used to describe the hot deformation during the extrusion (Sellars and McG. Tegart, 1972), for which the steady state effective flow stress, $\overline{\sigma}$, is given as

$$\overline{\sigma} = \frac{1}{\alpha}\sinh^{-1}\left(\frac{Z}{A}\right)^{\frac{1}{n}} \tag{1}$$

where $Z = \dot{\bar{\varepsilon}}\exp\left(\frac{Q}{RT}\right)$ is the Zener–Hollomon parameter, Q is the activation energy, R is the universal gas constant, T is the absolute temperature, and α, A, n, and Q are temperature independent material constants. The parameter values used for the AA6063 alloy in this work are obtained from the literature (Sheppard and Jackson, 1997) and is given in **Table 1**. These parameters are based on fitting of experimental compression and torsion data over a range of temperatures and strain rates relevant for the present work.

The deformation history for the center path (crossing of the horizontal and vertical symmetry planes), which ends at the exit of the 3 mm long bearing channel, was exported for further analysis and texture postsimulations.

Note that, FEM simulations were not carried out for the AA6082 alloy. The AA6082 has a different chemical composition; thus, the parameters of the constituent **Eq. 1**, including temperature, are different. The geometrical set-up is also different with a considerable smaller extrusion ratio. For the purpose of a qualitative comparison, the deformation path of the AA6063 was applied also for the texture simulations of the AA6082. This does not justify a quantitative comparison of simulated and measured textures. However, as it turns out, the extrusion texture contains a very strong Cube component that cannot be captured even qualitatively by the models. Note that an earlier reported texture of AA6082 (Ryen et al., 2004), measured after extrusion at a similar temperature, but with a higher extrusion ratio of about 50, showed a very similar, slightly sharper texture, with an even stronger Cube component.

The same modeling approach has recently been applied for the extrusion of round profiles of the same alloy (Zhang et al., 2018b). As compared to the previous work, only the center deformation path is considered for the subsequent texture simulations in the present work.

Crystal Plasticity Modeling

Two different crystal plasticity models, i.e., the FC-Taylor and the advanced Lamel model (Alamel) (Van Houtte et al., 2005) have been considered in this work.

The main assumption of the FC-Taylor model is that each single crystal experiences the same deformation as the polycrystalline aggregate (Van Houtte, 1988b), which implies that the FC-Taylor model ignore grain interactions. In Alamel-type models, on the other hand, local interactions across grain boundaries are considered by relaxing the constraints on the shear strain components, while constraints are imposed on the corresponding stress component. The Alamel model considers a cluster containing a common grain boundary and the two adjunct grains or regions. In the Alamel model, the grain boundary is represented by its normal vector and the shear components related with the normal of the common grain boundary can be relaxed.

Both the FC-Taylor and the Alamel model were implemented using the regularized single crystal yield surface (Holmedal, 2020). This approach enables activation of any number and type of slip systems in a very robust way. Moreover, the exponent a of the single crystal yield function is directly associated to the strain rate sensitivity defined by the power law (Hutchinson, 1976),

$$\tau^s = \tau_0 \mathrm{sgn}\left(\dot{\gamma}^s\right)\left|\frac{\dot{\gamma}^s}{\dot{\gamma}_0}\right|^m \tag{2}$$

As pointed out by Holmedal (2020),

$$m = \frac{1}{a-1} \tag{3}$$

In the FC-Taylor model, elastic deformation is neglected, i.e., the velocity gradient $\mathbf{L}$ provided by FEM simulations, is assumed to be equal to the plastic velocity gradient, $\mathbf{L}^{\mathrm{p}}$. After transformation into the crystal frame (quantities denoted by a hat) it reads $\widehat{\mathbf{L}}^{\mathrm{p}} = \mathbf{Q}\mathbf{L}^{\mathrm{p}}\mathbf{Q}^{\mathrm{T}}$, where $\mathbf{Q}$ is a rotation matrix between the global (laboratory) and the local (crystal) frame. In the crystal frame, for each time increment, the deviatoric Cauchy stress $\widehat{\boldsymbol{\sigma}}$ is found by solving the system of six nonlinear equations

$$\hat{\mathbf{D}}^{\mathrm{p}} = \dot{\lambda}\frac{\partial f}{\partial \hat{\boldsymbol{\sigma}}} \text{ and } f(\hat{\boldsymbol{\sigma}}) = 0 \tag{4}$$

by the Newton–Raphson method with line search (Scherzinger, 2017). $\hat{\mathbf{D}}^{\mathrm{p}} = \mathrm{sym}(\hat{\mathbf{L}}^{\mathrm{p}})$ is the plastic strain rate, f is the single crystal yield function, and $\dot{\lambda}$ is the plastic multiplier equal to the plastic work rate. The constitutive spin in the crystal frame, $\hat{\mathbf{W}}^{\mathrm{c}}$, is calculated as

$$\hat{\mathbf{W}}^{\mathrm{c}} = \hat{\mathbf{W}}^{\mathrm{p}} - \sum_{s} \hat{\boldsymbol{\Omega}}^{s}\dot{\gamma}^{s} \tag{5}$$

where $\hat{\mathbf{W}}^{\mathrm{p}} = \mathrm{skew}(\hat{\mathbf{L}}^{\mathrm{p}})$ is the plastic spin, $\dot{\gamma}^{s}$ is the slip rate on the slip system s, $\hat{\boldsymbol{\Omega}}^{s}$ is the skew-symmetric part of the Schmid matrix $\mathbf{m}^{s} = \mathbf{b}^{s}\otimes\mathbf{n}^{s}$, with the slip direction, $\mathbf{b}^{s}$, and the slip plane normal, $\mathbf{n}^{s}$. The orientation matrix of the single crystal is updated according to

$$\dot{\boldsymbol{Q}} = -\hat{\mathbf{W}}^{\mathrm{c}}\mathbf{Q} \tag{6}$$

In the Alamel model, in order to solve the plastic slip in the cluster, the nonlinear system given in **Eq. 4** is solved simultaneously for both grains. In addition, these are coupled by two nonlinear equations reading

$$\sigma_{23}^{\mathrm{B,G1}} - \sigma_{23}^{\mathrm{B,G2}} = 0, \tag{7a}$$

$$\sigma_{13}^{\mathrm{B,G1}} - \sigma_{13}^{\mathrm{B,G2}} = 0. \tag{7b}$$

Here, $\sigma_{ij}^{\mathrm{B,G}x}$ represents the ij-th Cauchy stress component of the grain x expressed in the boundary frame in a cluster. Solving **Eqs. 7a,b** results in two relaxation shears r_{23} and r_{13} so that

$$\begin{aligned}(\mathbf{L}^{\mathrm{p}})^{\mathrm{B,G1}} &= (\mathbf{L}^{\mathrm{p}})^{\mathrm{B}} + \begin{pmatrix} 0 & 0 & r_{13} \\ 0 & 0 & r_{23} \\ 0 & 0 & 0 \end{pmatrix} \text{ and} \\ (\mathbf{L}^{\mathrm{p}})^{\mathrm{B,G2}} &= (\mathbf{L}^{\mathrm{p}})^{\mathrm{B}} - \begin{pmatrix} 0 & 0 & r_{13} \\ 0 & 0 & r_{23} \\ 0 & 0 & 0 \end{pmatrix}\end{aligned} \tag{8}$$

where $(\mathbf{L}^{\mathrm{p}})^{\mathrm{B,G}x}$ is the plastic velocity gradient of grain x in the boundary frame, $(\mathbf{L}^{\mathrm{p}})^{\mathrm{B}}$ is the plastic velocity gradient prescribed by FEM and rotated into the boundary frame. After solving the relaxations and both grains, the update of respective orientation matrices is done in a similar fashion as **Eqs. 5**, **6**.

Besides the octahedral slip systems $\{111\}\langle 1\bar{1}0\rangle$, also the three nonoctahedral slip system classes $\{110\}\langle 1\bar{1}0\rangle$, $\{001\}\langle 1\bar{1}0\rangle$, and $\{112\}\langle 1\bar{1}0\rangle$ are considered here (Maurice and Driver, 1997a; Maurice and Driver, 1997b). The initial texture of the billet material is assumed to be random and is represented by a set of 1,000 randomly distributed orientations (uniformly distributed in Euler space). As described above, the considered grain interactions in the Alamel-type models take place on the common grain boundary shared by two adjacent grains. A set of 500 randomly distributed normal vectors in the spatial space are taken to represent the initial orientations of the grain boundaries, and they will reorientate during the deformation.

The crystal plasticity models use the deformation history provided by the FEM continuum plasticity flow simulations, notably the velocity gradient tensor **L** and the time increment Δt, to update the texture. The final deformation texture is exported to and analyzed using the MTEX toolbox in the Matlab software (Hielscher and Schaeben, 2008).

RESULTS

Experimental Results

The microstructure of the AA6063 profile extruded at T = 350°C, has been presented in a previous work (Zhang et al., 2018a). The as-extruded material for this condition shows a fibrous structure, i.e., a nonrecrystallized deformation structure. The overall texture in the form the ODF, representative for the center region, is shown in **Figure 1A**. It is noted that the texture is quite strong, with the Cu-component 26 times random, S 30 times random, Brass 20 times random, while Cube is only 3.6 times random.

For comparison, the deformation texture of the AA6082 alloy extruded at 500°C has also been recorded (**Figure 1B**). Also, this alloy, even at this high extrusion temperature, is in a fibrous, nonrecrystallized state after extrusion, and can as such be compared with the AA6063 alloy extruded at 350°C. Although different chemical compositions and extrusion ratios, the most important difference in this context is the extrusion temperature. The intensities of the main texture components are listed in **Table 2**. It is interesting to note that the texture is quite different, with the most notable difference the much stronger Cube (intensity 25). The relative intensities for the Copper, S, and Brass are also clearly different.

FEM Flow Simulations

The deformation microstructure is characterized by its deformation substructure and associated texture. As already mentioned, coupled FEM simulations and crystal plasticity (CP) modeling has recently successfully been performed to provide texture predictions comparable to the experiments (Zhang et al., 2015; Zhang et al., 2018b). In principle, any CP model can be used, nonetheless advanced CP models such as Alamel-type models have shown to perform better than the FC-Taylor model in predicting the deformation texture. The initial texture and the velocity gradient **L** along particle paths provided by the HyperXtrude FEM simulations are the main input to the CP models. The deformation texture simulations are realized by including just conventional octahedral slip as well as with also nonoctahedral slip systems included (Maurice and Driver, 1997a; Maurice and Driver, 1997b).

The deformation characteristics can be analyzed by means of the FEM flow simulations, using the same method developed by (Zhang et al., 2018b). Evolution of the strain rate along the center path is illustrated in **Figure 2**. It follows from **Figure 2** that the accumulated strain increases slowly far from the die inlet. At $\Gamma = -10$ mm, the strainrate increases rapidly, which corresponds to the flow into the extrusion gap.

With the definitions 1 = ED (extrusion direction), 2 = TD (transverse direction), and 3 = ND (normal direction, we have for uniaxial tension/compression

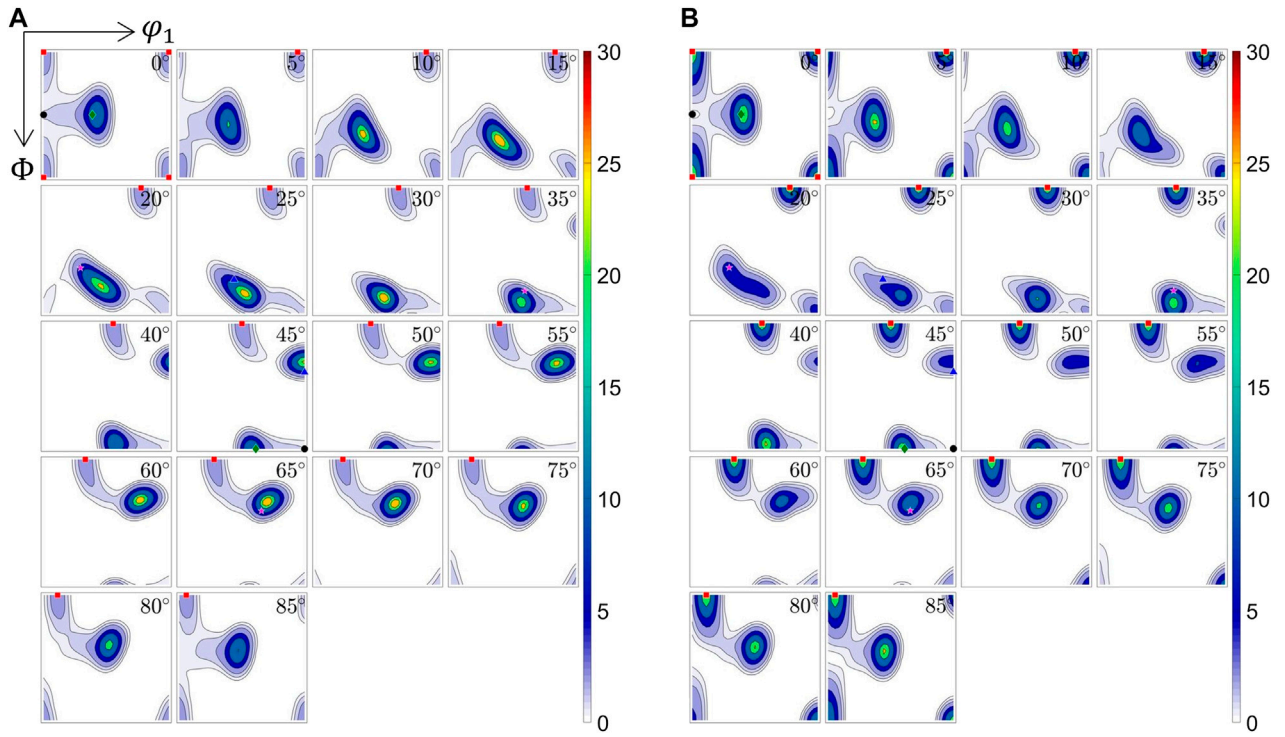

FIGURE 1 | The experimental texture of the as-extruded profile in the form of ODF for the center region **(A)** AA6063 extruded at 350°C and **(B)** AA6082 extruded at 500°C.

TABLE 2 | Intensity of the beta-fiber texture components and Cube texture in the AA6063 and AA6082 alloys extruded at different temperatures.

Texture component	Copper	S	Brass	Cube	Goss
AA6063, T = 350°C	26	30	20	3.6	1.1
AA6082, T = 500°C	8	17	26	25	0.4

$$\frac{\dot{\varepsilon}_{22}}{\dot{\varepsilon}_{33}} = 1 \text{ and } \frac{\dot{\varepsilon}_{11}}{\dot{\varepsilon}_{33}} = -2 \tag{9}$$

while for plane strain compression,

$$\frac{\dot{\varepsilon}_{22}}{\dot{\varepsilon}_{33}} = 0 \text{ and } \frac{\dot{\varepsilon}_{11}}{\dot{\varepsilon}_{33}} = -1 \tag{10}$$

From **Figure 2**, we clearly see that the flow changes from uniaxial tension in the container, to plane strain compression as one approach the bearings.

It is well known that during uniaxial tension of fcc alloys, a double ⟨100⟩/⟨111⟩ fiber texture develops (Zhang et al., 2018b). Consistent with the deformation analysis above, this is also what is observed experimentally by analyzing the texture of the material in the container (of the AA6063 alloy extruded at 350°C) before it enters the die (not shown in this paper), with a double ⟨111⟩ and ⟨100⟩ fiber texture, where the ⟨111⟩ component is considerably stronger than the ⟨100⟩. This was also what was previously observed during round profile extrusion of the same alloy. It is then interesting to see how these two components individually further develop during plane strain compression, which is the dominant deformation mode the material experiences during the die. This is analyzed in the Discussion part.

FEM Extrusion Texture Predictions

Rate-Sensitive CP Models With Only the Octahedral Slip Systems

The deformation texture was predicted by coupled FEM and CP modeling. Two different CP rate-insensitive models have been considered in this work, i.e., the FC-Taylor and the Alamel model. A description of both these models can be found in Mánik and Holmedal (2013); Mánik and Holmedal (2014) and Zhang et al. (2015). The FC-Taylor model ignores any grain interactions, whereas the Alamel model assumes grain interaction locally at the grain boundary by allowing relaxations of the strain constraints. Both models were formulated and implemented based on the regularized single crystal yield surface (Holmedal, 2020). This approach allows to introduce rate-sensitive behavior as well as activation of arbitrary number and type of slip systems in a robust way. In the first set of trials, only conventional octahedral slips were considered, i.e., the twelve {111}⟨110⟩ slip systems.

The texture predictions were conducted for the center path. Applying the velocity gradient and the temperature as a function of time, as predicted by the FEM simulations for the center path

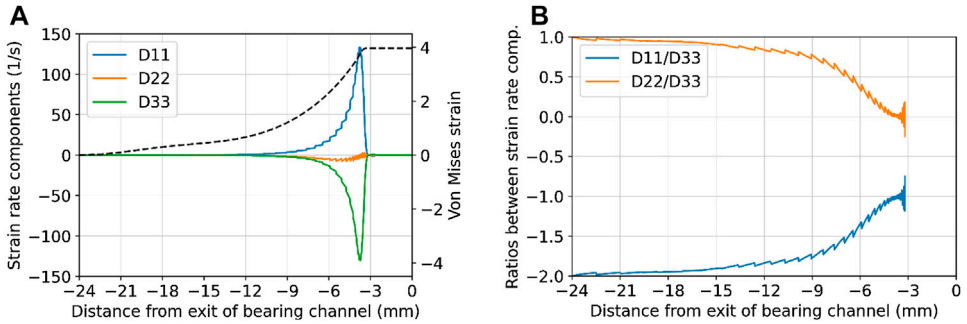

FIGURE 2 | Deformation mode analysis for the center deformation path; **(A)** plot of components of the deformation rate tensor; **(B)** ratios between these components.

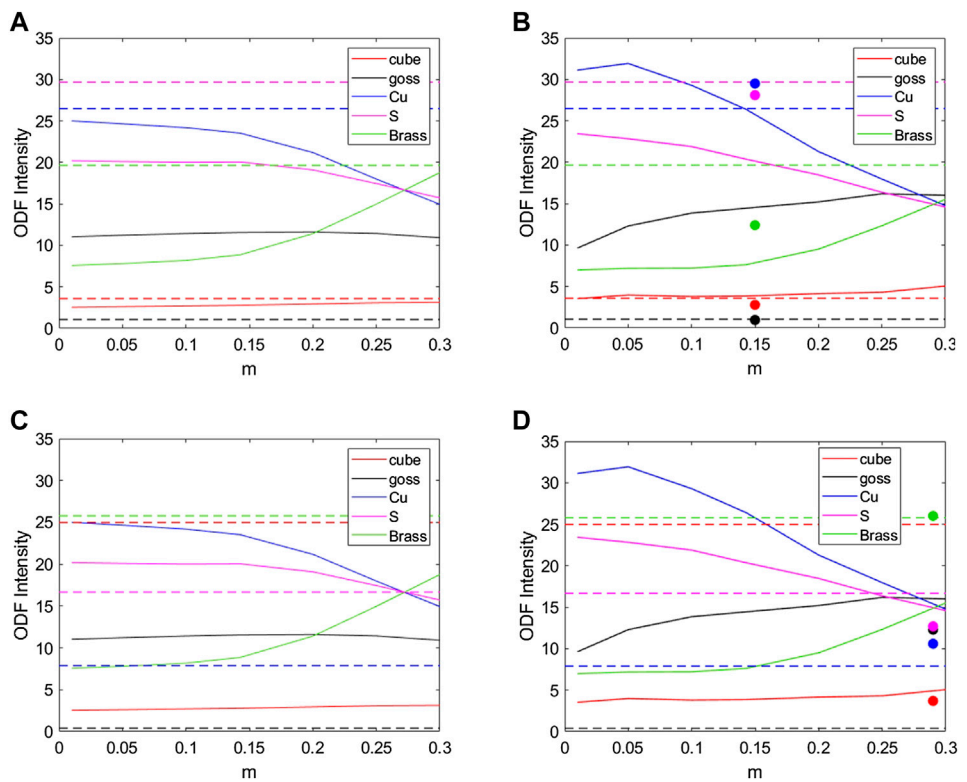

FIGURE 3 | Intensities of texture components as functions of the strain-rate sensitivity. Predicted by the Alamel model by solid lines in **(B)** and **(D)**, and computed by the FC-Taylor model by solid lines in **(A)** and **(C)** compared to measured values (dashed horizontal lines) for **(A)** and **(B)** T 350°C and **(C)** and **(D)** T 500°C. The filled circles in **(B)** and **(D)** indicate the results from the Alamel model with the optimal parameters including nonoctahedral slips (**Table 3**).

of the AA6063 alloy, the texture after extrusion was predicted by the CP models for this given deformation history for both alloys, in lack of detailed FEM simulations for the AA6082, as discussed above. The predicted results were processed in the MTEX toolbox in the Matlab software. When generating the ODF, the same parameters were used as for processing the experimental EBSD data.

As far as it concerns the predicted textures for the rate-insensitive variants of both the FC-Taylor and the Alamel model with only the octahedral slip, it is referred to a previous work (Zhang et al., 2018a).

Figure 3 shows the effect of the strain-rate sensitivity on the intensity of texture components obtained by the FC-Taylor (a, c) and Alamel model (b, d) with octahedral slips only. For the case of T = 350°C (**Figures 3A,B**), for a realistic strain-rate sensitivity expected to be between 0.1–0.2, the model predicted well Cube and Cu component intensities, while S and Brass were underpredicted, and Goss was significantly overpredicted. The too weak Brass component prediction occurred at both temperatures and is expected from Taylor type models (Mánik and Holmedal, 2014; Van Houtte, 1988a). For the case of 500°C (**Figures 3C,D**), the Alamel model predicted a significantly too

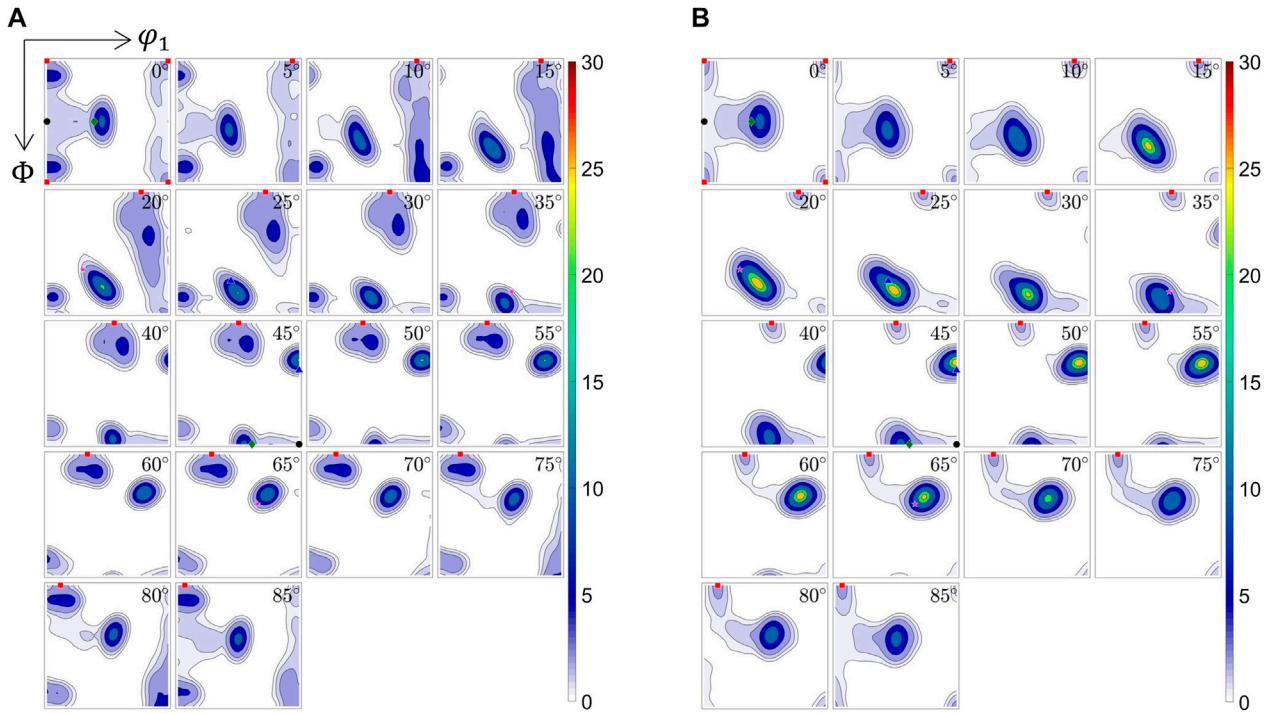

FIGURE 4 | Texture predictions computed by **(A)** FC-Taylor and **(B)** Alamel models with parameters giving the best match with the experimentally measured texture for AA6063, T 350°C.

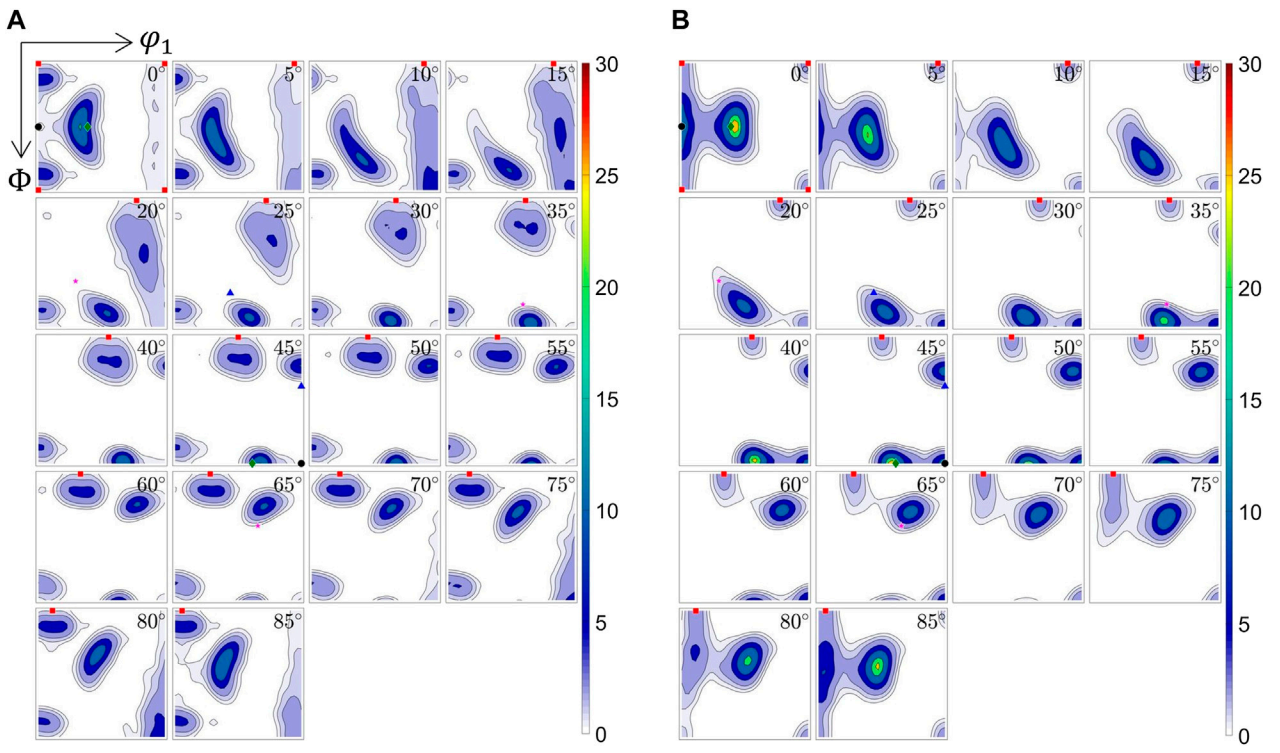

FIGURE 5 | Texture predictions computed by **(A)** FC-Taylor and **(B)** Alamel models with parameters giving the best match with the experimentally measured texture for AA6082, T 500°C.

TABLE 3 | Case of AA6063, T = 350°C. The best-fit relative critical resolved shear stress (CSSR) for the three nonoctahedral slip systems considered in the texture optimization for FC Taylor and Alamel, respectively.

Model	FC Taylor	Alamel
Strain-rate sensitivity	0.195	0.15
$\tau^c_{\{110\}\langle 1\bar{1}0\rangle}$	0.91	0.84
$\tau^c_{\{001\}\langle 1\bar{1}0\rangle}$	2.0[a]	1.52
$\tau^c_{\{112\}\langle 1\bar{1}0\rangle}$	1.74	2.0[a]

[a]*Not activated.*

low Cube, while the ED-rotated Cube, i.e., the Goss component, was too strong. The correct prediction of the Cube is important, because it is commonly assumed that the strong Cube, often present after recrystallization of hot deformed Al-alloys, stems from Cube already present in the deformed conditions (Daaland and Nes, 1996; Vatne et al., 1996).

Rate-Sensitive Models With Both Octahedral and Nonoctahedral Slip Systems

Maurice and Driver (1997a), Maurice and Driver (1997b) have shown that nonoctahedral slip may play a role at higher deformations temperatures. The deformation texture calculations are therefore made, including possible additional nonoctahedral slip systems, i.e., $\{110\}\langle 1\bar{1}0\rangle$, $\{001\}\langle 1\bar{1}0\rangle$, and $\{112\}\langle 1\bar{1}0\rangle$.

Both the strain rate sensitivity and the critical stresses of the nonoctahedral slip systems depend on the temperature. Several values have been previously suggested in the literature (Falkinger et al., 2020). Typically, the relative strengths of the nonoctahedral slips with respect to the octahedral slips are within the range of 0.75–1.5, the strain-rate sensitivity varies from 0.1 to 0.3, see e.g., (Perocheau et al., 1998; Falkinger et al., 2020).

In order to test the ability of the CP models to predict the measured textures, quantitatively at 350°C and qualitatively at 500°C, the strength of the nonoctahedral slips as well as the strain-rate sensitivity were varied by a global optimization algorithm within the given range until the best fit between the predicted and the measured texture was found. Strain-rate sensitivity variations were in the range from 0.1 to 0.4, the critical stresses of the nonoctahedral slips between 0.5 and 2, where the factor 2 represents deactivation of the given slip. The strength of the octahedral slips was fixed to unity. The particle swarm optimization algorithm in Matlab software (Mezura-Montes and Coello, 2011) was used for optimization. A brief outline of the algorithm is as follows:

1. The particle swarm algorithm begins by creating the initial particles and assigning them initial velocities.
2. It evaluates the objective function at each particle location and determines the best (lowest) function value and the best location.
3. It chooses new velocities, based on the current velocity, the particles' individual best locations, and the best locations of their neighbors and iteratively updates the particles locations.

For the case of T = 350°C, the residual $\mathcal{R}$ to be minimized was defined in the least-square sense as

$$\mathcal{R} = \left(\frac{I^{\mathrm{mod}}_{\mathrm{Cube}}}{I^{\mathrm{exp}}_{\mathrm{Cube}}} - 1\right)^2 + \left(\frac{I^{\mathrm{mod}}_{\mathrm{Goss}}}{I^{\mathrm{exp}}_{\mathrm{Goss}}} - 1\right)^2 + \left(\frac{I^{\mathrm{mod}}_{\mathrm{Cu}}}{I^{\mathrm{exp}}_{\mathrm{Cu}}} - 1\right)^2 + \left(\frac{I^{\mathrm{mod}}_{\mathrm{S}}}{I^{\mathrm{exp}}_{\mathrm{S}}} - 1\right)^2 + \left(\frac{I^{\mathrm{mod}}_{\mathrm{Brass}}}{I^{\mathrm{exp}}_{\mathrm{Brass}}} - 1\right)^2 \tag{11}$$

where $I^{\mathrm{exp}}_{\mathrm{X}}$ and $I^{\mathrm{mod}}_{\mathrm{X}}$ are intensities of the X texture component, read from the experimentally measured and the predicted ODFs, respectively. A global minimum was found for both the FC Taylor and the Alamel model, the corresponding model parameters are listed in **Table 3**.

In both models, $\tau^c_{\{111\}\langle 1\bar{1}0\rangle} = 1$. The final residuals were 0.285 and 0.2 for the FC Taylor and the Alamel, respectively. The simulated ODFs having closest match with the experimentally measured texture for AA6063 T = 350°C are shown in **Figure 4**

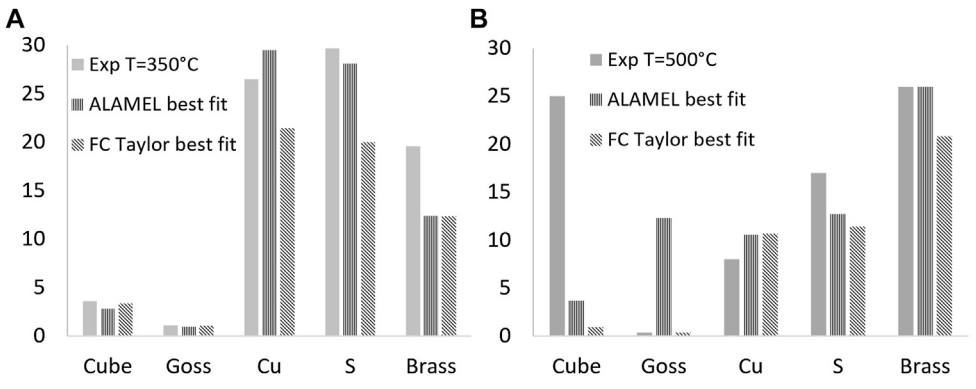

FIGURE 6 | Predicted and measured texture component intensities for **(A)** AA6063 T 350°C, **(B)** AA6082 T 500°C.

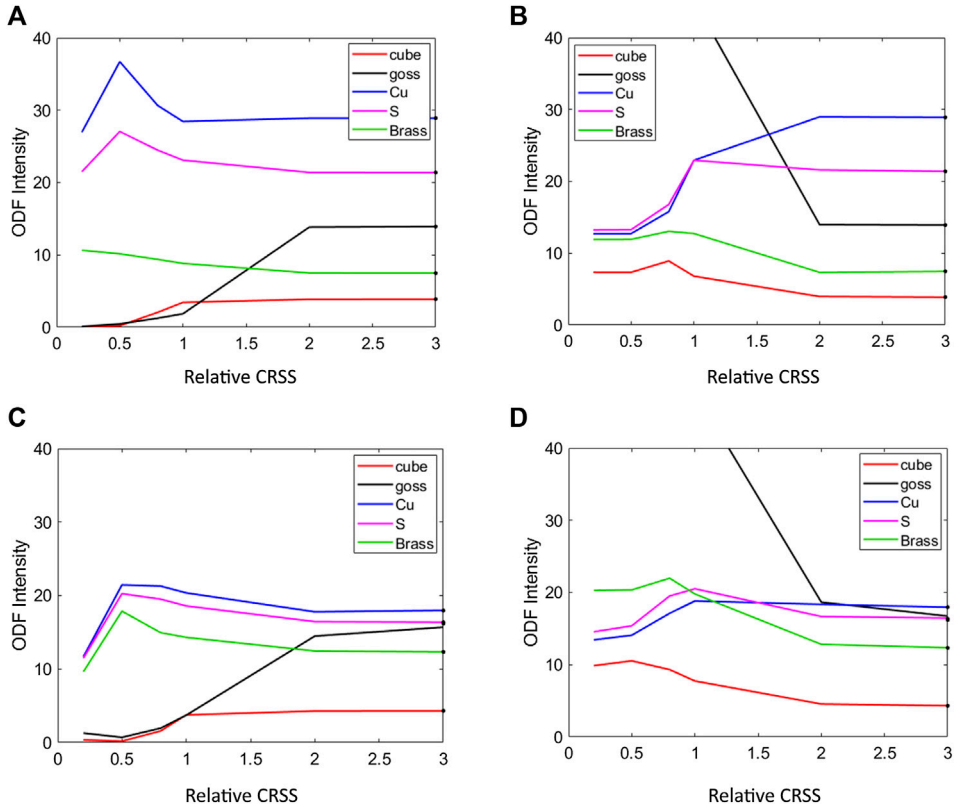

FIGURE 7 | Effect of the strain rate sensitivity and the activation of the non-octahedral slip systems on the texture component intensity prediction in the Alamelmodel. **(A)** m = 0.1, octahedral slip + $\{110\}\langle 1\bar{1}0\rangle$ **(B)** m = 0.1, octahedral slip + $\{112\}\langle 1\bar{1}0\rangle$ **(C)** m = 0.25, octahedral slip + $\{110\}\langle 1\bar{1}0\rangle$ **(D)** m = 0.25, octahedral slip + $\{112\}\langle 1\bar{1}0\rangle$.

and those for AA6082 T = 500 °C in **Figure 5**, and the intensities of the individual components are compared in **Figure 6**.

Both the strain-rate sensitivity and the critical resolved shear stresses that give the best fit for both models are within physically reasonable limits. According to **Table 3**, slip on the {110} planes has the lowest critical resolved shear stress, which means that this class of slip systems contributes more to the overall slip solution than slip on {001} and {112} planes, which have higher critical resolved shear stresses. The FC-Taylor model develops an extra undesired texture component, i.e., ~10° ED rotated Cube, which is not present in the Alamel's prediction. As this component is not stable for the plane-strain compression, it would continue to rotate if the deformation had continued.

For the case of AA6082, T = 500°C (**Figure 5**), neither of the texture models used can predict as high content of the Cube component as measured (intensity 25) (**Figure 1B** and Discussion chapter). Due to this, and because of the inaccuracy by applying the strain path from the AA6063 simulation also for the AA6082 texture simulation, the residual in the global optimization problem was instead chosen as $\mathcal{R} = \int_V (I^{\exp} - I^{\mathrm{mod}})^2 \mathrm{d}V$, i.e., to minimize the texture index of the difference between experimental and modeled textures. A global minimum was found for both the FC Taylor and the Alamel model, the corresponding model parameters are listed in **Table 4**.

TABLE 4 | Case of AA6082, T = 500°C. The best-fit relative critical resolved shear stress (CSSR) for the three nonoctahedral slip systems considered in the texture optimization for FC Taylor and Alamel, respectively.

Model	FC Taylor	Alamel
Strain-rate sensitivity	0.39	0.29
$\tau^c_{\{110\}\langle 1\bar{1}0\rangle}$	0.5	1.35
$\tau^c_{\{001\}\langle 1\bar{1}0\rangle}$	0.54	0.68
$\tau^c_{\{112\}\langle 1\bar{1}0\rangle}$	1.75	1.35

In both models, $\tau^c_{\{111\}\langle 1\bar{1}0\rangle}$ = 1. The final residuals were 2.330 and 1.8 for the FC Taylor and the Alamel, respectively. The simulated ODFs with the optimal set of parameters with respect to the experimentally measured texture for AA6082 T = 500°C are shown in **Figure 5**, and the intensities of the individual components are compared in **Figure 6B**.

A reasonable fit for S, Brass, and Cu components was obtained by both models. However, none of the models was capable to predict the strong Cube component observed experimentally after extrusion at this temperature. For the Alamel model, the

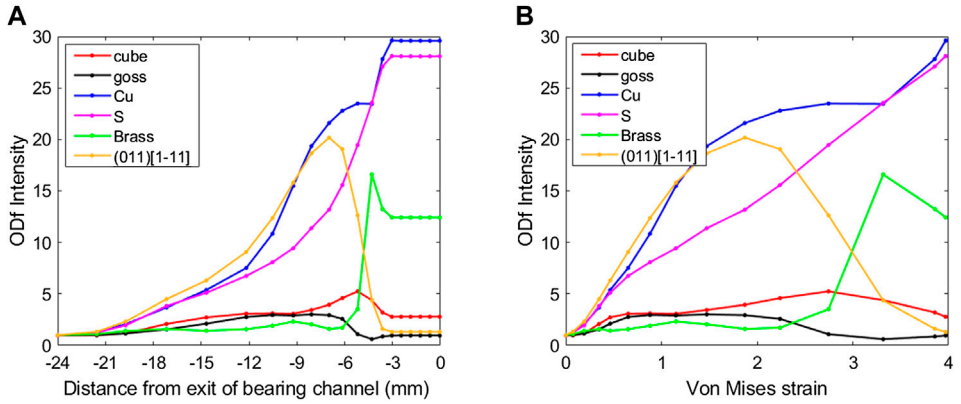

FIGURE 8 | Through-extrusion texture components development prediction by the Alamel model with parameters giving the best fit to the measured texture at 350°C, plotted as a function of **(A)** the Von Mises strain, **(B)** distance from exit of bearing channel along the extrusion direction.

optimal solution for the overall ODF resulted in the strong overprediction of Goss component.

DISCUSSION

Influence of the Nonoctahedral Slip Systems on Texture Prediction

The results presented in **Figure 6** show that by allowing slip on both octahedral and nonoctahedral slip systems, both FC Taylor and Alamel models were capable to model all the main components of the experimental texture after extrusion at 350°C. However, the Alamel model distinguished itself when considering the overall texture comparison. The activation of the nonoctahedral slip systems has proven to be crucial for obtaining good texture predictions. **Figures 3B,D** compare the Alamel model predictions for 350°C and 500°C, respectively, without considering slip on the nonoctahedral planes to the optimal solution obtained by the global optimization. The sole activation of the octahedral slip leads to strong overprediction of Goss, regardless of the strain-rate sensitivity. The effect of the activation of $\{110\}\langle 1\bar{1}0\rangle$ and $\{112\}\langle 1\bar{1}0\rangle$ slip systems at two different strain-rate sensitivities, i.e., $m = 0.1$ and 0.25, for the Alamel model (quite similar in the FC Taylor) is shown in **Figure 7**. Two main conclusions can be made:

1. Slip on the {110} planes can supress evolution of Goss.
2. Slip on the {112} planes can promote evolution of Goss and Cube.

Activation of the nonoctahedral slip systems affects the other texture components than Goss to somewhat less extent. Based on this observation, the reason for the very low Goss in the measured extrusion at 350°C is probably due to the activation of the {110} slip planes.

The good overall texture fit provided by the Alamel model for 350°C was not achieved for the case of 500°C. The individual predictions for the Cu, S, and Brass components are reasonably good; however, poor predictions for Goss and Cube are obtained. At 500°C, the strain-rate sensitivity is expected to be moderately high, i.e., in the range of 0.2–0.3. **Figure 7D** shows that by including the $\{112\}\langle 1\bar{1}0\rangle$ the amount of Cube can be increased with a strain rate sensitivity in this range. However, this is accompanied by a large increase in the Goss component, which clearly contradicts the experiments, in which quite limited Goss is observed. In any case, none of the current models, irrespective of parameters, are capable of predicting an intensity of Cube as high as ~25. For AA6082, one can argue that some error in the simulated texture should be expected, due to performing the simulation based on the strain path obtained from the AA6063 FEM simulation, which has an extrusion ratio of 80 as compared to 10 for the AA6082. With a higher extrusion ratio, a slightly sharper texture is expected, as well as some redistribution of the strength of the texture components. However, an even stronger Cube component was observed for extrusion of AA6082 at a similar temperature but with a higher, more comparable extrusion ratio (Ryen et al., 2004). Hence, the error introduced by using an unprecise strain path is small compared to the significant error not predicting the strong Cube component.

It is suspected that the large amount of Cube observed in AA6082 extruded at 500°C is not representative for the true deformation texture, but rather a result of fast recovery or early recrystallization of Cube at this high temperature.

Through Extrusion Texture Evolution Prediction

One of the main objectives behind the use of the texture model is to study and explain the origin of Cube texture component, as its presence in the deformation texture is believed to have important influence on the recrystallization of hot deformed Al-alloys (Daaland and Nes, 1996; Vatne et al., 1996). The clue to get any Cube at all is the deformation mode characteristics of the extrusion (**Figure 2**). The initial dominating deformation mode is uniaxial tension producing the $\langle 100\rangle$ and $\langle 111\rangle$ axisymmetric texture fibers. The Cube component is part of the $\langle 100\rangle$ fiber and remains present through further deformation close to and in the die, where the deformation mode is mainly plane strain compression. The good texture prediction at 350°C provided by the Alamel model legitimates to use this model for

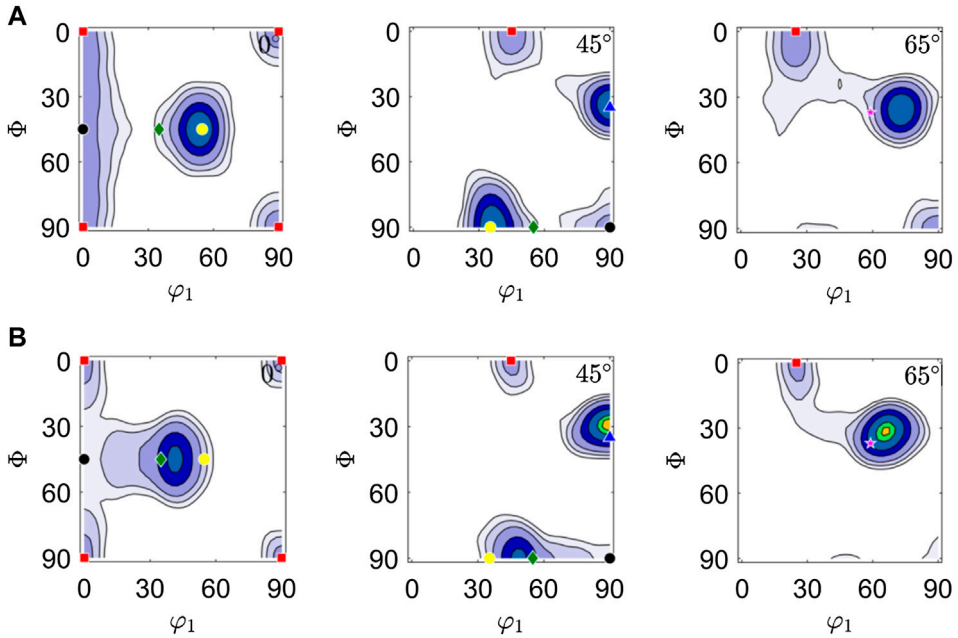

FIGURE 9 | Texture predictions **(A)** after Von Mises strain of ~1.5, which approximately corresponds to the transition from the uniaxial tensile mode to plane-strain compression mode; **(B)** at the end of the extrusion process.

assessing the texture evolution through the whole extrusion process.

Figure 8 shows texture component developments through the extrusion process, predicted by the Alamel model with parameters that give the best fit of the measured texture at 350°C. During the uniaxial tensile deformation mode, the ⟨111⟩ fiber, here represented by the {011}⟨1$\bar{1}$1⟩ and Cu components, develops stronger than the ⟨100⟩ fiber, represented by Cube and Goss components. The texture approximately at the end of the uniaxial tensile mode, i.e., at strain of 1.5 is shown in **Figure 9A**. During the following deformation mode of plane strain compression, the ⟨111⟩ fiber rotates into the β-fiber and forms the classical plane strain deformation texture (note interchanging of intensities between the {011}⟨1$\bar{1}$1⟩ tensile component and Brass both in **Figures 8**, **9**). The Cube continues to develop further during the last part of the extrusion where a mixed deformation mode took place, probably at the expense of Goss. Finally, the plane strain compression causes the intensity of the Cube to fall to approximately half the intensity. It is interesting to note that no Cube comes from the ⟨111⟩ fiber.

CONCLUSIONS

In the present work, the evolution of deformation textures during flat profile extrusion of AA6xxx aluminium alloys have been investigated numerically, by coupling FEM flow simulations and crystal plasticity simulations and compared to experiments. The simulations are based on implementations of the FC-Taylor at the Alamel grain cluster model, which allow for variations in strain-rate sensitivity and the inclusion of any type and number of nonoctahedral slip systems. The numerical simulated textures are compared to the measured ones and discussed. To assess the quality of the texture predictions at 350°C and 500°C, the strength of the nonoctahedral slips as well as the strain-rate sensitivity were varied by a global optimization algorithm. At 350°C, fairly good fits were obtained both with the FC Taylor and the Alamel model, and the selected optimal parameters had reasonable values as compared to their expected physical interpretations. Nonetheless, the Alamel model provided a significantly better overall texture prediction, predicting all the major texture components with correct intensities. A reasonable, qualitative fit for S, Brass, and Cu components can also be obtained at 500°C by both models. However, none of the models are capable of predicting the strong Cube component observed experimentally after extrusion at this temperature. Both models, in particular the Alamel model, tend to predict a too strong Goss component at 500°C, while this component can be suppressed by the activation of {110}⟨1$\bar{1}$0⟩ slip systems at the lower strain rate sensitivity at 350°C. Owing to strain rate sensitivity and activation of nonoctahedral slip systems, high predictability was obtained for 350°C. However, for 500°C, the poor predictions are likely due to that dislocation slip is no longer the sole responsible mechanism.

DATA AVAILABILITY STATEMENT

The raw data supporting the conclusion of this article will be made available by the authors, without undue reservation.

AUTHOR CONTRIBUTIONS

KZ was involved in experiments and initial texture simulations. TM was involved in texture simulations and texture optimization. AIA was involved in texture simulations. BH and KM was involved in

supervision, interpretation, funding acquisition, and suggestions. KM, TM, KZ, and BH wrote the manuscript. All authors discussed the results and reviewed and edited the manuscript.

ACKNOWLEDGMENTS

This research work has been supported by the IPN project COSMETEX (228918/O30) in Norway. The financial support by the Research Council of Norway and the industrial partner SAPA AS (Now Hydro Extruded Solutions) is gratefully acknowledged. We are grateful to Antonio Segatori, Hydro Extruded Solutions, Finspång, Sweden, for providing the extruded profiles for the texture analyses, and to Trond Aukrust, SINTEF Industry, Norway, for providing the FEM extrusion results, which are basis for the texture simulations.

REFERENCES

Aukrust, T., Tjøtta, S., Vatne, H. E., and Van Houtte, P. (1997). Coupled FEM and texture modelling of plane strain extrusion of an aluminium alloy. *Int. J. Plast.* 13, 111–125. doi:10.1016/s0749-6419(97)00003-x

Daaland, O., and Nes, E. (1996). Origin of cube texture during hot rolling of commercial Al-Mn-Mg alloys. *Acta Mater.* 44, 1389–1411. doi:10.1016/1359-6454(95)00290-1

Donati, L., Segatori, A., El Mehtedi, M., and Tomesani, L. (2013). Grain evolution analysis and experimental validation in the extrusion of 6XXX alloys by use of a Lagrangian FE code. *Int. J. Plast.* 46, 70–81. doi:10.1016/j.ijplas.2012.11.008

Dumoulin, S., Engler, O., Hopperstad, O. S., and Lademo, O. G. (2012). Description of plastic anisotropy in AA6063-T6 using the crystal plasticity finite element method. *Model. Simulat. Mater. Sci. Eng.* 20, 20. doi:10.1088/0965-0393/20/5/055008

Falkinger, G., Simon, P., and Mitsche, S. (2020). Viscoplastic self-consistent modeling of the through-thickness texture of a hot-rolled Al-Mg-Si plate. *Metall. Mater. Trans.* 51, 3066–3075. doi:10.1007/s11661-020-05743-y

Hielscher, R., and Schaeben, H. (2008). A novel pole figure inversion method: specification of theMTEXalgorithm. *J. Appl. Crystallogr.* 41, 1024–1037. doi:10.1107/s0021889808030112

Holmedal, B. (2020). Regularized yield surfaces for crystal plasticity of metals. *Crystals* 10, 1076. doi:10.3390/cryst10121076

Hutchinson, J. W. (1976). Bounds and self-consistent estimates for creep of polycrystalline materials. *Proc. Roy. Soc. Lond. Math. Phys. Sci.* 348, 101–127.

Mánik, T., and Holmedal, B. (2013). Additional relaxations in the Alamel texture model. *Mater. Sci. Eng.* 580, 349–354. doi:10.1016/j.msea.2013.05.071

Mánik, T., and Holmedal, B. (2014). Review of the Taylor ambiguity and the relationship between rate-independent and rate-dependent full-constraints Taylor models. *Int. J. Plast.* 55, 152–181. doi:10.1016/j.ijplas.2013.10.002

Maurice, C., and Driver, J. H. (1997a). Hot rolling textures of f.c.c. metals-Part I. Experimental results on Al single and polycrystals. *Acta Mater.* 45, 4627–4638. doi:10.1016/s1359-6454(97)00115-8

Maurice, C., and Driver, J. H. (1997b). Hot rolling textures of f.c.c. metals-Part II. Numerical simulations. *Acta Mater.* 45, 4639–4649. doi:10.1016/s1359-6454(97)00117-1

Mezura-Montes, E., and Coello Coello, C. A. (2011). Constraint-handling in nature-inspired numerical optimization: past, present and future. *Swarm and Evolutionary Computation.* 1, 173–194. doi:10.1016/j.swevo.2011.10.001

Perocheau, F., Driver, J. H., and Aukrust, T. (1998). "A viscoplastic simulation of texture evolution during extrusion of an aluminium alloy," in *Texture and anisotropy of polycrystals*. Editor R. A. Schwarzer (Aedermannsdor, Switzerland: Trans Tech Publications), 377–382.

Perocheau, F., and Driver, J. H. (2000). Texture gradient simulations for extrusion and reversible rolling of FCC metals. *Int. J. Plast.* 16, 73–89. doi:10.1016/s0749-6419(99)00048-0

Ralston, K. D., Birbilis, N., and Davies, C. H. J. (2010). Revealing the relationship between grain size and corrosion rate of metals. *Scripta Mater.* 63, 1201–1204. doi:10.1016/j.scriptamat.2010.08.035

Ryen, Ø., Holmedal, B., Li, S., Houtte, P. v., Roven, H. J., and Nes, E. (2004). "Plastic anisotropy in recrystallized and unrecrystallized extruded aluminium profiles," in 9th international conference on aluminium alloys, August, 2004. Editors J. F. Nie, A. J. Morton, and B. C. Muddle (Brisbane, Australia: © Institute of Materials Engineering Australasia Ltd), 1004–1009.

Scherzinger, W. M. (2017). A return mapping algorithm for isotropic and anisotropic plasticity models using a line search method. *Comput. Methods Appl. Mech. Eng.* 317, 526–553. doi:10.1016/j.cma.2016.11.026

Sellars, C. M., and Tegart, W. J. M. (1972). Hot workability. *Int. Metall. Rev.* 17, 1–24. doi:10.1179/imtlr.1972.17.1.1

Sheppard, T., and Jackson, A. (1997). Constitutive equations for use in prediction of flow stress during extrusion of aluminium alloys. *Mater. Sci. Technol.* 13, 203–209. doi:10.1179/mst.1997.13.3.203

Van Houtte, P. (1988a). A comprehensive mathematical formulation of an extended Taylor-Bishop-hill model featuring relaxed constraints, the Renouard-Wintenberger theory and a strain rate sensitivity model. *Textures Microstruct.* 8, 313–350. doi:10.1155/tsm.8-9.313

Van Houtte, P. (1988b). A comprehensive mathematical formulation of an extended taylor-bishop-hill model featuring relaxed constraints, the renouard-wintenberger theory and a strain rate sensitivity model. *Textures Microstruct.* 8, 313–350. doi:10.1155/tsm.8-9.313

Van Houtte, P., Li, S. Y., Seefeldt, M., and Delannay, L. (2005). Deformation texture prediction: from the Taylor model to the advanced Lamel model. *Int. J. Plast.* 21, 589–624. doi:10.1016/j.ijplas.2004.04.011

Vatne, H. E., Furu, T., and Nes, E. (1996). Nucleation of recrystallised grains from cube bands in hot deformed commercial purity aluminium. *Mater. Sci. Technol.* 12, 201–210. doi:10.1179/mst.1996.12.3.201

Zhang, K., Marthinsen, K., Holmedal, B., Aukrust, T., and Segatori, A. (2015). Coupled FEM and Alamel-type polycrystal plasticity modelling applied to extrusion of aluminium alloys. Aluminium Two Thousand World Congress and International Conference on Extrusion and Benchmark ICEB 2015, Florence, Italy, 12.-15 May, 2015. Editors L. Donati and L. Tomesani. Materials Today-Proceedings 2, 4898-4903.

Zhang, K., Marthinsen, K., Holmedal, B., Aukrust, T., and Segatori, A. (2018a). "Evolution in texture and through thickness variations in Al-Mg-Si-extrusions: experiments and modelling," in International conference on aluminium alloys (ICAA16). Montreal, Canada: Canadian Institute of Mining, Metallurgy & Petroleum, McGill University.

Zhang, K., Marthinsen, K., Holmedal, B., Aukrust, T., and Segatori, A. (2018b). Through thickness variations of deformation texture in round profile extrusions of 6063-type aluminium alloy: experiments, FEM and crystal plasticity modelling. *Mater. Sci. Eng.* 722, 20–29. doi:10.1016/j.msea.2018.02.081

Conflict of Interest: The authors declare that the research was conducted in the absence of any commercial or financial relationships that could be construed as a potential conflict of interest.

frontiers in Materials

ORIGINAL RESEARCH
published: 22 April 2021
doi: 10.3389/fmats.2021.656429

Wire and Arc Additive Manufacturing of High-Strength Al–Zn–Mg Aluminum Alloy

Xuewei Fang[1,2], Guopeng Chen[2], Jiannan Yang[2], Yang Xie[3], Ke Huang[1] and Bingheng Lu[1,2]*

[1] The State Key Laboratory for Manufacturing Systems Engineering, Xi'an Jiaotong University, Xi'an, China, [2] National Innovation Institute of Additive Manufacturing, Xi'an, China, [3] China Ship Design & Research Center, Wuhan, China

High-strength 7xxx series aluminum alloys are of great importance for the aerospace industries. However, this type of aluminum alloys has poor processability for most additive manufacturing techniques. In this paper, a newly designed Al–Zn–Mg alloy was used as a feeding wire to fabricate thin wall-shaped samples using the wire and arc additive manufacturing (WAAM) technique. These samples were fabricated based on the cold metal transfer (CMT) process with four different types of arc modes, that is, CMT, CMT-incorporated pulse (CMT + P), CMT-incorporated polarity (CMT + A), CMT-incorporated pulse and polarity (CMT + PA). The optical microscopy, x-ray computed tomography, and scanning electron microscopy equipped with energy-dispersive x-ray spectroscopy (EDS) and electron backscatter diffraction (EBSD) were employed to characterize the microstructure and phase constitution. The results clearly reveal that the porosity varies with the arc modes, and the densest sample with porosity of 0.97% was obtained using the CMT + P mode. The mechanical properties of the fabricated samples are also dependent on the arc modes. The tensile strength and yield strength of the sample manufactured by the CMT + PA arc mode are the highest. In terms of anisotropy, the strength differences in horizontal and vertical direction of the samples made by CMT + PA, CMT + A, and CMT modes are all large, which is mainly ascribed to the pores distributed at the interlayer region.

Keywords: wire and arc additive manufacturing, cold metal transfer, porosity, second phase particles, anisotropy, high strength aluminum alloy

OPEN ACCESS

Edited by:
Antonio Caggiano, Darmstadt University of Technology, Germany

Reviewed by:
Donghong Ding, Foshan University, China
Chen Zhang, Wuhan University, China

****Correspondence:***
Ke Huang
ke.huang@xjtu.edu.cn

Specialty section:
This article was submitted to Structural Materials, a section of the journal Frontiers in Materials

Received: *20 January 2021*
Accepted: *26 March 2021*
Published: *22 April 2021*

Citation:
Fang X, Chen G, Yang J, Xie Y, Huang K and Lu B (2021) Wire and Arc Additive Manufacturing of High-Strength Al–Zn–Mg Aluminum Alloy. Front. Mater. 8:656429. doi: 10.3389/fmats.2021.656429

INTRODUCTION

Additive manufacturing process is now an efficient technique to manufacture complex, large-scale parts (DebRoy et al., 2018). Weldability is an important factor to determine whether a metal is suitable for additive manufacturing (Oliveira et al., 2020). However, there are only a limited number of materials that exhibit good weldability, e.g., Ti6Al4V, Inconel 718, and AlSi10Mg (Kuo et al., 2017; Aboulkhair et al., 2019; Liu and Shin, 2019). Among these alloys, aluminum alloys are widely used in aerospace, aircraft, and automotive fields because of their good combination of light weight, high strength, and good ductility.

AlSi10Mg is, currently, the most suitable aluminum alloy for laser-based additive manufacturing process (Rosenthal et al., 2014; Girelli et al., 2019). However, its mechanical properties cannot meet

most of the aerospace requirements (Martin et al., 2017). Attempts have been made to fabricate high-strength aluminum alloys such as 7xxx series by selective laser melting (SLM) (Wang et al., 2017; Uddin et al., 2018). However, microcracks are often inevitable, due to their high solidification shrinkage and high susceptibility to liquation cracking in the fast cooling procedure (Montero-Sistiaga et al., 2016; Stopyra et al., 2020). Wire and arc additive manufacturing (WAAM), which is a variation of the direct energy deposition (DED) technology, uses an electric arc as the heat source to melt the metal wires layer by layer to form the near net shape three-dimensional (3D) components. This technique has been adopted to fabricate high-strength 7xxx aluminum since its high reflectivity of laser during SLM is no longer an issue. Cong et al. (2015) discussed the current research status of the WAAM technology and the future development trend. Cong et al. (2015) investigated the effect of the arc mode on the Al-6.3Cu alloy and proved that porosity is efficiently controlled by the low heat input. Generally, the mechanisms of pore formation were classified into the following: gas pores induced by hydrogen, which shows the sphere morphology, and the tortuous surface induced by solidification shrinkage (Cong et al., 2015). Ding et al. (2015) fabricated 7055-Al by WAAM to investigate its processability, mechanical properties, and microstructure evolution. 7055-Al shows quite good processability and medium tensile strength. However, the analysis of defects and their correlation with microstructure and mechanical properties are left unexploited. Klein et al. (2020) studied the Al–Zn–Mg–Cu alloy with a high-magnesium element and low-zinc element. It proved that this type of aluminum has a good deposition feasibility by WAAM (Klein et al., 2020). A similar aluminum alloy was investigated by Morais et al. (2020) and this aluminum alloy shows quite a high strength after heat treatment. Li et al. (2020) studied the Al–Zn–Mg alloy fabricated by the WAAM technique. The mechanical properties, microstructure, and pores distribution were tested and discussed; it was proved that the deteriorated mechanical properties, as compared to the forging counterparts, are related to the loss of the zinc and magnesium element as vapor, and the porosity clearly decreases the strength of the WAAM samples (Li et al., 2020, 2021). However, the detailed porosity, microstructure, and phase constitution in the high Zn/Mg ratio aluminum fabricated by WAAM remain uncertain.

In this paper, a new high-strength Al–Zn–Mg alloy with a high Zn/Mg ratio was designed and used to fabricate samples by the WAAM technique using four different arc modes associated with the different heat input. The microstructure and chemical composition of the samples were carefully characterized by scanning electron microscopy (SEM)/energy-dispersive x-ray spectroscopy (EDS)/electron backscatter diffraction (EBSD); x-ray CT was employed to examine the porosity in 3D, while tensile tests along both the horizontal and vertical direction of the fabricated samples were conducted to measure their mechanical properties. The correlation between the microstructure and second-phase particles, and the heterogeneous porosity of these four types of samples with mechanical properties are discussed in detail.

MATERIALS AND METHODSOLOGY

Materials and Samples Preparation

The chemical compositions of the Al–Zn–Mg feeding wire and the basal material 5083 aluminum plate are listed in **Table 1**, which were determined by inductively coupled plasma optical emission spectroscopy (ICP-OES). The diameter of the feeding wire is 1.2 mm, and the dimension of the base metal plate is 300 × 300 × 12 mm.

The as-deposited samples were prepared layer by layer by the WAAM manufacturing equipment, which consists of a KUKA robot, a Fronius cold metal transfer (CMT) advanced welding machine, and a welding platform. The base metal was a 12 mm-thick 5083-H112 plate. Before deposition, the basal metal was champed on the welding platform. Then, the oxide layer of the basal metal surface was removed by a grinder and then cleaned with acetone solution. The welding machine can produce four kinds of arc modes: pure CMT, the CMT process–incorporated pulse (CMT + P), the CMT process–incorporated polarity (CMT + A), and the CMT process–incorporated pulse and polarity (CMT + PA). The WAAM deposition parameters are listed in **Table 2**. The thin wall-shaped samples with a size of 220 × 85 × 8 mm were fabricated layer by layer with a 120s interval between layers. The metallographic samples were cut along the building direction, and dog-bone samples along the horizontal and vertical direction were cut by a wire electrical discharge machine for the tensile test, as shown in **Figure 1**.

Microstructure Characterization and Mechanical Testing

To detect the porosity of the fabricated WAAM samples, the x-ray CT (GE v| tome| x m) was employed to examine micropores distribution in the samples. Samples for microstructure characterization were grounded by a grit paper from 400# to 2000#, and then polished to a mirror facet through a standard metallographic procedure. The samples were etched by Keller's reagent for optical microstructure observation both in horizontal and vertical directions. Samples were further mechanically polished for the SEM-EDS analysis (SEM, JEOL-IT500) to

TABLE 1 | Chemical compositions of basal metal and filler wire (wt.%).

Material	Fe	Si	Cu	Mn	Zn	Mg
5083 plate	0.32	0.38	0.07	0.63	0.22	4.68
Al–Zn–Mg wire	0.079	<0.005	–	<0.005	5.28	2.70

TABLE 2 | Wire and arc additive manufacturing (WAAM) deposition parameters of the four samples.

Sample	Arc mode	Wire feeding speed	Deposition speed	Shielding gas Flow (99.99%)
A	CMT + A	0.6 m/min	6 m/min	20 L/min
B	CMT			
C	CMT + P			
D	CMT + PA			

obtain the microstructure, phase distribution, and chemical composition of phases. The EBSD (SEM, JEOL 7900F) samples were prepared by the electropolish method using a voltage of 30V for a duration of 88 s with the electrolyte composed of 10% perchlorate alcohol solution. The tensile tests were conducted using the INSTRON 5983 machine with a strain rate of 0.00025 s^{-1}.

RESULTS

Heat Input

The heat input of the four modes is quite different, and the calculation method is presented in Reference Fang et al. (2018). The heat input has a significant impact on the formation of microstructures and phase constitution (Su et al., 2019). The heat

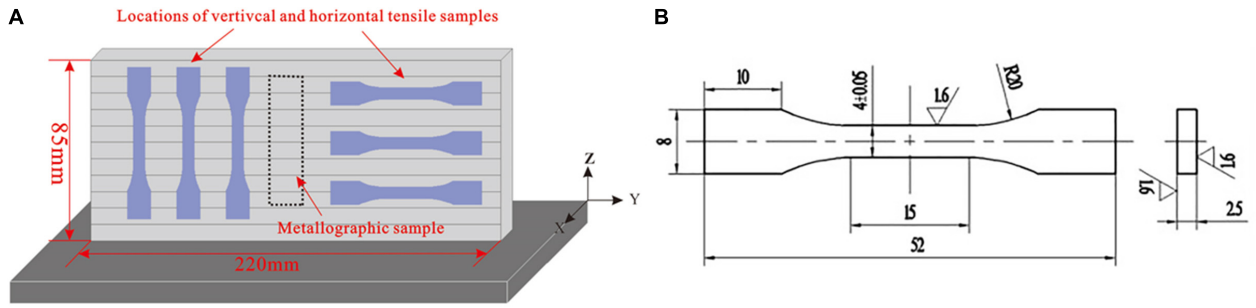

FIGURE 1 | (A) Schematic of the sampling positions and **(B)** the dimensions of tensile sample.

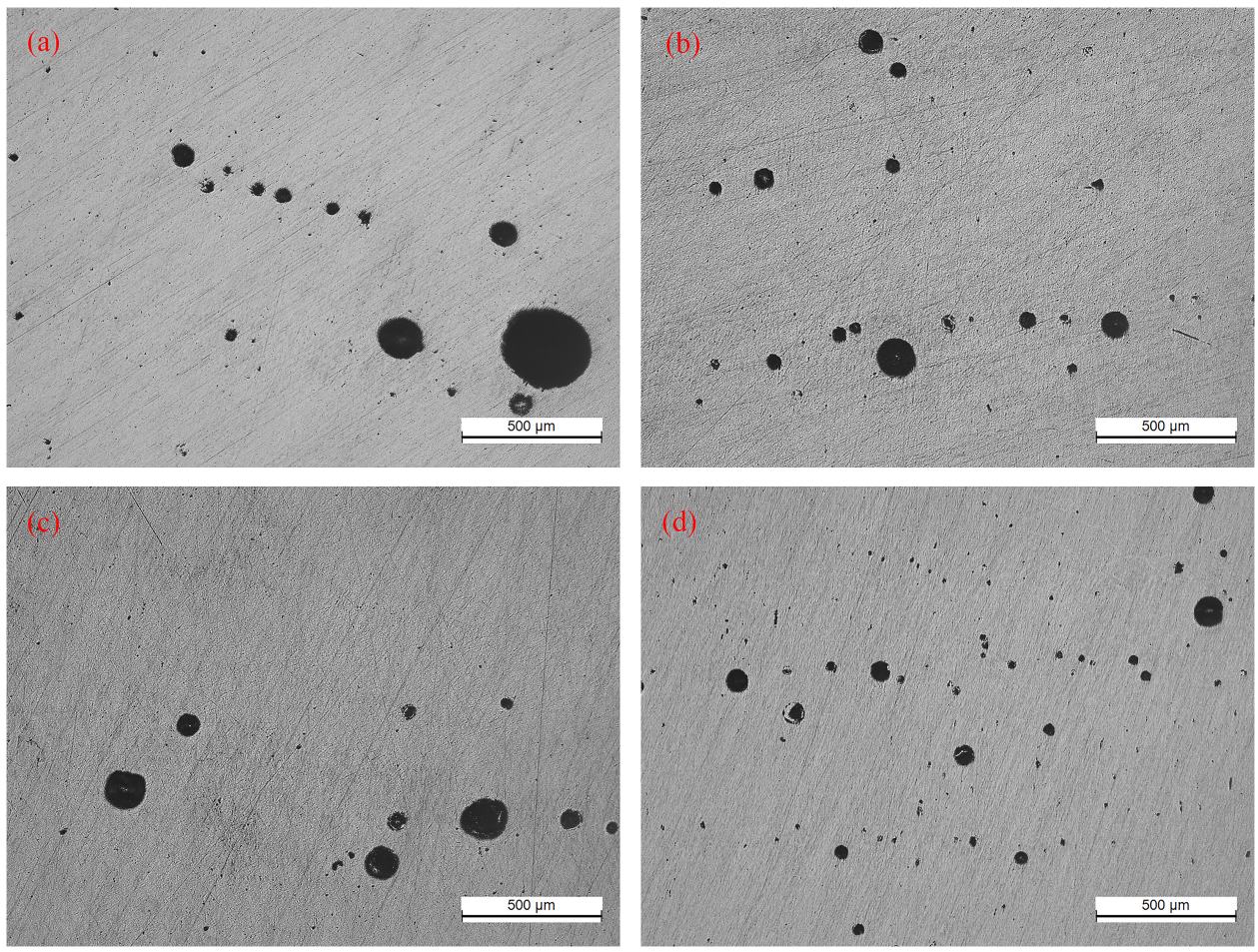

FIGURE 2 | Porosity morphology in **(a)** CMT + A, **(b)** CMT, **(c)** CMT + P, and **(d)** CMT + PA samples. CMT, cold metal transfer; CMT + A, cold metal transfer–incorporated polarity; CMT + P, cold metal transfer–incorporated pulse; and CMT + PA, cold metal transfer–incorporated pulse and polarity.

input of these four types of arc modes can be calculated by the following equation:

$$HI = \frac{\int_{t_1}^{t_2} U_i I i}{t_2 - t_1} \Big/ TS \quad (1)$$

where HI is heat input, U is voltage, I is current, t is time, and TS is the travel speed. The calculated heat input of the different arc modes is 206.3, 172.8, 162.1, and 121.3 J/mm in the CMT, CMT + P, CMT + A, and CMT + PA arc modes, respectively. It can be seen that the largest and lowest heat input are CMT and CMT + PA, respectively.

Micropores Distribution

Figure 2 depicts the micropore morphologies of the as-deposited sample with four different arc modes. The pores in all types of samples are close to spherical, and large pores in the CMT + A mode can be clearly seen, while the pore size in the CMT + PA sample is clearly much smaller than the other samples.

To further analyze the pores, the x-ray CT was employed to obtain the 3D distribution of pores in **Figure 3**. It can be clearly seen that the micropores mainly distribute at each interlayer zone, while the micropores at the innerlayer zone are quite small. The total volume ratio of pores is 2.07, 1.84, 1.76, and 0.97% in CMT, CMT + A, CMT + P, and CMT + PA samples, respectively.

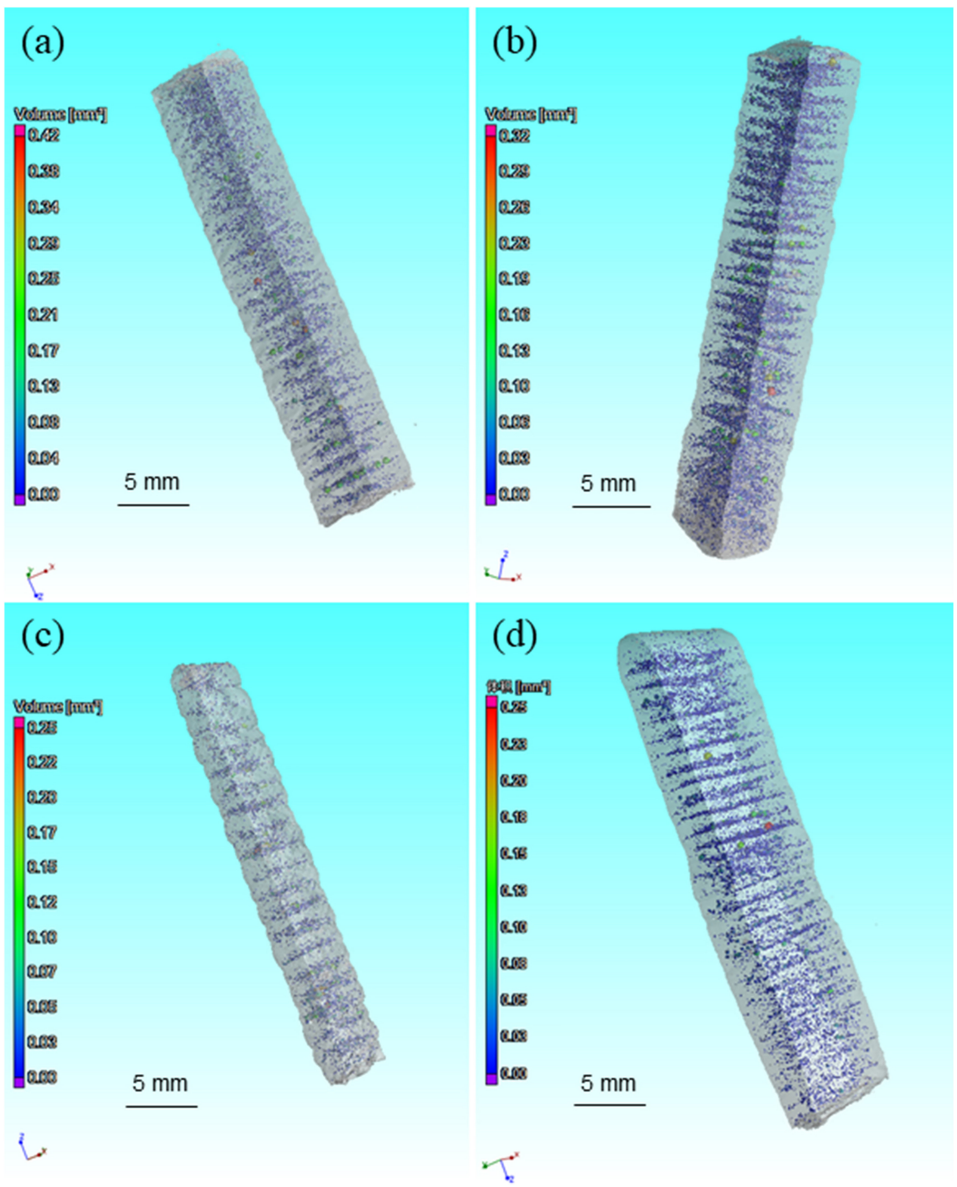

FIGURE 3 | Porosity distribution, 3D-morphology, and location inside the as-deposited samples **(a)** CMT + A, **(b)** CMT, **(c)** CMT + PA, and **(d)** CMT + P. CMT, cold metal transfer; CMT + A, cold metal transfer–incorporated polarity; CMT + P, cold metal transfer–incorporated pulse; and CMT + PA, cold metal transfer–incorporated pulse and polarity.

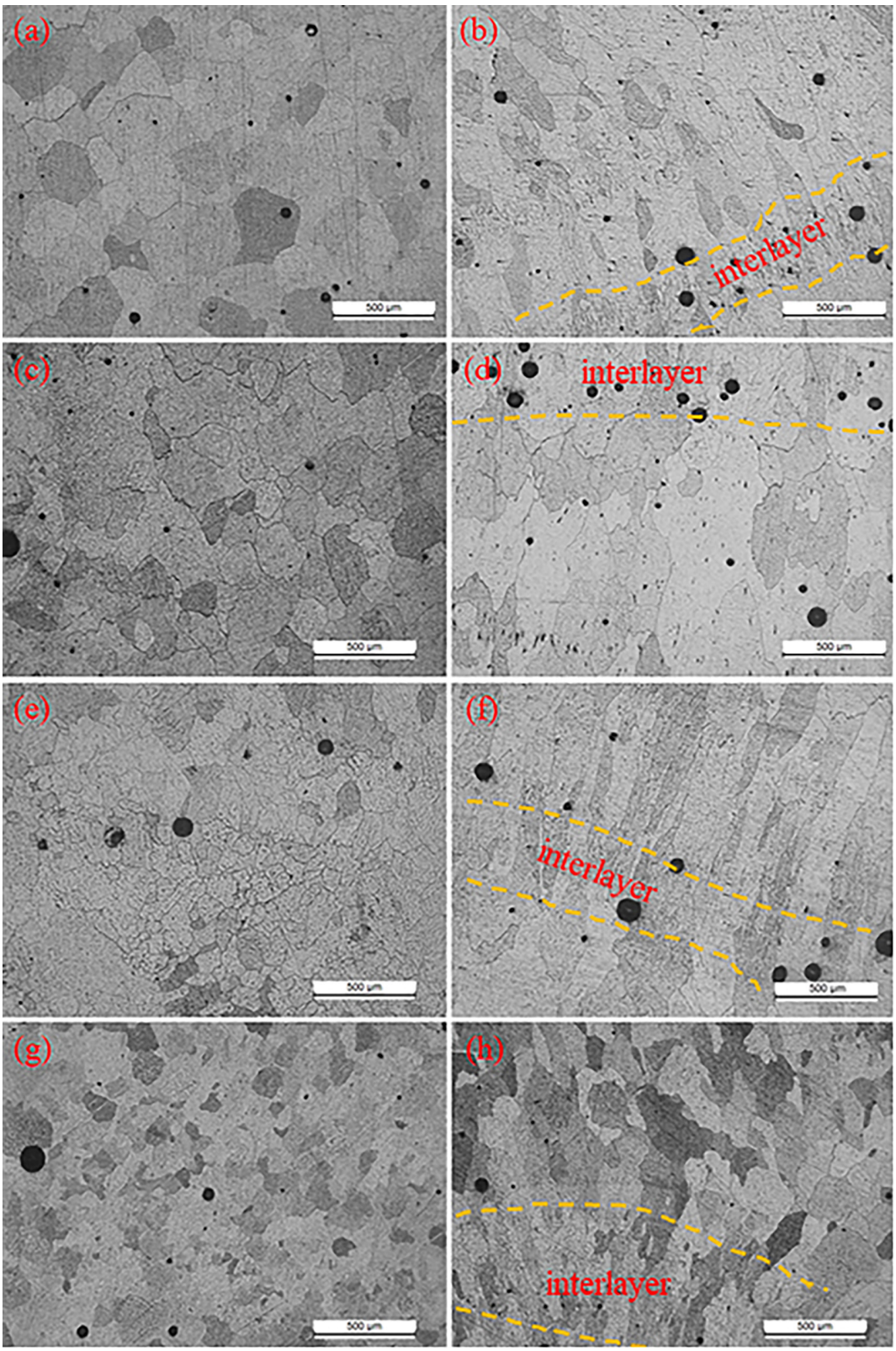

FIGURE 4 | Optical microstructure of these four samples in the horizontal and vertical section: **(a)** horizontal, **(b)** vertical section of the CMT + A mode, **(c)** horizontal and **(d)** vertical section of the CMT mode, **(e,f)** CMT + P mode, and **(g,h)** CMT + PA mode. CMT, cold metal transfer; CMT + A, cold metal transfer–incorporated polarity; CMT + P, cold metal transfer–incorporated pulse; and CMT + PA, cold metal transfer–incorporated pulse and polarity.

This proved that the arc mode has a significant effect on reducing pores in the samples. And the pulse and polarity arc modes have a positive effect in reducing the pore defects (Cong et al., 2015).

Microstructure Characterization

The mechanical properties of the as-deposited samples always depend on the microstructural changes and elemental distribution after experiencing an abrupt and cyclic thermal history. **Figure 4** displays the microstructures of these four samples along the vertical and horizontal sections from optical microscope (OM). These micrographs show the typical solidification characteristics of both the columnar dendritic and equiaxed dendritic structures. Each deposited layer can be divided into the interlayer and center regions. The grain structures in the four samples show a small difference. The grain structures of these four samples are all of equiaxed shape in the horizontal section, while nearly columnar structures are observed in the vertical section in the CMT and CMT + P sample. There are fine equiaxed grain regions at the interlayer region in CMT + A and CMT + PA samples, while the interlayer fine-grained regions are not obvious in the CMT + P and CMT samples. The grain size in the CMT + PA sample in the vertical section and horizontal section is almost the same, which is beneficial to eliminate the potential anisotropy of the material.

Element Distribution and Phase Constitution

It is widely accepted that the high strength of the 7075 alloy is mainly ascribed to a series of second-phase particles such as typical nanosize of $\eta(MgZn_2)$ (Davis, 1993). The solute contents and particles change significantly during WAAM, which plays an important role in the microstructure and mechanical properties variation.

Figure 5 exhibits the constituted second-phase particle distribution of the four as-deposited samples observed using the SEM. It can be seen from **Figure 5a** that most of the particles, with a rod-like morphology and an average size of less than

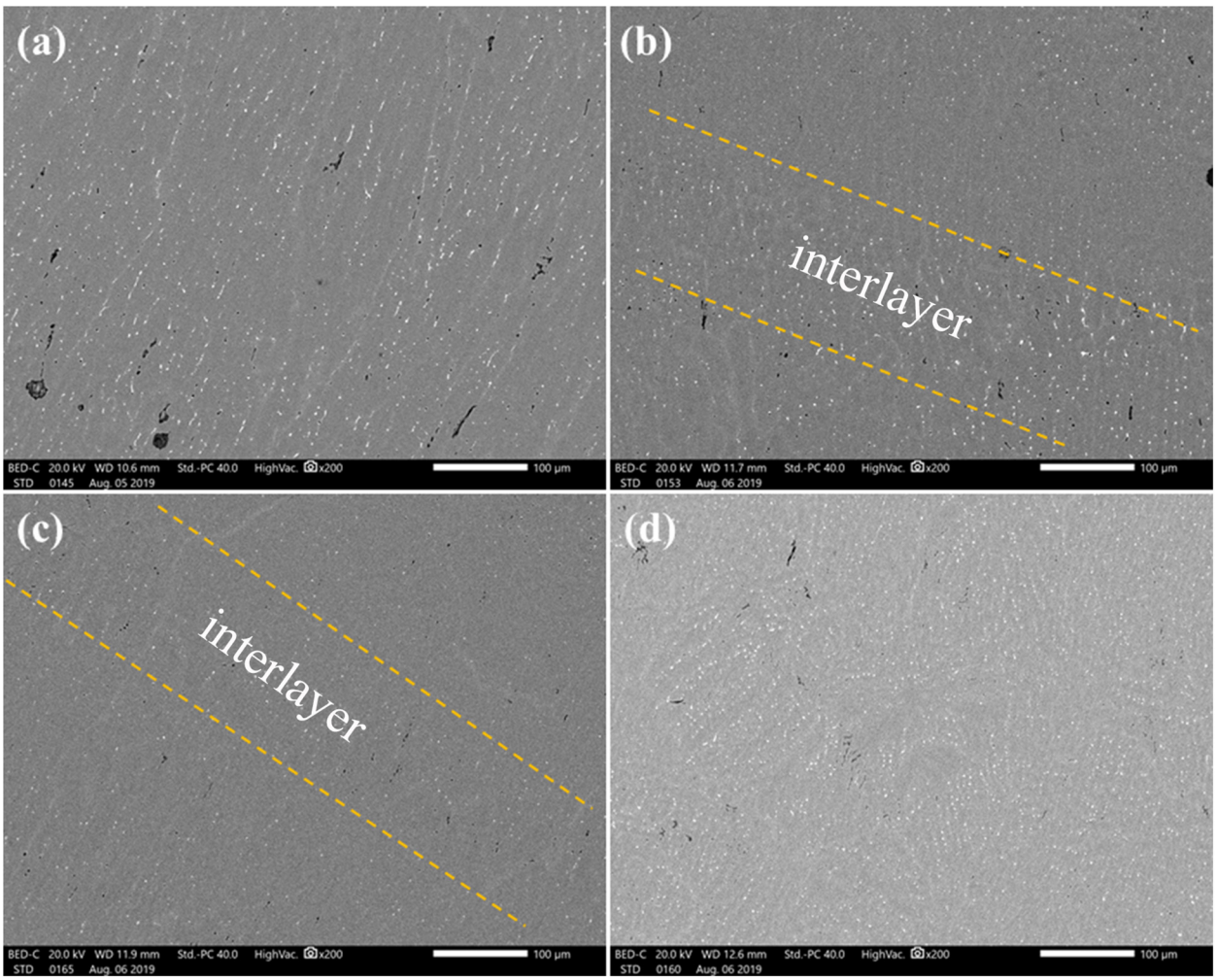

FIGURE 5 | BSE maps of the precipitation distribution in the as-deposited sample along the vertical direction **(a)** CMT, **(b)** CMT + A, **(c)** CMT + P, and **(d)** CMT + PA. CMT, cold metal transfer; CMT + A, cold metal transfer–incorporated polarity; CMT + P, cold metal transfer–incorporated pulse; and CMT + PA, cold metal transfer–incorporated pulse and polarity.

5 μm, distribute inside the α-Al matrix. In the four samples, the second-phase particles in CMT + A and CMT + P samples have a tendency to aggregate into a band-like distribution at the interlayer zone along the fusion line, as indicated by the yellow dotted line in **Figures 5b,c**. On the other hand, these white particles in the CMT + PA sample are almost uniformly distributed.

The backscattered-electron (BSE) images are shown in **Figure 6** to reveal more details of the fine and coarse particles. The morphology of the particles is mainly influenced by the alloy composition and cooling conditions, and different cooling conditions result in different morphologies. It can be seen in **Figure 6b** that some white particles in higher magnification show a net-like eutectic structure. These particles are most likely divorced eutectic particles formed during the final stage of cooling (Liu et al., 2019).

To further analyze the phase constitution of the white particles, EDS was performed on both the fine and coarse particles. The results show that the content of Zn and Mg in the α-Al matrix is 4.73wt.% and 1.78wt.%, respectively. Some of these fine white particles contain a large amount of Zn and only a little Fe, as shown in **Figure 6a**. Its chemical composition is 6.8wt.%Mg, 68.24wt.%Al, 6.74wt.%Fe, and 18.21wt.%Zn. This Fe-containing particle is considered to be detrimental to the

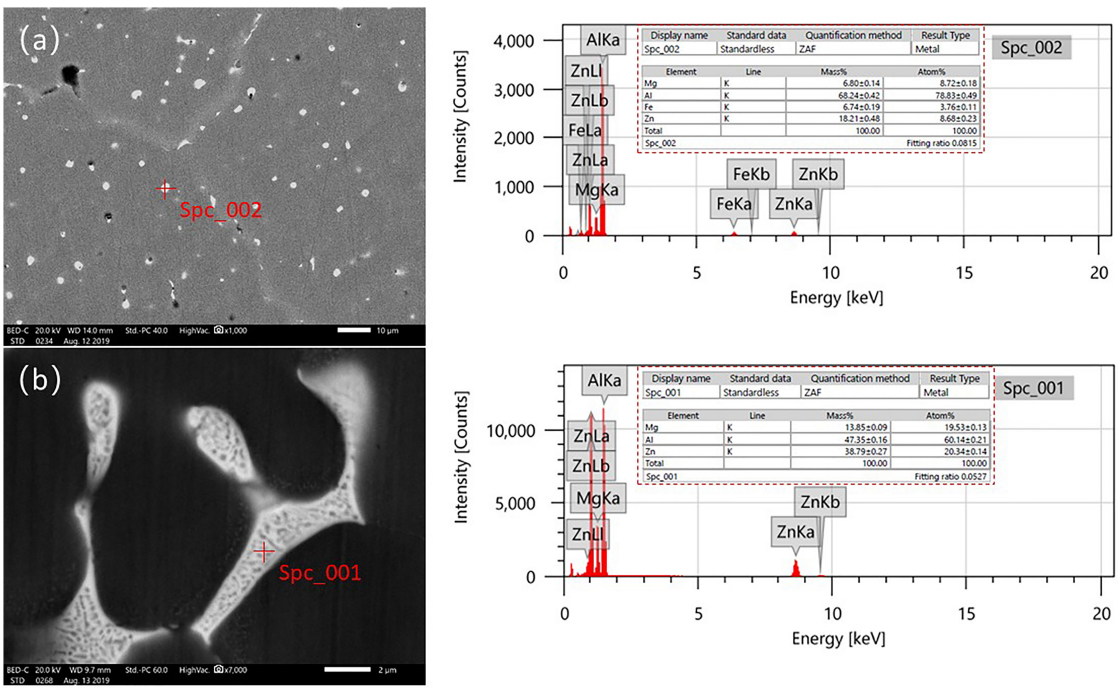

FIGURE 6 | (a) Particle morphology and spatial distribution in as-deposited CMT + PA sample and EDS analysis of the round particle and **(b)** eutectic structure of the white particle and its corresponding EDS analysis. EDS, energy-dispersive x-ray spectroscopy and CMT + PA, cold metal transfer–incorporated pulse and polarity.

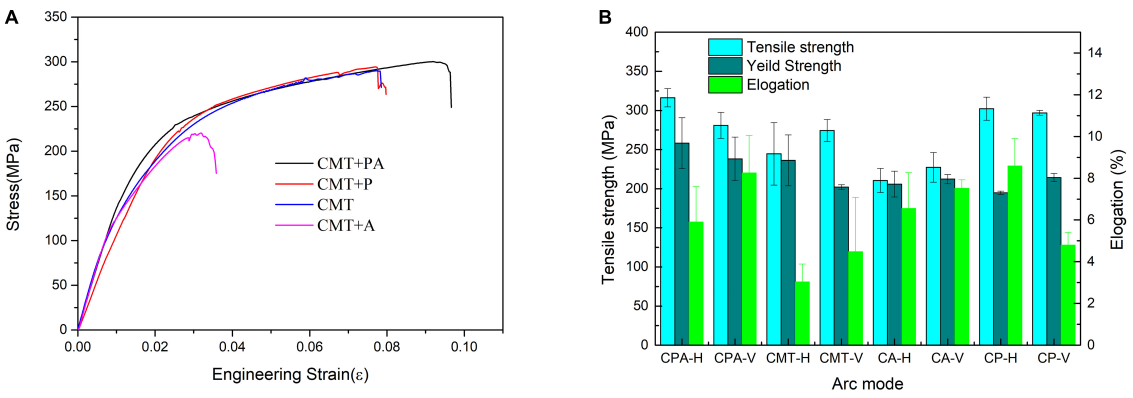

FIGURE 7 | (A) Tensile curves and **(B)** histogram of the tensile strength of the four samples.

strength of the material (Barbagallo et al., 2004). The composition of the coarse eutectic white particle is mainly Al, Mg, and Zn elements. The content of each element is 60.14, 19.53, and 20.34%, respectively (see **Figure 6b**), which are likely to be Al–Mg–Zn ternary compounds.

Mechanical Properties

The stress–strain curves and mechanical properties of the four as-deposited samples are shown in **Figure 7**. The overall mechanical properties, in terms of both strength and elongation, of the CMT + PA sample are the highest, while the tensile strength and yield strength of the CMT + A sample are the lowest. The mean value of horizontal and vertical tensile strength in the CMT + PA mode is 316.3 and 280.9 MPa, respectively, and the yield strengths are 258.3 and 238.1 MPa, respectively. The tensile strengths of the vertical and horizontal sample in the CMT + A mode are 210.6 and 227.4 MPa, and the yield strength is 205.9 and 212.3 MPa, respectively, which is the lowest among these samples. Except for the samples of the CMT + P mode, the vertical and horizontal mechanical properties are quite different in the other modes. The elongation of CMT + A is lower than other samples, which is 3% in the vertical direction and 4.2% in the horizontal direction, respectively, while the CMT + PA sample has an elongation of $>6.2\%$ in all samples.

DISCUSSION

Formation Mechanism of Porosity

The gas pores and lack of fusion pores are easily produced in additive manufacturing of metallic materials (DebRoy et al., 2018). The morphology of the gas pore is usually spherical, and the lack of the fusion pore is typically irregular. Since the majority of pores are spherical (see **Figures 2**, **3**), it can be concluded that the lack of fusion is not the main reason for the formation of pores. Normally, the most considerable factor of gas pore formation during additive manufacturing (AM) of the aluminum alloy is hydrogen element (Wu et al., 2013), but the entrapment of metal vapor also plays an important role. In the feeding wire, the content of Zn is 5.28wt.%, and the boiling point of Zn is 907°C, which is much lower than that of the Mg (1090°C) and Al (2518°C) element. **Table 3** lists the main chemical composition of these four samples. It can be clearly seen that the zinc element has reduced at least ∼0.5wt.% after WAAM. This means that zinc has vaporized in the deposited process. Therefore, zinc evaporation must have contributed to the gas pore formation. It is, therefore, reasonable to assume that these pores are a mixture of hydrogen gas pores and zinc evaporation pores. The fact that most of the gas pores are located near the interlayer region is unambiguously demonstrated from the x-ray CT, as presented in **Figure 3**. This non-uniformly distributed porosity should be held responsible for the anisotropic mechanical properties of the as-deposited samples, as will be detailed later.

TABLE 3 | Chemical compositions of the as-deposited samples obtained by inductively coupled plasma (ICP).

Arc mode	Mg	Zn	Fe
CMT	2.98	4.71	0.0092
CPA	2.54	4.76	0.1000
CA	2.98	4.72	0.0130
CP	3.00	4.68	0.0040

Microstructure and Second-Phase Particles

To further analyze the grain morphology and crystallographic texture, the inverse pole figure (IPF) EBSD maps of the CMT + PA and CMT samples were used, which are presented in **Figures 8a–h**. The effect of the arc mode on the grain morphology and grain size is evident. Equiaxed grain structure can be seen in the interlayer center region of the CMT + PA sample, while grains at the inner layer region show a larger grain size. Characteristic columnar structure is present at the inner layer region, and equiaxed grains can be seen at the interlayer region in the CMT, CMT + P, and CMT + A samples. The aspect ratio of the columnar grain in CMT, CMT + P, CMT + A, and CMT + PA samples is 3.4, 3.08, 2.88, and 2.31, respectively. The average grain size in the inner layer regions of CMT, CMT + P, CMT + A, and CMT + PA are 88, 78, 68.3, and 58.9 μm, respectively. It is, further, proved that the reduced heat input has a positive effect on columnar to equiaxed transition and decreasing the grain size; this is probably due to the fact that a faster cooling rate can be achieved at reduced heat input. **Figure 9** displays the pole figures of the CMT + PA and CMT samples. Although CMT + PA shows a lower maximum texture intensity (8.53) than that of the CMT sample (13.28), crystallographic texture was produced both in the CMT sample and CMT + PA sample. This means the crystallographic texture is not the dominating reason for the differences in the mechanical properties of the CMT + PA and CMT samples.

The arc mode also affects the status of the second-phase particles in the as-deposited samples. As shown in **Figure 6**, the second-phase particles may aggregate into a band-like distribution at the interlayer zone along the fusion line or being uniformly distributed, depending on the arc modes. Based on the Al–Zn–Mg ternary system, it can be concluded that the α-Al phase was the first to grow in the molten pool, since it developed a dendritic morphology (Liang et al., 1998). The liquid surrounding the solid–liquid interface was enriched with a solute (Zn and Mg). These solute elements cannot diffuse evenly due to the rapid solidification during the WAAM process. Therefore, the chemical composition of the retained liquid eventually reached the eutectic point in the ternary system; phases such as $MgZn_2$, τ-$Al_2Mg_3Zn_3$ intermetallic compounds and ($\alpha + \tau$-$Al_2Mg_3Zn_3$) eutectic structure can be formed, as echoed in Reference Alvarez et al. (2005). According to the EDS energy spectrum results and the chemical composition of the wire filler, it is inferred that the coarse second-phase particles may be the (α-Al + τ-$Al_2Mg_3Zn_3$) (Suarez et al., 2009).

Mechanical Properties

The strengthening of the aluminum alloy mainly includes solid solution strengthening, dispersion strengthening, and work hardening. The EDS energy spectrum shows that most Zn and

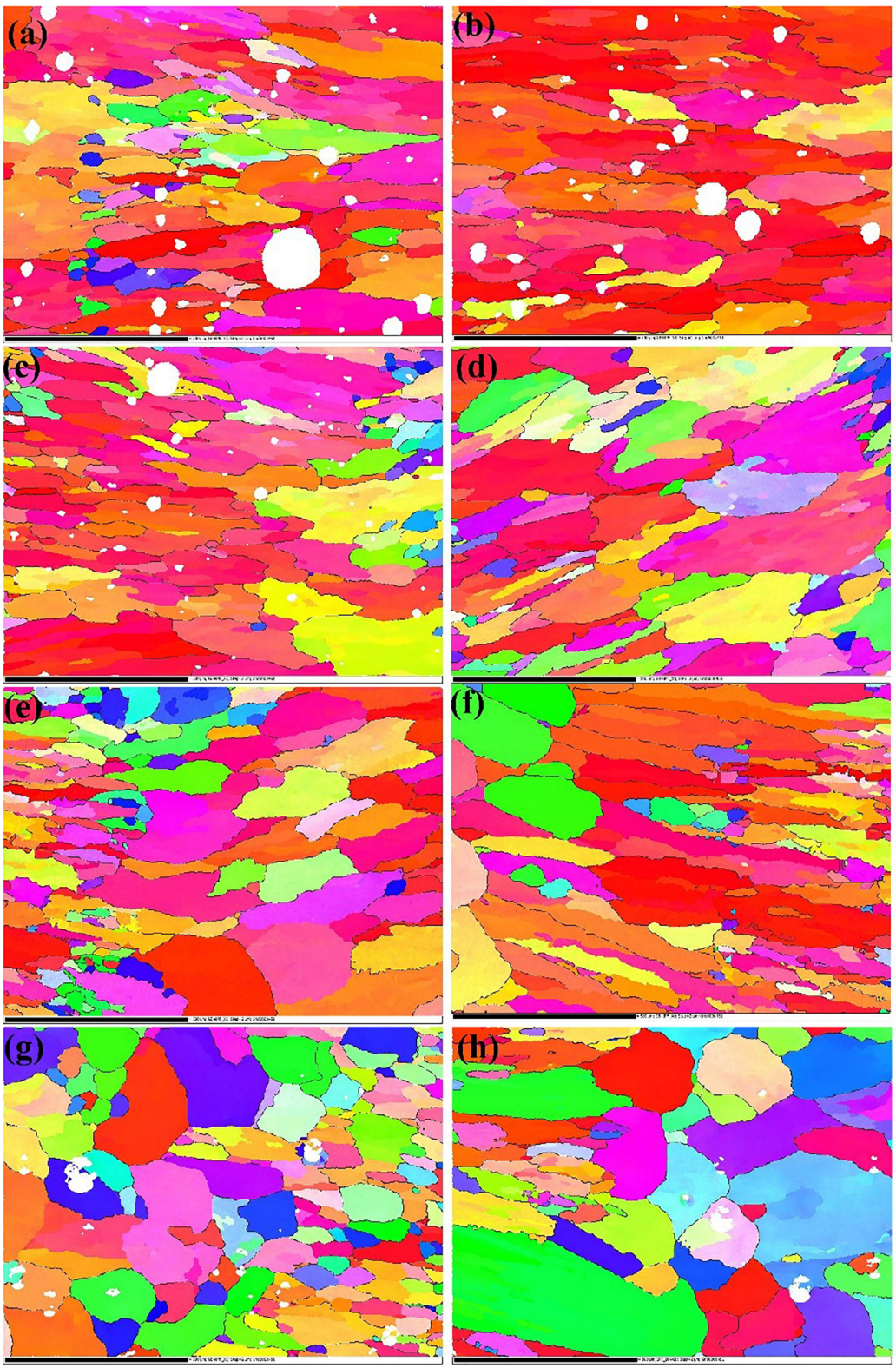

FIGURE 8 | The center and interlayer region IPF maps of these four samples: **(a)** center region of the CMT sample, **(b)** interlayer region of the CMT sample, **(c)** center region of the CMT + P sample, **(d)** interlayer region of the CMT + P sample, **(e)** center region of the CMT + A sample, **(f)** interlayer region of the CMT + A sample, **(g)** center region of the CMT + PA sample, and **(h)** interlayer region of the CMT + PA sample. CMT, cold metal transfer; CMT + A, cold metal transfer–incorporated polarity; CMT + P, cold metal transfer–incorporated pulse; CMT + PA, cold metal transfer–incorporated pulse and polarity, and IPF, inverse pole figure.

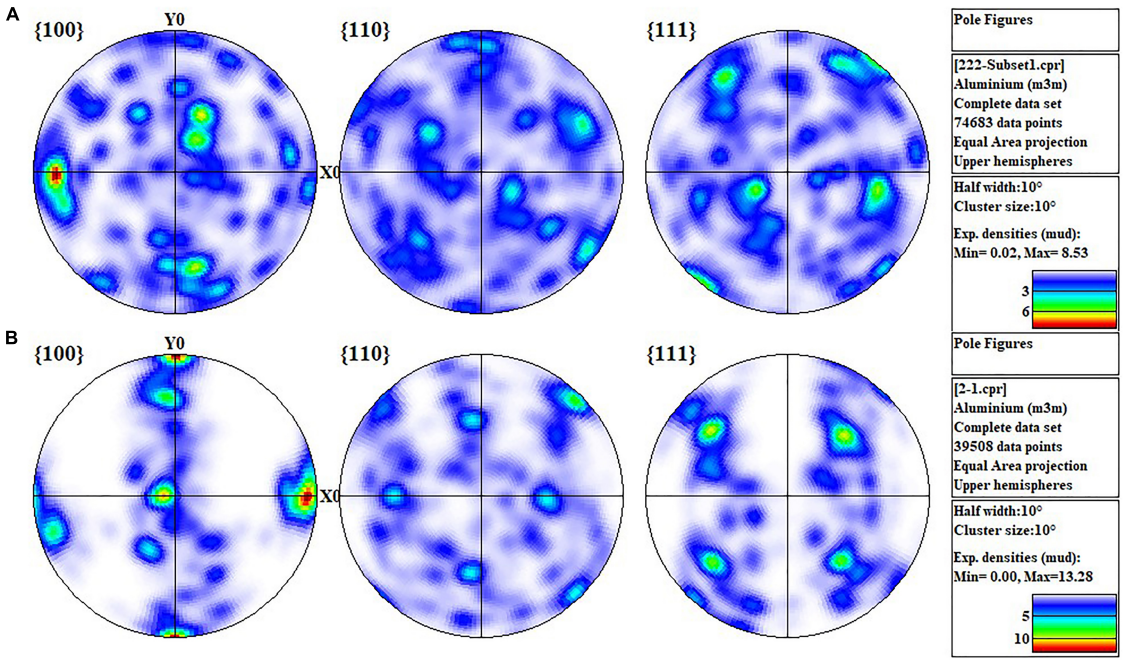

FIGURE 9 | (A) Pole figure of CMT + PA and **(B)** pole figure of CMT. CMT, cold metal transfer and CMT + PA, cold metal transfer–incorporated pulse and polarity.

Mg elements are dissolved into α-Al; the zinc content also increases from 4.13wt.% to 4.7wt.% in the α-Al phase under a different heat input; this contributes to the solid solution strengthening. The size of the constituent second phase in the deposited material is basically in the scale of 5 μm, as shown in **Figures 6**, **7**. Due to their large sizes, their contribution to the strength is very limited (Huang et al., 2018). During the cyclic heating and cooling process, some nanoscale second-phase dispersion and precipitation are expected, which may contribute to the strength improvement of the samples (Fang et al., 2021). It should be noted that the high strength of 7xxx alloys depends on the massive nanoscale precipitates after an appropriate solid solution and aging heat treatment; this is not covered here since it will be the topic of our next paper. The microstructure for the four samples shows inhomogeneous grains and heterogeneous distribution of precipitated particles. The grain sizes are within the range of ∼88 to ∼58.9 μm with various arc modes; the scale of grain refinement is too small to introduce significant grain boundary strengthening (Ding et al., 2015).

It should be noted that the porosity also significantly affects the mechanical properties of the as-deposited aluminum alloys (Zhou et al., 2020; Fang et al., 2021). The strength differences in the horizontal and vertical directions of the as-deposited samples are related to the heterogeneous distribution of pores at the interlayer, as shown in **Figure 3** from the x-ray CT. The fracture surfaces after the tensile testing are helpful to explain the fracture behavior; only the fractography of the sample fabricated by CMT + PA is further explained here. As shown in **Figure 10**, the fracture is mainly a mixture of the brittle fracture morphology and local plastic characteristics regardless of the horizontal or vertical direction. The brittle fracture of the samples is characterized by the intergranular brittle fracture with the dimple gliding surface (**Figures 10b,d**). The dimples are shallow and of small size (∼5 μm), as pointed out by the red arrow. This explains the low fracture elongation of the as-deposited samples. Besides, there are many pores distributed on the fracture surface. The interlayer pores can be clearly seen in **Figure 10a** (horizontal direction, as indicated by the red dotted lines), while pores are scattered in the vertical direction (**Figure 10c**, as indicated by the red dotted circles). This implies that microcracks may preferentially originate from these pores at the interlayer zone, and then these microcracks propagate and join together to form macrocracks until fracture takes place in the vertical direction. Therefore, the strength in the vertical direction is generally inferior to that of the horizontal direction in CMT + PA, CMT, and CMT + P sample. The porosity ratio in CMT + P is lower than that in the CMT + PA sample; this could be an explanation to the similar tensile strength in the horizontal and vertical direction. However, the pore accumulation at the interlayer zone in CMT + PA may cause the lower strength in the vertical direction. Even though the CMT + A sample has the lowest porosity, large pores (as illustrated in **Figure 3**) could be the main reason for its low tensile strength.

Generally, heat treatment is an indispensable step to increase the strength of the Al–Zn–Mg alloy. The work presented in this article is mainly a preliminary exploration of fabricating a high-strength Al–Zn–Mg component using the WAAM technology. Ongoing work will focus on tailoring the chemical composition of this alloy for the WAAM process, as well as reducing the porosity and performing appropriate heat treatment to improve the mechanical properties of Al–Zn–Mg materials.

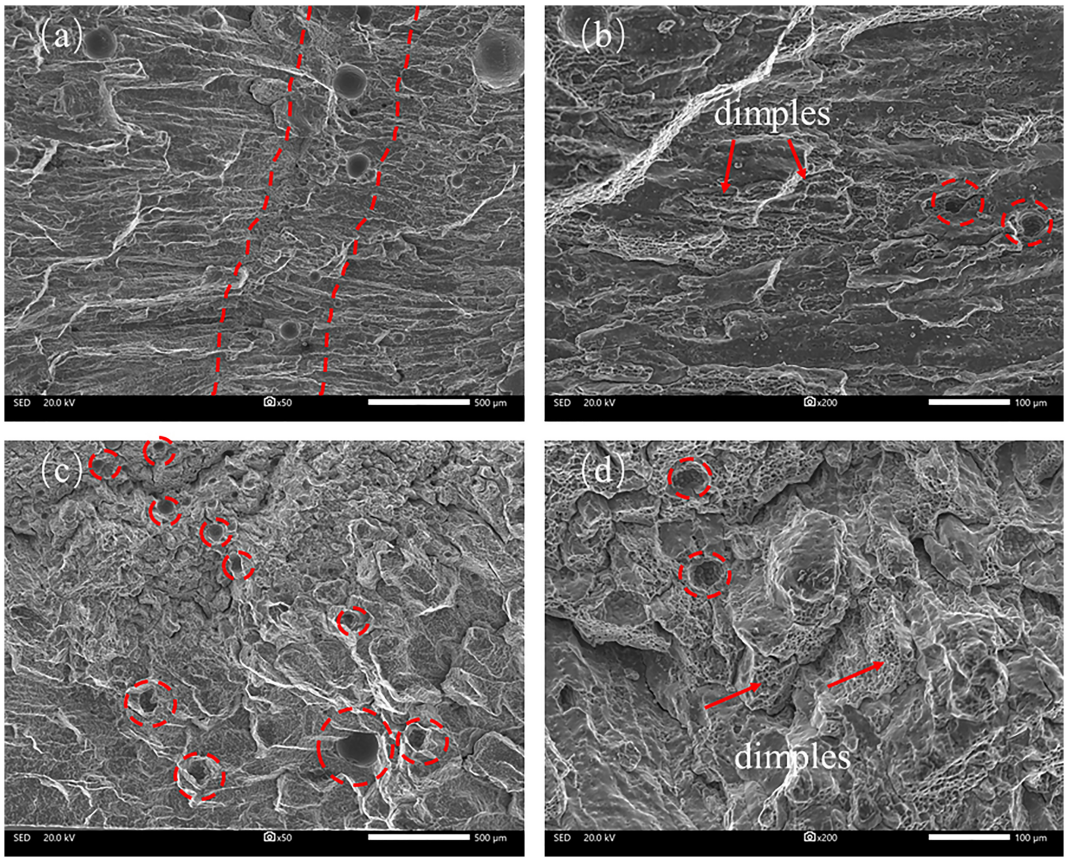

FIGURE 10 | Fracture morphology of the CMT + PA sample along the horizontal direction **(a)** low-magnification and **(b)** high-magnification photo and the vertical direction **(c)** low-magnification and **(d)** high-magnification photo. CMT + PA, cold metal transfer–incorporated pulse and polarity.

CONCLUSION

The Al–Zn–Mg alloy was successfully fabricated without a hot crack by WAAM. The correlation between the microstructure, second-phase particles, porosity, and mechanical properties was exploited. The following conclusion can be drawn:

(1) The heat input has a non-negligible influence on the microstructure and porosity of the Al–Zn–Mg alloy. Columnar grains tend to transform into equiaxed grains when the heat input is reduced.
(2) The pores in the as-deposited sample are dominated by gas pores. This type of porosity mainly consists of hydrogen gas pores and zinc vapor pores. The volume fraction of pores is reduced because of heat input decreasing.
(3) The tensile and yield strength of the CMT + PA sample show the optimum tensile properties among the samples fabricated by different arc modes. The mechanical anisotropy can be ascribed to the accumulated pores near the interlayer region. The fracture shows a mixture of the brittle fracture morphology with local plastic characteristics. The difference in strength along the horizontal and vertical directions is most likely caused by the heterogenous interlayer pores.

DATA AVAILABILITY STATEMENT

The original contributions presented in the study are included in the article/supplementary material, further inquiries can be directed to the corresponding author/s.

AUTHOR CONTRIBUTIONS

XF: methodology, investigation, and writing. GC: investigation, writing, and editing. JY: review and editing. YX: conceptualization and resources. KH: supervision, review, and editing. BL: project administration and supervision. All authors: contributed to the article and approved the submitted version.

FUNDING

This work was supported by the National Key Research and Development Program of China (Grant No. 2018YFB1105803), the China Postdoctoral Science Foundation (Grant No. 2019M663682), and the Fundamental Research Funds for the Central Universities (xzd012019033).

REFERENCES

Aboulkhair, N. T., Simonelli, M., Parry, L., Ashcroft, I., Tuck, C., and Hague, R. (2019). 3D printing of Aluminium alloys: additive manufacturing of aluminium alloys using selective laser melting. *Prog. Mater. Sci.* 106:100578. doi: 10.1016/j.pmatsci.2019.100578

Alvarez, O., Gonzalez, C., Aramburo, G., Herrera, R., and Juarez-Islas, J. A. (2005). Characterization and prediction of microstructure in Al-Zn-Mg alloys. *Mater. Sci. Eng. A* 402, 320–324. doi: 10.1016/j.msea.2005.05.022

Barbagallo, S., Laukli, H. I., Lohne, O., and Cerri, E. (2004). Divorced eutectic in a HPDC magnesium-aluminum alloy. *J. Alloy Compd.* 378, 226–232. doi: 10.1016/j.jallcom.2003.11.174

Cong, B., Ding, J., and Williams, S. (2015). Effect of arc mode in cold metal transfer process on porosity of additively manufactured Al-6.3% Cu alloy. *Int. J. Adv. Manuf. Tech.* 76, 1593–1606.

Davis, J. R. (1993). *Aluminum and Aluminum Alloys*. Novelty, OH: ASM international.

DebRoy, T., Wei, H. L., Zuback, J. S., Mukherjee, T., Elmer, J. W., and Milewski, J. O. (2018). Additive manufacturing of metallic components-process, structure and properties. *Prog. Mater. Sci.* 92, 112–224.

Ding, D., Pan, Z., Cuiuri, D., and Li, H. (2015). Wire-feed additive manufacturing of metal components: technologies, developments and future interests. *Intern. J. Adv. Manufact. Technol.* 81, 465–481.

Fang, X., Zhang, L., Chen, G., Dang, X., Huang, K., Wang, L., et al. (2018). Correlations between microstructure characteristics and mechanical properties in 5183 aluminium alloy fabricated by wire-arc additive manufacturing with different arc modes. *Materials* 11:2075. doi: 10.3390/ma11112075

Fang, X., Zhang, L., Chen, G., Huang, K., Xue, F., Wang, L., et al. (2021). Microstructure evolution of wire-arc additively manufactured 2319 aluminum alloy with interlayer hammering. *Mater. Sci. Eng. A* 800:140168. doi: 10.1016/j.msea.2020.140168

Girelli, L., Giovagnoli, M., Tocci, M., Pola, A., Fortini, A., Merlin, M., et al. (2019). Evaluation of the impact behaviour of AlSi10Mg alloy produced using laser additive manufacturing. *Mater. Sci. Eng. A* 748, 38–51. doi: 10.1016/j.msea.2019.01.078

Huang, K., Marthinsen, K., Zhao, Q., and Logé, R. E. (2018). The double-edge effect of second-phase particles on the recrystallization behaviour and associated mechanical properties of metallic materials. *Prog. Mater. Sci.* 92, 284–359.

Klein, T., Schnall, M., Gomes, B., Warczok, P., Fleischhacker, D., and Morais, P. J. (2020). Wire-arc additive manufacturing of a novel high-performance Al-Zn-Mg-Cu alloy: processing, characterization and feasibility demonstration. *Addit. Manuf.* 37:101663.

Kuo, Y. L., Horikawa, S., and Kakehi, K. (2017). Effects of build direction and heat treatment on creep properties of Ni-base superalloy built up by additive manufacturing. *Script. Mater.* 129, 74–78. doi: 10.1016/j.scriptamat.2016.10.035

Li, S., Ning, J., Zhang, G. F., Zhang, L. J., Wu, J., and Zhang, L. X. (2021). Microstructural and mechanical properties of wire-arc additively manufactured Al-Zn-Mg aluminum alloy: the comparison of as-deposited and heat-treated samples. *Vacuum* 184:109860. doi: 10.1016/j.vacuum.2020.109860

Li, S., Zhang, L. J., Ning, J., Wang, X., Zhang, G. F., Zhang, J. X., et al. (2020). Microstructures and mechanical properties of Al-Zn-Mg aluminium alloy samples produced by wire+ arc additive manufacturing. *J. Mater. Res. Technol.* 9, 13770–13780. doi: 10.1016/j.jmrt.2020.09.114

Liang, P., Tarfa, T., Robinson, J. A., Wagner, S., Ochin, P., Harmelin, M. G., et al. (1998). Experimental investigation and thermodynamic calculation of the Al-Mg-Zn system. *Thermochim. Acta* 314, 87–110. doi: 10.1016/S0040-6031(97)00458-9

Liu, S., and Shin, Y. C. (2019). Additive manufacturing of Ti6Al4V alloy: a review. *Mater. Design.* 164:107552. doi: 10.1016/j.matdes.2018.107552

Liu, Y., Deng, C., Gong, B., and Bai, Y. (2019). Effects of heterogeneity and coarse secondary phases on mechanical properties of 7050-T7451 aluminum alloy friction stir welding joint. *Mater. Sci. Eng. A* 764:138223. doi: 10.1016/j.msea.2019.138223

Martin, J. H., Yahata, B. D., Hundley, J. M., Mayer, J. A., Schaedler, T. A., and Pollock, T. M. (2017). 3D printing of high-strength aluminium alloys. *Nature* 549, 365–369. doi: 10.1038/nature23894

Montero-Sistiaga, M. L., Mertens, R., Vrancken, B., Wang, X., Van Hooreweder, B., Kruth, J. P., et al. (2016). Changing the alloy composition of Al7075 for better processability by selective laser melting. *J. Mater. Process. Tech.* 238, 437–445. doi: 10.1016/j.jmatprotec.2016.08.003

Morais, P. J., Gomes, B., Santos, P., Gomes, M., Gradinger, R., Schnall, M., et al. (2020). Characterisation of a high-performance Al-Zn-Mg-Cu alloy designed for wire arc additive manufacturing. *Materials* 13:1610.

Oliveira, J. P., Santos, T. G., and Miranda, R. M. (2020). Revisiting fundamental welding concepts to improve additive manufacturing: from theory to practice. *Prog. Mater. Sci.* 107:100590. doi: 10.1016/j.pmatsci.2019.100590

Rosenthal, I., Stern, A., and Frage, N. (2014). Microstructure and mechanical properties of AlSi10Mg parts produced by the laser beam additive manufacturing (AM) technology. *Metallogr. Microstruc. Analys.* 3, 448–453. doi: 10.1007/s13632-014-0168-y

Stopyra, W., Gruber, K., Smolina, I., Kurzynowski, T., and Kuźnicka, B. (2020). Laser powder bed fusion of AA7075 alloy: influence of process parameters on porosity and hot cracking. *Addit. Manuf.* 35:101270. doi: 10.1016/j.addma.2020.101270

Su, C., Chen, X., Gao, C., and Wang, Y. (2019). Effect of heat input on microstructure and mechanical properties of Al-Mg alloys fabricated by WAAM. *Appl. Surf. Sci.* 486, 431–440. doi: 10.1016/j.apsusc.2019.04.255

Suarez, M. A., Lara, A. G., Sánchez-Arévalo, F. M., Alvarez, O., Colin, J., and Juarez-Islas, J. A. (2009). Prediction and characterization of growth temperatures in Al-Zn-Mg alloys. *Mater. Charact.* 60, 420–424. doi: 10.1016/j.matchar.2008.11.002

Uddin, S. Z., Murr, L. E., Terrazas, C. A., Morton, P., Roberson, D. A., and Wicker, R. B. (2018). Processing and characterization of crack-free aluminum 6061 using high-temperature heating in laser powder bed fusion additive manufacturing. *Addit. Manuf.* 22, 405–415. doi: 10.1016/j.addma.2018.05.047

Wang, P., Li, H. C., Prashanth, K. G., Eckert, J., and Scudino, S. (2017). Selective laser melting of Al-Zn-Mg-Cu: heat treatment, microstructure and mechanical properties. *J. Alloy Compd.* 707, 287–290. doi: 10.1016/j.jallcom.2016.11.210

Wu, S. C., Yu, X., Zuo, R. Z., Zhang, W. H., Xie, H. L., and Jiang, J. Z. (2013). Porosity, element loss, and strength model on softening behavior of hybrid laser arc welded Al-Zn-Mg-Cu alloy with synchrotron radiation analysis. *Weld. J.* 92, 64–71.

Zhou, Y., Lin, X., Kang, N., Huang, W., and Wang, Z. (2020). Mechanical properties and precipitation behavior of the heat-treated wire+ arc additively manufactured 2219 aluminum alloy. *Mater. Charact.* 171:110735. doi: 10.1016/j.matchar.2020.110735

Conflict of Interest: YX was employed by company China Ship Design & Research Center.

The remaining authors declare that the research was conducted in the absence of any commercial or financial relationships that could be construed as a potential conflict of interest.

frontiers in Materials

REVIEW
published: 20 July 2021
doi: 10.3389/fmats.2021.661013

Mechanical Strength of Graphene Reinforced Geopolymer Nanocomposites: A Review

Chai Hua Tay[1†] *and Mazlan Norkhairunnisa*[2,3*†]

[1]*Institute of Tropical Forestry and Forest Products (INTROP), Universiti Putra Malaysia, Serdang, Malaysia,* [2]*Institute of Advanced Technology, Universiti Putra Malaysia, Serdang, Malaysia,* [3]*Department of Aerospace Engineering, Faculty of Engineering, Universiti Putra Malaysia, Serdang, Malaysia*

The emergence of high-strength graphene marks a new milestone in the material science field. With only a small percentage inclusion into the matrix system, this organic nanoparticle could tremendously improve the strength in vast arrays of composites. At the same time, there is a growing interest in using the low-cost, lightweight, and high early strength geopolymer as the new binder for concrete. Compared to the traditional Ordinary Portland Cement (OPC), geopolymer emits 80% less CO_2 during its production while exerting similar strength. Thus, the geopolymer has the potential to commercialize as new and green concrete. Geopolymer is a mixture of aluminosilicate powders and alkaline solutions. When incorporated with nano-sized graphene, the material forms a composite known as Graphene Reinforced Geopolymer Nanocomposite (GRGN). The addition of graphene enhances the strength of geopolymer, which can further improve its competitiveness. However, this depends on several factors, including the types of graphene, the surface modification of graphene, and the concentration of alkaline solutions. Generally, the presence of graphene alters the porous structure of geopolymer into a substantially filled porous structure, thus increasing compressive strength and flexural strength. On the other hand, Graphene Oxide (GO) undergoes a chemical reduction in the alkaline solution, producing epoxy functional groups. The chemical treatment results in two conditions which are weak interaction between graphene and geopolymer matrix, and better graphene dispersibility in geopolymer matrix. This review also highlights the analytical modelling aspect of GRGN. The dissolution of $Si(OH)^4$ and $Al(OH)^{4-}$ from the aluminosilicate source was consistent with experimental work and analytical modeling, while the dissolution of Si–OH on the surface-modified graphene indicated otherwise. Therefore, this paper will provide an insightful review of the GRGN mechanical properties.

Keywords: graphene, geopolymer, nanocomposite, flexural, compressive

OPEN ACCESS

Edited by:
Mohd Mustafa Al Bakri Abdullah, Universiti Malaysia Perlis, Malaysia

Reviewed by:
Neven Ukrainczyk, Darmstadt University of Technology, Germany
Romisuhani Binti Ahmad, Universiti Malaysia Perlis, Malaysia
Zarina Yahya, Universiti Malaysia Perlis, Malaysia
Yun Ming Liew, Universiti Malaysia Perlis, Malaysia

***Correspondence:**
Mazlan Norkhairunnisa
norkhairunnisa@upm.edu.my

[†]*Materials Processing and Technology Laboratory, Institute of Advanced Technology, Universiti Putra Malaysia, Selangor, Malaysia*

Specialty section:
This article was submitted to Structural Materials, a section of the journal Frontiers in Materials

Received: *30 January 2021*
Accepted: *05 July 2021*
Published: *20 July 2021*

Citation:
Tay CH and Norkhairunnisa M (2021) Mechanical Strength of Graphene Reinforced Geopolymer Nanocomposites: A Review. Front. Mater. 8:661013. doi: 10.3389/fmats.2021.661013

INTRODUCTION

The idea of geopolymer was first encountered by Joseph Davidovits in 1972 when he was initially searching for incombustible material due to the catastrophic fires in France at that time. The idea arose from the fact that a simple hydrothermal condition could govern the synthesis of plastics (polymer) in an alkaline medium (Davidovits, 2002). Davidovits then develop a three-dimensional,

semi-crystalline mineral polymer called geopolymer. The first application of geopolymer is a fire-resistant coating for wooden chipboard panels produced by compression. In 1975, he made the first breakthrough of producing a geopolymeric liquid binder with the combination of metakaolin (MK) and soluble alkali silicates. Due to its fluidity, the liquid binder gathers attention from industry for its use as cement (Davidovits, 2015a). Since then, various types of new geopolymers materials have been produced, including adhesives (Bell et al., 2005; He et al., 2011; Quan et al., 2017), waste encapsulations (Frizon, and Desbats-le-Chequer, 2010; Kupwade-Patil et al., 2013a; Mohajerani et al., 2019) and resin for fiber composites (Ruzaidi et al., 2014; Hron et al., 2018).

Not limited to MK, geopolymer can be made from other kinds of abundant aluminosilicate as well. The aluminosilicate includes slag, fly ash, clays, waste glass powder, volcanic tuffs, and calcined natural fibers such as rice husks, bamboo leaves, and elephant grass (Kriven, 2012). Ultimately, these aluminosilicate sources contain silica and alumina (Léonard and Su, 2007; Tulyaganov et al., 2013). When mixed with alkaline solution (either at room temperature or elevated temperature), the silica and alumina will react, following several steps in becoming a geopolymer. These steps include alkalinization, depolymerization of silicates, gel formation of olio-sialates, polycondensation, reticulation (networking), and lastly, geopolymer solidification (Habert, 2014; Davidovits, 2018).

Presence of low silica to alumina content, Si:Al ratio, is preferred for the high rigidity of geopolymer. When Si:Al ratio is between 1:1 and 2:1, the geopolymer material possesses a 3D network. When the ratio increases to 35:1, the network becomes 2D. The silica and alumina content varies with the aluminosilicate source. Thus, to achieve the desired Si:Al ratio and the intended resultant properties, one can utilize more than one type of aluminosilicate material in the production of geopolymer. On the other hand, the concentration of an alkaline solution affects the stability of geopolymer in water. This is because alkaline solution contains positive ions, for example Na^+ in NaOH solution and K^+ in KOH solution. These positive ions are often labeled as K. During geopolymerization, only positive ions can attach themselves to Al^- from the aluminosilicate source. When the content of positive ions exceeds alumina's content (K:Al>1), it will cause the positive ions in the geopolymer to be exposed and migrate easily in water. Therefore, in this scenario, the geopolymer structure will be broken (Davidovits, 2018). Thus, geopolymer rigidity and stability depend on silica and alumina content from aluminosilicate sources and positive ions from alkaline solutions.

Even with low Si:Al ratio and balanced K:Al ratio, the geopolymer has one main flaw, which is brittle. Like ceramic, geopolymer is highly susceptible to cracking under loading (Chi et al., 2018). The unstable geopolymer structure is due to its highly cross-linked framework. Filler reinforcement in the geopolymer matrix can improve fracture toughness and resist crack propagation in geopolymer, thus combating the brittleness of geopolymer material (Wang et al., 2016; Dac Ho, 2020). Variety types of reinforcement have been added into the geopolymer matrix to improve the geopolymer properties.

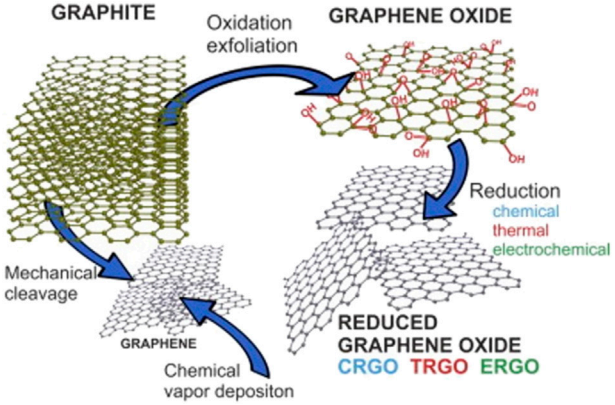

FIGURE 1 | Schematic diagram on the preparation of graphene and Graphene Oxide (GO) (Filip and Tkac, 2014).

This paper discusses in detail the effects of adding two-dimensional graphene and its derivatives on enhancing the mechanical performance of geopolymer nanocomposite.

GRAPHENE AND ITS DERIVATIVES

Graphene has been reinforced in polymer composite due to its attractive properties. Research on using graphene to modify the properties of the polymer (Carotenuto et al., 2012; Itapu and Jayatissa, 2018; Moharana et al., 2019), and ceramics (Porwal et al., 2013; Ikram and Farooq, 2019; Głuchowsk et al., 2020; Sun et al., 2020) have received much attention. The two-dimensional honeycomb structure of the graphene carbon network has multi functionally unique properties such as high thermal conductivity, which is in the range of 2000–5000 W/mK (Jauregui et al., 2010), large surface area which is more than 2,630 m^2/g (Lambert et al., 2009; Moon et al., 2010a), high Young Modulus of about 1 TPa (Liu et al., 2013), and high electrical conductivity. Graphite is the simplest form of crystalline carbon allotropes arranged in hexagonal manners with a C-C bond distance of only 0.142 nm (Anderson et al., 2013; Tiwari et al., 2020). The planar structure of graphene sheets creates a very high contact area with the host material because the top and bottom surface of the sheet is in close contact with the matrix (Lambert et al., 2009). The graphene sheet consists of a one-atom-thick lattice with carbon atoms arranged in a hexagonal ring structure (Roberts et al., 2010). The development of different types of graphene structures is shown in **Figure 1**.

Apart from Chemical Vapor Deposition (CVD) shown in **Figure 1**, graphene can be synthesized through methods such as micromechanical exfoliation of graphite (Novoselov et al., 2004), epitaxial growth (Huang et al., 2008), chemical intercalation (Malik et al., 2010), and the reduction of graphene oxide (Moon et al., 2010b). Preparation of graphene from GO stands out because it is promising for mass production of graphene based materials (Mao et al., 2012). GO can be synthesized in large quantity by oxidizing inexpensive graphite powders using strong oxidants where graphite powders are exfoliated and broken into layers with

increased interlayer distance. The landscape of the sp^2 carbon network is modified with oxygen containing functional groups and defects (holes) (Mao et al., 2012).

These oxygen-based functional groups such as epoxy (-COC) and hydroxyl (-OH) are randomly attached across the carbon backbone and carbonyl (C=O) and carboxylic acid (-COOH) are distributed at the edges of the graphene sheets (Lambert et al., 2009; Mao et al., 2012; Smith et al., 2019; Zhang Q. et al., 2020). These oxygen-containing moieties make GO hydrophilic and readily exfoliated when immersed in water (Ku Muhammad et al., 2016). In other words, GO can quickly disperse in an alkaline solution (Kuilla et al., 2010; Pei and Cheng, 2012). Good GO dispersion is said mainly due to the strong hydrogen bonding between GO functional groups and solvent molecules (Neklyudov et al., 2017). However, it has also been reported that GO sheets are highly negatively charged when dispersed in water as a result of ionization of the carboxylic acid and phenolic hydroxyl groups that are known to exist on GO sheets. Formation of stable GO colloids should be attributed to electrostatic repulsion rather than just hydrophilicity of GO (Li et al., 2008).

Reduced graphene oxide (rGO) has similar properties to GO but with reduced oxygen content. The rGO is produced by a thermal or chemical reduction process on GO. A range of reducing agent through chemical method includes hydrazine, alcohol, sodium borohydride, hydriodic acid with acetic acid, sodium/potassium hydroxide and many others (Mao et al., 2012). The defects introduced onto graphene oxide sheet due to oxidation degrades its unique properties, so it is important to reduce a much less defective rGO. The rGO still has good dispersibility in an alkaline medium which is suitable to be processed with geopolymer (Fan et al., 2008). This can be attributed mainly due to the residual of oxygen functional group on rGO. A one-step approach to reducing and functionalizing GO under alkaline solution has been reported (Yuan et al., 2014). Functionalized GO sheets display enhanced compatibility with polymer matrix. Thus, simultaneously reduced, and functionalized GO sheets exhibit better dispersion in matrix (Li et al., 2011; Ma et al., 2012; Mao et al., 2012).

GO sheets show that they are highly negatively charged when dispersed in water as a result of ionization of the carboxylic acid and phenolic hydroxyl groups that are known to exist on GO sheets. Formation of stable GO colloids should be attributed to electrostatic repulsion rather than just hydrophilicity of GO. It is worth nothing that the defects in GO and rGO causes reduction in electrical conductivity but offers a new applications that cannot be achieved with pristine graphene. This includes surfactant free graphene colloids. Graphene oxide can dispersion can be directly converted to stable graphene colloids through hydrazine reduction under controlled condition. The use of polymeric or surfactant is not required. Complete removal of metal salts and acids which often remain in the starting graphite oxide is critical to stability. These residual electrolytes can neutralize the charges on the sheets, destabilizing the resulting dispersion. As synthesized GO was suspended in water to give brown suspension which was subjected to dialysis to completely remove residual salts and acids (Li et al., 2008).

Reduction level of rGO is precisely controlled by heating temperature, gas environment and duration. To achieve a high reduction level, combination of chemical reduction with thermal reduction is proposed. Missing atoms or holes in GO carbon network could not be fixed with chemical reduction but by thermal reduction with carbon containing gas source, it is possible to repair the carbon network in GO. Overall, the properties of this nanoparticle depends on the type and distribution of functional groups, defects and holes from missing carbon in the GO carbon lattice (Mao et al., 2012).

Graphene nanoplatelet (GNP) is another type of graphene used as an additive in the geopolymer nanocomposites. GNP structure consists of several layers of graphene and less affected by agglomeration due to its thickness which is approximately 100 nm (Dusza et al., 2012). Compared to the single layer of graphene, GNP possesses good interaction with the matrix and can transfer stress efficiently in the composite. The multi-flakes structure of GNP and its ultrahigh surface areas imparts good interfacial adhesion with matrix (Yavari et al., 2010). GNP's presence aid in producing refine pores to prevent microcracks deflection and increased the geopolymer compactness (Wang et al., 2016). Owing to the excellent chemical bonding with the geopolymer matrix, the spatial arrangement of the GNP structure creates a tortuous path for water molecules in the geopolymer matrix (Du and Pang, 2018). It was reported that the high surface area of GNP arrests the initiation of microcracks in the geopolymer, which subsequently improves the compressive strength (Matalkah and Soroushian, 2020).

GRAPHENE REINFORCED GEOPOLYMER NANOCOMPOSITES

The improvement in mechanical properties brought by graphene in geopolymer composite is due to several factors such as high surface area of graphene structure, well disperse graphene in geopolymer matrix, and good bonding behavior of graphene in geopolymer. However, this is highly dependent on the type of graphene used. Dispersion of pristine graphene in geopolymer is complicated as the pristine graphene itself is hydrophobic. Graphene sheets are strongly attracted by van der Waals force and strong π-π stacking between graphene lamellae, leading to agglomeration (Fang et al., 2009; Liang et al., 2018). Moreover, the low surface activity of pristine graphene creates a weak bonding interaction with the matrix, making the dispersion challenging (Ma et al., 2013). Therefore, meticulous attention is needed to improve its dispersibility in the matrix.

Dispersion of graphene into the matrix can be carried out through physical, chemical, or thermal methods. Physical dispersion can be achieved through mechanical methods such as the use of a high-speed mechanical stirrer (Chun et al., 2017; Manigandan et al., 2017), ultrasonic dispersion (Liu et al., 2018; Zhang and Chen, 2019), and ball milling process (Kothiyal et al., 2016). High shear stress was applied onto the pristine graphene in the mechanical dispersion process to separate it into individual

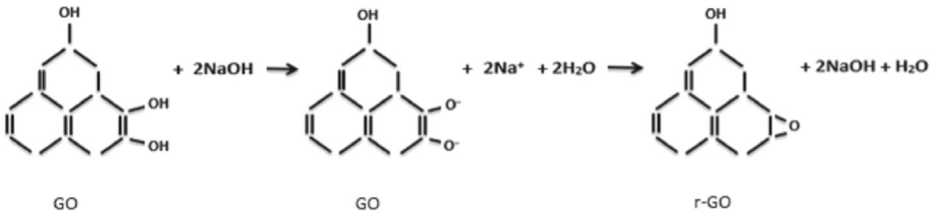

FIGURE 2 | Formation of epoxy groups by reaction with NaOH in GO/geopolymer nanocomposite (Amri et al., 2021).

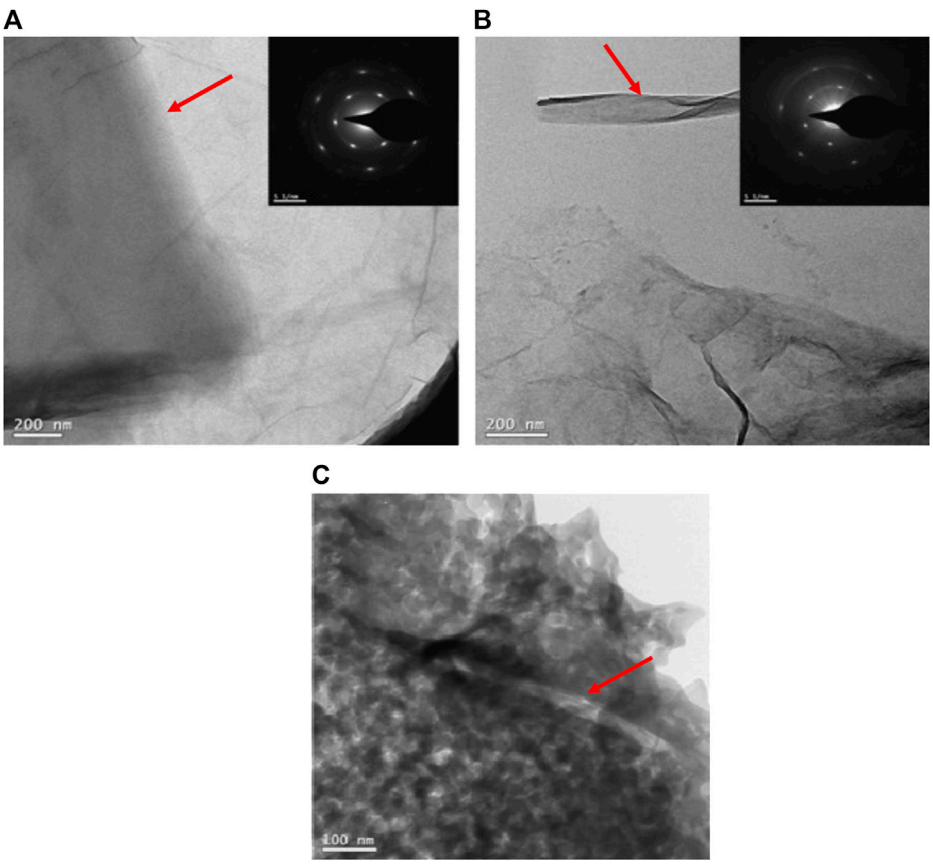

FIGURE 3 | Morphology observation under TEM on **(A)** Graphene Oxide (GO) sheet; **(B)** reduced Graphene Oxide (rGO); **(C)** rGO in geopolymer (Yan et al., 2015).

graphene sheets, allowing it to serve as a nanofiller instead of agglomerated micro filler. Graphene can be chemically dispersed within the matrix by altering its surface by covalent bonding or non-covalent bonding with various functional groups. Functionalization with covalent bonding forms functional oxygen-containing groups on the graphene surface, such as hydroxyl groups (-OH), carboxyl groups (-COOH), and epoxy groups (C-O-C). Meanwhile, non-covalent bonding occurs through the attachment of non-covalent functional groups by weak Van der Waals force, π-π interactions, ion interactions, and electrostatic interaction in the graphene basal plane (Naebe et al., 2014).

In the geopolymer synthesis process, the hydrophilic oxygen groups located on the basal plane of GO allowed it to be dispersed in water and mixed with the alkaline solution. The presence of a high concentration of functional groups on GO provides good interaction with geopolymer and improves matrix workability. In addition, the formation of a thick water layer around GO sheets aid in improved the rheology behavior for geopolymer workability (Zhong et al., 2017).

During geopolymer synthesis, the inclusion of GO into the alkaline solution will transform the GO to rGO by converting C=O to C-O bonds and eliminating some of the oxygen functional groups. X-ray photoelectron spectroscopy (XPS)

analysis can be used to confirm the reduction process, where the C/O ratio was found to increase after GO is immersed in an alkaline solution. The reaction between GO and sodium hydroxide (NaOH) to produce rGO is as follows (Amri et al., 2021):

$$GO - 2OH + 2NaOH \rightarrow GO - 2O - + 2Na + 2H2O \rightarrow rGO + 2NaOH.$$

The reaction between GO and strong alkaline solution such as NaOH produces epoxy as shown in **Figure 2**. Besides that, the GO will undergo deoxygenation, which then reduced the number of hydroxyl groups (Fan et al., 2008). The presence of epoxy groups can also reduce the interaction between the functional groups and the geopolymer matrix. Poor interaction is due to the low binding energy of the epoxy groups that may lower the strength of the geopolymer nanocomposite with an excessive amount of functional groups.

Figure 3A shows the thin GO sheets observed under the transmission electron microscope (TEM), which revealed the formation of single-layer GO (Yan et al., 2015). GO sheets contain electronegative characteristics that can react with cationic ions such as Na^+, K^+, and Ca^+ in a geopolymer solution. These reactions will then repels the presence of electronegative ions such as Al $(OH)^{4-}$ tetrahedral to balance out the negative charge from the substitution of Si with Al (Provis and Van Deventer, 2009). The repellant action is also said to accelerate geopolymerization as the electron binding energy of Al $(OH)^{4-}$ tetrahedral increases (Liu et al., 2020). Two factors were affecting the repellant reaction rate, which are activation energy and mass transfer rate. GO adsorbs free ions in geopolymer slurry as a high electron active material during the reaction and accelerates the mass transfer rate. (Guo et al., 2010).

When Al $(OH)^{4-}$ tetrahedral is repelled, it will reduce the Si/Al ratio in the geopolymer gel, while the Al element in the solution increased. Incomplete removal of negatively charged oxygen functional groups leads to repulsive effects between charged rGO sheets. Moreover, the van der Waals interaction between rGO sheets is weakened and leads to the electrostatic stabilization improvement of rGO, making it homogeneously dispersed in geopolymer solution (Yan et al., 2016b). Besides, the sheet edges of GO get scrolled up during the reduction process, as shown in **Figure 3B** (Yan et al., 2015). The intercalation of oxygen-containing groups indicates successful reduction process (Long et al., 2019b). The wrinkled and folded rGO has a higher surface area that can promote better interfacial adhesion with the geopolymer matrix (Kim et al., 2010; Liu et al., 2015). Good interfacial interaction between wrinkled rGO sheets and matrix improves mechanical strength. Besides, high concentrations of OH- ions attached to the RGO sheets can expedite the slag dissolution process (Sun and Vollpracht, 2018). The adhesion of rGO sheets onto geopolymer was observed, as shown in **Figure 3C**, where the arrow indicates the rGO is coated with a geopolymer matrix. Thus, it is expected that the addition of GO or rGO in the geopolymer system provides efficient load transfer from the matrix to the nano reinforcement.

COMPRESSION ANALYSIS ON THE GRAPHENE REINFORCED GEOPOLYMER NANOCOMPOSITES

Compressive analysis was done on the geopolymer to understand the ability of the materials to withstand the applied load. The compressive strength of the graphene reinforced geopolymer nanocomposite (GRGN) can be measured according to ASTM C293-10. The high elastic graphene cannot easily deform during compression of geopolymer nanocomposite due to its high rigidity structure. When a load is applied to the GRGN, the stress faces the geopolymer matrix. Then, cracks start to initiate from nano-scale and widen to micron-scale, which later the crack propagates to the graphene sheets. For the crack to move further, it must pass the high strength of graphene sheets. Therefore, graphene sheets can inhibit crack propagation by serving as a crack-bridging and crack blocking (Rehman et al., 2018). In addition, the well-distributed of high surface area of the graphene sheet in the matrix can facilitate the crack arrest effect in the nanocomposite (Zohhadi, 2014). The graphene thickness also may facilitate the stress transfer by inhibiting the crack propagation (Rehman et al., 2017). Thus, graphene sheets can interrupt the crack propagation, improve the fracture toughness, and make the composite more ductile than the unfilled geopolymer. **Figure 4** shows that when a load is applied to the GRGN in compression, the graphene sheets absorb high energy due to strong interaction with the matrix. The stress is initially transferred to the graphene sheets and then uniformly to other parts in the matrix, represented by yellow and pink arrows that distributes them in vertical and horizontal direction respectively. Then, as the load is released, the nanocomposite failed in a brittle manner. The nanocomposite failed due to the sudden release as the energy has been accumulated when the graphene is pulled out from the matrix (Ranjbar et al., 2015). The uniform stress transfer occurred as the graphene was distributed evenly in the geopolymer matrix. However, defects or overlapping of the graphene sheet will lead to non-uniform stress formation (Danial et al., 2019). Geopolymer composite filled with GO is much denser and more compact due to the strengthening mechanism of GO in the geopolymer matrix.

Geopolymer materials develop their strength properties with time. The voids within geopolymer structures will reduce with an increment in curing days (Yaghoubi et al., 2020). Reduction in voids number was contributed by the growth of the geopolymer network that consolidates and solidifies the material. This continuous cross-linking of geopolymerization occurs rapidly within the first few weeks of curing days, and the reaction slows down as it reaches months. Numerous studies reported the development of compressive strength on Day 1, Day 3, Day 7, Day 14, or Day 28 of curing for a more apparent result (Kim et al., 2014; Kupaei et al., 2014; Neupane et al., 2015).

Based on **Table 1**, the neat MK geopolymer (0% graphene) shows increasing compressive strength with longer curing days up to 28 days. Geopolymer filled with 1% of graphene shows enhancement of compressive strength at day 3 about 287%. The compressive strength increases due to well-distributed graphene in geopolymer and good interfacial adhesion with geopolymer

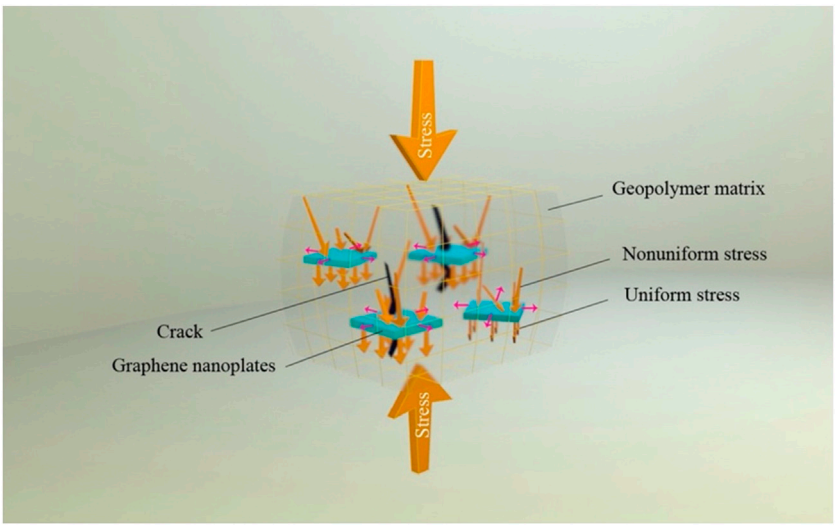

FIGURE 4 | Schematic diagram on the compressive behavior of graphene/geopolymer nanocomposite (Ranjbar et al., 2015)

TABLE 1 | Compressive strength of various Graphene Reinforced Geopolymer Nanocomposites.

Al-Si	Alkaline solution	Graphene		Compressive strength (MPa)				Ref
		Type	wt%	Day 3	Day 7	Day 14	Day 28	
MK	1. NaOH 8%	Graphene	0	8.2	12.8		14.1	Zhang and Lu, 2018
	2. Na_2SiO_3		1	28.8	29		32.5	
			2	30.5	31		34.5	
			3	31	31.2		35	
			4	30.2	30.5		32.8	
Fly ash	1. Na_2SiO_3	GO	0		18	26	35	Xu et al. (2018)
	2. Quicklime		0.02		24.8	32.8	43.1	
	3. Calcium Chloride							
Slag	1. NaOH	GO	0				38.06	Yeswanth sai and Durga Prasad (2020)
Fly ash class F	2. Na_2SiO_3		0.005				46.86	
Slag	1. Na_2SiO_3	TiO_2-RGO	0	38	48		68	Guo et al. (2020)
Fly ash class F	2. NaOH		0.02	47.6	58.1		73.5	
Slag	NaOH	Graphene, Zinc oxide (ZnO)	2	53.3	70.4		77.3	Zhang L. W. et al. (2020)

matrix. Simultaneously, the geopolymer hydration products become highly compacted, reducing the internal porosity, which increases its compressive strength. A similar observation was found for the same graphene geopolymer composite on Day 7 and Day 28, indicating that graphene does not interfere with the geopolymerization cross-linking with time. Similarly, the trend is consistent geopolymer loaded with 2, 3, and 4% graphene (Zhang and Lu, 2018). However, it is reported elsewhere that agglomeration and overlapping of above 1% graphene nanoplatelet can occur in the geopolymer system (Ranjbar et al., 2015). This is because the surface of graphene is hydrophobic which indicates that graphene has the potential to agglomerate in aqueous solutions and geopolymer composites (Jishnu et al., 2020). This indifference in result may be because Zhang uses a readily graphene dispersant liquid while Ranjbar personally sonicate graphene in water for 5 min (Zhang and Lu, 20188; Ranjbar et al., 2015). Ranjbar admitted that his method may not be suitable for high loading of graphene but high water content may be added to alter the experimental design to solve the issue. However, water must be added with care as excessive water would lead to composite weakening due to high porosity (Ranjbar et al., 2015). At the same time, it must be kept in mind that water is an important medium for destruction of raw materials and transfer of effective ions (Sagoe-Crentsil and Weng, 2007). Thus, an optimum amount of water is crucial for a good geopolymer fabrication.

GO was introduced into fly ash only based geopolymer system and improvement in compressive strength was observed at Day 7, Day 14, and Day 28. Thanks to its oxygen functional groups, GO can disperse well in geopolymer slurry (Xu et al., 2018). Well dispersed graphene promises long-term stability in geopolymeric solutions (Yuan et al., 2014). This is because the solvent has provided the necessary force for the GO molecules to move around in the medium. This force is stronger than that which hold the GO together. Thus, deagglomeration and sedimentation of graphene is minimized (Lahir, 2019). Moreover, the

mechanical interlocking adhesion between GO sheets and geopolymer binder contributes to the enhancement of the compressive strength. This is mainly due to the wrinkling effect on GO with respect to reduction in alkaline solution during fabrication. When wrinkled, GO provides a rough and higher surface area for adhesion with geopolymer binder (Bellum et al., 2020). In addition to this, it has been reported that reduction of GO induces hole defect onto the rGO. This is because the hole structures may allow polymer penetration through graphene sheets thus enhancing polymer-filler interaction (Lin et al., 2013).

Oxidation on parent graphene result in GO with 2% holes that form as CO and CO_2 are released during aggressive oxidation and sheet exfoliation. The defect hole here is usually less than 5 nm. Reduced and annealed graphene oxide has an increased area of holes with 5% now as CO and CO_2 formed during annealing. Even though all oxygen containing groups are completely removed from carbon network, the remaining functionalities and holes in rGO drastically differentiate from pristine graphene (Erickson et al., 2010).

From **Table 1**, Zhang uses MK while Xu uses FA in their geopolymer, which leads to the formation of different geopolymer material (Zhang and Lu, 2018; Xu et al., 2018). Frequently, MK contains low Si:Al ratio of about 1 (Constâncio Trindade et al., 2017 and Dousti et al., 2017) while FA contains higher Si:Al ratio of about 3 (Güneyisi et al., 2013 and Hariharan et al., 2015). According to Davidovits, a low Si:Al ratio of 1–3 leads to 3D geopolymer networking while higher Si:Al ratio results in 2D networking instead (Davidovits, 2015b). The problem incurs with 2D networking is that the linear structure can easily depolymerize, making the geopolymer weak (Davidovits, 2006; Davidovits, 2015c). Despite this, **Table 1** shows that the compressive strength of FA geopolymer is greater than the MK geopolymer. The presence of GO causes the difference in compressive strength value. Aside from great dispersibility of GO in alkaline solution, GO content has direct effect onto concentration of Al. In mole ratio analysis, increasing the GO content will increase the relative concentration of Al. Al mainly exerts a negative charge (for example, $Al(OH)^{4-}$. The oxygen group on GO also carries a negative charge (Skoda et al., 2014). When in the presence of both these groups, they repel each other, increasing Al concentration (Xu et al., 2018). On the other hand, positively charged ions like Ca^{2+}, Na^{+}, K^{+}, and Mg^{2+} likely to attract the oxygen functional group on GO. Due to this, the cationic ions are most likely to be entrapped via the -OH functional group, thus decreasing the positively charged ions concentration in the geopolymer solution (Ramesha et al., 2011; Archanjo et al., 2014). The effect of these charges is not significant toward Si as Si mainly exists as neutral Si $(OH)^4$ unit, and SiO $(OH)^{3-}$ and SiO_2 $(OH)_2{}^{2-}$ anions. In other words, the effect of GO on the distribution of Si is relatively weak (Xu et al., 2018).

A geopolymer nanocomposite with the most negligible graphene content of about 0.005 wt% only has been produced. The result still shows an encouraging increment in compressive strength up to 46.86 MPa (Yeswanth Sai and Durga Prasad, 2020). The improvement could be due to two reasons; lower weight of GO and synergistic effect among aluminosilicate materials. Firstly, GO is reduced to rGO and holes are formed, the weight of rGO is lowered. Therefore, for the same weight, there were more rGO used compared to pristine graphene. Secondly, it is due to the synergistic effect of two different types of aluminosilicate mixed in their formulation, which are slag and fly ash. Combining more than one aluminosilicate powder is known to result in high compressive strength (Kumar and Revathi, 2016; Vogt et al., 2019). Individual aluminosilicate sources do not have well-balanced characteristics to be the only source used in geopolymer production. For example, kaolin is one commonly used aluminosilicate source due to its abundance (Akinyele et al., 2017). In addition to this, kaolin has a low Si:Al ratio that is beneficial for producing 3D network geopolymers for bricks, ceramic, and fire protection applications (Davidovits, 2015c). Joseph Davidovits reported using kaolin in their earliest invention of geopolymer (Davidovits, 2015a). Indeed, various works have been reported recently on fabrications and properties of kaolin or calcined kaolin (called metakaolin, MK) in producing geopolymer (Jaya et al., 2016a; Jaya et al., 2016b; Hájková, 2018; Merabtene et al., 2019). However, kaolin has one dominating flaw, which it has high water demand. Kaolin is likely to absorb water due to its plate-like structure, which is still retained even after calcined to become MK. Despite benefiting from high reactivity, the high surface area ferociously increases the viscosity of geopolymer slurry (Provis et al., 2010). This forces researchers to add higher water content for good geopolymer workability.

A hybrid geopolymer nanocomposite was produced by adding titanium treated reduced graphene oxide (TiO_2-RGO) in the mixture of slag/fly ash geopolymer (Guo et al., 2020). The authors observed an increment of strength on the geopolymer with an increment of TiO_2-RGO loading. With the presence of TiO_2-RGO, the compressive strength jumped to 73.5 MPa. The unique spherical shape of titanium dioxide combined with rGO enhanced the geopolymer solution workability. Thus, it reduced the need to add extra during the processing of the geopolymer nanocomposite. Excessive water content is known to degrade the mechanical strength of geopolymer because water is not involved in geopolymerization and will be evaporated, which leaves behind empty spaces. Geopolymer material with less water content consistently exhibits high compressive strength. In addition to this, during evaporation, geopolymer tends to crack as it cannot sustain the previous shape held by water within. The failure will cause other problems like shrinkage (Asif et al., 2015; Raphaëlle et al., 2019). Aside from benefitting the lower water demand, TiO_2 also serves as an anti-aggregation particle and it can inhibit the interlaminar recombination of RGO sheets (Guo et al., 2020). Morphological observation under the transmission electron microscope (TEM), displays that TiO_2-RGO shows uniformly dispersed spherical morphology of TiO_2 nanoparticles onto the RGO sheets (Nainani and Thakur, 2016). This evident the prevention of RGO aggregation through adhesion of TiO_2

TABLE 2 | Compressive strength of Graphene Reinforced Geopolymer Nanocomposites at different alkaline solution concentration.

Al-Si	Graphene	Alkaline solution		Compressive strength (MPa)			Ref
		Na_2SiO_3 (%)	NaOH (%)	3 days	7 days	28 days	
MK	Graphene 4%	40	8	8.2	13	14	Zhang and Lu, 2018
			10	11	15	17	
			12	15.5	17	21.8	
			14	17.5	22.2	25	
			16	23	26	27.5	
Ground granulated blast furnace slag (GGBS), fly ash class F	GO 0.005%	43	17 8 M			40.53	Yeswanth sai et al., 2020
			10 M			41.7	
			12 M			46.86	

nanoparticles onto the RGO sheets. Interestingly, lamella graphene can also support zinc oxide in the geopolymer matrix, which subsequently improves the mechanical properties of the GRGN (Zhang L. W. et al., 2020).

Yeswanth Sai and Guo reported on selecting a similar aluminosilicate source which are slag and FA class F, in the fabrication of GRGN. They also reported a similar choice of alkaline solution, which are NaOH and Na_2SiO_3 used to fabricate the GRGN. The observation found that incorporation of 0.005 wt % GO increases the compressive strength at day 28, which is from 38.06 to 46.86 MPa. On the other hand, adding 0.02 wt% TiO_2-RGO shows a similar trend on strength increment at day 3, which is from 38 to 47.6 MPa. The high early strength for TiO_2-RGO geopolymer evident the advantage of using surface treated GO. Thanks to the low water demand, TiO_2-RGO geopolymer produces lesser pores during curing and therefore higher early strength (Guo et al., 2020; Yeswanth Sai and Durga Prasad, 2020).

Even though all geopolymer is known to develop its strength over time, the GO geopolymer cannot surpass the compressive strength of the TiO_2-RGO geopolymer. This is because it was reported that the compressive strength of slag/FA continues to develop over six months. However, the rate of strength development decreases each month. The compressive strength was enhanced by 10.4% from first month to second month of curing while from second month to the third, it was increased by 3.77%. Further reduction in percentage is observed in the following curing period. This is because slag is a highly reactive aluminosilicate source. Its presence in the slag/FA geopolymer slurry causes high reaction in the early period of curing. Thus, it achieves consolidation at a quicker rate (which in this case, is in the first month). Therefore, the strength development slows down as consolidation almost complete (Lloyd, 2009). Since GO geopolymer already achieved 46.86 MPa at day 28, its strength development is expected to slow down in the coming month and will not be able to overcome the strength of TiO_2-RGO geopolymer. Aside from this, it is essential to note that other factors could affect the strength of GRGN, which includes curing temperature and stirring speed.

In **Table 1**, it is clear that all GRGN exhibit higher compressive strength than their counterparts with no graphene. This is a clear indication that the strength of geopolymer is improved with graphene, no matter the type of graphene or treatment on graphene. As water is evaporated from geopolymer upon reaction, the porous spaces left behind is the source of geopolymer weakening when load is exerted. Any small sized particles that is incorporated into geopolymer matrix will act as filler that fills in these pores, aside from serving other advantages mentioned in the above paragraphs (Saafi et al., 2015; Ashfaq Alvi et al., 2020).

Table 2 shows the compressive strength of MK reinforced with graphene using a combination of two types of alkaline solution: sodium silicate (Na_2SiO_3) and sodium hydroxide (NaOH) (Zhang and Lu, 2018). In their experiment, the amount of MK, graphene, Na_2SiO_3, and water content is consistent, while the percentage of NaOH solution is varied (8, 10, 12, 14, and 16%). The change in the compressive strength was due to increasing the concentration of sodium cations from NaOH. Noticeably, the increment in compressive strength with the addition of NaOH percentage shows the same pattern at Day 3, Day 7, and Day 28. This can be attributed to the ease of reaction between NaOH and MK due to the smaller alkali cations present in the NaOH compared to Na_2SiO_3. The alkali cation from NaOH reacts with MK in generating polymeric chains of geopolymer. Thus, the addition of a high amount of NaOH percentage directly increases the reaction of MK, which accelerates hydration reaction and causing sufficient reaction (Zhang and Lu, 2018).

Variation in NaOH concentration at 8, 10, and 12 M in producing GO reinforced slag and fly ash geopolymer composite was reported. The authors observed that 12 M of NaOH gives the highest compressive strength with 46.86 MPa (Yeswanth sai and Durga Prasad, 2020). This value is high for only 0.005% of GO used in the geopolymer system, unlike other researchers, which often incorporate graphene in the range of 0.02–1 wt% (Yan et al., 2017; Xu et al., 2018). The difference was due to the high reactivity of NaOH with the aluminosilicate source in the geopolymer slurry. In addition to this, GO reinforced slag and fly ash geopolymer composite displays 70% higher compressive strength than the graphene reinforced MK geopolymer composite. The increment in compressive strength reveals the benefit of designing an excellent geopolymer recipe with various constituents compared to using only one type of aluminosilicate source with an excellently low Si:Al ratio. **Table 3** summarizes the compressive strength of all GRGN discussed.

TABLE 3 | Summary of compressive strength for Graphene Reinforced Geopolymer Nanocomposites.

Al-Si	Graphene type	Alkaline solution	Compressive strength at 28th day (MPa)	References
MK	Graphene	1. NaOH 2. Na_2SiO_3	35	Zhang and Lu, 2018
Fly ash	GO	1. Na_2SiO_3 2. Quicklime 3. Calcium Chloride	43.1	Xu et al. (2018)
Slag Fly ash class F	GO	1. NaOH 2. Na_2SiO_3	46.86	Yeswanth sai and Durga Prasad (2020)
Slag Fly ash class F	TiO_2-RGO	1. NaOH 2. Na_2SiO_3	73.5	Guo et al. (2020)
Slag	Graphene	NaOH	77.3	Zhang Q. et al. (2020)

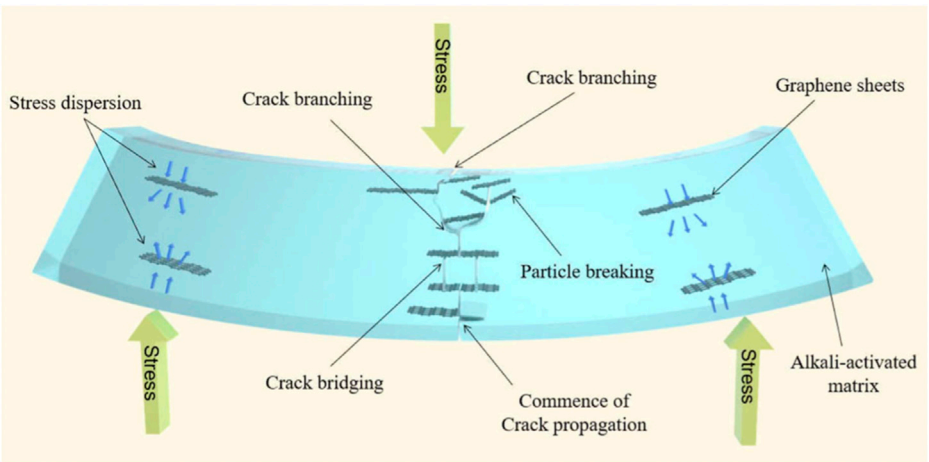

FIGURE 5 | Schematic diagram of toughening mechanism due to bending load applied on the graphene/geopolymer nanocomposite (Guo et al., 2020).

FLEXURAL ANALYSIS ON THE GRAPHENE REINFORCED GEOPOLYMER NANOCOMPOSITES

A bending test on a composite is performed to identify the amount of stress under the bending load that the materials can resist without breaking. The improvement in the flexural strength can be due to the numerous toughening mechanisms of graphene in the geopolymer matrix. **Figure 5** shows the toughening effect with the presence of graphene in geopolymer nanocomposite. Initially, when the load is applied onto the graphene/geopolymer nanocomposite, the crack will form at the sample center. The crack initiation at the center indicates that the highest bending stress was applied and that the crack begins to branch from the matrix to the graphene sheets. When the load is further applied, the graphene sheets in the geopolymer will form a bridge to slow down the crack formation, resulting in high stress transfer due to the greater energy absorption to break the nanocomposite sample. It was mentioned that the high stress exerted between the graphene sheets may break out the adjacent graphene sheets due to strong adhesion between graphene and the geopolymer matrix (Guo et al., 2020).

Figure 6 shows microscopic images of graphene nanoplatelet (GNP) as a toughening agent to improve the strength of the geopolymer matrix. With a high elastic modulus of GNP, the stress is transfer uniformly throughout the geopolymer matrix, and the nanocomposite is not easy to deform under stress when the load is applied. As the crack starts to initiate, it will propagate parallel to the direction of the loading. Then, the crack will reach the GNP sheets, and the GNP resists the crack by forming a bridge which results in toughening mechanism (**Figure 6A**). As the crack formation is harsh and sudden, the GNPs are broken and pulled out from the geopolymer matrix, leading to the formation of crack branching (**Figure 6B**) (Ranjbar et al., 2015).

The inclusion of rGO in the geopolymer matrix can affect the stiffness properties of the nanocomposite. As illustrated in **Figure 7**, a low amount of rGO sheets were separated by the geopolymer matrix and make the composite less brittle. By increasing the amount of rGO content to medium, some of the rGO sheets are overlapping and may restrict the movement of the geopolymer chain in the nanocomposite. However, as the rGO content is increased to a high amount,

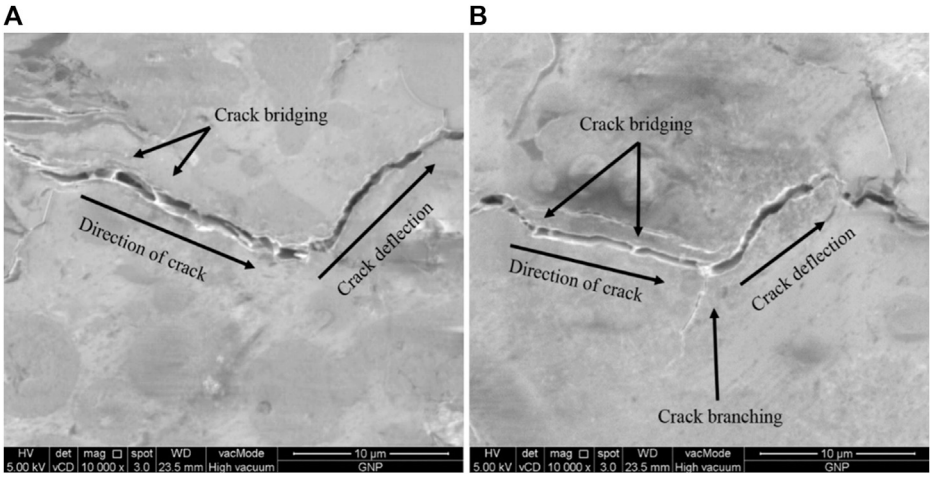

FIGURE 6 | Toughening effects by graphene nanoplatelet (GNP) in geopolymer (Ranjbar et al., 2015)

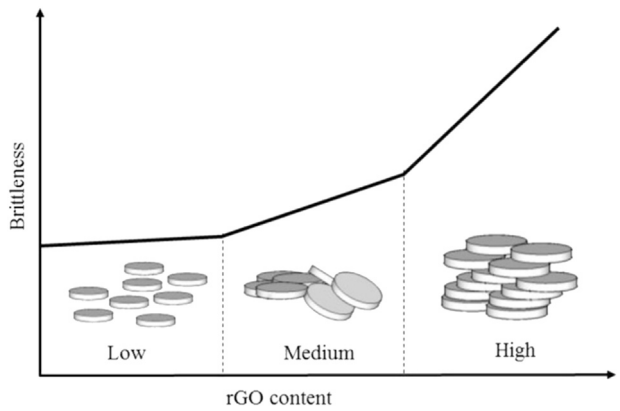

FIGURE 7 | Relationship between the amount of rGO and brittle properties (Saafi et al., 2015).

the geopolymer nanocomposite will become stiffer as the rGO constrains the geopolymer matrix's movement. High van der Waals forces between rGO sheets form a rigid laminate structure, making the geopolymer nanocomposite fail in a brittle manner (Saafi et al., 2015).

Table 4 shows the graphene content ranges from 0 to 4%, while the molarity and weight of NaOH and Na_2SiO_3 are kept constant. Each composite shows higher flexural strength proportional to increasing curing days, except for 4% graphene. The strength of geopolymer reinforced with 4% graphene reduces by 1.5% on Day 28 when compared to Day 7. According to Zhang, the possible reason for this is the uneven dispersion of graphene in alkaline solution due to excessive graphene content. Thus, in turn, decreases the strength of GRGN. Aside from this, Zhang also studied the effect of increasing NaOH concentration on the flexural strength of GRGN. In this experiment, the amount of other constituents is kept constant, while NaOH concentration is varied from 8 to 16% with an increment of 2%. The flexural strength increases as NaOH concentration increases due to the accelerated reaction between NaOH and geopolymer solution. However, the reaction reaches a threshold point at which strength began to decrease with higher NaOH concentration. According to the author, at this point, an excessive reaction has occurred. This excessive reaction is called carbonation, and it can cause the alkali content to react with CO_2 in the air (Zhang and Lu, 2018). At times, one can observe a blooming, whitish appearance on a geopolymer structure due to excessive alkalinity (Davidovits, 2016). Generally, carbonation occurred due to excess alkalinity when the K:Al ratio is very high. It can reduce the strength of geopolymer because it has a high destroying impact on geopolymer structure when exposed to moisture (Pandey, 2011).

It has been reported that the highest NaOH concentration gives the best strength of geopolymer (Yeswanth Sai and Durga

TABLE 4 | Flexural strength of Graphene Reinforced Geopolymer Nanocomposite based metakaolin.

Al-Si	Alkaline solution	Graphene		Flexural strength (MPa)			Ref
		Type	Wt %	Day 3	Day 7	Day 28	
MK	NaOH (16%), Na_2SiO_3	Graphene	0	2.69	3.18	3.29	Zhang and Lu, 2018
			1	3.25	3.75	3.85	
			2	3.63	4.35	4.38	
			3	3.71	4.51	4.61	
			4	3.95	4.61	4.54	

Prasad, 2020). However, this is in contrast with the finding from Zhang explained earlier (Zhang and Lu, 2018). In Zhang's reported work, there is a critical point in increasing NaOH concentration. For geopolymer without graphene, the oligomer chain and sodium silicate reacted with the soluble Al, which increase the reaction process and improve the geopolymer strength. However, the achievement in bending strength improvement is only at a certain threshold. Beyond the limit, the aggressive reaction occurred because an excessive amount of alkaline solution reacted with CO_2 in the air and subsequently reduced the composite strength. With the presence of 4% graphene in the geopolymer synthesizes with highly concentrated NaOH, the strength becomes less significant. Agglomeration of graphene in a highly alkali NaOH solution and lack of dispersion are the reasons for declining in strength properties. A different trend in results may occur if a different combination of the alkaline solution is used in the production of GRGN. This is an excellent insight for geopolymer studies that involve varying concentrations of NaOH solution (Zhang and Lu, 2018).

To prevent cracking and maintain the structural integrity of the cured geopolymer, a proper curing condition by controlling the temperature and curing time is essential (Shi et al., 2017). Rapid drying during curing must be avoided (Perera et al., 2007). It is vital to retain a small amount of water in the cured geopolymer to avoid dehydration and excessive shrinkage due to long curing times at high temperatures (Van Jaarsveld et al., 2002). It was found that the flexural strength increases to about 29% for slag geopolymer composite filled with rGO steamed cured for 48 h at 60°C (Long et al., 2019a). There are three reasons for the geopolymer strength improvement. Firstly, due to the presence of–OH ions on the rGO sheets that promote better dissolution of slag. At the same time, rGO sheets repel the negatively charged Al and adhere well with the geopolymer matrix, which contributes to the improvement in flexural strength. Secondly, the processing temperature of GO sheets in NaOH solution may affect the GO structure integrity. The 60°C treated rGO shows a higher ID/IG value in Raman Spectroscopy analysis, indicating a greater degree of structural defects which is optimum for adhesion to the geopolymer matrix (Kani and Allahverdi, 2009). Thirdly, steam curing has been reported to reduce porosity within geopolymer matrix, resulting in higher mechanical strength (Fekoua et al., 2021). For the geopolymer composites cured under steam condition, the obtained Si:Al ratio and K:Al ratio is closer to the designed composition than the same geopolymer composites that are cured in room temperature, which indicates a higher formation of aluminosilicate gel from the material source (Kani and Allahverdi, 2009).

Graphene also is famously known for its unique thermal properties, as reported by many (Kolhatkar et al., 2018; Phiri et al., 2018; Liu et al., 2019). The thermal properties of graphene are related to its anisotropic bonding and effective heat transfer by lattice vibrations. In addition, the two-dimensional (2D) and sp^2 covalent bonds between adjacent carbon atoms make graphene one of the strongest carbon allotrope. Thus, when geopolymer is sintered at an elevated temperature, the geopolymer structure becomes dense. Simultaneously, when GO is present during the sintering process, GO is reduced to rGO and forms a 3D network with a geopolymer matrix to create good interfacial bonding. The rGO restricts the crystal formation in geopolymer, and it may act as a barrier dislocation movement, which increases the composite's dislocation density. A work has been published on sintering process of graphene/leucite nanocomposite to 1,000°C. It was found that the sintering process managed to improve the flexural strength by 12 times and reduce GO together with change transformation of leucite grain structure. With the reduction of GO at high temperature to rGO, the rGO scrolled, folded, attached with leucite particles, and helps in refining the leucite grain structure, making the composite denser, leading to improved mechanical properties. As the sintering process increase beyond 1,000°C, making the rGO becomes much smaller, scrolled, and folded, which may lead to the degradation of rGO and easily debonded from the matrix when the load is applied. In addition, the amorphous geopolymer is fully transformed into leucite which subsequently degrades the composite strength (Yan et al., 2016a).

The presence of GO in geopolymer has been shown to promote better flexural strength at certain stirring temperature. When the processing temperature of graphene/aluminosilicate in alkaline solution is increased from room temperature to 40 and 60°C, the flexural strength of the produced GRGN increases correspondingly. The holes that formed onto GO during reduction acts as microscopic nets that made them highly flexible (Lin et al., 2013). At the same time, The residual oxygen functional group helps in dispersing rGO in alkaline solution. However, when stirring temperature is further increased to 80°C, the flexural strength is observed to decline due to severe structural defects of RGO (Long et al., 2019a). Extreme stirring heat in alkaline solution not only causes reduction of graphene to GO, but also exhibits wrinkles on GO structure (Deng and Berry, 2016). This severe defect onto rGO weakens its strength.

In addition to this, the right technique on adding sand in geopolymer fabrication is essential to understand. The addition of sand can lead to water trapped within the geopolymer pore structure. Calcareous sand, for example, has a pore diameter of at least 1 mm, while the diameter of one water molecule is only 0.27 nm (National Nanotechnology Coordinated Infrastructure, 2012; Zhu et al., 2013). Thus, the small size of water molecules can easily penetrate the bigger sand pore size and trapped within the pores. When graphene is added into geopolymer, the graphene is likely to be dispersed in distilled water to ensure the dispersibility or exfoliation of the layered graphene structure in the geopolymer matrix. However, if the graphene solution is trapped within sand pores, the reinforcing effect becomes less efficient. Moreover, if the aluminosilicate source or alkaline solution is trapped within the sand pores, the geopolymer reaction might be affected, and there is a possibility that the materials are not hardened. Thus, the suitable time to add sand is during the final mixing stage, where aluminosilicate powder has been well stirred with an alkaline solution, forming a geopolymer slurry. Homogeneous mixing of aluminosilicate and alkaline solution creates a viscous solution and less trapped problem when sand is added into it the mixture.

Graphene can be doped with various elements such as Si, N, B, P, and many more. By doping, active sites are created on the

TABLE 5 | Summary of flexural strength for Graphene Reinforced Geopolymer Nanocomposites.

Al-Si	Graphene type	Alkaline solution	Flexural strength (MPa)	References
MK	Graphene	1. NaOH 2. Na_2SiO_3	4.61	Zhang and Lu, 2018
Slag	Graphene	NaOH	10.2	Zhang et al. (2020)
Slag	rGO	1. NaOH 2. Na_2SiO_3	10.3	Long et al. (2019a)
MK	GO	1. Silica solution 2. KOH	91.1	Yan et al. (2016b)
MK	Si-graphene	1. K_2SiO_3 2. Na_2SiO_3	12	Cho et al. (2015)

graphene surface to alter the graphene properties and increase its catalytic activities. Doped graphene can foster better graphene dispersibility in a matrix medium. Cho investigated the properties of Si-doped graphene and found that the composite flexural strength increased from 11 to 12 MPa over pristine graphene (Cho, 2015). Meanwhile, Zhang studied the effects of pristine graphene, Si-doped graphene, and GO sheets in geopolymer composite. In water, the Si-doped graphene shows better dispersibility as water molecules easily penetrate the interlayer Si-doped graphene region and expand the graphene sheets. The hydrophilicity surface of Si-doped graphene was higher than GO as the hydrogen bonds per group are 16.9% higher than available in GO. While pristine graphene shows poor dispersion in water due to its hydrophobic behavior (Zhang L. W. et al., 2020).

Interestingly, Si-OH groups on the Si-doped graphene reacted well with the aluminate and silicate species in the geopolymer matrix by typical condensation reactions. Even though Si-doped graphene shows better dispersibility in the geopolymer matrix, the geopolymer composite strength decreased due to the transition of sp^2 to sp^3 bond on the Si-doped graphene layered structure deteriorates and affects its mechanical properties. However, the reinforcement effect of Si-doped graphene/geopolymer composite is still higher than unfilled geopolymer. It was mentioned that the Si-graphene is twice the weight of pristine graphene, which also makes sense, making Si-graphene geopolymer exhibiting higher density. The flexural strength of all GRGN is summarized in **Table 5** (Cho, 2015).

The condition of graphene before being incorporated into geopolymer matrix is equally important in effort to produced enhanced flexural strength of GRGN. During annealing process, microgasbags are constructed in Graphene Nanosheets (GNS). These microgasbags are closely packed and usually in dimension of several micrometers. It is said that during compression of paper sheet filled with GNS, microgasbags disappear and microfolds are formed. These microfolds are the factor that determine superflexibility of the thin sheet paper (Ding et al., 2017). This hints the importance of graphene condition before incorporation in geopolymer. There has also been a reported work on improving the flexibility of GNS film with aramid nanofiber framework (Xie et al., 2021). In addition to this, conventional method of exfoliating GO through vigorous sonication can destroy the GO structure, resulting in smaller sized GO nanosheets. To minimize this destruction, a homogenizer can be used to apply shear force in the solution. When compared, the average lateral size (mm^2) of sonicated GO was found to be 100 times smaller than homogenized GO (Han et al., 2018).

ANALYTICAL MODELING ASPECTS OF GRAPHENE REINFORCED GEOPOLYMER NANOCOMPOSITES

Material development has started from "materials by design" in the early 21st century, which involves in-depth knowledge of microscopic origins and later into processing that leads to new advanced materials. "Materials by design" or experimental work of geopolymers have been reported countless times (Zhang and Lu, 2018; Ren and Zhang, 2019; Yao et al., 2019; Cui et al., 2020; Yeddula and Karthiyaini, 2020). The optimum approach available to scientific research is to combine theory, experiment, and simulation (Landau, 2005). Generally, computer simulation can be used for prediction, qualitative or systemic predictions, giving us insight into materials system and behavior. This predictive capability is the catalyst to technological discovery and innovation in materials science and engineering (Murr, 2016). Several simulation techniques exist to understand the polymerization and gelation process in geopolymer materials. To date, the primary methods used to study geopolymer materials are density functional theory (DFT), molecular mechanics (MM), molecular dynamics (MD), and Monte Carlo (MC) simulations (Kupwade-Patil et al., 2013b).

Understanding the interfacial interaction mechanisms between Si-doped graphene and aluminosilicate source during geopolymerization is part of the comprehensive MD study done by Zhang (Zhang L. W. et al., 2020). The authors observe the dissolution of Si $(OH)^4$ and Al $(OH)^{4-}$ monomers from aluminosilicate source and ≡Si–OH groups from Si-doped graphene during geopolymerization. The Al $(OH)^{4-}$ monomers are fully consumed by condensation reaction after 30 ps as observed from the MD simulation. While for Si $(OH)^4$ monomers, there is almost no residual after 300 ps from simulation observation. This agrees with NMR analysis that proves almost entirely reacted Si $(OH)^4$ monomers (Duxson et al., 2005). However, the dissolution of ≡Si–OH groups of Si-doped graphene does not correlate between the simulation and experimental analysis. According to Zhang, the simulation analysis displays only 80% of ≡Si–OH groups chemically bonded

with geopolymer structure (Zhang L. W. et al., 2020). In other words, this means that only 80% of ≡Si–OH groups are polymerized. The reason to this is due to sequential attachment. Once active monomers are attached onto the 3D skeleton of geopolymer through condensation, they are unable to surface for reaction with ≡Si–OH groups. However, in reality, hydrolysis and polymerization processes occur simultaneously; thus ≡, Si–OH groups would attach to both the 3D skeleton of the geopolymer and the surface of Si-doped graphene. Besides, the ≡Si–OH monomers could dissolve in an alkaline solution in advance. The finding indicates that experimentally, ≡Si–OH groups can be fully polymerized, unlike simulation findings (Zuhua et al., 2009).

Various aluminosilicate sources were used to fabricate geopolymer composite, including different types of alkaline solution and varying concentrations of reinforcing fillers. A study investigated the physicochemical properties of rGO in geopolymer composite. The authors figure out that the higher strength in GO was due to the strong C-O bond with the electrostatic neutral carbon network in graphene. However, from their observation, inclusion of 0.5 wt% GO decreased the geopolymer compressive strength. Through inspection using fourier transform infrared (FTIR) analysis, a distinct peak occurs for 0.5 wt% GO geopolymer at 1,150 cm^{-1}, which corresponds to an excess epoxy group produced due to GO reduction in alkaline solution. The presence of epoxy groups on GO weakens the interaction between the functional group and geopolymer matrix due to the lower binding energy of the epoxy-functional group. Nevertheless, when epoxy functional groups form onto the graphene surface, a negative charge is entailed. DFT is a theoretical modeling that can be used to calculated the electronic structure of geopolymer (Kurth et al., 2005). Through DFT, rGO is configured by inserting oxygen atoms into the carbon skeleton of graphene, and epoxy groups are added to the C-C bridges. The epoxy-type atom in GO entails a negative charge of ~0.5 e, confirming the weakening of geopolymer composite with 0.5 wt% GO (Amri et al., 2021).

The difference in Si:Al ratio will affect the geopolymer strength properties. Low Si:Al ratio in geopolymer would lead to an improvement in mechanical properties. However, reported work on kaolinite-based geopolymers reveals a different outcome when comparing experimental and simulation analysis. DFT was used to model the geometry of geopolymer and discover that the total energy of geopolymer decreases as the Si:Al ratio increases. This indicates that at Si:Al of 1:1 ratio, the geopolymer has the most stable molecular orientation, which is translated as the highest rigidity. However, during experimental work at Si:Al ratio of 1, the geopolymer displays the lowest compressive strength. Upon an inspection of the microscopic images, it is revealed that there is the presence of a highly crystalline phase of zeolitic nuclei in geopolymer with Si:Al ratio of 1. The nuclei are not dispersed in the geopolymer matrix and lead to macropores formation, weakening the geopolymer structure when a compressive load is applied (Wan et al., 2017). Aside from this, there are also other reported work on low Si:Al ratio geopolymer but with weaker strength compared to higher Si:Al ratio. This includes slag based geopolymer (Mustofa and Pintowantoro, 2017) and fly ash based geopolymer (Asif et al., 2014). Both reported to observe homogenous binder at Si:Al ratio of two while lower ratio reveals insoluble aluminosilicate particles. It was mentioned in the work that silica content is increased by adding more sodium silicate. Therefore, in this case, the higher the Si:Al ratio, the higher the workability which leads to better particles dissolution (Asif et al., 2014). Despite the analytical modeling proving otherwise, experimental work represents real life situation. It is undeniable that simulations is useful in producing new knowledge just like experiments do, but the information and knowledge needed in running a good simulation is way more than running a good experiment (Guala, 2002).

To date, there are not many simulations works done on geopolymer and its reaction. A great insight has been made through the work done despite the limited modeling on graphene geopolymer composites. It is anticipated that a polymerization modeling would be made soon on the distribution of positive ions of alkaline solution on the 3D network of geopolymer. This is deemed necessary as the attachment of positive ions on alumina would stabilize the geopolymer structure in water. Any excess of positive ions may react with the water molecules form and disrupts the formation of a 3D network of geopolymer. In return, this may overall prevent geopolymerization from occurring. Based on the gathered information, **Table 6** is produced to summarize the pros and cons of the analytical modeling approach and **Table 7** on the pros and cons of the experimental approach.

RECOMMENDATIONS

Graphene is a unique and multi-functional nanoparticle for geopolymer composite. However, as a hydrophobic nanofiller with platelet like structure, graphene has high tendency to overlap and agglomerate in geopolymer matrix. Therefore, several types of treatments can be done to overcome this issue. Firstly, graphene can be doped with spherical shaped particles to improve workability of geopolymer slurry and to prevent interlaminar recombination of graphene sheets. Graphene can also be functionalized with hydrophilic elements to improve dispersibility in alkaline solution. Without treatment, the use of graphene dispersant liquid is recommended to prevent agglomerated graphene that could be the weakening point of geopolymer composite.

Since pristine graphene is often highly priced, its derivative which is GO is less expensive, making it a great alternative. During oxidation of graphene to produce GO, hole defects (<5 nm) are induced onto its surface. These holes are great for interlocking mechanism between GO and geopolymer matrix for enhanced mechanical properties. It is important to note that oftentimes geopolymer gel are reported to be in the range of micrometers (Temuujin et al., 2009; Kupaei et al., 2014; Mohammed et al., 2019). No work has been reported on impregnation of geopolymer nanogel into GO. The authors feel that an elucidation on this mechanism would give a new insight on the synergistic interaction between GO and geopolymer matrix in nano scale.

With presence of oxygen functional groups on GO, its dispersibility is better than pristine graphene. However, there

TABLE 6 | Pros and cons of analytical modeling in geopolymer.

Type	Aspect	Pros	Cons	Confirmation with experimental approach (type and confirmation)	References
MD (Molecular Dynamics)	Dissolution of Al $(OH)_4$ monomers from aluminosilicate source	100% -The condensation degree of the monomers were observed within 30 dps	None observed	NMR (Nuclear Magnetic Resonance) -Yes. Experimental approach shows fully dissolution of monomers	Zhang Q. et al. (2020)
MD	Dissolution of Si $(OH)_4$ monomers from aluminosilicate source	Almost 100% -The condensation degree of the monomers were observed within 300 dps	None observed	NMR -Yes. Experimental approach shows almost ully dissolution of monomers	
DFT (Density Functional Theory)	Minimum nanofiller content required for epoxy group detection	No -The presence of epoxy groups is directly displayed at any nanofiller loading depending on the number of epoxy atom configured	None observed	FTIR (Fourier Transform Infrared Spectroscopy) -No. Experimental approach reveals oxygen functional group starting at certain nanofiller loading	Amri et al. (2021)
DFT	Minimum Si:Al ratio required for true strength determination	The simulation reveals theoretical total energy of geopolymer at any given Si:Al ratio	Yes -The total energy does not take into account experimental factors like particles agglomeration and pores formation which affects geopolymer strength	Compressive test -No. Compressive strength peaks at Si:Al ratio of 2 FESEM (Field Emission Scanning Electron Microscopy) -No. Microscopic images reveals agglomeration of zeolitic nuclei at SiAl = 1 which produces pores thus reducing compressive strength	Wan et al. (2017)

TABLE 7 | Pros and cons of experimental modeling in geopolymer.

Type	Aspect	Pros	Cons	Confirmation with simulation approach (type and confirmation)	References
NMR	Dissolution of Al $(OH)_4$ monomers from aluminosilicate source	100% -The absence of peak at 78 ppm in ^{27}Al spectrum reveals fairly quick condensation of the monomer	None observed	MD -Yes. Simulation approach shows fully dissolution of monomers	Sagoe-Crentsil and Weng (2007)
NMR	Dissolution of Si $(OH)_4$ monomers from aluminosilicate source	Almost 100% -The absence of sharp peaks between -80 and -100 ppm in ^{29}Si spectra reveals almost fully reacted monomers	None observed	MD -Yes. Simulation approach shows almost fully dissolution of monomers	Duxson et al. (2005)
FTIR	Minimum nanofiller content required for epoxy group detection	None observed	Yes -A small peak at 1,150 cm^{-1} appears on FTIR spectra for 0.5 wt% of GO content, but not 0.1 wt% and 0.3 wt%	DFT -No. Simulation approach shows presence of epoxy group at any GO content	Amri et al. (2021)
Compressive test	Minimum Si:Al ratio required for strength determination	No. Compressive strength of geopolymer is correctly measured with respect to its constituent interfacial adhesion as observed through microscopic images	None observed	DFT -No. Simulation approach displays highest strength at Si:Al ratio = 1 which is not the same with data from compressive strength	Wan et al. (2017)

TABLE 8 | The cost of different types of graphenes.

Graphene type	Standard price (g)	Method	References
Pristine graphene	US$100	Chemical vapor deposition	Pistilli (2020)
GO in solution	US$46.62	Graphite treatment with strong oxidizers	Spasenovic (2020)
Pristine graphene	US$0.5	Synthesis of *Eucalyptus* bark	Taylor (2019)

is still a limit as to how much nanofiller can be reinforced into a matrix system. A high content of GO would lead to uneven dispersion in alkaline solution. To overcome this, a more reactive alkaline solution such as NaOH can be used to promote high early strength and high reaction of aluminosilicate source. This is because the small sodium cation eases the reaction with aluminosilicate source which increases geopolymerization. Despite providing high reaction, cautious action must be taken as high concentration of NaOH would lead to geopolymer carbonation which lead to harsh structure rupture under water. Besides that, during fabrication of geopolymer, GO will be reduced to rGO when in contact with alkaline solution. This causes enlargement of the hole, which will be severed when not controlled, thus resulting in detrimental effect on the graphene unique properties.

Oftentimes geopolymers are cured in high temperature to evaporate the high-water content added for workability. This can incur two problems: further reduction of GO and cracking of geopolymer. Aside from holes enlargement during GO reduction, the amount of oxygen functional group on GO will also be lowered. This would reduce the hydrophilicity of GO that is needed for good dispersibility. Rapid drying under high temperature would cause geopolymer to crack. To avoid this, steam curing is recommended to control moisture evaporation.

SUMMARY AND FUTURE WORK

Since 2004, graphene research has been extensively conducted, accelerating its academic publication to almost 120,000 papers as of March 2021 (Publons, 2021). With such immense interest in graphene from the academic field, the industry must keep up with current graphene technology processing (Randviir et al., 2014). The advancement in graphene research and technology will increase demands in graphene production which in the future, the cost of graphene production at maximum production can be minimized. **Table 8** shows the cost for several types of graphenes.

The most popular method in making graphene is through chemical vapor deposition (CVD), whereby the process involves a mixture of gases that reacts with a surface in producing a layer of graphene. This method produces high-quality graphene but detaching the graphene from its substrate often leads to damaged product (Pistilli, 2020). A cheaper way to produce graphene derivatives is from solution-based processes (Laurén, 2018). GO is created by attaching an oxygen-based functional group to increase the dispersion ability in the water. In addition, GO can be reduced to rGO in many ways, including thermal, chemical, and electrochemical techniques. In 2019, a group of researchers from RMIT University Australia discovered a new approach to produce graphene by using a *Eucalyptus* bark extract. In this way, more economical graphene sheets can be synthesized in which the price reduce almost 200 times cheaper than the conventional way (Taylor, 2019).

Graphene offers enhanced electrical properties for civil engineering applications, including bridges, buildings, and roads (Mohamed et al., 2014). However, the reduction of GO to rGO during geopolymerization is undesirable when an excess epoxy functional group is present on the rGO sheet due to its lower binding energy than hydroxyl groups. Interestingly, epoxy groups' negative charges have positive effects on the electrical properties in geopolymer composite, producing the material called Intrinsic self-sensing concrete (ISSC). By measuring the electrical resistance of ISSC, the stress, strain, crack, and damage of concrete can be monitored without embedding or attaching remote sensors (Han et al., 2015; Han et al., 2018). When implemented, ISSC made of graphene geopolymer composite can be very cost-effective in the long run.

While various works have been reported using geopolymer as green construction material, geopolymer can also be used for outer space application, where geopolymer is fabricated on the Moon using lunar regolith. Since geopolymer can be cured in average daytime temperature (127°C) and lunar regolith contains aluminosilicate materials, attempts have been made for *in-situ* materials utilization. It has been observed that vacuum conditions affect the geopolymerization process. Under vacuum treatment, the geopolymer crumbles into smaller pieces, which is suspected to fill in the pores in the structure (Davis et al., 2017). It has been discussed that the addition of graphene into geopolymer results in substantially filled pores, which would be useful in this case. On the other hand, graphene has been discussed for its potential to be used as a viable material in interstellar solar sail (Santoli, 2010; Matloff, 2012). When tested, graphene is lighter than the conventional polyester film and still successfully accelerates when shone with a 1 W laser. Perhaps, the use of graphene geopolymer lunar regolith-based composite could catalyst the production of geopolymer on lunar.

The mechanical strength of graphene/geopolymer nanocomposite was discussed based on various factors such as types of graphene, effects of graphene in alkaline solution, reaction between graphene and aluminosilicate particles, effects of graphene concentration on the workability of geopolymer, and geopolymer nanocomposite sintering temperature. Most of the studies observed that the strength of geopolymer filled with treated graphene surpasses pristine graphene in both compressive and flexural strength due to the higher dispersion and better reinforcement effects in the geopolymer matrix. Analytical modeling on graphene

geopolymer provides an insight into the interfacial reaction between graphene and geopolymer and its geopolymerization process that cannot be achieved experimentally. Nevertheless, current analytical modeling does not represent the simultaneous process in geopolymerization, which could not give an accurate and complete illustration. Therefore, it is expected to see a more commercialized application of graphene geopolymer composites with better detailed and thorough modeling.

AUTHOR CONTRIBUTIONS

All authors listed have made a substantial, direct, and intellectual contribution to the work and approved it for publication.

FUNDING

The research work was funded by the Ministry of Higher Education (MOHE), Malaysia, under Fundamental Research Grant Scheme (FRGS) with grant number 5540317.

ACKNOWLEDGMENTS

The authors thank the Universiti Putra Malaysia (UPM),especially the Department of Aerospace Engineering, Institute of Advanced Technology (ITMA), and Institute of Tropical Forestry and Forest Products (INTROP) for the infrastructures lend, allowing this project to be completed.

REFERENCES

Akinyele, J. O., Odunfa, S. O., Famoye, A. A., and Kuye, S. I. (2017). Structural Behaviour of Metakaolin Infused concrete Structure. *Nig. J. Tech.* 36 (2), 331–338. doi:10.4314/njt.v36i2.2

Amri, A., Najib, A. A., Olivia, M., Altarawneh, M., Aman Rahman, M. M., Saputro, S., et al. (2021). Physicochemical Properties of Geopolymer Composites with DFT Calculations of *In-Situ* Reduction of Graphene Oxide. *Ceram. Int.* 47 (10), 13440–13445. doi:10.1016/j.ceramint.2021.01.202

Anderson, M., Lloyd Spetz, A., and Pearce, R. (2013). "Chapter 4-Recent Trends in Silicon Carbine (SiC) and Graphene-Based Gas Sensors," in *Semiconductor Gas Sensors*. Editors R. Jaaniso and O. K. Tan (Cambridge: Woodhead Publishing Series).

Archanjo, B. S., Araujo, J. R., Silva, A. M., Capaz, R. B., Falcão, N. P. S., Jorio, A., et al. (2014). Chemical Analysis and Molecular Models for Calcium-Oxygen-Carbon Interactions in Black Carbon Found in fertile Amazonian Anthrosoils. *Environ. Sci. Technol.* 48, 7445–7452. doi:10.1021/es501046b

Ashfaq Alvi, M. A., Khalifeh, M., and Agonafir, M. B. (2020). Effect of Nanoparticles on Properties of Geopolymer Designed for Well Cementing Applications. *J. Pet. Sci. Eng.* 191, 1–16. doi:10.1016/j.petrol.2020.107128

Asif, A., Man, Z., Mohd Azizli, K. A., Nuruddin, M. F., and Ismail, L. (2014). The Effect of Si/Al Ratio and Sodium Silicate on the Mechanical Properties of Fly Ash Based Geopolymer for Coating. *Msf* 803, 355–361. doi:10.4028/www.scientific.net/msf.803.355

Asif, A., Man, Z., Mod Azizli, K. A., and Mohammed Hamidi, R. (2015). Effect of Alkali and Water Content on Setting Time and Strength of Fly Ash Based Geopolymer. *Appl. Mech. Mater.* 699, 93–98. doi:10.4028/www.scientific.net/amm.699.93

Bell, J. L., Gordon, M., and Kriven, W. M. (2005). Use of Geopolymeric Cements as a Refractory Adhesive for Metal and Ceramic Joins. *Ceram. Eng. Sci. Proc.* 26 (3), 407–413. doi:10.1002/9780470291238.ch46

Bellum, R. R., Muniraj, K., Indukuri, C. S. R., and Madduru, S. R. C. (2020). Investigation on Performance Enhancement of Fly Ash-GGBFS Based Graphene Geopolymer Concrete. *J. Build. Eng.* 32, 101659. doi:10.1016/j.jobe.2020.101659

Carotenuto, G., Romeo, V., Cannavaro, I., Roncato, D., Martorana, B., and Gosso, M. (2012). Graphene-polymer *Conference Series: Materials Science and Engineering*, 1-7. Bedforshire, UK: IOP Publishing Ltd.

Chi, H. L., Louda, P., Periyasamy, A. P., Bakalova, T., and Kovacic, V. (2018). Flexural Behaviour of Carbon Textile-Reinforced Geopolymer Composite Thin Plate. *Fibers* 6 (87), 1–14. doi:10.3390/fib6040087

Cho, S. (2015). *Gepolymer Composites and Their Applications in Stress Wave Mitigation*. Urbana-Champaign: University of Illinois. PhD Thesis.

Chun, W. W., Leng, T. P., Osman, A. F., and Keat, Y. C. (2017). The Properties of Epoxy/Graphene Conductive Materials Using High Speed Mechanical Stirrer and Bath Sonicator. *Mater. Sci. Forum* 888, 222–227. doi:10.4028/www.scientific.net/msf.888.222

Constâncio Trindade, A. C., Ahmed Alcamand, H., Ribeiro Borges, P. H., and Andrade Silva, F. d. (2017). "On the Durability Behaviour of Natural Fibre Reinforced Geopolymers," in Conference: 41st International Conference and Expo on Advanced Ceramics and Composites, Daytona Beach, FL, January 22–27, 2017 (USA: ICACC).

Cui, Y., Zhang, P., and Bao, J. (2020). Bond Stress between Steel-Reinforced Bars and Fly Ash-Based Geopolymer Concrete. *Adv. Mater. Sci. Eng.* 2020 (7), 1–11. doi:10.1155/2020/9812526

Dac Ho, V. (2020). *Development of Next-Generation Construction Materials with Graphene AdditivesPhD Thesis*. Australia: The University of Adelaide.

Danial, N. S., Che Halin, D. S., Ramli, M. M., Abdullah, M. M. A., Salleh, M. M. A., Mat Isa, S. S., et al. (2019). Graphene Geopolymer Hybrid: A Review on Mechanical Properties and Piezoelectric Effect. *IOP Conf. Ser. Mater. Sci. Eng.* 572, 1–10. doi:10.1088/1757-899x/572/1/012038

Davidovits, J. (2002). "30 Years in Successes and Failures in Geopolymer Applications. Market Trends and Potential Breakthroughs," in *Geopolymer 2002 Conference 2002*, 1–16. Melbourne, Australia.

Davidovits, J. (2006). *Difference between Geopolymer and Amorphous Zeolite*. Retrieved from: https://www.geopolymer.org/faq/difference-between-geopolymer-and-amorphous-zeolite/ (Accessed October 28, 2020).

Davidovits, J. (2015a). "Chapter 1-Introduction," in *Geopolymer-Chemistry and Applications*. Editor J. Davidovits 4th edition (France: Geopolymer Institute), 1–16.

Davidovits, J. (2015b). "Chapter 18-Quality Control," in *Geopolymer Chemistry and Applications*. Editor J. Davidovits 4th edition (France: Geopolymer Institute).

Davidovits, J. (2015c). "Part IV: Applications," in *Geopolymer Chemistry and Applications*. Editor J. Davidovits 4th edition (France: Geopolymer Institute).

Davidovits, J. (2016). *Webinar Spring 2016 Special Focus on Geopolymer Cement*. France: Geopolymer Insitute.

Davidovits, J. (2018). *Why Alkali-Activated Materials (AAM) Are Not Geopolymers*. Saint-Quentin: Geopolymer Institute. Technical Paper #25. 1–10.

Davis, G., Montes, C., and Eklund, S. (2017). Preparation of Lunar Regolith Based Geopolymer Cement under Heat and Vacuum. *Adv. Space Res.* 59 (7), 1–34. doi:10.1016/j.asr.2017.01.024

Deng, S., and Berry, V. (2016). Wrinkled, Rippled and Crumpled Graphene: an Overview of Formation Mechanism, Electronic Properties, and Applications. *Mater. Today* 19 (4), 197–212. doi:10.1016/j.mattod.2015.10.002

Ding, J., Zhao, H., Wang, Q., Dou, H., Chen, H., and Yu, H. (2017). An Ultrahigh thermal Conductive Graphene Flexible Paper. *Nanoscale* 9, 16871–16878. doi:10.1039/c7nr06667h

Dousti, A., Beaudoin, J. J., and Shekarchi, M. (2017). Chloride Binding in Hydrated MK, SF and Natural Zeolite-Lime Mixtures. *Constr. Build. Mater.* 154, 1035–1047. doi:10.1016/j.conbuildmat.2017.08.034

Du, H., and Pang, S. D. (2018). Dispersion and Stability of Graphene Nanoplatelet in Water and its Influence on Cement Composites. *Constr. Build. Mater.* 167, 403–413. doi:10.1016/j.conbuildmat.2018.02.046

Dusza, J., Morgiel, J., Duszová, A., Kvetková, L., Nosko, M., Kun, P., et al. (2012). Microstructure and Fracture Toughness of Si3N4+graphene Platelet Composites. *J. Eur. Ceram. Soc.* 32 (12), 3389–3397. doi:10.1016/j.jeurceramsoc.2012.04.022

Duxson, P., Provis, J. L., Lukey, G. C., Separovic, F., and van Deventer, J. S. J. (2005). 29Si NMR Study of Structural Ordering in Aluminosilicate Geopolymer Gels. *Langmuir* 21 (7), 3028–3036. doi:10.1021/la047336x

Erickson, K., Erni, R., Lee, Z., Alem, N., Gannett, W., and Zettl, A. (2010). Determination of the Local Chemical Structure of Graphene Oxide and Reduced Graphene Oxide. *Adv. Mater.* 22 (40), 4467–4472. doi:10.1002/adma.201000732

Fan, X., Peng, W., Li, Y., Li, X., Wang, S., Zhang, G., et al. (2008). Deoxygenation of Exfoliated Graphite Oxide under Alkaline Conditions: a green Route to Graphene Preparation. *Adv. Mater.* 20 (23), 4490–4493. doi:10.1002/adma.200801306

Fang, M., Wang, K., Lu, H., Yang, Y., and Nutt, S. (2009). Covalent Polymer Functionalization of Graphene Nanosheets and Mechanical Properties of Composites. *J. Mater. Chem.* 19, 7098–7105. doi:10.1039/b908220d

Fekoua, J. N. N., Kaze, C. R., Duna, L. L., Ghazouni, A., Ndassa, I. M., Kamseu, E., et al. (2021). Effect of Curing Cycles on Developing Strength and Microstructure of Goethite-Rich Aluminosilicate (Corroded Laterite) Based Geopolymer Composites. *Mater. Chem. Phys.* 270, 1–17. doi:10.1016/j.matchemphys.2021.124864

Filip, J., and Tkac, J. (2014). Is Graphene Worth Using in Biofuel Cells? *Electrochim. Acta* 136, 340–354. doi:10.1016/j.electacta.2014.05.119

Frizon, F., and Desbats-le-Chequer, C. (2010). Geopolymers as Waste Encapsulation Materials: Impact of Anions on the Materials Properties. *Ast* 69, 174–179. doi:10.4028/www.scientific.net/ast.69.174

Głuchowsk, P., Tomala, R., Jeżowski, A., Szeqwczyk, D., Macalik, B., Smolina, I., et al. (2020). Preparation and Physical Characteristics of Graphene Ceramics. *Sci. Rep.* 10, 11121. doi:10.1038/s41598-020-67977-5

Güneyisi, E., Gesoğlu, M., and İpek, S. (2013). Effect of Steel Fiber Addition and Aspect Ratio on Bond Strength of Cold-Bonded Fly Ash Lightweight Aggregate Concretes. *Constr. Build. Mater.* 47, 358–365. doi:10.1016/j.conbuildmat.2013.05.059

Guala, F. (2002). "Models, Simulations and Experiments," in *Model-based Reasoning*. Editors L. Magnani and N. J. Nersessian (Boston: Springer).

Guo, S., Qiao, X., Zhao, T., and Wang, Y. -S. (2020). Preparation of Highly Dispersed Graphene and its Effect on the Mechanical Properties and Microstructures of Geopolymer. *J. Mater. Civil Eng.* 32 (11), 1–10. doi:10.1061/(asce)mt.1943-5533.0003424

Guo, X., Shi, H., and Dick, W. A. (2010). Compressive Strength and Microstructural Characteristics of Class C Fly Ash Geopolymer. *Cem. Concr. Compos.* 32 (2), 142–147. doi:10.1016/j.cemconcomp.2009.11.003

Hájková, P. (2018). Kaolinite Claystone-Based Geopolymer Materials: Effect of Chemical Composition and Curing Conditions. *Minerals* 8 (10), 444. doi:10.3390/min8100444

Habert, G. (2014). "Chapter 10-Assessing the Environmental Impact of Conventional and 'Green' Cement Production," in *Eco-efficient Construction and Building Materials*. Editors F. Pacheco-Torgal, L. F. Cabeza, J. Labrincha, and A. de Magalhães (United Kingdom: . Woodhead Publishing).

Han, B., Ding, S., and Yu, X. (2015). Intrinsic Self-Sensing concrete and Structures: A Review. *Measurement* 59, 110–128. doi:10.1016/j.measurement.2014.09.048

Han, J. T., Jeong, S. Y., Jeong, H. J., and Lee, G.-W. (2018). *Chemically Exfoliated Graphene Nanosheets for Flexible Electrode Applications*. London, United Kingdom: Intech Open. doi:10.5772/intechopen.77284

Hariharan, R., Santhi, A. S., and Ganesh, N. (2015). Maximum Agreement Subtree (Of 2 Binary Trees). *Int. J. Civil Eng.* 13 (3), 1–5. doi:10.1007/978-3-642-27848-8_220-2

He, J., Zhang, G., Hou, S., and Cai, C. S. (2011). Geopolymer-based Smart Adhesives for Infrastructure Health Monitoring: Concept and Feasibility. *J. Mater. Civ. Eng.* 23 (2), 100–109. doi:10.1061/(asce)mt.1943-5533.0000140

Hron, R., Martaus, F., and Kadlec, M. (2018). "Compressive Properties of Geopolymer Matrix Composites," in 2nd international conference on mechanical, material and aerospace engineering, Wuhan, China, May 10–13, 2018, 179, 1–8. doi:10.1051/matecconf/201817902003

Huang, H., Chen, W., Chen, S., and Wee, A. T. S. (2008). Bottom-up Growth of Epitaxial Graphene on 6H-SiC(0001). *ACS Nano* 2 (12), 2513–2518. doi:10.1021/nn800711v

Ikram, M., and Farooq, M. U. (2019). *Ceramics (Si- and Al-Based Oxides)-Graphene Hybrids and Advanced Applications*. London, United Kingdom: IntechOpen, 1–22.

Itapu, B., and Jayatissa, A. (2018). A Review in Graphene/Polymer Composites. *Csij* 23 (3), 1–16. doi:10.9734/csji/2018/41031

Jauregui, L. A., Yue, Y., Sidorov, A. N., Hu, J. N., Yu, Q., Lopez, J., et al. (2010). Thermal Transport in Graphene Nanostructures: Experiments and Simulations. *Ecs Trans.* 28 (5), 73. doi:10.1149/1.3367938

Jaya, N. A., Al Bakri Abdullah, M. M., Ruzaidi Ghazali, C. M., Hussain, M., Hussin, K., and Ahmad, R. (2016a). Kaolin Geopolymer as Precursor to Ceramic Formation. *MATEC Web conf.* 78, 01061. doi:10.1051/matecconf/20167801061

Jaya, N. A., Al Bakri Abdullah, M. M., Ghazali, C. M. R., Binhussain, M., Hussin, K., and Ahmad, R. (2016b). Characterization and Microstructure of Kaolin-Based Ceramic Using Geopolymerization. *Kem* 700, 3–11. doi:10.4028/www.scientific.net/kem.700.3

Jishnu, A., S Jayan, J., Saritha, A., A S, S., and Venu, G. (2020). Superhydrophobic Graphene-Based Materials with Self-Cleaning and Anticorrosion Performance: An Appraisal of Neoteric Advancement and Future Perspectives. *Colloids Surf. A. Physicochem Eng. Asp* 606, 125395–125414. doi:10.1016/j.colsurfa.2020.125395

Kani, N. E., and Allahverdi, A. (2009). Effects of Curing Time and Temperature on Strength Development of Inorganic Polymeric Binder Based on Natural Pozzolan. *J. Mater. Sci.* 44 (12), 3088–3097. doi:10.1007/s10853-009-3411-1

Kim, H., Abdala, A. A., and Macosko, C. W. (2010). Graphene/Polymer Nanocomposites. *Macromolecules* 43 (16), 6515–6530. doi:10.1021/ma100572e

Kim, Y. Y., Lee, B.-J., Saraswathy, V., and Kwon, S.-J. (2014). Strength and Durability Performance of Alkali-Activated rice Husk Ash Geopolymer Mortar. *Scientific World J*, 2014, 1–10. doi:10.1155/2014/209584

Kolhatkar, G., Boucherif, A., Boucherif, A. R., Dupuy, A., Fréchette, L. G., Arès, R., et al. (2018). *Nanotechnology* 29 (14), 1–7. doi:10.1088/1361-6528/aaac40

Kothiyal, N. C., Sharma, S., Mahajan, S., and Sethi, S. (2016). Characterization of Reactive Graphene Oxide Synthesized from ball - Milled Graphite: its Enhanced Reinforcing Effects on Cement Nanocomposites. *J. Adhes. Sci. Technol.* 30 (9), 915–933. doi:10.1080/01694243.2015.1129214

Kriven, W. M. (2012). *The Geopolymer Route to High Tech Ceramics*. Geopolymer Institute Technical Paper. 2012. France: Geopolymer Institute, 1–72.

Ku Muhammad, K. S. S., Mohamed, F., Radiman, S., Hamzah, A., Sarmani, S., Siong, K. K., et al. (2016). Synthesis and Characterization of Exfoliated Graphene Oxide. *AIP Conf. Proc.* 174 (1), 1–6. doi:10.1063/1.4966799

Kuilla, T., Bhadra, S., Yao, D., Kim, N. H., Bose, S., and Lee, J. H. (2010). Recent Advances in Graphene Based Polymer Composites. *Prog. Polym. Sci.* 35 (11), 1350–1375. doi:10.1016/j.progpolymsci.2010.07.005

Kumar, M. L., and Revathi, V. (2016). Metakaolin Bottom Ash Blend Geopolymer Mortar-A Feasibility Study. *Constr. Build. Mater.* 114, 1–5. doi:10.1016/j.conbuildmat.2016.03.149

Kupaei, R. H., Alengaram, U. J., and Jumaat, M. Z. (2014). The Effect of Different Parameters on the Development of Compressive Strength of Oil Palm Shell Geopolymer Concrete. *Sci. World J.* 2014, 1–16. doi:10.1155/2014/898536

Kupwade-Patil, K., Allouche, E. N., Islam, M., and Gunasekaran, A. (2013a). Encapsulation of Solid Waste Incinerator Ash in Geopolymer Concretes and its Applications. *Aci Mater. J.*, 1–11.

Kupwade-Patil, K., Soto, F., Kunjumon, A., Allouche, E. N., and Mainardi, D. S. (2013b). Multi-scale Modeling and Experimental Investigations of Geopolymeric Gels at Elevated Temperatures. *Comput. Struct.* 122, 164–177. doi:10.1016/j.compstruc.2013.01.005

Kurth, S., Marques, M. A. L., and Gross, E. K. U. (2005). "Density-Functional Theory," in *Encyclopedia of Condensed Matter Physics*. Editors F. Bassani, G. L. Liedl, and W. Peter (Cambridge: Academic Press).

Lahir, Y. (2019). "Chapter 7-Graphene and Graphene-Based Nanomaterials Are Suitable Vehicles for Drug Delivery," in *Applications of Targeted Nano Drugs and Delivery Systems: Nanoscience and Nanotechnology in Drug Delivery*. Editors S. S. Mohapatra, S. Ranjan, N. Dasgupta, R. K. Misra, and S. Thomas (Amsterdam: Elsevier).

Lambert, T., Chavez, C. A., Hernandez-Sanchez, B., Lu, P., Bell, N. S., Ambrosini, A., et al. (2009). Synthesis and Characterization of Titania-Graphene Nanocomposites. *J. Phys. Chem.* 113 (46), 18912–19823. doi:10.1021/jp905456f

Landau, D. P. (2005). "The Future of Simulations in Materials Science," in *Handbook of Materials Modelling*. Editor S. Yip (Dordrecht: Springer).

Laurén, S. (2018). What Is Graphene Oxide? Retrieved from: https://www.biolinscientific.com/blog/what-is-graphene-oxide (Accessed November 28, 2020).

Léonard, A., and Su, B.-L. (2007). "A Mechanistic Study on the Degradation of Highly Ordered, Non-ionic Surfactant Templated Aluminosilicate Mesoporous Materials Al-CMI-1 in Boiling Water," in *Recent Progress in Mesostructured Materials*. Editors D. Zhao, S. Qiu, Y. Tang, and C. Yu, 113–116. doi:10.1016/s0167-2991(07)80278-3

Li, D., Müller, M. B., Gilje, S., Kaner, R. B., and Wallace, G. G. (2008). Processable Aqueous Dispersions of Graphene Nanosheets. *Nat. Nanotech* 3 (2), 101–105. doi:10.1038/nnano.2007.451

Li, W., Tang, X.-Z., Zhang, H.-B., Jiang, Z.-G., Yu, Z.-Z., Du, X.-S., et al. (2011). Simultaneous Surface Functionalization and Reduction of Graphene Oxide with Octadecylamine for Electrically Conductive Polystyrene Composites. *Carbon* 49 (14), 4724–4730. doi:10.1016/j.carbon.2011.06.077

Liang, A., Jiang, X., Hong, X., Jiang, Y., Shao, Z., and Zhu, D. (2018). Recent Developments Concerning the Dispersion Methods and Mechanisms of Graphene. *Coatings* 8 (1), 33. doi:10.3390/coatings8010033

Lin, Y., Watson, K. A., Kim, J-W., Baggett, D. W., Working, D. C., and Connell, J. W. (2013). Bulk Preparation of Holey Graphene via Controlled Catalytic Oxidation. *Nanoscale* 17 (2013), 7814–7824. doi:10.1039/c3nr02135a

Liu, X., Suk, J. W., Boddeti, N. G., Cantley, L., Wang, L., Gray, J. M., et al. (2013). Large Arrays and Properties of 3-Terminal Graphene Nanoelectromechanical Switches. *Adv. Mater.* 26 (10), 1571–1576. doi:10.1002/adma.201304949

Liu, F., Hu, N., Ning, H., Liu, Y., Li, Y., and Wu, L. (2015). Molecular Dynamics Simulation on Interfacial Mechanical Properties of Polymer Nanocomposites with Wrinkled Graphene. *Comput. Mater. Sci.* 108, 160–167. doi:10.1016/j.commatsci.2015.06.023

Liu, X., Wang, L.-Y., Zhao, L.-F., He, H.-F., Shao, X.-Y., Fang, G.-B., et al. (2018). Research Progress of Graphene-Based Rubber Nanocomposites. *Polym. Compos.* 39 (4), 1006–1022. doi:10.1002/pc.24072

Liu, F., Wang, M., Chen, Y., and Gao, J. (2019). Thermal Stability of Graphene in Inert Atmosphere at High Temperature. *J. Solid State Chem.* 276, 100–103. doi:10.1016/j.jssc.2019.04.008

Liu, X., Wu, Y., Li, M., Jiang, J., Guo, L., Wang, W., et al. (2020). Effects of Graphene Oxide on Microstructure and Mechanical Properties of Graphene Oxide-Geopolymer Composites. *Constr. Build. Mater.* 247, 1–12. doi:10.1016/j.conbuildmat.2020.118544

Lloyd, R. R. (2009). "Chapter 8-Accelerated Ageing of Geopolymers," in *Geopolymers: Structures, Processing, Properties and Industrial Applications*. Editors J. L. Provis and J. S. J. van Deventer (United Kingdom: Woodhead Publishing).

Long, W., Ye, T., Luo, Q., Wang, Y., and Mei, L. (2019a). Reinforcing Mechanism of Reduced Graphene Oxide on Flexural Strength of Geopolymers: a Synergistic Analysis of Hydration and Chemical Composition. *Nanomaterials* 9, 1–15. doi:10.3390/nano9121723

Long, W.-J., Ye, T.-H., Li, L.-X., and Feng, G.-L. (2019b). Electrochemical Characterization and Inhibiting Mechanism on Calcium Leaching of Graphene Oxide Reinforced Cement Composites. *Nanomaterials* 9 (2), 288. doi:10.3390/nano9020288

Ma, H.-L., Zhang, H.-B., Hu, Q.-H., Li, W.-J., Jiang, Z.-G., Yu, Z.-Z., et al. (2012). Functionalization and Reduction of Graphene Oxide with P-Phenylene Diamine for Electrically Conductive and Thermally Stable Polystyrene Composites. *ACS Appl. Mater. Inter.* 4 (4), 1948–1953. doi:10.1021/am201654b

Ma, J., Meng, Q., Michelmore, A., Kawashima, N., Izzuddin, Z., Bengtsson, C., et al. (2013). Covalently Bonded Interfaces for Polymer/graphene Composites. *J. Mater. Chem. A.* 1 (13), 4255–4264. doi:10.1039/c3ta01277h

Malik, S., Vijayaraghavan, A., Erni, R., Ariga, K., Khalakhan, I., and Hill, J. P. (2010). High Purity Graphenes Prepared by a Chemical Intercalation Method. *Nanoscale* 2 (10), 2139–2143. doi:10.1039/c0nr00248h

Manigandan, S., Gunasekar, P., Nithya, S., Revanth, G. D., and Anudeep, A. V. S. C. (2017). Experimental Analysis of Graphene Nanocomposite on Kevlar. *IOP Conf. Ser. Mater. Sci. Eng.* 225, 1–6. doi:10.1088/1757-899x/225/1/012061

Mao, S., Pu, H., and Chen, J. (2012). Graphene Oxide and its Reduction: Modeling and Experimental Progress. *RSC Adv.* 2 (7), 2643–2662. doi:10.1039/c2ra00663d

Matalkah, F., and Soroushian, P. (2020). Graphene Nanoplatelet for Enhancement the Mechanical Properties and Durability Characteristics of Alkali Activated Binder. *Constr. Build. Mater.* 249, 118773. doi:10.1016/j.conbuildmat.2020.118773

Matloff, G. L. (2012). Graphene, the Ultimate Interstellar Solar Sail Material? *J. Br. Interplanet. Soc.* 65, 1–5.

Merabtene, M., Kacimi, L., and Clastres, P. (2019). Elaboration of Geopolymer Binders from Poor Kaolin and Dam Sludge Waste. 5(6), 1–12. doi:10.1016/j.heliyon.2019.e01938

Mohajerani, A., Suter, D., Jeffrey-Bailey, T., Song, T., Arulrajah, A., Horpibulsuk, S., et al. (2019). Recycling Waste Materials in Geopolymer concrete. *Clean. Techn Environ. Pol.* 21, 493–515. doi:10.1007/s10098-018-01660-2

Mohamed, S., Leung, T., Jason, F., Mahbubur, R., Fiona, S., John, L., et al. (2014). Graphene/fly Ash Geopolymeric Composites as Self-Sensing Structural Materials. *Smart Mater. Struct.* 23 (6), 222–231. doi:10.1088/0964-1726/23/6/065006

Mohammed, B. S., Haruna, S., Wahab, M. M. A., Liew, M. S., and Haruna, A. (2019). Mechanical and Microstructural Properties of High Calcium Fly Ash One-Part Geopolymer Cement Made with Granular Activator. *Heliyon* 5, 1–9. doi:10.1016/j.heliyon.2019.e02255

Moharana, S., Kar, S. K., Mishra, M. K., and Mahaling, R. N. (2019). "Synthesis and Properties of Graphene and Graphene Oxide-Based Polymer Composites," in *Surface Engineering of Graphene*. Editors S. Sahoo, S. Tiwari, and G. Nayak (Cham, Switzerland: Springer).

Moon, K., Lee, J., Ruoff, R. S., and Lee, H. (2010a). Reduced Graphene Oxide by Chemical Graphitization. *Nat. Commun.* 1 (73), 1–6. doi:10.1038/ncomms1067

Moon, K., Li, Z., Yao, Y., Lim, Z., Liang, Q., Agar, J., Song, M., Liu, M., and Wong, C. P. (2010b). in Proceedings: 60th Electronic Components and Technology Conference (ECTC), Las Vegas, NV, June 1–4, 2010 (Las Vegas: IEEE). doi:10.1109/ectc.2010.5490644

Murr, L. E. (2016). "Computer Simulations in Materials Science and engineering," in *Handbook of Materials Structures, Properties, Processing and Performance* (Switzerland: Springer International Publisher), 1–17. doi:10.1007/978-3-319-01905-5_61-2

Mustofa, M., and Pintowantoro, S. (2017). The Effect of Si/Al Ratio to Compressive Strength and Water Absorption of Ferronickel Slag-Based Geopolymer. *Ijps*, 167–172. doi:10.12962/j23546026.y2017i2.2334

Naebe, M., Wang, J., Amini, A., Khayyam, H., Hameed, N., Li, L. H., et al. (2014). Mechanical Property and Structure of Covalent Functionalised Graphene/epoxy Nanocomposites. *Sci. Rep.* 4 (1), 1–7. doi:10.1038/srep04375

Nainani, R. K., and Thakur, P. (2016). Facile Synthesis of TiO2-RGO Composite with Enhanced Performance for the Photocatalytic Mineralization of Organic Pollutants. *Water Sci. Technol.* 73 (8), 1927–1936. doi:10.2166/wst.2016.039

National Nanotechnology Coordinated Insfrastructure (2012). Molecules: Lots of Shapes and Sizes. *Natl. Nanotechnol. Coord. Insfrastruct.* (11), 1–8.

Neklyudov, V. V., Khafizov, N. R., Sedov, I. A., and Dimiev, A. M. (2017). New Insights into the Solubility of Graphene Oxide in Water and Alcohols. *Phys. Chem. Chem. Phys.* 19, 17000–17008. doi:10.1039/c7cp02303k

Neupane, K., Kidd, P., Chalmers, D., Baweja, D., and Shrestha, R. (2015). Investigation on Compressive Strength Development and Drying Shrinkage of Ambient Cured Powder-Activated Geopolymer Concretes. *Aust. J. Civil Eng.* 14 (1), 72–83. doi:10.1080/14488353.2016.1163765

Novoselov, K. S., Geim, A. K., Morozov, S. V., Jiang, D., Zhang, Y., Dubunos, S. V., et al. (2004). Electric Field Effect in Atomically Thin Carbon Films. *Science* 306 (5696), 666–669. doi:10.1126/science.1102896

Pandey, B. (2011). Effect of Carbonation on Leachability and Compressive Strength of Cement Solidified and Geopolymer Solidified Synthetic Metal Wastes. Canada: Lakehead University. Master Thesis.

Pei, S., and Cheng, H.-M. (2012). The Reduction of Graphene Oxide. *Carbon* 50 (9), 3210–3228. doi:10.1016/j.carbon.2011.11.010

Perera, D. S., Uchida, O., Vance, E. R., and Finnie, K. S. (2007). Influence of Curing Schedule on the Integrity of Geopolymers. *J. Mater. Sci.* 42 (9), 3099–3106. doi:10.1007/s10853-006-0533-6

Phiri, J., Johansson, L.-S., Gane, P., and Maloney, T. (2018). A Comparative Study of Mechanical, thermal and Electrical Properties of Graphene-, Graphene Oxide- and Reduced Graphene Oxide-Doped Microfibrillated Cellulose Nanocomposites. *Composites B: Eng.* 147, 104–113. doi:10.1016/j.compositesb.2018.04.018

Pistilli, M. (2020). What Factors Impact Graphene Cost? Retrieved from: https://investingnews.com/daily/tech-investing/nanoscience-investing/graphene-investing/graphene-cost/#:~:text=Specific%20pricing%20data%20is%20hard,graphene%20has%20many%20exciting%20applications (Accessed November 28, 2020). doi:10.1109/icmew46912.2020.9105972

Porwal, H., Grasso, S., and Reece, M. J. (2013). Review of Graphene-Ceramic Matrix Composites. *Adv. Appl. Ceramics* 112 (8), 443–454. doi:10.1179/174367613x13764308970581

J. L. Provis and J. S. J. Van Deventer in *Geopolymers: Structures, Processing, Properties, and Industrial Applications* (Amsterdam: Elsevier).

Provis, J. L., Duxson, P., and van Deventer, J. S. J. (2010). The Role of Particle Technology in Developing Sustainable Construction Materials. *Adv. Powder Technol.* 21 (1), 2–7. doi:10.1016/j.apt.2009.10.006

Publons (2021). *Graphene Publications*. Retrieved from: https://publons.com/publon/?title=graphene (Accessed November 28, 2020).

Quan, J.-X., Zhang, H.-Y., Zhou, L.-Y., Zhou, Y., and Su, J.-W. (2017). Experimental Study of Geopolymer Used as Adhesive in anchorage of Steel Bars. *Proced. Eng.* 210, 45–52. doi:10.1016/j.proeng.2017.11.047

Ramesha, G. K., Vijaya Kumara, A., Muralidhara, H. B., and Sampath, S. (2011). Graphene and Graphene Oxide as Effective Adsorbents toward Anionic and Cationic Dyes. *J. Colloid Interf. Sci.* 361, 270–277. doi:10.1016/j.jcis.2011.05.050

Randviir, E. P., Brownson, D. A. C., and Banks, C. E. (2014). A Decade of Graphene Research: Production, Applications and Outlook. *Mater. Today* 17 (9), 426–432. doi:10.1016/j.mattod.2014.06.001

Ranjbar, N., Mehrali, M., Mehrali, M., Alengaram, U. J., and Jumaat, M. Z. (2015). Graphene Nanoplatelet-Fly Ash Based Geopolymer Composites. *Cem. Concr. Res.* 76, 222–231. doi:10.1016/j.cemconres.2015.06.003

Raphaëlle, P., Martin, C., and Raphaël, B. (2019). Influence of the Initial Water Content in Flash Calcined Metakaolin-Based Geopolymer. *Constr. Build. Mater.* 201, 421–429. doi:10.1016/j.conbuildmat.2018.12.201

Rehman, S., Ibrahim, Z., Memon, S., Javed, M., and Khushnood, R. (2017). A Sustainable Graphene Based Cement Composite. *Sustainability* 9 (7), 1229. doi:10.3390/su9071229

Rehman, S. K. U., Ibrahim, Z., Jameel, M., Memon, S. A., Javed, M. F., Aslam, M., et al. (2018). Assessment of Rheological and Piezoresistive Properties of Graphene-Based Cement Composites. *Int. J. Concr. Struct. Mater.* 12 (1), 1–23. doi:10.1186/s40069-018-0293-0

Ren, X., and Zhang, L. (2019). Experimental Study of Geopolymer concrete Produced from Waste concrete. *J. Mater. Civil Eng.* 31 (7), 1–14. doi:10.1061/(asce)mt.1943-5533.0002750

Roberts, M. W., Clemons, C. B., Wilber, J. P., Young, G. W., Buldum, A., and Quinn, D. D. (2010). Continuum Plate Theory and Atomistic Modeling to Find the Flexural Rigidity of a Graphene Sheet Interacting with a Substrate. *J. Nanotechnol.* 2010, 1–8. doi:10.1155/2010/868492

Ruzaidi, C. M., Abdullah, A., Mohd Mustafa, A. B. A., Kamarudin, H., and Ismail, A. N. (2014). Compressive Strength of Fly Ash Based Geopolymer/glass Fiber Composite via Filament Winding. *Key Eng. Mater.* 594-595, 78–82. doi:10.4028/www.scientific.net/kem.594-595.78

Saafi, M., Tang, L., Fung, J., Rahman, M., and Liggat, J. (2015). Enhanced Properties of Graphene/fly Ash Geopolymeric Composite Cement. *Cem. Concr. Res.* 67, 292–299. doi:10.1016/j.cemconres.2014.08.011

Sagoe-Crentsil, K., and Weng, L. (2007). Dissolution Processes, Hydrolysis and Condensation Reactions during Geopolymer Synthesis: Part II. High Si/Al Ratio Systems. *J. Mater. Sci.* 42 (9), 3007–3014. doi:10.1007/s10853-006-0818-9

Santoli, S. (2010). "Chapter: Carbon Nanotube Membrane Solar Sails: A challenge for Extremely Fast Space Flight," in *Carbon Nanotubes*. Editor J. M. Marulanda (Rijeka: InTech Open), 591–610.

Shi, C., Tu, Z., Guo, M.-Z., and Wang, D. (2017). "Accelerated Carbonation as a Fast Curing Technology for concrete Blocks," in *Sustainable and Nonconventional Construction Materials Using Inorganic Bonded Fiber Composites*. Editors H. S. Junior, J. Fiorelli, and S. F. dos Santos, 313–341. doi:10.1016/b978-0-08-102001-2.00015-2

Skoda, M., Dudek, I., Jarosz, A., and Szukiewicz, D. (2014). Graphene: One Material, many Possibilities-Application Difficulties in Biological Systems. *J. Nanomater.* 2014, 1–11. doi:10.1155/2014/890246

Smith, A. T., LaChance, A. M., Zeng, S., Liu, B., and Sun, L. (2019). Synthesis, Properties, and Applications of Graphene Oxide/reduced Graphene Oxide and Their Nanocomposites. *Nano Mater. Sci.* 1 (1), 31–47. doi:10.1016/j.nanoms.2019.02.004

Spasenovic, M. (2020). The price of Graphene. Retrieved from: https://www.graphenea.com/pages/graphene-price#.YGZZHrDitki (Accessed November 28, 2020).

Sun, Z., and Vollpracht, A. (2018). Isothermal Calorimetry and *In-Situ* XRD Study of the NaOH Activated Fly Ash, Metakaolin and Slag. *Cem. Concr. Res.* 103, 110–122. doi:10.1016/j.cemconres.2017.10.004

Sun, C., Huang, Y., Shen, Q., Wang, W., Pan, W., Zhong, P., et al. (2020). Embedding Two-Dimensional Graphene Array in Ceramic Matrix. *Sci. Adv.* 6 (39), 1–12. doi:10.1126/sciadv.abb1338

Taylor, G. (2019). *Branching Out: Making Graphene from Gum Trees*. Retrieved from: https://www.rmit.edu.au/news/all-news/2019/jun/graphene-from-gum-trees (Accessed November 28, 2020). doi:10.1007/978-3-030-30988-6

Temuujin, J., van Riessen, A., and Williams, R. (2009). Influence of Calcium Compounds on the Mechanical Properties of Fly Ash Geopolymer Pastes. *J. Hazard. Mater.* 167, 82–88. doi:10.1016/j.jhazmat.2008.12.1212009

Tiwari, S. K., Sahoo, S., Wang, N., and Huczko, A. (2020). Graphene Research and Their Outputs: Status and prospect. *J. Sci. Adv. Mater. Devices* 5 (1), 10–29. doi:10.1016/j.jsamd.2020.01.006

Tulyaganov, D. U., Reddy, A. A., Kharton, V. V., and Ferreira, J. M. F. (2013). Aluminosilicate-based Sealants for SOFCs and Other Electrochemical Applications – A Brief Review. *J. Power Sourc.* 242, 486–502. doi:10.1016/j.jpowsour.2013.05.099

Van Jaarsveld, J. G. S., van Deventer, J. S. J., and Lukey, G. C. (2002). The Effect of Composition and Temperature on the Properties of Fly Ash- and Kaolinite-Based Geopolymers. *Chem. Eng. J.* 89 (1-3), 63–73. doi:10.1016/s1385-8947(02)00025-6

Vogt, O., Ukrainczyk, N., Ballschmiede, C., and Koenders, E. (2019). Reactivity and Microstructure of Metakaolin Based Geopolymers: Effect of Fly Ash and Liquid/solid Contents. *Materials* 12 (3485), 1–21. doi:10.3390/ma12213485

Wan, Q., Rao, F., Song, S., García, R. E., Estrella, R. M., Patiño, C. L., et al. (2017). Geopolymerization Reaction, Microstructure and Simulation of Metakaolin-Based Geopolymers at Extended Si/Al Ratios. *Cem. Concr. Compos.* 79, 45–52. doi:10.1016/j.cemconcomp.2017.01.014

Wang, B., Jiang, R., and Wu, Z. (2016). Investigation of the Mechanical Properties and Microstructure of Graphene Nanoplatelet-Cement Composite. *Nanomaterials* 6 (11), 200. doi:10.3390/nano6110200

Xie, K., Liu, Y., Tian, Y., Wu, X., Wu, L., Mo, Y., et al. (2021). Improving the Flexibility of Graphene Nanosheets Films by Using Aramid Nanofiber Framework. *Compos. A: Appl. Sci. Manuf.* 142, 1–10. doi:10.1016/j.compositesa.2020.106265

Xu, G., Zhong, J., and Shi, X. (2018). Influence of Graphene Oxide in a Chemically Activated Fly Ash. *Fuel* 226, 644–657. doi:10.1016/j.fuel.2018.04.033

Yaghoubi, M., Arulrajah, A., Miri Disfani, M., Horpibulsuk, S., and Leong, M. (2020). Compressibility and Strength Development of Geopolymer Stabilized Columns Cured under Stress. *Soils Found.* 60 (5), 1241–1250. doi:10.1016/j.sandf.2020.07.005

Yan, S., He, P., Jia, D., Yang, Z., Duan, X., Wang, S., et al. (2015). *In Situ* fabrication and Characterization of Graphene/geopolymer Composites. *Ceram. Int.* 41 (9), 11242–11250. doi:10.1016/j.ceramint.2015.05.075

Yan, S., He, P., Jia, D., Duan, X., Yang, Z., Wang, S., et al. (2016a). *In Situ* Processing of Graphene/Leucite Nanocomposite Through Graphene Oxide/Geopolymer. *J. Am. Ceram. Soc.* 99 (4), 1164–1173. doi:10.1111/jace.14089

Yan, S., He, P., Jia, D., Yang, Z., Duan, X., Wang, S., et al. (2016b). Effect of Reduced Graphene Oxide Content on the Microstructure and Mechanical Properties of Graphene-Geopolymer Nanocomposites. *Ceram. Int.* 42 (1), 752–758. doi:10.1016/j.ceramint.2015.08.176

Yan, S., He, P., Jia, D., Duan, X., Yang, Z., Wang, S., et al. (2017). Effects of Graphene Oxide on the Geopolymerization Mechanism Determined by Quenching the Reaction at Intermediate States. *RSC Adv.* 7, 13498–13508. doi:10.1039/c6ra26340b

Yao, J., Qiu, H., He, H., Chen, X., and Hao, G. (2019). "Experimental Research and Application of Geopolymer in Soft Soil Foundation Treatment," in *Innovative Infrastructure Solutions Using Geosynthetics* (New York, NY: Springer), 82–94. doi:10.1007/978-3-030-34242-5_8

Yavari, F., Rafiee, M. A., Rafiee, J., Yu, Z.-Z., and Koratkar, N. (2010). Dramatic Increase in Fatigue Life in Hierarchical Graphene Composites. *ACS Appl. Mater. Inter.* 2 (10), 2738–2743. doi:10.1021/am100728r

Yeddula, B. S. R., and Karthiyaini, S. (2020). Experimental Investigations and Prediction of Thermal Behaviour of Ferrosialate-Based Geopolymer Mortars. *Arab J. Sci. Eng.* 45, 3937–3958. doi:10.1007/s13369-019-04314-7

Yeswanth sai, T., and Durga Prasad, P. N. V. (2020). Comparative Study on Flyash GGBS Based Geopolymer concrete Using Graphene. *J. Emerging Tech. Innovative Res.* 7 (4), 2094–2099.

Yuan, F.-Y., Zhang, H.-B., Li, X., Ma, H.-L., Li, X.-Z., and Yu, Z.-Z. (2014). *In Situ* chemical Reduction and Functionalization of Graphene Oxide for Electrically Conductive Phenol Formaldehyde Composites. *Carbon* 68, 653–661. doi:10.1016/j.carbon.2013.11.046

Zhang, B., and Chen, T. (2019). Study of Ultrasonic Dispersion of Graphene Nanoplatelets. *Materials* 12 (11), 1–20. doi:10.3390/ma12111757

Zhang, G., and Lu, J. (2018). Experimental Research on the Mechanical Properties of Graphene Geopolymer. *AIP Adv.* 8 (6), 1–10. doi:10.1063/1.5020547

Zhang, L. W., Kai, M. F., and Chen, X. H. (2020). Si-doped Graphene in Geopolymer: Its Interfacial Chemical Bonding, Structure Evolution and Ultrastrong Reinforcing Ability. *Cem. Concr. Compos.* 109, 1–12. doi:10.1016/j.cemconcomp.2020.103522

Zhang, Q., Gao, Y., Xu, Z., Wang, S., Kobayashi, H., and Wang, J. (2020). The Effects of Oxygen Functional Groups on Graphene Oxide on the Efficient Adsorption of Radioactive Iodine. *JMaterials* 13, 1–13. doi:10.3390/ma13245770

Zhong, J., Zhou, G.-X., He, P.-G., Yang, Z.-H., and Jia, D.-C. (2017). 3D Printing strong and Conductive Geo-Polymer Nanocomposite Structures Modified by Graphene Oxide. *Carbon* 117, 421–426. doi:10.1016/j.carbon.2017.02.102

Zhu, C-Q., Wang, X-Z., Wang, R., Chen, H-Y., and Meng, Q.-S. (2013). Experimental Microscopic Study of Inner Pores of Calcareous Sand. *J. Mater. Res. Innov.* 18 (2), 207–214. doi:10.1179/1432891714Z.000000000408

Zohhadi, N. (2014). *Functionalized Graphitic Nanoreinforcement for Cement Composites*. Columbia: University of South Carolina. PhD Thesis.

Zuhua, Z., Xiao, Y., Huajun, Z., and Yue, C. (2009). Role of Water in the Synthesis of Calcined Kaolin-Based Geopolymer. *Appl. Clay Sci.* 43 (2), 218–223. doi:10.1016/j.clay.2008.09.003

Conflict of Interest: The authors declare that the research was conducted in the absence of any commercial or financial relationships that could be construed as a potential conflict of interest.

frontiers in Materials

ORIGINAL RESEARCH
published: 29 July 2021
doi: 10.3389/fmats.2021.719716

A Nonlinear Macro-Model for the Analysis of Monotonic and Cyclic Behaviour of Exterior RC Beam-Column Joints

Ernesto Grande[1], *Maura Imbimbo*[2], *Annalisa Napoli*[3]*, *Riccardo Nitiffi*[2] and *Roberto Realfonzo*[3]

[1]Department of Engineering Sciences, University Guglielmo Marconi, Roma, Italy, [2]Department of Civil and Mechanical Engineering, University of Cassino and Southern Lazio, Cassino (FR), Italy, [3]Department of Civil Engineering, University of Salerno, Fisciano (SA), Italy

The study presents a numerical investigation on exterior reinforced concrete (RC) beam-column joints under seismic actions based on a macro-modelling approach proposed by the authors in a recent paper. The followed approach makes use of the well-known "scissors model" where two nonlinear rotational springs arranged in series were introduced to schematize the shear behavior of the joint panel and, moreover, the possible occurrence of the debonding of longitudinal steel rebars at the beam-joint interface. In this paper, the scissor model is employed in the context of a novel predictive approach with the twofold objective to: 1) develop a new model for the estimate of the maximum shear strength of RC joints by performing a multivariate linear regression analysis on a set of experimental tests and, 2) define a new multilinear backbone joint shear stress-strain law to be assigned to one of the mentioned springs. In particular, the identification of the shear strain parameters is obtained by performing a sensitivity analysis in which a number of monotonic load-drift numerical curves are derived by varying the strain values in ranges opportunely a-priori defined and compared with the experimental ones to investigate their accuracy. Finally, cyclic analyses on RC joints collected in the experimental database are carried out by considering the backbone joint shear stress-strain law identified in the calibration process. The analyses are performed by using the nonlinear open-source finite element platform, OpenSees, in which the "*pinching4*" uniaxial material model, available in the software library, is implemented to set the parameters governing the hysteresis rules and pinching effect. To this purpose, five literature proposals suggesting the values to use for such parameters are taken into account and their assessment is presented in the paper. The obtained outcomes have allowed, on the one hand, to identify the proposal providing the best numerical simulations of the experimental results and, on the other end, to draw useful indications on how to further improve the cyclic modelling by opportunely modifying the setting of the *"pinching4"* material model parameters.

Keywords: RC beam-column joints, shear capacity, numerical non-linear analysis, cyclic loading, pinching parameters, OpenSees code, experimental vs numerical comparison

OPEN ACCESS

Edited by:
Libo Yan,
Fraunhofer Institute for Wood Research, Germany

Reviewed by:
Ahmed Deifalla,
Future University in Egypt, Egypt
Gao Ma,
Hunan University, China

***Correspondence:**
Annalisa Napoli
annapoli@unisa.it

Specialty section:
This article was submitted to Structural Materials, a section of the journal Frontiers in Materials

Received: *02 June 2021*
Accepted: *12 July 2021*
Published: *29 July 2021*

Citation:
Grande E, Imbimbo M, Napoli A, Nitiffi R and Realfonzo R (2021) A Nonlinear Macro-Model for the Analysis of Monotonic and Cyclic Behaviour of Exterior RC Beam-Column Joints. Front. Mater. 8:719716. doi: 10.3389/fmats.2021.719716

INTRODUCTION AND RESEARCH BACKGROUND

The latest severe earthquakes occurred not only in Italy but also in many areas around the world have frequently highlighted that failure of beam-column joints represents a very recurring event in reinforced concrete (RC) frame buildings built prior to the introduction of the latest seismic codes. The main deficiencies include their poor structural details, lack of proper transverse reinforcements, inadequate anchorage of longitudinal steel bars crossing the joints as well as the quality of the concrete material employed at the time of manufacturing. In several cases, local failures of "old-type" joints, especially the exterior ones, like corner joints or those belonging to façade frames - being more seismically vulnerable than the internal joints, especially when unreinforced - were responsible for the global building collapse.

In the last 15 years the growing attention towards the assessment of the joint behavior has frequently promoted the cooperative collaboration between the construction industry and scientific community in the common twofold objective of: 1) better investigating the response of existing deficient beam-column joints and, eventually, proposing new solutions for the external retrofitting; 2) define specific and detailed recommendations for their design and analysis. To this purpose, the experimental research studies cited in the references (Bedirhanoglu et al., 2010; Al-Salloum et al., 2011; Akguzel and Pampanin, 2012; Del Vecchio et al., 2014; Realfonzo et al., 2014; De Risi et al., 2016; De Vita et al., 2017) are considered noteworthy, mostly focused on exterior joints. Among them, different strengthening solutions employing composites materials were investigated (Akguzel and Pampanin, 2012), (Shafaei et al., 2014) as also highlighted in the state-of-the-art published in (Bousselham, 2010).

More recent studies (Saleh et al., 2021) focused on the effect of web openings, often required by electromechanical layouts, on the performance of exterior joints under cyclic loading. These authors found that openings in the beams generally lead to a decrease in cracking and ultimate strengths and stiffness, due to opening proximity to support, opening aspect ratio, and opening reinforcements. Therefore, it is recommended to provide additional reinforcements around web openings (Deifalla et al., 2021).

Other relevant contributions found in the literature deal with the numerical modelling of the RC beam-column joints' behavior; in particular, starting from the first rough indications reported in some past technical codes (ASCE/SEI 41/06, 2006; ACI 369 R-11, 2011), more realistic and accurate modeling approaches were developed, i.e,: lumped–plasticity approaches (Alath and Kunnath, 1995), (Liel et al., 2010), multi–spring macro–models (Biddah and Ghobarah, 1999), (Lowes and Altoontash, 2003), nonlinear finite element (FE) modeling (Genesio, 2012).

Among the lumped-plasticity modeling techniques, one of the first proposals was provided by Giberson (1969), who reproduced the flexural behavior of beams and the shear deformation of joints through nonlinear rotational springs at each end of beams and columns, which were modeled through linear elastic elements. A similar model was used by Otani (1974), with the introduction of two parallel elements for beams and columns, representing the linear elastic behavior and the post–elastic behavior, respectively. The bar slippage was also taken into account through rotational springs at beam-joint and column-joint interfaces. The bond stress was assumed to be constant along the anchorage length and only the steel reinforcement under tension was assumed to slip. However, this model does not consider the deformability contribution due to the joint shear; this aspect was considered later by other modeling approaches with the introduction of a zero-length rotational spring inside the joint core (El-Metwally and Chen, 1988).

Alath and Kunnath (1995) modeled the joint shear deformation with a nonlinear rotational spring centered into the joint core. Rigid links with a finite size connect beams and columns, which are capable of independent rotations. This so-called "scissors model" is widely used in literature, due to its ease of implementation in several computer codes.

The multi-spring macro-model approaches are based on the use of more than a single spring to model different mechanisms of the joints. Among these, one of the first methods was proposed by Biddah and Ghobarah (1999), developing a modified version of the "scissors model". The method is based on the use of two different nonlinear rotational springs to simulate the shear behavior and the bond-slip phenomena; in their work the cyclic response of the joint is schematized throughout a tri-linear idealized hysteretic relationship without accounting for the pinching effect.

Youssef and Ghobarah (2001) used diagonal shear springs to link the hinges at the corner of joints; rigid elements connected these hinges to each other, with the addition of three concrete springs and three steel springs at the intersection between the joint and the adjacent elements to represent the bar-slip phenomenon. However, this model requires a large number of springs and a proper constitutive law for each spring and, therefore, it is difficult to implement.

Lowes and Altoontash (Liel et al., 2010) proposed a 4-node 12-degree-of-freedom macro-model element with eight zero-length translational bar slip springs, four interface shear springs, and a panel zone whose shear stress-strain relationship curve is defined through the "modified compression field theory" (MCFT) approach (Vecchio and Collins, 1986).

This model was simplified by Mitra and Lowes (2007), who introduced a model consisting of four zero-length bar-slip springs located at the beam-joint and column-joint interfaces and a zero-length shear spring in the middle of the panel zone.

However, the model may not be suitable to evaluate the hysteretic response of exterior joints without transverse reinforcement, since the experimental data used for the validation included only interior joints with a minimal amount of transverse reinforcement.

Shin and LaFave (2004) implemented two rotational springs in series at the beam–joint interfaces to simulate both the bar slip deformability contribution and the beam plastic rotation contribution. The panel zone was modeled following the

approach by Lowes and Altoontash (Liel et al., 2010). Experimental data were used to calibrate the cyclic behavior.

Another multi-spring approach was proposed by Sharma et al. (2011), who modeled the joint panel through one rotational spring located in the beam region and other two springs in the column portion. Lumped-plasticity elements were used for beams and columns. The backbones of these three springs were proposed for monotonic loading in principal stresses, and anchorage failure in the case of not sufficient beam bars anchorage length was also considered by reducing the critical principal stress.

Within this context, a wide overview of the mentioned existing joint modeling techniques was recently published by the authors in Grande et al. (2021) where a new macro-modelling approach was presented and implemented in the nonlinear open-source finite element platform, OpenSees (McKenna et al., 2010), with the aim to simulate the seismic performance of beam – column joints belonging to existing RC structures built according to past codes and guidelines.

By following the numerical study presented in Grande et al. (2021) - briefly summarized in *Numerical Analyses: Outcomes of the Previous Research and Insights* – a new formula for the estimate of the shear strength of exterior RC joints is, firstly, proposed by authors in the present paper. The analytical proposal was calibrated on experimental basis through a multivariate linear regression analysis; it is characterized by the same key parameters and structure of the strength models proposed by Kim and LaFave (2009), Kim and LaFave (2012) and Jeon (2013), Jeon et al. (2015) providing the most accurate predictions among all the accounted literature proposals.

Then, a new multilinear backbone joint shear stress-strain law is presented, which was identified after a proper definition of its characterizing parameters. In particular, for the strain parameters, a sensitivity analysis was carried out by considering the experimental database, from which a number of monotonic load-drift numerical curves were derived and compared with the experimental ones by varying the shear strain values in ranges opportunely a-priori defined. It is highlighted that the approach followed here is novel with respect to similar studies found in the literature (De Risi et al., 2016), (Shin and LaFave, 2004), (Sharma et al., 2011) in which the strain parameters were set to specific values just because they fitted well the (few) available experimental data.

Finally, cyclic analyses were performed on RC joints collected in the database, by accurately reproducing the test procedures adopted for each specimen. To this purpose, the "*pinching4*" uniaxial material model, available in the Opensees library (McKenna et al., 2010) and developed by Lowes et al. (2003), was used to set the parameters governing the hysteresis rule and pinching effect.

The found outcomes have allowed, on the one hand, to identify the best literature proposal and, on the other end, to draw useful indications on how to opportunely modify the values of the *"pinching4"* material model parameters with the purpose to further improve the simulation of the cyclic response of RC beam-column joints. Such aspect will be addressed in a future study under preparation.

KEY FEATURES OF THE PROPOSED MODEL FOR EXTERIOR "2D" JOINTS

A macro-model for numerically simulating the seismic behavior of exterior RC beam-column joints was recently developed and published by the authors in Grande et al. (2021). The model, of which only the main details are summarized herein, is suitable for the typically named "2D joints", i.e., unconfined joints made of just one transverse beam (see **Figure 1A**) which represent the typology most commonly investigated in the experimental studies published in the literature.

In the macro-modelling approach, frame elements and fiber discretization of the cross section were used for beams and columns, and the "*scissors model*" (Alath and Kunnath, 1995) was adopted for the joint element, which is generally preferred to other models due to its ease of implementation in several computer codes.

Figure 1B shows a scheme of the "*scissors model*", in which the two main mechanisms governing the overall behavior of the RC joints are considered by means of two nonlinear rotational springs in series; in particular, *spring 1* accounts for the shear deformation of the panel, while *spring 2* represents the "fixed-end-rotation" of the beam due to the debonding of the longitudinal steel rebars at the beam-joint interface. *Spring 1* connects a master node and a duplicated slave node located at the same position in the middle of the panel zone; these nodes are connected to the beam and the column members through rigid links.

The numerical analyses presented in Grande et al. (2021) as well as those described in this paper were carried out by using the open-source finite element platform "OpenSees" (McKenna et al., 2010).

The two rotational springs introduced to simulate the behavior of the joint panel were modelled through the "*Pinching4 Uniaxial Material*", which is based on a multilinear moment-rotation (M-θ) backbone law. The M-θ laws introduced for the two rotational springs are directly derived from multilinear shear stress-strain ($\tau - \gamma$) laws, in the case of the *spring 1,* and from bond-slip (τ-s) constitutive laws, in the case of the *spring 2*. The two relationships are qualitatively shown in **Figures 1C,D** respectively.

It is worth highlighting that, in the present study, the authors focus on the proper identification of the parameters characterizing the multilinear τ-γ constitutive law assigned to the joint shear rotational *spring 1* (to be converted into an M-θ relationship). Indeed, the experimental tests considered in the analyses discussed in the following sections are mostly related to beam-column assemblages experiencing the joint shear failure and, hence, their numerical modelling is generally affected by the activation of the *spring 1*. However, more details about the modelling of the rotational *spring 2,* omitted herein for the sake of brevity, can be found in Grande et al. (2021).

As shown in **Figure 1C**, the multilinear law is completely defined by four points identifying the main phases of the joint shear behavior, i.e.: the cracking of the joint attained at the shear stress τ_1, the pre-peak phase (acting until the pre-peak stress τ_2), the attainment of the peak strength τ_3, the softening branch with

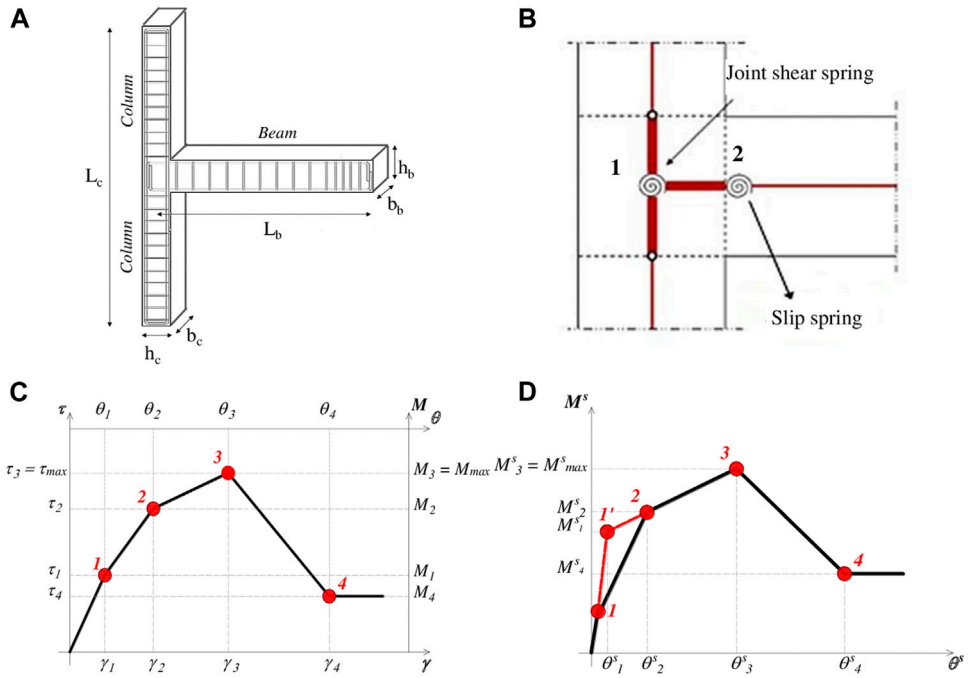

FIGURE 1 | Scheme of the 2D joint under consideration **(A)**; sketch of the used "scissors model" **(B)**; multilinear shear stress-strain (or moment-rotation) law assigned to *spring 1* **(C)**; multilinear moment-rotation law assigned to *spring 2* **(D)**.

TABLE 1 | Selected literature models for the estimate of peak shear stress $\tau 3 = \tau_{max}$.

Model ID	Authors	Describing equation[a]
1	Kim and LaFave (2009)	$\tau_{max} = 0.483\ (BI)^{0.3}\ (f_c)^{0.75}$ (MPa)
2	Vollum and Newman (1999)	$\tau_{max} = 0.642\,\lambda\left[1 + 0.555\left(2 - \frac{h_b}{h_c}\right)\right]\sqrt{fc}$ (MPa)
3	Reyes de Ortiz (1993)	$\tau_{max} = \frac{0.6 f_c\left(1 - \frac{f_c}{250}\right) b_c\, 0.45\,(h_c \sin\varphi + a_b \cos\varphi)\cos\varphi}{h_c b_b}$ (MPa)
4	Hwang and Lee (1999)	$\tau_{max} = \frac{\sqrt{fc}\left\{1 - \left[\frac{0.13(\sin\varphi - \cos\varphi)}{\sqrt{fc}\,(0.84\, h_c\, b_j + 2.85\frac{N}{f_c})}\right]\frac{A_{s,c} f_{yc}}{\sin^2\varphi}\right\}(0.84\, h_c\, b_j + 2.85\frac{N}{f_c})\cos\varphi}{h_c b_b}$ (MPa)
5	Jeon (2013)	$\tau_{max} = 0.409\ (BI)^{0.495}\ (f_c)^{0.941}$ (MPa)

[a]*For the meaning of all the symbols see the section "Glossary"*

the residual strength value, τ_4, and a final constant trend. In literature, this relationship has been repeatedly adopted in several studies (De Risi et al., 2016), (Jeon et al., 2015), (Celik and Ellingwood, 2008), but different choices were made in the estimate of the key $\tau - \gamma$ parameters.

In Shin and LaFave (2004), the proposal by Uzumeri (1977) was selected to estimate the shear stress value τ_1, which is expressed by:

$$\tau_1 = 0.29\sqrt{f_c}\sqrt{1 + 0.29\sigma_j}\ \text{(MPa)} \quad (1)$$

Where:

- f_c (MPa) is the cylinder compressive strength of concrete;
- σ_j (MPa) is the ratio between the column axial load (N) and the corresponding cross-section area (b_c h_c) of the column (**Figure 1A**).

Table 1 provides the equations describing the five models taken into account to estimate the maximum shear stress ($\tau_3 = \tau_{max}$), directly written for the investigated 2D joints without transverse steel reinforcement. Among them, *models 2* to *4* were developed by using a mechanical approach based on a strut-and-tie mechanism, whereas *model 1* and *model 5*, very similar to each other, were empirically derived. More details, omitted here for the sake of brevity, can be found in Grande et al. (2021).

For what concerns the remaining shear stresses τ_2 and τ_4, and the four shear strains (γ_1, γ_2, γ_3, γ_4), **Table 2** lists the models selected from the literature which provided specific indications.

As observed, the values of τ_2 and τ_4 are given as a percentage of the maximum shear strength τ_3, while the suggested values for the shear strains γ_1, γ_2, γ_3, γ_4, were calibrated on experimental basis.

TABLE 2 | Selected literature models providing values of τ_2, τ_4, γ_1, γ_2, γ_3, γ_4.

Model ID	Authors	τ_2	τ_4	γ_1	γ_2	γ_3	γ_4
A	De Risi et al. (2016)	0.85 τ_{max}	0.43 τ_{max}	0.0004	0.0017	0.0049	0.0441
B1	Celik and Ellingwood (2008)	0.75 τ_{max}	0.30 τ_{max}	0.0001	0.002	0.01	0.03
B2		0.75 τ_{max}	0.16 τ_{max}	0.0013	0.01	0.03	0.1
C1	Shin and LaFave (2004)	0.90 τ_{max}	0.30 τ_{max}	0.0005	0.002	0.01	0.03
C2		0.90 τ_{max}	0.30 τ_{max}	0.0005	0.01	0.03	0.05
D	Sharma et al. (2011)	0.90 τ_{max}	0.24 τ_{max}	0.0006	0.002	0.005	0.025

Unlike *model A* and *model D*, Celik and Ellingwood (2008) and Shin and LaFave (2004) provided a range of values for the shear strains γ_i. Therefore, the minimum (*models B1* and *C1*) and the maximum (*models B2* and *C2)* values of the range were reported in **Table 2**.

As mentioned earlier, the implementation of the τ-γ constitutive laws into the OpenSees numerical framework requires the conversion of the shear stresses into the moments M_j and the shear strains into the rotations θ_j of the joint shear spring. The rotation of the spring θ_j can be assumed equal to the joint panel strain γ_j, whereas the bending moment M_j is obtained from the joint shear stress τ_j according to **Eq. 2**:

$$M_j = \tau_j A \frac{1}{\frac{1-h_c/2L_b}{jd_b} - \frac{1}{L_c}} \quad (2)$$

which is obtained by using a simple equilibrium equation of the forces acting on the joint panel (Grande et al., 2021).

In **Eq. 2**, τ_j (MPa) is the shear stress of the multilinear law; A (mm^2) is the joint cross-section area; jd_b (mm) is the beam internal lever arm; h_c (mm) is the height column cross-section: L_b (mm) is the beam length; L_c (mm) is the column length.

NUMERICAL ANALYSES: OUTCOMES OF THE PREVIOUS RESEARCH AND INSIGHTS

In Grande et al. (2021) preliminary numerical analyses were performed by considering an experimental database assembled from the literature, including a set of fifteen cyclic tests performed on specimens representative of typical exterior beam – column joints. In order to avoid eventual uncertainties and heterogeneity related to the simulated tests, the collected specimens were rather similar in terms of geometric configurations, test set-ups, load conditions, loading procedures and observed failure modes. This is the case of: 1) joints J01 and J05 tested by Realfonzo et al. (2014); 2) joints TU3 and TU1 by Pantelides et al. (2002); 3) joints #4, T#1, TC3, T01, T0, BS-L tested, respectively, by Clyde et al. (2000), De Risi et al. (2016), Del Vecchio et al. (2014), Hadi and Tran (2016), El-Amoury and Ghobarah (2002), Wong (2005) and Hassan et al. (2018); 4) joints C1 and C2 tested by Antonopoulos and Triantafillou (2003); e) joints J2 and O1 tested, respectively, by Shafaei et al. (2014) and Tsonos (2002).

All the analyzed joints presented a 2D-configuration, i.e., they were not provided with orthogonal beams (**Figure 1A**). Beams and columns were reinforced with ribbed steel bars, which were symmetrical arranged, except for the case of the specimens T_C3 (Del Vecchio et al., 2014) and J2 (Shafaei et al., 2014). No transverse reinforcement was located in the joint panel zone, in accordance with past code prescriptions. All the specimens failed by joint shear failure except for the joints TU1 (Pantelides et al., 2002) and T0 (El-Amoury and Ghobarah, 2002) experiencing in the pull (negative) loading direction the bond failure due to the slippage of the longitudinal reinforcements in the beam. More details about the assembled experimental database are reported in Grande et al. (2021).

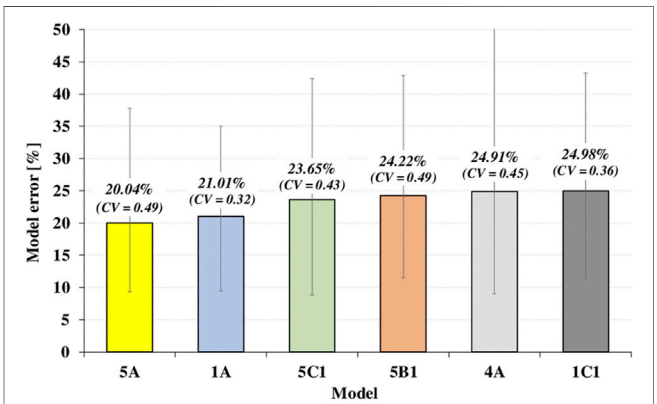

FIGURE 2 | Ranking of the best models yielding a mean absolute percentage error (MAPE) calculated on all the monotonic envelopes lower than 25%.

The numerical analyses were performed by employing the multilinear law in **Figure 1C** for the shear behavior and that in **Figure 1D** for the bond-slip behavior. For the *spring 1*, different values of τ and γ were selected by opportunely combining each model providing the estimate of the shear strength τ_{max} (*models 1, 2, 3, 4, 5*) with each model providing the other values of shear stress and strains (*models A, B1, B2, C1, C2, D*). Thus, the resulting 30 obtained τ-γ laws were implemented one at a time to carry out nonlinear static analyses by monotonically applying either downwards (positive direction) or upwards (negative direction) displacements at the end of the beam. The obtained results, expressed in terms of applied force vs. drift (the latter corresponding to the ratio between the displacement at the end of the beam and the beam length) were compared with the corresponding curves obtained from the envelope of the experimental hysteretic cycles up to 75% of the peak experimental force in the post-peak phase both in the positive

and negative direction; this assumption was made to represent the same conventional failure for all the considered specimens.

Then, in order to estimate the scatter between the numerical and the experimental curves, the mean absolute percentage error (MAPE) between the experimental and the numerical force for each specimen was calculated by means of the following formula:

$$E_{rr,F} = \frac{\sum_{i=1}^{n} \frac{|F_{exp,i} - F_{num,i}|}{F_{exp,i}} \cdot 100}{n} \quad (3)$$

where: $F_{exp,i}$ and $F_{num,i}$ are, respectively, the *i*th experimental force and the corresponding numerical one; n is the total number of measures considered in the analysis performed on each test specimen.

The bar chart in **Figure 2** shows the six model combinations between the analytical proposals providing the shear strength τ_{max} (*models 1, 2, 3, 4, 5*) and those suggesting the other values of shear stress and the strains (*models A, B1, B2, C1, C2, D*) for which the calculated errors on the whole monotonic curve for all the fifteen experimental joints were below the 25% threshold. The errors bars show the positive and negative deviation of the errors from the mean value computed for each model, while the corresponding coefficients of variation (CV) are reported in round brackets.

In particular, the plot shows that three over the best six combinations include *model 5* (i.e. the model by Jeon (2013) for evaluating the shear strength); similarly, two combinations entail *model 1* (i.e., that proposed by Kim and LaFave (2009)) which also yields the lowest coefficients of variation. As mentioned earlier, these two models were developed by considering the same parameters (i.e., BI and f_c) and the same formula at the basis of the calibration procedure (see **Table 1**).

At the same way, *model A* and *model C1*, respectively proposed by De Risi et al. (2016) and Shin and LaFave (2004), appear in five of the six best combinations.

Some Considerations on the Joint Shear Strength

The monotonic simulations in Grande et al. (2021) highlighted the strong correlation between the numerical evaluation of the global shear strength of joints and the correct estimate of the shear stress τ_{max} Therefore, some considerations were performed by comparing the values of τ_{max}^{th} estimated from the analyzed *models 1* to *5* with the experimental values of shear strength (τ_{max}^{exp}) obtained from the equilibrium of the forces acting on the joint panel as follows:

$$\tau_{max}^{exp} = \frac{T_b - V_{col}}{A} \text{ (MPa)} \quad (4)$$

where T_b is the tensile force acting in the longitudinal bars of the beam, V_{col} is the column shear force, A is the cross-section area of the joint.

The scatter between the numerical and the experimental strength was calculated through the mean absolute percentage error (MAPE) as follows:

$$E_{rr,\tau} = \frac{\sum_{i=1}^{n} \frac{\left|\tau_{max,i}^{exp} - \tau_{max,i}^{th}\right|}{\tau_{max,i}^{exp}} \cdot 100}{m} \quad (5)$$

where $\tau_{max,i}^{exp}$ and $\tau_{max,i}^{th}$ are the *i*th experimental and the *i*th numerical shear strength, respectively, while m is the number of available measures.

The bar charts in **Figures 3A,B** depict the errors for both the positive ("+") and negative ("−") direction of loading in terms of τ_{max} estimated for all the collected specimens according to the considered five models. An exception is represented by the specimen TU1 (Pantelides et al., 2002) and T0 (El-Amoury and Ghobarah, 2002) for which only the errors in the push (positive) direction were calculated since, as mentioned before, an anchorage failure due to loss of bond was experienced in the pull direction.

The bar chart in **Figure 4**, instead, shows the model errors in the estimate of τ_{max} computed all the considered tests and considering both the positive and negative directions together; the errors bars show the positive and negative deviation of the error from the mean value computed for each model.

From these graphs it can be noted that the accuracy of the all models is rather variable with the considered test. Overall, *model 1* (Kim and LaFave, 2009) and *model 5* (Jeon, 2013) seem to provide values of the shear strength closer to the those emerged from experimental tests, since the mean errors amount to 13.11 and 14.39%, respectively (see **Figure 4**).

It is mentioned that these two empirical models derived from the study on the shear strength performed on a wide experimental database, considering several geometric configurations. On the contrary, the *models 2, 3* and *4* were developed using a mechanical approach based on a strut-and-tie mechanism, but considering only few experimental cases investigated by the authors.

CALIBRATION OF A CONSTITUTIVE MODEL FOR 2D-JOINTS

The numerical study presented in Grande et al. (2021) and briefly summarized in *Numerical Analyses: Outcomes of the Previous Research and Insights* was basically devoted to 1) identify the literature models best estimating the joint shear strength and, 2) find, based on the literature proposals, the multilinear joint shear stress-strain constitutive law that, implemented in the proposed model for 2D-joints, be able to provide the best simulation of then monotonic envelopes of load-displacement experimental curves.

The study presented in this paper, instead, is aimed at deriving a new constitutive model for the analysis of both the monotonic and cyclic behavior of 2D-joints, with the purpose to further improve the simulation of the considered experimental tests. To this end, a calibration procedure is carried out by considering just the mentioned experimental database concerning RC beam-column joints in 2D configuration. In particular, while the first application of the procedure specifically regards the shear strength of the joint, presented in the following, the subsequent applications are devoted to derive: 1) a multi-linear shear stress-slip law for the monotonic response, described in *The Proposed*

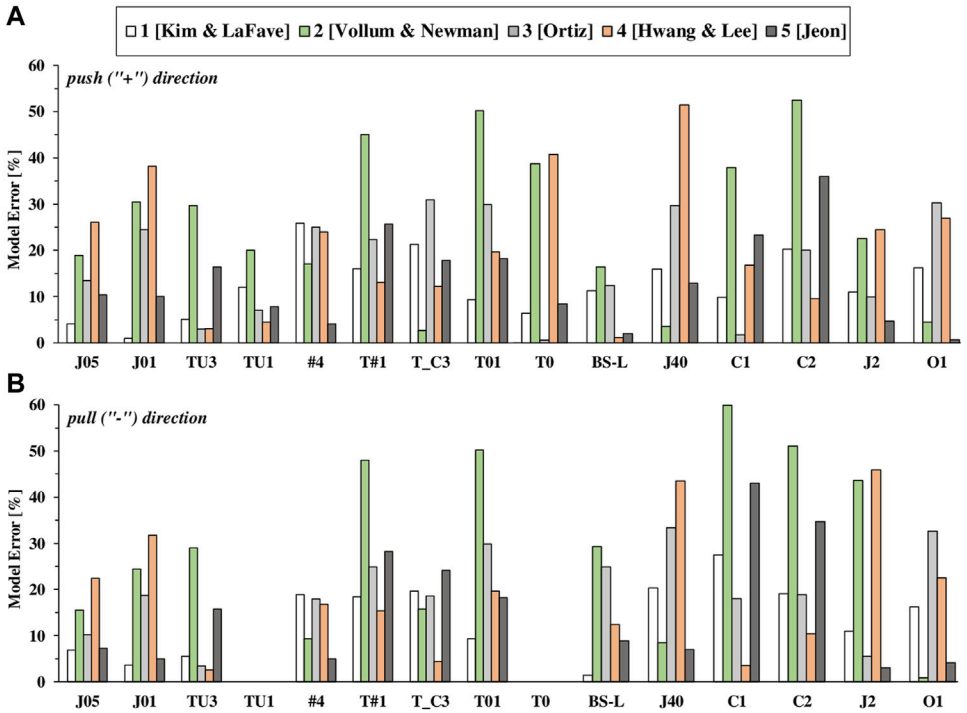

FIGURE 3 | Model errors in terms of τ_{max} for each considered experimental test: push direction **(A)**; pull direction **(B)**.

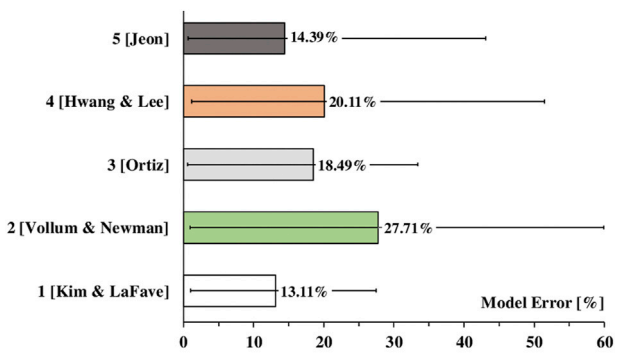

FIGURE 4 | Model errors in terms of τ_{max} calculated per each considered literature model by considering all experimental tests.

Backbone Joint Shear Stress-strain Law, and 2) a model able to predict the response of 2D joints under cyclic loads, presented in *Modeling of Cyclic Response of Joints – "Pinching4" Model.*

Joint Shear Strength Model Prediction

The assessment of the literature models in predicting the shear strength of the experimental database, presented in the previous section, showed that the models proposed by Kim and LaFave (2009) and by Jeon (2013) provided the lowest values of MAPE (13.11 and 14.39% respectively). As observed from **Table 1**, both models identified the beam reinforcement index, *BI*, and the concrete compressive strength, f_c, as the key parameters affecting the joint shear strength; the only difference between the two equations relies into the numerical coefficients calibrated by the authors based on their own accounted set of experimental cases.

In the present study, considering an experimental database containing 2D-joint configurations only, a multivariate linear regression analysis is performed by taking into account the same predictor variables (*BI* and f_c) and the same structure of the formula used by *model 1* and *model 5* for deriving the shear strength:

$$\tau_{max} = a \cdot (BI)^b \cdot (f_c)^c \tag{6}$$

where *a*, *b* and *c* are the numerical coefficients to be opportunely calibrated.

It is worth highlighting that the use of a multivariate linear regression analysis instead of a simple linear regression method allows to study the relationship between a dependent variable and more than one independent variable.

The general functional equation is expressed by an additive model expressed in a logarithmic scale as follows:

$$\ln(Y) = \beta_0 + \beta_1 \ln(X_1) + \beta_2 \ln(X_2) + \cdots + \beta_n \ln(X_n) \tag{7}$$

where:

- Y is the response (dependent) variable;
- X_j ($j = 1,2...n$) are the predictor (independent) variables;
- β_j ($j = 1,2...n$) are the coefficients of the regression analysis.

In the literature, this functional form was employed in several empirical models for estimating the main variables affecting the

TABLE 3 | Regression results for the proposed empirical model.

F test	*RMSE*	R^2	*p-value*
31.61	0.153	0.716	1.43e-7

shear strength of beam and column elements in RC framed structures (Jeon, 2013), (Haselton et al., 2016).

Once the numerical coefficients of the relationship are evaluated, **Eq. 10** can be equivalently rewritten in the original multiplicative form:

$$Y = e^{\beta 0}(X1)^{\beta 1}(X2)^{\beta 2}\cdots(Xn)^{\beta n} \tag{8}$$

The coefficient of determination R^2 and the residual standard error σ quantify the effectiveness of the predictive model and are evaluated based on the regression analysis carried out using the form in **Eq. 7**.

By focusing on the prediction of the shear strength of exterior joints, the dependent variable is, of course, represented by the shear strength τ_{max}, while the considered independent variables are BI and f_c. Therefore, **Eq. 7** can be converted into:

$$\ln(\tau_{max}) = \ln(a) + \ln(BI)^b + \ln(f_c)^c \tag{9}$$

whereas **Eq. 8** can be converted into an expression coinciding with **Eq. 6**.

In order to examine the accuracy of the two predictor variables BI and f_c on the response variable τ_{max}, an analysis of variance (ANOVA) was performed in a log-transformed space. In the ANOVA analysis, the following two different statistic tests proved the accuracy of the regression method adopted: the "*F test*" and "*t test*". In particular, the "*F test*" checks the hypothesis of no significant relationship between the predictive independent variables (in this case, BI and f_c) and the single dependent variable τ_{max} (null hypothesis). On the other hand, the "*t test*" is used to check the hypothesis of no significant relationship between a single independent variable and the dependent variable (null hypothesis). Both tests must meet the condition of significance at the 95% level, or equivalently, a *p-value* less than the 5%, so that the null hypothesis can be rejected. In the "*F test*", this condition ensures that at least one of the coefficients β_j in **Eq. 7** is statistically significant; on the other hand, in the "t test", a *p-value* less than the significant level implies that the single predictor variable is significant.

Usually, a stepwise elimination process is performed until all the remaining variables are all significant at the 95% level based on the "*F test*".

The regression analysis, in conjunction with the ANOVA test, was performed by considering both the positive and the negative values of the shear strength τ_{max} available for each experimental test collected in the database; an exception is represented by the tests TU1 (Pantelides et al., 2002) and T0 (El-Amoury and Ghobarah, 2002) for which the two negative values of τ_{max} were excluded from the analysis since they are associated to the occurrence of bond failure in place of the joint shear one.

Table 3summarizes the results obtained from the regression analysis in terms of "*F test*" value, root mean square error (RMSE), correlation of determination (R^2) and *p-value*, while **Table 4** shows the results of each predictor variable in terms of numerical coefficients, "*t test*" value and *p-value*.

As observed, both the variables *BI* and f_c are significant at the 95% level based on the "*F test*" and each of them, including the intercept (ln(a) in **Eq. 9**), are significant at the 95% based on the individual "*t test*". Thus, the null hypothesis can be rejected for both the statistic tests; moreover, the coefficients resulting from the multiple linear regression can be deemed relevant for the purposes of the predictive capacity model.

Before definitively accepting the results derived from the multiple regression analysis, it is necessary to perform an outlier detection plan in order to identify whether the obtained model is appropriate. To this aim, the residuals are plotted against the predicted values and against the predictor variables to determine whether some data points must be eliminated to get a final model. If the residuals are distributed within a horizontal band centred around the zero, the model can be deemed accurate and it does not show any trend in overestimating or underestimating the output of the independent variable. Furthermore, the normal probability plot must be displayed to assess the normality of the distribution of the residuals. This condition is achieved if the points in the plot lie approximately on a straight line.

Figure 5A shows the residual plot against both the fitted values $\ln(\tau_{max})$ and the two significant predictor variables: ln(BI) and $\ln(f_c)$. From this plot, it is observed that the residuals are evenly scattered and no curve trend is observed, indicating a reasonable accuracy of the predictive model. Moreover, the normal probability plot in **Figure 5B** shows an approximately linear trend. These outcomes prove the effectiveness of the predictive shear strength model for exterior joints described in **Eq. 9**.

Therefore, the functional form of the predictive model can be expressed by **Eq. 10**, with the numerical coefficients derived from the ANOVA test:

$$\ln(\tau_{max}) = -0.5634 + \ln(BI)^{0.4448} + \ln(f_c)^{0.783} \tag{10}$$

that, converted into the original multiplicative form expressed by **Eq. 6**, provides the following predictive model for the joint shear strength:

$$\tau_{max} = 0.569 \cdot (BI)^{0.445} \cdot (f_c)^{0.783} \tag{11}$$

Comparison Between the New Proposal and the Literature *Models 1 and 5*

By comparing the new proposal with the counterpart models by Kim and LaFave (2009) *(model 1)* and by Jeon (2013) (*model 5*), it

TABLE 4 | Regression results for each predictor variable.

Predictor variables	*Coefficient*	*t test*	*p-value*
ln(BI)	0.4448	5.77	5.12e-6
ln(fc)	0.783	7.81	3.64e-8
ln(a) *(intercept)*	−0.5634	-2.1	0.04

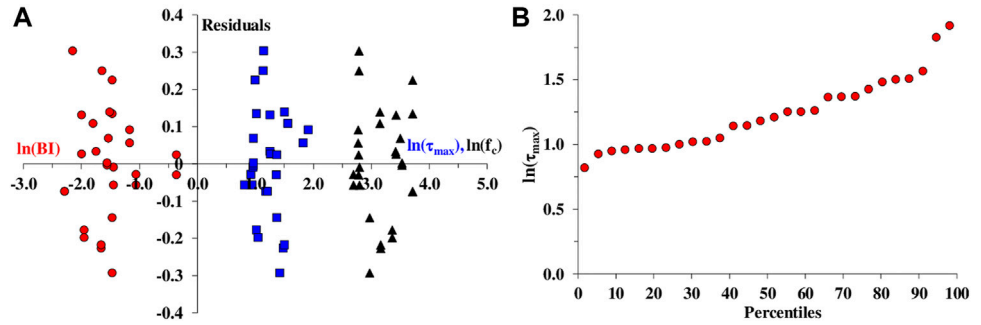

FIGURE 5 | Residual plots for $\ln(\tau_{max})$ *(blue points)*, $\ln(f_c)$ *(black points)* and ln(BI) *(red points)* **(A)**; normal probability plot of the predicted values **(B)**.

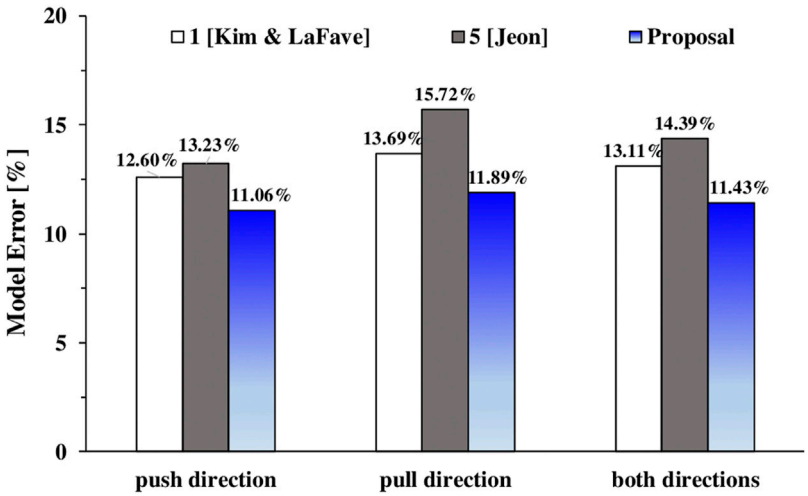

FIGURE 6 | Comparisons between the new proposal and Models 1 & 5 in terms of mean errors calculated according to MAPE on all the considered experimental tests.

is noted that the main difference lies in the coefficient multiplying the parameter BI and f_c (= 0.569), which is higher than those of the two literature models (0.483 and 0.409, respectively); the coefficient term (0.445), representing the power of BI, is higher than that provided by Kim and LaFave (0.3), but lower than that provided by Jeon (0.495); the coefficient representing the power of f_c (0.783), instead, is slightly higher than that found by Kim and LaFave (0.75), but lower than that proposed by Jeon (0.941). Of course, differences in the found numerical coefficients are strictly related to the experimental database used for the calibration procedure; to this purpose, as already mentioned, the new proposal was specifically found by considering an experimental database including a homogeneous set of RC exterior joints.

In order to compare the accuracy of the proposed strength model with that of the counterpart formula, the bar chart in **Figure 6** shows the mean errors in terms of τ_{max} calculated according to MAPE (see **Eq. 5**) for all the experimental tests by considering the following three case: *a)* τ_{max} in the push ("+") loading direction only; *b)* τ_{max} in the pull ("−") loading direction only, and *c)* τ_{max} in both loading directions.

As observed, all the three models always provide the highest errors in the pull loading direction; however, the application of proposed model yields an overall error reduction of about 13–15% and 20–30% with respect to *model 1* (Kim and LaFave, 2009) and *model 5* (Jeon, 2013), respectively.

Finally, in **Figure 7** the theoretical values τ_{max}^{th}, estimated for all the tests by applying the three considered models, were compared with the experimental ones τ_{max}^{exp}, relatively to the push (**Figure 7A**) and pull direction (**Figure 7B**). The bisector corresponds to perfect agreement between prediction and tests; therefore, points falling in the lower part of the graph indicate conservative predictions whereas points falling over the line represent non-conservative situations.

As shown, the application of the new strength model leads, except for a few cases, to the best agreement between prediction and tests, with points (blue circles) mostly distributing about the bisector line. Conversely, points related to the application of the model by Kim and LaFave (2009) (white squares) are mostly distributed below the bisector line, thus indicating conservative predictions; an opposite trend, instead, is observed for points

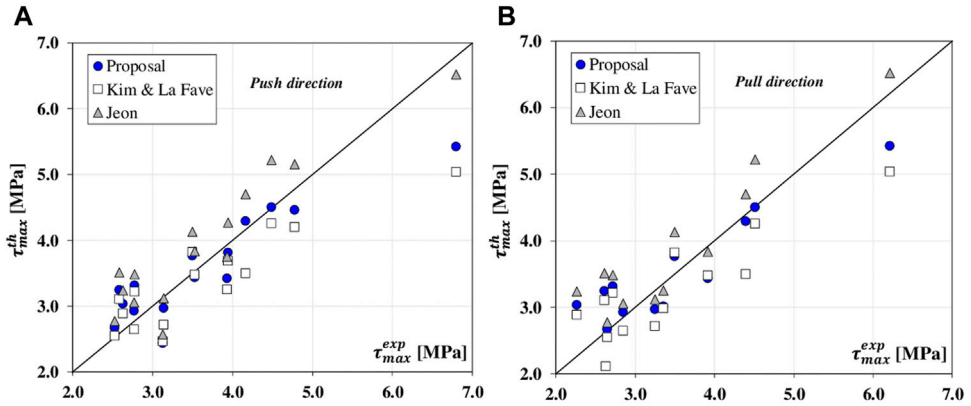

FIGURE 7 | Numerical vs experimental τmax values: comparisons between the new proposal and Models 1 & 5: push loading direction **(A)**; pull loading direction **(B)**.

referred to the use of the formulation by Jeon (2013), generally providing non-conservative predictions.

THE PROPOSED BACKBONE JOINT SHEAR STRESS-STRAIN LAW

By following the development of a sound analytical model for the estimate of the maximum shear stress ($\tau_{max} = \tau_3$), a new backbone $\tau - \gamma$ law was identified by properly defining the remaining stress and strain parameters of the multilinear relationship assigned to the rotational *spring 1* (**Figure 1C**).

In particular, the stress values (τ_1, τ_2, τ_4) were determined by both following the indications provided from literature studies and accounting for the conclusions drawn from the preliminary numerical analyses published in Grande et al. (2021). The strain parameters (γ_1, γ_2, γ_3, γ_4), instead, were identified by carrying out new monotonic numerical analyses in which their associated values were varied within specific ranges chosen by authors. Then, by computing the errors emerged from the numerical vs experimental comparisons in terms of force – drift monotonic envelopes, the best set of γ_i parameters was identified.

It is worth highlighting that the whole calibration procedure, better detailed in the following sections, consists of, firstly, defining the values of the stress parameters, and, secondly, identifying the best values for the strains γ_i among the investigated ones. Of course, the two steps of the applied procedures are not decoupled, since the percentage errors emerged from the sensitivity analyses are affected on both the stress and strain assessments.

Definition of the Stress Parameters (τ_1, τ_2, τ_4)

Cracking Shear Strength τ_1

Based on the examined literature studies, the cracking shear strength τ_1 can be reasonably estimated through the formula proposed by Uzumeri (1977) (see **Eq. 1**). In particular, the results of the preliminary numerical analyses published in Grande et al. (2021), which were performed by implementing the 30 τ-γ model combinations briefly described in *Numerical Analyses: Outcomes of the Previous Research and Insights*, highlighted that this first stress point can be roughly set, on average, to 57% of τ_{max}.

Pre-Peak Strength τ_2

The pre-peak strength τ_2 can be assumed equal to $0.85\tau_{max}$, according to the model proposed by De Risi et al. (2016), which showed the best agreement in predicting the pre-peak branch of the monotonic experimental envelopes (Grande et al., 2021). Moreover, since the minimum pre-peak strength assessed from the literature models is $0.75\tau_{max}$ (as proposed by Celik and Ellingwood (2008)), while the maximum value is $0.9\tau_{max}$ (model by Shin and LaFave (2004) and model by Sharma et al. (2011)), an average value between the two ends of the range (i.e., $\tau_3 = 0.85\tau_{max}$) can reasonably assumed.

Residual Strength τ_4

The residual strength point τ_4 of the backbone law is assumed equal to $0.3\tau_{max}$ which is the value approximately suggested by the most of considered literature models (Shin and LaFave, 2004; Sharma et al., 2011; Celik and Ellingwood, 2008) (see also **Table 2**) and fitting quite well the experimental monotonic curves in the post-peak phase (Grande et al., 2021).

The second column of **Table 5** summarizes the four τ_i stress values identified by authors for the proposed constitutive law.

Definition of the Strain Parameters (γ_1, γ_2, γ_3, γ_4)

A higher uncertainty affects the strain parameters of the $\tau - \gamma$ relationship, since the proposed values from the literature are merely derived from experimental observations on each individual test, and do not depend on neither particular geometric or mechanical properties nor other theoretical considerations. However, the assessment of the monotonic analyses in terms of load-drift published in Grande et al. (2021) provided preliminary indications on the range of strain values which best meet the experimental results. Thus, a

TABLE 5 | Selected shear stress values and proposed ranges for γ_i parameters.

Backbone Point	Shear stress, τ_j	Shear strain, γ_j
1	$\tau_1 = 0.29\sqrt{f_c}\sqrt{1+0.29\sigma_j}$ Uzumeri (1977)	γ_1 = 0.0004 – 0.0008 – 0.0013
2	$\tau_2 = 0.85\tau_{max}$	γ_2 = 0.0017 – 0.002 – 0.004
3	$\tau_{max} = 0.569 \cdot (Bl)^{0.445} \cdot (f_c)^{0.783}$	γ_3 = 0.004 – 0.006 – 0.007 – 0.009 – 0.010 – 0.012 – 0.014 – 0.016 – 0.018 – 0.020
4	$\tau_4 = 0.3\tau_{max}$ Lowes et al. (2003), Shin and LaFave (2004), Sharma et al. (2011)	γ_4 = 0.025 – 0.030 – 0.035 – 0.0441 – 0.050 – 0.060 – 0.070 – 0.080

sensitivity analysis was carried out on all the 15 experimental tests, with the aim to identify a set of strain parameters to propose in the $\tau - \gamma$ constitutive model for exterior joints.

Table 5 provides the four proposed ranges of strains to assess (γ_1, γ_2, γ_3, γ_4) which were associated to the corresponding backbone points. The motivations for investigating such ranges are provided in the following.

Strain γ_1

Regarding the strain corresponding to the cracking shear strength τ_1, investigating only three values was considered sufficient for the purpose of the study; indeed, the monotonic analyses previously performed by implementing the 30 mentioned model combinations showed that a larger variation of this parameter does not lead to a significant scatter in terms of errors calculated between experimental and numerical enveloped in the first loading branch. In detail, these analyses highlighted that, relatively to γ_1 parameter, the lowest errors were generally obtained by considering *model B2* in which the value γ_1 = 0.0013 (upper end of the range provided in **Table 5**) coincides with the upper end of the range proposed by Celik and Ellingwood (2008); such a value is also the highest among those proposed by the various authors (see **Table 2**). However, numerical analyses related to some few tests showed that the first branch of the experimental monotonic envelope was better reproduced by setting γ_1 to 0.0004 (lower end of the range provided in **Table 5**); such a value is that proposed by De Risi et al. (2016) but it is not significantly different from other proposals (Shin and LaFave, 2004), (Sharma et al., 2011) (see **Table 2**). Finally, γ_1 = 0.0008 in **Table 5** is the average value of the range and represents a third alternative considered by authors.

Strain γ_2

Regarding the strain corresponding to the pre-peak strength τ_2, it is worth mentioning that the previous analyses highlighted that the implementation of the *models B2* and *C2* in **Table 2**, both suggesting γ_2 = 0.01, led to the highest scatter in terms of errors between the numerical drift and the experimental one; conversely, the adoption of lower γ_2 values, such as those provided by the other models, showed to provide better simulations. Therefore, the first two γ_2 values included in the range reported in **Table 5** coincide, respectively, with those of *model A* (De Risi et al., 2016) and *models B1* (Celik and Ellingwood, 2008), *C1* (Shin and LaFave, 2004) and *D* (Sharma et al., 2011). The upper end of the range, instead, was arbitrarily chosen by the authors with the aim to consider a third alternative; as shown later, this value was found to be optimal in carrying out the numerical analyses.

Strain γ_3

With respect to γ_1 and γ_2, the strain corresponding to the peak stress, γ_3, is characterized by greater uncertainty; indeed, the previous numerical analyses performed on the considered experimental tests have highlighted the wide range of values that such parameter can assume to fit the experimental data well. The same literature models in **Table 2** propose very different values for γ_3. However, it is worth mentioning that the previous analyses showed that, as for γ_2, the implementation of the *models B2* and *C2* in **Table 2**, both suggesting γ_3 = 0.03, led to the highest scatter in terms of errors between the numerical drift and the experimental one. Conversely, the models yielding the lowest errors were found to be *models B1* and *C1* (both suggesting γ_3 = 0.01), in the push loading direction, and *models A* and *D* (suggesting γ_3 = 0.0049 and γ_3 = 0.005, respectively) in the pull loading direction. Therefore, in order to cover the widest range of possible values, γ_3 spans from 0.004 (value close to the minimum one proposed in literature, equal to 0.0049 (De Risi et al., 2016)), to 0.02 (the highest value found from the previous numerical analyses fitting some experimental curves well). Within this range, a thickening of the values was considered towards the lower end, where the higher uncertainty was identified in the numerical analyses; conversely, by moving towards the upper end of the range, a lower number of values were considered, being less likely.

Strain γ_4

As for γ_3, high uncertainties affect the correct identification of the strain γ_4 corresponding to the residual strength τ_4. These are related, on one hand, to the test procedures used in some experimental investigations (as that carried out by Realfonzo et al. (2014), where tests were stopped at a predetermined conventional collapse in order to not significantly damage the specimens) and, on the other end, to the significant scatter of values proposed in the literature models (see **Table 2**). Therefore, in this case, the lower end of the range coincides with the minimum value suggested in literature (γ_3 = 0.025 (Sharma et al., 2011)); then, such a value was increased up to 0.050 (value adopted by *model C2* (Shin and LaFave, 2004)) by also including the other literature proposals. Finally, in order to account for experimental cases in which high values of drift were experienced, the remaining values of γ_4, equal to 0.06, 0.07 and 0.08, were also taken into consideration.

TABLE 6 | Strain parameters minimizing the mean absolute percentage errors.

Joint	γ_1	γ_2	γ_3	γ_4	*MAPE [%]*
J05	0.0004	0.0040	0.0060	0.0441	6.67
J01	0.0013	0.0020	0.0040	0.0300	9.74
TU3	0.0013	0.0040	0.0120	0.0700	8.90
TU1	0.0013	0.0040	0.0070	0.0800	10.19
#4	0.0004	0.0017	0.0090	0.0250	15.02
T#1	0.0013	0.0040	0.0060	0.0500	16.33
T_C3	0.0013	0.0017	0.0200	0.0441	12.08
T01	0.0013	0.0040	0.0060	0.0500	11.30
T0	0.0013	0.0020	0.0060	0.0350	10.88
BS-L	0.0008	0.0040	0.0100	0.0441	5.19
J40	0.0004	0.0017	0.0070	0.0500	8.04
C1	0.0013	0.0040	0.0060	0.0350	20.33
C2	0.0013	0.0040	0.0060	0.0350	13.87
J2	0.0013	0.0040	0.0200	0.0800	7.52
O1	0.0013	0.0040	0.0060	0.0600	7.11
μ_{γ_i}; μ_{MAPE}	***0.001087***	***0.003273***	***0.008733***	***0.04882***	***10.87***

Sensitivity Analysis and Results

In order to assess the influence of each γ_i parameter on the global response in terms of force – drift results, the sensitivity analysis was performed by varying every single value of the strain parameter within the predetermined range, thus requiring a hard computation effort. Indeed, a total of 21600 monotonic analyses were carried out by considering the 720 values of the strain parameters [= (#3γ_1) x (#3γ_2) x (#10γ_3) x (#8γ_4)] applied on the 15 experimental specimens in the 2 directions of loading (therefore, 720 × 15 × 2 = 21600 analyses). Of course, a wider variation of γ_i values within each considered range would have led to an even more accurate identification of the strain parameters but, according to the authors, the choices made herein represent the right compromise with the required computational effort.

Each of the monotonic curves resulting from the sensitivity analysis was compared to the experimental envelope of each test and the MAPE value was calculated according to **Eq. 3**.

It is highlighted that the errors between the *i*th experimental force and the corresponding numerical one were calculated considering the total length of the numerical monotonic curve (i.e., until the point $\tau_4 - \gamma_4$, or, equivalently, until the final point of the experimental curve).

For each experimental test, the combination of (γ_1, γ_2, γ_3, γ_4) minimizing the mean absolute percentage error on the monotonic envelope was, then, identified.

The resulting combinations are shown in **Table 6** for each experimental test, together with the related percentage error. The last row of **Table 6** also reports in *bold italics* the combination of "mean" γ_i, i.e., the set of γ_i obtained by averaging the values obtained from all the 15 experimental tests, together with the corresponding mean value of the errors. Such set of γ_i values is that proposed by the authors in conjunction with the stress parameters τ_i to define a new backbone joint shear stress-strain law to implement and validate in the numerical analyses described in the following section. For better clarity, the four couples of (τ_i – γ_i) parameters of the proposed law are summarized in **Table 7**.

Validation of the Proposed τ – γ Law

In order to check the accuracy of the proposed model, new monotonic analyses were carried out by implementing the proposed $\tau - \gamma$ law in the OpenSees computer code, both in the positive and negative direction of the loading. Then, the MAPE value between the experimental and numerical curve was calculated by applying **Eq. 6** over the whole monotonic envelope of each test.

In **Table 8**, the errors per each test related to the implementation of the proposed constitutive law (namely "*proposed model*") are compared with those obtained by considering the best three literature $\tau - \gamma$ models identified in *Numerical Analyses: Outcomes of the Previous Research and Insights*, i.e., "*model 5A*", "*model 1A*" and "*model 5C1*" (see the ranking in **Figure 2**). Furthermore, the errors resulting from considering the optimal set of γ_i parameters – found test by test in the minimization error procedure (see **Table 6**) – in place of the proposed average values in **Table 7**, are reported for a better comparison (see column "*optimal solution*" in **Table 8**).

As expected, test by test the MAPE values related to the "*proposed model*" are higher than those derived by the "*optimal solution*"; on average, the mean error computed on all the experimental tests (μ_{MAPE}) is about 45% greater (compare 15.86% with 10.87% in the last raw of **Table 8**). In particular, it is observed that for some specimens (specifically, J05, T#1, T01, BS-L, J40, O1), there is not a large scatter between the "*proposed model*" and the "*optimal solution*", while some others (J01, TU3, #4, C1, C2, J2) show a higher difference in the error between these two models.

The mean error provided by the "*proposed model*" is, however, lower than that derived from the literature *models 5A, 1A* and *5C1*, which show μ_{MAPE} values equal to 20.04, 21.01 and 23.65%, respectively.

Of course, in some tests the error for the "*proposed model*" is higher than that related to the literature models. This is the case of: a) the *model 5A* which provides better results for the tests TU3 (Pantelides et al., 2002), #4 (Clyde et al., 2000), C1; b) the *model 1A* which shows lower errors for the tests J01 (Realfonzo et al., 2014), #4 (Clyde et al., 2000), C1 (Antonopoulos and Triantafillou, 2003), and *c)* the *model 5C1* furnishes better results for the specimen #4 (Clyde et al., 2000). Only in the case of the joint #4 (Clyde et al., 2000), the "*proposed model*" works worse than all the three literature models. However, it is worth mentioning that the percentage errors related to the literature models, published in Grande et al. (2021) and provided in **Table 8** for the sake of comparison, have been computed until the 75% of the maximum strength, while the errors of both the "*proposed model*" and the "*optimal solution*" are evaluated considering the whole monotonic envelope.

Finally, **Figure 8** shows the resulting force – drift monotonic curves plotted for all the 15 specimens. In particular, in each graph the red curve and green one represent the monotonic envelope numerically obtained by implementing the $\tau - \gamma$ law identified as "*optimal solution*" and "*proposed model*", respectively; the black dotted curve, instead, is the experimental monotonic envelope.

The Figure clearly highlights the greater accuracy in matching the experimental behavior when the "*optimal solution*" is

TABLE 7 | Shear stress and strain parameters of the proposed constitutive law.

Backbone point	Shear stress, τ_j	Shear strain, γ_j
1	$\tau_1 = 0.29\sqrt{f_c}\sqrt{1+0.29\sigma_j}$ Uzumeri (1977)	$\gamma_1 = 0.001087$
2	$\tau_2 = 0.85\tau_{max}$	$\gamma_2 = 0.003273$
3	$\tau_{max} = 0.569 \cdot (Bl)^{0.445} \cdot (f_c)^{0.783}$	$\gamma_3 = 0.008733$
4	$\tau_4 = 0.3\tau_{max}$ Lowes et al. (2003), Shin and LaFave (2004), Sharma et al. (2011)	$\gamma_4 = 0.048820$

TABLE 8 | Mean absolute percentage errors and their mean values calculated for: a) the best three literature models (5A, 1A and 5C1); b) the proposed model, and c) the optimal solution.

Specimen	*MAPE [%]*				
	Model 5A	**Model 1A**	**Model 5C1**	**Proposed model[a]**	**Optimal solution[b]**
J05	11.00	12.44	8.87	*8.63*	6.67
J01	23.71	14.58	19.42	*18.92*	9.74
TU3	14.43	19.13	25.43	*15.60*	8.90
TU1	17.35	21.95	24.42	*16.47*	10.19
#4	9.88	19.01	11.69	*22.96*	15.02
T#1	32.75	22.41	42.44	*18.52*	16.33
T_C3	20.09	22.01	28.35	*17.20*	12.08
T01	33.52	26.31	32.91	*13.43*	11.30
T0	30.68	26.54	30.19	*14.99*	10.88
BS-L	9.30	13.87	13.42	*5.55*	5.19
J40	10.47	29.08	16.54	*9.07*	8.04
C1	17.23	22.47	29.61	*27.42*	20.33
C2	37.77	35.02	38.13	*22.98*	13.87
J2	23.13	20.91	22.97	*17.49*	7.52
O1	9.35	9.46	10.29	*8.71*	7.11
μ_{MAPE}	*20.04*	*21.01*	*23.65*	*15.86*	*10.87*

[a]*strain parameters γ_i reported in **Table 7** and in the last row of **Table 6** as well.*
[b]*optimal set of strain parameters γ_i found test by test in the minimization error procedure (**Table 6**)*

implemented in the numerical simulations, but the *"proposed model"* also provides good results for all the analyzed joints.

Both the numerical curves match the first elastic branch of the experimental envelope better than the softening phase; this issue is also common to all the numerical models investigated in the previous study (Grande et al., 2021). In fact, the main difference between the *"optimal solution"* and the *"proposed model"* stands after the peak point for most of the cases. As also shown from the errors in **Table 8**, the proposed numerical model (green curve in **Figure 8**) meets well the experimental outcomes in the following cases: J05, BS-L, J40, O1. On the other hand, the worst results are shown for the tests #4, T#1, TC_3, C1 and C2. Even in this analysis, the negative envelopes of the specimens TU1 and T0 are related to the nonlinear rotational spring describing the anchorage failure of the bottom bars at the beam-joint interface.

It is noticed that, in the case of the joints showing the higher errors, the main difference between the numerical and the experimental results relies in the values of the peak force, i.e. in the maximum shear strength. This aspect confirms that the assessment of this parameter is a crucial preliminary step in the definition of the shear behavior of beam – column joints.

Moreover, in the cases of joints TU3, TU1, T#1, T01, the *"proposed model"* is characterized by a constant trend after the residual strength point (τ_4-γ_4 in the constitutive law) since the corresponding experimental envelopes experienced high excursions in terms of drift in the post-peak phase.

MODELING OF CYCLIC RESPONSE OF JOINTS : "PINCHING4" MODEL

The modelling of the cyclic behavior represents a key aspect in the study of the seismic performance of the RC beam-column joints and is characterized by a greater complexity with respect to the simulation of the monotonic response. To this aim, the "*pinching4*" uniaxial material model (see **Figure 9**), available in the OpenSees library (McKenna et al., 2010), and developed by Lowes et al. (2003), was still used to set the parameters governing the hysteresis rule and pinching effect. This model has been widely used in several studies available in literature to simulate the hysteretic behavior of shear critical elements like beam – column joints or infilled frames (De Risi, 2015).

The model is based on a multilinear envelope response (backbone curve) and a trilinear unload – reload path, as illustrated in **Figure 9**. The cyclic degradation is simulated by three damage rules, that is, unloading stiffness degradation, reloading stiffness degradation (i.e. deterioration in strength developed in the vicinity of the maximum and minimum deformation demands) and strength degradation (i.e. deterioration in strength achieved at previously unachieved deformation demands).

Figure 10 shows the different effect of these three damage modes on the hysteretic response of the material.

Each of the three hysteretic damage modes is characterized by a modified version of the damage index proposed by Park and

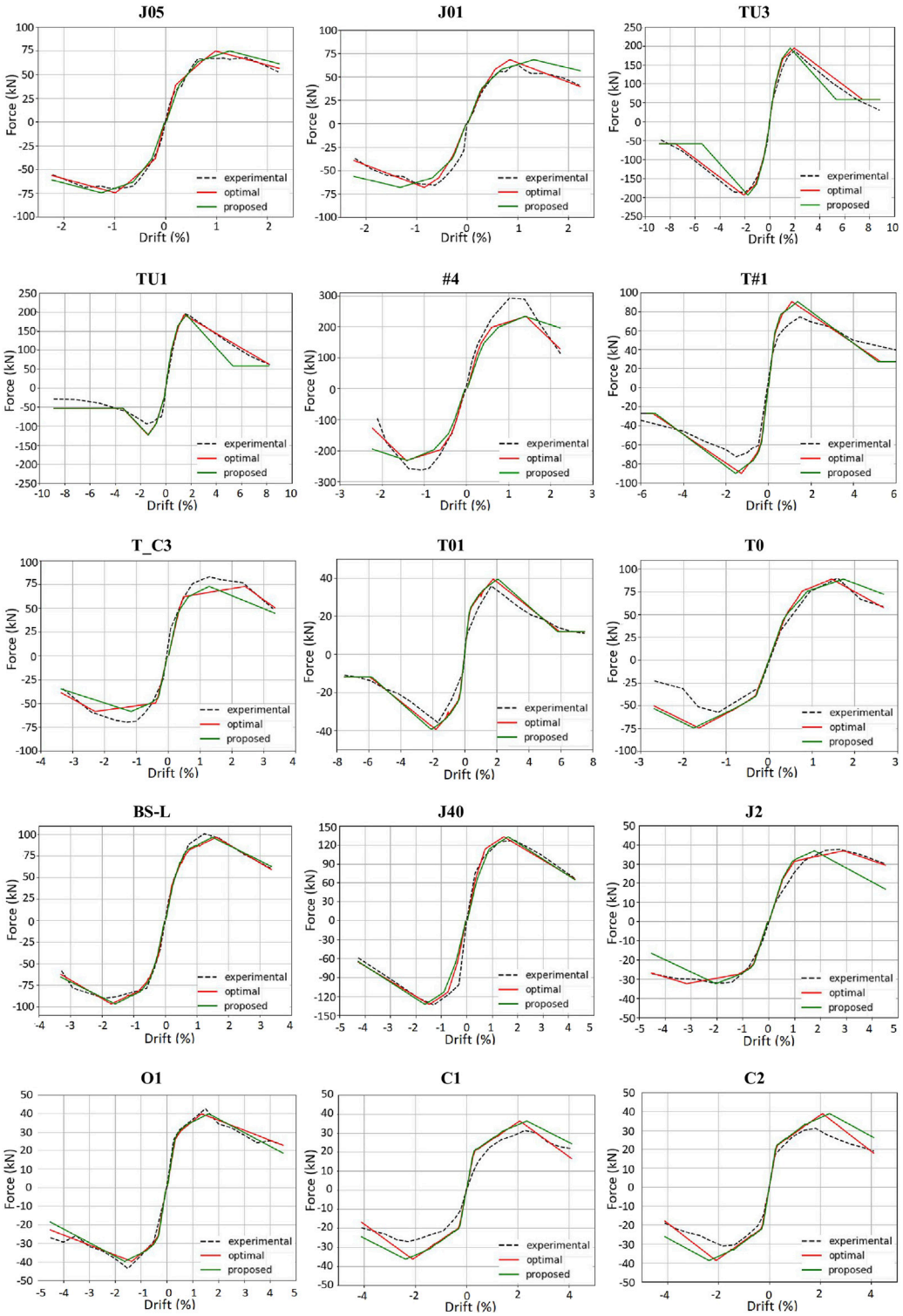

FIGURE 8 | Numerical vs Experimental comparison of the monotonic envelopes considering the *"optimal solution"* (red curve) and the *"proposed model"* (green curve).

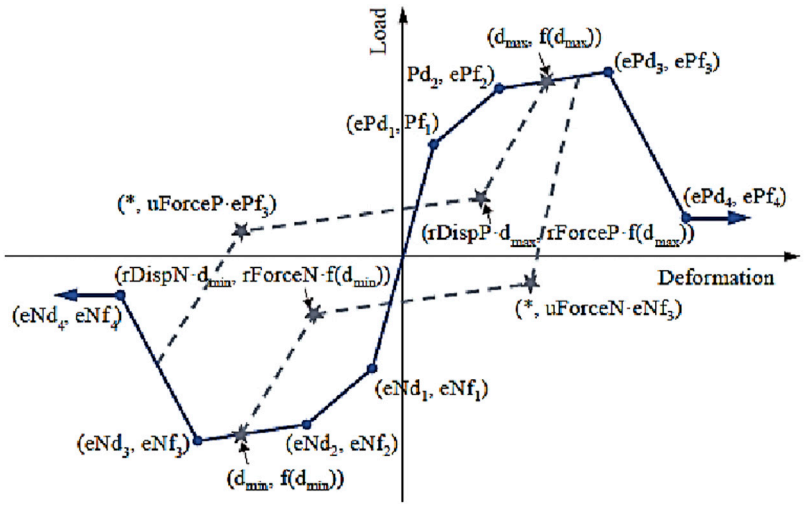

FIGURE 9 | *"Pinching4"* material model (adapted from Lowes et al. (Kim and LaFave, 2012)).

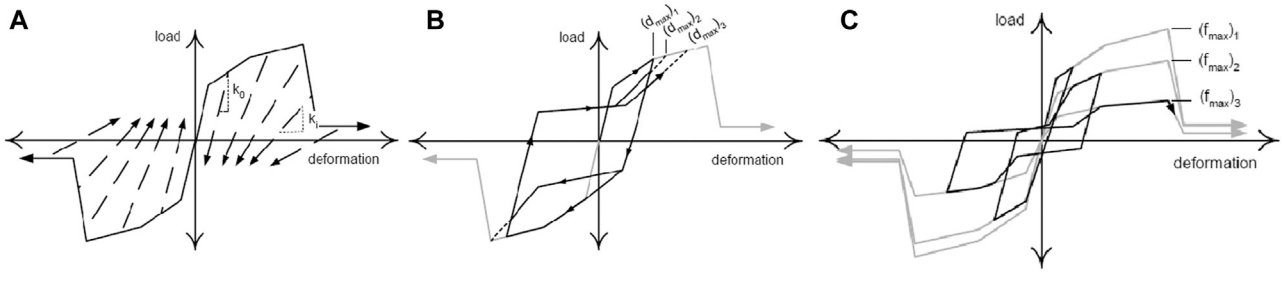

FIGURE 10 | Damage modes of the *"pinching4"* material: unloading stiffness degradation **(A)**; reloading stiffness degradation **(B)**; strength degradation **(C)** (Genesio, 2012).

Ang (1985), dependent on the displacement history and the accumulated energy, as follows:

$$\delta_i = \left(\alpha_1 (d_{max})^{\alpha_3} + \alpha_2 \left(\frac{E_i}{E_{monotonic}}\right)^{\alpha_4}\right) \leq \delta_{lim} \tag{12}$$

where:

$$d_{max} = \max\left[\frac{(d_{max})_i}{def_{max}}, \frac{(d_{min})_i}{def_{min}}\right] \tag{13}$$

$$E_i = \int_{loadhistory} dE \tag{14}$$

$$E_{monotonic} = gE\left(\int_{monotonic\,load} dE\right) \tag{15}$$

In **Eqs 12–15**:

- the subscript *i* refers to the current displacement increment;
- δ_i is the damage index (0 in case of no damage, 1 in case of maximum damage);
- α_j are parameters required to fit the damage rule to experimental data;
- E_i is the accumulated hysteretic energy;
- $E_{monotonic}$ is the energy required to achieve under monotonic loading the deformation that defines failure;
- def_{max} and def_{min} are the positive and negative deformations that define failure;
- d_{max} and d_{min} are the maximum and minimum historic deformation demands;
- δ_{lim} is the maximum possible value of the damage index;
- gE is a multiplication factor used to define the maximum energy dissipation under cyclic loading.

The same basic equations are used to describe deterioration in strength, unloading stiffness and reloading stiffness. For the case of stiffness degradation (**Figure 10A**):

$$k_i = k_0 (1 - \delta k_i) \tag{16}$$

where: k_i is the current unloading stiffness; k_0 is the initial unloading stiffness for the case of no damage; δk_i is the current value of the stiffness damage index.

The same relationship describes the envelope strength degradation (**Figure 10C**), as follows:

TABLE 9 | Pinching4" material model parameters and their role.

Parameter type		Parameter name	Description
Pinching parameters		*rDispP, rDispN*	Ratio of deformation at which reloading occurs to the maximum/minimum historic deformation demand
		rForceP, rForceN	Ratio of the force at which reloading begins to force corresponding to the maximum/minimum historic load demand
		uForceP, uForceN	ratio of the load developed upon unloading, from a negative (positive) load, to the maximum (minimum) of the load envelope
model degradation parameters	*Unloading stiffness degradation parameters*	*gK1, gK2, gK3, gK4*	Control unloading stiffness degradation (parameter related to δk_i index)
		gKlim	Damage index limit for unloading stiffness degradation (parameter related to δk_i index)
	Reloading stiffness degradation parameters	*gD1, gD2, gD3, gD4*	Control reloading stiffness degradation (parameter related to δd_i index)
		gDlim	Damage index limit for reloading stiffness degradation (parameter related to δd_i index)
	Strength degradation parameters	*gF1, gF2, gF3, gF4*	Control strength degradation (parameter related to δf_i index)
		gFlim	Damage index limit for strength degradation (parameter related to δf_i index)
Energy dissipation		*gE*	Floating point value used to define maximum energy dissipation under cyclic loading. The total energy dissipation capacity is given by this factor multiplied by the energy dissipated under monotonic loading

$$f_{max,i} = f_{max,0}\left(1 - \delta f_i\right) \tag{17}$$

where: $f_{max,i}$ is the current envelope maximum strength; $f_{max,0}$ is the initial envelope maximum strength for the case of no damage; δf_i is the current value of the strength damage index.

The case of reloading stiffness degradation (**Figure 10B**) is defined by applying an increase in the maximum (decrease in the minimum) historic deformation demand:

$$d_{max,i} = d_{max,0}\left(1 - \delta d_i\right) \tag{18}$$

where: $d_{max,i}$ is the current deformation that defines the end of the reload cycle for increasing deformation demand; $d_{max,0}$ is the maximum or minimum historic deformation demand; δd_i is the current value of the reloading – strength damage index.

The damage rule of **Eq. 12** requires the definition of 4 parameters (α_j) which must be calibrated for each of the three damage indices on the basis of experimental data. In the "*pinching4*" model, these α_j parameters are replaced by proper degradation model parameters to be defined for each damage index (δk_i, δf_i, δd_i); all these 15 parameters are indicated in **Table 9**.

Also, as observed in **Table 9**, the "*pinching4*" model requires the definition of other parameters, i.e.: 1) *gE*, already introduced in **Eq. 15**, and 2) three couples of parameters (*rDispP, rDispN*; *rForceP, rForceN*; *uForceP, uForceN*) describing the pinching behavior of the unload-reload path in **Figure 9**.

It is worth mentioning that the correct setting of these 22 parameters characterizing the material model (specifically, 15 degradation parameters + "*gE*" + 6 unloading–reloading pinching parameters), is a key task in the numerical simulation of the joint cyclic response. To this purpose, several studies were published in the literature, in which the calibration of these parameters was always based on a fitting process of experimental cyclic responses of beam-column joints. In this paper, the studies performed by Lowes and Altoontash (2003), Theiss (2005), Hassan (2011), De Risi (2015), Jeon (2013) were taken under consideration for the definition of the "*pinching4*" material model. The main details of these studies are provided in the following section.

Selected Literature Studies

In each selected literature study the researchers defined a set of "*pinching4*" parameters even though generally calibrated by using their own experimental data. In particular, the study by Lowes and Altoontash (2003) represents one of the first attempts to provide specific indications on the hysteretic rules defined by the "*pinching4*" material model. The proposed unload-reload path and the damage law were assessed through the comparison between the simulated and the observed response for a series of four joint sub-assemblages with different design details. The backbone envelope was defined through the *modified compression field theory* (MCFT) approach proposed by Vecchio and Collins (1986). Experimental data provided by Stevens et al. (1991) were, then, used to define the response under cyclic loading. These data showed an extremely pinched shear stress-strain behavior, which was attributed to the opening and closing of cracks in the concrete-steel composite. The numerical simulations showed that the proposed model represented well the fundamental characteristics of the observed response, including energy dissipation within the joint and the shear failure mode. However, due to the limited number of experimental tests investigated by the authors, the accuracy of the model should be further assessed for a higher number of joints.

Theiss (2005) investigated five laboratory tests previously carried out by Walker (2001) and Alire (2002). Different cyclic analyses were performed, employing simulation and no simulation of the joint's strength and stiffness deteriorations under cyclic loading. The results showed that simulating the strength and stiffness deteriorations had a significant impact on the global hysteretic response of the joints, especially in terms of

maximum drift demands. The effect of the joint modeling was also evaluated through dynamic analyses on a three-story RC frame building.

The study by Hassan (2011) aimed at evaluating the seismic performance of four full-scale corner beam-column joint sub-assemblies until total collapse. The model incorporates the effect of axial load level, overturning seismic moment, joint aspect ratio, joint failure mode and the post-shear damage residual axial capacity. To validate the appropriateness of the proposed joint model, six additional unconfined exterior and corner tests were selected from literature and investigated through numerical simulations.

The study by De Risi (2015) focused on proposing a modelling approach for exterior RC joints under cyclic loading in order to assess the seismic vulnerability of existing RC buildings typical of Italian/Mediterranean building stock, and to evaluate the impact of joints' response on such a performance. To this purpose, the calibration of the key parameters governing the joint panel hysteretic behavior was based on an experimental database including 10 tests of which 2 were performed by the same author; from the calibration procedure, the mean values of the parameters calibrated from each test were finally proposed. In particular, the applied procedure was performed starting from the experimental shear stress-strain backbones and minimizing the error in terms of dissipated energy between the numerical and the experimental responses. No degradation in strength was introduced (namely all *gF* parameters in **Table 9** were set equal to zero) since it was already included in the backbone of the joint response obtained from the experimental data.

Finally, the study by Jeon (2013) was based on the most complete experimental database, which gathered 28 exterior sub-assemblages from literature. The mean values of the "*Pinching4*" material parameters, extracted from the model validation in terms of strength, stiffness and energy dissipation, were then utilized in the simulations of RC structures for a probabilistic risk assessment.

Table 10 shows the values of the pinching parameters proposed by the selected literature studies. From this table, the following considerations can be made:

- in most of the cases, the pinching parameters (*rDisp, rForce, uForce*) are assumed to be equal – in absolute value – between the positive and negative unload – reload path; only Hassan (2011) proposed different values between the two branches (in particular, $rForceP = 0.35$ and $rForceN = -0.40$, whereas $uForceP = -0.10$ and $uForceN = -0.40$);
- the models by Lowes and Altoontash (2003), De Risi (2015) and Jeon (2013) assumed the unloading stiffness damage to be a function of the displacement history only, since the parameters gK_2 and gK_4, related to the energy accumulation damage, are set equal to zero. The same observation can be made for reloading stiffness degradation parameters; in this case, also the model by Theiss (2005) shows that the stiffness loss is determined primarily by the maximum deformation demand (d_{max}) ($gD_2 = 0.005$; $gD_4 = 0$);
- both the unloading and the reloading stiffness damage indices limits (gk_{lim} and gD_{lim}) assumed similar values among all the models; in fact, the maximum value of gk_{lim} is equal to 0.99 (Theiss, 2005), (Hassan, 2011) and the minimum is 0.89 (Lowes and Altoontash, 2003), while gD_{lim} assumes a maximum of 0.99 (Theiss, 2005), (Hassan, 2011) and a minimum of 0.95 (Lowes and Altoontash, 2003; Jeon, 2013);
- the displacement history is taken as main factor of the strength degradation index for the models by Lowes and Altoontash (2003), Theiss and Jeon (gF_2 and gF_4 equal to zero) (Theiss, 2005; Jeon, 2013);
- the strength degradation limit (gF_{lim}) is equal to 0.99 for the models by Theiss (2005) and Hassan (2011) (note that this limit value is also assumed for the other damage indices by these authors), whereas much lower values are assumed by the models by Lowes and Altoontash (2003), and Jeon (2013) (0.13 and 0.25, respectively);
- as mentioned earlier, the strength degradation parameters assumed by De Risi (2015) are all set equal to zero, i.e., no strength degradation is included in this model. Indeed, due to these parameters, a reduction in the envelope curve of the hysteretic cycles would have been shown, leading to a mismatch if the monotonic backbone had been previously calibrated through specific analyses and assumptions as done by De Risi (2015); the author proposed the multilinear response envelope, based on some experimental tests, before the definition of the degradation laws concerning the cyclic behavior of joints;
- the energy dissipation factor *gE* is assumed equal to 10 by all the models, with the exception of the model by Theiss (2005), which proposed an energy multiplication factor equal to 2.

Assessment of the Model Parameters Proposed in Literature

The considerations made on the literature values assigned to the *"pinching4"* model parameters represent a useful starting point for carrying out cyclic analyses on the experimental tests available in the database. Therefore, the obtained results have allowed, on one hand, to identify the literature proposal fitting the experimental best and, on the other end, to catch valuable indications on how to properly modify the values of some "*pinching4*" model parameters.

To this purpose, the finite element model geometry used to simulate the monotonic envelope of the experimental joints, was again considered to carry out cyclic analyses for the same set of 15 specimens in the OpenSees platform (McKenna et al., 2010).

Even in this case, the macro – modeling approach adopted the "*scissors model*" to simulate the joint element, with the two rotational *springs 1* and *spring 2* in series, representing the shear behavior of the joint panel and the bond – slip mechanism at the beam – joint interface. In particular, the multilinear moment – rotation (M–θ) law in **Figure 1C** was adopted to describe the envelope backbone of the shear rotational spring, of which the key parameters were derived from the τ and γ values previously calibrated by the authors (see **Table 7**).

TABLE 10 | Values of the "Pinching4" material parameters selected from the literature.

Parameter type		Parameter ID	Lowes and Altoontash (2003)	Theiss (2005)	Hassan (2011)	De Risi (2015)	Jeon (2013)
Pinching parameters		*rDispP*	0.25	0.11	0.15	0.16	0.2
		rForceP	0.15	0.25	0.35	0.23	0.2
		uForceP	0	0	−0.1	−0.22	0
		rDispN	−0.25	−0.11	0.15	0.16	0.2
		rForceN	−0.15	−0.25	0.15	0.23	0.2
		uForceN	0	0	−0.4	−0.22	0
model degradation parameters	*Unloading stiffness degradation parameters*	*gK1*	1.3	0.42	0.5	0.85	0.95
		gK2	0	0.35	0.2	0	0
		gK3	0.24	0.2	0.1	0.12	0.1
		gK4	0	0.028	0.4	0	0
		gKLim	0.89	0.99	0.99	0.96	0.95
	Reloading stiffness degradation parameters	*gD1*	0.12	0.046	0.1	0.38	0.35
		gD2	0	0.005	0.4	0	0
		gD3	0.23	1.385	1	0.34	0.15
		gD4	0	0	0.5	0	0
		gDLim	0.95	0.99	0.99	0.96	0.95
	Strength degradation parameters	*gF1*	1.11	1	0.05	0	0.05
		gF2	0	0	0.02	0	0
		gF3	0.32	2	1	0	0.32
		gF4	0	0	0.05	0	0
		gFLim	0.13	0.99	0.99	0	0.25
Energy dissipation		*gE*	10	2	10	10	10

The "*pinching4*" uniaxial material model was, hence, assigned to the two rotational springs. Of course, besides the implementation of the backbone envelope in terms of moment-rotation multilinear laws, the "*pinching4*" material model requires, for cyclic analyses, the mentioned additional 22 parameters describing the unloading-reloading path, the strength and stiffness degradation and pinching effect (see **Table 9**).

Therefore, for each of the 15 experimental specimens, a set of 5 cyclic analyses were carried out by implementing the corresponding 5 sets of cyclic degradation parameters listed in **Table 10**.

It is worth highlighting that that no strength degradation was considered in all the 5 models, meaning that the strength damage index parameters (gF_1, gF_2, gF_3, gF_4, gF_{lim}) were always set equal to zero whatever the accounted model. Indeed, like the numerical study performed by De Risi (2015), even in this work the monotonic envelope of each joint has been separately calibrated by performing specific monotonic analyses. The introduction of the strength loss phenomenon, indeed, would have reduced the envelope backbone, leading to a worsening with respect to the experimental monotonic curve.

In order to assure a perfect correspondence between numerical and experimental curves, the cyclic analyses were performed by implementing, for each single experimental test, the same displacement history described in literature by the authors.

Results and Discussion

In order to identify the model which best approximate the cyclic behavior of the tests, an assessment was carried out on the basis of the difference between the numerical and the experimental response in terms of dissipated energy ($E_{d,i}$) and stiffness degradation (K_i) at each cycle. In fact, these are the properties mainly controlling the shape of the hysteretic loops and their evaluation is a relatively simple issue in the post – processing phase of the force – drift cyclic response. In particular, by summing up the area enclosed by each force-displacement cycle, the total cumulative dissipated energy was obtained, which obviously increases with the imposed displacement. On the other hand, the secant stiffness K_i was calculated through the relationship proposed by Mayes and Clough (1975) as follows:

$$K_i = \frac{\left|F^+_{max,i}\right| + \left|F^-_{max,i}\right|}{\left|D^+_{max,i}\right| + \left|D^-_{max,i}\right|} \tag{19}$$

where: $F^+_{max,i}$ and $F^-_{max,i}$ are the peak lateral forces applied to the beam in the two directions of loading; $D^+_{max,i}$ and $D^-_{max,i}$ are the corresponding displacements.

Unlike the cumulative energy, the secant stiffness decreases with imposed displacement.

To compare the accuracy of the numerical simulations resulting from the implementation of the five sets of "*pinching4*" model parameters, the mean absolute percentage error was calculated between the experimental and the numerical values for both energy and stiffness at each cycle by applying the following equation:

$$\mathrm{E}_{rr,E_d} = \frac{\sum_{\mathrm{i}=1}^{\mathrm{n}} \frac{\left|E^{exp}_{d,i} - E^{num}_{d,i}\right|}{E^{exp}_{d,i}} \cdot 100}{\mathrm{n}}; \quad \mathrm{E}_{rr,K} = \frac{\sum_{\mathrm{i}=1}^{\mathrm{n}} \frac{\left|K^{exp}_{i} - K^{num}_{i}\right|}{K^{exp}_{i}} \cdot 100}{\mathrm{n}} \tag{20}$$

where n is the total number of measures in terms of energy and stiffness available for each specimen, $E^{exp}_{d,i}$ and $E^{num}_{d,i}$ are,

TABLE 11 | Mean absolute percentage errors for energy dissipation and stiffness degradation.

Test	*MAPE [%] Energy*					*MAPE [%] Stiffness*				
	Lowes and Altoontash (2003)	Theiss (2005)	Hassan (2011)	De Risi (2015)	Jeon (2013)	Lowes and Altoontash (2003)	Theiss (2005)	Hassan (2011)	De Risi (2015)	Jeon (2013)
J05	80	61	79	58	54	9	12	8	9	13
J01	84	67	77	65	63	16	13	14	14	15
TU3	27	43	36	23	15	29	31	26	22	21
TU1	22	60	27	24	26	46	48	49	45	54
#4	76	70	80	69	63	43	26	40	37	39
T#1	39	39	38	35	30	28	36	27	21	18
T_C3	44	29	45	28	28	69	72	61	52	44
T01	25	45	12	23	24	23	30	23	21	19
T0	26	22	36	30	22	24	27	24	20	20
BS-L	29	14	33	23	27	16	21	15	9	8
J40	55	41	52	45	48	42	30	36	29	27
C1	25	75	34	64	58	24	22	25	20	18
C2	33	76	44	60	69	31	24	27	25	22
J2	40	21	34	16	21	11	27	16	17	18
O1	18	10	21	9	17	20	44	19	15	15
μ_{MAPE}	*41.53*	*44.87*	*43.20*	*38.13*	*37.67*	*28.73*	*30.87*	*27.33*	*23.73*	*23.40*

respectively, the experimental and numerical dissipated energy calculated at the *i-th* displacement cycle; K_i^{exp} and K_i^{num} are, respectively, the experimental and numerical stiffness calculated at the *i-th* displacement cycle according to Eq. (19).

The MAPE values emerged from the analysis are reported in **Table 11** for both energy and stiffness parameters; the mean value (μ_{MAPE}) calculated per each model on all the experimental tests is also provided in the last row of **Table 11**.

As observed, the model by Jeon (2013) yields the lowest μ_{MAPE} values both in terms of energy and stiffness, being equal to 37.67 and 23.40%, respectively. In the ranking, the model by De Risi (2015) follows, providing overall mean values equal to 38.13% for the dissipated energy and 23.73% for the stiffness degradation. For both the properties, the model leading to the highest mismatch is the model by Theiss (2005).

By analyzing the tests case by case, some observations can be made regarding the joints J05 and J01 (Realfonzo et al., 2014), since they are characterized by high values of errors for the energy, but very low values for the stiffness if compared to corresponding results found for the other tests. This particular outcome is probably due to the fact that the experimental data of the entire cyclic load history were available for these tests. Thus, the analysis on the dissipated energy and stiffness degradation was made possible also for the first small imposed displacements, which have been proven to furnish the highest mismatch in terms of loop width and, consequently, in terms of energy dissipation. No substantial differences are observed in terms of secant stiffness at each cycle, since the monotonic backbone of the numerical models provided a good approximation with the experimental envelope.

Moreover, it is highlighted that, the cases that already had showed the highest errors in terms of monotonic envelopes (see §5) are also characterized by high errors in terms of energy dissipation and stiffness loss (see joints #4, T#1, T_C3, C1, C2 in **Table 11**). This observation remarks the importance of defining a proper monotonic backbone curve before studying the hysteretic cyclic behavior.

Figure 11 and **Figure 12** depict the cumulative dissipated energy and the stiffness degradation, respectively; for each test, all the five numerical outcomes are displayed and compared among them and with the experimental trend as well.

As observed, a large scatter among the considered models is found in terms of numerical energy dissipation (**Figure 11**), whereas only slight differences are noted in terms of stiffness decay (**Figure 12**).

As emerged from the outcomes shown in **Table 11**, the numerical model derived by adopting the pinching parameters proposed by Theiss (2005) provided the less accurate results in terms of dissipated energy and stiffness degradation. Conversely, the best numerical simulations are those generally obtained considering the proposal by Jeon (2013) The good accuracy is also confirmed by analyzing the plots in terms of force – drift hysteretic cycles shown in **Figure 13** where the experimental curves are compared to the numerical ones obtained by using the pinching parameters proposed by Jeon (2013) (the cyclic simulations obtained by using the pinching parameters suggested by the other proposals are omitted for the sake of brevity). Of course, in order to further improve the cyclic modelling of the considered RC joints, an *ad-hoc* calibration procedure of the "*pinching4*" model parameters should be performed by considering the collected experimental database; to this purpose, a good starting point is represented by the outcomes of the numerical study performed herein, suggesting to focus on the sets of parameters proposed by Jeon (2013) and by

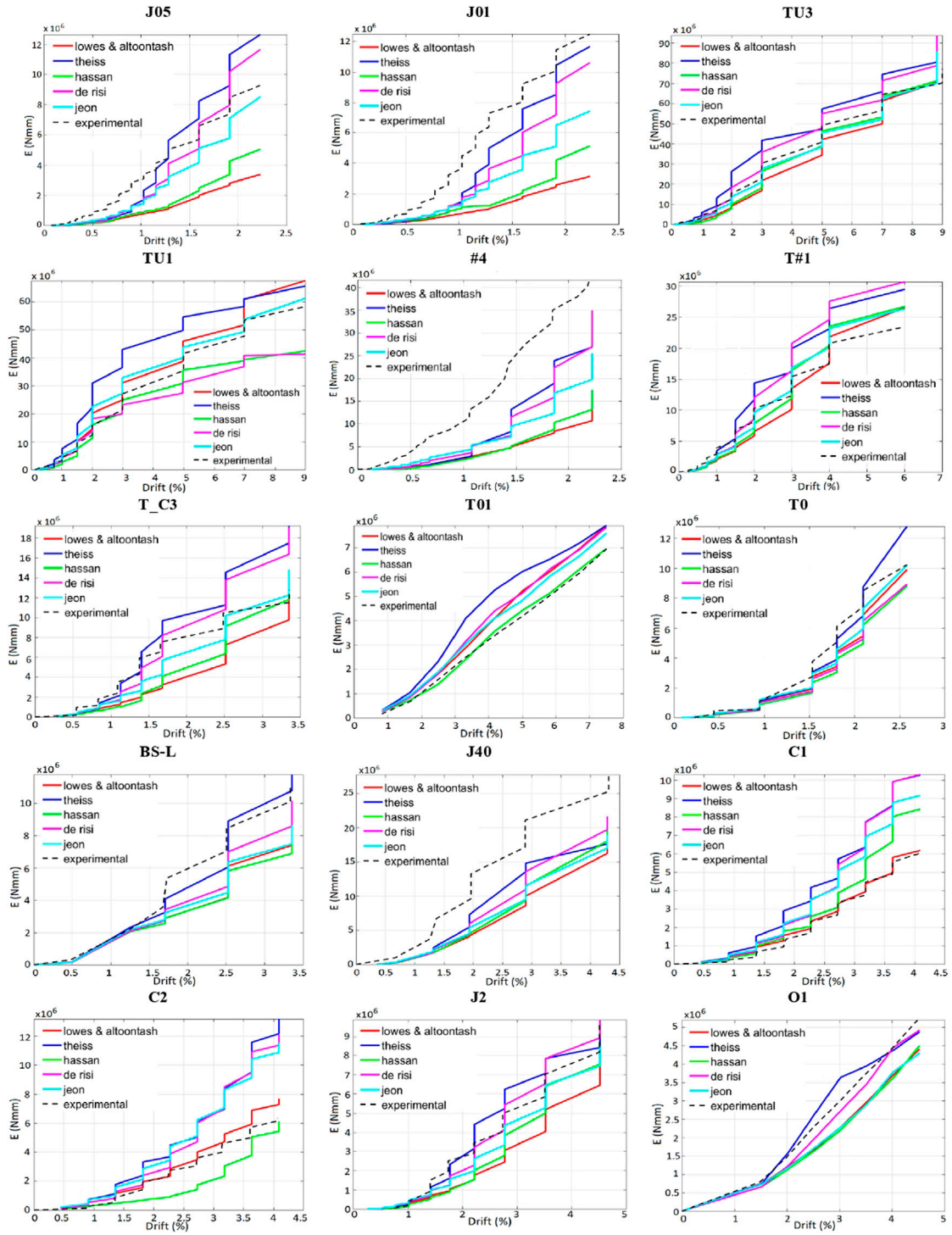

FIGURE 11 | Cumulative dissipated energy: comparison among the literature models.

De Risi (2015), and opportunely modify them by spanning within the values proposed by these authors. However, this aspect is omitted herein and will be addressed in another paper under preparation.

CONCLUSION

Past and recent earthquake events have underlined a behavior of existing RC frame structures in some cases characterized by

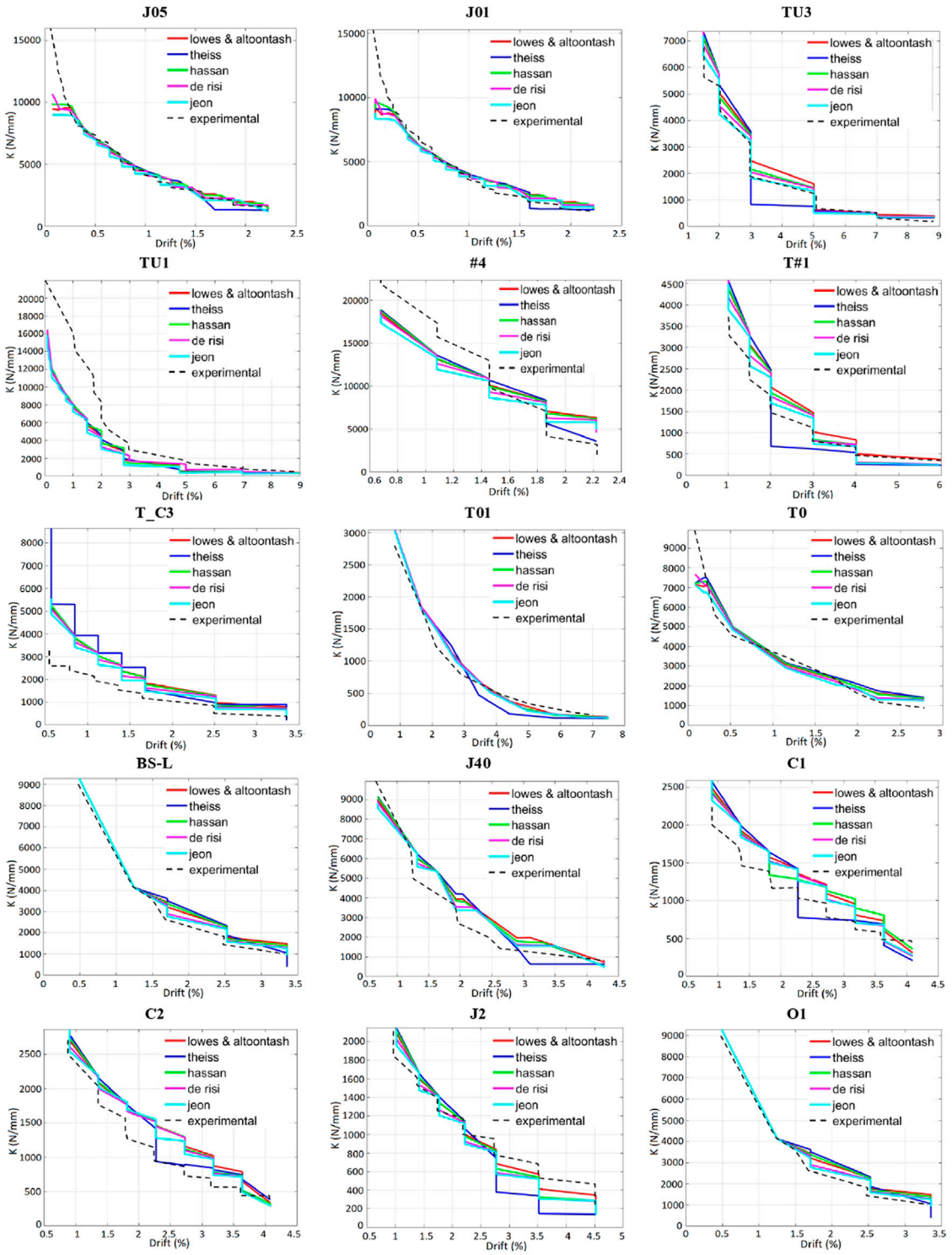

FIGURE 12 | Stiffness degradation: comparison among the literature models.

significant damages and failure of beam-column joints. This unexpected behavior has led to a particular attention of the scientific community toward the assessment, verification and design of this important component of RC frames.

In this study, a numerical modelling approach to evaluate the behavior of exterior RC beam – column joints has been presented. In particular, starting from the outcomes of a previous study carried out by the authors, a calibration process based on a set of

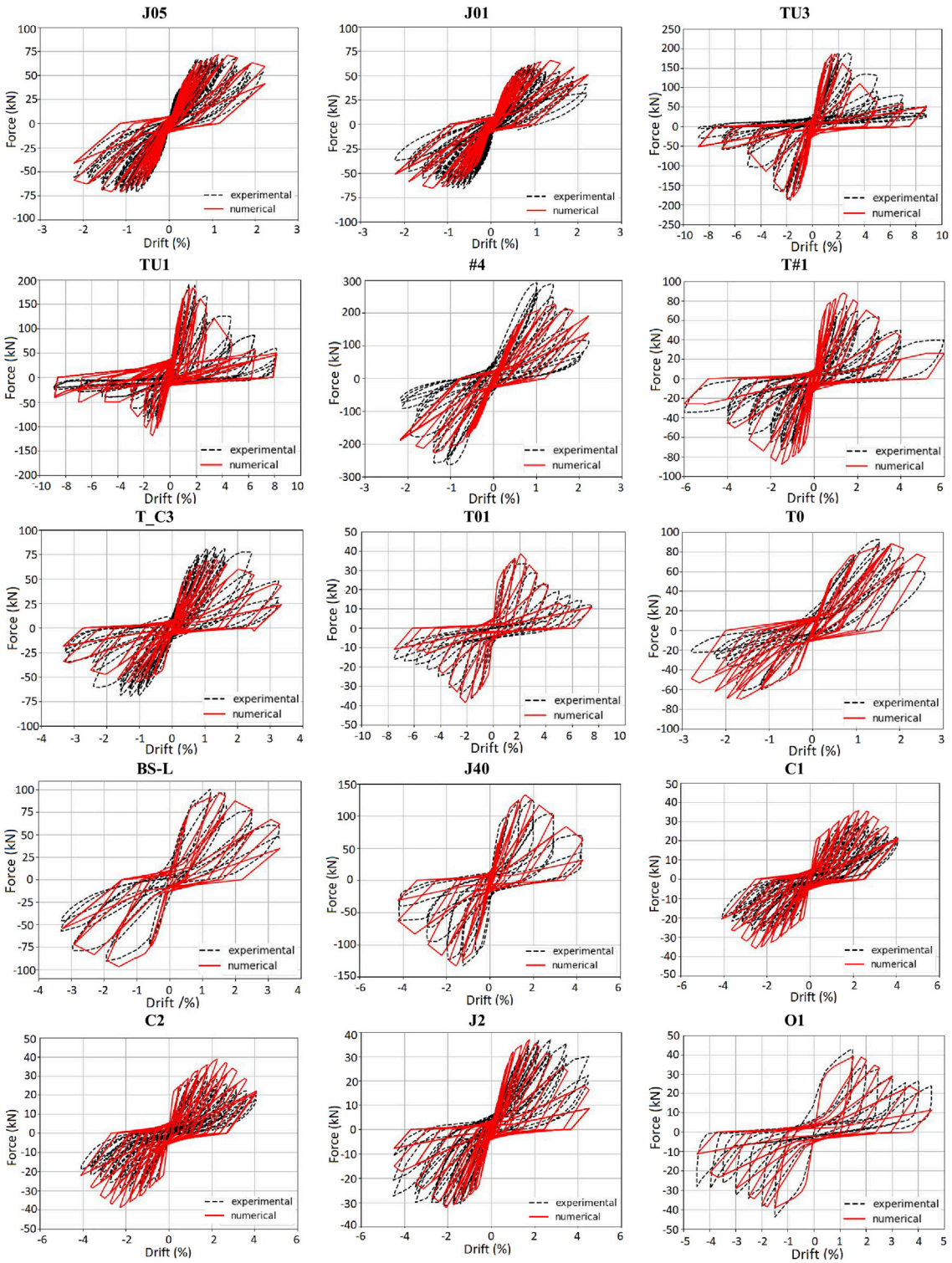

FIGURE 13 | Force – drift cyclic response using the pinching parameters proposed by Jeon (Mitra and Lowes, 2007).

experimental tests has been carried out in order to derive an efficient constitutive model for exterior RC joints.

To this end, non-linear static analyses carried out by implementing the scissor model in the software OpenSees have been performed by simulating both the monotonic experimental behavior and the cyclic response of the selected experimental cases.

The monotonic analyses have been preliminary finalized to identify among the models of literature the ones that better

simulate the experimental behavior of the selected specimens. From these analyses it has been observed that the model by Kim and LaFave (2009) and the model by Jeon (2013) are the most reliable in predicting the shear strength of the examined joints, while the deformability level is better approximated by the strain parameters proposed by the model by De Risi et al. (2016). Subsequently, the calibration process has been carried out to improve the capacity of the model to simulate the monotonic response of exterior RC joints.

Moreover, cyclic analyses have been carried out considering the model derived from the calibration process here presented and some literature proposals for defining the set of parameters governing the hysteresis rules and pinching effect. The obtained results, although have clearly emphasized the great complexity in simulating the cyclic response, have pointed out the reliability of the proposed model and, also, provided useful indications on how to further improve the cyclic modelling of the considered RC joints.

DATA AVAILABILITY STATEMENT

The raw data supporting the conclusions of this article will be made available by the authors, without undue reservation.

AUTHOR CONTRIBUTIONS

EG, AN and RN contributed to: Conceptualization, Methodology, Investigation, Validation, Software, Formal analysis, Data curation, Writing-original draft. MI and RR contributed to: Conceptualization, Methodology, Investigation, Resources, Visualization, Writing-review and editing, Supervision, Project administration, Funding acquisition. All authors approved the submitted version.

FUNDING

Funding received from University of Salerno for open access publication fees.

ACKNOWLEDGMENTS

The financial support by ReLUIS (Network of the Italian University Laboratories for Seismic Engineering–Italian Department of Civil Protection) is gratefully acknowledged (Executive Project 2019-21 - WP14/WP2 CARTIS). Further support has been given by University of Salerno (FARB 2020).

REFERENCES

ACI 369 R-11 (2011). *Guide for Seismic Rehabilitation of Existing Concrete Frame Buildings and Commentary*. Farmington Hills, MI: American Concrete Institute.

Akguzel, U., and Pampanin, S. (2012). Assessment and Design Procedure for the Seismic Retrofit of Reinforced Concrete Beam-Column Joints Using FRP Composite Materials. *J. Compos. Constr.* 16 (1), 21–34. doi:10.1061/(ASCE)CC.1943-5614.0000242

Al-Salloum, Y. A., Siddiqui, N. A., Elsanadedy, H. M., Abadel, A. A., and Aqel, M. A. (2011). Textile-reinforced Mortar versus FRP as Strengthening Material for Seismically Deficient RC Beam-Column Joints. *J. Compos. Constr.* 15, 920–933. doi:10.1061/(asce)cc.1943-5614.0000222

Alath, S., and Kunnath, S. K. (1995). "Modeling Inelastic Shear Deformations in RC Beam–Column Joints," in Engineering mechanics proceedings of 10th conference 1995. ASCE, New York, May 21-24, 1995 (Boulder, Colorado: University of Colorado at Boulder), 822–825.

Alire, D. A. (2002). "Seismic Evaluation of Existing Unconfined Reinforced Concrete Beam–Column Joints,"M.Sc. Thesis (University of Washington).

Antonopoulos, C. P., and Triantafillou, T. C. (2003). Experimental Investigation of FRP-Strengthened RC Beam-Column Joints. *J. Compos. Constr.* 7 (1), 39–49. doi:10.1061/(asce)1090-0268(2003)7:1(39)

ASCE/SEI 41/06 (2006). *Seismic Rehabilitation of Existing Buildings*. Reston, Virginia: American Society of Civil Engineers.

Bedirhanoglu, I., Ilki, A., Pujol, S., and Kumbasar, N. (2010). Behavior of Deficient Joints with plain Bars and Low-Strength concrete. *ACI Struct. J.* 107, 300–310.

Biddah, A., and Ghobarah, A. (1999). Modelling of Shear Deformation and Bond Slip in Reinforced concrete Joints. *Struct. Eng. Mech.* 7 (4), 413–432. doi:10.12989/sem.1999.7.4.413

Bousselham, A. (2010). State of Research on Seismic Retrofit of RC Beam-Column Joints with Externally Bonded FRP. *J. Compos. Constr.* 14, 49–61. doi:10.1061/(asce)cc.1943-5614.0000049

Celik, O. C., and Ellingwood, B. R. (2008). Modeling Beam-Column Joints in Fragility Assessment of Gravity Load Designed Reinforced Concrete Frames. *J. Earthquake Eng.* 12, 357–381. doi:10.1080/13632460701457215

Clyde, C., Pantelides, C. P., and Reavely, L. D. (2000). "Performance-Based Evaluation of Exterior Reinforced concrete Building Joints for Seismic Excitation,". PEER report 2000/05 (Berkeley, CA: Pacific Earthquake Engineering Research Center, College of Engineering, University of California).

De Risi, M. T. (2015). "Seismic Performance Assessment of RC Buildings Accounting for Structural and Non-structural Elements,"Ph.D. Thesis (University of Napoli, Federico II).

De Risi, M. T., Ricci, P., and Verderame, G. M. (2016). Modelling Exterior Unreinforced Beam-Column Joints in Seismic Analysis of Non-ductile RC Frames. *Earthquake Engng Struct. Dyn.* 46 (6), 899–923. doi:10.1002/eqe.2835

De Vita, A., Napoli, A., and Realfonzo, R. (2017). Full Scale Reinforced concrete Beam-Column Joints Strengthened with Steel Reinforced Polymer Systems. *Front. Mater.* 4, 1–17. doi:10.3389/fmats.2017.00018

Deifalla, A., Ahmed, F., Saleh, A., Elwan, S., Hamad, M., and Elzeiny, S. (2021). Effect of Reinforcement Around Web Opening on the Cyclic Behavior of Exterior RC Beam-Column Joints. *Future Eng. J.* 2 (1).

Del Vecchio, C., Di Ludovico, M., Balsamo, A., Prota, A., Manfredi, G., and Dolce, M. (2014). Experimental Investigation of Exterior RC Beam-Column Joints Retrofitted with FRP Systems. *J. Composites Construction* 18 (4), 1–13. doi:10.1061/(ASCE)CC.1943-5614.0000459

El-Amoury, T., and Ghobarah, A. (2002). Seismic Rehabilitation of Beam-Column Joint Using GFRP Sheets. *Eng. Structures* 24, 1397–1407. doi:10.1016/S0141-0296(02)00081-0

El-Metwally, S. E., and Chen, W. F. (1988). Moment-Rotation Modeling of Reinforced Concrete Beam-Column Connections. ACI Struct. *J.* 85 (4), 384–394.

Genesio, G. (2012). "Seismic Assessment of RC Exterior Beam-Column Joints and Retrofit with Haunches Using post-installed Anchors,". Ph.D. thesis (Germany: University of Stuttgart). doi:10.18419/OPUS-472

Giberson, M. F. (1969). Two Nonlinear Beams with Definitions of Ductility. *J. Struct. Div.ASCE* 95, 137–157. doi:10.1061/jsdeag.0002184

Grande, E., Imbimbo, M., Napoli, A., Nitiffi, R., and Realfonzo, R. (2021). A Macro-Modelling Approach for RC Beam-Column Exterior Joints: First Results on Monotonic Behavior. *J. Building Eng.* 39, 1–16. doi:10.1016/j.jobe.2021.102202

Hadi, M. N. S., and Tran, T. M. (2016). Seismic Rehabilitation of Reinforced concrete Beam-Column Joints by Bonding with concrete Covers and Wrapping with FRP Composites. *Mater. Struct.* 49, 467–485. doi:10.1617/s11527-014-0511-4

Haselton, C. B., Liel, A. B., Taylor-Lange, S. C., and Deierlein, G. G. (2016). Calibration of Model to Simulate Response of Reinforced concrete Beam-Columns to Collapse. *ACI Struct. J.* 113 (6), 1141–1152. doi:10.14359/51689245

Hassan, W., Al-Zahraa Refaie, F., and Belal, A. (2018). "Seismic Vulnerability of concrete Beam-Column Joints in Older Construction under High Axial Loads". In: Proceeding of the 16th European Conference on earthquake engineering, Thessaloniki, Greece, June 18–21 (Springer), 1–10.

Hassan, W. M. (2011). "Analytical and Experimental Assessment of Seismic Vulnerability of Beam-Column Joints without Transverse Reinforcement in Concrete Buildings,". Ph.D. Thesis (Berkeley: University of California).

Hwang, S., and Lee, H. (1999). Analytical Model for Predicting Shear Strengths of Exterior Reinforced concrete Beam-Column Joints for Seismic Resistance. *ACI Struct. J.* 96 (5), 846–857.

Jeon, J.-S., Lowes, L. N., DesRoches, R., and Brilakis, I. (2015). Fragility Curves for Non-ductile Reinforced concrete Frames that Exhibit Different Component Response Mechanisms. *Eng. Structures* 85, 127–143. doi:10.1016/j.engstruct.2014.12.009

Jeon, J. S. (2013). "Aftershock Vulnerability Assessment of Damaged Reinforced concrete Buildings in California,". Ph.D. Thesis (GA: School of Civil and Environmental Engineering, Georgia Institute of Technology). doi:10.1061/9780784412848.230

Kim, J., and LaFave, J. M. (2009). "Joint Shear Behavior of Reinforced concrete Beam-Column Connections Subjected to Seismic Lateral Loading,"Report No. NSEL-020 (IL: Department of Civil and Environmental Engineering, University of Illinois at Urbana-Champaign).

Kim, J., and LaFave, J. M. (2012). A Simplified Approach to Joint Shear Behavior Prediction of RC Beam-Column Connections. *Earthquake Spectra* 28 (3), 1071–1096. doi:10.1193/1.4000064

Liel, A. B., Haselton, C. B., and Deierlein, G. G. (2010). Seismic Collapse Safety of Reinforced concrete Buildings. II: Comparative Assessment of Nonductile and Ductile Moment Frames. *J. Struct. Eng.* 137 (4), 492–502.

Lowes, L. N., Mitra, N., and Altoontash, A. (2003). *A Beam-Column Joint Model for Simulating the Earthquake Response of Reinforced Concrete Frames. University of California*. Berkeley: Pacific Earthquake Engineering Research Center.

Lowes, L. N., and Altoontash, A. (2003). Modeling Reinforced-Concrete Beam-Column Joints Subjected to Cyclic Loading. *J. Struct. Eng.* 129, 1686–1697. doi:10.1061/(asce)0733-9445(2003)129:12(1686)

Mayes, R. L., and Clough, R. W. (1975). "State of the Art in Seismic Shear Strength of Masonry – an Evaluation and Review,". EERC Report (CA: University of Berkeley).

McKenna, F., Fenves, G. L., and Scott, M. H. (2010). *OpenSees: Open System for Earthquake Engineering Simulation, Pacific Earthquake Engineering Research Center*. Berkeley, CA, USA: University of California. http://opensees.berkeley.edu.

Mitra, N., and Lowes, L. N. (2007). Evaluation, Calibration, and Verification of a Reinforced Concrete Beam-Column Joint Model. *J. Struct. Eng.* 133 (1), 105–120. doi:10.1061/(asce)0733-9445(2007)133:1(105)

Otani, S. (1974). Inelastic Analysis of R/C Frame Structures. *J. Struct. Division* 100, 1433–1449. doi:10.1061/jsdeag.0003821

Pantelides, C. P., Hansen, J., Nadauld, J., and Reavely, L. D. (2002). "Assessment of Reinforced concrete Building Exterior Joints with Substandard Details,". PEER Report 2002/18 (Berkeley, CA: Pacific Earthquake Engineering Research Center, College of Engineering, University of California).

Park, Y. J., and Ang, A. H. S. (1985). Mechanistic Seismic Damage Model for Reinforced concrete. *J. Struct. Eng.* 111 (4), 722–739. doi:10.1061/(asce)0733-9445(1985)111:4(722)

Realfonzo, R., Napoli, A., and Pinilla, J. G. R. (2014). Cyclic Behavior of RC Beam-Column Joints Strengthened with FRP Systems. *Construction Building Mater.* 54, 282–297. doi:10.1016/j.conbuildmat.2013.12.043

Reyes de Ortiz, I. (1993). "Strut-and-Tie Modeling of Reinforced Concrete Short Beams and Beam-Column Joints,". Ph.D. Thesis (London, United Kingdom: University of Westminster).

Saleh, A., Elwan, S. K., Elzeiny, S., Hamad, M., and Deifalla, A. (2021). Numerical Modeling the Effect of an Opening on the Behavior of Exterior Beam-Column Connections under Cyclic Loading. *J. Building Eng.* 40, 102742. doi:10.1016/j.jobe.2021.102742

Shafaei, J., Zareian, M. S., Hosseini, A., and Marefat, M. S. (2014). Effects of Joint Flexibility on Lateral Response of Reinforced concrete Frames. *Eng. Structures* 81, 412–431. doi:10.1016/j.engstruct.2014.09.046

Sharma, A., Eligehausen, R., and Reddy, G. R. (2011). A New Model to Simulate Joint Shear Behavior of Poorly Detailed Beam-Column Connections in RC Structures under Seismic Loads, Part I: Exterior Joints. *Eng. Structures* 33 (3), 1034–1051. doi:10.1016/j.engstruct.2010.12.026

Shin, M., and LaFave, J. M. (2004). Modeling of Cyclic Joint Shear Deformation Contributions in RC Beam-Column Connections to Overall Frame Behavior. *Struct. Eng. Mech.* 18 (5), 645–669. doi:10.12989/sem.2004.18.5.645

Stevens, N. J., Uzumeri, S. M., and Collins, M. P. (1991). Reinforced-Concrete Subjected to Reverse-Cyclic Shear – Experiment and Constitutive Model. *ACI Struct. J.* 88 (2), 135–146.

Theiss, A. G. (2005). "Modeling the Earthquake Response of Older Reinforced Concrete Beam-Column Building Joints,"M.Sc. Thesis (University of Washington).

Tsonos, A. G. (2002). Seismic Repair of Exterior R/C Beam-To-Column Joints Using Two-Sided and Three-Sided Jackets. *Struct. Eng. Mech.* 13 (1), 17–34. doi:10.12989/sem.2002.13.1.017

Uzumeri, S. M. (1977). "Strength and Ductility of Cast-In-Place Beam-Column Joints," in American Concrete Institute Annual Convention. Symposium on Reinforced Concrete Structures in Seismic Zones, 293–350.

Vecchio, F. J., and Collins, M. P. (1986). The Modified Compression-Field Theory for Reinforced Concrete Elements Subjected to Shear. *ACI J.* 83 (2), 219–231.

Vollum, R. L., and Newman, J. B. (1999). Strut and Tie Models for Analysis/design of External Beam-Column Joints. *Mag. Concrete Res.* 51 (6), 415–425. doi:10.1680/macr.1999.51.6.415

Walker, S. G. (2001). "Seismic Performance of Existing RC Beam–Column Joints,". M.Sc. Thesis (University of Washington).

Wong, H. F. (2005). "Shear Strength and Seismic Performance of Non-seismically Designed Reinforced concrete Beam-Column Joints,". Ph.D. Thesis (The Hong Kong University of Science and Technology, Department of Civil Engineering). doi:10.14711/thesis-b914043

Youssef, M., and Ghobarah, A. (2001). Modelling of RC Beam-Column Joints and Structural walls. *J. Earthquake Eng.* 5 (1), 93–111. doi:10.1080/13632460109350387

Conflict of Interest: The authors declare that the research was conducted in the absence of any commercial or financial relationships that could be construed as a potential conflict of interest.

Publisher's Note: All claims expressed in this article are solely those of the authors and do not necessarily represent those of their affiliated organizations, or those of the publisher, the editors and the reviewers. Any product that may be evaluated in this article, or claim that may be made by its manufacturer, is not guaranteed or endorsed by the publisher.

GLOSSARY

The symbols used within the paper are reported herein:

A (mm^2) joint cross-section area

$A_{s,b}$ (mm^2) area of the beam longitudinal reinforcement in tension

$A_{s,c}$ (mm^2) total area of the column longitudinal reinforcement

BI (-) beam reinforcement index equal to $(A_{s,b} \cdot f_{yb})/(b_b \cdot h_b \cdot f_c)$

$D^+_{max,i}$ (mm) displacement corresponding to $F^+_{max,i}$

$D^-_{max,i}$ (mm) displacement corresponding to $F^-_{max,i}$ (kN)

E_i (N mm) accumulated hysteretic energy at the *i*th displacement increment

$E_{monotonic}$ (N mm) energy required to achieve under monotonic loading the deformation that defines failure

$E^{exp}_{d,i}$ (N mm) experimental dissipated energy calculated at the *i-th* displacement cycle

$E^{num}_{d,i}$ (N mm) numerical dissipated energy calculated at the *i-th* displacement cycle

$E_{rr,En}$ (%) mean absolute percentage error calculated on the dissipated energy parameter

$E_{rr,F}$ [%] mean absolute percentage error calculated on the force parameter

$E_{rr,K}$ (%) mean absolute percentage error calculated on the stiffness degradation parameter

$E_{rr,\tau}$ (%) mean absolute percentage error calculated on the shear strength parameter

$F_{exp,i}$ (kN) *i*th value of the experimental force

$F^+_{max,i}$ (kN) peak lateral force applied to the beam in the push loading direction at the *i*th displacement cycle

$F^-_{max,i}$ (kN) peak lateral force applied to the beam in the pull loading direction at the *i*th displacement cycle

$F_{num,i}$ (kN) *i*th value of the numerical force

K_i (N/mm) stiffness loss at *i*th displacement cycle

K^{exp}_i(N/mm) experimental stiffness calculated at the *i-th* displacement cycle

K^{num}_i(N/mm) numerical stiffness calculated at the *i-th* displacement cycle

L_b (mm) beam length

L_c (mm) column length

M (kN m) generic bending moment corresponding to the joint shear stress

M_j (kN m) *j*th bending moment corresponding to the *j*th shear stress τ_j

M^s_1 (kN mm) bending moment at beam cracking associated to the slip s_1

M^s_2 (kN mm) bending moment at pre-peak phase associated to the slip s_2

M^s_3 (= Mmaxs) (kN m) maximum bending moment associated to the slip s_3

M^s_4 (kN m) residual bending capacity associated to the slip s_4

N (N) axial force applied to the column

T_b (N) tensile force acting in the beam longitudinal bars

V_{col} (N) column shear force

X_j (-) *j*th predictor (independent) variable

Y (-) response (dependent) variable

a_b (mm) depth of the neutral axis in the beam, evaluated assuming plane section

b_b (mm) width of the beam cross-section

b_c (mm) width of the column cross-section

b_j (mm) effective joint width, equal to bj = minbc; (bc + bb/2]

d-d′ (mm) distance between the longitudinal reinforcements in tension and compression of the beam

d_{max} (mm) maximum historic deformation demands

d_{min} (mm) minimum historic deformation demands

$d_{max,i}$ (mm) current deformation defining the end of the reload cycle for increasing deformation demand

$d_{max,0}$ (mm) maximum (or minimum) historic deformation demand

def_{max} (mm) positive deformations that define failure

def_{min} (mm) negative deformations that define failure

f_c (MPa) cylinder compressive strength of concrete

$f_{max,i}$ (kN) current envelope maximum strength

$f_{max,0}$ (kN) initial envelope maximum strength for the case of no damage

$f_{stm,tr}$ (MPa) mean value of the maximum tensile stress developed in the bar that can be transferred by bond

$f_{st,0}$ (MPa) maximum bond stress estimated in absence of confining effect

f_{yb} (MPa) steel yield strength of beam reinforcement

f_{yc} (MPa) steel yield strength of column reinforcement;

gE (-) multiplication factor used to define the maximum energy dissipation under cyclic loading

k_i (N/mm) current unloading stiffness

k_0 (N/mm) k_0 is the initial unloading stiffness for the case of no damage

h_b (mm) height of the beam cross-section

h_c (mm) height of the column cross-section

jd_b (mm) beam internal lever arm

l_b (mm) anchorage length of the longitudinal bar (the bond stress is assumed uniform over this length)

m (-) number of available measures

n (-) total number of measures considered in the analysis

p_{tr} (MPa) the transverse pressure in the column (equal to σj)

s (mm) slip of the beam's reinforcing bars under tension

s_1 (mm) slip s associated to the bending moment at beam crackingM1s

s_2 (mm) slip s associated to the bending moment at pre-peak phase M2s

s_3 (mm) slip s associated to the maximum bending moment M3s

s_4 (mm) slip s associated to the residual bending capacity M4s

θ (mm) longitudinal bar diameter;

α_j (-) *j*th parameter required to fit the damage rule to experimental data

β_j (-) coefficient of the regression analysis

γ (-) generic shear strain value

γ_j (-) *j*th joint shear strain

γ_1 (-) shear strain corresponding to τ_1

γ_2 (-) shear strain corresponding to τ_2

γ_3 (-) shear strain corresponding to $\tau_3 = \tau_{max}$

γ_4 (-) shear strain corresponding to τ_4

δ_i (-) damage index at the *i*th displacement increment (0 in case of no damage, 1 in case of maximum damage)

δ_{lim} (-) maximum possible value of the damage index

δd_i (-) current value of the reloading – strength damage index

δf_i (-) current value of the strength damage index

δk_i (-) current value of the stiffness damage index

θ (rad) generic rotation corresponding to the joint shear strain

θ_j (rad) *j*th joint rotation

θ^s (rad) joint rotation due to slip of the beam's reinforcing bars under tension

λ (-) parameter accounting for the bending shape of the beam's longitudinal steel bar end inside the joint ($\lambda = 1.0$ in the case of a "L-shape" configuration; $\lambda = 0.9$ in the case of a "U-shape" one)

σ_j (MPa) ratio between the column axial load (N) and the corresponding cross-section area bc·hc of the column

τ (MPa) generic shear stress value

τ_j (MPa) *j*th joint shear stress

τ_1 (MPa) shear stress at joint craking

τ_2 (MPa) shear stress at pre-peak phase

τ_3 ($= \tau_{max}$) (MPa) shear stress at peak

τ_4 (MPa) residual shear strength

φ angle between the strut and the longitudinal beam axis

frontiers in Materials

ORIGINAL RESEARCH
published: 06 September 2021
doi: 10.3389/fmats.2021.737646

Mechanical Behavior of Reactive Powder Concrete Made From Local Material Subjected to Axial Pressure

Jing Ji[1,2], Wei Kang[1], Liangqin Jiang[1], Yunhao Li[1], Hongguo Ren[3], Sixue Hao[3], Lingjie He[1], Yubo Lin[1] and Chenyu Yu[1]*

[1]Heilongjiang Key Laboratory of Disaster Prevention, Mitigation and Protection Engineering, Northeast Petroleum University, Daqing, China, [2]Key Laboratory of Structural Disaster and Control of the Ministry of Education, Harbin Institute of Technology, Harbin, China, [3]Handan Key Laboratory of Building Physical Environment and Regional Building Protection Technology, School of Architecture and Art, Hebei University of Engineering, Handan, China

In order to investigate the influence of various parameters on the compressive strength and fluidity of reactive powder concrete (RPC) made from local materials, 22 groups of RPC cubic specimens and 3 groups of RPC prism specimens were designed, and the main parameters included water to binder ratio, the ratio of silica fume to cement, the ratio of slag powder to cement, the ratio of quartz sand to cement, volume fraction of steel fiber, and steam curing time. The stress-strain curves and failure mode of RPC cubic specimens were obtained by the axial compression test. The influence of various parameters on the compressive mechanical properties and the mixture fluidity of RPC cubic specimens was analyzed. The results showed that the ultimate compressive strength (f_{cu}) of RPC gradually decreases with the increase in the water to binder ratio; however, f_{cu} increases with the increase in the volume fraction of steel fiber. f_{cu} increases firstly and then decreases with the increase in the ratio of silica fume to cement, the ratio of slag powder to cement, and the ratio of quartz sand to cement, so there exists a peak point. The fluidity of RPC mixture increases with the increase in the water to binder ratio and the ratio of slag powder to cement; on the contrary, it decreases with the increase in the ratio of silica fume to cement, the ratio of quartz sand to cement, and volume fraction of steel fiber. Based on the analysis of the parameters, the optimal mix proportion of the RPC made from local materials is proposed. The constitutive model of RPC is established according to the stress-strain curves of RPC prism specimens. Finally, the relationship between compressive strength and elastic modulus of RPC made of local materials is regressed statistically.

Keywords: reactive powder concrete, fluidity, compressive strength, optimal mix proportion, constitutive model

OPEN ACCESS

Edited by:
Kequan Yu,
Tongji University, China

Reviewed by:
Wenyang Liu,
IFET College of Engineering, India
Yan Kai,
Shandong Jianzhu University, China

****Correspondence:***
Hongguo Ren
renhongguo771126@163.com

Specialty section:
This article was submitted to Structural Materials, a section of the journal Frontiers in Materials

Received: *07 July 2021*
Accepted: *04 August 2021*
Published: *06 September 2021*

Citation:
Ji J, Kang W, Jiang L, Li Y, Ren H, Hao S, He L, Lin Y and Yu C (2021) Mechanical Behavior of Reactive Powder Concrete Made From Local Material Subjected to Axial Pressure. Front. Mater. 8:737646. doi: 10.3389/fmats.2021.737646

INTRODUCTION

Reactive powder concrete (RPC), as a new type of high performance concrete material, has excellent mechanical properties, durability, and volume stability, which has been applied in practical projects (Abid et al., 2017; Salahuddin et al., 2020). As we know, there are great differences between RPC and ordinary concrete in composition and microstructure; therefore, it is necessary to study the mechanical properties of RPC made from local material (Xia et al., 2015). Many research studies on the mix proportion, mechanical properties, and durability of RPC materials have been carried out around the world, and it is certain that the mix proportion is the key factor affecting the performance of the RPC material.

The principles of mix proportion design, mechanical properties, durability, and high-temperature resistance of RPC were summarized by W. Zheng, and it could be known that RPC possessed excellent performance of chloride ion permeability resistance, carbonation resistance, frost thawing resistance, and sulfate resistance (Zheng et al., 2015). Based on the orthogonal experiment, the influence of different parameters on the mechanical properties and mixing flow of RPC was studied, and the mix proportion design of RPC was optimized by He et al. (2016). The mix proportion design and curing technology of RPC were obtained by Ola et al. (2021), and the results showed that the compressive strength could be improved obviously by adding the content of the quartz powder in RPC, and RPC cured by autoclave could achieve higher compressive strength than that cured by steam. Fiber reinforced polymers (steel fiber, glass fiber, carbon fiber, and basalt fiber) were added to RPC by some researchers, and the mechanical behavior of RPC mixed with FRP was obtained, and the results showed that the toughness of RPC was greatly improved with the increase in FRP (Deng et al., 2016; Syed et al., 2021). RPC had been used in steel-concrete composite structures, and the shear bearing capacity formula of RPC beams under bending and shear was proposed by Maha et al. (2018). The flexural behavior of reinforced concrete beams strengthened by RPC would be greatly improved, and the test results showed that, due to the existence of RPC, the high ductility of reinforcement was fully utilized in the process of plastic hinge formation (Zbigniew et al., 2020). The failure experiments of RPC materials under complex stress states were carried out successively. Based on the triaxial compression test of RPC under different peripheral pressure, the failure mode and failure criterion of RPC were obtained by X. Qin, and the results showed that the RPC specimens under different peripheral pressures mainly showed oblique shear failure (Qin, 2011). The biaxial compression test of RPC was carried out by Z. Li, and the failure criterion of RPC under biaxial compression was obtained. Based on the Ottosen constitutive model, the constitutive model of RPC under biaxial compression was proposed (Li, 2013). Subsequently, the biaxial tension-compression test of RPC was conducted by Y. Jiang, and the constitutive model in the tensile direction was established according to Weibull distribution (Jiang, 2014). Although the mix proportion of RPC has been widely studied around the world, there exist great differences in selecting materials in different area, and the performance of RPC obtained by different studies is discrete and lacks unified reference significance. Therefore, the mix proportion of RPC made from local materials should be optimized to accurately grasp its mechanical properties, which is crucial for the application of RPC materials in the local area.

The mix proportion design, material selection, and mixing process of RPC are introduced in this paper, and the influence of various parameters on the mechanical properties and fluidity of RPC is analyzed. Based on the test results, the constitutive model of RPC and the relationship between elastic modulus and compressive strength are established.

EXPERIMENTAL PROGRAM

Specimens Design

In order to study the compressive mechanical properties and the fluidity of reactive powder concrete made from local materials, water to binder ratio (w/b), the ratio of silica fume to cement (s/c), the ratio of slag powder to cement (p/c), the ratio of quartz sand to cement (q/c), volume fraction of steel fiber (f), and steam curing time (t) were taken as main parameters, and 22 groups of RPC cubic specimens and 3 groups of RPC prism specimens were designed. The specific parameters were shown in **Table 1**. The dimensions of Fi, Gi, and Hi groups were 70.7 × 70.7 × 230 mm (prism specimens), and the other groups were 70.7 × 70.7 × 70.7 mm (cubic specimens). The parameters of three groups of prism specimens were selected from cube specimens. The volume fraction of steel fiber in **Table 1** was the volume ratio of steel fiber to mixture, and other components were their mass ratio to cement. The number after F, G, and H indicated the days of steam curing.

The water to binder ratio referred to the mass ratio of water to gel material, and the expression was as follows:

$$w/b = \frac{M_w}{M_b} \tag{1}$$

$$M_b = M_c + M_s + M_p \tag{2}$$

where M_w and M_b were the mass of water and gel material, respectively. M_c, M_s, and M_p were the mass of cement, silica fume, and slag powder, respectively.

MATERIALS

Cement and Silica Fume

The cement was P.O 42.5 ordinary Portland cement produced by Jilin Yatai company. The bulk density of silica fume was 200–250 kg/m^3, and the fineness less than 1 μm accounted for more than 80%, and the average particle size was 0.1–0.3 μm, and the specific surface area was 20–80 m^2/kg. The SiO_2 content in silica fume was 75–96%.

Quartz Sand and Slag Powder

The graded quartz fine sand with two particle sizes of 40–70 mesh and 70–140 mesh (produced by Harbin Jinghua water treatment material company) was selected as quartz sand, and its physical indexes and chemical composition were shown in **Table 2**. S95 blast furnace slag was selected as slag powder.

Steel Fiber and Superplasticizer

The steel fiber was selected from Anshan Changhong steel fiber factory with a diameter of 0.22 mm and a length of 13 mm. FDN concentrated superplasticizer which can be purchased locally was selected as superplasticizer, and the product was yellowish brown powder.

Mixing Process and Fluidity Measurement

Due to the great difference between RPC and ordinary concrete, the mixing method of traditional concrete could not be used.

TABLE 1 | The main parameters of RPC specimens.

Specimen number	Cement *c/c*	Water to binder ratio *w/b*	The ratio of silica fume to cement *s/c*	The ratio of slag powder to cement *p/c*	The ratio of quartz sand to content *q/c*	Volume fraction of steel fiber *f* (%)
A1	1	0.22	0.3	0.25	1.2	0
A2	1	0.2	0.3	0.25	1.2	0
A3	1	0.18	0.3	0.25	1.2	0
A4	1	0.16	0.3	0.25	1.2	0
B1	1	0.2	0.2	0.25	1.2	0
B2	1	0.2	0.4	0.25	1.2	0
B3	1	0.2	0.5	0.25	1.2	0
C1	1	0.2	0.3	0.15	1.2	0
C2	1	0.2	0.3	0.35	1.2	0
C3	1	0.2	0.3	0.4	1.2	0
D1	1	0.2	0.3	0.25	1.4	0
D2	1	0.2	0.3	0.25	1.6	0
D3	1	0.2	0.3	0.25	1.8	0
E1	1	0.2	0.3	0.25	1.2	1
E2	1	0.2	0.3	0.25	1.2	2
E3	1	0.2	0.3	0.25	1.2	3
F0	1	0.2	0.3	0.25	1.2	0
G0	1	0.16	0.3	0.25	1.2	0
H0	1	0.2	0.3	0.25	1.2	2
F6	1	0.2	0.3	0.25	1.2	0
G6	1	0.16	0.3	0.25	1.2	0
H6	1	0.2	0.3	0.25	1.2	2
Fi	1	0.2	0.3	0.25	1.2	0
Gi	1	0.16	0.3	0.25	1.2	0
Hi	1	0.2	0.3	0.25	1.2	2

TABLE 2 | Physical indexes and chemical composition of quartz sand.

Specifications		Chemical composition/%	
Mesh number	Particle size/*μm*	SiO_2	Al_2O_3
40~70 mesh	0.38~0.212	≥99.6	≥0.02
70~140 mesh	0.212~0.106	≥99.6	≥0.02

According to the mixing experience obtained from existing research, the mixing process was adopted as shown in **Figure 1**.

1) The cementitious materials such as quartz sand, cement, silica fume, and slag powder were weighed according to the mix proportion.
2) The materials were poured into JJ-5 cement blender and were mixed for 2 min to make them even.
3) Water and superplasticizer were added to blender, and the mixture was stirred slowly for 4 min and then stirred quickly for 4 min.
4) For the experimental groups with steel fiber, steel fiber was added after stirring quickly; then the mixture was stirred for 5 min again.
5) Once the mixing was completed, the mixture was put into the fluidity test mold, and the fluidity of RPC mixture was measured according to the principle of jump table method proposed by test method for fluidity of cement mortar.

Preparation and Curing of Specimens

After the fluidity was measured, we poured the mixture into the triple rubber sand mold and vibrated it with ZHDG-80 concrete shaking table and then levelled it with a spatula. After the specimens were formed, some specimens were cured by steam at 80°C for 3 days or 6 days, and the other specimens were not cured by steam. At last, all the specimens were cured by spraying water at room temperature until being tested after 28 days, as shown in **Figure 2**.

Specimen Test

In order to obtain the compressive stress-strain curve, elastic modulus, and Poisson's ratio of RPC specimens, the compressive strength test was conducted on the axial compression testing machine in Heilongjiang Key Laboratory of Disaster Prevention, Mitigation, and Protection Engineering. To measure the transverse and longitudinal strain of the specimens, the strain gauges were pasted on two sides of the specimens along longitudinal and transverse directions, as shown in **Figure 3**.

The double control automatic loading of load and displacement was adopted in this experiment. The formal loading of the specimens was carried out after preloading. At the initial period of formal loading, the load control at a rate of 0.5 kN/s was adopted as loading mode. When the load reached 50% of the predicted peak load, it turned into displacement control at a rate of 0.02 mm/s until the specimens failed.

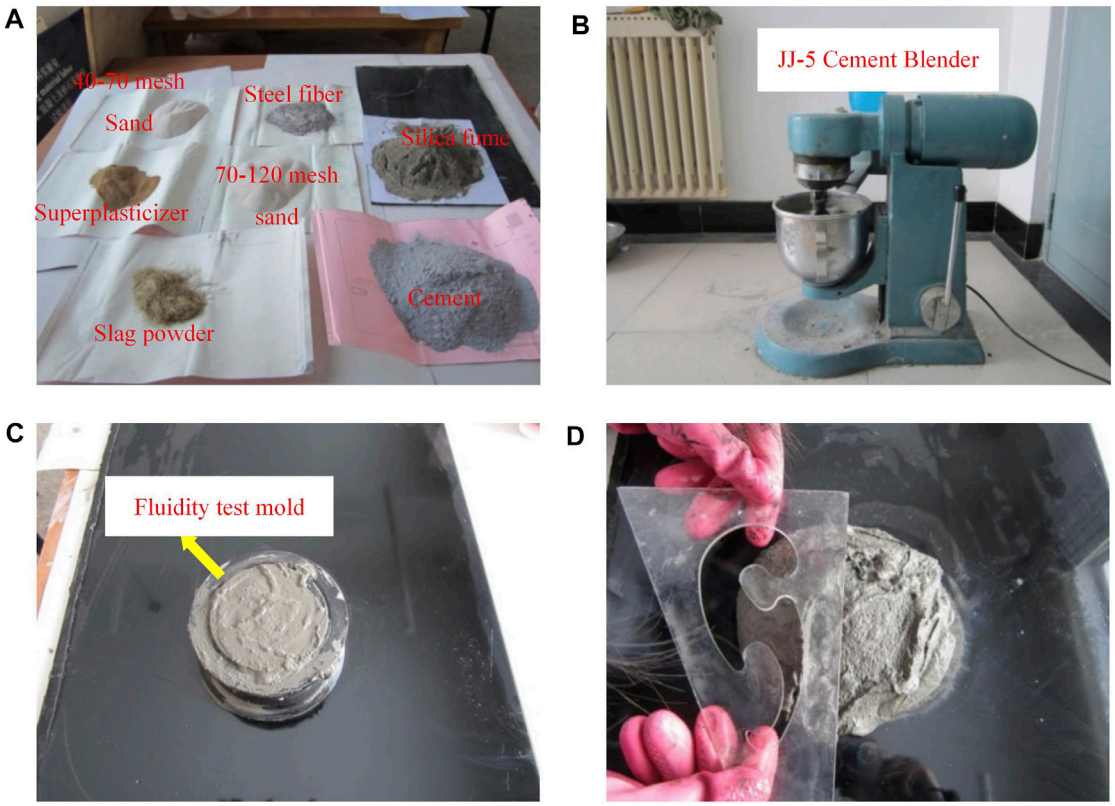

FIGURE 1 | Mixing process: **(A)** Weighing of components; **(B)** mixing of materials; **(C)** fluidity test mold; **(D)** fluidity measurement.

Test Phenomena

The RPC specimens without steel fiber had no obvious change at the initial formal loading. With the increase in the load, the phenomenon of the concrete spalling could be seen at the surface of the specimens. Later on, the failure of specimens happened accompanied by loud sound and violent reaction as the peak loads were reached. For the RPC specimens with steel fiber, the stress-strain relationship was linear at the initial loading period, and there was no obvious phenomenon on the surface of specimens. When the load approximately reached 0.5 times of the peak load, the splitting sound began to appear. With the increase in the load, the width and number of cracks increased gradually, and the debris began to peel off from the surface of the specimens accompanied by louder splitting sound. Then, the specimens entered unstable state, and the cracks showed a trend of penetration. The compressive stress-strain curves of the specimens entered the plastic stage. After reaching peak stress, obvious vertical cracks appeared on the surface of the specimens, and the stress-strain curves began to decline. It could be seen that, compared with the RPC specimens without steel fiber, the RPC specimens with steel fiber had a certain buffer for the development of cracks due to the anticracking of steel fiber. As a result, brittle failure did not occur. The failure modes of the two kinds of specimens were shown in **Figure 4**.

RESULTS AND DISCUSSION

Test Results

The test result of fluidity (h) and ultimate compressive strength (f_{cu}) of 22 groups of cube specimens are shown in **Table 3**, and the test values of compression mechanical indexes of 3 groups of prism specimens are shown in **Table 4**. The data value of elastic modulus in **Table 4** is obtained according to the slope of the elastic stage of the stress-strain curves.

Parameter Analysis

Water to Binder Ratio

The comparison of the stress-strain curves of the specimens with different water to binder ratios is shown in **Figure 5A**, and the influence of different water to binder ratios on the ultimate compressive strength and mixture fluidity of RPC specimens is shown in **Figure 5B**. It can be seen from **Figure 5** and **Table 3** that when the water to binder ratio of the specimens decreases from 0.22 to 0.20, 0.18, and 0.16 in turn, the ultimate compressive strength of the specimens increases from 84.83 to 93.42, 95.43, and 99.74 Mpa in order, which increases by 10.13, 12.50, and 17.58%, respectively. When the water to binder ratio of the mixture decreased from 0.22 to 0.20, 0.18, and 0.16 in turn, the fluidity of RPC mixture decreased from 159 to 139, 104, and 98 mm in order, which decreases by 12.58, 34.59, and 38.36%,

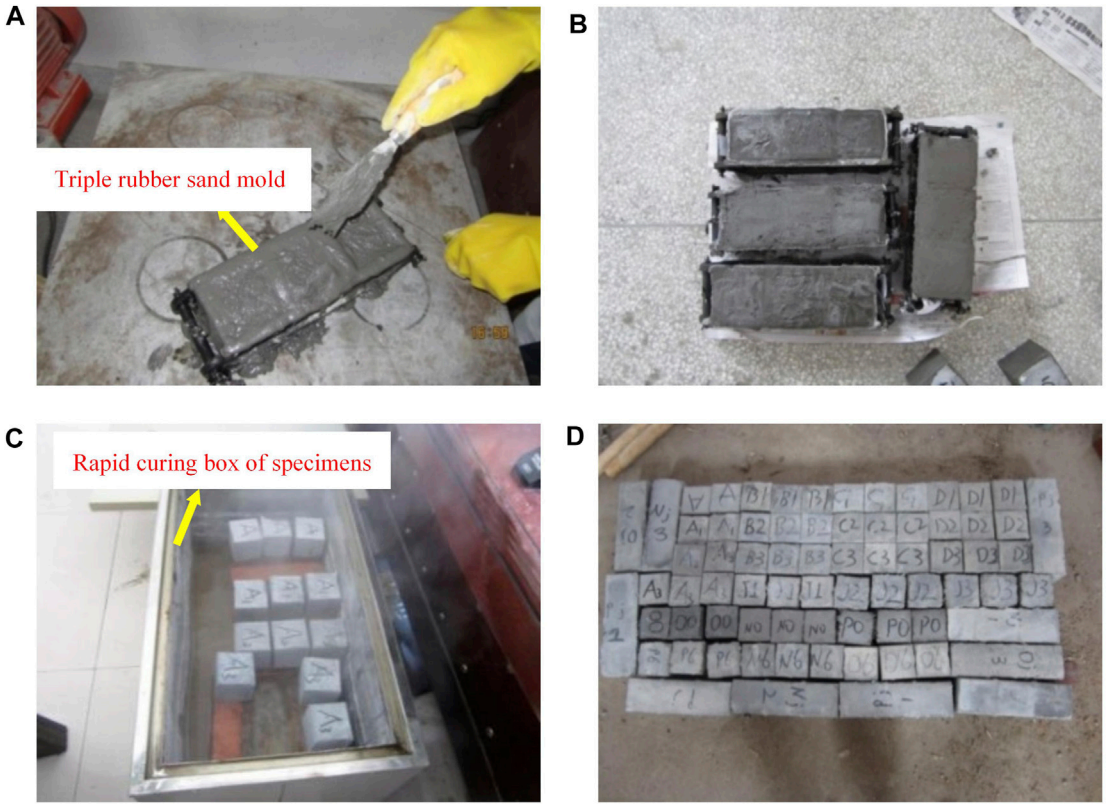

FIGURE 2 | Specimens production process; **(A)** concrete mold forming; **(B)** room temperature curing. **(C)** Rapid curing box of specimens. **(D)** Specimens.

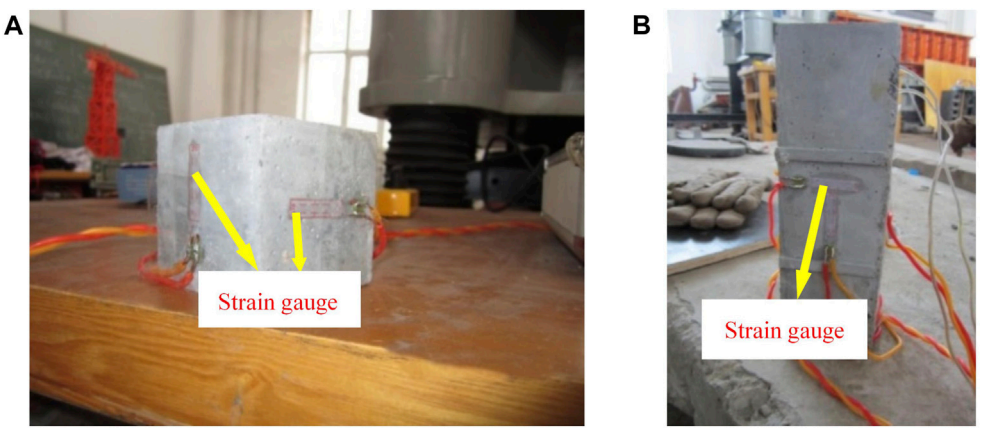

FIGURE 3 | Strain gauge layout of specimens. **(A)** Strain gauge layout of cube specimen; **(B)** strain gauge layout of prism specimen.

respectively. It can be seen that, with the increase in the water to binder ratio, the fluidity of RPC mixture increases, while the ultimate compressive strength of the cube specimen decreases.

The Ratio of Silica Fume to Cement

The comparison of stress-strain curves of specimens with different ratios of silica fume to cement is shown in **Figure 6A**, and the influence of different ratios of silica fume to cement on the ultimate compressive strength and mixture fluidity of RPC specimens is shown in **Figure 6B**. It can be seen from **Figure 6** and **Table 3** that when the ratio of silica fume to cement of the specimen increases from 0.2 to 0.3, 0.4, and 0.5 in turn, the ultimate compressive strength of the specimen increases from 73.82 to 93.42, 77.23, and 87.58 Mpa in order, which increases by 26.55, 4.61, and 18.65%, respectively. When the ratio of silica fume to cement of the mixture increases from 0.2 to 0.3, 0.4, and 0.5 in turn, the fluidity of RPC

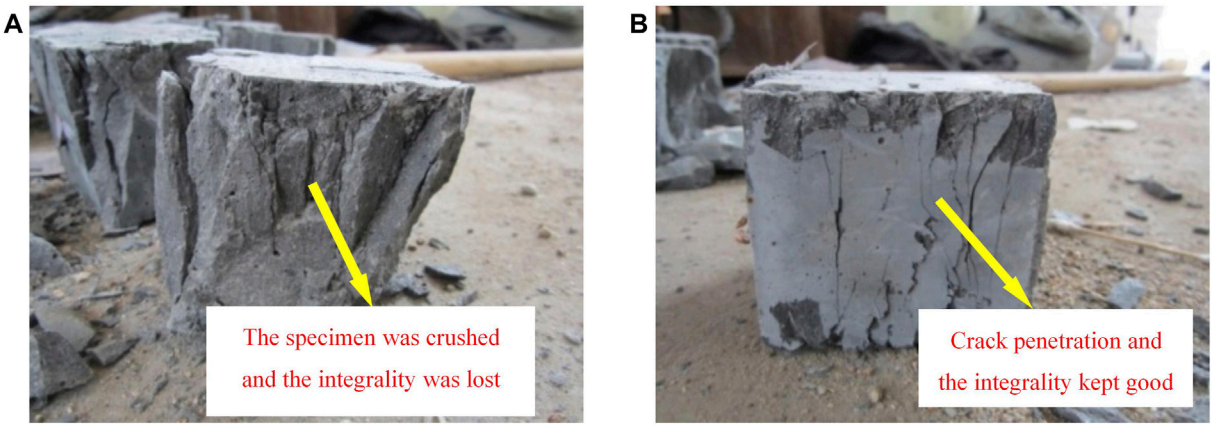

FIGURE 4 | Failure mode of specimen. **(A)** Failure mode of specimens without steel fiber; **(B)** failure mode of specimens with steel fiber.

TABLE 3 | Compression test results of 22 groups of cube specimens.

Specimen number	*c/c*	*w/b*	*s/c*	*p/c*	*q/c*	*f* (%)	*h*/mm	f_{cu}/Mpa
A1	1	0.22	0.3	0.25	1.2	0	159	84.83
A2	1	0.20	0.3	0.25	1.2	0	139	93.42
A3	1	0.18	0.3	0.25	1.2	0	104	95.43
A4	1	0.16	0.3	0.25	1.2	0	98	99.74
B1	1	0.2	0.2	0.25	1.2	0	144	73.82
B2	1	0.2	0.4	0.25	1.2	0	124	77.23
B3	1	0.2	0.5	0.25	1.2	0	98	87.58
C1	1	0.2	0.3	0.15	1.2	0	120	85.20
C2	1	0.2	0.3	0.35	1.2	0	140	91.39
C3	1	0.2	0.3	0.4	1.2	0	143	76.16
D1	1	0.2	0.3	0.25	1.4	0	138	80.36
D2	1	0.2	0.3	0.25	1.6	0	135	83.99
D3	1	0.2	0.3	0.25	1.8	0	117	75.23
E1	1	0.2	0.3	0.25	1.2	1	122	130.45
E2	1	0.2	0.3	0.25	1.2	2	123	154.18
E3	1	0.2	0.3	0.25	1.2	3	124	167.02
F0	1	0.2	0.3	0.25	1.2	0	136	56.35
G0	1	0.16	0.3	0.25	1.2	0	100	60.53
H0	1	0.2	0.3	0.25	1.2	2	107	82.50
F6	1	0.2	0.3	0.25	1.2	0	136	74.16
G6	1	0.16	0.3	0.25	1.2	0	100	84.18
H6	1	0.2	0.3	0.25	1.2	2	107	159.96

mixture decreases from 144 to 139, 124, and 98 mm in order, which decreases by 3.47, 13.89, and 31.94%, respectively. It can be seen that, with the increase in the ratio of silica fume to cement, the fluidity of the mixture decreases gradually, and the ratio of silica fume to cement corresponding to the peak of ultimate compressive strength of the cube specimens is taken as 0.3.

The Ratio of Slag Powder to Cement

The comparison of stress-strain curves of RPC specimens with different ratios of slag powder to cement is shown in **Figure 7A**, and the influence of different ratios of slag powder to cement on the ultimate compressive strength and mixture fluidity of RPC specimens is shown in **Figure 7B**. It can be seen from **Figure 7** and **Table 3** that when the ratio of slag powder to cement of the specimens increases from 0.15 to 0.25, 0.35, and 0.4 in turn, the ultimate compressive strength of the specimens increases from 85.20 to 93.42, 91.39, and 76.16 Mpa in order, which increases by 9.65%, 7.27%, and −10.61%, respectively. When the ratio of slag powder to cement of the mixture increases from 0.15 to 0.25, 0.35, and 0.4 in turn, the fluidity of RPC mixture increases from 120 to 139, 140, and 143 mm in order, which increases by 15.83, 16.67, and 19.17%, respectively. It can be seen that, with the increase in the ratio of slag powder to cement, the fluidity of mixture increases. The ratio of slag

TABLE 4 | Test values of compressive mechanical indexes of 3 groups of prism specimens.

Specimen number	Compressive strength of prism f_c'/MPa	Strain corresponding to peak stress *Mε*	Elastic modulus *E*/GPa	Poisson's ratio *υ*
Fi-1	72.52	2,166	37.59	0.182
Fi-2	89.31	2,987	40.10	0.173
Fi-3	87.41	2,788	39.20	0.169
Gi-1	89.22	2,230	40.08	0.165
Gi-2	93.65	2,580	41.20	0.176
Gi-3	85.76	2,660	39.88	0.167
Hi-1	113.11	3,372	46.80	0.252
Hi-2	99.04	3,445	45.03	0.220
Hi-3	90.94	3,556	42.05	0.246

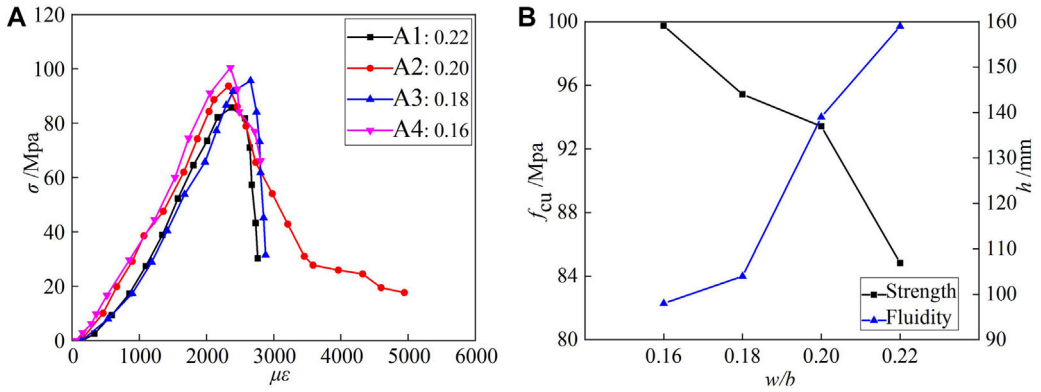

FIGURE 5 | The influence of different water to binder ratios on RPC mechanical properties. **(A)** Stress-strain curves of RPC specimens with different water to binder ratios. **(B)** Ultimate compressive strength and mixture fluidity of RPC with different water to binder ratios.

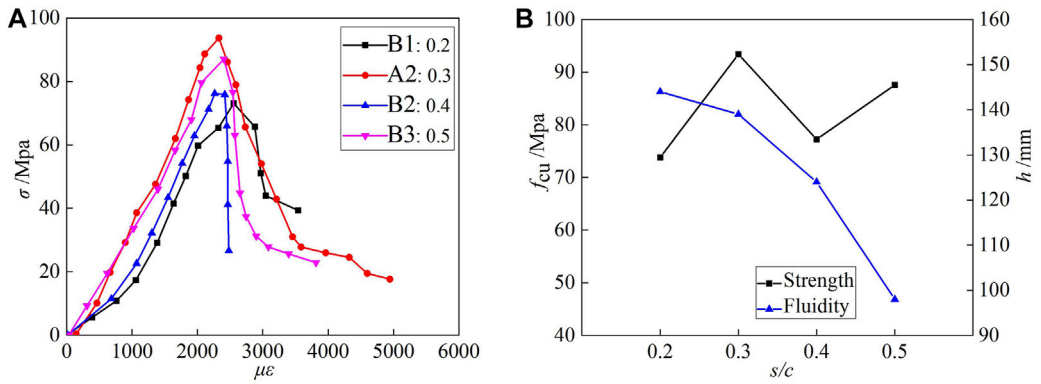

FIGURE 6 | The influence of different ratios of silica fume to cement on RPC mechanical properties. **(A)** Stress-strain curves of RPC specimens with different ratios of silica fume to cement; **(B)** ultimate compressive strength and mixture fluidity of RPC with different ratios of silica fume to cement.

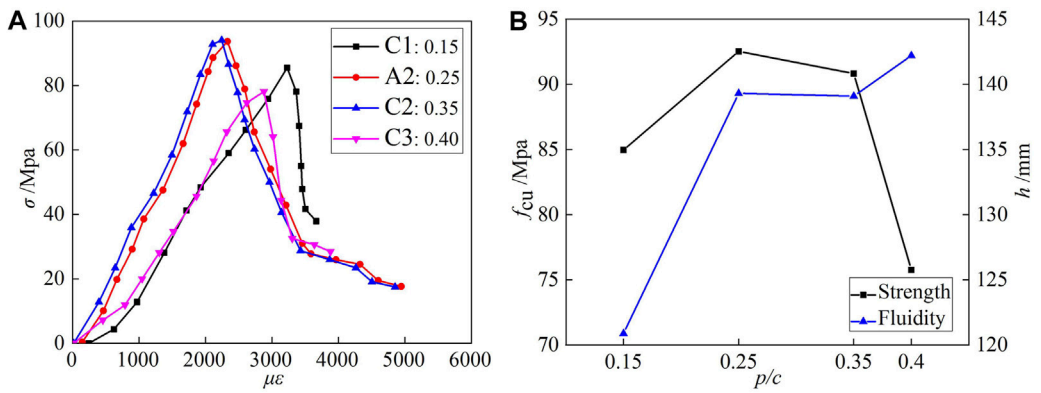

FIGURE 7 | The influence of different ratios of slag powder to cement on RPC mechanical properties. **(A)** Stress-strain curves of RPC specimens with different ratios of slag powder to cement; **(B)** ultimate compressive strength and mixture fluidity of RPC with different ratios of slag powder to cement.

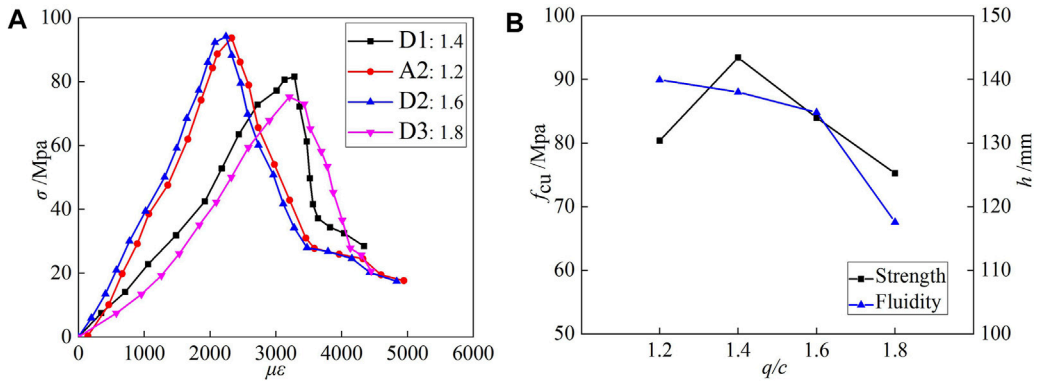

FIGURE 8 | The influence of different ratios of quartz sand to cement on RPC mechanical properties. **(A)** Stress-strain curves of RPC specimens with different ratios of quartz sand to cement. **(B)** Ultimate compressive strength and mixture fluidity of RPC with different ratios of quartz sand to cement.

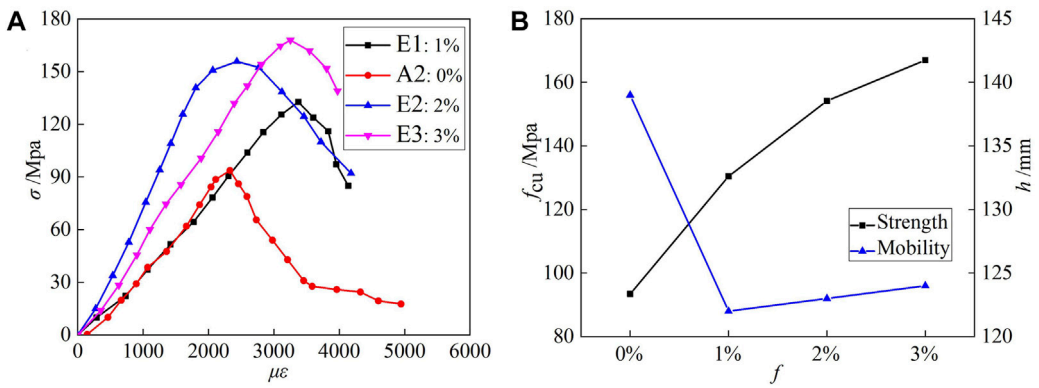

FIGURE 9 | The influence of different volume fractions of steel fiber on RPC mechanical properties. **(A)** Stress-strain curves of RPC specimens with different volume fractions of steel fiber. **(B)** Ultimate compressive strength and mixture fluidity of RPC with different volume fractions of steel fiber.

powder to cement corresponding to the peak of ultimate compressive strength of the cube specimens is taken as 0.25.

The Ratio of Quartz Sand to Cement

The comparison of stress-strain curves of specimens with different ratios of quartz sand to cement is shown in **Figure 8A**, and the influence of different ratios of quartz sand to cement on the ultimate compressive strength and mixture fluidity of RPC specimens is shown in **Figure 8B**. It can be seen from **Figure 8** and **Table 3** that when the ratio of quartz sand to cement of the specimen increases from 1.2 to 1.4, 1.6, and 1.8 in turn, the ultimate compressive strength of the specimen decreases from 80.36 to 93.42, 83.99, and 75.23 Mpa in order, which increases by 16.25, 4.52, and −6.36%, respectively. When the ratio of quartz sand to cement of the mixture increases from 1.2 to 1.4, 1.6, and 1.8 in turn, the fluidity of RPC mixture decreases from 139 to 138, 135, and 117 mm in order, which decreases by 0.72, 2.88, and 15.83%, respectively. It can be seen that, with the increase in the ratio of quartz sand to cement, the fluidity of the mixture increases, and the ratio of quartz sand to cement corresponding to the peak of ultimate compressive strength of the cube specimens is taken as 1.4.

The Volume Fraction of Steel Fiber

The comparison of stress-strain curves of specimens with different volume fractions of steel fiber is shown in **Figure 9A**, and the influence of different volume fractions of steel fiber on the ultimate compressive strength and mixture fluidity of RPC specimens is shown in **Figure 9B**. It can be seen from **Figure 9** and **Table 3** that when the volume fraction of steel fiber of the specimens increases from 0 to 1, 2, and 3% in turn, the ultimate compressive strength of the specimen increases from 93.42 to 130.45, 154.18, and 167.02 Mpa in order, which increases by 28.39, 65.04, and 80.92%, respectively. When the volume fraction of steel fiber of the mixture increases from 0 to 1, 2, and 3% in turn, the fluidity of RPC mixture decreases from 139 to 122, 123, and 124 mm in turn, which decreases by 12.23, 11.51, and 10.79%, respectively. It can be seen that, with the increase in the volume fraction of steel fiber, the fluidity of mixture decreases, while the ultimate compressive strength of the cube specimens increases gradually.

Normal Pressure Steam Curing Time

Under 80°C normal pressure steam environment, specimens A2, A4, and E2 are cured for 3 days, and specimens F6, G6, and H6

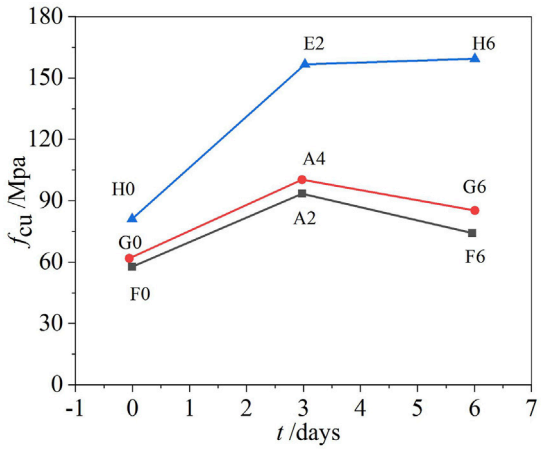

FIGURE 10 | The influence of different atmospheric steam curing time on ultimate compressive strength of RPC.

TABLE 5 | Optimal RPC mix proportion without steel fiber.

w/b	*c/c*	*s/c*	*p/c*	*q/c*	Superplasticizer (%)
0.20	1	0.3	0.25	1.2	2

are cured for 6 days; however specimens F0, G0, and H0 are not cured under 80°C normal pressure steam environment. The influence of steam curing time on RPC is investigated according to the ultimate compressive strength of specimens, as shown in **Figure 10**. The comparison results show that the ultimate compressive strength of all specimens without steam curing is relatively low. For the group of G0, A4, and G6 and the group of F0, A2, and F6, the specimens can reach the highest ultimate compressive strength when cured by steam for 3 days; nevertheless the ultimate compressive strength of the specimens cured by steam for 6 days is lower than that of the specimens cured by steam for 3 days. For the group of H0, E2, and H6, the ultimate compressive strength of specimen H6 cured by steam for 6 days is higher slightly than that of specimen E2 cured by steam for 3 days, and both are basically the same; therefore, there is little difference for ultimate compressive strength between the specimens cured by steam for 3 and 6 days. It could be drawn that the best steam curing time for RPC specimens is 3 days.

Optimal Mix Proportion of RPC

Based on the results of cube specimen tests in **Table 3**, the optimal mix proportion of RPC is proposed through the comprehensive consideration of the fluidity behavior, compressive strength, and economic index, meanwhile taking the materials that can be purchased locally into consideration. With the addition of steel fiber, the cost of RPC will increase greatly and its failure mode will change, so two groups of optimal mix proportion are obtained in this paper. One group is not mixed with steel fiber, and the other group contains steel fiber, as seen **Tables 5**, **6**.

TABLE 6 | Optimum RPC mix proportion with steel fiber.

w/b	*c/c*	*s/c*	*p/c*	*q/c*	*F* (%)	Superplasticizer (%)
0.20	1	0.3	0.25	1.2	2	2

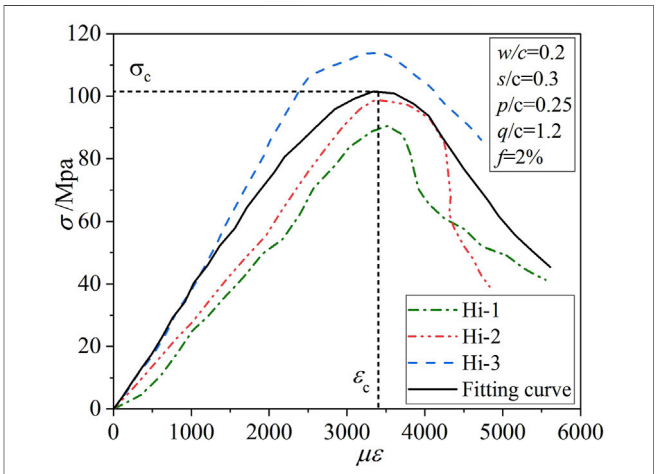

FIGURE 11 | Comparison of fitting stress-strain curve and test curves.

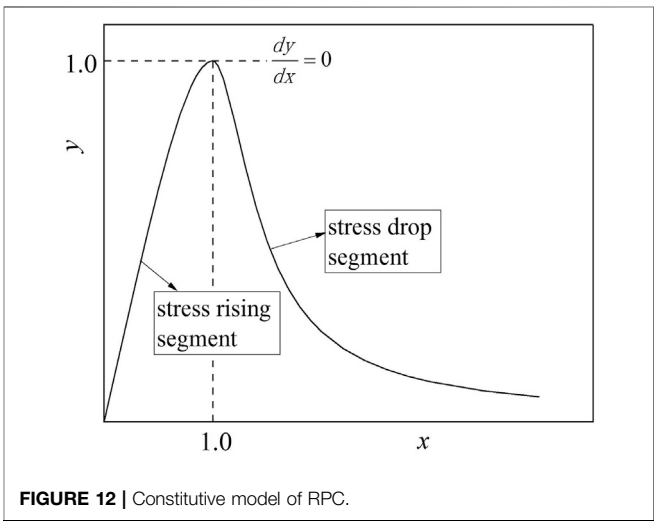

FIGURE 12 | Constitutive model of RPC.

Constitutive Model of RPC

According to the above research conclusion, when 2% steel fiber was added to RPC, the compressive strength of the material could be greatly improved. Therefore, the results of H group prism specimens are selected for regression of constitutive model. Based on the stress-strain curves of prism specimens, a fitting stress-strain curve is obtained by using lstOpt software regression. The comparison between the fitting curve and the three test curves of group H is shown in **Figure 11**.

In order to obtain the constitutive model of RPC, firstly, the stress and strain are transformed into dimensionless quantities. Let $x = \varepsilon/\varepsilon_c$, $y = \sigma/\sigma_c$, where ε_c is the strain corresponding to the peak

TABLE 7 | The comparison between E and E_w.

Test specimens	*E*/Gpa	*E*w/Gpa	$\frac{\lvert E-E_w \rvert}{E}$/%
Fi-1	37.59	36.92	1.79
Fi-2	40.10	40.97	2.17
Fi-3	39.20	40.53	3.40
Gi-1	40.08	40.95	2.17
Gi-2	41.20	41.95	1.83
Gi-3	39.88	40.15	0.67
Hi-1	46.80	46.11	1.48
Hi-2	45.03	43.14	4.19
Hi-3	42.05	41.34	1.68

stress, and σ_c is the peak stress. Referring to the constitutive model of ordinary concrete, the constitutive model of RPC in the stress rising segment at the optimal mix proportion is established:

$$y = 1.33x - 0.32x^4 - 0.01x^5 \tag{3}$$

In view of the limitations of laboratory conditions, the compressive stress-strain curves of some RPC specimens in the stress drop segment are very discrete, so it is inadequate to regress the constitutive model of the stress drop segment. Therefore, the corresponding formula given in Wang (2008) is adopted as the constitutive model of RPC stress drop segment in this paper. The constitutive model is shown in **Figure 12**, and the expression is as follows:

$$y = \begin{cases} 1.33x - 0.32x^4 - 0.01x^5 & 0 \le x \le 1 \\ \dfrac{x}{6(x-1)^2 + x} & x > 1 \end{cases} \tag{4}$$

Relationship Between Compressive Strength and Elastic Modulus

According to the relationship between elastic modulus and compressive strength of RPC in Ahmad et al. (2015), the expression is as follows:

$$E = 4.36\sqrt{f_c'} \quad (R^2 = 0.85) \tag{5}$$

The relationship between elastic modulus and compressive strength of RPC prism specimens is established; the expression is as follows:

$$E = a\sqrt{f_c'} \tag{6}$$

Based on the experimental data in **Table 4**, the global optimization algorithm (Leveberg Marquardt) in lstOpt software is used to calculate the coefficient a in **Eq. 6**. After 23 iterations, the convergence standard is reached, and the coefficient a is 4.34. The relationship between the elastic modulus and compressive strength of RPC made from local materials is obtained as follows:

$$E = 4.34\sqrt{f_c'} \quad (R^2 = 0.88) \tag{7}$$

where E is the modulus of elasticity of RPC (Gpa), and $f_c^{'}$ is the compressive strength of RPC (Mpa).

The coefficient of regression formula in Ahmad et al. (2015) is 4.36, and the coefficient of regression in this test is 4.34, which indicates that there is a universal relationship between the elastic modulus and compressive strength of RPC. The square sum of the correlation coefficients of the regression formula in Ahmad et al. (2015) is $R^2 = 0.85$, while the square sum of the correlation coefficients of the regression formula in this experiment is $R^2 = 0.88$, which indicates that the data of this test is more aggregated.

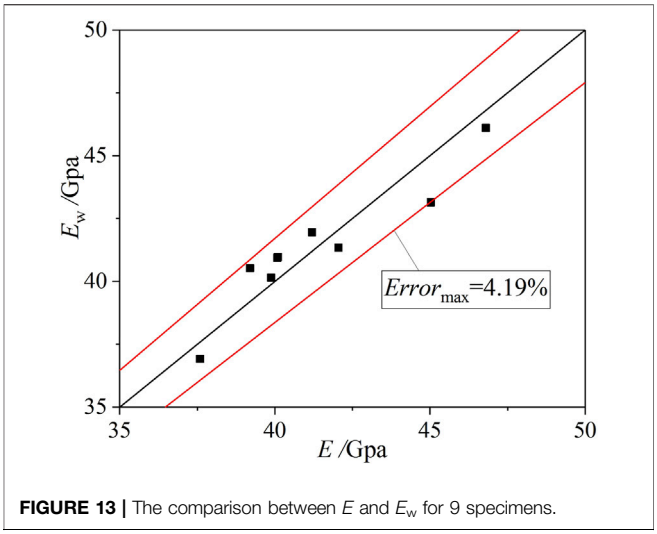

FIGURE 13 | The comparison between E and E_w for 9 specimens.

According to **Eq. 7**, the modulus of elasticity (E_w) of 9 specimens is calculated by using RPC compressive strength, as shown in **Table 7**. The dispersion comparison of E and E_w of 9 specimens is shown in **Figure 13**. Through the comparison, it can be seen that the maximum error is 4.19%, which shows that the two are in good agreement and meet the engineering requirements.

CONCLUSION

In this paper, 22 groups of RPC cubic specimens and 3 groups of RPC prism specimens were carried out, and two groups of optimal mix proportion were obtained. From the results of comparisons and analysis presented in this paper, the following conclusions are obtained.

1) When the load approximately reached 0.5 times of the peak load, the cracks of RPC specimens with steel fiber began to develop. After reaching peak stress, obvious vertical cracks appeared on the surface of the specimens. It can be concluded that the crack resistance of steel fiber has a certain buffer for the development of cracks, and the RPC specimens with steel fiber do not show brittle failure.
2) The ratio of silica fume to cement, the ratio of slag powder to cement, the ratio of quartz sand to cement, the volume fraction of steel fiber, and water to binder ratio have greater influence on the compressive strength of RPC specimens. The compressive strength of RPC specimens reaches the maximum when the ratio of silica fume to cement is 0.3, the ratio of slag powder to cement is 0.25, and the ratio of quartz sand to cement is 1.4, respectively. When the volume fraction of steel fiber is 1~ 3%, the compressive strength of the specimens increases with the increasing of the volume fraction of steel fiber. With the

increase in the water to binder ratio in a certain range, the compressive strength gradually decreases; however the fluidity gradually increases. The recommended value of water to binder ratio is 0.2, which could ensure the mechanic behavior of RPC specimens.

3) Steam curing time has some influence on the compressive strength of RPC. The strength of specimens without steam curing is very low, and RPC can reach the highest strength after steam curing for 3 days; however the compressive strength of the specimens of steam curing for 6 days is lower than the compressive strength of the specimens of steam curing for 3 days.
4) Based on the stress-strain curves of RPC prism specimens, the constitutive model of RPC made from local materials is established. The relationship between compressive strength and elastic modulus for RPC is regressed statistically, which is in good agreement with the existing expression.

DATA AVAILABILITY STATEMENT

The original contributions presented in the study are included in the article/supplementary material, and further inquiries can be directed to the corresponding author.

AUTHOR CONTRIBUTIONS

JJ contributed to testing and writing; WK contributed to writing and translation; LJ contributed to testing; YL contributed to translation; HR contributed to writing; SH, LH, YL, and CY contributed to translation. All authors contributed to the article and approved the submitted version.

FUNDING

The authors are grateful to the financial support received from the National Natural Science Foundation of China (Grant no. 51808173); the Natural Science Foundation of Heilongjiang Province (Grant no. LH 2020E018); the Opening Fund for Key Laboratory of the Ministry of Education for Structural Disaster and Control of Harbin Institute of Technology (Grant no. HITCE201908); the Social Science Foundation of Hebei Province (grant no. HB20GL055); the Northeast Petroleum University Guided Innovation Fund (grant no. 2020YDL-02); and the Research on Risk Identification and Emergency Management of Residential Buildings from the Perspective of COVID-19 (grant no. SQ2021115).

REFERENCES

Abid, M., Hou, X., Zheng, W., and Hussain, R. R. (2017). High Temperature and Residual Properties of Reactive Powder concrete - A Review. *Construction Building Mater.* 147, 339–351. doi:10.1016/j.conbuildmat.2017.04.083

Ahmad, S., Zubair, A., and Maslehuddin, M. (2015). Effect of Key Mixture Parameters on Flow and Mechanical Properties of Reactive Powder concrete. *Construction Building Mater.* 99, 73–81. doi:10.1016/j.conbuildmat.2015.09.010

Deng, Z. C., and Feng, Q. (2016). Fracture Properties of Hybrid Fibers Reinforced Reactive Powder Concrete. *J. Building Mater.* 19, 14–21. doi:10.3969/j.issn.1007-9629.2016.01.003

He, X. Y., Qin, L., Zhang, H. Y., Zhang, S. Y., Li, H., and Zhao, Y. R. (2016). Mixture Ratio Design of Basalt Fiber Reactive Powder Concrete Based on Orthogonal Theory. *Building Chin. Ceram. Soc.* 35, 1402–1406+1412. doi:10.16552/j.cnki.issn1001-1625.2016.05.013

Jiang, Y. R. (2014). *Experimental Investigation on Mechanical Behavior of Reactive Powder Concrete under Tension-Compression Stress State*. Beijing: Beijing Jiaotong University.

Li, Z. G. (2013). *Experimental Study of Practical Failure Criterion of Reactive Powder Concrete under Biaxial Compression*. Beijing: Beijing Jiaotong University.

Mayhoub, O. A., Nasr, E.-S. A. R., Ali, Y. A., and Kohail, M. (2021). The Influence of Ingredients on the Properties of Reactive Powder Concrete: A Review. *Ain Shams Eng. J.* 12, 145–158. doi:10.1016/j.asej.2020.07.016

Perkowski, Z., Czabak, M., Grzeszczyk, S., Frączek, D., Tatara, K., Matuszek-Chmurowska, A., et al. (2020). Experimental Research on Concrete Beams Reinforced with High Ductility Steel Bars and Strengthened with A Reactive Powder Concrete Layer in the Compression Zone. *Materials* 13, 4173. doi:10.3390/ma13184173

Qin, X. (2011). *Under Various Stress the Constitutive Relation and Failure Criterion of Reactive Powder Concrete*. Beijing: Beijing Jiaotong University.

Raza, S. S., Qureshi, L. A., Ali, B., Raza, A., and Khan, M. M. (2021). Effect of Different Fibers (Steel Fibers, Glass Fibers, and Carbon Fibers) on Mechanical Properties of Reactive Powder Concrete. *Struct. Concrete* 22, 334–346. doi:10.1002/suco.201900439

Ridha, M. M. S., Al-Shaarbaf, I. A. S., and Sarsam, K. F. (2018). Experimental Study on Shear Resistance of Reactive Powder Concrete Beams without Stirrups. *Mech. Adv. Mater. Structures* 27, 1006–1018. doi:10.1080/15376494.2018.1504258

Salahuddin, H., Qureshi, L. A., Nawaz, A., and Raza, S. S. (2020). Effect of Recycled Fine Aggregates on Performance of Reactive Powder Concrete. *Construction Building Mater.* 243, 118223. doi:10.1016/j.conbuildmat.2020.118223

Wang, Z. N. (2008). *Research on Flexural Behavior of Reactive Powder Concrete Rectangular Beam with Steel Bar*. Beijing: Beijing Jiaotong University.

Xia, H., Wang, W., and Shi, Z. (2015). Mechanical Properties of Reactive Powder Concrete with Ultra-short Brass-Coated Steel Fibres. *Mag. Concrete Res.* 67, 308–316. doi:10.1680/macr.14.00184

Zheng, W. Z., and Lv, X. Y. (2015). Literature Review of Reactive Powder Concrete. *J. Building Structures* 36, 44–58. doi:10.14006/j.jzjgxb.2015.10.006

Conflict of Interest: The authors declare that the research was conducted in the absence of any commercial or financial relationships that could be construed as a potential conflict of interest.

Publisher's Note: All claims expressed in this article are solely those of the authors and do not necessarily represent those of their affiliated organizations, or those of the publisher, the editors and the reviewers. Any product that may be evaluated in this article, or claim that may be made by its manufacturer, is not guaranteed or endorsed by the publisher.

frontiers in Materials

ORIGINAL RESEARCH
published: 17 September 2021
doi: 10.3389/fmats.2021.714455

Hot Tensile Deformation Behavior of Mg-4Li-1Al-0.5Y Alloy

Ting Yang, Zhuohua Li, Jinhui Wang and Peipeng Jin*

Qinghai Provincial Key Laboratory of New Light Alloys, Qinghai University, Xining, China

The microstructure evolution and deformation mechanism of the as-extruded-annealed Mg-4Li-1Al-0.5Y alloy (denoted as LAY410) were investigated during the hot tensile deformation at the temperatures between 150°C and 300°C with strains from 8×10^{-5} s^{-1} to 1.6×10^{-3} s^{-1}. The results show that when the strain rate decreases and/or the deformation temperature increases, the peak stress of the alloy gradually decreases, and the elongations to fracture gradually increases. The true stress–strain curves show typical dynamic recrystallization (DRX) softening characteristics. It is observed that the microstructure in the magnesium (Mg) alloy deformed at 150°C is mainly composed of the deformed grains and a few recrystallized grains. The microstructures in the Mg alloy deformed at 200°C consisted of substructures and a slightly increasing number of dynamic recrystallized grains. When the deformation temperature reaches 250°C, the number of recrystallized grains increases significantly, and the microstructures are dominated by recrystallized grains. Moreover, through theoretical calculation and result analysis, the activation energy was about 99.3 kJ/mol, and the hot tensile deformation mechanism was the alternate coordinated deformation mechanism among grain boundary slip (GBS), intragranular slip, and DRX.

Keywords: Mg–Li alloy, dynamic recrystallization (DRX), grain boundary slip, work hardening, hot tensile, deformation mechanism

OPEN ACCESS

Edited by:
Liang-Yu Chen,
Jiangsu University of Science and Technology, China

Reviewed by:
Jinhua Peng,
Jiangsu University of Science and Technology, China
Qianhao Zang,
Jiangsu University of Science and Technology, China
Bo Song,
Southwest University, China

****Correspondence:***
Jinhui Wang
ahui1004@163.com

Specialty section:
This article was submitted to Structural Materials, a section of the journal Frontiers in Materials

Received: *25 May 2021*
Accepted: *15 July 2021*
Published: *17 September 2021*

Citation:
Yang T, Li Z, Wang J and Jin P (2021) Hot Tensile Deformation Behavior of Mg-4Li-1Al-0.5Y Alloy. Front. Mater. 8:714455. doi: 10.3389/fmats.2021.714455

INTRODUCTION

Compared with steel and aluminum (Al) alloy, Mg alloy not only has lower density but also good thermal conductivity and machinability. It has great application potential in aerospace, automobile manufacturing, and electronics industry (Luo et al., 1995; Wang, 2007; Hadadzadeh and Wells, 2013). However, Mg alloy is an HCP structure, and its slipping systems are less than five independent slip systems at lower temperatures (lower than 225°C). Therefore, it does not meet the requirements of the five slip systems required for continuous coordinated deformation of materials (He et al., 2019), which severely limits the wider application of Mg alloys. When the plastic forming temperatures are higher than 225°C, the <a> slipping system of the prismatic plan and <c+a> slipping system of the pyramidal plan II can be activated, although the plastic formability of the Mg alloys are improved at this situation, the costs have risen.

To improve the plastic formability of Mg alloys at room temperature, the alloying elements such as lithium (Li), Al, zinc (Zn), and rare earth element (RE) are usually added to Mg alloys to improve its plastic formability. The literatures (Al-Samman, 2009; Tang et al., 2017; Tu et al., 2020; Wang et al., 2020) found that adding Li to Mg alloys can effectively reduce the density and lattice spacing (c/a axis ratio) of Mg alloys. This makes the non-basal slip system of the alloy easier to be activated during deformation, thereby effectively improving the plastic formability of the alloy. In addition, Kumar et al. (2012) found that adding Li to Mg–Al alloy can promote the precipitation process of the $MgAlLi_2$ phase, which strengthens the alloy by the precipitation phase and thus improves the mechanical properties of the alloy. However, $MgAlLi_2$ is not thermally stable and tends to be decomposed at 50–70°C, and is further

TABLE 1 | Chemical composition of the LAY410 alloy (wt%).

Material	Composition (wt%)			
LAY410	Mg	Li	Al	Y
	94.17	4.26	1.05	0.52

decomposed to form the AlLi phase, which leads to a significant decrease in the mechanical properties of the Mg–Li–Al alloy at elevated temperatures. This phenomenon prevents Mg–Li–Al alloys from having ultra-low density and high strength simultaneously (Cui et al., 2011; Hagihara et al., 2019; Li et al., 2019). Therefore, it is important to improve the comprehensive mechanical properties of Mg–Li–Al alloy. The previous studies (Hantzsche et al., 2010; Bao et al., 2013; Zhu et al., 2014; Fei et al., 2015) have shown that the addition of rare earth element yttrium (Y) can effectively improve the comprehensive mechanical properties of Mg–Li–Al alloys. Guo et al. (2014) studied Mg-9Li-6Al-xY (x = 0, 2) and found that adding rare earth element Y could not only precipitate Al_2Y phase in the alloy to suppress the precipitation of AlLi phase, but effectively refine the grains as well, thus improving the comprehensive mechanical properties of the alloy. In addition, Sun et al. (2018) found that the addition of rare earth element Y can increase the bonding force between atoms, thus effectively inhibiting dislocation slip during deformation. Therefore, the work hardening rate in the hot deformation is increased, and the mechanical properties of the alloy at elevated temperatures are significantly improved.

Recently, many researchers have studied the hot deformation behavior and microstructure evolution of Mg–Li–Al alloy in order to improve the mechanical properties and plastic formability of the alloy (Yang et al., 2016; Chen D et al., 2020; Guo et al., 2020). Xu et al. (2015) studied the hot deformation behavior of Mg–Li–Al–Nd alloy at varied temperatures and strain rates. It is found that unlike the LAY410 alloy, in this alloy, Li exists in the form of β-Li phase. The DRX easily occurs in the β-Li phase, whereas in the α-Mg phase, it is retarded. Moreover, the deformation temperatures and strain rates have great influence on the occurrence of DRX, and DRX can easily occur at higher temperatures and lower strain rates. Therefore, for the Mg–Li–Al–Nd alloy, the improvement of plastic formability of the alloy can be attributed to DRX softening and non-basal slip system activation during the hot deformation. Li et al. (2021) studied the hot tensile deformation behavior of LAZ532 alloy. It is found that the hot tensile deformation mechanism of the alloy is more complicated, which is an alternate coordinated deformation mechanism between GBS, intragranular slip, and DRX. However, there are few reports on the hot deformation behavior of Mg-Li-Al-Y alloy and the microstructure evolution during hot tensile deformation.

In this article, the microstructure evolution and deformation mechanism of LAY410 alloy during hot tensile deformation were studied in detail. Furthermore, the fracture mechanisms of LAY410 alloy during hot tensile are discussed.

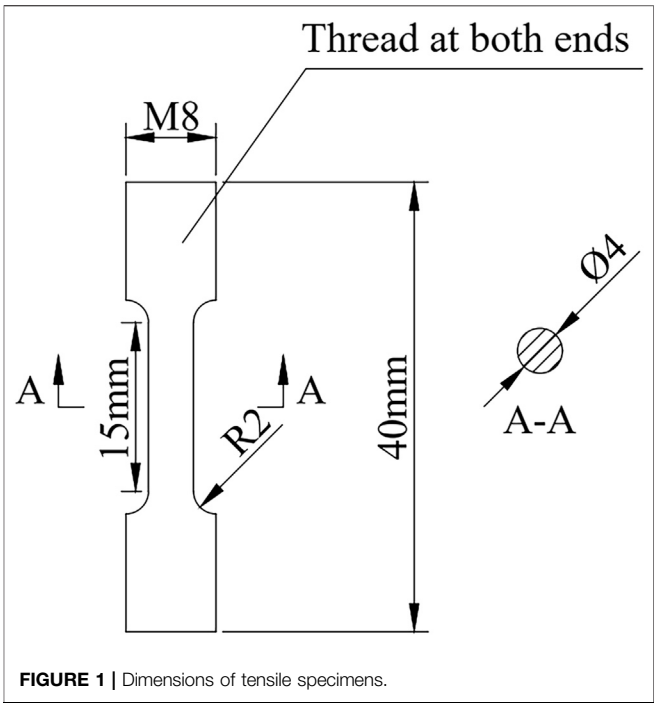

FIGURE 1 | Dimensions of tensile specimens.

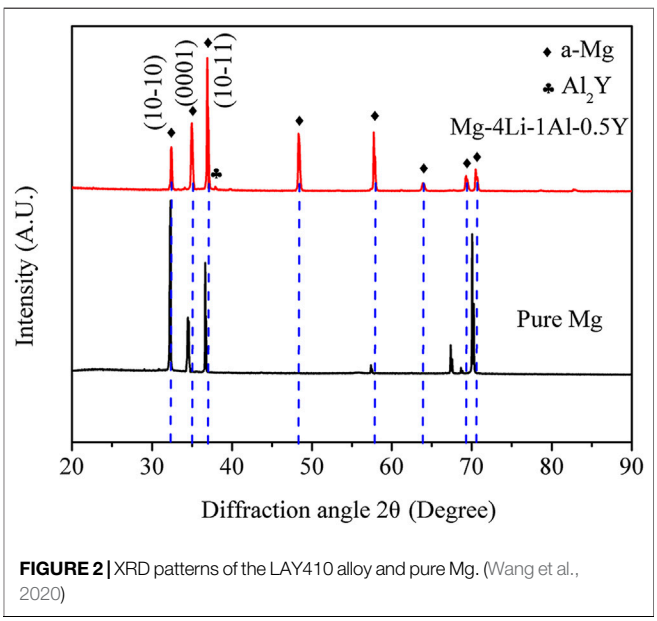

FIGURE 2 | XRD patterns of the LAY410 alloy and pure Mg. (Wang et al., 2020)

TABLE 2 | Lattice parameters of α-Mg.

Lattice parameters	A/nm	C/nm	c/a
Pure Mg	0.320 936	0.521 120	1.623 75
LAY410	0.319 993	0.513 743	1.605 48

EXPERIMENT METHOD

Industrial pure Mg (99.95 wt%), Mg-30wt.%Y master alloy, pure Li (99.99wt%), and pure Al (99.99wt%) were used as experimental raw materials. The LAY410 (wt%) alloy was fabricated by melt casting. The concrete melt-casting method is as follows. First, the clean crucible was preheated to 300°C, and then the Mg ingot was placed in the crucible and the temperature was raised to 720°C. After

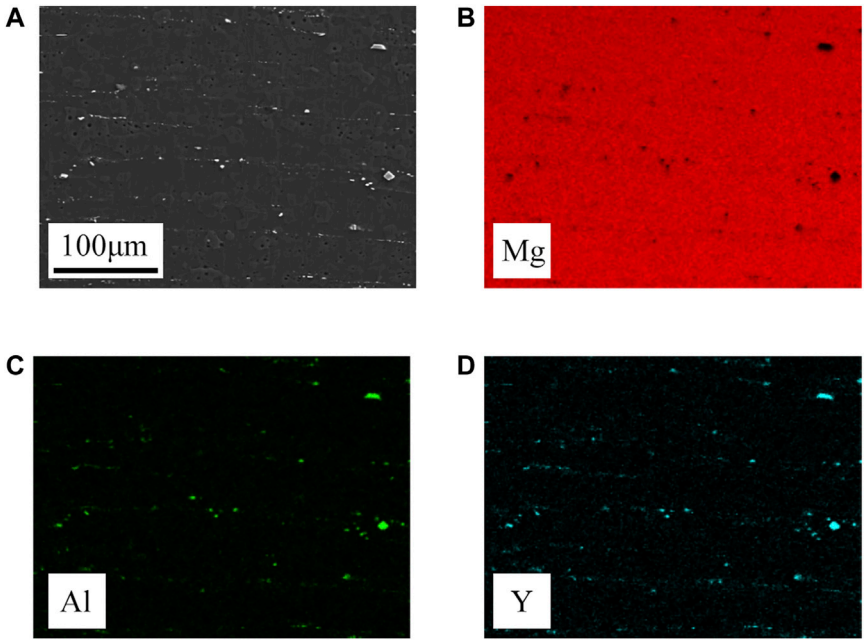

FIGURE 3 | Microstructures of the LAY410 alloy.

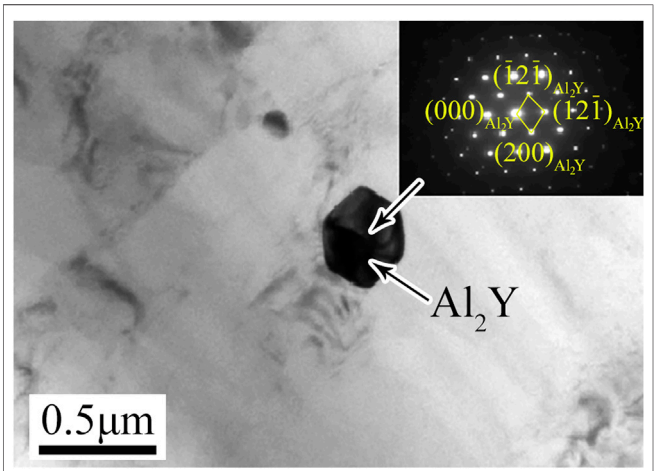

FIGURE 4 | TEM BF image of the Al_2Y in the LAY410 alloy and its SAED pattern (inset).

the Mg ingot was completely melted, the Mg-30wt%Y master alloy and pure Al were successively added into Mg melt, and stirred for 10 min. Subsequently, the temperature was lowered to 680°C and pure Li was added, and stirred for 10 min. After the temperature rose to 740°C, the alloy melt was left standing for 20 min, and the alloy melt was fully stirred and the slag was removed to make the melt clear and clean. Finally, after the melt temperature was further reduced to 710°C, the alloy melt was cast into a mold to obtain a LAY410 alloy ingot. During the whole melting process, sulfur hexafluoride (SF_6) and argon (Ar) were used as a mixed shielding gas. Next, the ingot was processed into an extruded billet of Ø44 mm × 40 mm and held at 350°C for 2 h. Then, the four-column hydraulic press (equipment model: IM-Y300) was used to extrude at an extrusion ratio of 13:1 and then air cooling was performed to obtain an extruded bar with a diameter of 12 mm. Finally, the extruded sample was put into a heat treatment furnace at 350°C and then taken out and water cooled immediately after holding for 1 h to prevent the grain growth and retain the grain structure. The alloy was called the LAY410 alloy.

The actual chemical composition of the prepared LAY410 alloy tested by inductively coupled plasma optical emission spectrometer (ICP-OES) is shown in **Table 1**. As can be seen from **Table 1**, the actual content of each element in the alloy has a small gap with the design composition, indicating that there was almost no element burning loss in the smelting process. After heat preservation for 10 min, the hot tensile test of the LAY410 alloy was carried out at temperatures between 150°C and 300°C with the strain rates from 8×10^{-5} s^{-1} to 1.6×10^{-3} s^{-1} via an Instron-5982 equipped with a heating device. The tensile specimens were prepared along the extrusion direction (ED), and their dimensions are shown in **Figure 1**. Furthermore, through scanning electron microscopy (SEM, ZEISS-6035 field-emission) and electron back-scattering diffraction (EBSD) technology, the microstructure of the specimens after hot tensile deformation was analyzed to explore the microstructure evolution during hot tensile deformation.

RESULTS AND DISCUSSIONS

Analysis of Phases and Microstructures in the Alloy

The X-ray diffraction (XRD) patterns of LAY410 alloy as shown in our previous study (Wang et al., 2020) (**Figure 2** in this article). There are not only diffraction peaks of the α-Mg phase, but the

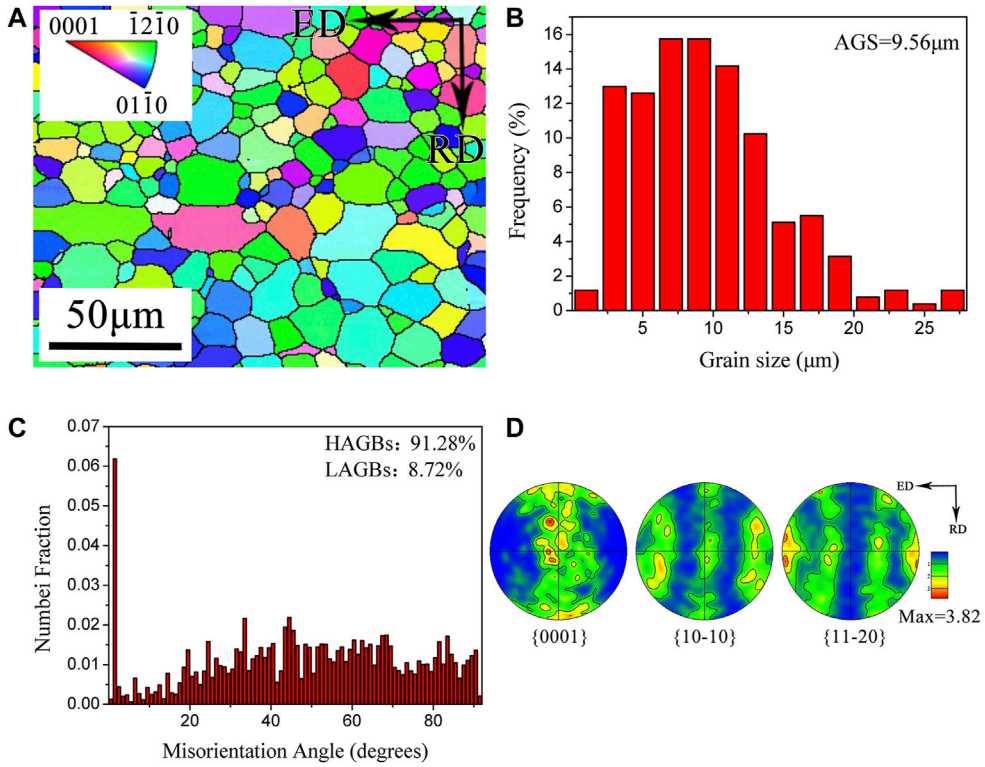

FIGURE 5 | Microstructure and texture of the LAY410 alloy: **(A)** inverse pole figure, **(B)** grain size map, **(C)** misorientation angle distribution histogram, **(D)** pole figures.

diffraction peaks of the Al_2Y phase as well. There is only one diffraction peak of the Al_2Y phase with a low intensity in the XRD patterns due to the high solid solubility of Y in Mg (Stanford et al., 2015). Most of the Y atoms are dissolved in the Mg matrix. As a result, the content of Al_2Y phase formed in LAY410 alloy is very low. In addition, compared with pure Mg, the diffraction peak of the α-Mg phase in LAY410 alloy is shifted to the right, which indicates that the axial ratio value (c/a) of the α-Mg phase decreases as described in our previous study (Wang et al., 2020) and the results are reanalyzed in this article. In order to confirm the above conclusions, Jade 6.0 software is used to calculate the lattice constants of the α-Mg phase in pure Mg and LAY410 alloy. The calculated results are shown in **Table 2**. Compared with pure Mg, the lattice constants a and c of the α-Mg phase in Mg–Li alloy are reduced by 0.29 and 1.41%, respectively. The axial ratio value (c/a) value dropped from 1.624 to 1.605. This is mainly because when the added amount of Li is less than 5.7%, it can be completely dissolved in Mg, thereby reducing the axial ratio value (c/a) of Mg (Koike et al., 2005; Zhou et al., 2017).

To prove the existence of Al_2Y phase in LAY410 alloy, further, EDS-Mapping of the alloy is carried out as shown in **Figure 3**. It can be clearly observed from **Figure 3** that a small amount of submicron white precipitates are distributed in the grain boundary and grain interior, and the main elements are Al and Y. Combined with the binary phase diagram of Al–Y alloy (Liu et al., 2004), it is concluded that the white precipitated phase in **Figure 3A** is the Al_2Y phase. In addition, by observing the transmission electron microscope (TEM) bright-field image of the precipitated phase as shown in **Figure 4** and the corresponding selected area electron diffraction pattern (inset), it is further proved that the white particles in the alloy are of the Al_2Y phase. Because the Al_2Y phase is a hard phase, it can hinder the dislocation movement. Therefore, the formation of Al_2Y phase can improve the strength of LAY410 alloy effectively due to dispersion strengthening (Zhao et al., 2016).

In order to determine the grain size and texture type of LAY410 alloy, EBSD technology is used to characterize the alloy. The results are shown in **Figure 5**. From **Figures 5A,B**, it can be seen that there are a large number of equiaxed grains in the alloy. And there are many fine recrystallized grains around the equiaxed grains. The average grain size (AGS) is 9.56 μm. As shown in **Figure 5C**, the misorientation angle of the alloy is mainly high-angle grain boundaries (HAGBs> 10°) with a number fraction of 91.28. This also proves that there is a large amount of DRX in the alloy, which weakens the {0001} basal fiber texture due to forming fresh DRXed grains without a preferred orientation selection. **Figure 5D** shows the polar figure of the LAY410 alloy, where ED and RD represent the extrusion direction and radial direction, respectively. The pole density points in the {0001} pole figure are distributed along the RD, while the pole density points in the {10–10} and {11–20} pole figures are distributed along the edges. This indicates that there is a weak {0001} basal fiber texture in the alloy, and its texture strength value is 3.82.

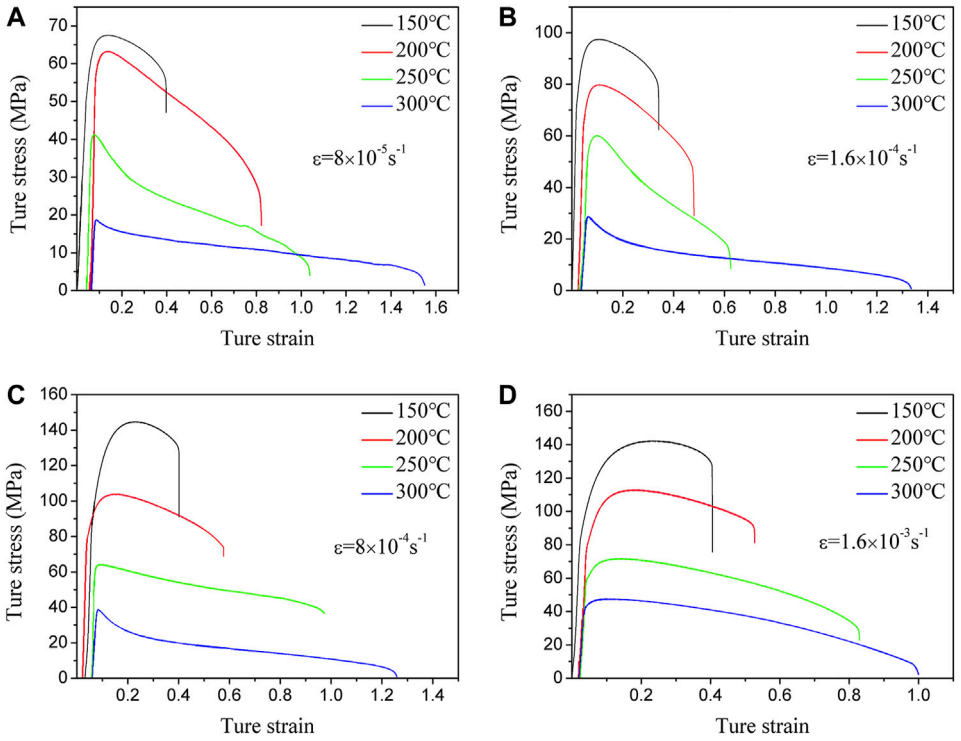

FIGURE 6 | True stress–strain curves of the LAY410 alloy: **(A)** $\varepsilon = 8 \times 10^{-5}\ s^{-1}$, **(B)** $\varepsilon = 1.6 \times 10^{-4}\ s^{-1}$, **(C)** $\varepsilon = 8 \times 10^{-4}\ s^{-1}$, and **(D)** $\varepsilon = 1.6 \times 10^{-3}\ s^{-1}$.

High-Temperature Mechanical Properties of Alloy

The hot tensile true stress–strain curves of LAY410 alloy at the temperatures between 150°C and 300°C with strain rates from $8 \times 10^{-5}\ s^{-1}$ to $1.6 \times 10^{-3}\ s^{-1}$ are shown in **Figure 6**. According to the observation of the curves, the alloy exhibits a typical DRX softening curve. This is mainly due to the decrease in the axial ratio value (c/a) of the alloy, which leads to the increase in dislocation density and the occurrence of cross-slip. It is conducive to nucleation of DRX, causing a certain degree of dynamic softening (Yang et al., 2009; Li et al., 2011). In addition, the strain rate and deformation temperature have a significant effect on the flow stress of the alloy. The flow stress gradually decreases with the strain rate decrease and/or deformation temperature increase. That is, the curves show a positive strain rate effect and negative temperature effect. The change of flow stress curve is mainly manifested in three stages. In the elastic deformation stage, the true-stress increases sharply due to the volumetric expansion, but the shape remaining unchanged of the crystal induced an increase in the distance of atoms in the α-Mg HCP crystal structure (Huang and Huang, 2013). The flow stress rapidly increases to the critical stress. The second stage of tensile deformation is the deformation process in which the flow stress reaches the peak stress from the critical stress after yielding. The strain hardening effect caused by dislocation proliferation is gradually offset by the strain softening effect caused by partial dislocation annihilation. This causes the dislocation propagation rate to decrease gradually until it reaches equilibrium with the dislocation annihilation rate. At this time, the flow stress reaches the peak stress, and the strain hardening rate gradually decreases to zero. The third stage of tensile deformation is the process in which the flow stress gradually decreases until the specimen fracture. As the strain increases, the dislocation annihilation rate is gradually greater than the dislocation propagation rate. It makes the strain softening effect stronger than the strain hardening effect, leading to the strain softening phenomenon in the rheological curve (Xu et al., 2009).

Effect of Deformation Temperature on Microstructure of Alloy

To further investigate the influence of deformation temperatures on the hot tensile deformation behavior of the alloy, the microstructures at the same strain position of the hot tensile specimen are selected for analysis at the same strain rate ($\varepsilon = 1.6 \times 10^{-4}\ s^{-1}$) with different deformation temperatures (T = 150°C–250°C).

The IPF maps, grain boundary maps, and misorientation angle distribution histograms near the fracture of the hot tensile specimen of LAY410 alloy at the same rate ($\varepsilon = 1.6 \times 10^{-4}\ s^{-1}$) with different deformation temperatures (T = 150°C, 200°C, 250°C) are shown in **Figure 7**. As shown in **Figure 7A**, when the deformation temperature is 150°C, the microstructures near the fracture of tensile specimen are mainly composed of fine recrystallized grains and coarse deformed grains. The

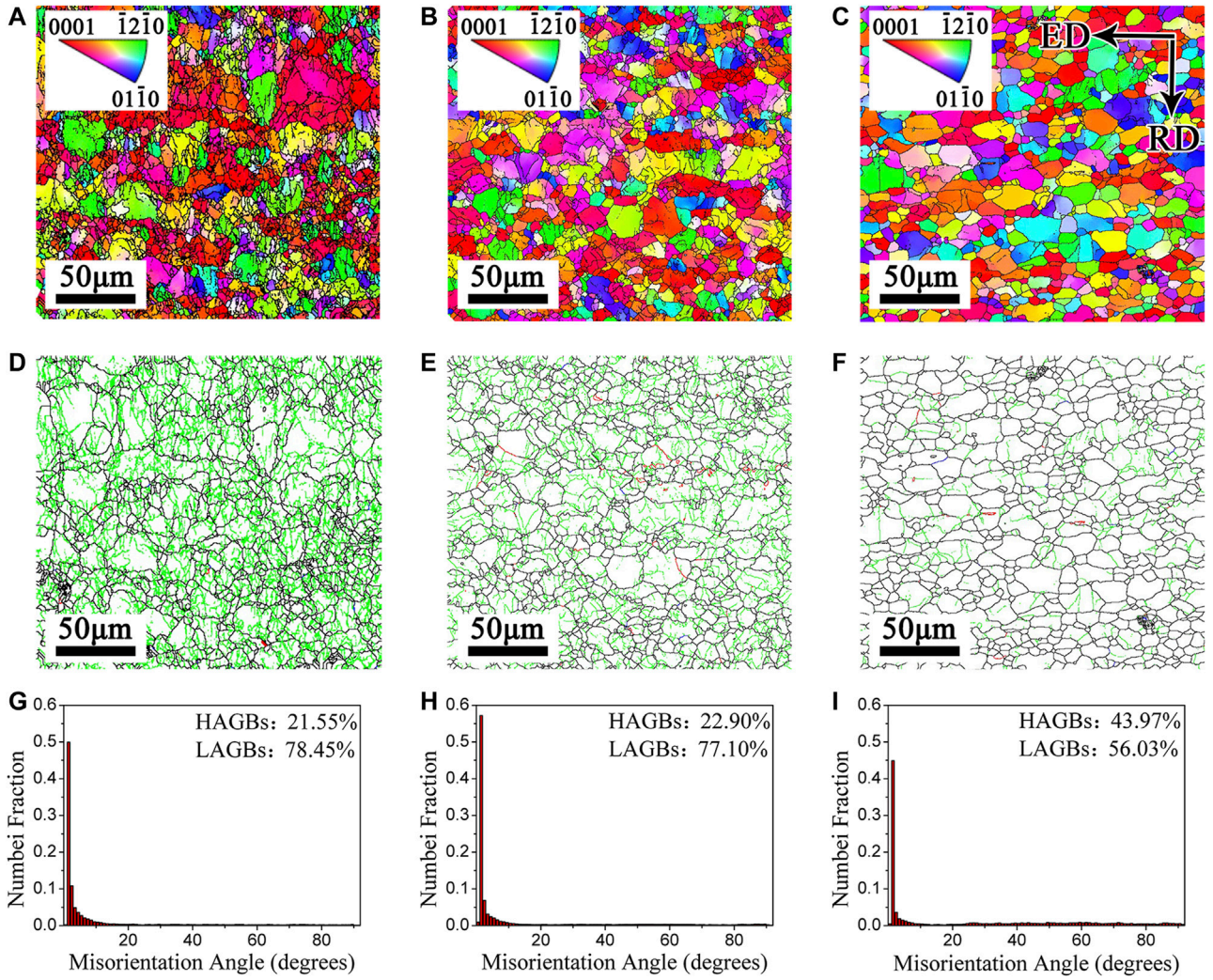

FIGURE 7 | IPF maps, grain boundary maps, and misorientation angle distribution histograms of the LAY410 alloy at the same rate with different temperatures: **(A,D,G)** T = 150°C, **(B,E,H)** T = 200°C, **(C,F, and I)** T = 250°C.

recrystallized grains are mainly distributed at the trigeminal grain boundaries composed of coarse deformed grains, which show obvious discontinuous dynamic recrystallization (DDRX) characteristics. And the traces of the band-like structure can still be seen in the **Figure 7A**, indicating that some of the crystal grains are not fully rotated and are still connected in series to show a band-like shape. In addition, there is a clear color orientation gradient inside the coarse crystals, which indicates that there are abundant slip activities inside. The corresponding grain boundary distribution of size angle is shown in **Figure 7D**, where the green line represents LAGBs and the black line represents HAGBs. It can be seen that a large number of LAGBs are mainly distributed in the coarse grains and at the grain boundaries, which indicates that there are a large number of dislocations inside the coarse deformed grains. As shown in **Figure 7G**, the corresponding misorientation angle is mainly concentrated in LAGBs with a number fraction of 78.45%. It shows that the microstructures in the Mg alloy are mainly composed of the deformed grains and a few of the recrystallized grains. As the deformation temperature increases to 200°C, the fine recrystallized structure inside the alloy increases slightly, and the grain size is mostly kept between 10 and 20 μm, as shown in **Figures 7B,E,H**. In addition, the LAGBs inside the coarse deformed grains also decreased slightly, and the corresponding misorientation angle shifted slightly to the HAGBs. When the deformation temperature reaches 250 °C, the recrystallized grain structure inside the alloy increases significantly, at this time, HAGBs with a number fraction of 22.90%, as shown in **Figures 7C,F,I**. The crystal grains rotate and connect to a network and begin to grow up. It is clearly observed that the content of the LAGBs inside the coarse grains is lowered, the number fraction of which is reduced to 56.03%, and the corresponding misorientation angle is obviously shifted to the HAGBs. This is mainly due to the increase in temperature that accelerates the grain boundaries migration and further promotes the occurrence of complete DRX (Chen T et al., 2020). This leads

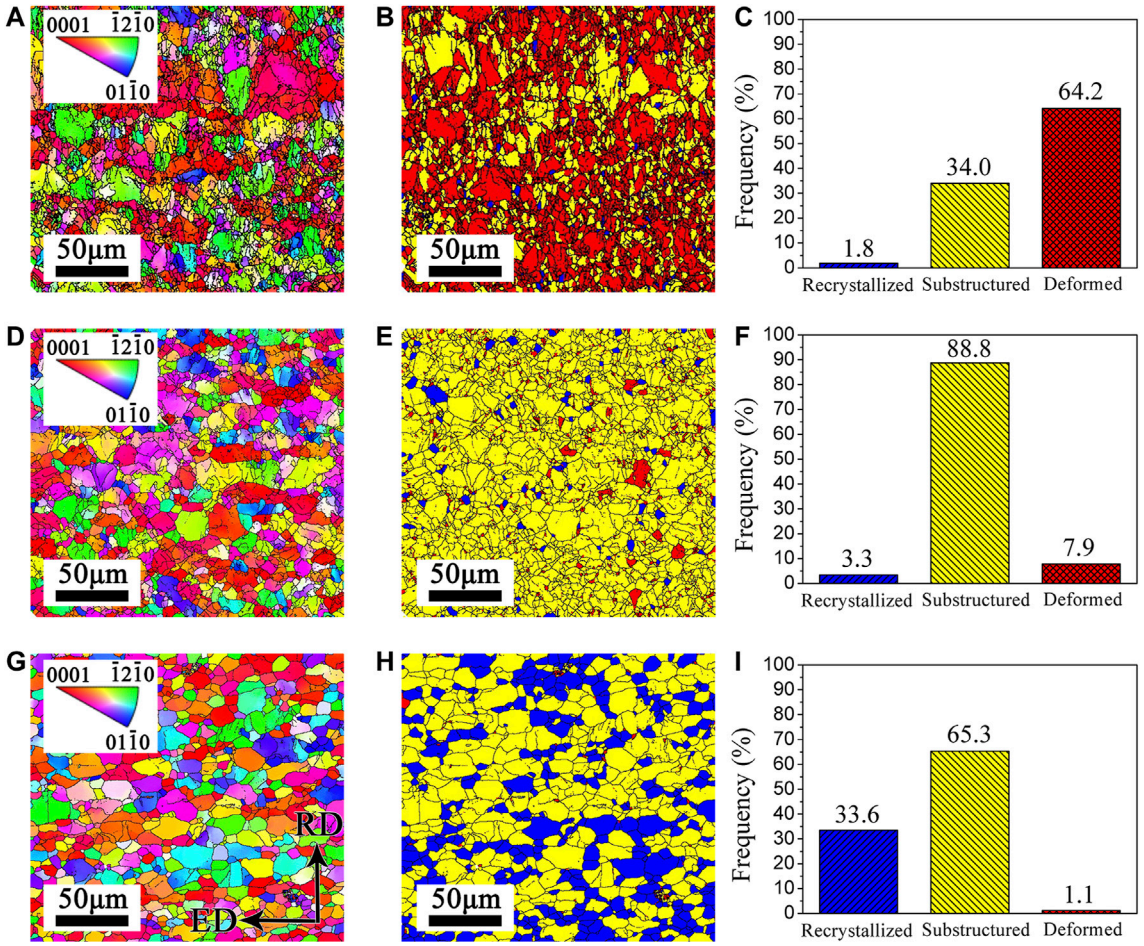

FIGURE 8 | Microstructures of the LAY410 alloy at the same rate with different temperatures: **(A,B,C)** T = 150°C, **(D,E,F)** T = 200°C, **(G,H,I)** T = 250°C.

to an increase in the HAGBs and a decrease in the LAGBs. Small new grains without distortion are produced in the original deformed structure, which makes the overall grain size significantly reduced (Sun et al., 2019).

The distribution of microstructures and the proportion of each microstructure near the fracture of the hot tensile specimens of LAY410 alloy at the same rate ($\varepsilon = 1.6 \times 10^{-4}$ s^{-1}) with different deformation temperatures (T = 150°C, 200°C, 250°C) are shown in **Figure 8**. The red, yellow, and blue grains in the **Figure 8** represent deformed grains, substructure and recrystallized grains, respectively. As shown in **Figures 8A–C**, when the deformation temperature is 150°C, the microstructures of the alloy are mainly composed of deformed grains and substructures, with a number fraction of 64.2 and 34.0%, respectively. The recrystallized grains accounted for only a small part, with a number fraction of 1.8%. It indicates that DRX is incomplete at 150°C, which is consistent with the results in **Figure 7**. At 150°C, recrystallization is mainly distributed at the intersection of deformed grains and substructures. This is mainly because not only the grain boundary energy is high at the intersection, but dislocation plugging is prone to occur, resulting in a high dislocation density. Therefore, it is conducive to DRX. Related studies (Malik et al., 2020) have shown that the nucleation temperature of DRX in Mg alloys is about 200°C. In this experiment, the nucleation of DRX can be observed clearly at 150°C, indicating that the decrease in axial ratio value (c/a) is conducive to the nucleation of DRX. As shown in **Figures 8D–F**, when the deformation temperature reaches 200°C, the deformed grains decrease significantly, and the alloy structure is mainly composed of substructures. The number of dynamic recrystallized grains increased slightly, indicating that the DRX is nucleating and growing. As the diffusion speed between atoms and the migration speed of grain boundaries are accelerated, dislocations are more likely to slip and may be accompanied by cross-slip. Therefore, it is conducive to substructures formation and DRX. When the temperature reaches 250°C, the phenomenon of DRX becomes more obvious and the number increases significantly (see **Figures 8G–I**). It indicates that when the temperature is higher, the rate of DRX and growth is faster. With the recrystallized grains increase, the softening degree caused by recrystallized grains also increases. Therefore, DRX also contributes to the increase in alloy elongation (Hadadzadeh et al., 2018). In summary, with the deformation temperature increases, the atomic diffusion rate increases. The nucleation and

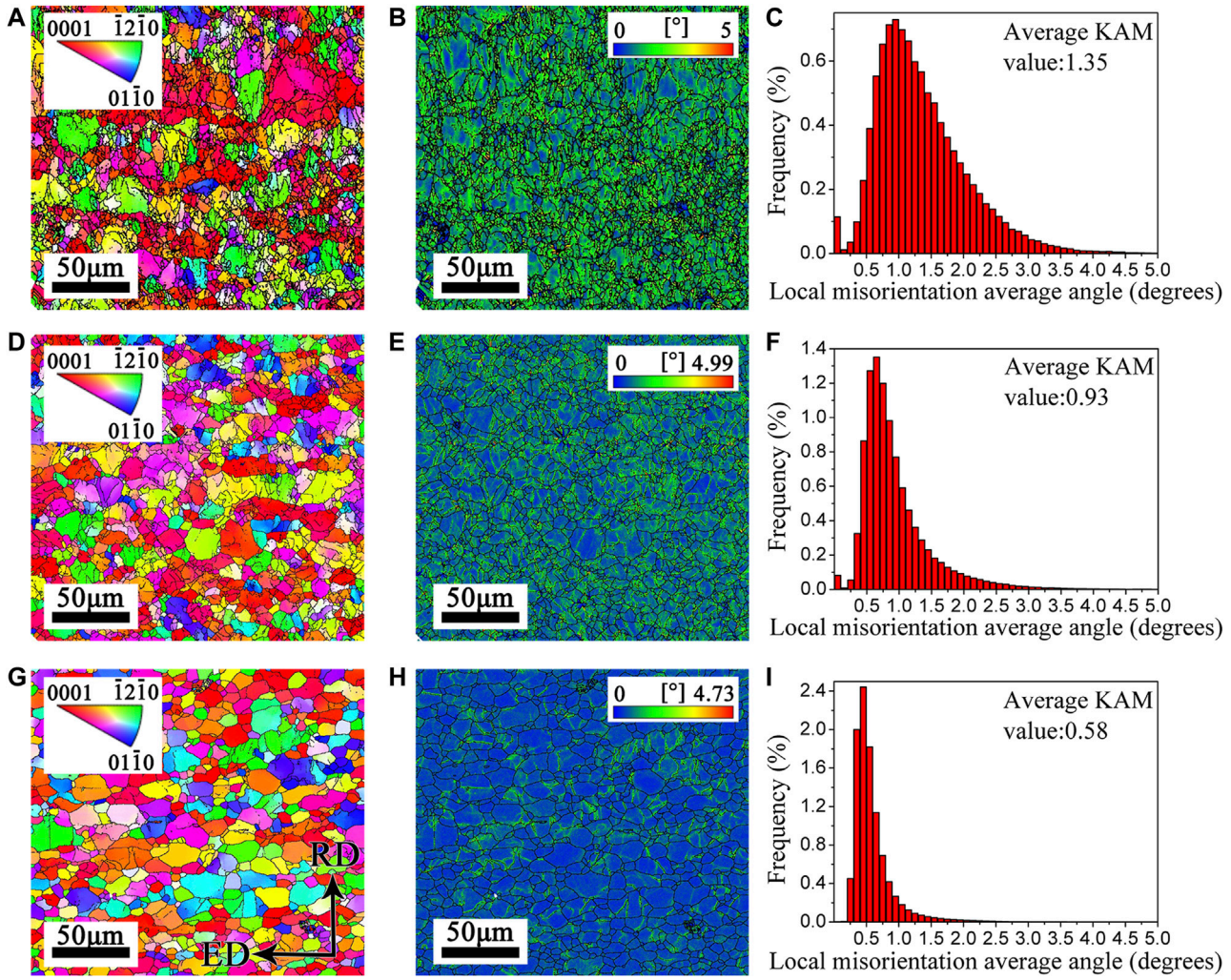

FIGURE 9 | KAM maps of the LAY410 alloy at the same rate with different temperatures: **(A,B, and C)** T = 150°C, **(D,E,F)** T = 200°C, **(G,H,I)** T = 250 °C.

growth of dynamic recrystallized grains are promoted, which leads to flow stress decrease and elongation increase.

The kernel average misorientation (KAM) maps near the fracture of the hot tensile specimen of LAY410 alloy at the same rate ($\varepsilon = 1.6 \times 10^{-4}$ s^{-1}) with different deformation temperatures (T = 150°C, 200°C, and 250°C) are shown in **Figure 9**. KAM value is an indicator of defect density, especially dislocation density, and can indirectly reflect deformation mechanism. It means that the evolution of dislocation density at different temperatures can be reflected in the KAM diagrams during tensile. When the deformation temperature is 150°C, the average KAM value is 1.35, as shown in **Figures 9A–C**. Meanwhile, the internal stress in the alloy is relatively concentrated, the dislocation density is relatively high, and the internal defects are relatively high. The number of dynamic recrystallized grains is small, and no obvious twins are observed. Therefore, the deformation mechanism is dominated by slippage, and the nucleation of a small number of recrystallized grains plays an auxiliary role in coordinating deformation. As the deformation temperature increases, the average KAM value decreases to 0.58, as shown in **Figures 9D–I**. Due to the occurrence of DRX, the stress in the alloy is released, and the stress concentration phenomenon is alleviated, resulting in a significant reduction in internal defects of the alloy. There is no obvious stress concentration phenomenon, only a small amount of stress is concentrated at the LAGBs.

The polar figures near the fracture of the hot tensile specimen of LAY410 alloy at the same rate ($\varepsilon = 1.6 \times 10^{-4}$ s^{-1}) with different deformation temperatures (T = 150°C, 200°C, 250°C) are shown in **Figure 10**. As can be seen from **Figure 10A**, when the deformation temperature is 150°C, the polar density points of {0001} basal plane are distributed along RD. The polar density points of {11–20} plane and {10–10} plane are distributed along the edge, showing a typical {0001} basal plane fiber texture, that is, the {0001} basal plane of the grains is approximately parallel to the ED, and the texture strength is 9.66. When the deformation temperature reaches 200°C, as shown in **Figure 10B**, the texture distribution becomes random. The texture strength is reduced, and its value is 8.31, but there is no significant change in the

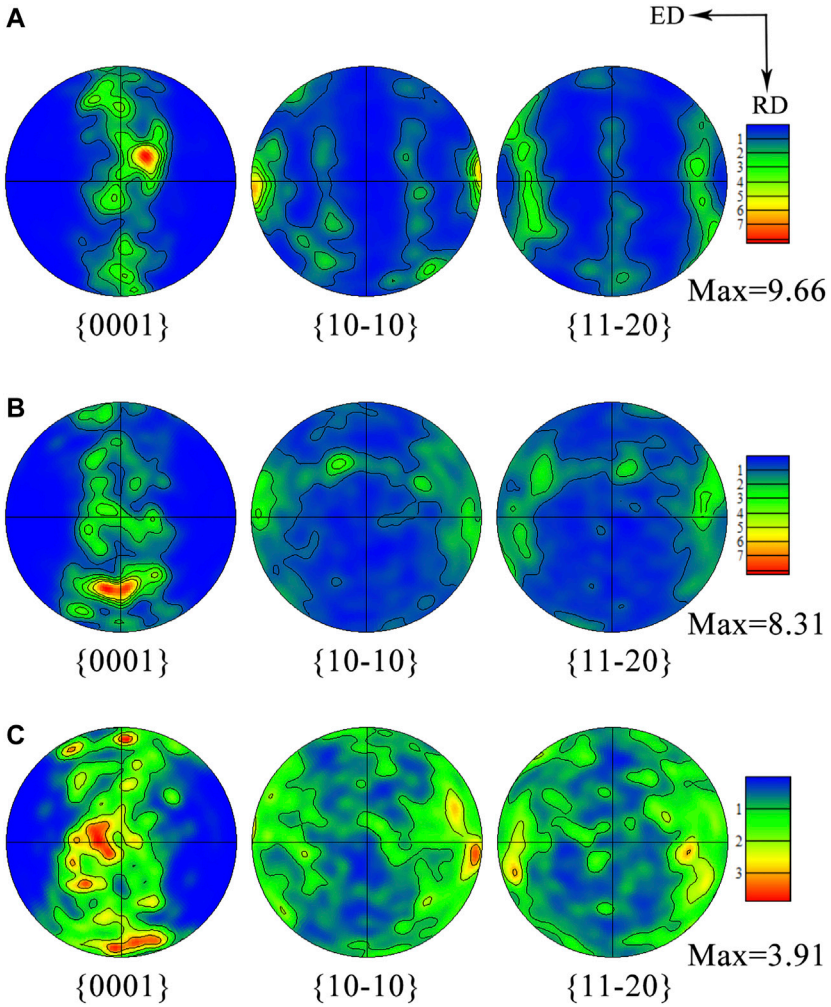

FIGURE 10 | Pole figures of the LAY410 alloy at the same rate with different temperatures: **(A)** T = 150°C, **(B)** T = 200°C, **(C)** T = 250°C.

texture type. The increase in temperature is conducive to non-basal slip system activation, which leads to the randomization of alloy texture and the decrease in texture strength (Barrett et al., 2018). When the temperature reaches 250°C, the texture strength decreases to 3.91, as shown in **Figure 10C**. The recrystallized grain structure inside the alloy increases significantly, which leads to a significant decrease in the texture strength. In general, the above results indicate that the deformation temperature has a certain influence on the texture strength of the alloy but does not change the texture type. Therefore, the {0001} basal fiber texture of LAY410 alloy still exists after hot tensile deformation.

Hot Tensile Fracture Morphology of Alloy

The fracture morphologies of LAY410 alloy after tensile at the same rate ($\varepsilon = 1.6 \times 10^{-4}\ s^{-1}$) with different deformation temperatures (T = 150°C, 200°C, and 250°C) is shown in **Figure 11**. It can be seen from **Figure 11** that the presence of cleavage steps, dimples, and quasi-cleavage tearing ridges leads to uneven fracture after hot tensile, showing the characteristics of ductile-brittle mixed fracture. When the temperature is 150°C, the existence of grain boundary indicates that the fracture mechanism is intergranular fracture. As the temperature reaches 250°C, the number of dimples gradually increases and the color of dimples becomes darker. It shows that the dominated fractures mechanisms of the alloys are gradually transferred from the fragile fracture mechanism to the ductile dimple mechanism due to the stress relaxation and the microstructure homogenization induced by DRX increase as deformation temperatures elevated (Bao et al., 2021).

Hot Tensile Plastic Deformation Mechanism of Alloy

To investigate the plastic deformation mechanism of LAY410 alloy during hot tensile, the Arrhenius model is used to calculate the relationship between various factors and flow stress during deformation. Its specific expression is shown in **Eq. 1** (Ji et al., 2011):

$$\dot{\varepsilon} = A\sigma^n \exp\left(-\frac{Q}{RT}\right), \quad (1)$$

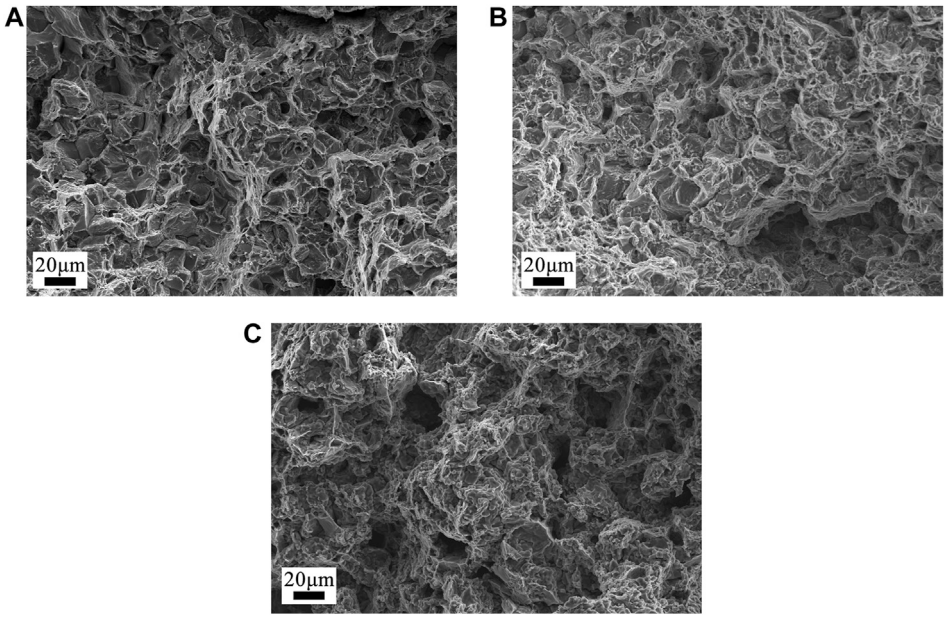

FIGURE 11 | Fracture morphologies of the LAY410 alloy at the same rate with different temperatures: **(A)** T = 150°C, **(B)** T = 200°C, **(C)** T = 250°C.

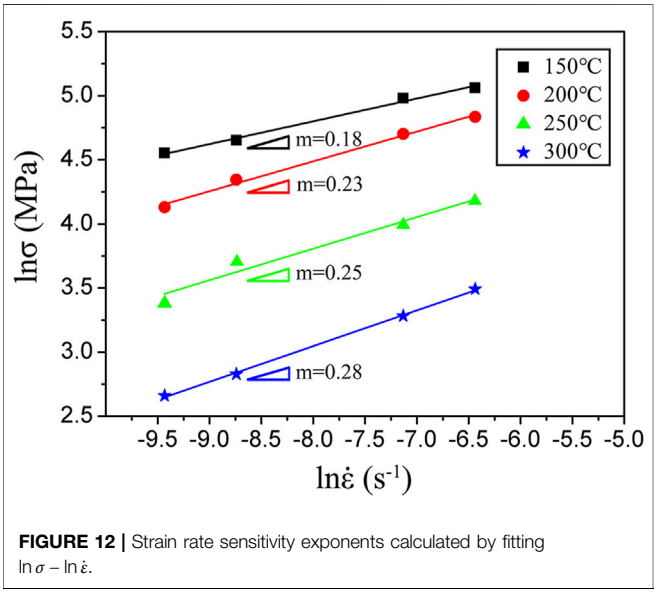

FIGURE 12 | Strain rate sensitivity exponents calculated by fitting $\ln\sigma - \ln\dot{\varepsilon}$.

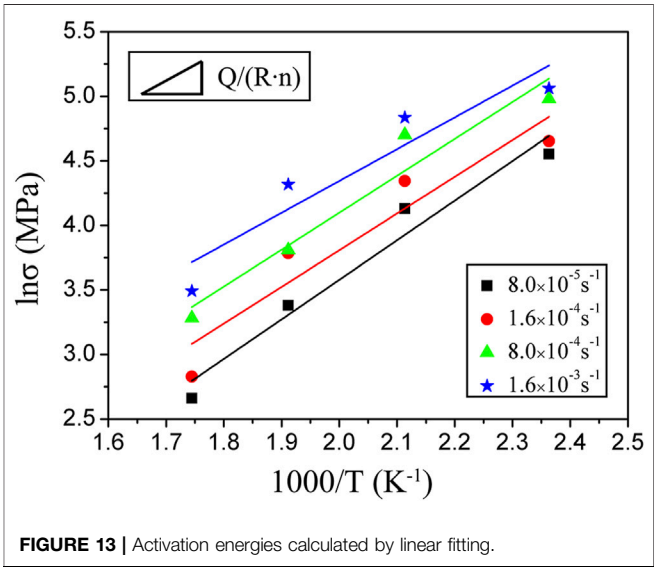

FIGURE 13 | Activation energies calculated by linear fitting.

where $\dot{\varepsilon}$ is the strain rate, σ is the flow stress, Q is the activation energy, T is the deformation temperature, R is the molar gas constant, and its value is 8.314 $Jmol^{-1}$ k^{-1}. A and n are the material constants, n = 1/m. m is the strain rate sensitivity exponent, usually used to reflect the upper limit of the plastic deformation of metal materials.

When the deformation temperature and strain rate are both constants, the strain rate sensitivity exponent can be calculated by **Eq. 2** (Huang et al., 2014) as follows:

$$m = \frac{\partial ln\sigma}{\partial ln\varepsilon}|\varepsilon, T, \tag{2}$$

where σ represents the flow stress and $\dot{\varepsilon}$ represents the strain rate.

When the deformation temperatures are 150°C, 200°C, 250°C, and 300°C, and the strain rates are 8×10^{-5} s^{-1}, 1.6×10^{-4} s^{-1}, 8×10^{-4} s^{-1}, and 1.6×10^{-3} s^{-1}, the calculated results are shown in **Figure 12**. According to the analysis, it is obvious that as the deformation temperature increases from 150°C to 300°C, the m value gradually increases from 0.18 to 0.28. In general, the value of m is used to reflect the ability to inhibit local necking. When the value of m is larger, the ability to inhibit tensile necking is stronger, indicating that the alloy exhibits higher elongation. When m = 1, the alloy reaches the ideal infinitely extendable state. Therefore, it can be concluded that LAY410 alloy shows

good plastic formability when the deformation temperature is 300°C.

To calculate activation energies in **Eq. 1**, **Equation 1** is converted into **Eq. 3**:

$$\dot{\varepsilon} \cdot exp\left(\frac{Q}{RT}\right) = A\sigma^{n}. \tag{3}$$

Take the natural logarithm on both sides of **Eq. 3** to obtain **Eq. 4** which is as follows:

$$ln\sigma = \frac{ln\dot{\varepsilon} - lnA}{n} + \frac{1}{T} \cdot \frac{Q}{R \cdot n}. \tag{4}$$

Eq. 4 can be further expressed as follows:

$$Q = R \cdot n \cdot \left|\frac{\partial \ ln\, \sigma}{\partial (1/T)}\right|_{\dot{\varepsilon}} = R \cdot \frac{1}{m} \cdot \left|\frac{\partial ln\sigma}{\partial (1/T)}\right|_{\dot{\varepsilon}} \tag{5}$$

By linear fitting $\ln\sigma - \ln 1/T$, the relevant slope can be obtained, and the calculation results are shown in **Figure 13**. Finally, by substituting the values of $Q/(R \cdot n)$ into **Eq. 4**, it can be obtained that the activation energy of the alloy is about 99.3 kJ/mol, which is smaller than the lattice diffusion activation energy of pure Mg (135 kJ/mol) and slightly higher than the grain boundary diffusion activation energy of pure Mg (92 kJ/mol) (Atkins, 1984). Therefore, based on the above analysis, it is further proved that the dominant hot tensile deformation mechanism of LAY410 alloy is the alternate coordinated deformation mechanism among GBS, intragranular slip, and DRX.

CONCLUSION

1) In the LAY410 alloy, with the strain rate decreases and/or deformation temperature increases, the peak stress gradually decreases and the elongations to fracture gradually increases. In addition, with temperature increases, an obvious steady-state rheological characteristic appears at the later stage of deformation, and the fracture morphology of the alloy gradually transfers from the ductile-brittle mixed fracture mode to the ductile fracture mode.
2) The microstructures of LAY410 alloy are obviously different at varied temperatures. When the deformation temperature is low (T = 150°C), the alloy microstructures are mainly composed of deformed grains with LAGBs. There are many internal defects in the alloy, and the recrystallized grains nucleate but the number is small. When the temperature rises to 250°C, the number of recrystallized grains increases significantly, and the DRX is completed more fully.
3) The deformation mechanism of LAY410 alloy is affected by temperature. When the deformation temperature is low, the deformation of the alloy is dominated by slippage, and the twinning plays a supplementary coordinating role. When the deformation temperature is high, DRX plays a dominant role.
4) In the LAY410 alloy, the activation energy of hot tensile deformation is about 99.3 kJ/mol, and the hot tensile deformation mechanism is the alternate coordinated deformation mechanism among GBS, intragranular slip, and DRX.

DATA AVAILABILITY STATEMENT

The raw data supporting the conclusions of this article will be made available by the authors, without undue reservation.

AUTHOR CONTRIBUTIONS

TY wrote and organized the manuscript. JW conducted the final review and revision of the manuscript. ZL and PJ made important contribution in the revision. All authors approved it for publication.

FUNDING

The authors would like to express thanks to the financial support from the Science and Technology Department of Qinghai Province (No. 2018-ZJ-783).

ACKNOWLEDGMENTS

We acknowledge Mengna Zhang for assistance in SEM, TEM, and EBSD experiments.

REFERENCES

Al-Samman, T. (2009). Comparative Study of the Deformation Behavior of Hexagonal Magnesium-Lithium Alloys and a Conventional Magnesium AZ31 alloy. *Acta Materialia* 57, 2229–2242. doi:10.1016/j.actamat.2009.01.031

Atkins, A. G. (1984). Deformation-mechanism Maps (The Plasticity and Creep of Metals and Ceramics). *J. Mech. Working Tech.* 9, 224–225. doi:10.1016/0378-3804(84)90015-9

Bao, J., Wu, Z., Wu, S., Withers, P. J., Li, F., Ahmed, S., et al. (2021). Hot Dwell-Fatigue Behaviour of Additively Manufactured AlSi10Mg alloy: Relaxation, Cyclic Softening and Fracture Mechanisms. *Int. J. Fatigue* 151, 106408. doi:10.1016/j.ijfatigue.2021.106408

Bao, L., Le, Q., Zhang, Z., Cui, J., and Li, Q. (2013). Effect of Homogenization Treatment on Microstructure Evolution and the Distributions of RE and Zr Elements in Various Mg-Li-RE-Zr Alloys. *J. Magnesium Alloys* 1, 139–144. doi:10.1016/j.jma.2013.07.003

Barrett, C. D., Imandoust, A., and El Kadiri, H. (2018). The Effect of Rare Earth Element Segregation on Grain Boundary Energy and Mobility in Magnesium and Ensuing Texture Weakening. *Scripta Materialia* 146, 46–50. doi:10.1016/j.scriptamat.2017.11.004

Chen, D., Xu, S., and Kulkarni, Y. (2020). Atomistic Mechanism for Vacancy-Enhanced Grain Boundary Migration. *Phys. Rev. Mater.* 4, 33602. doi:10.1103/PhysRevMaterials.4.033602

Chen, T., Chen, Z., Shao, J., Wang, R., Mao, L., and Liu, C. (2020). The Role of Long Period Stacking Ordered Phase in Dynamic Recrystallization of a Mg-Zn-Y

alloy during Hot Compression. *J. Alloys Comp.* 818, 152814. doi:10.1016/j.jallcom.2019.152814

Cui, C., Wu, L., Wu, R., Zhang, J., and Zhang, M. (2011). Influence of Yttrium on Microstructure and Mechanical Properties of As-Cast Mg-5Li-3Al-2Zn alloy. *J. Alloys Comp.* 509, 9045–9049. doi:10.1016/j.jallcom.2011.04.030

Fei, P., Qu, Z., and Wu, R. (2015). Microstructure and Hardness of Mg-9Li-6Al- X La (X =0, 2, 5) Alloys during Solid Solution Treatment. *Mater. Sci. Eng. A* 625, 169–176. doi:10.1016/j.msea.2014.12.014

Guo, F., Liu, L., Ma, Y., Jiang, L., Zhang, D., and Pan, F. (2020). Mechanism of Phase Refinement and its Effect on Mechanical Properties of a Severely Deformed Dual-phase Mg-Li alloy during Annealing. *Mater. Sci. Eng. A* 772, 138792. doi:10.1016/j.msea.2019.138792

Guo, X., Wu, R., Zhang, J., Liu, B., and Zhang, M. (2014). Influences of Solid Solution Parameters on the Microstrucuture and Hardness of Mg-9Li-6Al and Mg-9Li-6Al-2Y. *Mater. Des.* 53, 528–533. doi:10.1016/j.matdes.2013.07.011

Hadadzadeh, A., Mokdad, F., Amirkhiz, B. S., Wells, M. A., Williams, B. W., and Chen, D. L. (2018). Bimodal Grain Microstructure Development during Hot Compression of a Cast-Homogenized Mg-Zn-Zr alloy. *Mater. Sci. Eng. A* 724, 421–430. doi:10.1016/j.msea.2018.03.112

Hadadzadeh, A., and Wells, M. A. (2013). Mathematical Modeling of Thermo-Mechanical Behavior of Strip during Twin Roll Casting of an AZ31 Magnesium alloy. *J. Magnesium Alloys* 1, 101–114. doi:10.1016/j.jma.2013.04.001

Hagihara, K., Mori, K., and Nakano, T. (2019). Enhancement of Plastic Anisotropy and Drastic Increase in Yield Stress of Mg-Li Single Crystals by Al-Addition Followed by Quenching. *Scripta Materialia* 172, 93–97. doi:10.1016/j.scriptamat.2019.07.012

Hantzsche, K., Bohlen, J., Wendt, J., Kainer, K. U., Yi, S. B., and Letzig, D. (2010). Effect of Rare Earth Additions on Microstructure and Texture Development of Magnesium alloy Sheets. *Scripta Materialia* 63, 725–730. doi:10.1016/j.scriptamat.2009.12.033

He, J., Mao, Y., Lu, S., Xiong, K., Zhang, S., Jiang, B., et al. (2019). Texture Optimization on Mg Sheets by Preparing Soft Orientations of Extension Twinning for Rolling. *Mater. Sci. Eng. A* 760, 174–185. doi:10.1016/j.msea.2019.06.007

Huang, K. Z., and Huang, Y. G. (2013). *Advanced Solid Mechanics*. Beijing: Tsinghua University Press. in Chinese.

Huang, Y.-C., Lin, Y. C., Deng, J., Liu, G., and Chen, M.-S. (2014). Hot Tensile Deformation Behaviors and Constitutive Model of 42CrMo Steel. *Mater. Des.* 53, 349–356. doi:10.1016/j.matdes.2013.06.070

Ji, G., Li, F., Li, Q., Li, H., and Li, Z. (2011). A Comparative Study on Arrhenius-type Constitutive Model and Artificial Neural Network Model to Predict High-Temperature Deformation Behaviour in Aermet100 Steel. *Mater. Sci. Eng. A* 528, 4774–4782. doi:10.1016/j.msea.2011.03.017

Koike, J., Kobayashi, T., Mukai, T., Watanabe, H., Suzuki, M., Maruyama, K., et al. (2005). The Activity of Non-basal Slip Systems and Dynamic Recovery at Room Temperature in fine-grained AZ31B Magnesium Alloys. *Acta Mater.* 51, 2055–2065. doi:10.1016/S1359-6454(03)00005-3

Kumar, V., Govind, R., Balasubramaniam, R., and Balani, K. (2012). Microstructure Evolution and Texture Development in Thermomechanically Processed Mg-Li-Al Based Alloys. *Mater. Sci. Eng. A* 547, 38–50. doi:10.1016/j.msea.2012.03.074

Li, J., Qu, Z., Wu, R., Zhang, M., and Zhang, J. (2011). Microstructure, Mechanical Properties and Aging Behaviors of As-Extruded Mg-5Li-3Al-2Zn-1.5Cu alloy. *Mater. Sci. Eng. A* 528, 3915–3920. doi:10.1016/j.msea.2011.01.025

Li, X., Cheng, C., Le, Q., Zhou, X., Liao, Q., Chen, X., et al. (2019). Ex-situ EBSD Analysis of Yield Asymmetry, Texture and Twinning Development in Mg-5Li-3Al-2Zn alloy during Tensile and Compressive Deformation. *J. Alloys Comp.* 805, 947–956. doi:10.1016/j.jallcom.2019.07.099

Li, X., Le, Q., Li, D., Wang, P., Jin, P., Cheng, C., et al. (2021). Hot Tensile Deformation Behavior of Extruded Laz532 alloy with Heterostructure. *Mater. Sci. Eng. A* 801, 140412. doi:10.1016/J.MSEA.2020.140412

Liu, T., Wang, Y. D., Wu, S. D., Peng, R. L., Huang, C. X., Jiang, C. B., et al. (2004). Textures and Mechanical Behavior of Mg-3.3%Li alloy after ECAP. *Scr. Mater.* 51, 1057–1061. doi:10.1016/j.scriptamat.2004.08.007

Luo, A., Renaud, J., Nakatsugawa, I., and Plourde, J. (1995). Magnesium Castings for Automotive Applications. *JOM* 47, 28–31. doi:10.1007/BF03221226

Malik, A., Wang, Y., Huanwu, C., Nazeer, F., Ahmed, B., Khan, M. A., et al. (2020). Constitutive Analysis, Twinning, Recrystallization, and Crack in fine-grained ZK61 Mg alloy during High Strain Rate Compression over a Wide Range of Temperatures. *Mater. Sci. Eng. A* 771, 138649. doi:10.1016/j.msea.2019.138649

Stanford, N., Marceau, R. K. W., and Barnett, M. R. (2015). The Effect of High Yttrium Solute Concentration on the Twinning Behaviour of Magnesium Alloys. *Acta Materialia* 82, 447–456. doi:10.1016/j.actamat.2014.09.022

Sun, Y., Wang, R., Peng, C., and Feng, Y. (2018). Effects of Sn and Y on the Microstructure, Texture, and Mechanical Properties of As-Extruded Mg-5Li-3Al-2Zn alloy. *Mater. Sci. Eng. A* 733, 429–439. doi:10.1016/j.msea.2018.05.030

Sun, Y., Wang, R., Ren, J., Peng, C., and Feng, Y. (2019). Hot Deformation Behavior of Mg-8Li-3Al-2Zn-0.2Zr alloy Based on Constitutive Analysis, Dynamic Recrystallization Kinetics, and Processing Map. *Mech. Mater.* 131, 158–168. doi:10.1016/j.mechmat.2019.02.005

Tang, Y., Le, Q., Jia, W., Fu, L., Liu, X., and Cui, J. (2017). Microstructure evolution and strengthening mechanism study of Mg-Li alloys during deformation and heat treatment. *Materials Science and Engineering: A* 704, 344–359. doi:10.1016/j.msea.2017.08.043

Tu, T., Chen, X., Zhao, C., Yuan, Y., and Pan, F. (2020). A simultaneous increase of elastic modulus and ductility by Al and Li additions in Mg-Gd-Zn-Zr-Ag alloy. *Materials Science and Engineering: A* 771, 138576.1–138576.5. doi:10.1016/j.msea.2019.138576

Wang, J., Zhang, M., Shi, B., Zhang, L., and Jin, P. (2020). Ex-situ EBSD Investigation of the Reduced C/a Values and Work Hardening Behavior in Mg-4Li-1Al-0.5Y alloy under Hot Compression. *Mater. Sci. Eng. A* 797, 140113. doi:10.1016/j.msea.2020.140113

Wang, X. L. (2007). *Preparation of Mg-Li Mg-Li-Zr Zn-Zr Alloys by Electrolysis in Molten Salt*. Harbin: Harbin Institute of Technology.

Xu, S. W., Kamado, S., Matsumoto, N., Honma, T., and Kojima, Y. (2009). Recrystallization Mechanism of As-Cast AZ91 Magnesium alloy during Hot Compressive Deformation. *Mater. Sci. Eng. A* 527, 52–60. doi:10.1016/j.msea.2009.08.062

Xu, T. C., Peng, X. D., Qin, J., Chen, Y. F., Yang, Y., and Wei, G. B. (2015). Dynamic Recrystallization Behavior of Mg-Li-Al-Nd Duplex alloy during Hot Compression. *J. Alloys Comp.* 639, 79–88. doi:10.1016/j.jallcom.2015.03.144

Yang, X., Wang, G., Dong, G., Gong, F., Gong, F., and Zhang, M. (2009). Rare Earth Conversion Coating on Mg-8.5Li Alloys. *J. Alloys Comp.* 487, 64–68. doi:10.1016/j.jallcom.2009.07.113

Yang, Y., Peng, X., Ren, F., Wen, H., Su, J., and Xie, W. (2016). Constitutive Modeling and Hot Deformation Behavior of Duplex Structured Mg-Li-Al-Sr alloy. *J. Mater. Sci. Tech.* 32, 1289–1296. doi:10.1016/j.jmst.2016.11.015

Zhao, J., Zhang, J., Liu, W., Wu, G., and Zhang, L. (2016). Effect of Y Content on Microstructure and Mechanical Properties of As-Cast Mg-8Li-3Al-2Zn alloy with Duplex Structure. *Mater. Sci. Eng. A* 650, 240–247. doi:10.1016/j.msea.2015.10.067

Zhou, Y., Chen, Z., Ji, J., and Sun, Z. (2017). Dynamic Nano Precipitation Behavior of As-Cast Mg-4Li-4Zn-Y alloy during High Temperature Deformation. *Mater. Sci. Eng. A* 707, 110–117. doi:10.1016/j.msea.2017.09.050

Zhu, T., Sun, J., Cui, C., Wu, R., Betsofen, S., Leng, Z., et al. (2014). Influence of Y and Nd on Microstructure, Texture and Anisotropy of Mg-5Li-1Al alloy. *Mater. Sci. Eng. A* 600, 1–7. doi:10.1016/j.msea.2014.02.017

Conflict of Interest: The authors declare that the research was conducted in the absence of any commercial or financial relationships that could be construed as a potential conflict of interest.

frontiers in Materials

ORIGINAL RESEARCH
published: 07 October 2021
doi: 10.3389/fmats.2021.712551

Multi-Objective Optimization of Nano-Silica Modified Cement-Based Materials Mixed With Supplementary Cementitious Materials Based on Response Surface Method

Xiuzhi Zhang[1,2], Liming Lin[1,2], Mengdi Bi[3], Hailong Sun[1,2], Heng Chen[1,2], Qinfei Li[1,2] and Ru Mu[3]*

[1]School of Materials Science and Engineering, University of Jinan, Jinan, China, [2]Shandong Provincial Key Laboratory of Preparation and Measurement of Building Materials, University of Jinan, Jinan, China, [3]School of Civil and Transportation Engineering, Hebei University of Technology, Tianjin, China

This paper investigates the effect of supplementary cementitious materials (SCMs) on the fresh and mechanical properties of nano-silica modified cement-based materials (NSMCBM) based on the response surface method (RSM). Fly ash (FA), ground granulated blast-furnace slag (GGBFS), and silica fume (SF) were selected and the Box-Behnken design (BBD) method was used to design mix proportion. Besides, the quadratic term model was used to describe the relationship between independent variables and responses including fluidity, yield stress, plastic viscosity, thixotropy, and 3, 7, 28, and 56 d compressive strength. Based on the quadratic term model, the response surface of each response was drawn to understand the influence of SCMs. Results showed that FA had significant effect on fluidity and thixotropy while three kinds of SCMs had extremely significant effect on plastic viscosity. Response surface plot showed that NS could increase the plastic viscosity of NSMCBM to 1.445 Pa•s (M16). However, the addition of FA and GGBFS decreased the plastic viscosity to 0.9 Pa•s, which was comparable with the reference sample (M17). Such value was 37.7% lower than that of M16. Meanwhile, NS complemented the reduction of compressive strength caused by SCMs. Thus, the synergy effect of SCMs and NS could improve both fresh and mechanical properties. At last, multi-objective optimization was utilized to optimize the proportion of SCMs considering the interaction between SCMs to achieve desirable parameters.

Keywords: response surface method (RSM), multi-objective optimization, nano-silica, supplementary cementitious materials (SCM), rheology

OPEN ACCESS

Edited by:
Kequan Yu,
Tongji University, China

Reviewed by:
Jian Huang,
Wuhan University of Technology, China
Yun Gao,
Southeast University, China

****Correspondence:***
Xiuzhi Zhang
mse_zhangxz@ujn.edu.cn

Specialty section:
This article was submitted to Structural Materials, a section of the journal Frontiers in Materials

Received: *20 May 2021*
Accepted: *30 August 2021*
Published: *07 October 2021*

Citation:
Zhang X, Lin L, Bi M, Sun H, Chen H, Li Q and Mu R (2021) Multi-Objective Optimization of Nano-Silica Modified Cement-Based Materials Mixed With Supplementary Cementitious Materials Based on Response Surface Method. Front. Mater. 8:712551. doi: 10.3389/fmats.2021.712551

INTRODUCTION

With the development of concrete technology, supplementary cementitious materials (SCMs) have grown up to be indispensable components in concrete. It not only reduces cost but also improves the workability and durability of concrete (Cheng et al., 2018; Dhanya et al., 2018). However, the incorporation of SCMs decreases the early strength significantly, especially with the incorporation of large amounts of SCMs such as in pumped concrete and self-compacting concrete (SCC). Even

though adding accelerators such as calcium chloride (Riding et al., 2010), triethanolamine (Yan-Rong et al., 2016), and nitrate (Pizoń et al., 2016) can compensate for the adverse effects caused by the large amount of SCMs, but the improvement of early strength is limited and some accelerators also lead to the reduction of long term mechanical properties of concrete (Pizoń, 2017).

Due to its higher pozzolanic reactivity and nucleation effect (García-Taengua et al., 2015; Flores et al., 2017), nano-silica (NS) is regarded as a promising modifying material for concrete, which can improve the mechanical strength and durability of the cement-based materials and thus complement the reduction of early strength caused by SCMs. However, the consequent disadvantage is that the NS has a large specific surface area, so the rheological properties have deteriorated when it is incorporated into the cement paste (Ghafari et al., 2014). It is worth noting that a large number of literatures have reported that SCMs can improve the workability of nano-silica modified cement-based materials (NSMCBM) owing to the "morphological effect" and "filling effect" (Jalal et al., 2019; Roshani and Fall 2020; Hosan and Shaikh, 2021). Thus, the combination of NS and SCMs can improve various aspects of properties (workability, rheology, and mechanical properties) and has achieved satisfying results (Flores et al., 2017; Nandhini and Ponmalar, 2018; Ramezanianpour and Moeini, 2018; Liu et al., 2019). However, the optimum dosage of SCMs lacks a theoretical basis to achieve desirable properties. Besides, the interaction effect between SCMs also makes the properties of NSMCBM complicated and hard to predict. For this reason, it is important to investigate the influence of SCMs on workability and mechanical properties of NSMCBM. At the same time, the proportion of SCMs should be optimized to obtain satisfying properties.

The most widely used method for optimizing parameters is the response surface method (RSM). RSM is a statistical method to solve multivariate problems, which includes central composite design (CCD) method and Box-Behnken design (BBD) method (Pratama et al., 2020). Compared with the control variates method, RSM has less workload and more scientific experimental design (Ghalehnovi et al., 2020). As an effective statistical method, the RSM method has been widely employed in civil engineering to optimize the properties of concrete. For the CCD method, Jiao et al. (2018) optimized the mixture design of concrete based on the rheological properties. Li et al. (2018) optimized the mix proportion to prepare high-performance alkali-activated concrete with a slump of more than 200 mm. For the BBD method, Ahmed et al. (2020) employed the BBD method to get the optimum solution for designing parameters, which attained maximum mechanical properties and recycled aggregate, as well as minimum fiber percentage. However, few literatures can be found about the SCMs optimization due to their complex compositions, especially the incorporation of NS, which should be further researched to explore the synergy effect between SCMs and NS.

In this paper, three kinds of SCMs, namely, fly ash (FA), ground granulated blast-furnace slag (GGBFS), and silica fume (SF), were selected to explore the effect of the types, dosage, and interaction on the fluidity, rheology, and compressive strength of nano-silica modified cement-based materials (NSMCBM) based on RSM. Among them, the Box-Behnken design (BBD) method was used to design the mix proportion. Analysis of variance (ANOVA) was utilized to describe the significance of the factors and the fitting equation was determined according to the experimental results, and then, the combined effect of SCMs on fluidity, rheology, and compressive strength of NSMCBM was analyzed. Finally, the proportion of SCMs was optimized according to the fitting equation to achieve desirable properties. The authors hoped this study can provide an approach for optimizing mix proportion, especially multi-blending SCMs.

MATERIALS AND METHODS

Materials

The cement used here was Portland cement (P.O 42.5), which complies with Chinese standard GB 175-2007 (Committee, 2016). FA, GGBFS, and SF, these three kinds of supplementary cementitious materials (SCMs) were selected. The chemical compositions of cement and SCMs are shown in **Table 1**. The characteristic particle size measured by laser particle size analyzer and specific surface area measured by BET are given in **Table 2**. The microscopic morphology photographed by scanning electron microscope (SEM) is presented in **Figures 1–4**. There are many kinds of nano-silica (NS) and the pyrogenic fumed nano-silicas were used in this study. The nano-silica with 99.8% of powder concentration was used and its particle size is 7–40 nm. The characteristic particle size and specific surface area are presented in **Table 2**. A polycarboxylate-based superplasticizer (SP) with a water-reducing rate of 40% was used and its solid content is 45%.

Mix Proportion and Sample Preparation

In this study, the effect of SCMs was only focused on. Therefore, the effect of fine and coarse aggregate was neglected and the nano-silica modified cement-based paste was prepared in which the amount of SP was 0.5% by mass of binder, and the water-to-binder ratio was 0.3. NS was determined as 1% by mass of binder because Ref. (Hou et al., 2012; Hou et al., 2013) showed that NS would be difficult to disperse when the amount of NS is larger than 1.2%, even if ultrasonic dispersion is used. Besides, FA, GGBFS, and SF were used to replace cement for preparing ternary (cement, NS, and any one of the three SCMs), quaternary (cement, NS, and any two of the three SCMs), and quinary (cement, NS, and three SCMs) paste. The replacement levels for various SCMs were differed as 0, 15, and 30% for FA and GGBFS and 0, 3, and 6% for SF. Each of the SCMs was replaced by a percentage of the mass of the cement. According to the Box-Behnken design (BBD) method, fifteen groups of mix proportion were required and the corresponding lowest, median, and maximum values of replacement levels of SCMs were coded by −1, 0, and +1, respectively. Besides, to understand the effect of NS on workability and mechanical strength, two groups of paste that only contained cement and only contained cement and NS were prepared. The schematic of BBD is shown in **Figure 5** and the detailed mix proportion can be found in **Table 3**. It should be noted that for convenience, each group was marked by letter plus number, where F stood for fly ash, G stood for ground

TABLE 1 | Chemical composition of cement and SCMs.

	CaO	SiO_2	Al_2O_3	MgO	Fe_2O_3	SO_3	Na_2O	TiO_2	K_2O	Others
Cement	59.5	19.18	4.93	3.95	3.10	3.47	0.21	—	0.32	5.34
FA	3.79	47.20	41.29	1.10	2.51	1.17	0.91	0.69	—	1.34
GGBFS	39.8	35.4	12.8	7.9	0.2	1.9	0.3	—	0.4	1.3
SF	0.43	97.20	0.08	0.27	—	0.57	0.46	—	0.83	0.16

TABLE 2 | Characteristic particle size and specific surface area of cement, SCMs, and NS.

	D_{10}/μm	D_{50}/μm	D_{90}/μm	Mean/μm	Specific surface area/(m^2/kg)
Cement	1.29	13.24	35.57	16.54	328
FA	0.61	6.27	22.64	8.62	640
GGBFS	1.26	8.38	24.85	10.66	594
SF	0.056	0.14	0.21	0.15	20,000
NS	0.0065	0.023	0.04	0.029	2,96,000

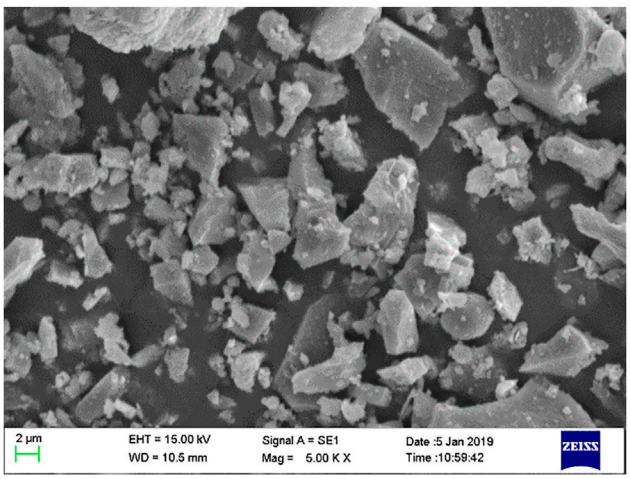

FIGURE 1 | SEM images of cement and SCMs, cement.

granulated blast-furnace slag, and S stood for silica fume. The number after the letter represented the corresponding amounts.

NS is easy to agglomerate due to its ultra-fine particle size when mixed with water (Kong et al., 2012). Therefore, high-intensity ultrasonication (SB25-12 DTD, 600 W, 40 Hz) was used to disperse suspension. Different mixing orders of raw materials will lead to significant deviation or uncertainty of the experimental results (Wang et al., 2019). In order to improve the accuracy of the results and reduce the deviation, each group of mixture was prepared according to the following mixing protocol. Firstly, the nano-silica suspension, water, and superplasticizer were mixed and poured into the mixing container to mix with cement and/or supplementary cementitious materials. Secondly, it was mixed at a lower speed of 150 r/min for 2 minutes and then at a higher speed of 300 r/min for additional 2 minutes to get evenly paste (Xiuzhi et al., 2021). After finishing the preparation, the measurement of fluidity and rheological parameters was carried out.

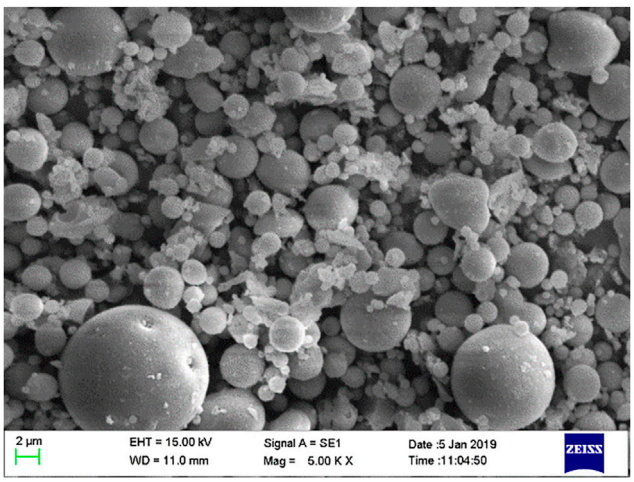

FIGURE 2 | SEM images of cement and SCMs, fly ash.

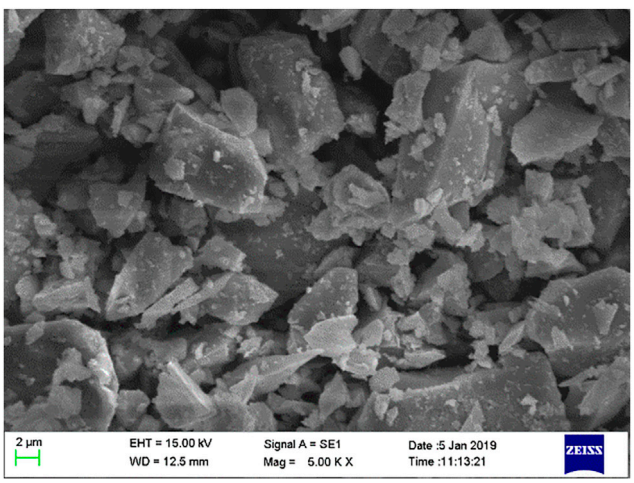

FIGURE 3 | SEM images of cement and SCMs, ground granulated blast-furnace slag.

Testing Methods

Fluidity

According to the American standard ASTM C230 (ASTM International, 2014), the fluidity was measured with a mini cone whose top diameter was 36 mm, the bottom diameter was 60 mm, and the height was 60 mm. At first, the mini cone was laid on a wet horizontal glass board and filled with paste and

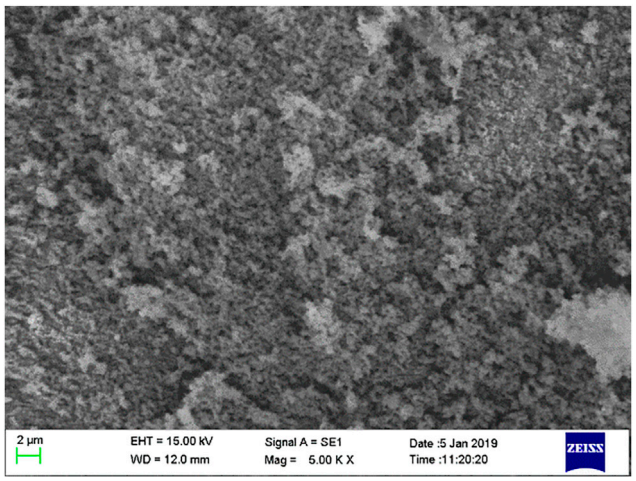

FIGURE 4 | SEM images of cement and SCMs, silica fume.

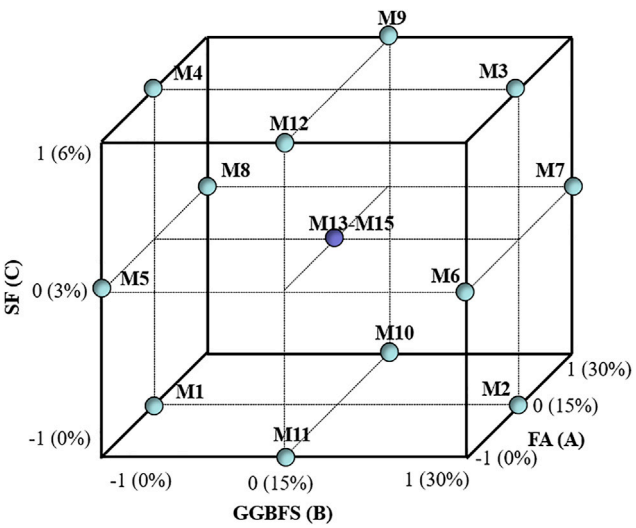

FIGURE 5 | The schematic of BBD.

then the mini cone was lifted. After waiting for 30 s, two diameters perpendicular to each other of each paste were measured and the average value was recorded as fluidity.

Rheological Parameters

The rheological parameters were determined by a Malvern Kinexus rotary rheometer. The measurement procedures were as follows: the sample was pre-sheared for 30 s at a shear rate of 100 s^{-1}. After resting for 30 s, the shear rate increased from 0 to 150 s^{-1} uniformly in 120 s and finally dropped to 0 s^{-1} with the same rotation speed gradient. The detailed process can be seen in **Figure 6**. This measurement procedure can minimize the internal flocculation structure of the paste before testing the rheological parameters, making the test results more accurate (Park et al., 2005; Senff et al., 2009).

According to the data measured by the rheometer, the descending section was selected to draw the shear stress-shear rate curve and the Herschel–Bulkley model was used to fit the rheological curve:

$$\tau = \tau_0 + K\dot{\gamma}^n, \tag{1}$$

where τ and $\dot{\gamma}$ are shear stress and shear rate, respectively; τ_0 is yield stress; K is the consistency coefficient; n is the power exponent.

The plastic viscosity η was calculated according to the method proposed by de Larrard (Hu and de Larrard, 1996; de Larrard et al., 1998). The equation is as follows:

$$\eta = \frac{3K}{n+2}\dot{\gamma}_{max}^{n-1}. \tag{2}$$

Several methods have been utilized to measure the thixotropy (Qian et al., 2018): shear rate decay method (Kawashima et al., 2013), yield stress growth rate (Roussel, 2006), and thixotropy hysteresis loop (Ferron et al., 2007). In this study, the thixotropy hysteresis loop was applied. According to the data measured by the rheometer, the thixotropic hysteresis loops can be obtained and the area of loops can be used to characterize the thixotropy.

Compressive Strength

After the fresh properties were measured, the paste was cast into 20 × 20 × 20 mm^3 molds and covered by a plastic film. After 1 day, the species were demolded and put into a standard curing room at 20 ± 2°C and relative humidity higher than 95% to cure for 3, 7, 28, and 56 days. Finally, CMT-5504 electronic universal testing machine was used to measure the compressive strength. The displacement velocity was 2.0 mm/min. The compressive strength of species was measured according to Chinese standard GB/T 17671-1999 (Supervision, 1999) and the average value of three species of each group was recorded as the final compressive strength.

Analyzing Methods

In most RSM problems, the relationship between the response (dependent variable) and the independent variable is unknown, so the first step of RSM is to seek a suitable approximation of the true functional relationship between the response (y) and the independent variable (x). Generally speaking, if the response is suitable for modeling with a linear function of independent variables, the approximate function is a linear model:

$$y = \beta_0 + \beta_1 x_1 + \beta_2 x_2 + \cdots + \beta_k x_k + \varepsilon. \tag{3}$$

Otherwise, higher-order polynomials must be used. For example, the expression of the quadratic term model is

$$y = \beta_0 + \sum_{i=1}^{k}\beta_i x_i + \sum_{i=1}^{k}\beta_{ii}x_i^2 + \sum_{i=1}^{k}\sum_{j>1}^{k}\beta_{ij}x_i x_j + \varepsilon, \tag{4}$$

where y is the response variable; x_i, x_i^2, $x_i x_j$ are the independent variables; k is the number of independent variables; β represents the regression coefficients; $\varepsilon$is the random error. In this study, the quadratic term model was used to fit the data to obtain the

TABLE 3 | Mix proportion of nano-silica modified cement-based paste containing SCMs.

Groups	Coded values			Cementitious mass/%				
	FA (A)	GGBFS (B)	SF (C)	A	B	C	Cement	NS
M1 (F15)	0	−1	−1	15	0	0	84	1
M2 (F15G30)	0	1	−1	15	30	0	54	1
M3 (F15G30S6)	0	1	1	15	30	6	48	1
M4 (F15S6)	0	−1	1	15	0	6	78	1
M5 (S3)	−1	−1	0	0	0	3	96	1
M6 (G30S3)	−1	1	0	0	30	3	66	1
M7 (F30G30S3)	1	1	0	30	30	3	36	1
M8 (F30S3)	1	−1	0	30	0	3	66	1
M9 (F30G15S6)	1	0	1	30	15	6	48	1
M10 (F30G15)	1	0	−1	30	15	0	54	1
M11 (G15)	−1	0	−1	0	15	0	84	1
M12 (G15S6)	−1	0	1	0	15	6	78	1
M13 (F15G15S3)	0	0	0	15	15	3	66	1
M14 (F15G15S3)	0	0	0	15	15	3	66	1
M15 (F15G15S3)	0	0	0	15	15	3	66	1
M16 (only NS)	—	—	—	0	0	0	99	1
M17 (no NS)	—	—	—	0	0	0	100	0

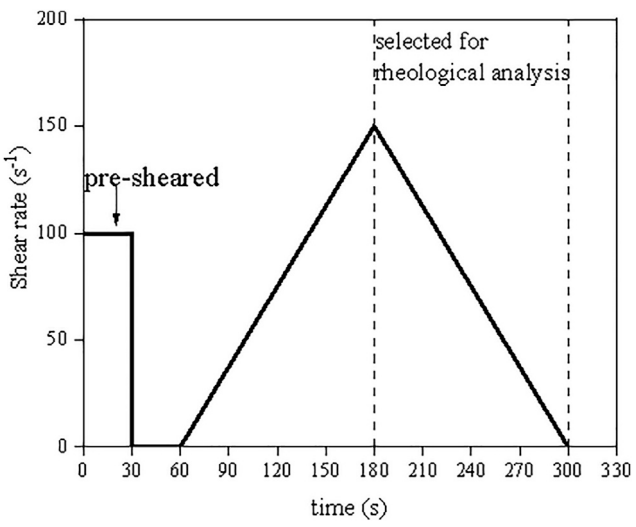

FIGURE 6 | The shear procedure of rheometer.

regression coefficients (β_i, β_{ii}, β_{ij}). R^2 was used to determine the degree of fitting of the quadratic term model to the data. At the same time, analysis of variance (ANOVA) was used to test the significance of the variables. The flow chart of the research can be seen in **Figure 7**.

RESULTS AND DISCUSSION

Experimental and RSM Results

The experimental results of fluidity, yield stress, plastic viscosity, thixotropy, 3 d compressive strength (C_{3d}), 7 d compressive strength (C_{7d}), 28 d compressive strength (C_{28d}), and 56 d compressive strength (C_{56d}) are shown in **Table 4**, respectively. According to the data, ANOVA and quadratic term model fitting were carried on, respectively. The significance of variables and the regression coefficients (β_i, β_{ii}, β_{ij}) is shown in **Table 5**.

It can be seen from **Table 4** that compared with the group without NS (M17), the addition of NS (M16) remarkably decreased the fluidity and increased the yield stress, which can be due to the ultra-fine particle size led to the increase of friction and water demand (Chithra et al., 2016). Plastic viscosity and thixotropy are closely related to flocculation and C-S-H. NS has a higher pozzolanic effect, so the addition of NS accelerates the cement hydration to form additional C-S-H (Mendoza Reales et al., 2019). As a result, the plastic viscosity and thixotropy were

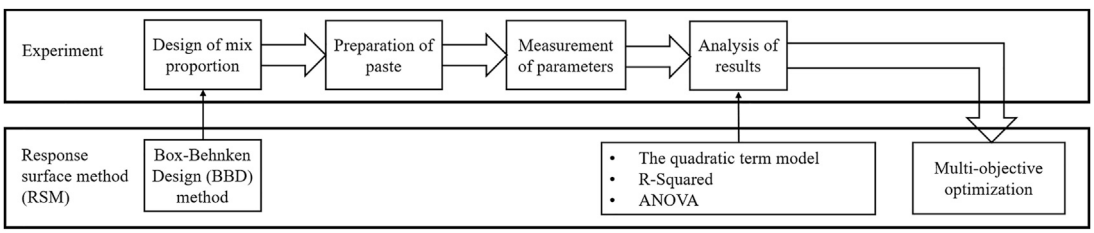

FIGURE 7 | The flow chart of the research.

TABLE 4 | Experimental results of nano-silica modified cement-based paste containing SCMs, fluidity.

Groups	Fluidity (mm)	Yield stress (Pa)	Plastic viscosity (Pa`s)	Thixotropy ($Pa•s^{-1}$)	C_{3d} (MPa)	C_{7d} (MPa)	C_{28d} (MPa)	$C_{56d.}$ (MPa)
M1 (F15)	268	4.81	1.137	2,837	42.27	82.03	108.14	108.74
M2 (F15G30)	256	5.44	1.048	2,557	47.36	81.87	102.64	109.97
M3 (F15G30S6)	265	5.03	1.069	2,325	34.27	63.36	88.29	93.34
M4 (F15S6)	262	4.99	1.48	3,631	36.14	80.21	111.06	112.36
M5 (S3)	249	7.61	1.382	3,740	60.32	90.88	112.39	112.37
M6 (G30S3)	253	4.13	1.22	3,167	47.56	84.02	103.90	105.34
M7 (F30G30S3)	257	5.3	1.011	2,086	33.40	72.50	98.26	107.88
M8 (F30S3)	279	6.12	1.259	2,944	41.04	77.78	98.08	112.39
M9 (F30G15S6)	263	5.33	1.193	2,929	38.17	65.77	93.91	107.30
M10 (F30G15)	280	6.04	1.051	2,934	36.58	75.80	101.52	111.77
M11 (G15)	260	6.09	1.13	3,233	48.57	74.12	107.39	101.05
M12 (G15S6)	254	4.61	1.48	2,953	56.98	83.69	110.77	110.13
M13 (F15G15S3)	265	4.92	1.127	2,683	43.01	84.49	111.18	94.21
M14 (F15G15S3)	260	4.88	1.121	2,689	42.89	84.21	110.98	94.68
M15 (F15G15S3)	263	4.97	1.132	2,678	43.26	84.71	111.59	94.11
M16 (only NS)	253	5.17	1.445	4,629	59.38	98.05	110.77	108.87
M17 (no NS)	295	0.36	0.968	2,113	38.01	61.23	81.59	92.31

TABLE 5 | Results of ANOVA and regression coefficients.

Terms		Fluidity (mm)	Yield stress (Pa)	Plastic viscosity (Pa`s)	Thixotropy ($Pa•s^{-1}$)	C_{3d} (MPa)	C_{7d} (MPa)	C_{28d} (MPa)	$C_{56d.}$ (MPa)
Regression coefficients	Intercept	262.67	4.92	1.13	2,683.33	43.05	84.47	111.25	94.33
	A (x_1)–FA	7.88*	0.04	–0.09***	–275.00*	–8.03*	–5.11**	–5.33**	1.30
	B (x_2)–GGBFS	–3.38	–0.45	–0.11***	–377.13*	–2.15	–3.64*	–4.57*	–3.67*
	C (x_3)–SF	–2.50	–0.30	0.11***	34.63	–1.15	–2.60	–1.96	–1.05
	AB (x_1x_2)	–6.50*	0.67	–0.02	–71.25	1.28	0.39	2.17	0.63
	AC (x_1x_3)	–2.75	0.19	–0.05**	68.75	–1.70	–4.90**	–2.75	–3.39
	BC (x_2x_3)	3.75	–0.15	–0.08**	–256.50	–1.74	–4.17	–4.32	–5.06*
	A^2 (x_1^2)	–0.83	0.66	0.06**	237.83	3.80	–2.60	–3.61	8.31**
	B^2 (x_2^2)	–2.33	0.21	0.03	63.08	–1.27	–0.58	–4.48	6.85**
	C^2 (x_3^2)	2.42	–0.06	0.03	91.08	–1.77	–7.03*	–4.24	4.92*
	R^2	0.9007	0.9213	0.9898	0.9851	0.9648	0.9635	0.9254	0.9401
	Adjusted R^2	0.8979	0.8934	0.9715	0.9218	0.9046	0.8935	0.8692	0.8323

increased in M16. Besides, the higher pozzolanic reactivity, nucleation effect, and filler effect also contributed to the increase of early strength through improving the microstructure (García-Taengua et al., 2015; Lu et al., 2020).

The regression coefficients obtained by fitting the quadratic term model can be seen in **Table 5** and the significance of the corresponding independent variable is also marked with * after the regression coefficient. If the *p*-value of the independent variable calculated through ANOVA is less than 0.001, it meant that it has an extremely significant effect on the corresponding parameters and marked with ***. ** represents highly significant $p < 0.01$ and * represents significant $p < 0.05$. Otherwise, the independent variable is not significant. Besides, the R^2 and the adjusted R^2 demonstrate the credibility of the quadratic term model. It can be seen from **Table 5** that the R^2 and the adjusted R^2 were both close to one demonstrating that the quadratic term model can be used to fit the data. In the next three sections, the quadratic term equation about every parameter was listed according to regression coefficients shown in **Table 5**. Moreover, response surface plots of the quadratic term model were also generated to understand the effect of the

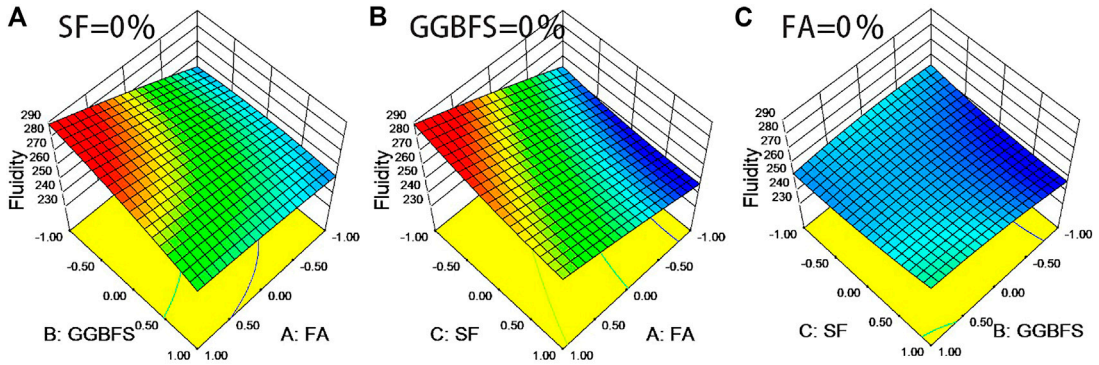

FIGURE 8 | The combined effect of SCMs on fluidity of nano-silica modified cement-based paste.

independent variables on the dependent variable (WARDROP and MYERS, 1990; Garlapati and Roy, 2017).

Effect of SCMs on Fluidity

The relative influence of the independent variables can be evaluated by comparing their regression coefficients. The greater the absolute value, the greater the significance of the independent variable to the dependent variable. Besides, the positive value indicates that the factor can increase the parameter while the negative value demonstrates that the parameter decreases with increasing the factor. As can be seen from **Table 5** the effect of FA showed a significant positive effect on fluidity while the interaction of FA and GGBFS showed a significant negative effect. According to the regression coefficients, the quadratic term equation about fluidity can be written as follows and the combined effect of SCMs on fluidity is shown in **Figure 8**.

$$Y_{fluidity} = 262.67 + 7.88A - 3.38B - 2.5C - 0.83A^2 - 2.33B^2 + 2.42C^2 - 6.5AB - 2.75AC + 3.75BC. \quad (5)$$

It can be seen from **Eq. 5** that FA could increase the fluidity while the increase of GGBFS and SF led to the fluidity decrease. The effect of SCMs on fluidity can be ascribed to the morphology effect (Giergiczny, 2019). As can be seen from **Figure 2**, the spherical shape of FA can exhibit ball-bearing effect to decrease the friction between particles and increase the fluidity. However, GGBFS and SF have an irregular surface, which may increase the friction (Li and Wu, 2005; Jiao et al., 2017). Moreover, the specific surface area of SF is much larger than that of cement and the replacement of cement with SF can increase the demand for water to lubricating (Wu et al., 2019). As a result, the addition of GGBFS and SF decreased the fluidity. **Figure 8** shows the combined effect of SCMs on fluidity. **Figures 8A,B** illustrate that when the replacement of FA was 0% (that is FA−−1 level), the effect of GGBFS and SF on fluidity was not significant and the fluidity was kept at the range of 240–260 mm, which is consisted in **Figure 8C**. However, with the presence of FA, the addition of GGBFS and SF reduced the fluidity gradually and GGBFS reduced the most. This phenomenon is also reflected in **Table 5** in which FA*GGBFS showed a significant effect on fluidity compared with FA*SF. It also can be seen in **Figures 8A,B** that without SF and GGBFS, the incorporation of FA could increase the fluidity up to about 290 mm, which was comparable with the fluidity of M17 shown in **Table 4**. That indicated that the influence of FA and NS on fluidity could offset each other. Similar results are reported by other investigations (Shirdam et al., 2019; Xie et al., 2019). To increase fluidity, FA should be incorporated and the amount of GGBFS and SF should be as small as possible. At the same time, **Figure 8C** indicates that the combination of GGBFS and SF was not advisable.

Effect of SCMs on Rheology

From **Table 5**, it also can be observed that the effect of SCMs on yield stress was not significant, but had a highly significant effect on plastic viscosity. Specifically, FA, GGBFS, and SF had an extremely significant effect and FA*SF and GGBFS*SF as well as FA^2 had a highly significant effect. Moreover, FA and GGBFS exhibited a negative effect on plastic viscosity while SF displayed a positive effect, which are consistent with Ref. (Ting et al., 2019; Duan et al., 2020; Jiang et al., 2020). As for thixotropy, FA, and GGBFS had a significant effect on thixotropy and the rest of the terms were not significant, the quadratic term model of the yield stress, plastic viscosity, and thixotropy are as follows:

$$Y_{yield\ stress} = 4.92 + 0.04A - 0.45B - 0.3C + 0.66A^2 + 0.21B^2 - 0.06C^2 + 0.67AB + 0.19AC - 0.15BC, \quad (6)$$

$$Y_{plastic\ viscosity} = 1.13 - 0.09A - 0.11B + 0.11C + 0.06A^2 + 0.03B^2 + 0.03C^2 - 0.02AB - 0.05AC - 0.08BC, \quad (7)$$

$$Y_{thixotropy} = 2683.33 - 275A - 377.13B + 34.63C + 237.83A^2 + 63.08B^2 + 91.08C^2 - 71.25AB + 68.75AC - 256.5BC. \quad (8)$$

The combined effect of SCMs on yield stress, plastic viscosity, and thixotropy is illustrated in **Figures 9–11**, respectively.

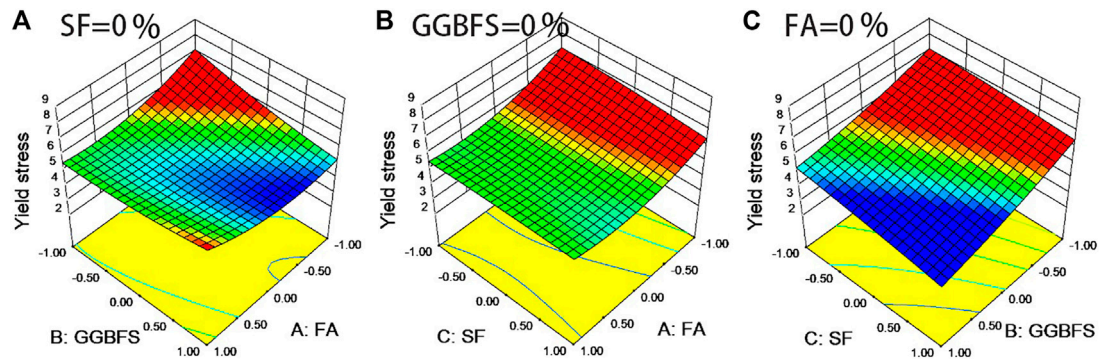

FIGURE 9 | The combined effect of SCMs on yield stress of nano-silica modified cement-based paste.

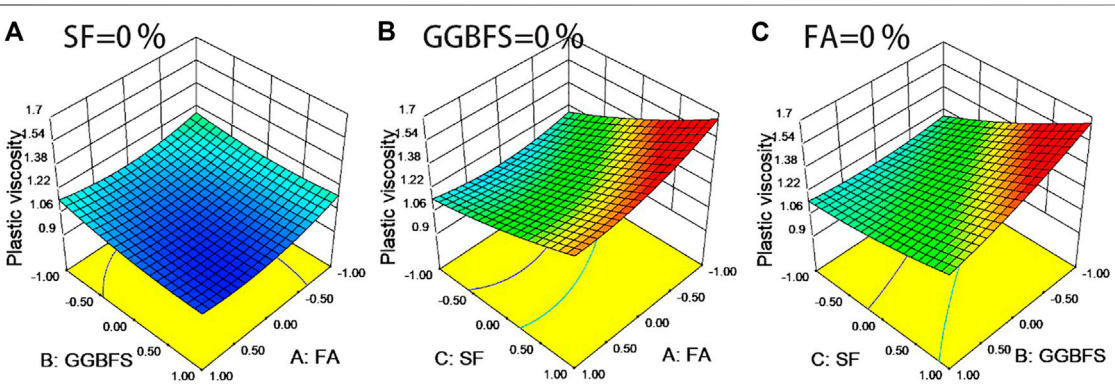

FIGURE 10 | The combined effect of SCMs on plastic viscosity of nano-silica modified cement-based paste.

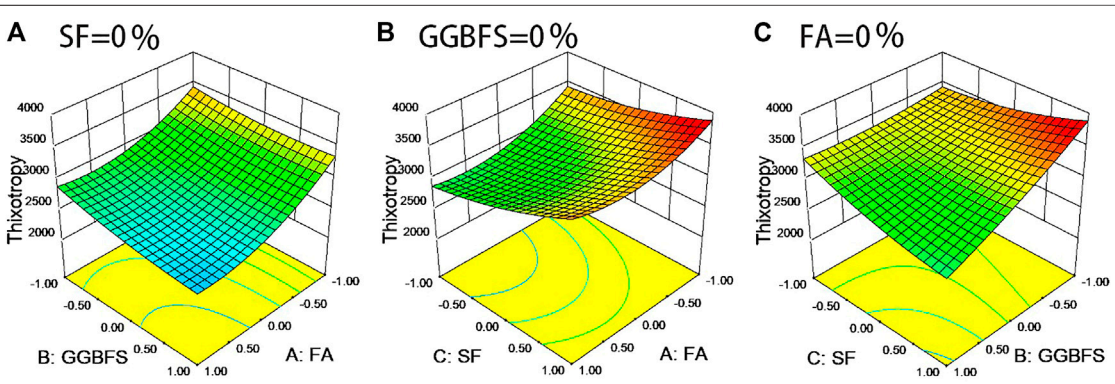

FIGURE 11 | The combined effect of SCMs on thixotropy of nano-silica modified cement-based paste.

It can be seen from **Eq. 6** that FA could increase the yield stress while GGBFS and SF made it decrease. However, **Figure 9A** shows that the incorporation of 30% FA (that is FA−1 level) made the yield stress increase slightly with GGBFS, which was not consistent with **Eq. 6**. At the same time, the incorporation of GGBFS made the lowest yield stress occurred at about FA−0 level, which indicated that there existed an interaction effect between FA and GGBFS. **Figure 9B** illustrates that whether or not FA was added, the effect of SF on yield stress was not significant. On the contrary, the incorporation of FA decreased the yield stress sharply. That is in agreement with the result from Ref. (Shanahan et al., 2016). Banfill (Banfill, 1991) reported that the combination of GGBFS with SF resulted in lower yield stress, which is consistent with **Figure 9C** and **Eq. 6**. Based on

the discussion above, conclusions can be drawn that SF needs to be mixed with FA or GGBFS to reduce the yield stress. Among them, SF and GGBFS can exert a synergy effect to decrease the yield stress sharply. However, the amount of FA should be about 15% when mixed with GGBFS.

Equations 7, **8** show that both FA and GGBFS could decrease the plastic viscosity and thixotropy, but the addition of SF led to the two parameters' increase. From the perspective of microstructure, the plastic viscosity characterizes the deformation rate of the paste, which is mainly related to the amount of flocculated structure (Ke et al., 2020). Thixotropy can be explained by the formation and destruction of flocculated structures (Roussel et al., 2012). Moreover, the formation and amount of flocculated structure are related to the chemical reactivity of SCMs (Muzenda et al., 2020). The higher the chemical reactivity of SCMs, the more flocculated structure is generated and the less deformable the paste is, which leads to the higher plastic viscosity and thixotropy. Compared with cement, SF has higher chemical activity; as a result, the incorporation of SF leads to the formation of a large amount of flocculation rapidly (Benaicha et al., 2015). Jiao (Xiao et al., 2020) stated that GGBFS has lower hydraulic activity compared with cement, thus the addition of GGBFS decreases plastic viscosity. Moreover, the unburnt carbon coated on FA particles may decrease the chemical activity, thus decreasing the plastic viscosity and thixotropy (Alberici et al., 2017).

Figure 10A shows that the addition of FA and GGBFS decreased the plastic viscosity to about 0.9 Pa·s, which was comparable with the plastic viscosity of M17 shown in **Table 4**. On the contrary, SF increased the plastic viscosity up to about 1.7 Pa·s and adding FA or GGBFS may slightly decrease the plastic viscosity, which can be seen in **Figures 10B,C**. As for thixotropy, **Figures 11A,C** plot that the synergy effect of GGBFS and FA as well as GGBFS and SF could reduce thixotropy significantly. Among them, the addition of GGBFS changed the effect of SF on thixotropy, which indicated that SF was suitable for incorporation in the presence of GGBFS. However, the combination of FA and SF was not desirable because the lowest thixotropy was about 2,800 and occurred at FA–1 level and SF−−1 level, which demonstrated that FA was not suitable for mixing with SF. Self-compacting concrete (SCC) often requires smaller plastic viscosity and thixotropy to obtain higher flow velocity (Alberici et al., 2017). From this point of view, the combinations of FA and GGBFS or SF and GGBFS are preferable while the combination of FA and SF is not advisable.

Effect of SCMs on Compressive Strength

Table 5 indicates that only FA had a significant effect on 3 d compressive strength. FA and FA*SF imposed a highly significant effect on 7 d compressive strength and followed by GGBFS and SF^2. Besides, GGBFS and FA exhibited significant and highly significant effects on 28 d compressive strength, respectively. Moreover, FA^2 and $GGBFS^2$ showed a highly significant effect on 56 d compressive strength and followed by GGBFS, GGBFS*SF, and SF^2. The fitted quadratic term equations of compressive strength are as follows:

$$Y_{3d\ C.S.} = 43.05 - 8.03A - 2.15B - 1.15C + 3.8A^2 - 1.27B^2 - 1.77C^2 + 1.28AB - 1.7AC - 1.74BC, \quad (9)$$

$$Y_{7d\ C.S.} = 84.47 - 5.11A - 3.64B - 2.6C - 2.6A^2 - 0.58B^2 - 7.03C^2 + 0.39AB - 4.9AC - 4.17BC, \quad (10)$$

$$Y_{28d\ C.S.} = 111.25 - 5.33A - 4.57B - 1.96C - 3.61A^2 - 4.48B^2 - 4.24C^2 + 2.17AB - 2.75AC - 4.32BC, \quad (11)$$

$$Y_{56d\ C.S.} = 94.33 + 1.3A - 3.67B - 1.05C + 8.31A^2 + 6.85B^2 + 4.92C^2 + 0.63AB - 3.39AC - 5.06BC. \quad (12)$$

It can be seen from **Eqs. 9–12** that SCMs can decrease the compressive strength, except FA which increased the 56 d compressive strength. This is because SCMs delay the early hydration and generate less C-S-H in an early age, which is closely related to compressive strength (Ting et al., 2020; Wang et al., 2020). The combined effect of SCMs on 3, 7, 28, and 56 d compressive strength is depicted in **Figures 12–15**, respectively. It can be seen from **Figures 12A,B** that the presence of FA decreased the 3 d compressive strength to about 36 MPa, which was similar to M17 shown in **Table 4**. However, the combination of SF and GGBFS kept the 3 d compressive strength at a higher level, which is shown in **Figure 12C**. **Figures 13**, **14** indicate that SF played an important role to increase 7 and 28 d compressive strength. At the same time, in the presence of SF, the incorporation of FA or GGBFS would reduce the strength. Therefore, FA or GGBFS was not suitable to be incorporated into blends containing SF at a large amount. **Figure 14A** shows that the combination of GGBFS−−0.5 level and FA−−0.5 level contributed to the highest 28 d compressive strength while **Figure 15A** shows the same level to the lowest 56 d compressive strength, which indicated that the same combination of SCMs may have a different effect on compressive strength of different ages. Besides, in the presence of SF, the effect of FA and GGBFS on 56 d compressive strength was different. Specifically, the 56 d compressive strength decreased initially but then increased with the increase of FA while decreased steadily with the GGBFS. Moreover, it also can be seen from **Figures 13–15** that regardless of the amount of SCMs, the synergy effect of SCMs and NS increased the compressive strength compared with M17 shown in **Table 4**. Based on the above analysis, conclusions can be drawn that SF contributes to the compressive strength and GGBFS has a beneficial effect on 3 d strength. To obtain higher 7 and 28 d compressive strength, FA or GGBFS cannot be incorporated at a large amount in the presence of SF. As for 56 d compressive strength, the combination of FA and SF shows a satisfactory result compared with the other two combinations.

It can be seen from the above analysis that different SCMs have different effects on fluidity, rheology, and compressive strength of different ages. At the same time, the interaction between SCMs makes the effect more complicated. As a result, a more scientific

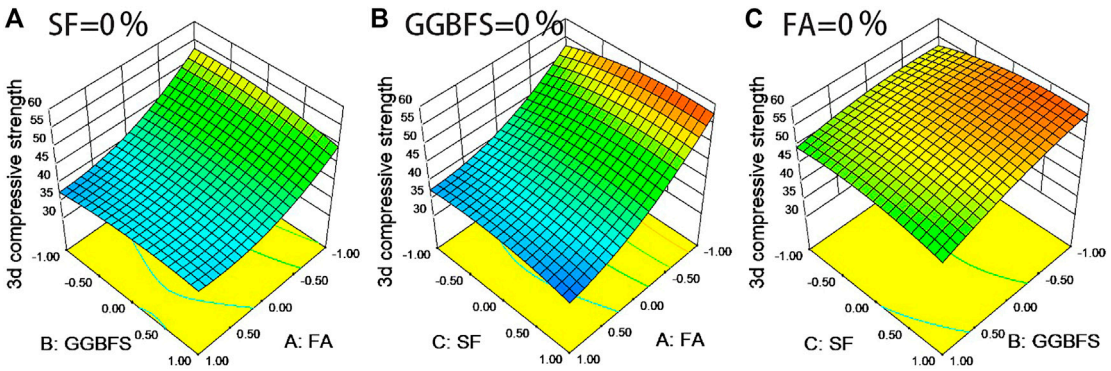

FIGURE 12 | The combined effect of SCMs on 3 d compressive strength of nano-silica modified cement-based paste.

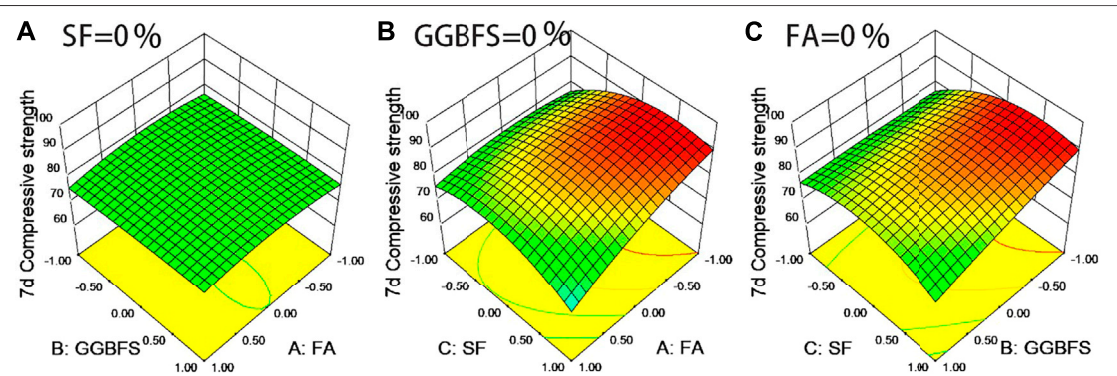

FIGURE 13 | The combined effect of SCMs on 7 d compressive strength of nano-silica modified cement-based paste.

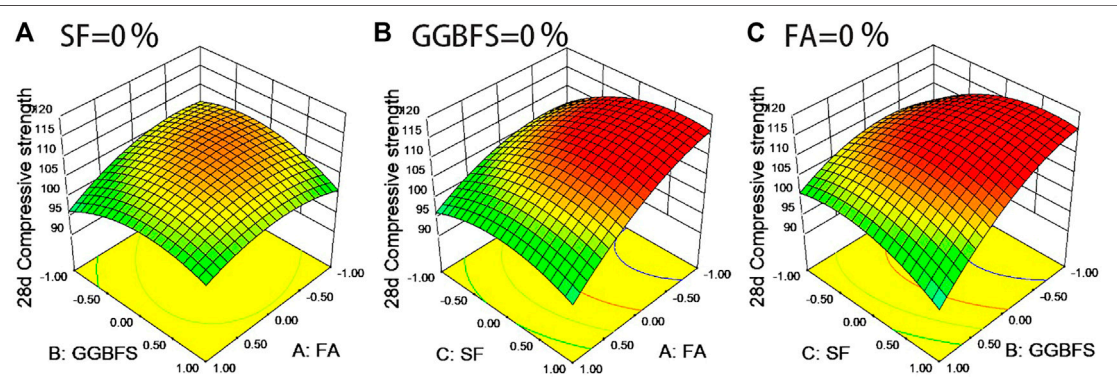

FIGURE 14 | The combined effect of SCMs on 28 d compressive strength of nano-silica modified cement-based paste.

method should be utilized to optimize the mix proportion to achieve desirable properties.

MULTI-OBJECTIVE OPTIMIZATION

In this part, a multi-objective optimization technique was employed to find out the optimum solution (the appropriate dosage of SCMs to satisfy target parameters). The criterion used to evaluate the response optimization is the desirability function. If one single response is needed to be optimized, then the individual desirability function should be used. Otherwise, the composite desirability function should be used. For example, if one wants to get maximum response, the desirability function is as follows (Ferdosian and Camões, 2017):

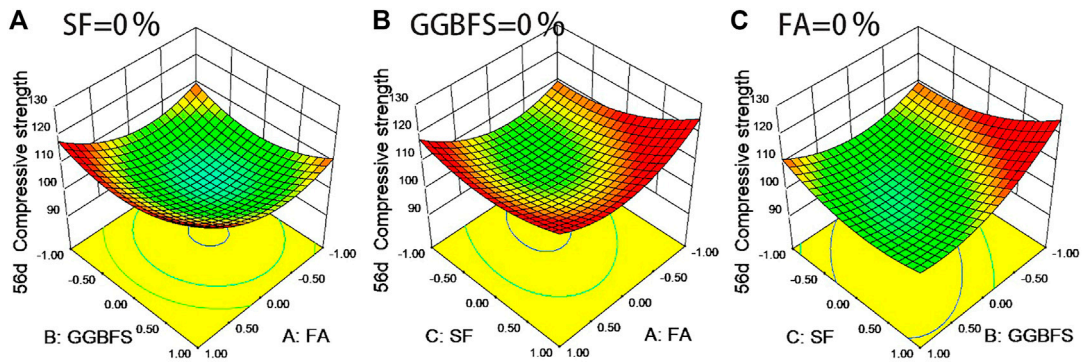

FIGURE 15 | The combined effect of SCMs on 56 d compressive strength of nano-silica modified cement-based paste.

TABLE 6 | The results of multi-objective optimization of nano-silica modified cement-based paste containing SCMs.

Coded values			Predicted values			Desirability
FA	GGBFS	SF	Fluidity (mm)	Plastic viscosity (Pa•s)	56 d compressive strength (MPa)	
0.96	−0.24	−0.97	280	1.08	112.39	0.947

$$d_i = \begin{cases} 0 & (Y_i < L_i) \\ \left[\dfrac{Y_i - L_i}{T_i - L_i}\right]^{w_i} & (L_i < Y_i < T_i), \\ 1 & (Y_i < T_i) \end{cases} \quad (13)$$

where d_i is the desirability; L_i is the lowest acceptable value of the i_{th} response; T_i is the highest acceptable value of the i_{th} response; w_i is the weight of the desirability function corresponding to the i_{th} response.

Besides, if the weight of the responses is equal, the composite desirability is calculated by

$$D = \sqrt[n]{d_1 \times d_2 \times \cdots \times d_n}, \quad (14)$$

where n is the number of response.

Multi-objective optimization aims to find out the appropriate dosage of FA, GGBFS, and SF to satisfy the target parameters. Generally speaking, self-compacting concrete (SCC) needs the highest fluidity to satisfy its filling ability, the lowest plastic viscosity to provide higher flow velocity, and the highest compressive strength. In this part, taking the fluidity, plastic viscosity, and 56 d compressive strength as examples to perform multi-objective optimization and obtain the optimal proportion of SCMs, it should be noted that the primary objective is to obtain the maximum fluidity, minimum plastic viscosity, and maximum 56 d compressive strength. At the same time, the weights of the responses are supposed to be equal. The results of multi-objective optimization are shown in **Table 6**.

The dosage of SCMs corresponding to the coded value in **Table 6** can be calculated according to the linear relationship between the coded value and dosage in **Table 3**. It can be seen from **Table 6** that, to obtain the maximum fluidity, minimum plastic viscosity, and maximum 56 d compressive strength, the optimum additions of FA, GGBFS, and SF were 29.4, 11.4, and 0.45%, respectively, and the desirability was 0.947. The abovementioned analysis showed that multi-objective optimization can be used to optimize the mix proportion.

CONCLUSION

In this study, the response surface method (RSM) was used to investigate the effect of SCMs on workability, rheology, and compressive strength of nano-silica modified cement-based paste. Box-Behnken design (BBD) method was used to design mix proportion and analysis of variance (ANOVA) was used to determine the significance of the factors. The quadratic term model was used for fitting the data and multi-objective optimization. Based on the results presented in this research, the following conclusions can be drawn:

(1) FA could increase the fluidity and yield stress while GGBFS and SF made them decrease. FA should be incorporated in blends containing SF or GGBFS in order to obtain adequate fluidity. However, for the purpose of getting lower yield stress, SF needs to be mixed with FA or GGBFS and 15% of FA was advisable when mixed with GGBFS.

(2) FA and GGBFS decreased the plastic viscosity and thixotropy, but SF led these two parameters to increase. Response surface plot indicated that, adding 30% GGBFS and 30% FA into nano-silica modified cement-based paste could decrease the plastic viscosity from 1.445 to 0.9 Pa·s, which was similar with reference sample (M17). Thus, SCMs could improve the rheology of nano-silica modified cement-based paste. In terms of quaternary blends, the combinations of FA and GGBFS or SF and GGBFS were preferable to achieve lower plastic viscosity and thixotropy.

(3) Regardless of the amount of SCMs, the synergy effect of SCMs and NS increased the 7, 28, and 56 d compressive strength higher than that of reference sample (M17). The amount of FA and GGBFS should be less than 15% when mixed with SF in order to obtain higher 7 and 28 d compressive strength. As for 56 d compressive strength, the combination of FA and SF was acceptable compared with other two combinations.
(4) The optimal mix proportion of SCMs was difficult to calculate to obtain satisfied parameters due to the interaction between SCMs. Therefore, multi-objective optimization can be successfully applied to optimize the mix proportion to achieve desirable target.

DATA AVAILABILITY STATEMENT

The raw data supporting the conclusions of this article will be made available by the authors, without undue reservation.

AUTHOR CONTRIBUTIONS

All authors listed have made a substantial, direct, and intellectual contribution to the work and approved it for publication.

FUNDING

The authors gratefully acknowledge financial supports from the National Natural Science Foundation of China (Grant No. 51778269), National Key Research and Development Program of China (Grant No. 2017YFC0703100), and Case-by-Case Project for Top Outstanding Talents of Jinan.

ACKNOWLEDGMENTS

The authors thank Tafadzwa Ronald Muzenda for his help in proofreading.

REFERENCES

Ahmed, T. W., Ali, A. A. M., and Zidan, R. S. (2020). Properties of High Strength Polypropylene Fiber concrete Containing Recycled Aggregate. *Construction Building Mater.* 241, 118010. doi:10.1016/j.conbuildmat.2020.118010

Alberici, S., Beer, J. d., Hoorn, I. v. d., and Maarten, S. (2017). *Fly Ash and Blast Furnace Slag for Cement Manufacturing*. BEIS Research. Paper No. 19.

Banfill, P. F. G. (1991). Rheology of Fresh Cement and Concrete. *Rheology Reviewers*, J537, 61–130. Rheology of fresh cement and concrete. doi:10.4324/9780203473290

Benaicha, M., Roguiez, X., Jalbaud, O., Burtschell, Y., and Alaoui, A. H. (2015). Influence of Silica Fume and Viscosity Modifying Agent on the Mechanical and Rheological Behavior of Self Compacting concrete. *Construction Building Mater.* 84, 103–110. doi:10.1016/j.conbuildmat.2015.03.061

Cheng, S., Shui, Z., Sun, T., Yu, R., and Zhang, G. (2018). Durability and Microstructure of Coral Sand concrete Incorporating Supplementary Cementitious Materials. *Construction Building Mater.* 171, 44–53. doi:10.1016/j.conbuildmat.2018.03.082

Chithra, S., Senthil Kumar, S. R. R., and Chinnaraju, K. (2016). The Effect of Colloidal Nano-Silica on Workability, Mechanical and Durability Properties of High Performance Concrete with Copper Slag as Partial fine Aggregate. *Construction Building Mater.* 113, 794–804. doi:10.1016/j.conbuildmat.2016.03.119

Committee, C. N. S. M. (2016). *Common Portland Cement (GB175-2007*. BeiJing: Chinese Standard Publishing.

de Larrard, F., Ferraris, C. F., and Sedran, T. (1998). Fresh concrete: A Herschel-Bulkley Material. *Mat. Struct.* 31, 494–498. Fresh concrete. doi:10.1007/bf02480474

Dhanya, B. S., Santhanam, M., Gettu, R., and Pillai, R. G. (2018). Performance Evaluation of Concretes Having Different Supplementary Cementitious Material Dosages Belonging to Different Strength Ranges. *Construction Building Mater.* 187, 984–995. doi:10.1016/j.conbuildmat.2018.07.185

Duan, Z., Hou, S., Xiao, J., and Singh, A. (2020). Rheological Properties of Mortar Containing Recycled Powders from Construction and Demolition Wastes. *Construction Building Mater.* 237, 117622. doi:10.1016/j.conbuildmat.2019.117622

Ferdosian, I., and Camões, A. (2017). Eco-efficient Ultra-high Performance concrete Development by Means of Response Surface Methodology. *Cement and Concrete Composites* 84, 146–156. doi:10.1016/j.cemconcomp.2017.08.019

Ferron, R., Gregori, A., Sun, Z., and Shah, S. P. (2007). Rheological Method to Evaluate Structural Buildup in Self-Consolidating concrete Cement Pastes. *ACI MATERIALS JOURNAL* 107, 104. doi:10.1088/0957-4484/18/17/17560110.14359/18669

Flores, Y. C., Cordeiro, G. C., Toledo Filho, R. D., and Tavares, L. M. (2017). Performance of Portland Cement Pastes Containing Nano-Silica and Different Types of Silica. *Construction Building Mater.* 146, 524–530. doi:10.1016/j.conbuildmat.2017.04.069

García-Taengua, E., Sonebi, M., Hossain, K. M. A., Lachemi, M., and Khatib, J. (2015). Effects of the Addition of Nanosilica on the Rheology, Hydration and Development of the Compressive Strength of Cement Mortars. *Composites B: Eng.* 81, 120–129. doi:10.1016/j.compositesb.2015.07.009

Garlapati, V. K., and Roy, L. (2017). Utilization of Response Surface Methodology for Modeling and Optimization of Tablet Compression Process. *Jyp* 9 (3), 417–421. doi:10.5530/jyp.2017.9.82

Ghafari, E., Costa, H., Júlio, E., Portugal, A., and Durães, L. (2014). The Effect of Nanosilica Addition on Flowability, Strength and Transport Properties of Ultra High Performance concrete. *Mater. Des.* 59, 1–9. doi:10.1016/j.matdes.2014.02.051

Ghalehnovi, M., Rashki, M., and Ameryan, A. (2020). First Order Control Variates Algorithm for Reliability Analysis of Engineering Structures. *Appl. Math. Model.* 77, 829–847. doi:10.1016/j.apm.2019.07.049

Giergiczny, Z. (2019). Fly Ash and Slag. *Cement Concrete Res.* 124, 105826. doi:10.1016/j.cemconres.2019.105826

Hosan, A., and Shaikh, F. U. A. (2021). Influence of Nano Silica on Compressive Strength, Durability, and Microstructure of High-volume Slag and High-volume Slag-Fly Ash Blended Concretes. *Struct. Concrete* 22, E474–E487. doi:10.1002/suco.202000251

Hou, P., Wang, K., Qian, J., Kawashima, S., Kong, D., and Shah, S. P. (2012). Effects of Colloidal nanoSiO2 on Fly Ash Hydration. *Cement and Concrete Composites* 34 (10), 1095–1103. doi:10.1016/j.cemconcomp.2012.06.013

Hou, P., Kawashima, S., Kong, D., Corr, D. J., Qian, J., and Shah, S. P. (2013). Modification Effects of Colloidal nanoSiO2 on Cement Hydration and its Gel Property. *Composites Part B: Eng.* 45 (1), 440–448. doi:10.1016/j.compositesb.2012.05.056

Hu, C., and de Larrard, F. (1996). The Rheology of Fresh High-Performance Concrete. *Cement Concrete Res.* 26, 283–294. doi:10.1016/0008-8846(95)00213-8

ASTM International (2014). *ASTM C230/C230M-20, Standard Specification for Flow Table for Use in Tests of Hydraulic Cement*.

Jalal, M., Teimortashlu, E., and Grasley, Z. (2019). Performance-based Design and Optimization of Rheological and Strength Properties of Self-Compacting Cement Composite Incorporating Micro/Nano Admixtures. *Composites Part B: Eng.* 163, 497–510. doi:10.1016/j.compositesb.2019.01.028

Jiang, D., Li, X., Lv, Y., Zhou, M., He, C., Jiang, W., et al. (2020). Utilization of limestone Powder and Fly Ash in Blended Cement: Rheology, Strength and Hydration Characteristics. *Construction Building Mater.* 232, 117228. doi:10.1016/j.conbuildmat.2019.117228

Jiao, D., Shi, C., Yuan, Q., An, X., Liu, Y., and Li, H. (2017). Effect of Constituents on Rheological Properties of Fresh concrete-A Review. *Cement and Concrete Composites* 83, 146–159. doi:10.1016/j.cemconcomp.2017.07.016

Jiao, D., Shi, C., Yuan, Q., An, X., and Liu, Y. (2018). Mixture Design of concrete Using Simplex Centroid Design Method. *Cement and Concrete Composites* 89, 76–88. doi:10.1016/j.cemconcomp.2018.03.001

Nandhini, K., and Ponmalar, V. (2018). Microstructural Behaviour and Flowing Ability of Self-compacting concrete Using Micro- and Nano-silica. *Micro Nano Lett.* 13 (8), 1213–1218. doi:10.1049/mnl.2018.0105

Kawashima, S., Chaouche, M., Corr, D. J., and Shah, S. P. (2013). Rate of Thixotropic Rebuilding of Cement Pastes Modified with Highly Purified Attapulgite Clays. *Cement Concrete Res.* 53, 112–118. doi:10.1016/j.cemconres.2013.05.019

Ke, G., Zhang, J., Xie, S., and Pei, T. (2020). Rheological Behavior of Calcium Sulfoaluminate Cement Paste with Supplementary Cementitious Materials. *Construction Building Mater.* 243, 118234. doi:10.1016/j.conbuildmat.2020.118234

Kong, D., Du, X., Wei, S., Zhang, H., Yang, Y., and Shah, S. P. (2012). Influence of Nano-Silica Agglomeration on Microstructure and Properties of the Hardened Cement-Based Materials. *Construction Building Mater.* 37, 707–715. doi:10.1016/j.conbuildmat.2012.08.006

Li, G., and Wu, X. (2005). Influence of Fly Ash and its Mean Particle Size on Certain Engineering Properties of Cement Composite Mortars. *Cement Concrete Res.* 35 (6), 1128–1134. doi:10.1016/j.cemconres.2004.08.014

Li, N., Shi, C., Zhang, Z., Zhu, D., Hwang, H.-J., Zhu, Y., et al. (2018). A Mixture Proportioning Method for the Development of Performance-Based Alkali-Activated Slag-Based concrete. *Cement and Concrete Composites* 93, 163–174. doi:10.1016/j.cemconcomp.2018.07.009

Liu, M., Tan, H., and He, X. (2019). Effects of Nano-SiO2 on Early Strength and Microstructure of Steam-Cured High Volume Fly Ash Cement System. *Construction Building Mater.* 194, 350–359. doi:10.1016/j.conbuildmat.2018.10.214

Lu, J., Jiang, J., Lu, Z., Li, J., Niu, Y., and Yang, Y. (2020). Pore Structure and Hardened Properties of Aerogel/cement Composites Based on Nanosilica and Surface Modification. *Construction Building Mater.* 245, 118434. doi:10.1016/j.conbuildmat.2020.118434

Mendoza Reales, O. A., Duda, P., Silva, E. C. C. M., Paiva, M. D. M., and Filho, R. D. T. (2019). Nanosilica Particles as Structural Buildup Agents for 3D Printing with Portland Cement Pastes. *Construction Building Mater.* 219, 91–100. doi:10.1016/j.conbuildmat.2019.05.174

Muzenda, T. R., Hou, P., Kawashima, S., Sui, T., and Cheng, X. (2020). The Role of limestone and Calcined clay on the Rheological Properties of LC3. *Cement and Concrete Composites* 107, 103516. doi:10.1016/j.cemconcomp.2020.103516

Park, C. K., Noh, M. H., and Park, T. H. (2005). Rheological Properties of Cementitious Materials Containing mineral Admixtures. *Cement Concrete Res.* 35 (5), 842–849. doi:10.1016/j.cemconres.2004.11.002

Pizoń, J., Miera, P., and Łaźniewska-Piekarczyk, B. (2016). Influence of Hardening Accelerating Admixtures on Properties of Cement with Ground Granulated Blast Furnace Slag. *Proced. Eng.* 161, 1070–1075. doi:10.1016/j.proeng.2016.08.850

Pizoń, J. (2017). Long-term Compressive Strength of Mortars Modified with Hardening Accelerating Admixtures. *Proced. Eng.* 195, 205–211. doi:10.1016/j.proeng.2017.04.545

Pratama, H. B., Supijo, M. C., and Sutopo, H. B. (2020). Experimental Design and Response Surface Method in Geothermal Energy: A Comprehensive Study in Probabilistic Resource Assessment. *Geothermics* 87, 101869. doi:10.1016/j.geothermics.2020.101869

Qian, Y., Lesage, K., El Cheikh, K., and De Schutter, G. (2018). Effect of Polycarboxylate Ether Superplasticizer (PCE) on Dynamic Yield Stress, Thixotropy and Flocculation State of Fresh Cement Pastes in Consideration of the Critical Micelle Concentration (CMC). *Cement Concrete Res.* 107, 75–84. doi:10.1016/j.cemconres.2018.02.019

Ramezanianpour, A. A., and Moeini, M. A. (2018). Mechanical and Durability Properties of Alkali Activated Slag Coating Mortars Containing Nanosilica and Silica Fume. *Construction Building Mater.* 163, 611–621. doi:10.1016/j.conbuildmat.2017.12.062

Riding, K., Silva, D. A., and Scrivener, K. (2010). Early Age Strength Enhancement of Blended Cement Systems by CaCl2 and Diethanol-Isopropanolamine. *Cement Concrete Res.* 40 (6), 935–946. doi:10.1016/j.cemconres.2010.01.008

Roshani, A., and Fall, M. (2020). Flow Ability of Cemented Pastefill Material that Contains Nano-Silica Particles. *Powder Tech.* 373, 289–300. doi:10.1016/j.powtec.2020.06.050

Roussel, N., Ovarlez, G., Garrault, S., and Brumaud, C. (2012). The Origins of Thixotropy of Fresh Cement Pastes. *Cement Concrete Res.* 42 (1), 148–157. doi:10.1016/j.cemconres.2011.09.004

Roussel, N. (2006). A Thixotropy Model for Fresh Fluid Concretes: Theory, Validation and Applications. *Cement Concrete Res.* 36 (10), 1797–1806. doi:10.1016/j.cemconres.2006.05.025

Senff, L., Labrincha, J. A., Ferreira, V. M., Hotza, D., and Repette, W. L. (2009). Effect of Nano-Silica on Rheology and Fresh Properties of Cement Pastes and Mortars. *Construction Building Mater.* 23 (7), 2487–2491. doi:10.1016/j.conbuildmat.2009.02.005

Shanahan, N., Tran, V., Williams, A., and Zayed, A. (2016). Effect of SCM Combinations on Paste Rheology and its Relationship to Particle Characteristics of the Mixture. *Construction Building Mater.* 123, 745–753. doi:10.1016/j.conbuildmat.2016.07.094

Shirdam, R., Amini, M., and Bakhshi, N. (2019). Investigating the Effects of Copper Slag and Silica Fume on Durability, Strength, and Workability of Concrete. *Int. J. Environ. Res.* 13 (6), 909–924. doi:10.1007/s41742-019-00215-7

Supervision, N. B. o. Q. a. T. (1999). *GB/T 17671-1999, Method of Testing Cements-Determination of Strength*.

Ting, L., Qiang, W., and Shiyu, Z. (2019). Effects of Ultra-fine Ground Granulated Blast-Furnace Slag on Initial Setting Time, Fluidity and Rheological Properties of Cement Pastes. *Powder Tech.* 345, 54–63. doi:10.1016/j.powtec.2018.12.094

Ting, L., Qiang, W., and Yuqi, Z. (2020). Influence of Ultra-fine Slag and Silica Fume on Properties of High-Strength concrete. *Mag. Concrete Res.* 72 (12), 610–621. doi:10.1680/jmacr.18.00492

Wang, X., Huang, J., Ma, B., Dai, S., Jiang, Q., and Tan, H. (2019). Effect of Mixing Sequence of Calcium Ion and Polycarboxylate Superplasticizer on Dispersion of a Low Grade Silica Fume in Cement-Based Materials. *Construction Building Mater.* 195, 537–546. doi:10.1016/j.conbuildmat.2018.11.032

Wang, L., Guo, F., Lin, Y., Yang, H., and Tang, S. W. (2020). Comparison between the Effects of Phosphorous Slag and Fly Ash on the C-S-H Structure, Long-Term Hydration Heat and Volume Deformation of Cement-Based Materials. *Construction Building Mater.* 250, 118807. doi:10.1016/j.conbuildmat.2020.118807

Wardrop, D. M., and Myers, R. H. (1990). Some Response Surface Designs for Finding Optimal Conditions. *J. Stat. Plann. inference* 25 (1), 7–28. doi:10.1016/0378-3758(90)90003-D

Wu, Z., Khayat, K. H., and Shi, C. (2019). Changes in Rheology and Mechanical Properties of Ultra-high Performance concrete with Silica Fume Content. *Cement Concrete Res.* 123, 105786. doi:10.1016/j.cemconres.2019.105786

Xiao, Y., Ye, K., and He, W. (2020). An Improved Response Surface Method for Fragility Analysis of Base-Isolated Structures Considering the Correlation of Seismic Demands on Structural Components. *Bull. Earthquake Eng.* 18, 4039–4059. doi:10.1007/s10518-020-00836-w

Xie, J., WangRao, J. R., Rao, R., Wang, C., and Fang, C. (2019). Effects of Combined Usage of GGBS and Fly Ash on Workability and Mechanical Properties of Alkali Activated Geopolymer concrete with Recycled Aggregate. *Composites Part B: Eng.* 164, 179–190. doi:10.1016/j.compositesb.2018.11.067

Xiuzhi, Z., Hailong, S., Haibo, Y., Ru, M., and Heng, C. (2021). Rheological Properties of Nanosilica-Modified Cement Paste at Different Temperatures and Hydration Times. *J. Mater. Civil Eng.* 33 (1), 4020404. doi:10.1061/(ASCE)MT.1943-5533.0003488

Yan-Rong, Z., Xiang-Ming, K., Zi-Chen, L., Zhen-Bao, L., Qing, Z., Bi-Qin, D., et al. (2016). Influence of Triethanolamine on the Hydration Product of Portlandite in Cement Paste and the Mechanism. *Cement Concrete Res.* 87, 64–76. doi:10.1016/j.cemconres.2016.05.009

Conflict of Interest: The authors declare that the research was conducted in the absence of any commercial or financial relationships that could be construed as a potential conflict of interest.

Publisher's Note: All claims expressed in this article are solely those of the authors and do not necessarily represent those of their affiliated organizations, or those of the publisher, the editors, and the reviewers. Any product that may be evaluated in this article, or claim that may be made by its manufacturer, is not guaranteed or endorsed by the publisher.

frontiers in Materials

ORIGINAL RESEARCH
published: 12 October 2021
doi: 10.3389/fmats.2021.755241

Reactive Transport Modelling of Chloride Ingress in Saturated Coral Aggregate Concrete

Bingbing Guo[1,2,3], Zhenming Li[4]*, Qiang Fu[1,2,3], Yan Wang[2,3], Daguan Huang[5] and Ditao Niu[1,2,3]*

[1]School of Civil Engineering, Xi'an University of Architecture and Technology, Xi'an, China, [2]National Key Laboratory of Green Building in West China, Xi'an University of Architecture and Technology, Xi'an, China, [3]Key Lab of Engineering Structural Safety and Durability, Xi'an University of Technology, Xi'an, China, [4]Department of Materials and Environment, Faculty of Civil Engineering and Geoscience, Delft University of Technology, Delft, Netherlands, [5]School of Civil Engineering and Architecture, Xi'an University of Technology, Xi'an, China

Utilizing coral aggregate concrete (CAC) for construction on remote islands can significantly reduce construction cost and period, CO_2 emission, and consumption of non-renewable energy. The durability of reinforced CAC structures is critically influenced by their resistance to chloride attack. In this study, a reactive transport modelling was developed to investigate chloride ingress in CAC, in which a COMSOL-PHREEQC interface based on MATLAB language was established. The experiment from the literature was taken as a benchmark example. The results show that the developed numerical model can accurately predict chloride transport in CAC. Differing from ordinary aggregate concrete (OAC), Kuzel's salt does not appear in cement hydrate compounds of CAC during chloride ingress. The numerical results indicate that the penetration depth of chloride in CAC gradually increases as the exposure time is prolonged. When CAC is exposed to an external chloride solution, the decrease in the pH of the pore solution affects the precipitation of Friedel's salt, which is detrimental to the chemical binding of chloride.

Keywords: coral aggregates concrete, chloride ingress, reactive transport modelling, chloride binding, corrosion

OPEN ACCESS

Edited by:
Anuj Kumar,
Natural Resources Institute Finland (Luke), Finland

Reviewed by:
Petr Lehner,
VSB-Technical University of Ostrava, Czechia
Deju Zhu,
Hunan University, China

****Correspondence:***
Bingbing Guo
guobingbing212@163.com
Zhenming Li
Z.li-2@tudelft.nl

Specialty section:
This article was submitted to Structural Materials, a section of the journal Frontiers in Materials

Received: *08 August 2021*
Accepted: *22 September 2021*
Published: *12 October 2021*

Citation:
Guo B, Li Z, Fu Q, Wang Y, Huang D and Niu D (2021) Reactive Transport Modelling of Chloride Ingress in Saturated Coral Aggregate Concrete. Front. Mater. 8:755241. doi: 10.3389/fmats.2021.755241

INTRODUCTION

In recent decades, increasing number of islands and reefs, which are generally far from the mainland, have been constructed to meet the needs of rapidly developing of marine industry. Concrete is a primary building material for island and reef construction. Enormous amounts of raw materials, such as river sand, gravel, and freshwater, need to be shipped to produce concrete. This is associated with high cost, long period, CO_2 emission, and the consumption of non-renewable energy (Zhou et al., 2021). A sustainable solution is to use locally available materials to produce concrete, such as seawater, sea sand, and coral reefs (Gui et al., 2020; Liu et al., 2020; Wu et al., 2020). There are abundant coral sources in remote islands and reefs, and using crushed coral as coarse and fine aggregates to produce concrete has been proven feasible (Da et al., 2016; Liang et al., 2021, Liang et al., 2021a).

The corrosion of reinforcing steel caused by chloride ingress is the primary threat to the durability of reinforced concrete (RC) structures located in marine environments (Angst et al., 2009; Li et al., 2014; Hou et al., 2017). Through field surveys, Yu et al. (2017) found that the corrosion rates of reinforcing steel embedded in concrete in tropical islands and reefs were very high, which led to cracking, spalling, and collapse of the concrete cover. Coral reefs contain chloride salt (Yu et al.,

2020). When coral reefs are used as coarse or fine aggregates, the chloride salt will inevitably be mixed into concrete (Da et al., 2016; Huang et al., 2020a; Zhang et al., 2020). Hence, corrosion of reinforcing steel embedded in coral aggregate concrete (CAC) is supposed to be more serious than that of ordinary aggregate concrete (OAC). It is commonly accepted that the initiation of steel corrosion depends on the ratio of $[Cl^-]/[OH^-]$ in the pore solution near the reinforcing steel. When the $[Cl^-]/[OH^-]$ ratio exceeds the threshold value, the passive layer at the steel surface is destroyed, and the corrosion will occur. Therefore, the transport behaviour of chloride in CAC is closely related to the durability of CAC and the service life of CAC structures.

In addition to the fact that coral aggregates contain chloride salt, coral reefs are a type of porous and light rock, which differs completely from ordinary aggregates. These two features make CAC more vulnerable to chloride attack than OAC (Wattanachai et al., 2009). The experimental results in (Yu et al., 2017) indicated that the free chloride concentration is much higher in OAC than CAC when exposed to the same chloride environment. Da et al. (2016) and Huang et al. (2020a) found that the surface chloride concentration in CAC and its apparent chloride diffusion coefficient were higher than those of OAC.

Numerical modelling of ionic transport can predict the spatial-temporal distributions of chloride and pH in the pore solution of concrete, providing a theoretical basis for the durability design of CAC and the service life prediction of structures. Thus, in addition to experimental investigations, numerical modelling is also a powerful tool for studying chloride ingress in cement-based materials (Lehner et al., 2021). However, to our best knowledge, no studies related to the numerical modelling of chloride transport in CAC have been reported.

Numerical models based on the Nernst-Planck equations are widely used to simulate the ionic transport in concrete materials (Baroghel-Bouny et al., 2011; Liu et al., 2015; Yuan et al., 2011). The chloride binding behaviour has a significant effect on ionic transport in concrete materials. Binding isotherms, i.e., linear, Langmuir, Freundlich, and BET binding isotherms, are widely used to describe chloride binding behaviours in the numerical models from Baroghel–Bouny et al. (2011), Liu et al. (2015), and Yuan et al. (2011). However, there are two problems when using the binding isotherms: 1) none of these can accurately describe this relationship between free and bound chlorides with the global free chloride concentration range (Yuan et al., 2009); 2) the parameters in these isotherms need to be fitted from the experimental data, while each concrete material has specific parameters (Tran et al., 2018). Chloride binding in cement-based materials is dependent on the physical and chemical interactions between the cement hydrate and pore solution (Elakneswaran et al., 2010; Guo et al., 2018). Reactive transport modelling coupled with physical and chemical interactions can resolve the above-mentioned problems. Recently, reactive transport modelling of chloride ingress in cement-based materials has attracted great attention from researchers (Kari et al., 2013; Guo et al., 2018; Van Quan et al., 2018; Angst, 2019; Guo et al., 2021). In this study, reactive transport modelling was developed to simulate chloride ingress for saturated CAC.

TABLE 1 | Equilibrium constants of the surface site reactions at 25 °C (Elakneswaran et al., 2010).

Surface site reactions	Log K_i
$\equiv SiOH + K^+ \rightarrow \equiv SiOK + H^+$	−13.6
$\equiv SiOH + Ca^{2+} \rightarrow \equiv SiOCa^+ + H^+$	−9.4
$\equiv SiOH + Na^+ \rightarrow \equiv SiONa + H^+$	−13.6
$\equiv SiOH + Cl^- \rightarrow \equiv SiOHCl^-$	−0.35
$\equiv SiOH + OH^- \rightarrow \equiv SiO^- + H_2O$	−12.7

Reactive Transport Modelling of Chloride Ingress in CAC

Physical and Chemical Interactions Between Pore Solution and Cement Hydrate

Chloride in CAC exists in two forms: free chloride in the pore solution and bound chloride by cement hydrate. When external chloride penetrates CAC, it will cause physical and chemical interactions between the pore solution and cement hydrate, and the amount of chloride bound by the cement hydrate will increase (Huang et al., 2020a), significantly affecting the ionic transport in CAC. The physical and chemical interactions include the adsorption between the surface silanol sites (≡SiOH) of calcium silicate hydrate (C–S–H) and the aqueous species in the pore solution, and the dissolution/precipitation reactions of hydrate phases (Elakneswaran et al., 2010; Tran et al., 2018). The adsorption and dissolution/precipitation reactions can be described using the surface complexation model (Elakneswaran et al., 2009) and the phase-equilibrium model (Elakneswaran et al., 2010), respectively.

According to (Elakneswaran et al., 2008; 2009) and (Guo et al., 2018), in cement-based materials, the aqueous species in the pore solution that participates in the adsorption reactions of the C–S–H surface are mainly Na^+, K^+, Ca^{2+}, OH^-, and Cl^-, and other species can be neglected. The surface charge density is calculated using the following equation:

$$\sigma = F[\Gamma_H - \Gamma_{OH} - \Gamma_{Cl} + 2\Gamma_{Ca} + \Gamma_{Na} + \Gamma_K] \quad (1)$$

where σ is the surface charge density (C/m^2); F is the Faraday constant (96,485 C/mol); Γ_H, Γ_{OH}, Γ_{Cl}, Γ_{Ca}, Γ_{Na}, and Γ_K denote the densities (mol/m^2) of bound protons, hydroxyl, chloride, calcium, sodium, and potassium, respectively. Based on the Gouy-Chapman diffuse theory, σ is related to the surface potential (ψ_0) for a symmetrical electrolyte with valence z:

$$\sigma = -0.1174 \cdot c^{\frac{1}{2}} \sinh\left(19.46 \cdot z\psi_0\right) \quad (2)$$

where c denotes the electrolyte concentration (mol/L). Combining Eqs 1, 2, we obtain:

$$F[\Gamma_H - \Gamma_{OH} - \Gamma_{Cl} + 2\Gamma_{Ca} + \Gamma_{Na} + \Gamma_K] + 0.1174 \cdot c^{\frac{1}{2}} \sinh(19.46 \cdot z\psi_0) = 0 \quad (3)$$

The mass action law is used to describe the surface site reactions in the equilibrium state:

$$K_i = \left(\prod_m (\gamma_{m,i} c_{m,i})^{n_{m,i}} \right) \exp\left(\frac{F\psi_0}{RT} \Delta z_i\right) \quad (4)$$

where K_i is the equilibrium constant of the surface site reaction of C–S–H with the ion i in the pore solution, and the surface site reactions, as presented in **Table1**, are considered; $\gamma_{m,i}$ is the activity coefficient of mass specie m in the surface site reaction; $c_{m,i}$ is the concentration of mass specie m; $n_{m,i}$ is the stoichiometric coefficient; F (9.6485 × 10^4 C/mol), R (8.314 J/(mol·K)), and T (K) denote the Faraday constant, universal gas constant, and absolute temperature, respectively; Δz_i denotes the net charge at the surface of C–S–H.

When external chloride ions penetrate CAC, it produces new Kuzel's and Friedel's salts, causing an increase in the their content. This is considered to be a result of the precipitation reactions of the species (such as SO_4^{2-}, Cl^-, $Al(OH)_4^-$, OH^-, and Ca^{2+}) in the pore solution, which is accompanied by other dissolution and precipitation reactions between cement hydrate and pore solution. Similarly, the mass action law is used to describe the phase equilibrium of the dissolution and precipitation reactions.

$$K_p = \prod_i (\gamma_{i,p} c_{i,p})^{n_{i,p}} \quad (5)$$

where K_p is the equilibrium constant of the dissolution/precipitation reaction between the pore solution and hydrate phase p. The dissolution/precipitation reactions considered in this study are presented in the next section. $c_{i,p}$ and $\gamma_{i,p}$ denote the concentration of ion i in the pore solution and its activity coefficient, respectively; the Davies or extended Debye–Huckel equation is used to express the activity coefficient $\gamma_{i,p}$, [more details about this equation can be seen in (Parkhurst and Appelo, 2013)]; $n_{i,p}$ denotes the stoichiometric coefficient of ion i in the associated reaction. The equilibrium constants for nearly all the hydration products in cement-based materials can be seen in the CEMDATA18 database (Lothenbach et al., 2019).

Transport Equations

In saturated CAC, diffusion and electromigration are two driving forces that cause the transport of free ions in the pore solution, which can be described using the Nernst–Planck equation:

$$J_i = -D_i \left[\nabla c_i + \frac{z_i c_i F}{RT} \nabla \phi \right] \quad (6)$$

where J_i (mol/m^2/s) denotes the flux of free ion i; D_i (m^2/s) is the diffusion coefficient of free ion i in CAC, which will be discussed in detail later; c_i (mol/m^3) and z_i (−) denote the ionic concentration and electric charge number, respectively; ϕ (V) denotes the electric potential. The electric neutrality in CAC should be satisfied when subjected to chloride ingress, and hence,

$$F \sum_i z_i J_i = 0 \quad (7)$$

Combining Eqs 6, 7, the following can be deduced:

$$J_i = -D_i \left(\nabla c_i - \frac{RT}{F} \frac{\sum_i z_i D_i \nabla c_i}{\sum_i z_i^2 D_i c_i} \right) \quad (8)$$

According to the continuity equation, we can obtain:

$$\frac{\partial c_i}{\partial t} + \nabla \cdot J_i = Q_i \quad (9)$$

where Q_i denotes the source term, which is determined by the physical and chemical interactions between the pore solution and cement hydrate, which is calculated *via* thermodynamic modelling in *Physical and Chemical Interactions Between Pore Solution and Cement Hydrate*.

The diffusion coefficient (D_i) of free ion i in the pore solution of a porous material is completely different from that in free water because it is affected by the constrictivity and tortuosity of the pore structure (Appelo et al., 2010). Considering that the diffusion coefficient (D_{Cl}) of chloride in saturated cement-based materials can be easily measured by rapid chloride migration testing, the diffusion coefficient (D_i) of free ion i in CAC is expressed using the following equation:

$$D_i = \frac{D_{Cl}}{D_{Cl\_free}} \cdot D_{i\_free} \quad (10)$$

where $\frac{D_{Cl}}{D_{Cl\_free}}$ represents the effect of tortuosity and constrictivity of the pore structure (Tang and Nilsson, 1995), including the effect of the porous property of the coral aggregate. D_{i_free} denotes the diffusion coefficient of ion i in free water, which can be measured experimentally, and their values for Ca^{2+}, Na^+, K^+, OH^-, SO_4^{2-}, and Cl^- are 0.791 × 10^{-9} m^2/s, 1.33 × 10^{-9} m^2/s, 1.96 × 10^{-9} m^2/s, 5.27 × 10^{-9} m^2/s, 1.07 × 10^{-9} m^2/s, and 2.03 × 10^{-9} m^2/s at 20°C (Haynes et al., 2014).

NUMERICAL IMPLEMENTATION

Numerical Calculation Procedures

Reactive transport modelling is divided into two modules using the operator splitting algorithm, i.e., the reaction and transport modules (Nardi et al., 2014). The PHREEQC program, a geochemical simulator developed by the United States Geological Survey (USGS), can solve the reaction module (Parkhurst and Appelo, 2013). COMSOL Multiphysics, a commercial finite element method (FEM) software, can solve the transport module (COMSOL, 2021). Hence, a COMSOL-PHREEQC interface must be developed to achieve the interaction between these two modules (Guo et al., 2018; Nardi et al., 2014). COMSOL Multiphysics with MATLAB can connect COMSOL Multiphysics to the MATLAB script (COMSOL, 2021). The

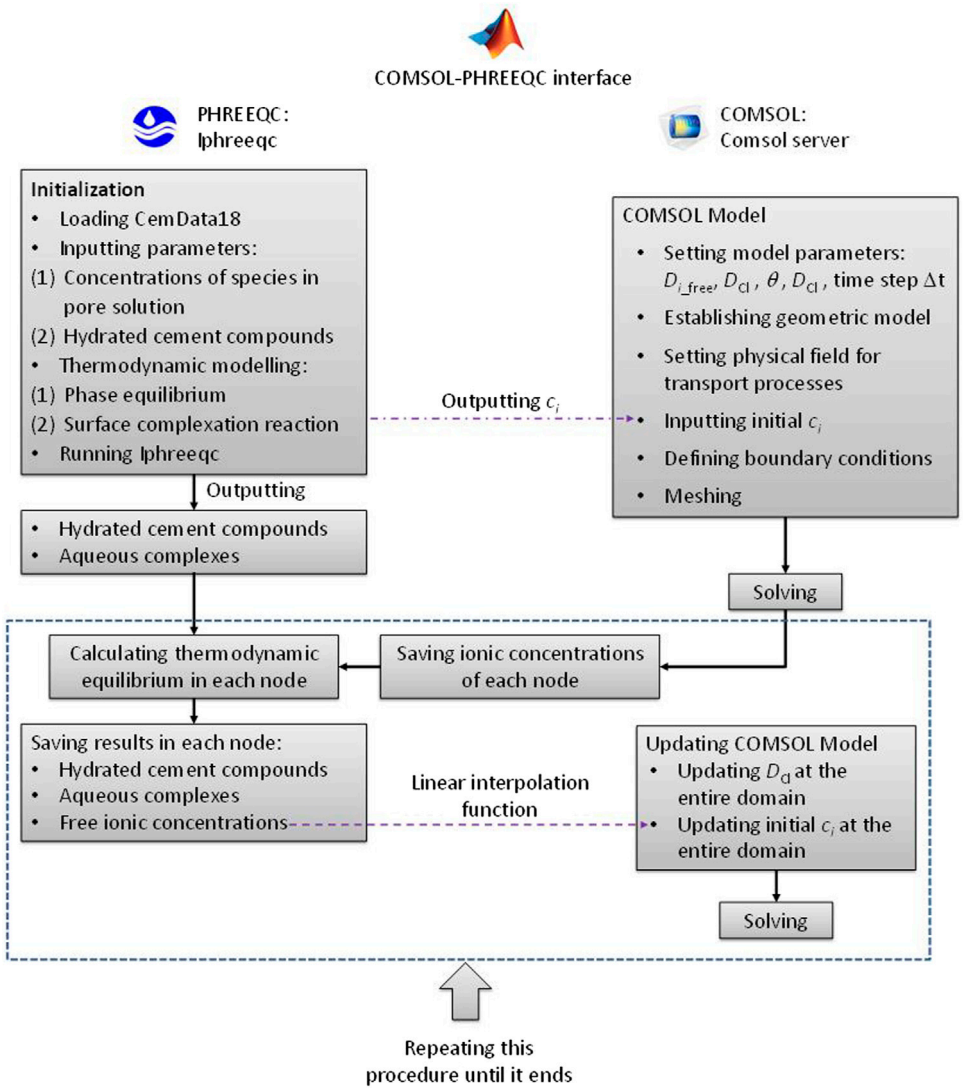

FIGURE 1 | Main structure and workflow of the COMSOL-PHREEQC interface to calculate the reactive transport model.

IPhreeqc COM allows PHREEQC to be used as a COM server for MATLAB (Charlton and Parkhurst, 2011). Therefore, in this study, the MATLAB scripting environment was selected to establish the COMSOL-PHREEQC interface. The main structure and workflow of the interface are illustrated in **Figure 1**.

The hydrated cement compounds and concentrations of species in the pore solution are necessary to solve the reactive transport model in cement-based materials and can be obtained from experiments or calculation of GEMS (Kulik et al., 2013; Lothenbach and Winnefeld, 2006; Lothenbach and Zajac, 2019). However, the pore solution and hydrated cement compounds from experiments or GEMS may not be in an equilibrium state in PHREEQC. Thus, as shown in **Figure 1**, the first step is to initialize such that they are in an equilibrium state in PHREEQC. Simultaneously, the COMSOL model needs to be established, which includes building geometric model, setting material parameters and physical fields, and defining boundary conditions. Then, the concentrations of the free ions from the initialization are output to the COMSOL model as the initial values to calculate the transport process in the first time step. COMSOL is based on FEM, and the concentrations of free ions at each node can be obtained. The values are saved in matrix and then passed to PHREEQC to solve the thermodynamic equilibrium at each FEM node with the hydrated cement compounds from the initialization. When completing the thermodynamic equilibrium calculations at all the nodes, the concentrations of the free ions at the nodes are updated, and then sent back to the COMSOL model as initial values *via* linear interpolation function to calculate the transport process in the second time step. Meanwhile, the hydrated cement compounds at all the nodes are saved in the form of a

FIGURE 2 | (A) Corals; **(B)** coral fine aggregate; **(C)** coral coarse aggregate (Huang et al., 2020a).

TABLE 2 | Mix proportion of CAC in kg/m^3, and primary characteristics (Huang et al., 2020a).

Concrete	C30F15
Cement	446.25
Pre-wetting water	120
Water	183.75
FA	78.75
Coral aggregate	600
Coral sand	900
Compressive strength/MPa	35
Porosity accessible to water θ_0 (%)	13.6
Chloride diffusion coefficient D_{Cl} ($\times 10^{-12}$ m/s)	13.81
Slump (mm)	182

TABLE 3 | Chemical compositions (%) of cement and FA (Huang et al., 2020a; Huang, 2020).

Item	SiO_2	Al_2O_3	Fe_2O_3	CaO	MgO	SO_3	K_2O	Na_2O
Cement	21.18	5.02	3.14	63.42	3.12	2.30	0.65	0.42
FA	35.71	16.57	8.92	21.14	1.41	1.94	0.80	1.02

TABLE 4 | Hydrated cement compounds.

Hydrate phase	Formula	Amount (mol/L of concrete)
C–S–H	$4(CaO)\cdot3(SiO_2)\cdot6.5(H_2O)$	2.124
CH	$Ca(OH)_2$	1.9018
AFt	$Ca_6Al_2(SO_4)_3(OH)_{12}\cdot26H_2O$	0.1549
AFm	$Ca_4Al_2(SO_4)(OH)_{12}\cdot6H_2O$	0.1481
Fs	$Ca_4Al_2Cl_2O_6\cdot10H_2O$	0.054
Ks	$Ca_4Al_2Cl(SO_4)_{0.5}O_6\cdot12H_2O$	0
Hydrotalcite	$Mg_4Al_2(OH)_7\cdot3(H_2O)$	0.051

matrix for calculating the thermodynamic equilibrium in the third time step. The above procedure is repeated until the calculation ends.

Spiesz et al. (2012) reported that the time to achieve a new thermodynamic equilibrium between the pore solution and cement hydrate is approximately 10 days. Therefore, this 10 was selected as the time step in this model.

Benchmark Example and Required Input Data

To investigate chloride ingress in CAC, CAC cubic specimens with the size of 100 mm × 100 mm × 100 mm were exposed to 3.5% NaCl solution in the literature (Huang, 2020; Huang et al., 2020a), and the free chloride concentrations in the CAC were measured at 30, 60, 90, 120, and 180 days. The coral aggregates presented in **Figure 2** were used in their experiment. The chloride ion contents of coral fine and coarse aggregates are 0.6284% and 0.6375, respectively (Wang et al., 2019). In this study, the CAC specimen C30F15 in their experiment was taken as a benchmark example to show the implementation of the reactive transport modelling of chloride ingress in CAC. The experimental results about the free chloride concentration at different exposure times were used to verify the numerical model. The mix proportion, chloride diffusion coefficients, porosity accessible to water, and slump are listed in **Table 2**. Other details regarding the preparation procedure of CAC and the experiments to measure these characteristics can be found in the literature (Huang et al., 2020a; Huang, 2020). Among the parameters listed in **Table 2**, the mix proportion is used to calculate the hydrated cement compounds and pore solution, which will be further discussed in the next paragraph. Because CAC itself contains a certain amount of chloride, the rapid chloride migration method cannot measure the chloride diffusion coefficient. Hence, the chloride diffusion coefficient of CAC fitted at the minimum exposure time in Huang et al. (2020a) is used although it is a little unreasonable, as given in **Table 2**.

The chemical compositions of the cement and FA used in the literature (Huang, 2020; Huang et al., 2020a) are presented in **Table 3**. According to the mix proportion in **Table 2**, the hydrated cement compounds and the pore solution can be calculated by employing the GEMS software with the CEMDATA18 and Nagra/PSI TDB thermodynamic databases (Kulik et al., 2013; Lothenbach et al., 2019). It is assumed that the CAC is completely hydrated, and the effect of ageing is neglected. The effect of CO_2 in the water or atmosphere on cement hydration is also neglected. The hydrated cement compounds that are considered to participate in the dissolution/precipitation reactions of hydrate phases are calcium silicate hydrate (C–S–H), portlandite (CH), monosulfoaluminate

TABLE 5 | Ionic concentration and pH of pore solution.

Ion	Cl^-	Na^+	K^+	Ca^{2+}	SO_4^{2-}	AlO_2^-	$HSiO_3^-$	Mg^{2+}	pH
Concentration (mmol/L of pore solution)	105.99	74.80	203.13	0.12	0.24	0.61	4.85×10^{-5}	3.24×10^{-7}	13.44

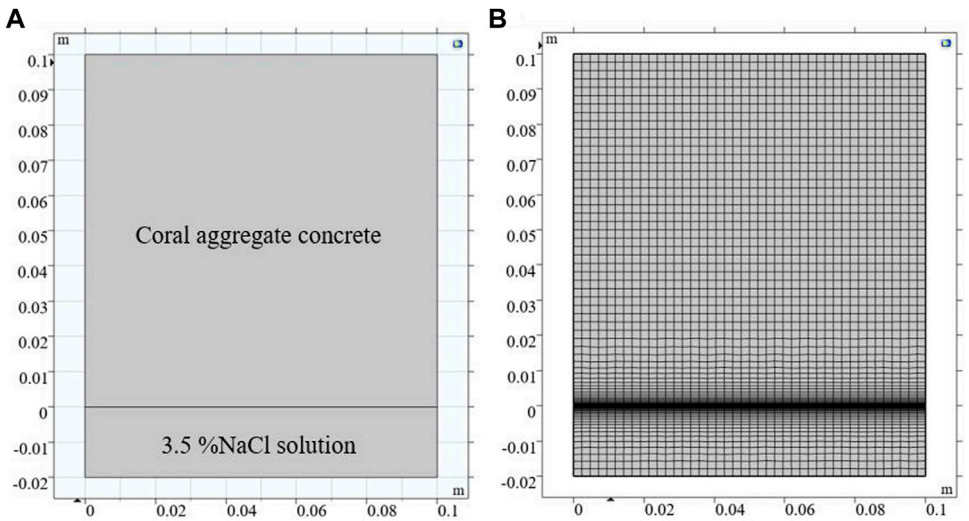

FIGURE 3 | (A) Geometrical model; **(B)** finite element meshing.

(AFm), ettringite (AFt), Friedel's salt (Fs), Kuzel's salt (Ks), and hydrotalcite. Free ions (including Ca^{2+}, K^+, Na^+, OH^-, SO_4^{2-}, and Cl^-) and aqueous complexes (such as AlO_2^-, $HSiO_3^-$, etc.) in the CAC pore solution are taken into account. Therefore, the initial hydrated cement compounds and pore solution obtained by GEMS calculation are given in **Tables 4**, **5**. It has been reported that when the free chloride concentration in pore solution is low, the chemical binding of chloride in cement-based materials is primarily through Kuzel's salt formation (Mesbah et al., 2011). However, the chloride concentration in CAC is high because coral aggregates contain a considerable amount of chloride. In the experimental study by Wang et al. (2019), Friedel's salt in CAC was found, which is in line with the results in **Table 4**. In the study of Huang et al. (2020a), when the exposure time was 30d, the chloride penetration depth was less than 18 mm. The free chloride concentration in the interior of the CAC specimen where the external chloride cannot penetrate should be nearly equal to its initial concentration, and it is 0.17% of concrete weight. Then, according to the mix proportion of CAC and the porosity of CAC, it is 89.29 mol/L of pore solution. The calculation result of the chloride concentration in **Table 5** is 105.99. There is a small and acceptable gap between the calculation and experimental results.

The specific surface area and surface site density of C–S–H are two key parameters for calculating the surface complexation reactions, and their values are 500 m^2/g and 4×10^3 mol/g, respectively (Pointeau et al., 2006).

Geometric Model and Boundary Conditions

According to the experiment of Huang et al. (2020a), the size of the CAC specimen was $100 \times 100 \times 100$ mm^3; one surface was exposed to a 3.5% NaCl solution (approximately 0.6 mol/L), and the others were sealed with epoxy resin. In addition, to ensure a constant concentration of chloride, the NaCl solution was periodically replaced. This meant that the Na^+ and Cl^- concentrations in the external solution nearly maintained 0.6 mol/L throughout the experimental process. In the numerical model, the operator splitting algorithm was used, and the initial values of the ionic concentration in the domain were redefined at each time step (see **Figure 1**). Thus, the initial values of the Na^+ and Cl^- concentrations in the external solution were defined as 0.6 mol/L at each time step, instead of the fixed boundary condition widely used in the ionic transport modelling. To reduce the calculation time, the height of the domain of the solution should be as small as possible. The two-dimensional geometrical model was built as shown in **Figure 3A**, in which the height of the domain of the external solution was chosen as 0.02 m to balance the calculation time and the accuracy. A quadrilateral mesh was adopted, as shown in **Figure 3B**. The difference in the initial ionic concentrations between the external solution and the CAC specimen was significant, and hence, to improve the convergence of the numerical model, the boundary layer mesh was used to densify the finite element mesh at the interface between the CAC specimen and the external solution. All boundaries in the domain were insulated. In the study of Huang et al. (2020a) The longest time that the specimen was exposed to NaCl solution was 180 days. Herein, the period for simulating chloride ingress for CAC was setas 360 days, giving 36 time steps of 10 days.

RESULTS AND DISCUSSION

The developed numerical model for the reactive transport in CAC is capable of predicting the variations in the hydrate phases, the

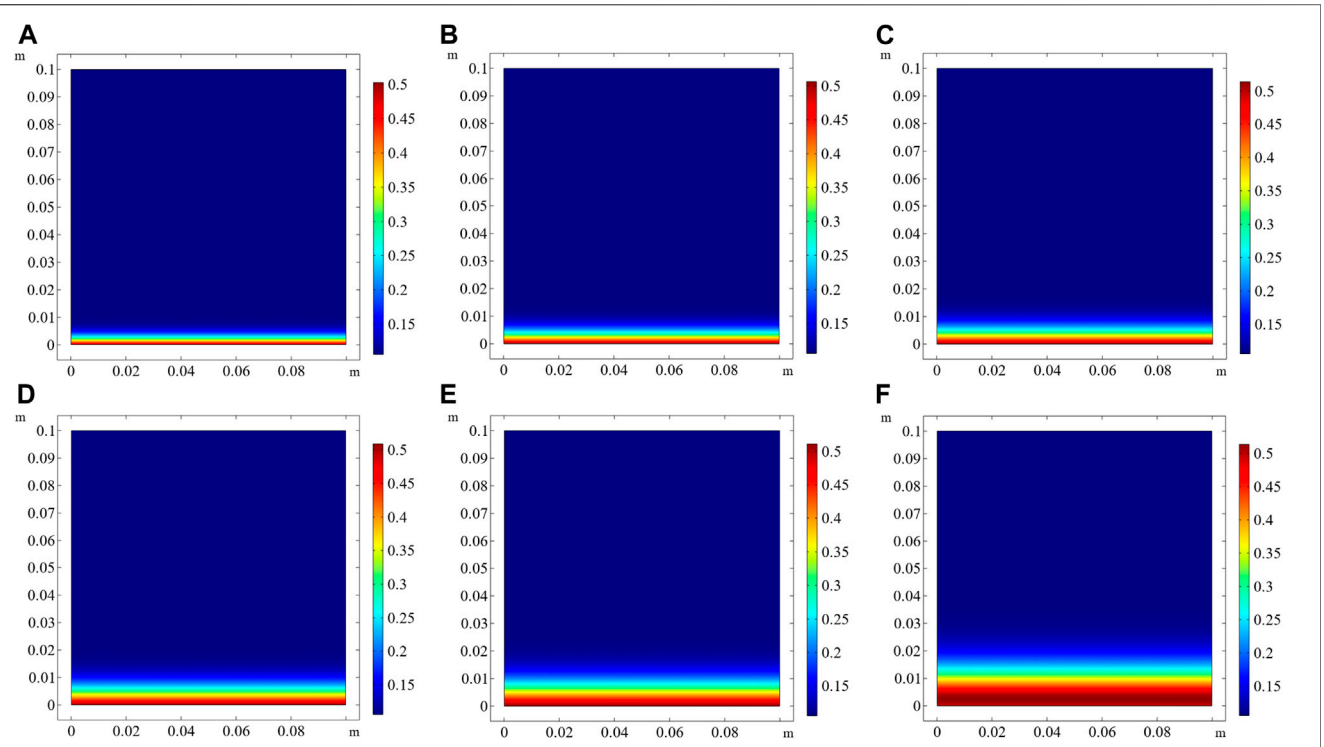

FIGURE 4 | Free chloride concentration in the pore solution of CAC at different exposure times (unit: mol/L of pore solution). **(A)** 30 days, **(B)** 60 days, **(C)** 90 days, **(D)** 120 days, **(E)** 180 days, **(F)** 360 days.

concentrations of free ions in the pore solution, and the amounts of ions bound by C–S–H with time and space. Considering that the $[Cl^-]/[OH^-]$ ratio in the pore solution determines the corrosion initiation of reinforcing steel embedded in CAC, the numerical results related to chloride and pH are presented and discussed, including the results of the free chloride concentration and pH in the pore solution, the content of chloride bound by C–S–H, and the amount of Friedel's salt. In addition, the experimental results for the free chloride concentration in the pore solution in Huang et al. (2020a) are used to verify the numerical model.

Concentration of Free Chloride and pH in CAC Pore Solution

When the exposure times are 30, 60, 90, 120, 180, and 360 d, the concentrations of free chloride in the pore solution are shown in **Figures 4A-F** respectively. Coral aggregates contain chloride, and hence, free chloride exists in the pore solution of CAC before exposure to the NaCl solution. As presented in **Table 5**, the initial free chloride concentration is 0.106 mol/L. Thus, the minimum free chloride concentration in the entire domain is 0.106 mol/L of pore solution. The free chloride concentration at the exposure side is the highest, and it gradually decreases with increasing distance from the exposed surface, becoming zero beyond a certain depth. The numerical results in **Figure 4** clearly show that the penetration depth of chloride increases with prolonged exposure time. When the CAC specimen is exposed to the external solution for 360 days, the penetration depth of chloride is 23.85 mm (**Figure 4F**).

The numerical model predicts the pH of the pore solution when the exposure times are 30, 60, 90, 120, 180, and 360 d, which are shown in **Figures 5A-F** respectively. Due to the presence of a concentration gradient, OH^- moves from high-concentration regions to low-concentration regions. The external solution is neutral, and OH^- will move from the pore solution to the external solution. Hence, the pH in the pore solution near the exposed side decreases with increasing exposure time. When the exposure time is 360 days, the pH near the surface is lower than 11.5 (**Figure 5F**). In addition, similar to the penetration depth of chloride, the regions with reduced pH of the pore solution become thicker with the elapse of time.

Physically and Chemically Bound Chloride

The physical and chemical binding of chloride has a significant effect on chloride transport in cement-based materials because it can slow down chloride transport, and prolong the time before chloride arrives at the steel surface. When the free chloride concentration decreases, the bound chloride is released into the pore solution as free chloride. The predicted chloride content physically bound by C–S–H at different exposure time is shown in **Figure 6**. Prior to the ingress of external chloride, some chloride ions in CAC have already been bound by C–S–H or chemically bound by producing Friedel's salt. With increasing exposure time, increasing number of external chloride ions penetrate CAC, and hence, the amount of chloride bound by C–S–H increases, as shown in **Figure 6**. The amount of chloride physically bound by C–S–H is closely related to the free chloride concentration in the pore solution. The free chloride concentration at the exposed side is the highest and remains constant (**Figure 4**). Thus,

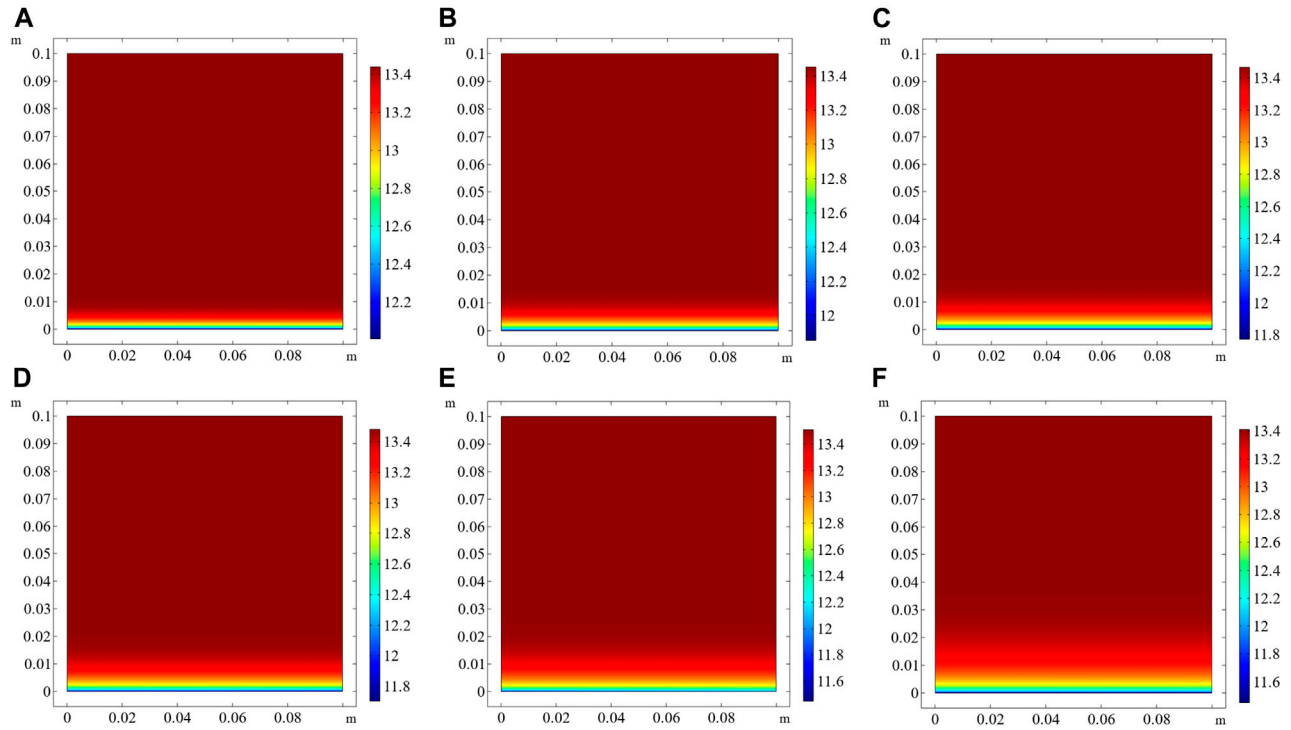

FIGURE 5 | pH in the pore solution of CAC at different exposure times. **(A)** 30 days, **(B)** 60 days, **(C)** 90 days, **(D)** 120 days, **(E)** 180 days, **(F)** 360 days.

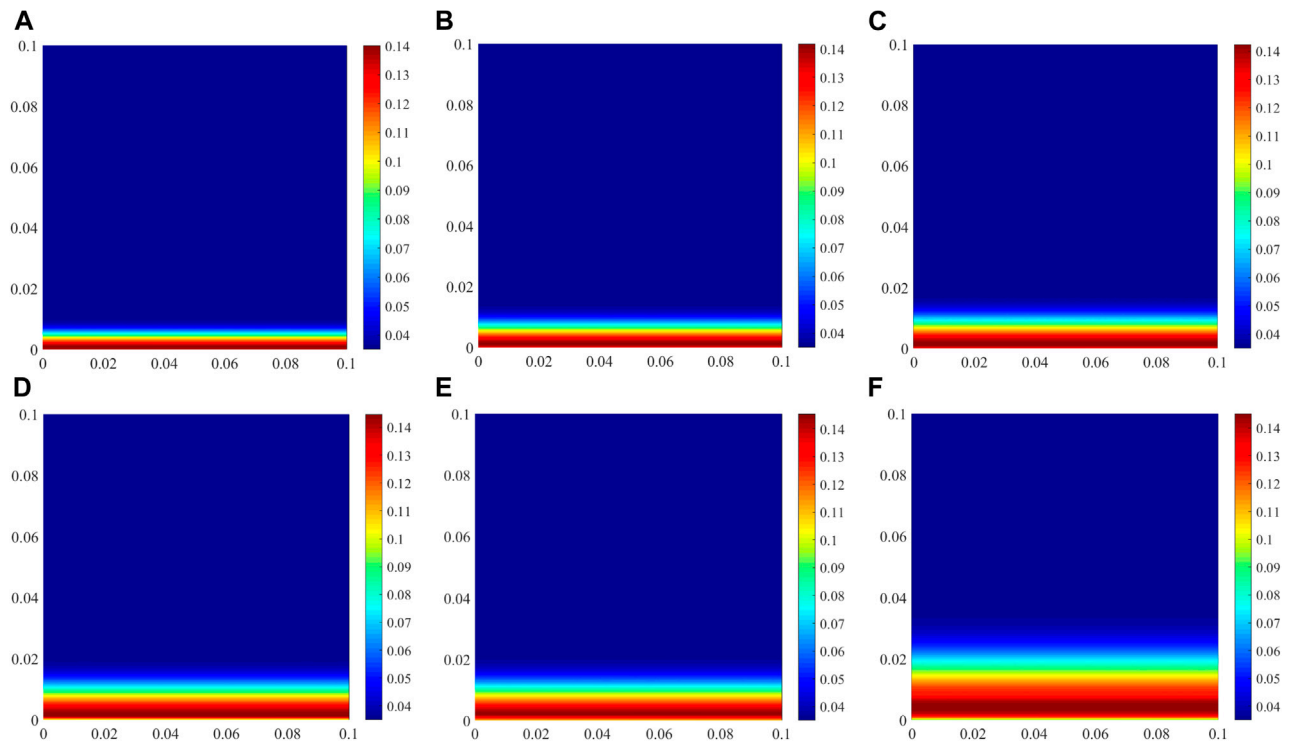

FIGURE 6 | Physically bound chloride by C–S–H at different exposure times (unit: mol/L of concrete). **(A)** 30 days, **(B)** 60 days, **(C)** 90 days, **(D)** 120 days, **(E)** 180 days, **(F)** 360 days.

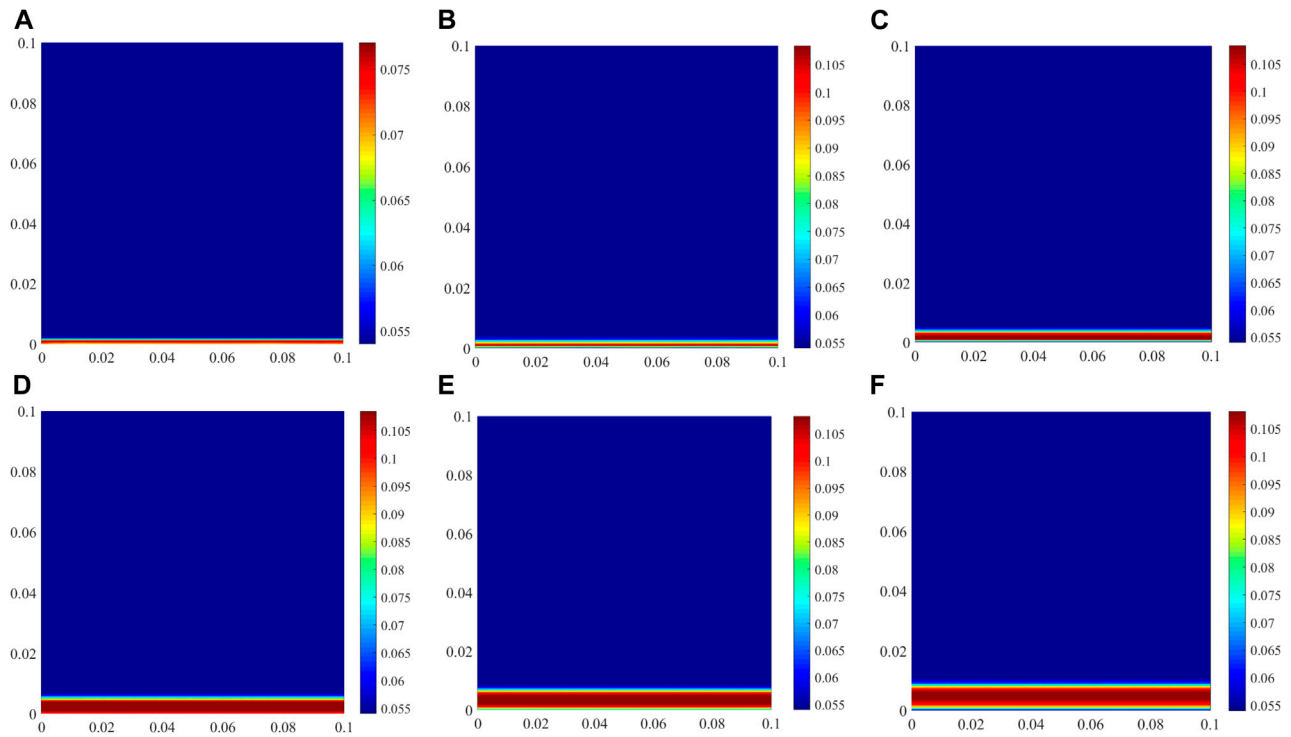

FIGURE 7 | Amount of Friedel's salt in CAC at different exposure times (unit: mol/L of concrete). **(A)** 30 days, **(B)** 60 days, **(C)** 90 days, **(D)** 120 days, **(E)** 180 days, **(F)** 360 days.

the amount of chloride physically bound at the exposed side is also the most, which is barely affected by the exposure time.

The amount of chemically bound chloride is expressed in the form of the content of Friedel's salt in the cement hydrate compounds, as shown in **Figure 7**. As is well known, when OAC is subjected to chloride attack, the chloride concentration in OAC is lower at the early stage, and some chlorides are bound by Kuzel's salt formation (Mesbah et al., 2011; Tran et al., 2018). With increasing the chloride concentration in OAC from the external environment, Kuzel's salt is converted into Friedel's salt (Zibara, 2001), which means that chloride is bound by Friedel's salt formation. However, because coral aggregates contain chloride, prior to chloride ingress, there are plenty of free chloride ions in the initial pore solution (**Table 5** and **Figure 4**), and some chlorides are directly bound by Friedel's salt formation (**Figure 6**). Thus, Kuzel's salt does not appear in CAC during chloride ingress.

One molar of Friedel's salt contains two molars of chloride, which can be seen from the formula in **Table 4**. The amount of Friedel's salt in CAC directly reflects the amount of chemically bound chloride. The amount of bound chloride at the exposed side decreases with prolonging the exposure time. When the exposure time exceeds 60 days, the amount of chloride chemically bound at the exposed side is not the highest in the whole specimen although the free chloride concentration is the highest. Some experimental results indicate that the stability of Friedel's salt is dependent on the pH of the pore solution, and a decrease in the pH can lead to the dissolution of Friedel's salt (Suryavanshi and Swamy, 1996). The pH at the exposed side is the lowest in the entire specimen owing to the OH^- movement from the pore solution to the external solution, and it decreases with increasing the exposure time (**Figure 5**). This is unfavourable for the formation of Friedel's salt. Therefore, the amount of Friedel's salt on the exposed side decreases, which differs from the physical binding of chloride. However, the variation in the amount of Friedel's salt in the interior region of the specimen is similar to that of the physical binding.

TABLE 6 | Hydrated cement compounds of CACs with C20F15 and C40F15.

Hydrate phase	Formula	Amount (mol/L of concrete)	
		C20F15	C40F15
C–S–H	$4(CaO)\ 3(SiO_2)\ 6.5(H_2O)$	2.013	2.132
CH	$Ca(OH)_2$	1.8121	1.9231
AFt	$Ca_6Al_2(SO_4)_3(OH)_{12}{\cdot}26H_2O$	0.1389	0.1601
AFm	$Ca_4Al_2(SO_4)(OH)_{12}{\cdot}6H_2O$	0.1375	0.1507
Fs	$Ca_4Al_2Cl_2O_6{\cdot}10H_2O$	0.048	0.059
Ks	$Ca_4Al_2Cl(SO_4)_{0.5}O_6{\cdot}12H_2O$	0	0
Hydrotalcite	$Mg_4Al_2(OH)_7\ 3(H_2O)$	0.046	0.054

Validation of the Model

Huang et al. (2020a) measured the free chloride concentration in CACs with different proportions at different exposure time. Their experimental results of C25F15, C30F15 and C40F15 CAC at 60 days and 180 days are used to verify the numerical model. In *Numerical Implementation*, C30F15 CAC is used a benchmark example to illustrate the implementation of the numerical model

and how to obtain the required parameters from the study of Huang et al. (2020a). Similarly, the required parameters of C25F15 and C40F15 can be obtained. The initial parameters are listed in **Tables 6**, **7**. The diffusion coefficients of chloride in C25F15 and C40F15 CAC used in the numerical model are 15.28 $\times 10^{-12}$ and 12.71 $\times 10^{-12}$, respectively.

Comparisons between the experimental and numerical results for free chloride in C25F15, C30F15 and C40F15 are shown in **Figures 8A-C** respectively. The results for C30F15 CAC are presented in **Figure 4**, which are represented in **Figure 8B** using traditional 2D plots. It is noted that the free chloride concentration is versus the CAC weight in their experimental results, and the free chloride concentration in the numerical results needs to be converted according to the mix proportion of CAC and the porosity of CAC.

By comparing the numerical and experimental results in **Figure 8**, it is clear that the numerical model overestimates the free chloride concentration in the surface layer of the specimen, especially when the distance from the exposed side is less than 5 mm. However, the numerical results agree well with the experimental results in the interior of the specimen. Doubt may arise as to whether the developed numerical model can accurately predict the chloride transport in CAC. In the experiment of Huang et al. (2020a), free chloride was obtained from CAC powder using distilled water extraction. At the end of the exposure, all the specimens were placed indoors for 7 days and then dried for 24 h to remove the moisture in the surface layer of CAC before they were milled using a concrete pulveriser. These processes to remove moisture significantly affect the chloride transport, especially in the surface layer of the CAC specimen. It should be noted that these processes occurred at the end of the chloride ingress for CAC, and it is unnecessary to consider them in the reactive transport modelling of chloride ingress for saturated CAC. In other words, the post-processing about the experimental results of (Huang et al., 2020) was not included by the numerical model. This is the primary reason why the numerical model does not agree with the concentration of the

TABLE 7 | Ionic concentration and pH of pore solution of CACs with C20F15 and C40F15.

Ion	Concentration (mmol/L of pore solution)	
	C20F15	C40F15
Cl^-	118.99	108.12
Na^+	71.8	98.8
K^+	198.13	221.41
Ca^{2+}	0.11	0.19
SO_4^{2-}	0.22	0.35
AlO_2^-	0.59	0.76
$HSiO_3^-$	3.76×10^{-5}	5.98×10^{-5}
Mg^{2+}	2.84×10^{-7}	3.58×10^{-7}
pH	13.31	13.65

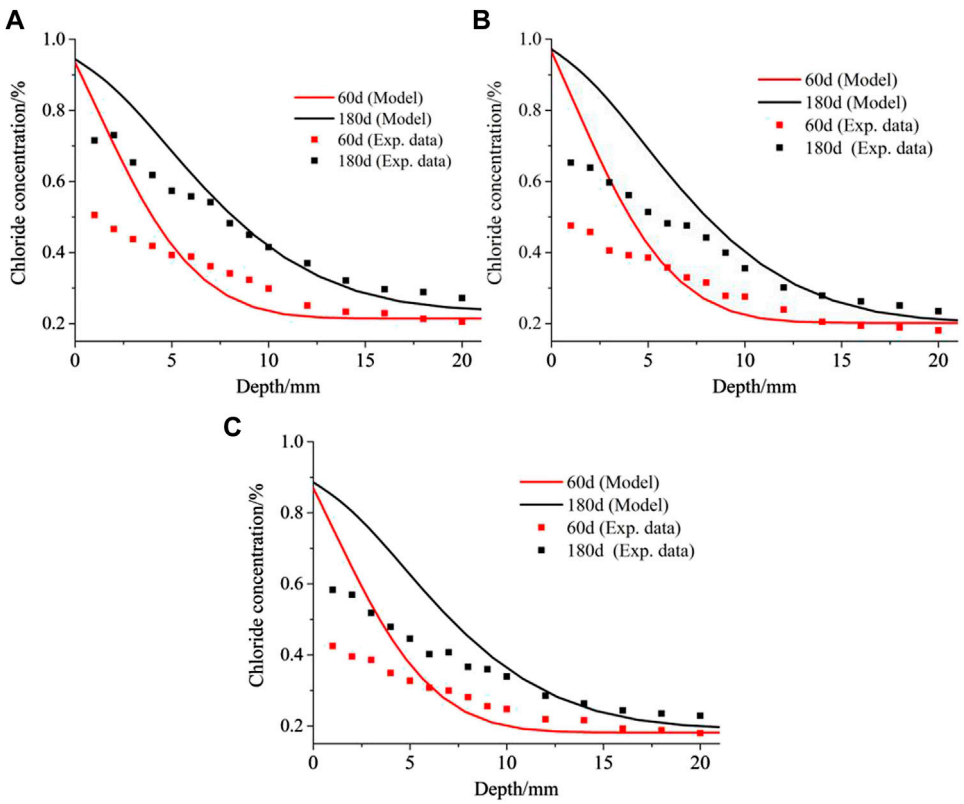

FIGURE 8 | Comparison between experimental and numerical results about free chloride concentration: **(A)** C25F15; **(B)** C30F15; **(C)** C40F15. Note that all the experimental data in the figure are from Huang et al. (2020a).

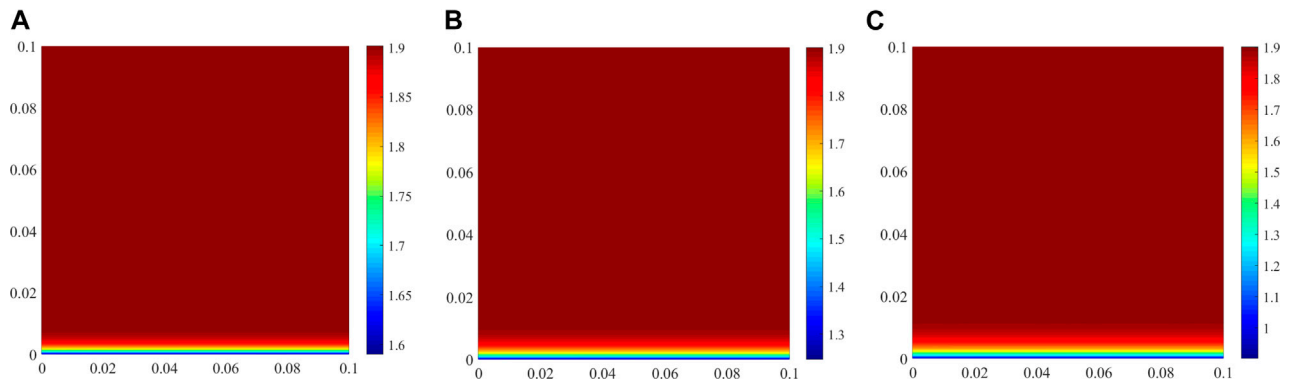

FIGURE 9 | Amount of CH in CAC at different exposure times (unit: mol/L of concrete). **(A)** 30 days, **(B)** 180 days, **(C)** 360 days.

free chloride ion in the surface layer of the CAC specimen. However, the processes hardly affect the free chloride concentration measurement in the interior of the CAC specimen, and the chloride ingress is predicted well with the numerical model in this region. Thus, the numerical model can predict the chloride ingress for saturated CAC.

Limits of the Model

The diffusion coefficient of chloride in the pore solution of CAC is a key input parameter for simulating ionic transport, and this parameter is constant in this study. However, Friedel's salt formation during chloride ingress causes a less porous structure of cement-based materials (Yuan et al., 2009). Thus, chloride ingress results in a decrease in the diffusion coefficient of chloride owing to the increase in the content of Friedel's salt (see **Figure 7**). In practice, chloride ingress into saturated CAC generally occurs in an underwater environment, which is accompanied by the decalcification of cement hydrates. This can also be seen from the benchmark example, in which the numerical model predicts the CH content in CAC at different exposure time, as shown in **Figure 9**. It is clear that the CH amount decreases with prolonged exposure time, especially in the vicinity of the exposed side. Decalcification would result in a more porous structure of CAC, leading to an increase in the diffusion coefficient of chloride in the pore solution of CAC. However, the positive effect of decalcification and the negative effect of Friedel's salt formation on the diffusion coefficient of chloride only appears in the local region close to the external solution. These effects are more significant with time, and the local region will increase. Thus, the diffusion coefficient of chloride varies with time and space. However, it is difficult to consider this in the reactive transport modelling. This is the limit of the model developed in this study. This may also be another reason for the gap between the numerical and experimental results shown in **Figure 8**.

CONCLUSION

Reactive transport modelling was developed in this study to investigate chloride ingress in CAC. A COMSOL-PHREEQC interface was established to solve the numerical model based on the MATLAB program. The experimental investigation of Huang et al. (2020a) was taken as an example to illustrate the implementation of reactive transport modelling in CAC. The free chloride concentration and pH in the CAC pore solution, and the physically and chemically bound chloride are predicted. The results indicate that the developed numerical model is capable of predicting chloride transport behaviour in CAC.

Kuzel's salt does not appear in the cement hydrate compounds of CAC during chloride ingress, which is different from OAC. The numerical results clearly indicate that the penetration depth of chloride in CAC gradually increases as the exposure time is prolonged. When exposed to external chloride solution, the decrease in the pH of the CAC pore solution has a significant influence on the formation of Friedel's salt, which is detrimental to the chemical binding of chloride.

DATA AVAILABILITY STATEMENT

The raw data supporting the conclusions of this article will be made available by the authors, without undue reservation.

AUTHOR CONTRIBUTIONS

BG: Numerical modelling, Writing-Original draft preparation, Funding acquisition. ZL: Investigation, Writing-Review and Editing. QF: Analysis, Methodology. YW: Conceptualization, Analysis. DH: Conceptualization, Methodology. DN: Conceptualization, Supervision.

FUNDING

This study is supported by the Nature Science Foundation of China (51908453), China Postdoctoral Science Foundation (2020M673607XB and 2020T130497), Scientific Research of Shanxi Provincial Department of Education (20JK0710), Independent Research and Development project of State Key Laboratory of Green Building in Western China (LSZZ202113).

REFERENCES

Angst, U., Elsener, B., Larsen, C. K., and Vennesland, Ø. (2009). Critical Chloride Content in Reinforced concrete - A Review. *Cement Concrete Res.* 39 (12), 1122–1138. doi:10.1016/j.cemconres.2009.08.006

Angst, U. M. (2019). A Critical Review of the Science and Engineering of Cathodic protection of Steel in Soil and concrete. *Corrosion Journal.ORG.* 12 (75), 1420–1433. doi:10.5006/3355

Appelo, C. A. J., Van Loon, L. R., and Wersin, P. (2010). Multicomponent Diffusion of a Suite of Tracers (HTO, Cl, Br, I, Na, Sr, Cs) in a Single Sample of Opalinus clay. *Geochimica et Cosmochimica Acta* 74 (4), 1201–1219. doi:10.1016/j.gca.2009.11.013

Baroghel-Bouny, V., Thiéry, M., and Wang, X. (2011). Modelling of Isothermal Coupled Moisture-Ion Transport in Cementitious Materials. *Cement Concrete Res.* 41 (8), 828–841. doi:10.1016/j.cemconres.2011.04.001

Charlton, S. R., and Parkhurst, D. L. (2011). Modules Based on the Geochemical Model PHREEQC for Use in Scripting and Programming Languages. *Comput. Geosciences* 37 (10), 1653–1663. doi:10.1016/j.cageo.2011.02.005

COMSOL (2021). COMSOL Multiphysics. Version 5.5. Available from: www.comsol.com.

Da, B., Yu, H., Ma, H., Tan, Y., Mi, R., and Dou, X. (2016). Chloride Diffusion Study of Coral concrete in a marine Environment. *Construction Building Mater.* 123, 47–58. doi:10.1016/j.conbuildmat.2016.06.135

Elakneswaran, Y., Iwasa, A., Nawa, T., Sato, T., and Kurumisawa, K. (2010). Ion-cement Hydrate Interactions Govern Multi-Ionic Transport Model for Cementitious Materials. *Cement Concrete Res.* 40 (12), 1756–1765. doi:10.1016/j.cemconres.2010.08.019

Elakneswaran, Y., Nawa, T., and Kurumisawa, K. (2009). Electrokinetic Potential of Hydrated Cement in Relation to Adsorption of Chlorides. *Cement Concrete Res.* 39 (4), 340–344. doi:10.1016/j.cemconres.2009.01.006

Elakneswaran, Y., Nawa, T., and Kurumisawa, K. (2009). Influence of Surface Charge on Ingress of Chloride Ion in Hardened Pastes. *Mater. Struct.* 42, 83–93. doi:10.1617/s11527-008-9368-8

Gui, W., Hu, X., and Liang, L. (2020). Normal Distribution Analysis of Fracture Parameters of Alkali-Activated Slag Seawater Column Coral Aggregate concrete. *Theor. Appl. Fracture Mech.* 110, 102794. doi:10.1016/j.tafmec.2020.102794

Guo, B., Hong, Y., Qiao, G., and Ou, J. (2018). A COMSOL-PHREEQC Interface for Modeling the Multi-Species Transport of Saturated Cement-Based Materials. *Construction Building Mater.* 187, 839–853. doi:10.1016/j.conbuildmat.2018.07.242

Guo, B., Hong, Y., Qiao, G., Ou, J., and Li, Z. (2018). Thermodynamic Modeling of the Essential Physicochemical Interactions between the Pore Solution and the Cement Hydrates in Chloride-Contaminated Cement-Based Materials. *J. Colloid Interf. Sci.* 531, 56–63. doi:10.1016/j.jcis.2018.07.005

Guo, B., Qiao, G., Li, D., and Ou, J. (2021). Multi-species Reactive Transport Modeling of Electrochemical Corrosion Control in Saturated concrete Structures Including Electrode Reactions and Thermodynamic Equilibrium. *Construction Building Mater.* 278, 122228. doi:10.1016/j.conbuildmat.2020.122228

Haynes, W. M., Lide, D. R., and Bruno, T. J. (2014). *Handbook of Chemistry and Physics*. Boca Raton: CRC Press.

Hou, B., Li, X., Ma, X., Du, C., and Zhang, D. (2017). The Cost of Corrosion in China. *NPJ Mat. Degrad.* 1 (1), 1–10. doi:10.1038/s41529-017-0005-2

Huang, D. (2020). *Chloride Transport Behavior of Coral Aggregate concrete under Extreme Hot and Humid Environment, PhD Thesis*. China: Xi'an University of Architecture and Technology.

Huang, D., Niu, D., Zheng, H., Su, L., Luo, D., and Fu, Q. (2020a). Study on Chloride Transport Performance of Eco-Friendly Coral Aggregate concrete in marine Environment. *Construction Building Mater.* 258, 120272. doi:10.1016/j.conbuildmat.2020.120272

Kari, O. P., Elakneswaran, Y., Nawa, T., and Puttonen, J. (2013). A Model for a Long-Term Diffusion of Multispecies in concrete Based on Ion-Cement-Hydrate Interaction. *J. Mater. Sci.* 48 (12), 4243–4259. doi:10.1007/s10853-013-7239-3

Kulik, D. A., Wagner, T., Dmytrieva, S. V., Kosakowski, G., Hingerl, F. F., Chudnenko, K. V., et al. (2013). GEM-selektor Geochemical Modeling Package: Revised Algorithm and GEMS3K Numerical Kernel for Coupled Simulation Codes. *Comput. Geosci-uk* 17 (1), 1–24.

Lehner, P., Konečný, P., and Ghosh, P. (2021). Variation of Durability and Strength Parameters of Pumice Based Mixtures. *Materials* 14, 3674. doi:10.3390/ma14133674

Li, H., Xiao, H., Guan, X., Wang, Z., and Yu, L. (2014). Chloride Diffusion in concrete Containing Nano-TiO2 under Coupled Effect of Scouring. *Composites B: Eng.* 56, 698–704. doi:10.1016/j.compositesb.2013.09.024

Liang, X., Yin, S., and Hu, C. (2021). Environmental Reduction Factors of BFRP Bars in Coral Aggregate concrete in High Temperature and High Humidity Environments. *Structures* 33, 3017–3024. doi:10.1016/j.istruc.2021.06.021

Liang, X., and Yin, S. (2021a). Mechanical Properties and Gas Permeability of Coral Aggregate concrete Incorporating Supplementary Cementitious Materials. *Construction Building Mater.* 302, 124237. doi:10.1016/j.conbuildmat.2021.124237

Liu, B., Guo, J., Zhou, J., Wen, X., Deng, Z., Wang, H., et al. (2020). The Mechanical Properties and Microstructure of Carbon Fibers Reinforced Coral concrete. *Construction Building Mater.* 249, 118771. doi:10.1016/j.conbuildmat.2020.118771

Liu, Q.-f., Easterbrook, D., Yang, J., and Li, L.-y. (2015). A Three-phase, Multi-Component Ionic Transport Model for Simulation of Chloride Penetration in concrete. *Eng. Structures* 86, 122–133. doi:10.1016/j.engstruct.2014.12.043

Lothenbach, B., Kulik, D. A., Matschei, T., Balonis, M., Baquerizo, L., Dilnesa, B., et al. (2019). Cemdata18: A Chemical Thermodynamic Database for Hydrated Portland Cements and Alkali-Activated Materials. *Cement Concrete Res.* 115, 472–506. doi:10.1016/j.cemconres.2018.04.018

Lothenbach, B., and Winnefeld, F. (2006). Thermodynamic Modelling of the Hydration of portland Cement. *Cement Concrete Res.* 36 (2), 209–226. doi:10.1016/j.cemconres.2005.03.001

Lothenbach, B., and Zajac, M. (2019). Application of Thermodynamic Modelling to Hydrated Cements. *Cem. Concr. Res.* 105779 (13). doi:10.1016/j.cemconres.2019.105779

Mesbah, A., François, M., Cau-dit-Coumes, C., Frizon, F., Filinchuk, Y., Leroux, F., et al. (2011). Crystal Structure of Kuzel's Salt 3CaO·Al2O3·1/2CaSO4·1/2CaCl2·11H2O Determined by Synchrotron Powder Diffraction. *Cement Concrete Res.* 41 (5), 504–509. doi:10.1016/j.cemconres.2011.01.015

Nardi, A., Idiart, A., Trinchero, P., de Vries, L. M., and Molinero, J. (2014). Interface COMSOL-PHREEQC (iCP), an Efficient Numerical Framework for the Solution of Coupled Multiphysics and Geochemistry. *Comput. Geosciences* 69, 10–21. doi:10.1016/j.cageo.2014.04.011

Parkhurst, D. L., and Appelo, C. A. J. (2013). Description of Input and Examples for PHREEQC Version 3–A Computer Program for Speciation, Batch-Reaction, One-Dimensional Transport, and Inverse Geochemical Calculations. *U.S. Geol. Surv.*

Pointeau, I., Reiller, P., Macé, N., Landesman, C., and Coreau, N. (2006). Measurement and Modeling of the Surface Potential Evolution of Hydrated Cement Pastes as a Function of Degradation. *J. Colloid Interf. Sci.* 300 (1), 33–44. doi:10.1016/j.jcis.2006.03.018

Spiesz, P., Ballari, M. M., and Brouwers, H. J. H. (2012). RCM: A New Model Accounting for the Non-linear Chloride Binding Isotherm and the Non-equilibrium Conditions between the Free- and Bound-Chloride Concentrations. *Construction Building Mater.* 27 (1), 293–304. doi:10.1016/j.conbuildmat.2011.07.045

Suryavanshi, A. K., and Narayan Swamy, R. (1996). Stability of Friedel's Salt in Carbonated concrete Structural Elements. *Cement Concrete Res.* 26 (5), 729–741. doi:10.1016/s0008-8846(96)85010-1

Tang, L., and Nilsson, L.-O. (1995). A New Approach to the Determination of Pore Distribution by Penetrating Chlorides into concrete. *Cement Concrete Res.* 25 (4), 695–701. doi:10.1016/0008-8846(95)00058-k

Tran, V. Q., Soive, A., and Baroghel-Bouny, V. (2018). Modelisation of Chloride Reactive Transport in concrete Including Thermodynamic Equilibrium, Kinetic Control and Surface Complexation. *Cement Concrete Res.* 110, 70–85. doi:10.1016/j.cemconres.2018.05.007

Van Quan, T., Soive, A., Bonnet, S., and Khelidj, A. (2018). A Numerical Model Including Thermodynamic Equilibrium, Kinetic Control and Surface Complexation in Order to Explain Cation Type Effect on Chloride Binding Capability of concrete. *Constr. Build. Mater.* 191, 608–618.

Wang, Y., Zhang, S., Niu, D., Su, L., and Luo, D. (2019). Effects of Silica Fume and Blast Furnace Slag on the Mechanical Properties and Chloride Ion Distribution of Coral Aggregate concrete. *Construction Building Mater.* 214, 648–658. doi:10.1016/j.conbuildmat.2019.04.149

Wattanachai, P., Otsuki, N., Saito, T., and Nishida, T. (2009). A Study on Chloride Ion Diffusivity of Porous Aggregate Concretes and Improvement Method. *Jsce J. Mater. Concrete Structures Pavements* 65 (1), 30–44. doi:10.2208/jsceje.65.30

Wu, Z., Zhang, J., Yu, H., and Ma, H. (2020). 3D Mesoscopic Investigation of the Specimen Aspect-Ratio Effect on the Compressive Behavior of Coral Aggregate concrete. *Composites Part B: Eng.* 198, 108025. doi:10.1016/j.compositesb.2020.108025

Yu, H., Da, B., Ma, H., Dou, X., and Wu, Z. (2020). Service Life Prediction of Coral Aggregate concrete Structure under Island Reef Environment. *Construction Building Mater.* 246, 118390. doi:10.1016/j.conbuildmat.2020.118390

Yu, H., Da, B., Ma, H., Zhu, H., Yu, Q., Ye, H., et al. (2017). Durability of concrete Structures in Tropical Atoll Environment. *Ocean Eng.* 135, 1–10. doi:10.1016/j.oceaneng.2017.02.020

Yuan, Q., Shi, C., De Schutter, G., Audenaert, K., and Deng, D. (2009). Chloride Binding of Cement-Based Materials Subjected to External Chloride Environment - A Review. *Construction Building Mater.* 23 (1), 1–13. doi:10.1016/j.conbuildmat.2008.02.004

Yuan, Q., Shi, C., De Schutter, G., Deng, D., and He, F. (2011). Numerical Model for Chloride Penetration into Saturated concrete. *J. Mater. Civ. Eng.* 23 (3), 305–311. doi:10.1061/(asce)mt.1943-5533.0000168

Zhang, L., Niu, D., Wen, B., Peng, G., and Sun, Z. (2020). Corrosion Behavior of Low alloy Steel Bars Containing Cr and Al in Coral concrete for Ocean Construction. *Construction Building Mater.* 258, 119564. doi:10.1016/j.conbuildmat.2020.119564

Zhou, L., Guo, S., Zhang, Z., Shi, C., Jin, Z., and Zhu, D. (2021). Mechanical Behavior and Durability of Coral Aggregate concrete and Bonding Performance with Fiber-Reinforced Polymer (FRP) Bars: A Critical Review. *J. Clean. Prod.* 289, 125652. doi:10.1016/j.jclepro.2020.125652

Zibara, H. (2001). *Binding of External Chloride by Cement Pastes, PhD Thesis*. Canada: University of Toronto.

Conflict of Interest: The authors declare that the research was conducted in the absence of any commercial or financial relationships that could be construed as a potential conflict of interest.

Publisher's Note: All claims expressed in this article are solely those of the authors and do not necessarily represent those of their affiliated organizations, or those of the publisher, the editors and the reviewers. Any product that may be evaluated in this article, or claim that may be made by its manufacturer, is not guaranteed or endorsed by the publisher.

frontiers in Materials

ORIGINAL RESEARCH
published: 03 November 2021
doi: 10.3389/fmats.2021.778833

Research on Microstructure, Mechanical Properties and Electromagnetic Shielding Properties of Mg-6Zn-3Sn-0.5Cu Alloy

Yan Hui Liu[1,2,3], *Ming Long Ma*[1,2,3]*, *Xing Gang Li*[1,2,3], *Yong Jun Li*[1,2,3], *Guo Liang Shi*[1,2,3], *Jia Wei Yuan*[1,2,3] *and Kui Zhang*[1,2,3]*

[1]State Key Laboratory of Nonferrous Metals and Processes, GRINM Co., Ltd., Beijing, China, [2]GRIMAT Engineering Institute Co., Ltd., Beijing, China, [3]General Research Institute for Nonferrous Metals, Beijing, China

In this paper, the microstructure, electromagnetic shielding properties and mechanical properties of Mg-6Zn-3Sn-0.5Cu alloys are studied. As indicated from the results, the phases in the as-cast alloy comprise α-Mg, MgZnCu, Mg_2Sn and Mg_2Zn_3 phases. After homogenization, Mg_2Sn and Mg_2Zn_3 phases are decomposed, but the MgZnCu phase remains. During extrusion, complete dynamic recrystallization (DRX) occurs, and the spherical Mg_2Sn phase precipitates dynamically. Due to considerable rod-like β'_1 phases precipitate by complying with the $[0001]_{Mg}$ direction, the mechanical properties of aged alloys are remarkably enhanced. The peak-aged alloy achieves the tensile strength of 366 MPa, the yield strength of 358 MPa and the elongation of 7%. With the increase in the size of the β'_1 phase, the mechanical properties of the over-aged alloy are reduced. Since the phases precipitate, the electrical conductivity of the alloy is enhanced, and the internal reflective interface increases, so the aged alloys exhibit improved electromagnetic shielding performance. The electromagnetic shielding efficiency of the peak-aged alloy exceeds 105 dB in the range of 30–1500 MHz, showing the best match between mechanical and electromagnetic shielding properties.

Keywords: Mg-Zn-Sn-Cu alloy, extrusion, aging treatment, mechanical properties, electromagnetic shielding properties

OPEN ACCESS

Edited by:
Lai-Chang Zhang,
Edith Cowan University, Australia

Reviewed by:
Xiaodong Peng,
Chongqing University, China
Bo Song,
Southwest University, China
Xianhua Chen,
Chongqing University, China

***Correspondence:**
Ming Long Ma
maminglong@grinm.com
Kui Zhang
zhkui@grinm.com

Specialty section:
This article was submitted to Structural Materials, a section of the journal Frontiers in Materials

Received: *17 September 2021*
Accepted: *20 October 2021*
Published: *03 November 2021*

Citation:
Liu YH, Ma ML, Li XG, Li YJ, Shi GL, Yuan JW and Zhang K (2021) Research on Microstructure, Mechanical Properties and Electromagnetic Shielding Properties of Mg-6Zn-3Sn-0.5Cu Alloy. Front. Mater. 8:778833. doi: 10.3389/fmats.2021.778833

INTRODUCTION

As modern electronic technology is advancing, people's production life has been facilitated, while the issue of electromagnetic pollution has arisen. Electromagnetic waves are capable of affecting the life and health of living organisms and interfering with the normal operation of electronic equipment. Moreover, the risk of information leakage in national defense will be raised if electromagnetic waves are not effectively shielded (García et al., 2008; Shen et al., 2013; Shahzad et al., 2016; Kim et al., 2017). On the whole, the existing electromagnetic shielding materials complies with polymer composites and metal-based materials, whereas polymer materials exhibit poor mechanical properties, and metal-based materials face a problem of high density (Geetha et al., 2009). For this reason, the development of lightweight electromagnetic shielding materials with high mechanical properties has become one of the hotspots in materials research.

Magnesium alloys have been extensively employed in automotive, aerospace, defense and military industries for their low density, high specific strength over stiffness, good damping properties and

TABLE 1 | Chemical composition of the experimental alloy (wt.%).

Alloy	Nominal compositions	Actual compositions			
		Zn	Sn	Cu	Mg
ZT63-0.5Cu	Mg-6Zn-3Sn-0.5Cu	5.8	3.38	0.48	Bal.

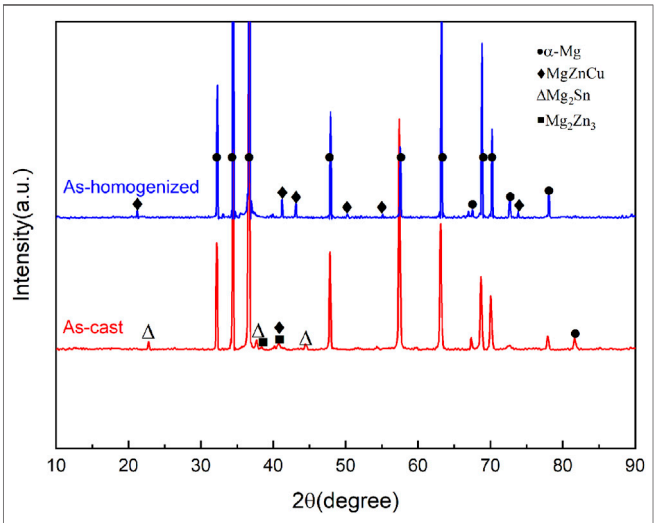

FIGURE 1 | X-ray diffraction patterns of as-cast and as-homogenized alloys.

easy recycling (Ali et al., 2015; You et al., 2017). At present, in addition to studying the microstructure and mechanical properties of magnesium alloys, the study of their functional properties has also become an emerging research hotspot (Yang et al., 2021). Electromagnetic shielding performance as an important functional property of magnesium alloys has also attracted the attention of researchers. Pandey et al. (2019) found that the addition of Ti can improve the electromagnetic shielding performance of pure magnesium. Wang et al. (2019) developed an Mg-Li alloy with high mechanical and electromagnetic shielding properties by rolling. Ye et al. (2021) prepared an Mg-Sn-Zn alloy with a tensile strength of 337 MPa and an electromagnetic shielding efficiency of 97–114 dB, which had a good comprehensive performance. Chen et al. (2012), Chen et al. (2013), and Chen et al. (2015a) revealed that aging treatment could improve the electromagnetic shielding properties of Mg-Zn alloys. By introducing suitable alloying elements to the alloy, combined with plastic deformation and aging treatment, magnesium alloys with high electromagnetic shielding properties and prominent mechanical properties can be prepared, which is critical to expanding the application of magnesium alloys.

Mg-Zn alloys can be strengthened by heat treatment, and their cost is significantly lowered compared with rare-earth magnesium alloys. However, the mechanical properties of Mg-Zn alloys are poor, and further alloying is required to enhance the properties of the alloys. For example, elements such as Sn, Ca, Mn, and Cu are added to the Mg-Zn alloys to improve their mechanical properties (Liu et al., 2020; Wang et al., 2021). As reported by Wei et al. (2013) and Qi et al. (2014), the addition of Sn elements to Mg-Zn alloys resulted in grain refinement and improvement of mechanical properties. Wang et al. (2018) reported that the Cu element could refine the second phase in Mg-Sn-Zn alloy and enhance the mechanical properties of the alloy.

As indicated from recent studies, Mg-Zn alloys also exhibit high electromagnetic shielding properties (Chen et al., 2012; Chen et al., 2013; Chen et al., 2015a). However, Research on structural-functional integration Mg-Zn alloys is still relatively rare Rare research has been reported on. Thus, to further expand the application of Mg-Zn alloy and enrich its basic theoretical data as structural-functional materials, we prepared Mg-6Zn-3Sn-0.5Cu alloy based on Mg-6Zn-3Sn alloy with the addition of a trace amount of Cu elements. The microstructure evolution of the alloy was studied, and the mechanical properties and electromagnetic shielding properties of the extruded, peak-aged and over-aged alloy were analyzed. such a study will provide novel ideas for preparing low-cost and high-performance magnesium alloys.

MATERIALS AND METHODS

The raw materials applied for preparing the alloy included pure Mg (99.95%), pure Zn (99.95%), pure Sn (99.99%) and pure Cu (99.99%), which were melted in a medium frequency induction furnace. A mixture of argon and tetrafluoroethane (Ar: CH_2FCF_3 = 20:1) was introduced in the melting to protect the melt, the final size of the ingot reached Φ100 × 360 mm. The element content of the ingots was determined with Inductively Coupled Plasma-Atomic Emission Spectrometry (ICP-AES), and the results are listed in **Table 1**. The ingots were homogenized at 335°C–24h + 420°C–24h and then extruded at 370 °C at an extrusion speed of 0.6 mm/s as well as an extrusion ratio of 23:1. The final extruded bar with a diameter of 25 mm was obtained. The alloy was aged at 180°C under an aging period of 0–100 h.

The microstructure of the alloy was explored under an optical microscope (OM, Carl Zeiss Axiovet2000MAT), a field emission scanning electron microscope (FE-SEM, JEOL JSM-7600), an X-ray diffractometer (XRD, Smartlab), as well as a transmission electron microscope (TEM, Tecnai G2 F20). JEOL JSM-7900F equipped with an electron backscattered diffraction (EBSD) system was used to analyze the texture of the alloy. The etchant for the alloy is a mixture of ethanol (l0 ml) + picric acid (0.3 g) + glacial acetic acid (1 ml) + distilled water (1 ml). EBSD samples were electropolished in a 10% nitric acid alcohol solution. The average grain size of the alloy was determined by the linear intercept method. The tensile properties for the different state alloy were obtained by a SANS universal testing machine. Cylindrical samples of diameter 5 mm and gauge length 25 mm were used for tensile tests. Three tensile tests were

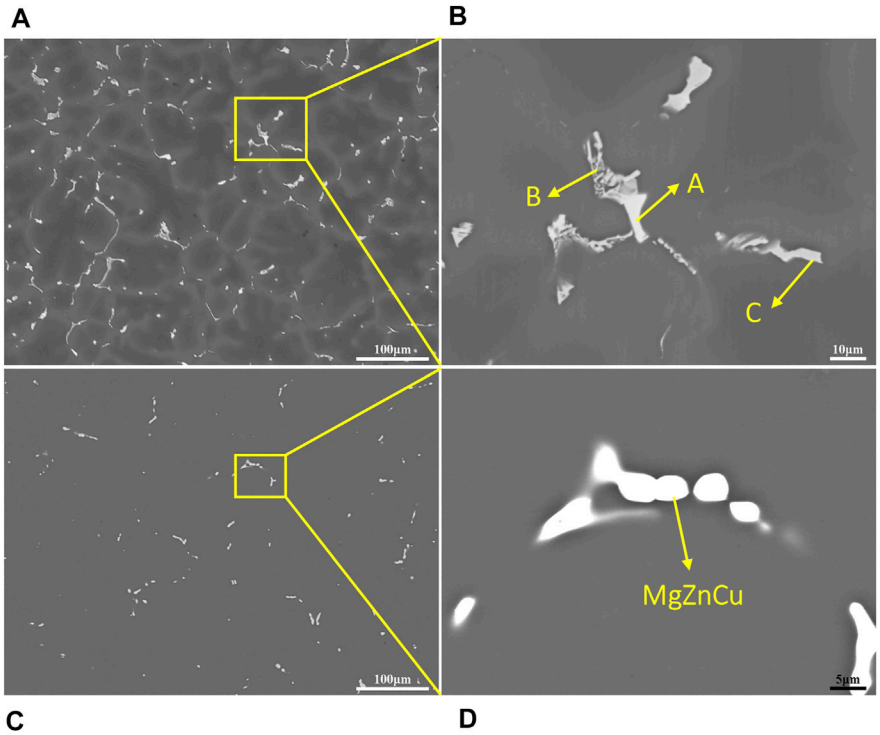

FIGURE 2 | SEM images of as-cast and as-homogenized alloys: **(A,B)** as-cast alloy, **(C,D)** as-homogenized alloy.

TABLE 2 | EDS results for different positions of as-cast alloy.

Point	Mg		Sn		Zn		Cu	
	At. %	Wt.%	At. %	Wt.%	At. %	Wt.%	At. %	Wt.%
A	72.32	35.47	26.05	62.39	1.24	1.64	0.39	0.50
B	70.76	47.32	0.32	1.03	21.94	39.46	6.98	12.19
C	64.99	40.21	1.13	3.41	33.88	56.38	—	—

performed, and the strength and elongation were taken as the mean value. A Brinell hardness tester (HBS 62.5) was employed to examine the hardness of the alloy during aging. The load during the test was 30 kg and the loading time was 25 s. Each sample was tested five times, and the average hardness value was taken. The electrical conductivity of the alloy was tested with a WD-Z eddy current conductivity tester, with the respective sample being tested five times, and the final result was taken as the mean value. The standard coaxial cable method was employed to measure the electromagnetic shielding properties of the different state alloys. The electromagnetic shielding test equipment involved an E6063A vector network analyzer and a DR-S04 micro-coaxial shield effectiveness tester. The samples were taken from the cross-section of the bar, with a diameter of 20 mm and a thickness of 0.9 mm. The electromagnetic wave frequency range of the test was 30–1500 MHz. Each sample was tested five times, and the final shielding effectiveness was taken as its average value.

RESULTS AND DISCUSSION

Microstructure of As-Cast and As-Homogenized Alloys

The XRD patterns of the as-cast and as-homogenized alloys are illustrated in **Figure 1**. α-Mg, MgZnCu phase, Mg_2Sn phase and Mg_2Zn_3 phase are found in the as-cast alloy. After the homogenization treatment, the diffraction peaks belonging to the Mg_2Sn and Mg_2Zn_3 phases disappear, and only the diffraction peak of the MgZnCu phase existed except for the α-Mg, which demonstrates that the homogenization can make the Mg_2Sn and Mg_2Zn_3 phases decompose, and the Zn and Sn atoms dissolve back into the matrix, while the MgZnCu phase is not decomposed.

Figure 2 presents the SEM images of the as-cast and as-homogenized alloys. As indicated from the low magnification SEM image (**Figure 2A**), the as-cast alloy displays a typical petal-like dendritic structure, with the eutectic compounds primarily distributed on the grain boundaries. As suggested from the high magnification SEM image (**Figure 2B**), the eutectic compounds are mainly skeletal and massive in shape. The results of the EDS composition analysis of the eutectic compounds at different locations (marked as A, B, and C in **Figure 2B**) are listed in **Table 2**. Given the EDS and XRD results, the skeletal phase is the MgZnCu phase and the bulk phase refers to the Mg_2Sn phase or Mg_2Zn_3 phase. **Figure 2C** shows that the dendritic morphology of the alloy disappears after homogenization, the segregation of elements at the grain boundaries is noticeably reduced and the

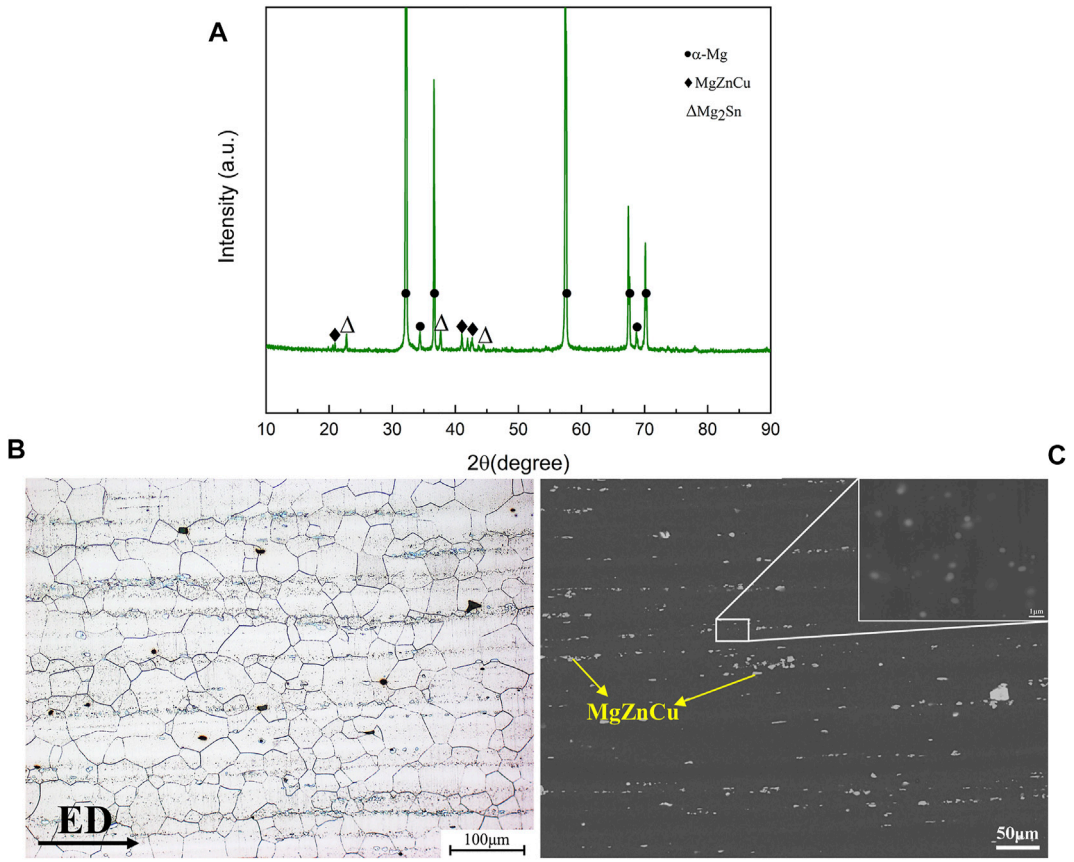

FIGURE 3 | X-ray diffraction pattern and microstructure images of the extruded alloy: **(A)** XRD pattern, **(B)** OM image, **(C)** SEM image (inset: high magnification SEM image of the precipitated phase).

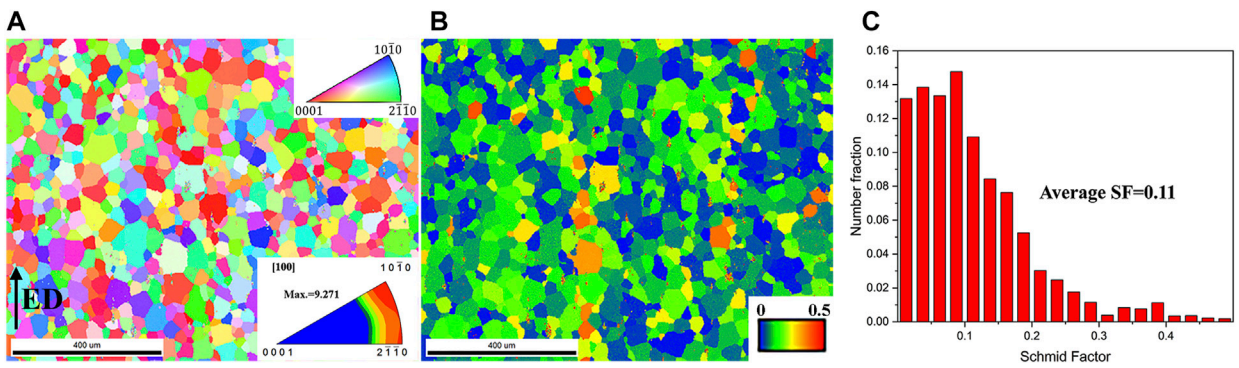

FIGURE 4 | Inverse pole figure, Schmid factor map, and Schmid factor distribution of the extruded alloy: **(A)** inverse pole figure (inset: ED inverse pole figure), **(B)** Schmid factor map, **(C)** Schmid factor distribution.

eutectic compounds are largely decomposed, but some of the granular or lumpy phases remain at the grain boundaries. Given the XRD results, the residual second phase is the MgZnCu phase (**Figure 2D**), which is a thermally stable phase that fails to decompose during homogenization.

Microstructure of the Extruded Alloy

Figure 3 presents the XRD pattern, OM and SEM images of the extruded alloy. XRD pattern reveals that the Mg_2Sn phase appears in the extruded alloy besides the MgZnCu phase and the α-Mg, thereby indicating that the dynamic precipitation of the Mg_2Sn

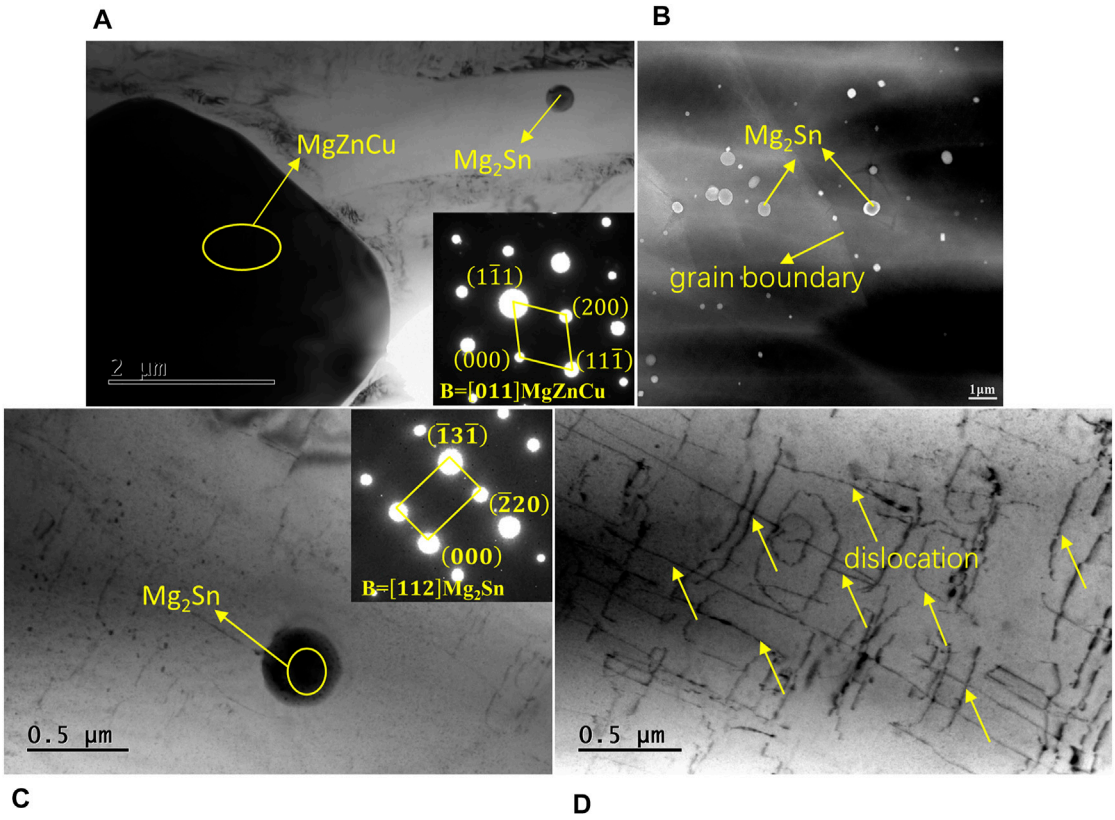

FIGURE 5 | TEM images of the extruded alloy: **(A)** MgZnCu phase (inset: SEAD pattern of MgZnCu phase), **(B)** distribution of Mg_2Sn phase, **(C)** Mg_2Sn phase (inset: SEAD pattern of Mg_2Sn phase), **(D)** dislocations in the alloy.

phase occurs in the extrusion (**Figure 3A**). **Figure 3B** shows that complete dynamic recrystallization (DRX) takes place in the extrusion, and the dynamically recrystallized grains are equiaxed with an average size of approximately 39 μm. As indicated in **Figure 3C**, besides the broken MgZnCu phase, there are also numerous dispersed spot phases in the alloy. Combined with the XRD results, it can be concluded that the phase is the Mg_2Sn phase.

For the extruded alloy, texture also affects its properties. The inverse pole figure of the extruded alloy (**Figure 4A**) reveals that it exhibits a basal fiber texture, in which the (0001) plane is preferentially parallel to the extrusion direction (ED). The texture type is < 10-10>//ED, <2-1-10>//ED and the maximum intensity is 9.271. Schmid factor (SF) map and Schmid factor distribution for the basal slip system of the alloy indicate that the alloy has a low SF value of 0.11 (**Figure 4B**). The low Schmid factor means that basal slip is difficult to activate, enabling the alloy to exhibit a high yield strength.

TEM images of the extruded alloy are presented in **Figure 5**. The larger phase can be identified as the MgZnCu phase (**Figure 5A**). **Figure 5B** indicates that the dynamically precipitated Mg_2Sn phase is spherical, distributed near the grain boundaries, with sizes ranging from 200–500 nm. SEAD pattern of the phase reveals it has a face-centered cubic structure (FCC, a = 0.6763 nm) (**Figure 5C**). Moreover, a certain number of dislocations in the alloy are observed in the TEM bright-field image (**Figure 5D**).

The precipitation of the Mg_2Sn phase is closely related to the deformation temperature and the stress state during the deformation process. The eutectic temperature of Mg-Sn is 567°C, and the solid solubility of Sn increases with the rise of the temperature (Ghosh et al., 2012). With the deformation temperature lower than the homogenization temperature, the Mg_2Sn phase exerts a certain precipitation driving force. In addition, the compressive stress in the extrusion process also facilitates the precipitation of the Mg_2Sn phase (Kabir et al., 2014). Accordingly, under the combined effect of temperature and stress, the Mg_2Sn phase with a high eutectic temperature can precipitate from the matrix. The statically precipitated Mg_2Sn phase has a range of forms, whereas the dynamically precipitated Mg_2Sn phase during extrusion is subjected to stress, thereby leading to its spherical precipitation. In addition, it has been shown that Zn elements can reduce the activation energy of the Mg_2Sn phase nucleation by reducing the interfacial energy at the Mg_2Sn-Mg interface, thus promoting the precipitation of the Mg_2Sn phase (Sasaki et al., 2011; Liu et al., 2016). Zn elements solid dissolved in the matrix during homogenization undoubtedly facilitate the precipitation of the Mg_2Sn phase. The precipitated Mg_2Sn, in turn, hinders the growth of recrystallized grains (Sasaki

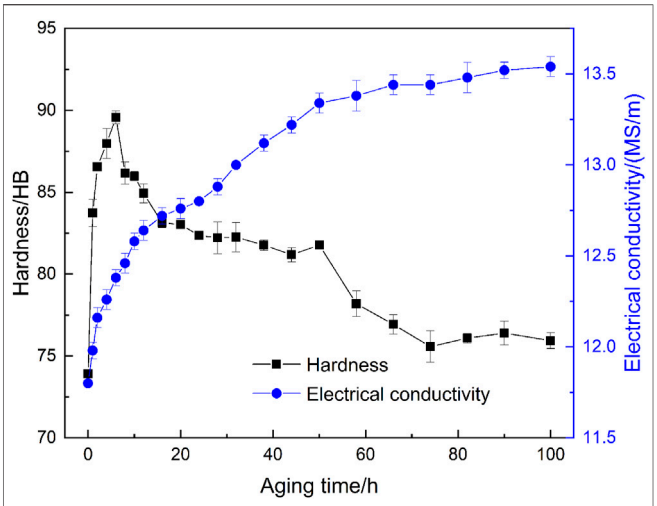

FIGURE 6 | Curves of hardness and electrical conductivity of the extruded alloy during aging at 180°C.

et al., 2008), thereby improving the mechanical properties of the alloy.

Microstructure of the Aged Alloy

Figure 6 presents the changes in hardness and electrical conductivity of the extruded alloy during aging at 180°C. The hardness of the alloy increases rapidly first and then decreases with time, reaching a peak at 6 h. Compared with the extruded alloy, the hardness of the peak-aged alloy increases significantly, which demonstrates a strong aging strengthening effect. At the early stage of aging, the second phase gradually precipitates, and the phase density increases. The denser the phase is distributed, the stronger its resistance to dislocation motion (Kim and Park, 2016). Therefore, the hardness of the alloy continues to increase until reaches its peak. With the extension of time, the size of the precipitated phase increases, leading to a decrease in dislocation hindrance efficiency and a drop in hardness. In addition, the electrical conductivity of the alloy rises continuously over time. This is because the scattering effect of the second phase on the electrons is significantly weaker than that of the solid solution atoms (Pan et al., 2013). As the second phase continues to precipitate, the content of solute solution atoms in the matrix is reduced, the lattice distortion of the matrix declines, the chance of being scattered during electron transport is lowered, and the conductivity of the alloy increases continuously.

Figure 7 gives TEM images of the peak-aged alloy. Considerable rod-shaped phases precipitate in the alloy, complying with the long axis of $[0001]_{Mg}$ and ranging from 10 to 20 nm in the size (**Figure 7A**). Based on their morphology and orientation as well as high-resolution TEM image, they are identified as β'_1 precipitates (Rashkova et al., 2008; Ren et al., 2021). They stand for the main strengthening precipitates in Mg-Zn alloys (Rosalie and Pauw, 2014; Alizadeh et al., 2021). The

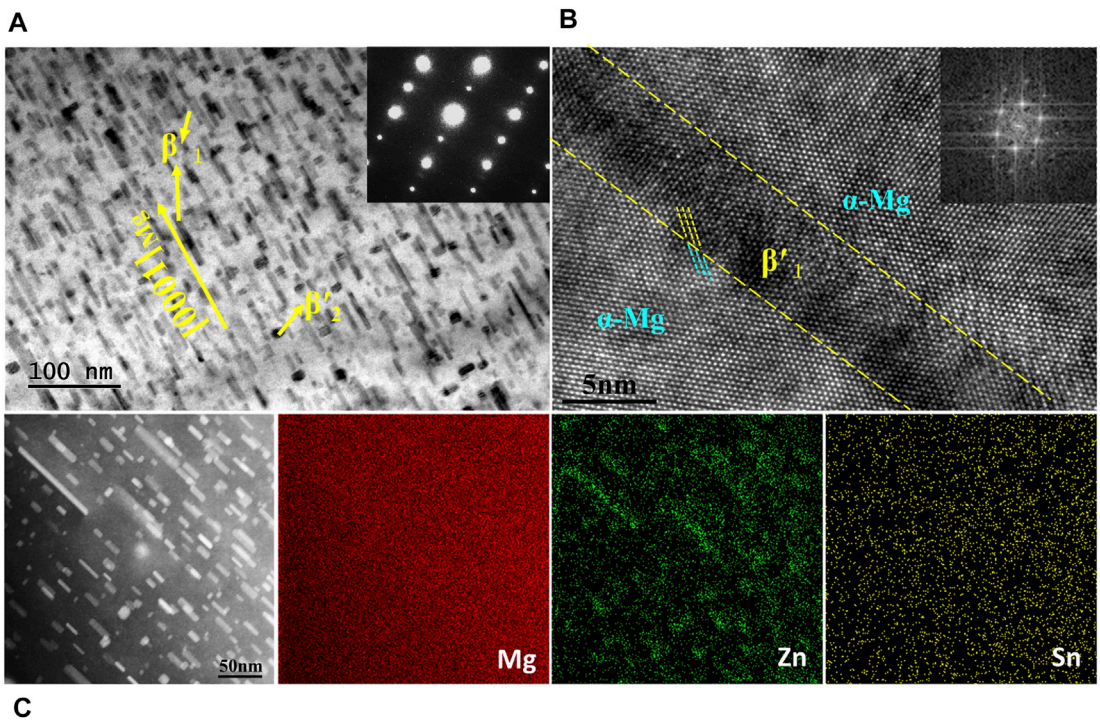

FIGURE 7 | TEM images of peak-aged alloy (180°C–6 h): **(A)** Bright-field TEM image of peak-aged alloy, taken along the $[11\bar{2}0]$ zone axis (inset: $[11\bar{2}0]_{Mg}$ Mg diffraction pattern), **(B)** HR-TEM image of β'_1 phase (inset: FFT pattern obtained from the β'_1 phase), **(C)** HADDF-STEM image and corresponding EDS mapping images of peak-aged alloy.

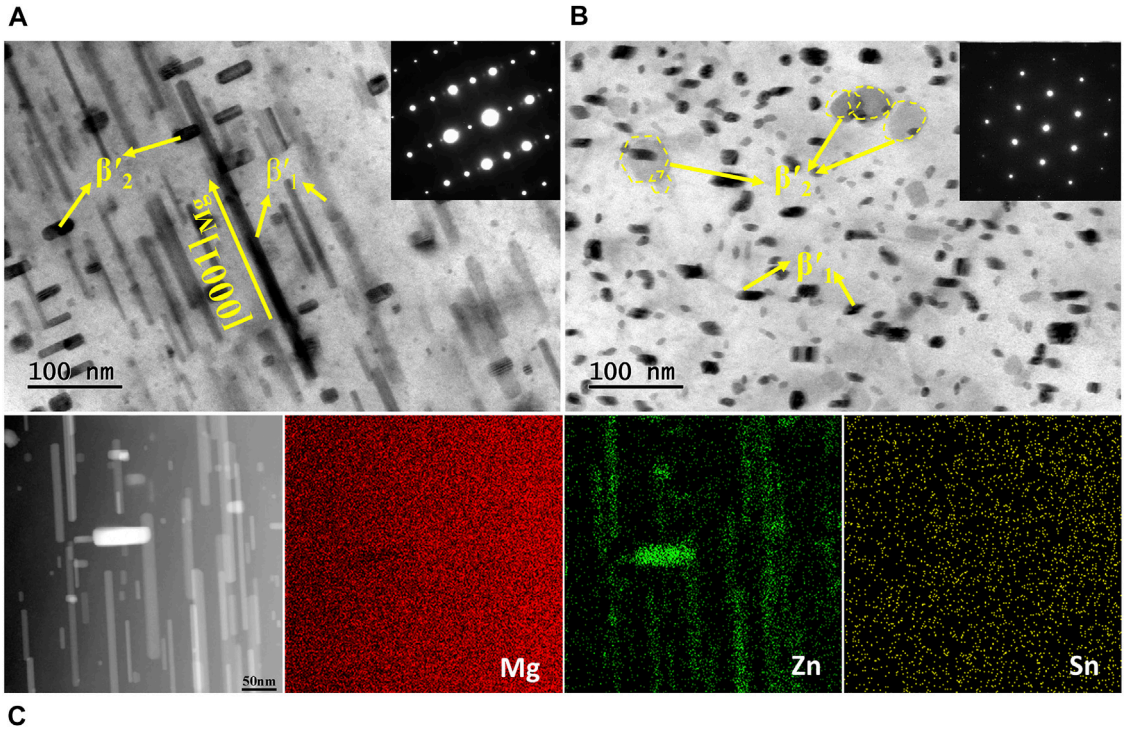

FIGURE 8 | TEM images of over-aged alloy (180°C–100 h): **(A)** Bright-field TEM image of over-aged alloy, taken along the [11$\bar{2}$0] zone axis (inset: [11$\bar{2}$0] $_{Mg}$ Mg diffraction pattern), **(B)** Bright-field TEM image of over-aged alloy, taken along the [0001] zone axis (inset: [0001] $_{Mg}$ Mg diffraction pattern), **(C)** HADDF-STEM image and corresponding EDS mapping images of over-aged alloy.

high-resolution TEM image of the β'_1 phase in **Figure 7B** indicates that the β'_1 phase is fully coherent with the α-Mg matrix. The precipitates in this coherent relationship with the matrix are more effective in impeding the movement of dislocations, increasing the hardness, and improving the mechanical properties of the alloy. Besides the densely distributed β'_1 phase, there are also precipitated phases perpendicular to the β'_1 phase in orientation. They are identified as the β'_2 phase, which are distributed on the basal plane (0001) of α-Mg (Ren et al., 2021). According to **Figure 7C**, only Mg-Zn phases precipitate during aging, and no precipitation of the Mg-Sn phase is observed.

Figure 8 illustrates the TEM images of the over-aged alloy. Both the β'_1 and β'_2 phases grow significantly with the prolonging of the aging time, and the β'_1 phase is converted into a slender rod shape (**Figure 8A**). Moreover, the β'_2 phase is observed to be disk-shaped from the [0001] $_{Mg}$ direction (**Figure 8B**), which has a lower amount compared with the β'_1 phase. It is noteworthy that the precipitation of the Mg-Zn phase is predominant in the aging process, and no precipitation of the Mg-Sn phase is observed even with the aging time extended to 100 h (**Figure 8C**). This phenomenon may be explained as the dynamic precipitation of the Mg_2Sn phase in the extrusion consumes considerable Sn elements, and the low Sn content in the matrix, together with the low aging temperature, results in a lack of motivation for the precipitation of the Mg-Sn phase.

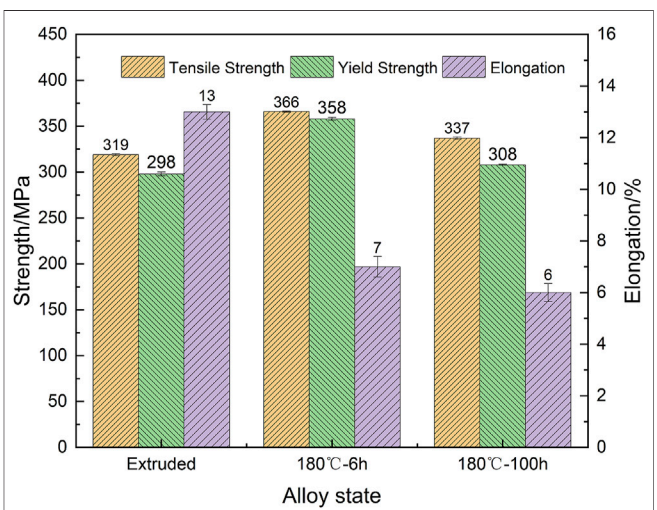

FIGURE 9 | Mechanical properties of the extruded, peak-aged and over-aged alloys.

Mechanical Properties of the Alloys

The room temperature tensile mechanical properties of the extruded, peak-aged and over-aged alloys are illustrated in **Figure 9**. The tensile strength, yield strength and elongation of the extruded alloy reach 319 MPa, 298 MPa and 13%,

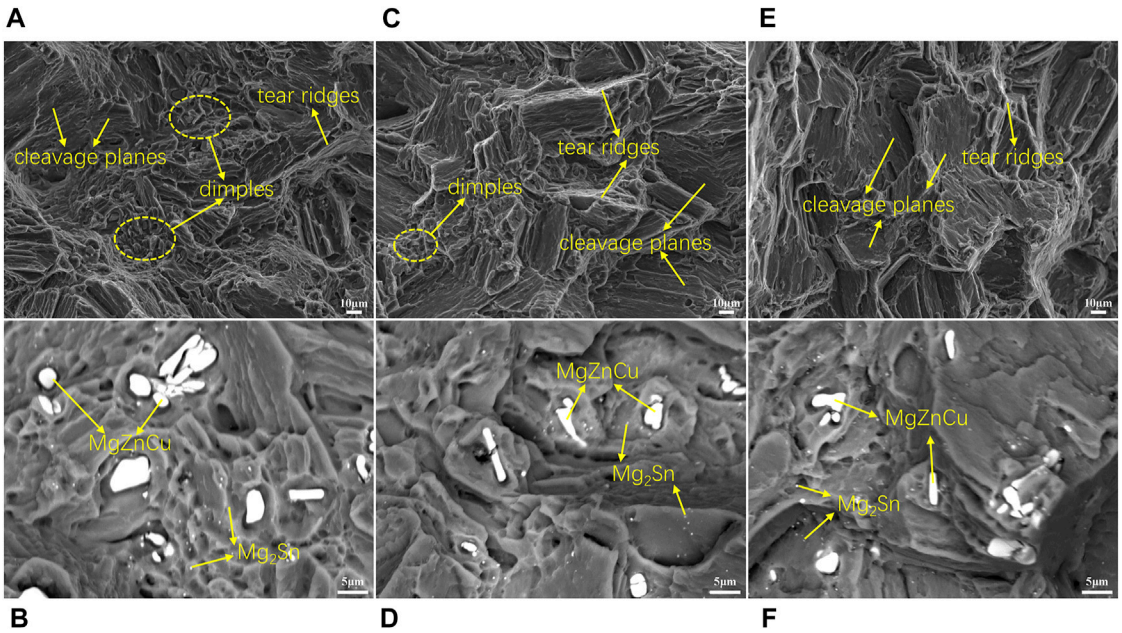

FIGURE 10 | SEM images of fracture surfaces for different state alloy: **(A,B)** extruded alloy, **(C,D)** peak-aged alloy, **(E,F)** over-aged alloy.

respectively. The tensile and yield strengths of the peak-aged alloy substantially increase compared with the extruded alloy, with the tensile strength increasing by 47 MPa and the yield strength by 60 MPa, whereas the elongation is reduced to only 7%. In comparison with the peak-aged alloy, the mechanical properties of the over-aged alloy are reduced, to be specific, the tensile strength is reduced to 337 MPa, the yield strength declines to 308 MPa, and the elongation is approximately 6%.

Many factors are affecting the mechanical properties of the alloy. For the extruded alloy, complete dynamic recrystallization takes place, forming recrystallized grain structure, which can be the basis for high mechanical properties. Secondly, considerable Zn atoms are solid dissolved in the extruded alloy. The solid dissolved Zn atoms interact with dislocation, hindering dislocation movement and improving the mechanical properties of the alloy. In addition, the size of the Mg_2Sn phase precipitated during extrusion ranges from 200 to 500 nm, thereby exerting a small effect on dislocation, whereas it can hinder the sliding of grain boundaries and thus improve the mechanical properties of the alloy. Lastly, the extruded alloy develops a strong fiber texture with the basal plane (0001)//ED. When the alloy is deformed under the tensile stress in the ED, the Schmid factor (SF) along the basal plane equaled to 0, and the basal slip is difficult to activate, thereby improving the yield strength of the alloy (Chen et al., 2005; Wu et al., 2020; Li et al., 2021). In general, the high mechanical properties of the extruded alloy are attributed to the combined strengthening mechanisms (e.g., grain refinement, solid solution strengthening, precipitation strengthening, as well as texture strengthening). For the peak-aged alloys, the fine and dense short rod-like β'_1 phase precipitates along with the $[0001]_{Mg}$ orientation, completely coherent with the matrix, and a large coherent strain field is generated, thereby interacting with dislocations and hindering dislocation slip. On that basis, the mechanical properties of the peak-aged alloy are improved. As the aging process continues, the size of the β'_1 phase increases, the number of the β'_1 phase is lowered, and the corresponding strengthening effect weakens. Therefore, the mechanical properties of the over-aged alloy decrease. In general, the precipitation strengthening effect of β'_1 phases is the main reason for the improved mechanical properties of the peak-aged alloy.

To analyze the fracture mode of the extruded, peak-aged and over-aged alloys, SEM images of fracture surfaces for these alloys are illustrated in **Figure 10**. There are a certain amount of dimples in the fracture surface of the extruded alloy; moreover, part of the cleavage planes and tearing ridges are founded, so a ductile-brittle mixed fracture mode is presented (**Figure 10A**). The number of dimples in the peak-aged alloy (**Figure 10C**) decreases significantly compared with that of extruded alloy, and the cleavage plane rises, which demonstrates that the plasticity of the alloy decreases, as reflected in a decrease in the elongation. The smooth cleavage plane in the over-aged alloy (**Figure 10E**) further increases, and dimples are hardly visible, which demonstrates that the fracture mechanism of the over-aged alloy is characterized by the brittle fracture mode. In addition, as indicated from the high-magnification BEI images of fracture surfaces for the extruded, peak-aged and over-aged alloys (**Figures 10B,D,F**), some MgZnCu phases are distributed at the bottom of dimples, and the MgZnCu phases are partially broken. In addition, precipitated Mg_2Sn phase during extrusion is also observed, mainly distributed near the dimple. The MgZnCu phase is brittle (Cheng et al., 2014), its presence accounts for the fracture failure of the alloy. When the alloy is subjected to external forces, stress concentration will occur near the MgZnCu phase, and MgZnCu particles can be the nucleation sites of microcracks formed by a void nucleation and coalescence mechanism (Zhu et al., 2011), eventually leading to the fracture failure of the alloy.

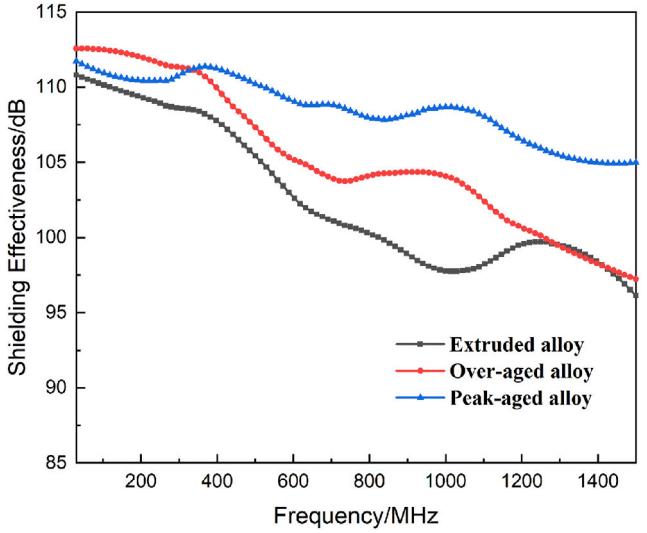

FIGURE 11 | Electromagnetic shielding properties of the extruded, peak-aged and over-aged alloys.

Electromagnetic Shielding of the Alloys

Figure 11 presents the frequency dependence of EMI shielding performance of the extruded, peak-aged and over-aged alloys. In the frequency range of 30–1500 MHz, the electromagnetic shielding effectiveness of the alloys gradually decreases with the increase in the electromagnetic wave frequency. The shielding efficiency of the extruded alloy exceeds 95 dB throughout the whole range, while the peak-aged alloy exhibits a significantly higher shielding efficiency than the extruded alloy, higher than 105 dB throughout the range. Moreover, the over-aged alloy exhibits a lower shielding performance compared with the peak-aged alloy, with a shielding efficiency between 97 and 112 dB, which can still be better than that of the extruded alloy. The peak-aged alloy exhibits the optimal electromagnetic shielding performance. **Table 3** gives a comparison of tensile strengths and SE results of the studied alloy with other alloys in the literature. Obviously, the alloys obtained in this paper have excellent comprehensive performance.

According to the transmission line theory, the attenuation of electromagnetic waves by a shield is achieved by three mechanisms, i.e., reflection attenuation, absorption attenuation and multiple reflection attenuation. The electromagnetic shielding efficiency can be calculated by the following equations (Schulz et al., 1988; Tong, 2009).

$$SE = SE_A + SE_R + SE_M \quad (1)$$

$$SE_A = 131.43t\sqrt{f\mu_r\sigma_r} \quad (2)$$

$$SE_R = 168.2 + 10\,lg\left[\sigma_r/\left(f\mu_r\right)\right] \quad (3)$$

$$SE_M = 20\,lg\left(1 - e^{-2t/\delta}\right) \quad (4)$$

where A denotes the absorption attenuation; R represents the reflection attenuation; M expresses the multiple reflection attenuation; t is the thickness of the material (m); f denotes the electromagnetic wave frequency (Hz); μ_r and σ_r are relative magnetic permeability and electrical conductivity relative to copper, respectively; δ expresses the skin depth of the material, $\delta = \sqrt{1/\pi\mu\sigma f}$, with μ and σ as the intrinsic magnetic permeability and electrical conductivity of the material, respectively. As indicated from the equations, the electromagnetic shielding performance of the alloy is significantly impacted by its electrical conductivity. A schematic diagram of the electromagnetic shielding mechanism of the alloy is shown in **Figure 12A**. In addition, it has also been shown that the presence of a large number of second phases will enhance the multiple reflection attenuation and improve the electromagnetic shielding properties of the alloy (Chen et al., 2015b).

TABLE 3 | Comparison of tensile strengths and SE results between the studied alloys and alloys in the literature.

Alloys	Tensile strength/MPa	SE/dB	References
Extruded alloy	319	96–110	This work
Peak-aged alloy	366	106–111	
Over-aged alloy	337	97–112	
ZK50-2.5Cu	306	84–118	Chen et al. (2015b)
ZK60	~300	65–85	Chen et al. (2013)
Mg-9Li-3Al-1Zn	241	98–107	Wang et al. (2020)

The electrical conductivity for the extruded, peak-aged and over-aged alloy are 11.7 Ms/m, 12.4 Ms/m, 13.5 Ms/m, respectively. Notably, the conductivity of the alloy increases after aging treatment, whereas the electromagnetic shielding performance exhibited by the alloy fails to increase monotonically with the increase in conductivity. Thus, electrical conductivity can not be a single factor affecting the electromagnetic shielding performance of the alloy, and the transmission line theory has certain limitations. The effect of the fine structure of the alloy on its electromagnetic shielding performance should be further considered. In general, the conductivity of the precipitated phase is significantly lower than that of the matrix, and there is a serious impedance mismatch at the interface between the precipitated phase and the matrix. Thus, electromagnetic waves will be reflected when reaching the phase interface. Accordingly, the precipitation of Mg_2Sn, β'_1 and β'_2 phases will remarkably increase the phase interface in the alloy, and the multiple reflections of electromagnetic waves will be noticeably enhanced as they advance in the alloy, thereby improving the electromagnetic shielding performance of the alloy (Chen et al., 2015a; Wang et al., 2020). The diagram of the multiple reflections of electromagnetic waves for different second phases is presented in **Figure 12B**. As obviously indicated from the figure, the precipitation of the dense β'_1 phase in the peak-aged alloy results in a significant increase in the proportion of phase interface area in the alloy, thereby endowing the alloy with excellent electromagnetic shielding properties. After the aging period is extended to 100h, the electromagnetic shielding performance of the over-aged alloy decreases compared with the peak-aged alloy, which demonstrates that the size of the precipitated phase also impacts the electromagnetic shielding performance of the alloy. As illustrated in **Figure 12B**, the size of the β'_1 phase increases significantly in the over-aged alloy. The phase interface in the over-aged alloy is significantly reduced compared with the peak-aged alloy, and the multiple reflection attenuation of the precipitated phase on the

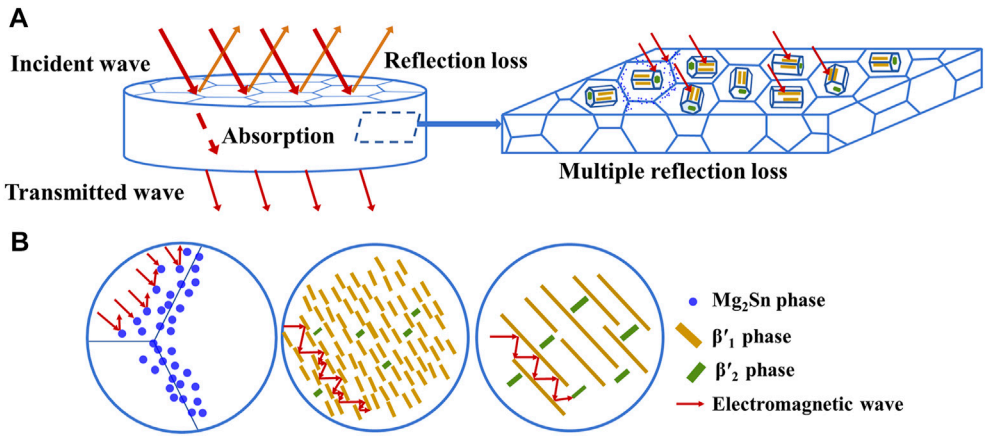

FIGURE 12 | Schematic diagram of the electromagnetic shielding mechanism: **(A)** reflection attenuation, absorption attenuation and multiple reflection attenuation, **(B)** multiple reflection attenuation of different second phases for electromagnetic waves.

electromagnetic waves is correspondingly weakened (Chen et al., 2013), so the electromagnetic shielding performance of the over-aged alloy decreased. The factors influencing the electromagnetic shielding performance of the alloy are complex, whereas it can be generally conducive to obtaining the alloy exhibiting high electromagnetic shielding properties through appropriate alloy composition design combined with deformation and heat treatment means to endow the alloy with higher electrical conductivity and more reflective interfaces.

CONCLUSION

The microstructure, mechanical properties and electromagnetic shielding properties exhibited by Mg-6Zn-3Sn-0.5Cu alloy are explored, and possible shielding mechanisms and strengthening mechanisms are analyzed. The conclusions are drawn below:

1) The phases in the as-cast alloy are comprised of α-Mg, MgZnCu, Mg_2Sn, and Mg_2Zn_3 phases. During homogenization, only the MgZnCu phase remains. Complete dynamic recrystallization (DRX) takes place in the extrusion, and the spherical Mg_2Sn phase precipitates dynamically. Considerable β'_1 phase along $[0001]_{Mg}$ precipitates in the peak-aged alloy. The size of the β'_1 phase increases as the aging time is prolonged.
2) The mechanical properties of the peak-aged alloy are improved compared to the extruded alloy due to the strengthening effect of the β'_1 phase, with a tensile strength of 366 MPa and elongation of 7%. The mechanical properties of the over-aged alloy decrease as the strengthening effect of β'_1 is weakened. The fracture mode of the extruded and peak-aged alloys can be a ductile-brittle mixed fracture, and the over-aged alloy is a brittle fracture mode.
3) The electromagnetic shielding performance of the aged alloy is improved in comparison with the extruded alloy. The growth of precipitates results in a decrease in the electromagnetic shielding property of the over-aged alloy. The peak-aged alloy exhibits the optimal electromagnetic shielding performance, with the shielding effectiveness exceeds 105 dB in the 30–1,500 MHz frequency.

DATA AVAILABILITY STATEMENT

The raw data supporting the conclusion of this article will be made available by the authors, without undue reservation.

AUTHOR CONTRIBUTIONS

YHL and MM contributed conception and design of the study. YHL organized the database and analytic results and wrote the draft of the manuscript. All authors participated in the preparation of the material. YHL and MM did the writing-review and editing.

FUNDING

This study was financially supported by The Project of Achievement Transformation of Jiangsu Province (BA2017044).

REFERENCES

Ali, Y., Qiu, D., Jiang, B., Pan, F., and Zhang, M.-X. (2015). Current Research Progress in Grain Refinement of Cast Magnesium Alloys: A Review Article. *J. Alloys Comp.* 619, 639–651. doi:10.1016/j.jallcom.2014.09.061

Alizadeh, R., Wang, J., and Llorca, J. (2021). Precipitate Strengthening of Pyramidal Slip in Mg-Zn Alloys. *Mater. Sci. Eng. A* 804, 140697. doi:10.1016/j.msea.2020.140697

Chen, X., Liu, J., and Pan, F. (2013). Enhanced Electromagnetic Interference Shielding in ZK60 Magnesium alloy by Aging Precipitation. *J. Phys. Chem. Sol.* 74, 872–878. doi:10.1016/j.jpcs.2013.02.003

Chen, X., Liu, J., Zhang, Z., and Pan, F. (2012). Effect of Heat Treatment on Electromagnetic Shielding Effectiveness of ZK60 Magnesium alloy. *Mater. Des.* 42, 327–333. doi:10.1016/j.matdes.2012.05.061

Chen, X., Liu, L., Liu, J., and Pan, F. (2015). Microstructure, Electromagnetic Shielding Effectiveness and Mechanical Properties of Mg-Zn-Y-Zr Alloys. *Mater. Des. (1980-2015)* 65, 360–369. doi:10.1016/j.matdes.2014.09.034

Chen, X., Liu, L., Pan, F., Mao, J., Xu, X., and Yan, T. (2015). Microstructure, Electromagnetic Shielding Effectiveness and Mechanical Properties of Mg-Zn-Cu-Zr Alloys. *Mater. Sci. Eng. B* 197, 67–74., doi:10.1016/j.mseb.2015.03.012

Chen, Z. H., Xia, W. J., Cheng, Y. Q., and Fu, D. F. (2005). Texture and Anisotropy in Magnesium Alloys. *Chin. J. Nonferrous Met.* 15, 1–11. doi:10.3321/j.issn:1004-0609.2005.01.001

Cheng, L., Shuai, Z., Yu, Z., Da-Wei, Z., Chao-Zheng, H., and Zhi-Wen, L. (2014). Insights into Structural and Thermodynamic Properties of the Intermetallic Compound in Ternary Mg-Zn-Cu alloy under High Pressure and High Temperature. *J. Alloys Comp.* 597, 119–123. doi:10.1016/j.jallcom.2014.01.210

García, A. M., Sisternas, A., and Hoyos, S. P. (2008). Occupational Exposure to Extremely Low Frequency Electric and Magnetic fields and Alzheimer Disease: a Meta-Analysis. *Int. J. Epidemiol.* 37, 329–340. doi:10.1093/ije/dym295

Geetha, S., Satheesh Kumar, K. K., Rao, C. R. K., Vijayan, M., and Trivedi, D. C. (2009). EMI Shielding: Methods and Materials-A Review. *J. Appl. Polym. Sci.* 112, 2073–2086. doi:10.1002/app.29812

Ghosh, P., Mezbahul-islam, M., and Medraj, M. (2012). Critical Assessment and Thermodynamic Modeling of Mg-Zn, Mg-Sn, Sn-Zn and Mg-Sn-Zn Systems. *Calphad* 36, 28–43. doi:10.1016/j.calphad.2011.10.007

Kabir, A. S. H., Sanjari, M., Su, J., Jung, I.-H., and Yue, S. (2014). Effect of Strain-Induced Precipitation on Dynamic Recrystallization in Mg-Al-Sn Alloys. *Mater. Sci. Eng. A* 616, 252–259. doi:10.1016/j.msea.2014.08.032

Kim, J. T., Park, C. W., and Kim, B.-J. (2017). A Study on Synergetic EMI Shielding Behaviors of Ni-Co alloy-coated Carbon Fibers-Reinforced Composites. *Synth. Met.* 223, 212–217. doi:10.1016/j.synthmet.2016.11.027

Kim, S.-H., and Park, S. H. (2016). Influence of Ce Addition and Homogenization Temperature on Microstructural Evolution and Mechanical Properties of Extruded Mg-Sn-Al-Zn alloy. *Mater. Sci. Eng. A* 676, 232–240. doi:10.1016/j.msea.2016.08.093

Li, R. G., Li, H. R., Pan, H. C., Xie, D. S., Zhang, J. H., Fang, D. Q., et al. (2021). Achieving Exceptionally High Strength in Binary Mg-13Gd alloy by strong Texture and Substantial Precipitates. *Scripta Materialia* 193, 142–146. doi:10.1016/j.scriptamat.2020.10.052

Liu, C., Chen, H., and Nie, J.-F. (2016). Interphase Boundary Segregation of Zn in Mg-Sn-Zn Alloys. *Scripta Materialia* 123, 5–8. doi:10.1016/j.scriptamat.2016.05.035

Liu, C., Chen, X., Chen, J., Atrens, A., and Pan, F. (2020). The Effects of Ca and Mn on the Microstructure, Texture and Mechanical Properties of Mg-4 Zn alloy. *J. Magnesium Alloys* 9, 1084–1097. doi:10.1016/j.jma.2020.03.012

Pan, H., Pan, F., Peng, J., Gou, J., Tang, A., Wu, L., et al. (2013). High-conductivity Binary Mg-Zn Sheet Processed by Cold Rolling and Subsequent Aging. *J. Alloys Comp.* 578, 493–500. doi:10.1016/j.jallcom.2013.06.082

Pandey, R., Tekumalla, S., and Gupta, M. (2019). Enhanced (X-Band) Microwave Shielding Properties of Pure Magnesium by Addition of Diamagnetic Titanium Micro-particulates. *J. Alloys Comp.* 770, 473–482. doi:10.1016/j.jallcom.2018.08.147

Qi, F., Zhang, D., Zhang, X., and Xu, X. X. (2014). Effect of Sn Addition on the Microstructure and Mechanical Properties of Mg-6Zn-1Mn (wt.%) alloy. *J. Alloys Compd.* 585, 656–666. doi:10.1016/j.jallcom.2013.09.156

Rashkova, B., Prantl, W., Görgl, R., Keckes, J., Cohen, S., Bamberger, M., et al. (2008). Precipitation Processes in a Mg-Zn-Sn alloy Studied by TEM and SAXS. *Mater. Sci. Eng. A* 494, 158–165. doi:10.1016/j.msea.2008.04.005

Ren, Y., Liu, B., Xie, H., Li, H., Jiang, M., and Qin, G. (2021). Characterization of Precipitates in Aged Mg-4 wt%Zn alloy. *Mater. Today Commun.* 26, 102017. doi:10.1016/j.mtcomm.2021.102017

Rosalie, J. M., and Pauw, B. R. (2014). Form-free Size Distributions from Complementary Stereological TEM/SAXS on Precipitates in a Mg-Zn alloy. *Acta Materialia* 66, 150–162. doi:10.1016/j.actamat.2013.11.029

Sasaki, T. T., Oh-ishi, K., Ohkubo, T., and Hono, K. (2011). Effect of Double Aging and Microalloying on the Age Hardening Behavior of a Mg-Sn-Zn alloy. *Mater. Sci. Eng. A* 530, 1–8. doi:10.1016/j.msea.2010.05.010

Sasaki, T. T., Yamamoto, K., Honma, T., Kamado, S., and Hono, K. (2008). A High-Strength Mg-Sn-Zn-Al alloy Extruded at Low Temperature. *Scripta Materialia* 59, 1111–1114. doi:10.1016/j.scriptamat.2008.07.042

Schulz, R. B., Plantz, V. C., and Brush, D. R. (1988). Shielding Theory and Practice. *IEEE Trans. Electromagn. Compat.* 30, 187–201. doi:10.1109/15.3297

Shahzad, F., Alhabeb, M., Hatter, C. B., Anasori, B., Man Hong, S., Koo, C. M., et al. (2016). Electromagnetic Interference Shielding with 2D Transition Metal Carbides (MXenes). *Science* 353, 1137–1140. doi:10.1126/science.aag2421

Shen, B., Zhai, W., Tao, M., Ling, J., and Zheng, W. (2013). Lightweight, Multifunctional polyetherimide/graphene@Fe3O4 Composite Foams for Shielding of Electromagnetic Pollution. *ACS Appl. Mater. Inter.* 5, 11383–11391. doi:10.1021/am4036527

Tong, X. C. (2009). *Advanced Materials and Design for Electromagnetic Interference Shielding*. CRC Press, Taylor & Francis Group.

Wang, C., Luo, T., Liu, Y., Huang, Q., and Yang, Y. (2021). Residual Stress and Precipitation of Mg-5Zn-3.5Sn-1Mn-0.5Ca-0.5Cu alloy with Different Quenching Rates. *J. Magnesium Alloys* 9, 604–612. doi:10.1016/j.jma.2020.02.021

Wang, J., Wu, R., Feng, J., Zhang, J., Hou, L., and Zhang, M. (2019). Influence of Rolling Strain on Electromagnetic Shielding Property and Mechanical Properties of Dual-phase Mg-9Li alloy. *Mater. Characterization* 157, 109924. doi:10.1016/j.matchar.2019.109924

Wang, J., Xu, L., Wu, R., Feng, J., Zhang, J., Hou, L., et al. (2020). Enhanced Electromagnetic Interference Shielding in a Duplex-phase Mg-9Li-3Al-1Zn Alloy Processed by Accumulative Roll Bonding. *Acta Metall. Sin. (Engl. Lett.* 33, 490–499. doi:10.1007/s40195-020-01017-z

Wang, Y., Peng, J., and Zhong, L. (2018). On the Microstructure and Mechanical Property of As-Extruded Mg-Sn-Zn alloy with Cu Addition. *J. Alloys Comp.* 744, 234–242. doi:10.1016/j.jallcom.2018.02.013

Wei, S., Zhu, T., Hodgson, M., and Gao, W. (2013). Effects of Sn Addition on the Microstructure and Mechanical Properties of As-Cast, Rolled and Annealed Mg-4Zn Alloys. *Mater. Sci. Eng. A* 585, 139–148. doi:10.1016/j.msea.2013.07.051

Wu, J., Jin, L., Dong, J., Wang, F., and Dong, S. (2020). The Texture and its Optimization in Magnesium alloy. *J. Mater. Sci. Tech.* 42, 175–189. doi:10.1016/j.jmst.2019.10.010

Yang, Y., Xiong, X., Chen, J., Peng, X., Chen, D., and Pan, F. (2021). Research Advances in Magnesium and Magnesium Alloys Worldwide in 2020. *J. Magnesium Alloys* 9, 705–747. doi:10.1016/j.jma.2021.04.001

Ye, J., Chen, X., Luo, Z., Li, J., Yuan, Y., Tan, J., et al. (2021). Improving Strength and Electromagnetic Shielding Effectiveness of Mg-Sn-Zn-Ca-Ce Alloy by Sn Addition. *Adv. Eng. Mater.* 23, 2100166. doi:10.1002/adem.202100166

You, S., Huang, Y., Kainer, K. U., and Hort, N. (2017). Recent Research and Developments on Wrought Magnesium Alloys. *J. Magnesium Alloys* 5, 239–253. doi:10.1016/j.jma.2017.09.001

Zhu, H. M., Sha, G., Liu, J. W., Wu, C. L., Luo, C. P., Liu, Z. W., et al. (2011). Microstructure and Mechanical Properties of Mg-6Zn-xCu-0.6Zr (wt.%) Alloys. *J. Alloys Compd.* 509, 3526–3531. doi:10.1016/j.jallcom.2010.12.165

Conflict of Interest: Authors YHL, MM, XL, YJL, GS, JY, and KZ were employed by the company GRINM Co., Ltd. Authors YHL, MM, XL, YJL, GS, JY, and KZ were employed by the company GRIMAT Engineering Institute Co., Ltd. Authors YHL, MM, XL, YJL, GS, JY, and KZ were employed by the company General Research Institute for Nonferrous Metals.

Publisher's Note: All claims expressed in this article are solely those of the authors and do not necessarily represent those of their affiliated organizations, or those of the publisher, the editors and the reviewers. Any product that may be evaluated in this article, or claim that may be made by its manufacturer, is not guaranteed or endorsed by the publisher.

Advantages of publishing in Frontiers

OPEN ACCESS
Articles are free to read for greatest visibility and readership

FAST PUBLICATION
Around 90 days from submission to decision

HIGH QUALITY PEER-REVIEW
Rigorous, collaborative, and constructive peer-review

TRANSPARENT PEER-REVIEW
Editors and reviewers acknowledged by name on published articles

Frontiers
Avenue du Tribunal-Fédéral 34
1005 Lausanne | Switzerland

Visit us: www.frontiersin.org
Contact us: frontiersin.org/about/contact

REPRODUCIBILITY OF RESEARCH
Support open data and methods to enhance research reproducibility

DIGITAL PUBLISHING
Articles designed for optimal readership across devices

FOLLOW US
@frontiersin

IMPACT METRICS
Advanced article metrics track visibility across digital media

EXTENSIVE PROMOTION
Marketing and promotion of impactful research

LOOP RESEARCH NETWORK
Our network increases your article's readership